Development of Nanoparticles for Imaging Applications

by

Sunil Claire

A thesis submitted for the degree of Doctor of Philosophy

School of Chemistry

University of Birmingham

March 2016

Abstract

Nanoparticles have attracted considerable recent research interest for a variety of applications and can be used to visualize and characterise biological processes at the molecular and cellular level. They can be exploited as contrast agents for imaging and functionalised to incorporate luminescent moieties to a provide multi-modal imaging capability. This thesis presents a detailed series of studies on a luminescently labelled gold and silica nanoparticles, with the use of optical and electron microscopies to examine their applications.

Using surfactant and peptide pre-coatings gold nanoparticles were coated with an organic dye developed bind to the nanoparticle surface. The imaging potential of these novel nanoprobes is explored by examining uptake in vitro in cancer cells. Confocal laser scanning and transmission electron microscopies indicate significant cellular uptake. Nuclear uptake is also observed and possible methods of translocation to the nucleus are discussed. Cell cycle dysregulation is also assessed with no statistically significant perturbations observed.

The cellular uptake of 13 nm and 100 nm gold nanoparticles coated with a luminescent ruthenium polypyridyl complex was also investigated. Microscopy studies demonstrated the imaging potential of luminescent nanoprobes upon cellular uptake which was not accompanied significant cytotoxicity.

Finally an investigation in to the interaction of luminescent silica particles with dentine is presented. Confocal and scanning electron microscopies enable qualitative comparisons of the dentinal tubule occluding ability of particles coated with surfactants. The data indicate surfactant hydrophobicity is important factor in governing interactions with the dentine and illustrate the potential of luminescence imaging in dentistry.

This thesis is dedicated to my dearest family

Whoever tries to understand the human values of truth, righteous conduct, peace, love and non-violence properly, who practises these values and propagates them with zeal and sincerity can alone be described as a truly educated person.

$\sim$ *Sri Sathya Sai Baba*

Acknowledgements

ॐ भूर्भुवः स्वः
ॐ तत्सवितुर्वरेण्यं भर्गो देवस्य
धीमहि धियो यो नः प्रचोदयात्।

Foremost gratitude I express to my parents Sukhdev Raj Claire and Bhajno Claire, your love and encouragement throughout my life has and always will be my strength. Thank you to my dearest sisters Sangeta and Daljeet and my little brother Rajan, you deserve my wholehearted thanks for the immeasurable support you have always given me.

My sincere thanks to my supervisors Prof. Pikramenou, Dr. Hodges, Dr. Styles and mentor Prof. Damien Walmsley. Their support, expertise and the time they have invested in me has given me the confidence to traverse a challenging field of research. I am also immensely grateful to all the Pikramenou and Hodges research group members, both past and present, and the PSIBS Doctoral Training Centre for their support throughout my PhD.

ਧੰਨ ਧੰਨ
ਸੀ ਨਾਭ ਕੰਵਲ ਰਾਜਾ ਸਾਹਿਬ ਜੀ

Contents

List of Figures

List of Tables

1 Introduction

1.1 Luminescence Imaging

Luminescence imaging can yield valuable morphological and functional information within a variety of scientific disciplines. A great advantage of luminescence imaging is the capability of imaging with high contrast, sensitivity, temporal and spatial resolution. A variety of measurements can be performed with luminescent sensing modes such as intensity, lifetime and polarization detection. For imaging at the nanoscale transmission electron microscopy (TEM) can provide nanometre imaging resolution of a range of specimens, however the technique can involve extensive sample preparation making it relatively time consuming in comparison to luminescence based experiments. The field of nanotechnology has undergone an exponential growth over the past two decades, providing great potential for the design of nanoprobes for luminescence imaging.

1.1.1 Nanoparticles for Luminescence Imaging

Nanomaterials are defined as substances with at least one dimension below 100 nm and often display novel physical and chemical properties.[1] The unique physico-chemical properties can be attributed to their small size, chemical composition, surface structure, solubility, shape and aggregation characteristics.[2] For the purposes of luminescent imaging the inherent properties of the nanomaterial can be exploited or alternatively imaging moi-

eties can be incorporated either in or on the nanomaterial.[3–8] Luminescent nanoprobes aim to offer an alternative to the use of molecular probes which can also be used as imaging agents. Spatial specificity is improved with the use of nanoparticles, for example they can be functionalised to target specific organelles or biological processes of interest via the binding of targeting ligands such as peptides, proteins and antibodies. Greater temporal control may also be demonstrated, for example the time taken to internalise different sizes of nanoparticles by a cell may vary owing to differences in the kinetics of their uptake due to their size. This can be exploited to deliver the particles at a desired rate, in contrast to molecular probes which may be rapidly internalised by a cell without a trivial method of controlling uptake rate. Detection platforms utilising nanoparticles thus overcome such limitations offering improved sensitivity, stability and the potential for multiplexing with the integration of multiple probes on a single platform.[9–13]

Integrating multiple lumiphores with nanoprobes can offer a higher brightness and the potential for imaging via a range of imaging modalities depending on the nature of the nanoprobe. Transmitted-light and reflected-light configurations on microscopes for example can be used when the nanoprobe exhibits the appropriate light scattering or absorption properties. In a biological context the nanoprobes can also be targeted to specific cells and/or tissues by surface modification with targeting vectors, opening new avenues for disease diagnosis and therapy.[14–17]

Nanoparticles engineered to simultaneously express therapeutic and diagnostic potential and are said to possess a 'theranostic' capability.[18,19] Research in the field of 'nanotheranostics has the potential to eventually offer personalised treatment where therapy is tailored to address a patient's specific disease and genetic profile, of particular importance in cancer therapy.[20,21] Directing such treatment to specific cells or tissues can also diminish the side-effects of off-target accumulation. In cancer treatment improved biodistribution may also improve the therapy of the metastatic aspect of the disease with the potential for eradication of cancer stem cells which are thought to be responsible for primary and metastatic cancer growth.[21]

A variety of nanoparticles have been engineered including those consisting of polymers,[22] dendrimers,[23] silica,[24,25] semiconductor quantum dots,[26–28] carbon,[29] magnetite,[30,31] upconversion nanoparticles[32] and noble metals such as gold[33,34] and silver.[35] The aforementioned constructs each have their distinct advantages and disadvantages. Quantum dots for example have several useful properties such as large Stokes shifts, high quantum yields and broad excitation spectra making them useful luminescent nanoprobes.[23,36–38] Their luminescence properties are however size dependant and surface functionalisation can be non-trivial. Quantum dots also tend to be limited in size to the order of 5 nm or less.[39] Crucially with regard to biomedicinal applications quantum dots may be toxic to cells. Cadmium, selenium or tellurium quantum dots may for example leach cytotoxic heavy metal atoms in the intracellular environment and induce programmed cell death (apoptosis).[40,41]

Upconversion nanoparticles, consisting of an inorganic lattice doped with lanthanide ions, luminesce by the conversion of two or more low-energy photons into a higher-energy photon.[32] They offer a useful alternative to quantum dots as they do not suffer from blinking and can be excited in the near infra-red region of the spectrum, ideal for biological tissue.[42] A large drawback however is the synthesis of such particles with reproducability, yield and growth-control all proving non-trivial.[43]

Noble metal nanoparticles offer several distinct advantages for use as luminescent probes.[44–46] The relative ease of synthesis and surface functionalisation of gold nanoparticles in particular has enabled their use as an inert scaffold for a myriad of purposes, and has led to an exponential growth in gold nanotechnology based research over the last two decades.[47]

1.2 Gold Nanoparticles for Imaging

The use of gold in human civilisation spans several thousand years with gold nanoparticles in particular possessing a rich history. In Roman times they were used to stain glass

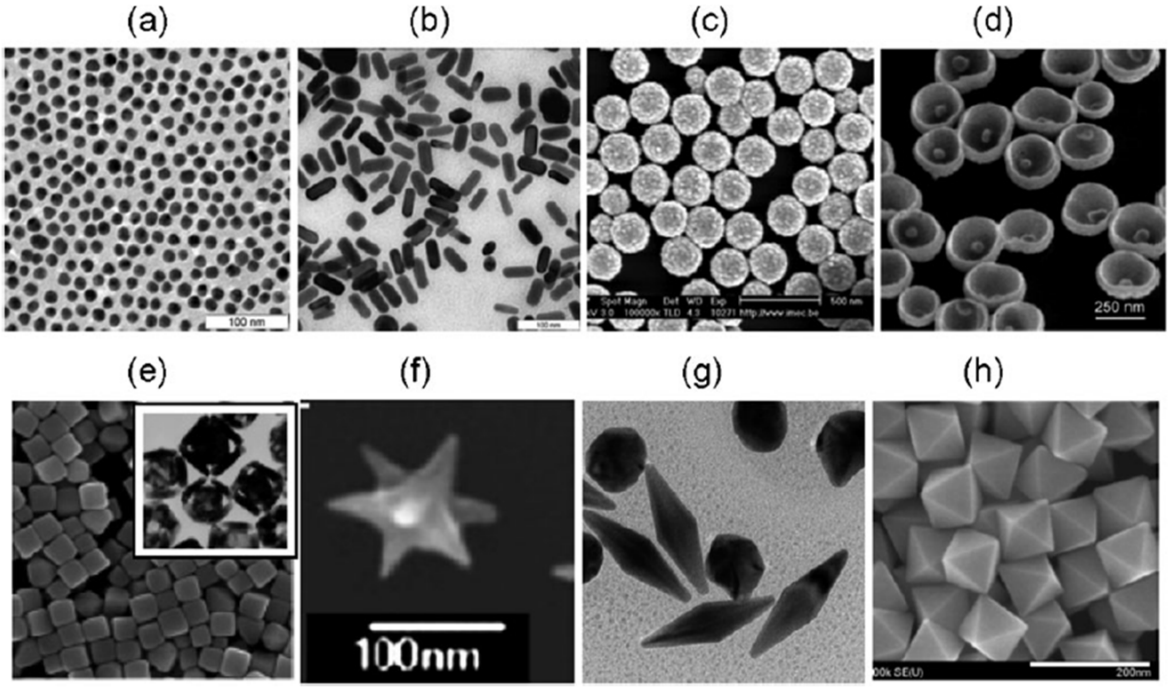

Figure 1.1: Transmission electron microscopy images of (a) 15 nm colloidal AuNPs, (b) 15-by-50 nm gold nanorods, (c) core/shell silica/gold nanoshells, (d) 250 nm gold nanobowls containing 55 nm gold seeds, (e) silver cubes and gold nanocages, (f) gold nanostars, (g) gold bipyramids and (h) gold octahedrals . Image adapted from Khlebtsov and Lev.[48]

for decorative purposes and over the centuries have even been recommended as cures for numerous diseases.[11] The first scientific report on gold nanoparticles was in 1857 when Faraday reported their red appearance as an attribute of their colloidal nature and observed that colloidal gold solutions have differing properties to bulk gold.[17,49] In 1908 Mie went on to characterise their visible absorption using the electromagnetic wave equations of Maxwell.[50]

Gold nanoparticles are relatively easily synthesised with numerous synthetic routes available. Most methods use the commercially available $HAuCl_4$ for citrate reduction of Au^{III} to Au^0 in water using a technique first introduced by Turkevitch *et al.* in 1951.[51,52] Gold nanoparticles can be manufactured in a variety of shapes including nanospheres, nanorods, nanobelts, nanocages and nanostars[53] (Figure 1.1). Their relative ease of synthesis coupled with their unique physico-chemical properties make them ideally suited for translation from the laboratory to the clinic. The large surface to volume ratio of spherical nanoparticle allows for a high loading of functionalising ligands and water solubility

also affords biocompatibilty.[48]

Strategies for conjugation of ligands to gold nanoparticles can be broadly categorised as covalent and non-covalent, with the former often yielding a more stable conjugate. This is particularly relevant for imaging purposes where it is important to have a strong link between the luminescent moiety and the nanoparticle. An example of a popular covalent conjugation strategy is the direct attachment of a thiolated moeity to the gold surface via an Au-S bond.[54] Conjugation to gold via such functional groups on luminescent probes, oligonucleotides, proteins and antibodies can be used to impart a huge array of functionality to gold nanoparticles, allowing for numerous applications in biomedicine.[11,17,55]

An important physical property of gold nanoparticles is the surface plasmon resonance (SPR) and the size related absorption peak from 500 to 550 nm exhibited by particles ranging 1 to 100 nm in size. The SPR can be determined using UV-Vis (Ultraviolet-Visible) Absorption Spectroscopy which can be used to monitor changes in the SPR of the gold nanoparticles as they undergo surface functionalisation. A schematic showing a typical UV-Vis Spectrophotometer is shown in Figure 1.2. In brief this spectroscopic analysis involves passing light of a known wavelength through a simple and measuring how much light is absorbed as a function of wavelength. Molecules absorb radiation of different wavelengths depending on their structural composition. The absorption of UV or visible radiation for organic molecules for example correspond to electronic transitions, where outer electrons are promoted to excited states such as the π to $\pi^{\star}$ transition.

With regards to gold nanoparticles an important feature of the UV-Vis spectrum is the aforementioned SPR. According to Mie theory the SPR arises from the absorption of electromagnetic radiation resulting in the collective oscillation of conduction electrons on the nanoparticles surface, providing the wavelength of the incident radiation is small with respect to size of the nanoparticle.[50] The SPR absorption wavelength is in the visible region for gold nanoparticles 520 nm in diameter, and is furthermore also dependent on the gold nanoparticle shape, solvent/environment (dielectric properties), surface ligands and inter-particle distance to other nanoparticles.[56,57] The SPR wavelength also undergoes a

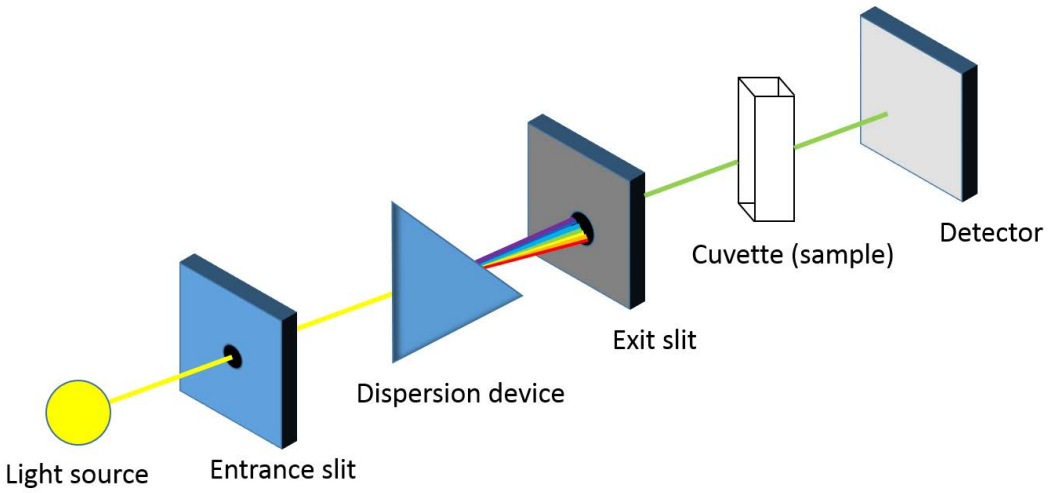

(a)

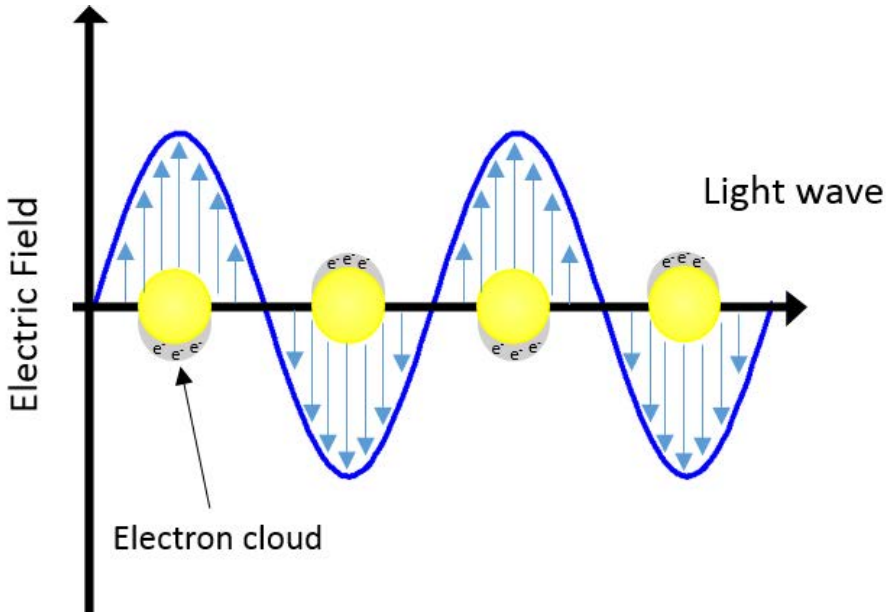

(b)

Figure 1.2: (a) Schematic diagram of a double-beam UV-Vis spectrophotometers. UV-Vis spectrophotometers consist of a (tungsten) filament lamp employed as the light source. The polychromatic light from the lamp light passes through an entrance slit and is directed through a dispersion device (prism/grating) by a collimating lens (not shown). A focusing lens (not shown) directs monochromatic light through an exit slit, through the sample and on to a detector, usually a photo-multiplier tube. By moving the dispersing device or the exit slit, radiation of a particular wavelength can be selected to leave through the exit slit. (b) Schematic diagram of the surface plasmon resonance effect on a gold nanoparticle. The interaction of light of a specific wavelength with electrons on the surface of the gold nanoparticle causes their collective oscillation, resulting in an effect called the surface plasmon resonance. This causes the strong absorption/scattering of light at that wavelength that is evident by a broad band in the UV-Vis spectrum. The SPR peak is strongly dependant on the gold nanoparticle size, shape, surface and agglomeration state, and thus an important parameter for their characterisation.

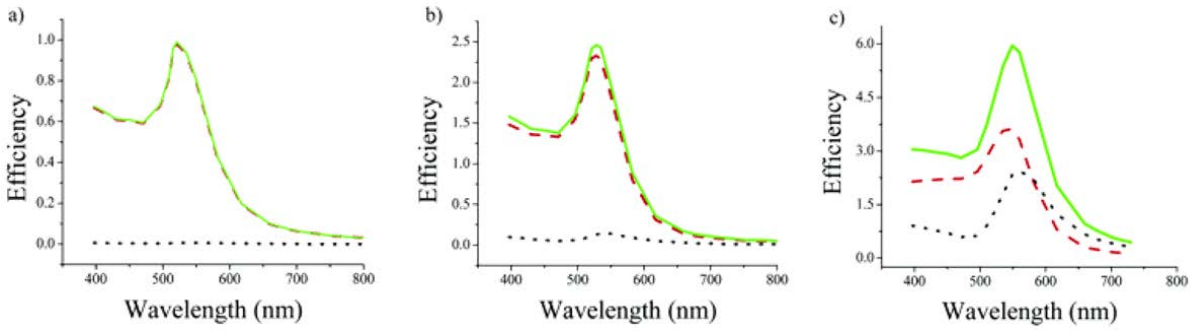

Figure 1.3: Theoretical spectra of the efficiency of absorption (red dashed line), scattering (black dotted line) and extinction (green solid line) observed for spherical gold nanoparticles as a function of the wavelength of incident light. Diameter (a) = 20 nm, (b) = 40 nm and (c) = 80 nm. (Figure adapted from Jain et al.[59]).

significant redshift upon nanoparticle aggregation and is accompanied by a broadening of the SPR band and a colour change of colloid from red to blue.[58] The high sensitivity of the SPR to the physico-chemical properties of gold nanoparticles make it an important diagnostic in their surface functionalisation.[59]

Total light extinction, defined as the energy loss of an electromagnetic wave after passing through matter, comprises of scattering as well as the aforementioned absorption. Light absorption occurs due to inelastic scattering of incident photons resulting in a dissipation of energy. Scattering occurs in the form of Rayleigh scattering, where scattered light is emitted at the same frequency as the incident light, or in the form of Raman scattering where it is emitted at a different frequency. The SPR, scattering and total extinction of nanoparticles are characterised by Mie theory and for nanoparticles larger than 20 nm in diameter, high order electron oscillations become significant and must be accounted for when characterising light absorption.[50]

Using Mie theory it was shown by El-Sayed **et al.** that optical absorption and scattering is highly dependent on nanoparticle size.[59] It was found that for 20 nm gold nanoparticles the total extinction is contributed to nearly entirely by absorption. Scattering then becomes an increasing contributor to light extinction for 40 nm nanoparticles, whilst at 80 nm size scattering and absorption contribute to the total extinction to a similar degree (Figure 1.3). This is particularly relevant for biomedical theranostic applications. Larger

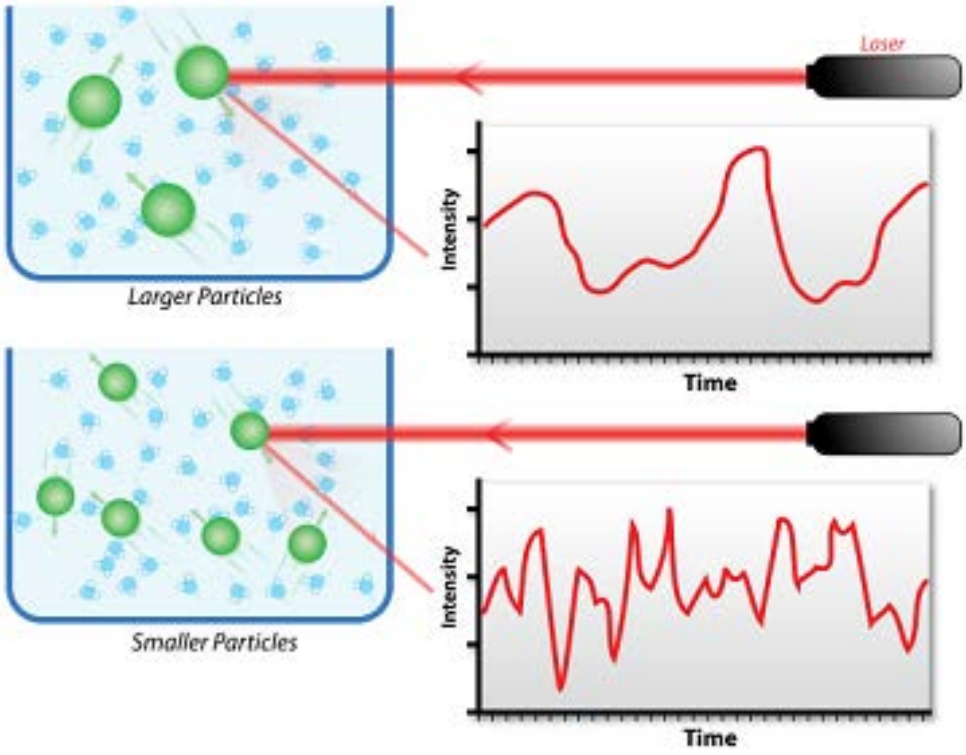

Figure 1.4: Schematic of the hypothetical fluctuations in scattering intensity observed from large and small particles. The rate of change of intensity fluctuations depends on particle velocity, that is in turn related to particle size (smaller particles in Brownian motion diffuse faster and vice-versa). Thus the size distribution of particles in a solution can be acquired through measurement of scattered light. (Image adapted from M. Jones[63]).

gold nanoparticles are often preferred for their greater scattering efficiency, a property that has been readily exploited for the imaging of cancer cells by with dark field microscopy and confocal microscopy.[60] Contrastingly due to their greater absorption smaller nanoparticles are preferred for photothermal therapy due to their greater efficiency at converting incident light to heat.[61,62]

Nanoparticle size is an important property that must be measured once they are synthesised and furthermore to monitor changes upon their functionalisation. Dynamic Light Scattering (DLS) is a technique often employed to measure the size of sub-micron particles. DLS determines the size of particles by measuring their Brownian motion; the random movement of particles due to collisions with the surrounding solvent molecules. The velocity of the Brownian motion is characterised by a parameter known as the translational diffusion coefficient (D). The size of the particle is calculated using the Stokes-Einstein

equation which also relates temperature (T) and viscosity η to the translational diffusion coefficient. The particle size is referred to the particle's hydrodynamic diameter *d(H)*, and with the Boltzmann constant defined as k the Stokes-Einstein equation is thus:

$$d(H) = \frac{kT}{3\pi\eta D}$$

Particle size is defined as the so-called hydrodynamic diameter because it refers to the diameter of a sphere that has the same translational diffusion as the sample particle. This is dependant on the surface structure/morphology of the particle and any surrounding ionic layers, not just on the size of the core, thus the concentration of particles and the ionic nature of the medium can affect diffusion speed and perceived particle size.

In practice the DLS machine measures the extent to which intensity of scattered light fluctuates using a signal correlator that measures the degree of similarity between two signals or indeed the same signal over time. The amount of correlation measured over time is a signature of particle size with large particles exhibiting slowly changing correlation and vice-versa. Computational algorithms are then applied to determine the translational diffusion coefficient. Particle size can therefore be calculated in addition to the polydispersity index (PDI); a measure of a sample's polydispersity. Nanoparticle size and monodispersity are useful parameters to measure upon their synthesis and functionalisation, providing an indication as to whether successful ligand conjugation has been achieved and colloidal stability maintained.

Another important phyiscal property of nanoparticles that requires characterisation is the zeta potential ζ. This refers to the electrokinetic potential in a colloidal dispersion and is essentially the potential difference between the dispersion medium and the stationary layer of fluid surrounding the dispersed particle. To examine this in greater detail, one must consider the dispersed particle being surrounded by a layer of ions. A net charge on the particle surface will affect the distribution of ions in the surrounding region resulting in an increased concentration of counter ions close to the surface. This liquid layer surrounding the particle comprises of an electrical double layer, consisting of an inner region (Stern layer) where ions are strongly bound, and a diffuse outer region where

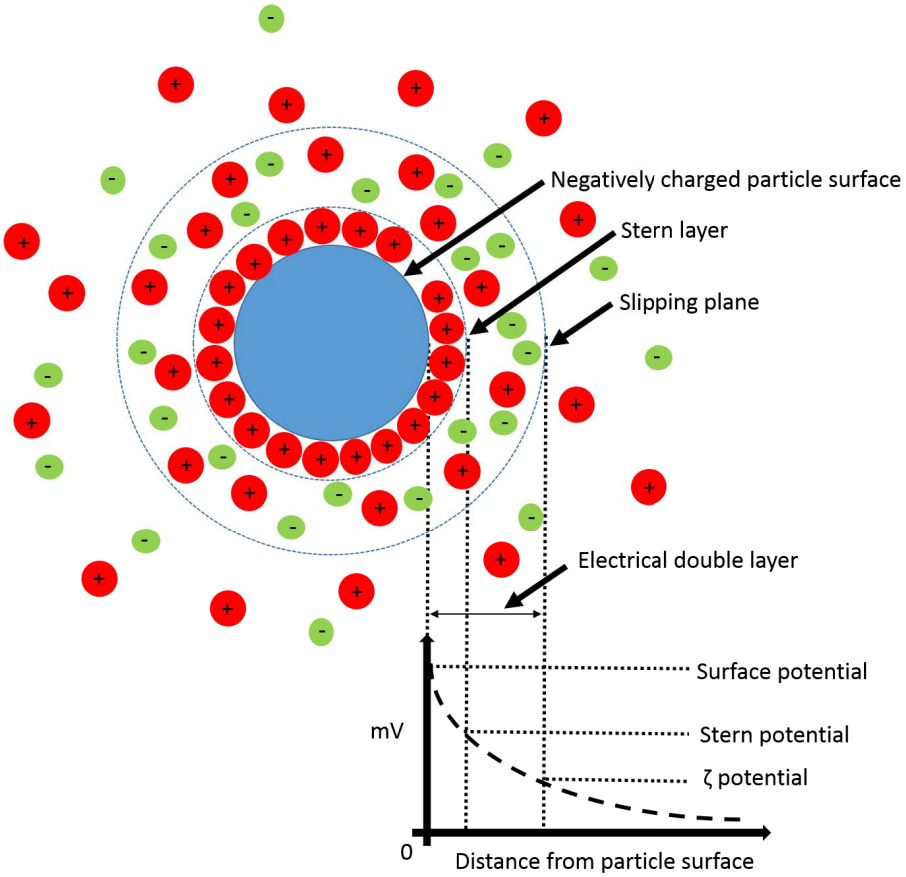

Figure 1.5: Schematic illustrating a negatively charged particle in solution surrounding by ions. Ionic concentration is depicted and electric potential as a function of distance from the charged particle surface is depicted graphically. Also shown are the boundaries comprising the electrical double layer namely the inner (Stern) layer and diffuse outer layer. The zeta potential is defined at the slipping plane interface, as depicted in the diagram.

they are loosely bound. Within the diffuse outer layer there exists a notional boundary where if the particle moves, ions within the boundary move with it but ions beyond it do not. This boundary is referred to as the slipping plane and the potential that exists at this boundary defines the zeta potential.

The stability of a colloid can be assessed by measuring the magnitude of the zeta potential. If the particles have a large negative or positive potential they will electrostatically repel each other. If not the particles may exhibit a tendency to flocculate as the lack of an electrostatic repulsion allows them to come in closer proximity to each other and flocculate. Generally colloids with zeta potentials more positive than +30 mV or less negative than -30 mV are considered stable. In practice the zeta potential is measured using

electrophoresis where an electric field is applied across a sample causing charged samples to move toward the electrode of opposite charge. Particle velocity is determined using the intensity of the scattered light as particles move through a laser beam directed through the sample[64,65] (Figure 1.4). Exploiting the proportional relationship between the frequency of the intensity fluctuations and particle speed, a property known as the Electrophoretic mobility (U_E) can be determined using the Henry equation. The electrophoretic mobility is related to the zeta potential by the dielectric constant (ε), viscosity (η) and Henry's function ($f(Ka)$) that is usually approximated as either 1.5 or 1.0:

$$U_E = \frac{2\varepsilon\zeta f(Ka)}{3\eta}$$

Nanoparticle conjugation can alter the zeta potential of the particles due the displacement of ions on the nanoparticle surface and/or through the addition of species to the nanoparticle surface. This affects particle diffusion and thus zeta potential, allowing nanoparticle functionalisation and colloidal stability to be characterised.

Although gold nanoparticles exhibit intrinsic luminescence the emission mechanism is not fully understood.[66] The emission properties are also very sensitive to particle size, surface roughness and surface functionalisation.[67,68] The design and synthesis of gold nanoprobes to exploit these luminescence characteristics can therefore be problematic due low quantum yields and variable luminescence properties. Imaging has however been achieved using gold nanostars and plasmon-enhanced two-photon luminescence *in vitro* in BT549 breast cancer cells and *in vivo* in laboratory mouse studies.[69]

An alternative to the use of the inherent gold nanoparticle luminescence is the functionalisation of the nanoparticle surface with luminescent moieties. A wide variety of functional molecular linkers are currently being employed to enable conjugation of such probes to gold nanoparticles including thiolate,[70,71] dithiolate,[72] carboxylate[73] and phosphine[74] moieties. A schematic showing use of a gold nanoparticle as a scaffold for multiple luminescent groups is shown in Figure 1.6. Functionalising gold nanoparticles with luminescent probes in this manner can enable construction of a nanoprobe that bears the

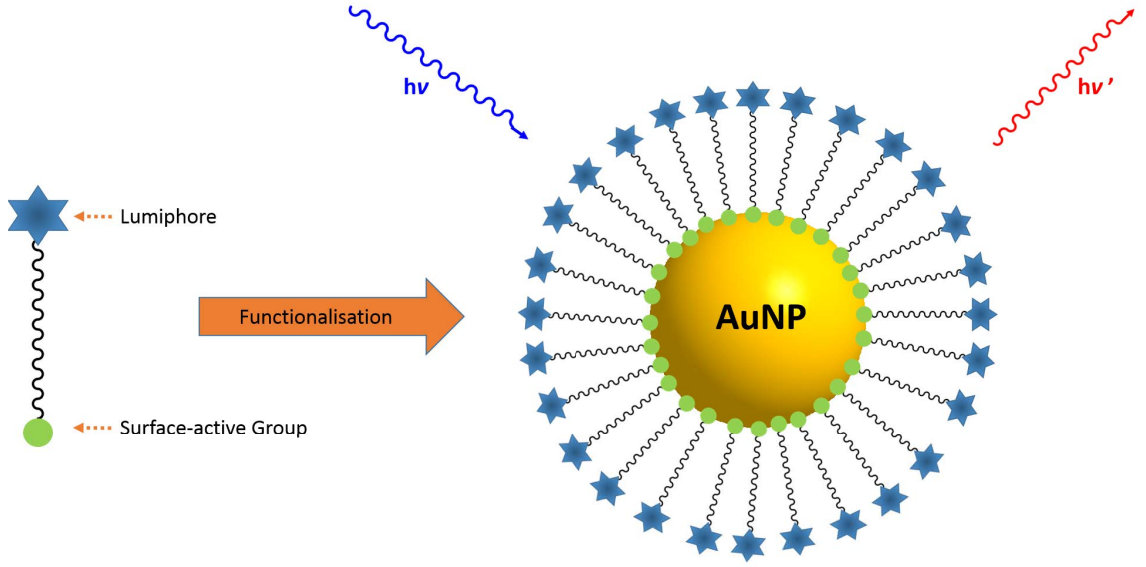

Figure 1.6: Schematic illustrating the functionalisation of gold nanoparticles with surface-active lumiphores.

distinct optical signature of the luminescent agent, independent of the particle properties.[75–77] Such probes can also exploit the high electron density of gold to offer multimodal imaging and do not suffer from blinking as observed in quantum dots.

For biomedicinal applications gold nanoparticles may encounter complex environments such as those of cells and tissues and many such studies on uptake have been conducted both *in vivo*[78,79] and *in vitro*.[80,81] Some of the commonly used methods of imaging or assessing gold nanoparticle uptake are transmission electron microscopy (TEM), exploiting the high atomic mass of gold, and inductively coupled plasma mass spectrometry (ICPMS). These techniques are however destructive in nature and therefore provide impetus to use luminescent based imaging modalities. Furthermore gold nanoparticles of the order of tens of nanometres in diameter can be imaged by phase contrast or differential interference contrast microscopy with an optical microscope. The aforementioned gold scattering can also be exploited by reflection and dark field microscopies,[59,77,82–85] thus a number of complementary techniques to luminescence based imaging are possible allowing for a broad spectrum of biomedical applications.[86–89]

The majority of nanoparticle uptake studies in cells presented in this thesis are per-

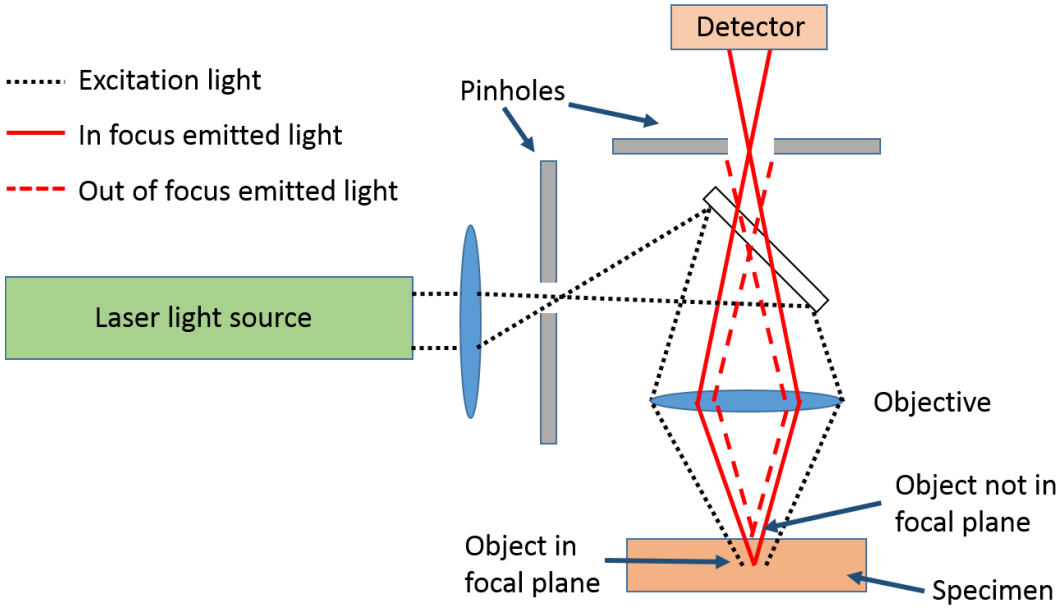

Figure 1.7: Schematic of a Confocal Microscope

formed with confocal microscopy. Confocal microscopy has the distinct ability to perform optical sectioning by means of a pinhole at the detector that works to eliminate out-of-focus light and enable the reconstruction three-dimensional structures from the recorded images. These reconstructions, referred to as "z-stacks" allow specimens to be visualised through their vertical planes by creating a coronal ("yz") and transverse ("xz") projection image through the data set. Confocal image data presented using these "side" views are referred to as "orthogonal views" for the remainder of the thesis.

In brief a confocal microscope operates with the use of a laser as an excitation source which is raster scanned across the sample by motorised mirrors. The emitted light is directed by the (dichroic) mirrors and focused on to a detector (photomultiplier tube) through a pinhole which eliminates out-of-focus light. The confocal microscope is extremely useful for looking at stained cells that have been stained to indicate particular organelles of interest via fluorescence. Nanoparticles can also be imaged by a confocal microscope by exploiting their aforementioned light absorption/scattering properties in addition to their luminescence or conjugated luminescent moieties.

An important issue to consider when examining nanoparticle uptake in cells is the

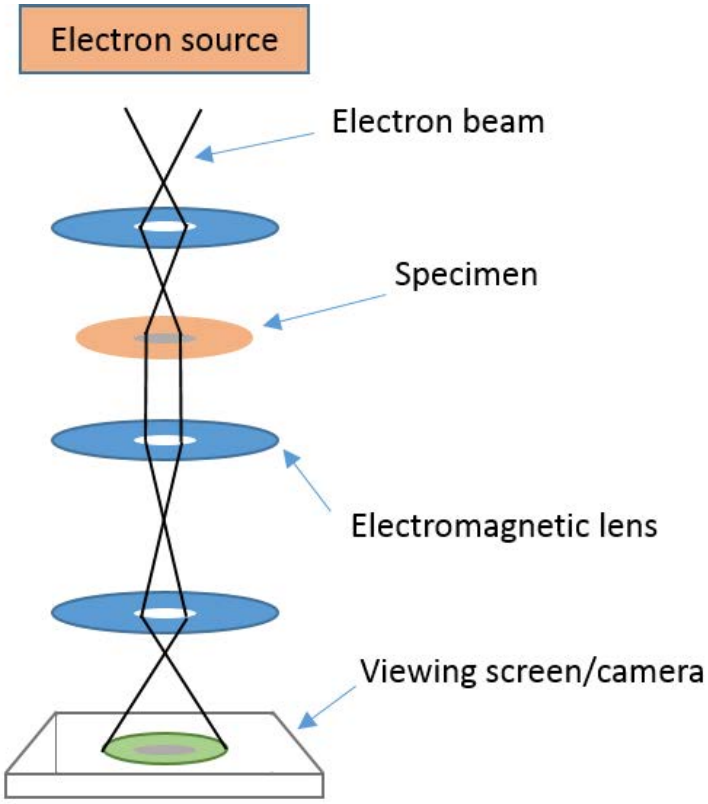

Figure 1.8: Schematic of a Transmission Electron Microscope

potential for artefacts from the fixation processes required for preparing cells microscopy. Ideally all confocal and indeed all microscopy studies on biological samples would be performed on living specimens, such that the biological specimen is imaged in its most native physiological state and any processes/featured imaged cannot be attributed to fixation artefacts. Furthermore many light microscopy fixation techniques were developed for two-dimensional imaging, thus retaining the three-dimensional structure of a sample is often not possible. In practice however live specimen imaging is not always trivial with cell movement and keeping cells in a physiologically "happy" state important considerations. Imaging cells in liquid media and staining the cells can also be non-trivial, as such many imaging studies are performed on fixed samples.

Fixatives are used to essentially "fix" biological specimens and render any macromolecular processes inert by causing the cessation of metabolic reactions, thus preserving

microstructures for an extended period of time. Three general categories of fixation protocols exist for biological specimens, namely chemical fixation that works by coagulating proteins or chemically cross-linking them, freeze substitution and microwave fixation.[90] An example of a popular chemical fixative is formaldehye and is was the method adopted by the author to fix cells for confocal microscopy. Ideally a fixative should penetrate the specimen quickly and act rapidly to preserve the physical structure however chemical fixation of this type can cause permeabilisation of some cellular structures such as the cell membrane. It can also damage lipids and in the case of formaldehyde damage DNA structure.[91] It is thus of great importance that fixed-cell imaging be complemented with live-cell imaging, particularly when scrutinising the spatial localisation of features of interest such as nanoparticles in cells. As such the author adopts both fixed and live-cell confocal imaging in this thesis. A complementary modality that allows for imaging of cells and nanoparticles is the aforementioned transmission electron microscopy (TEM) imaging modality. TEM utilises a beam of electrons that is focused and transmitted through an ultra-thin sample of the specimen, as depicted schematically in Figure 1.8. An image is formed by the interaction of electrons with the sample with the absorption of electrons according to the thickness and composition of the specimen providing image contrast. Electron microscopes are capable of achieving a much higher resolution than light microscopes due to the small de Broglie wavelength of electrons, thus intracellular and single nanoparticle imaging can be performed with relative ease.

1.2.1 Cellular Uptake of Gold Nanoparticles

Numerous developments in biomedical science involve studying the interaction of artificially produced nanoparticles with living organisms not only as imaging agents but also as therapeutic agents on the cellular level.[6,92] Colloidal nanoparticles are naturally "ingested" by cells, thus functionalised luminescent gold nanoparticles have the potential to probe the intracellular environment and a wide array of biomolecular interactions that occur therein.[77,93] Of particular interest is the ability to functionalise particles for prefer-

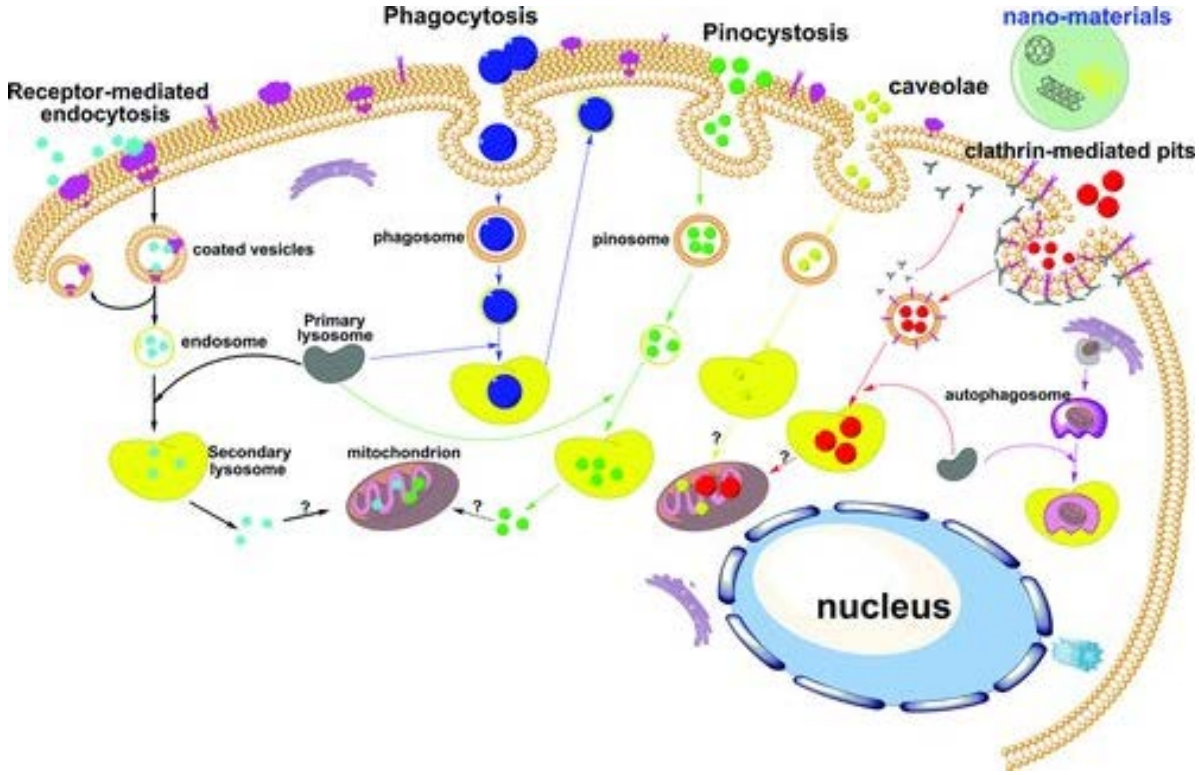

Figure 1.9: Schematic of the known pathways for intracellular uptake of nanoparticles. Adapted from Zhao et al.[7]

ential accumulation in cancer cells through the use of targeting ligands. These ligands may be specific to receptors which are overexpressed on the surface of cancer cells, providing a method of cancer diagnosis and therapy.[83,94]

For *in vitro* applications nanoparticles are required to achieve cellular uptake which involves the traversal of the dynamic structure of lipid bilayers and membrane proteins comprising the cell membrane. A range of experimental findings have indicated that engineered nanoparticle such as metal clusters, carbon nanotubes and quantum dots can achieve membrane penetration in a variety of cell lines such as endothelial cells,[95,96] pulmonary epithelial cells,[97,98] intestinal epithelial cells,[99] alveolar macrophages[100] and neuronal cells[101] A host of uptake mechanisms have been suggested broadly categorised as active[102] or passive[103] forms of nanoparticle transport, with the latter referring to ATP independant mechanisms and not requiring cellular machinery for uptake (Figure 1.9).

A common form of active transport is endocytosis in which the cell internalises objects by enclosing them in vesicles which pinch off the cell membrane (Figure 1.9). The endocy-

totic energy-dependant mechanisms are phagoytosis, pinocytosis and caveolae-dependant or clathrin-mediated endocytosis.[104–108] Phagocytosis is a process usually utilised by specialised mammalian cells such as macrophages and neutrophils to ingest large solid particles larger than approximately 750 nm in diameter, leading to the formation of an internal phagosome.[7] The processes of pinocytosis or macropinocytosis occurs in nearly all cell types and is a method used by cells to internalise particles ranging from a few to several hundred nanometres in size.

Clathrin-mediated endocytosis is the mechanism believed to be responsible for most of the cellular uptake of nanoparticles.[109–113] Also referred to as receptor-mediated endocytosis, this mechanism involves binding of the nanoparticles to receptors which span the cell membrane. The formation of a membrane invagination then internalizes the particles in clathrin-coated vesicles which go on to fuse with early-stage endosomes.[114] Caveolae-mediated endocytosis in the context of nanoparticle uptake is of particular importance in endothelial cells,.[115,116] This pathway involves uptake via invaginations in the cell membrane 50-80 nm in size consisting of cholesterol, sphingolipids and caveolins.[117]

Despite the vast number of investigations on the interaction of nanoparticles with cells, relating their physico-chemical properties with the uptake is still a largely unresolved problem. It is likely that the effect of size, surface chemistry, cell line and colloidal stability are all contributory factors to the method of uptake. Generally each type of nanoparticle has a preferred mechanism for cellular uptake, for example gold nanoparticles are usually internalised by cells by clathrin-mediated endocytosis. Once internalised by endocytosis it is believed that the nanoparticles remain trapped in the endosomes created by the endocytotic pathway[118]

A study demonstrating some of the hitherto discussed uptake mechanisms is the investigation by Nativo *et al.* which involved a TEM study of the uptake of 16 nm surface-modified gold nanoparticles by HeLa cells[119] It was found that citrate-stabilised gold nanoparticles were readily internalised by cells in to endosomes which eventually became densely populated with internalised nanoparticles (Figure 1.10a). As no nanoparticles

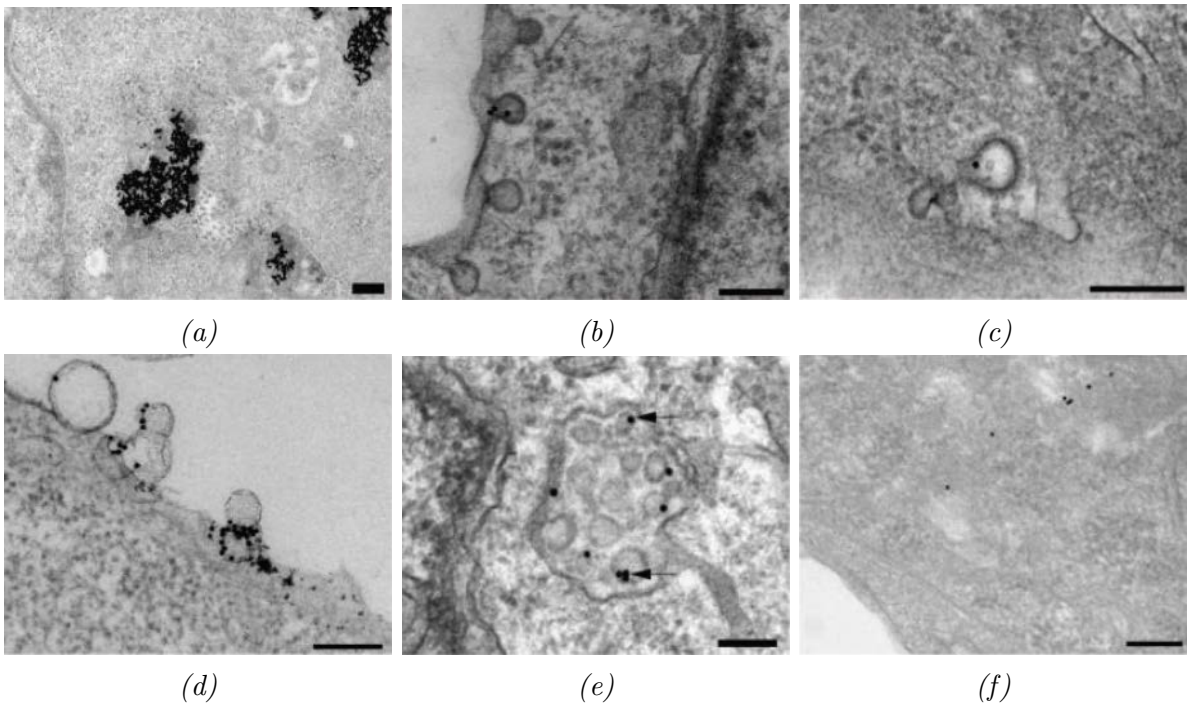

Figure 1.10: (a) Typical TEM images of citrate-stabilized gold nanoparticles confined to the endosome after cellular uptake in HeLa cells. (b-f) Uptake of PEG-modified gold nanoparticles in the presence of liposomes. Uptake mechanisms observed without apparent direct involvement of the liposomes include (b) caveolae and (c) clathrin-mediated endocytosis. (c) Nanoparticle delivery by liposomes. PEG-modified gold nanoparticles are found in the endosome (d) or free in the cytosol (e). Arrows indicate nanoparticles in the endosome that are surrounded by an additional membrane, indicating that they have been taken up by the endosome from the cytosol. (Scale bars - 200 nm). Figure adapted from Nativo et al.[119]

were found freely dispersed in the cytoplasm of the HeLa cells, commercially available neutral liposomes that could deliver nanoparticles directly to the cell cytoplasm by fusion with the cell membrane were used. In the presence of these liposomes it was found that Poly(ethylene glycol) (PEG) modified gold nanoparticles were internalised by the cells by a number of different pathways, surprisingly not all of which were directly mediated by the liposomes.[120] For example caveolae-mediated uptake was observed which was particularly surprising considering that in the absence of the liposomes the PEG-modified nanparticles were not internalised at all (Figure 1.10b). The caveolae mechanism is the major non-clathrin dependant route of uptake from the cell surface into the endosomal pathway (Figure 1.10c),[121] however uptake via clathrin-coated vesicles was also observed in the presence of the liposomes (Figure 1.10d). It was therefore concluded that the presence

of the liposomes induces employment of both the major routes of endocytosis (caveolae and clathrin) for particle internalisation. The majority of nanoparticles internalised in the HeLa cells were thus found in endosomes (Figure 1.10e). As a result of direct delivery by the liposomes to the cytoplasm however, some particles were also found free in the cytoplasm (Figure 1.10f).

A further point of discussion in this study regarded the introduction of nanoparticles to a biological cell culture medium and the diverse range of biomolecules, including proteins, carbohydrates and lipids, they subsequently encounter. When introduced into a serum containing media with such molecules a so-called "protein corona" will form on the nanoparticle surface. The protein corona can have important consequences on the stability of the nanoparticles.[122–126] In the study by Nativo *et al.* it was observed that citrate-coated gold nanoparticles remained stable after their addition to cell culture medium.[119] This was indicated by retention of the characteristic red colour of the gold colloid and confirmed by UV-Vis absorption spectroscopy, which indicated no signifcant red-shift or SPR broadening. It was concluded that proteins secreted by the cells and the presence of fetal bovine serum (FBS) in the cell culture medium were responsible for the observed nanoparticle stability.[120] Another consequence of the protein corona is that the cell surface may potentially encounter a nanoparticle much different to the original engineered nanoparticle. This is of great relevance for the design and manufacture of nanoparticles with targeted uptake.

In addition to the active uptake processes discussed nanoparticles may also enter cells by passive penetration of the cell membrane,[127–129] as indicated by the uptake of nanoparticles into cells that lack endocytotic machinery such as erythrocytes.[130] Uptake may occur through diffusion across the cell membrane or via protein channels in the cell membrane.[131] This method of uptake may often go unnoticed because of the dominance of endocytotic uptake.

A typical mammalian cell membrane is negatively charged and cationic gold nanoparticles have been shown to exhibit greater adhesion to neutral or negative regions of the

membrane and subsequently achieve uptake.[132] It has however also been reported that anionic gold nanoparticles can bypass endocytotic uptake with direct entry into the cytoplasm particles into the cytosol by passing directly through the cell membrane in an example of passive uptake.[133] Simulations of gold nanoparticle interactions with cell membranes reported by Lin *et al.* also indicated that electrostatic interactions with the surface ligands on the nanoparticle can affect membrane interaction and uptake.[132]

Overall there are numerous factors to consider when assessing nanoparticle internalisation in cells, particularly passive uptake which is much less characterised than active uptake. Passive uptake may indeed even be the main contributor to uptake in the long-term exposure to low concentrations of nanoparticles, where the threshold for active uptake of nanoparticles across the cell membrane is not achieved.[134]

Nanoparticles can also be internalised by cells by methods categorised as facilitated delivery mechanisms. These involve the use of cell penetrating peptides (CPPs) and localisation signals on the particles to direct the nanoparticles to organelles of interest. Peptide sequences can also be used to stabilise aqueous gold nanoparticles. The CALNN peptide created in 2004 by Levy *et al.* is a short sequence incorporating a cysteine residue to promote binding to gold nanoparticles via the functional thiol group.[135] The uptake of gold nanoparticles stabilised with the CALNN peptide has been demonstrated by Nativo *et al.*[119] and Sun *et al.*[136] in HeLa cells.

Peptide functionalised gold nanoparticles can also demonstrate active cellular targeting in biological applications. Cancer cells for example can suffer from oxygen deprivation when their blood supply is insufficient. As a result they often adapt to this hypoxic environment by developing alternative metabolic pathways which result in acidic extracellular environments. The resulting reduction in pH can be used as biomarker for cancer and also as a strategy for the delivery of nanoparticles via the use of peptides activated in an acidic environment.[137] One such example is the pH low insertion peptide (pHLIP) developed by Engelman *et al.*[138,139] At neutral pH the peptide is hydrophilic and hence water soluble, enabling weak association with the cell membrane. At slightly acidic pH

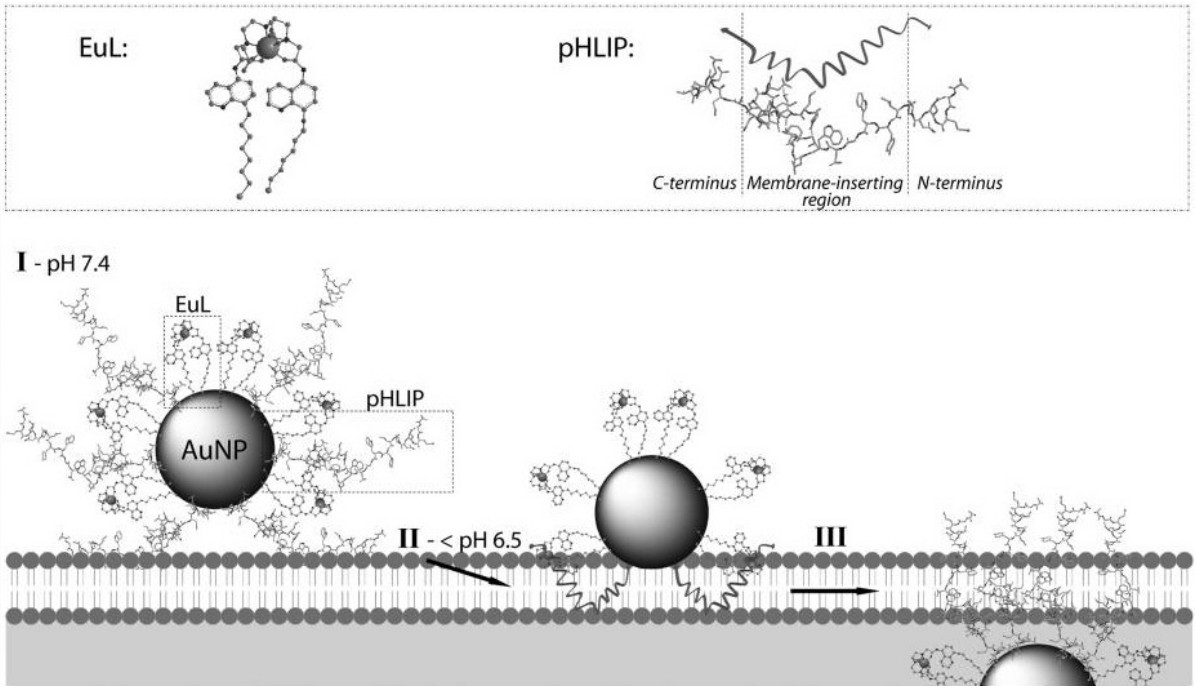

Figure 1.11: Schematic representation of gold nanoparticles coated with the pHLIP peptide and luminescent europium complex. At neutral pH, the nanoparticles are loosely associated with the lipid membrane. Upon a decrease in pH to 6.5, pHLIP peptide molecules form alpha-helical structures and insert across the lipid membrane, allowing translocation of the luminescent nanoparticles across the lipid membrane into the cytoplasm. Image adapted from Davies et al.[82]

(<7) the peptide becomes hydrophobic (due to protonation of the carboxylic side chains on the aspartic acid residues), causing insertion into the cell membrane through formation of an alpha-helix structure.[140,141]

Delivery of 13 nm gold nanoparticles into platelets using the pHLIP peptide has been reported by Davies *et al.*[82] The peptide was attached to the gold nanoparticles through the thiol group of the cysteine residue. A luminescent europium(III) probe was also attached to the nanoparticles to enable optical imaging of the nanoprobes. A schematic of the insertion mechanism showing the translocation mechanism of the gold nanoparticle-pHLIP-europium construct is shown in Figure 1.11.

The uptake of pHLIP coated gold nanoparticles 1 nm in diameter were also investigated in HeLa cells by Yao *et al.*[142] Gold nanoparticles modified with pHLIP peptide showed higher uptake relative to unmodified particles at both the neutral and acidic conditions tested. A pH dependence was observed with a 3-fold greater uptake at pH 7.4 and a 6.4-

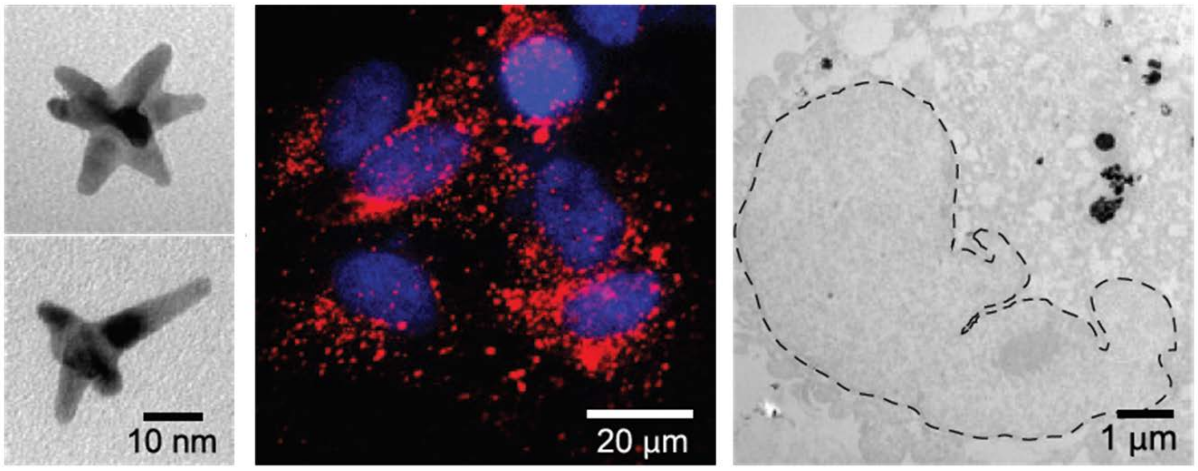

Figure 1.12: TEM image of nanoconstructs composed of nucleolin-specific aptamers and gold nanostars (left) were actively transported to the nucleus as indicated by confocal luminescence microscopy (middle) [nucleus - blue, Cy5 labelled nanoparticles - red]. TEM images indicated nanoparticles induced major changes to the nuclear phenotype in the form of nuclear envelope invaginations near the site of the nanoparticle localisation (right). Adapted from Dam et al.[148]

fold greater uptake at pH 6.5. The pH dependence is perhaps expected but it is interesting to note that the pHLIP coated particles show greater uptake than the uncoated particles even at neutral pH. This may be because at neutral pH the pHLIP peptide exists in an equilibrium between it's water soluble and membrane-bound unstructured forms.[143,144]

The pHLIP peptide has demonstrated further versatility with silica nanoparticles. Mesoporous silica nanoparticles 140 nm in diameter were loaded with a chemotherapy drug (doxorubucin) and delivered to tumorous tissue through pHLIP mediation, again exploiting the characteristics of the pHLIP peptide in the acidic tumour microenvironment.[145]

Functionalising nanoparticles with localisation signals as well as peptides can also provide a targeting capability to nanoparticles as mentioned previously. Of particular interest is the cell nucleus where the majority of the genetic material in cells is located, thus making the nucleus most important organelle in the cell. Responsible for controlling cellular growth, proliferation and apoptosis it is a particularly desirable target for nanoparticles used for drug delivery and gene therapy.[146] Nanoparticles present a viable alternative to the use of viral vectors, the conventional method of nuclear drug delivery, which often illicit an immunogenic response.[147]

Nuclear uptake is inherently non-trivial as it requires that a nanoprobe first gain cellular entry via a mechanism that avoids endosomal restriction. Furthermore the nanoprobe may also require a nuclear localisation signal (NLS) to achieve translocation to the nucleus via traversal of the nuclear envelope, which like the cell membrane consists of a phospholipid bilayer.[149] Nuclear uptake of gold nanoparticles coated with PEG and conjugated with an arginine-glycine-aspartic acid peptide and a nuclear localization signal was demonstrated in human oral squamous cancer cells.[150] In this study by Kang *et al.* cytokinetic arrest was also observed, referring to the ability of the nanoparticles to disturb the cell cycle of the cancer cells. This was indicated by binucleate cell formation in the late stages of mitosis which resulted in the failure of complete cell division. Confocal microscopy and a flow cytometry based investigations into the cell cycle also indicated DNA damage and apoptosis accompanying the cytokinetic arrest.

Active nuclear targeting has also been achieved with gold nanoparticles modified with CPPs and an adenovirus nuclear localization signal in the HeLa and HepG2 cell lines.[147] Video-enhanced colour differential interference contrast microscopy and TEM indicated the transport of nanoparticles into the cytoplasm and nucleus. Another study aimed at direct visualization of interaction between drug loaded nanoparticles and the nuclei of HeLa cells was conducted by *Dam et al.*,[148] whose approach consisted of the construction of gold nanostars functionalised with nucleolin-specific aptamers and a Cy5 red fluorescent marker (Figure 1.12). Nuclear uptake was achieved by taking advantage of the nuclear trafficking ability of the nucleolin phosphoprotein which is over expressed in the cytoplasm and cell membrane in metastatic and rapidly dividing cells.[151] A striking result from this study were major changes to the shape of the nuclear envelope in areas where the nanoconstructs localised after uptake. Cells displaying these foldings in the nuclear envelope showed increased apoptosis and decreased cell viability, thus revealing a new correlation between changes in nuclear phenotype and potential therapeutic efficacy in potential anti-cancer therapies using gold nanoparticles.

The preceding discussion illustrates the wide range of biological effects gold nanoparti-

cles can elicit in cells, however the detailed mechanisms by which such interactions occur are only just being understood.[152] Gold nanoparticles can be targeted to specific organelles such as the nucleus with the aforementioned nuclear localisation signals, however non-targeted gold nanoparticles can also illicit cell damage in the form of photothermal ablation,[153] mechanical injury[152] or be utilised for localised drug delivery.[154,155] The development of gold nanoparticle based therapeutics in cancer cell eradication is of particular importance as rapidly metastasising cancers often lack effective treatment.[156] Imaging of gold nanoparticle uptake in cancer cells and examining the intracellular fate of the nanoparticles is thus of great importance.

Optimal therapeutic outcome is based on organelle targeting in cells such that accumulation in specific compartments affects important intrinsic cell functioning. Targeted treatment methods also have the benefit of reduced side-effects. As mentioned the cell nucleus is a particularly desirable target for nanoparticles, responsible for growth, proliferation and apoptosis; all of which anti-cancer treatments would hope to disrupt.[146] Nuclear phenotypes are usually altered in cancer cells relative to normal healthy cells with changes in nuclear size, shape, envelope and genetic organisation.[157–159] Crucially nucleo-cytoplasmic trafficking may be enhanced in cancer cells with nuclear translocation of gold nanoparticles resultantly more efficient.[160–162]

The permeability characteristics of the nuclear envelope have also been demonstrated to vary during different phases of cellular activity. Diffusion rates across the nuclear envelope of gold nanoparticles stabilised with bovine serum albumin (BSA) for example have been shown to correlate directly with known rates of nuclear pore formation, suggesting greater nuclear permeability during or just after nuclear envelope reformation in cell division.[160] In this study by Feldherr *et al.* it was also found that the nuclei of dividing cells could incorporate larger nanoparticles (23 nm) compared to non-dividing cells (19 nm).[160]

It is of great interest that non-targeted i.e. nanoparticles lacking functionalisation with a specific targeting signal have demonstrated nuclear uptake accompanied by varying

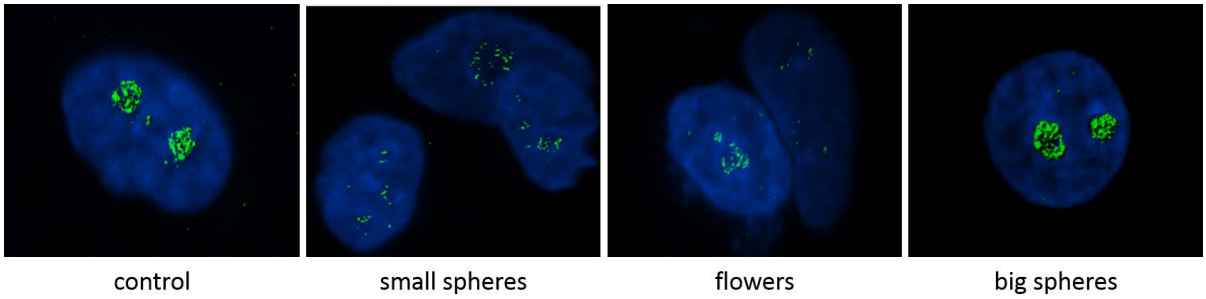

Figure 1.13: Small gold nanospheres and gold nanoflowers inhibit RNA synthesis (green) in the nucleolus of MCF7 breast cancer cells, co-stained with DAPI (blue nuclear stain). (Scale bar 3 μm). Adapted from Kodiha et al.[163]

degrees of toxicity. Gold nanoparticles 3.7 nm in diameter have been shown to accumulate in HeLa cell nuclei with cell viability measured at 85 % after 24 hours and 70 % after 72 hours suggesting a low cytotoxic effect.[164] Gold nanoclusters (Au55) 1.4 nm in size have demonstrated nuclear uptake accompanied with significant toxic effects attributed to the ability of the gold clusters to interact with nuclear DNA. A particularly interesting study performed by Kodiha *et al.* illustrates the complexities of the nuclear uptake mechanisms of nanoparticles.[163] Although Pante *et al.* state that the nuclear pore complex is able to transport macromolecules no greater than 39 nm in size,[165] the study by Kodiha *et al.* observed large gold nanoflowers 40 - 120 nm in size entering the nuclei of breast cancer cells. Nuclear uptake was observed to disrupt nuclear homeostasis via inhibition of RNA synthesis (Figure 1.13).

In summary cellular uptake of gold nanoparticles is achieved through a variety of mechanisms. Whilst nuclear targeting of gold particles is achieved predominantly through the hitherto discussed nuclear localisation signals, non-targeted gold nanoparticles have also demonstrated nuclear uptake. The major restriction on gold nanoparticles in cells is compartmentalisation to endosomal/lysosomal compartments. As nanoparticles are internalised in cells through a variety of mechanisms, including those which are non-endocytotic e.g. passive diffusion, nanoparticles may still find free dispersion in the cytoplasm. Furthermore compartmental release may be promoted by endosomal swelling, possibly as a result of pH dependant aggregation or lipid membrane rupture.[166] Several studies have

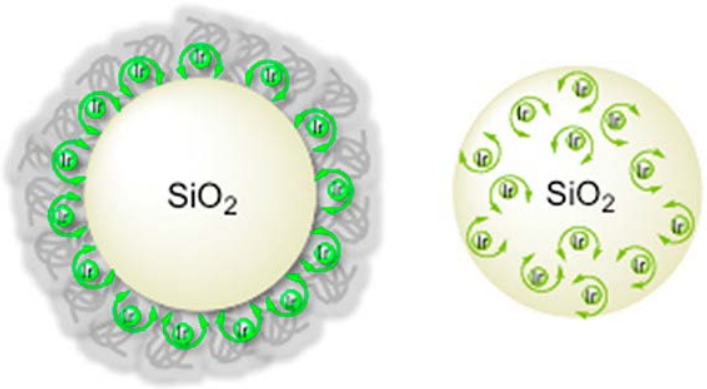

Figure 1.14: Schematic illustrating iridium complexes covalently incorporated at the surface of a preformed 500 nm silica nanoparticle using a fluorinated polymer (left), and encapsulation of the iridium complex within the silica nanoparticle (right). Adapted from Lewis et al.[169]

demonstrated nuclear uptake of nanoparticles much larger than those originally believed to be able to traverse nuclear pore complexes, thus illustrating the complexities of uptake mechanics but also the diverse potential of the therapeutic and imaging applications of gold nanoparticles in cells.

1.3 Silica Nanoparticles for Imaging

The gold nanoparticles discussed hitherto are surface functionalised however nanomaterials can also be engineered to encapsulate lumiphores for imaging applications. One such example are silica nanoparticles which can be synthesised to encapsulate luminescent probes. Wang *et al.* incorporated quantum dots in a silica based nanosphere which was able to measure local pH in a ratiometric fashion.[167] Sung *et al.* also incorporated quantum dots in to porous silica nanoparticles which were able to sense for Cu^{2+} ions.[168] Zhang *et al.* demonstrated surface functionalisation of silica nanoparticles with pairs of DNA strands that "uncap" in the presence of Hg^{2+} ions, releasing a fluorescent dye resulting in a measurable increase in fluorescence signal.

Encapsulation of multiple lumiphores enables a much higher signal intensity compared to single lumiphores. Lewis *et al.* demonstrated this with the caging of luminescent ruthenium(II) tris-bipyridyl in 500 nm diameter colloidal silica nanoparticles.[170] The particles

were used for the analysis of fluid flow in microchannels by exploiting the luminescence from the encapsulated ruthenium. A subsequent study established a method of immobilizing a cyclometalated iridium(III) complex on to the surface of silica nanoparticles using a fluorinated polymer.[169] These particles exhibited better stability than those prepared without the polymer in addition to a seven-fold increase in the luminescence intensity and luminescence lifetime. The surfactant prepared particles were also successfully used in fluid flows for microparticle imaging velocimetry, exploiting the enhanced particle brightness and demonstrating the potential for using the nanoparticles as nanotracers in microchannels. Many such studies have been conducted where the silica nanoparticles have been used as sensors however silica nanoparticles also have great potential in biological applications due to their robustness, mechanical stability, transparency and protection they offer to the encapsulated lumiphore.

One such example in which silica based nanoparticles have found a biological application is in cancer research. Their relatively simple synthesis, uniform and controllable morphology, size and pore volume as well as their easy functionalisation make them well suited as imaging and drug delivery agents.[171–174] The two main types of silica nanoparticles developed for cancer imaging and therapy are the hitherto discussed mesoporous silica nanoparticles[174] and core/shell silica nanoparticles.[173] The unique ability of mesoporous nanoparticles to release encapsulated payloads, not only of fluorescent dyes as discussed in the example above, but also drugs through the surface pores with easily controllable release are of particular relevance in tumour therapy. Core/shell nanoparticles are particularly useful as imaging agents as they are easily doped with flurophores, quantum dots and gold nanoparticles which are protected by the shell structure, thus the imaging signal obtained yields the precise location of the nanoparticle. These properties in addition to the biocompatibility both types of nanoparticles exhibit make them ideally suited theranostic agents.[175,176]

The robust nature of silica nanoparticles has also seen their application in the field of dentistry. Most studies involving silica nanoparticles have involved their development

in resin-based composite technology[177–179] or for caries (tooth decay) prevention as they can be used to polish tooth surfaces to prevent bacterial adhesion.[180] Silica nanoparticles can also be used to address the issue of dentin hypersensitivy, a common dental problem caused by the exposure dentinal tubules.[181,182] It is theorised that external irritation can induce movement of fluid in and out of dentinal tubules, which can stimulate the sensory nerve endings within and lead to hypersensitivity.[183] The stability and ability of the silica nanoparticle to adhere, as a result of surface hydroxyl groups interacting with the dentine surface,[184] has led to their application for the attempted occlusion of dentinal tubules.[185] Their water solubility allows them to be easily deposited into the irregular spaces composing the dentine surface[186] and their large surface area allows for further functionalisation to enhance tubule occlusion.[169,187]

Successful tubule occlusion has been demonstrated by Besinis *et al.* who evaluated the size dependence of the nanoparticles in relation to their tubule occluding ability using electron microscopy.[188] Tian *et al.* also investigated dentinal tubule occlusion with mesoporous silica nanoparticles using electron microscopy, demonstrating almost complete occlusion over 100 μm deep in to the tubule.[189] These results illustrate the great potential for silica based nanomaterials for applications in clinical dentistry.

1.4 Thesis Outline

In the last few decades nanoparticles have attracted considerable research interest. Their variable composition, structure and surface characteristics yield physico-chemical properties that can be finely-tuned for a variety of applications. Functionalised nanomaterials have been afforded use as drug delivery agents, diagnostic sensors, labelling and imaging agents. This thesis details the use of gold and silica particles for applications in imaging, exploring additional capabilities as a result of their specific functionalisation.

Chapter Two details the labelling strategy utilised to attach a luminescent organic dye to gold nanoparticles. This involved development of the Hoechst DNA binding dye to

incorporate a surface-active thiol group for attachment to gold, with the subsequent addition to gold nanoparticles achieved via surfactant and peptide mediation. The resulting luminescent nanoparticles are characterised and explored in cellular imaging applications. Confocal microscopy and transmission electron microscopy in particular enable the uptake and intracellular fate of the nanoparticles to be examined and with evidence of nuclear uptake observed cell cycle dysregulation is also evaluated.

Chapter Three details the cellular imaging of 13 nm and 100 nm gold nanoparticles coated with a luminescent ruthenium complex. The luminescent nanoparticles were produced and characterised by Dr. Nicola Rogers.[77,190] Confocal microscopy of the nanoparticles in cells was performed in collaboration with Dr. Robert Harris (School of Biosciences, University of Birmingham). Transmission electron microscopy and toxicity studies further characterised the cellular interactions of these nanoparticles. The work performed in this chapter contributes to the first appended publication.

Chapter Four examines the use of silica particles for application in dentistry to address the problem of dental hypersensitivity. Specifically the interaction of sub-micron silica particles with dentine is evaluated in the context of their ability to occlude dentinal tubules. Silica particles bearing an encapsulated ruthenium luminescent complex are coated with surfactants and assessed for achieving tubule occlusion via confocal microscopy and scanning electron microscopy. Imaging was performed with Sophie Glinton, Hayley Floyd (EPSRC Doctoral Training Centre for the Physical Sciences of Imaging in the Biomedical Sciences, School of Chemistry, University of Birmingham) in collaboration with Prof. Damien Walmsley (School of Dentistry, University of Birmingham). The work performed in this chapter contributes to the second appended publication.

2 Labelling of Gold Nanoparticles with Thiol Functionalised Hoechst

2.1 Introduction

Nanoparticles possess numerous characteristics that make them ideal imaging agents. Targeting capability can be incorporated in to nanoparticles to offer specificity, many lumiphores can be conjugated to a single nanoparticle producing bright luminescence, lumiphore stability can be enhanced upon nanoparticle conjugation, and the potential for drug delivery mean nanoparticles offer a great theranostic potential.[9–13] Luminescent nanoprobes can be imaging with multiple modalities depending on their composition and can be functionalised to target specific cells and/or tissues, exhibit a sensing ability or to interrogate a range of biomolecular processes.[14–17,77] Gold nanoparticles and quantum dots in particular have been used for a wide range of biochemical and therapeutic applications.[13,17,47,119] Functionalising gold nanoparticles with luminescent probes enables construction of nanoprobes that bear the distinct optical signature of the luminescent agent, independent of the particle properties.[75] Such probes can also exploit the high electron density of gold to offer multimodal imaging and do not suffer from blinking as observed in quantum dots.

2.1.1 Functionalisation of Gold Nanoparticles

A variety of nanomaterials have been developed for imaging applications. For the purposes of luminescent imaging the inherent properties of the nanomaterial can be exploited or imaging moieties incorporated within or on the surface of the nanomaterial.[3–8] Luminescent imaging of gold nanoparticles functionalised with neutral lanthanide lumophores and co-coated with a pH sensitive peptide have demonstrated this concept with selective cell uptake and luminescent imaging of the probe in the intracellular environment.[82] Associating luminescent ruthenium complexes with gold nanoparticles has previously been studied using electrostatic interactions,[191] thiol exchange methods using Brust-type nanoparticles,[192] or by direct reduction of Au^{3+} by $NaBH_4$.[193–195] All of these methods however have their limitations as nanoparticles are restricted to sizes smaller than 10 nm, are relatively polydisperse and offer limited control over the coating of the ruthenium probe.

An alternative coating method has been developed with gold nanoparticles 13 and 100 nm in diameter. The large Au cores of these nanoparticles enable extensive labelling with a ruthenium(II) polypyridyl complex producing a luminescent water soluble gold colloid.[77] Addition of the ruthenium complex was achieved by pre-coating the nanoparticle with Zonyl 7950, a non-ionic fluorinated surfactant, prior to addition of the surface-active ruthenium complex.[77,196] Uptake of the luminescent nanoparticles was investigated in A549 human lung cancer cells and revealed uptake of nanoparticles undergoing interesting biomolecular interactions including nuclear uptake. Such nanoparticles may thus offer significant improvements in sensitivity, selectivity and practicality over conventional diagnostic methods in biological assays for DNA and protein markers.[197] Furthermore exploiting nanoparticle binding with DNA has seen their use in molecular diagnosis, gene therapy and sensing.[198]

Functionalisation of nanoparticles is a crucial step in their design to achieve optimal biological and physico-chemical properties.[199] In addition to luminescence capabilities nanoparticles may also be designed to undergo specific biomolecular interactions. The binding of nanoparticles with DNA in particular must be characterised in the context

of their biocompatibility, as it is of particular relevance in a cellular environment where binding to DNA can have a number of important implications.[200] It is therefore necessary to study such nanoprobes in a cellular environment and to examine their uptake and interactions with cell membranes, organelles and indeed the cell nucleus. The nucleus contains the cells' genetic material, responsible for controlling cellular growth, proliferation and apoptosis and is a particularly desirable target for nanoparticles.[146] After passing through the cellular membrane nanoparticles may achieve nuclear uptake which may be instigated by attaching targeting ligands to the particles, for example with a ligand that exhibits a response to nuclear localisation. This furthermore requires endosomal release of the nanoparticles if internalisation occurs through an endocytotic uptake mechanism.[147]

Gold nanoparticles are particularly suited for cellular uptake and imaging as they can be easily functionalised to aid uptake, for example with peptides, aptamers or antibodies which help in their internalisation and specificity. Their large surface-to-volume ratio also means multiple such ligands can be attached to a single particle. Nanoparticles functionalised with multiple lumiphores can thus exhibit a greater luminescence that single lumiphores alone. Gold nanoparticles are furthermore relatively easily synthesised with good monodispersity.

Functionalisation can be classified as covalent or non-covalent. Covalent methods include the use of -SS, -SH, -OH, -NH_2 or -COOH derivatised moieties. Gold nanoparticles for example can be functionalized with thiolated oligonucleotides to achieve specific DNA hybridization through recognition of complementary sequences of interest.[198] A study by Cima et al. found that the -SH thiol link, most frequently used in biomedical applications for attachment to gold nanoparticles, remains stably adsorbed for up to 35 days in physiological conditions. It is therefore the most commonly used functional group for attachment of biomolecules to gold surface binding for biomedical applications.[201]

The non-specific binding between DNA and nanoparticles can be also achieved by simple adsorption via non-covalent interactions. Gold nanoparticles may be used to achieve DNA binding however it is believed that the electrostatic repulsion between the negatively

charged DNA and the negatively charged surface of citrate-stabilised gold nanoparticles would not be favourable. This is particularly an issue with double-stranded DNA which has a higher surface charge density, and therefore more electrostatic repulsion, than single-stranded-DNA.[202] An obvious and widely used strategy for promoting DNA interaction is functionalising nanoparticles with positively charged organic moieties, exploiting their electrostatic affinity for the negatively charged phosphate backbone of DNA.[197]

2.1.2 Hoechst Organic Dye

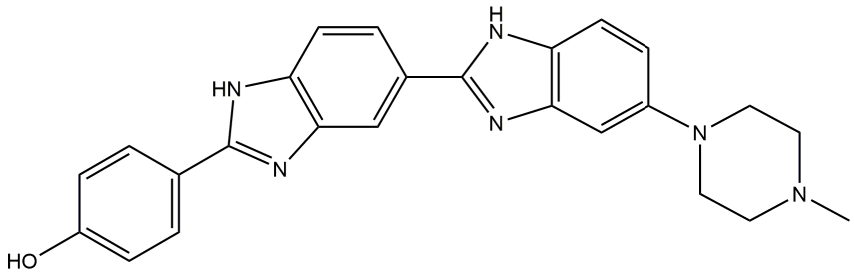

Figure 2.1: Structure of ***Hoechst 33258***

The approach discussed in this chapter to produce luminescent gold nanoparticles which can achieve cellular uptake, involves functionalisation of the **Hoechst 33258** organic dye to achieve surface binding to gold nanoparticles. The **Hoechst 33258** (2-(4-hydroxyphenyl)-5-[5-(4-methylpiperazine-1-yl) benzimidazo-2-yl]-benzimidazole) stain is part of a family of three bis-benzamide dyes developed by Hoechst AG (Figure 2.1). Stains and dyes are frequently used in biomedicine to highlight structures of interest in cells for microscopy. The Hoechst dyes can bind to all nucleic acids but have a preference for sequences rich in adenine and thymine bases and binding to DNA blueshifts and enhances the fluorescence considerably, as shown in Section 2.3.2.

A result of the Hoechst dyes' DNA binding ability in living cells is the suppression of protein synthesis and cell division as binding can interfere with DNA transcription and translation,[203] thus the bis-benzamide family of dye molecules may exhibit further potential as anticancer drugs.[204,205]

2.1.3 Uptake and Imaging of Nanoparticles in Cells

As discussed gold nanoparticles are well-suited to surface functionalisation and courtesy of their water-solubility are biocompatible. They also exhibit a relative lack of toxicity and as such find uses in many biomedical applications[11,13,206] including imaging,[206,207] chemical sensing[208] and nanotheranostics.[19] Numerous studies on gold nanoparticle interaction with cells have also explored their uptake, fate and toxicity.[13,17,78,79,81] The investigations indicate that nanoparticle uptake is affected by several physico-chemical properties, including particle size and surface functionality.[13,15,119,209,210] A host of uptake mechanisms have been suggested and can be broadly categorised as active[102] or passive[103] forms of transport, the latter referring to ATP independant mechanisms not requiring cellular machinery.

The majority of uptake studies have suggested that nanoparticle internalisation is achieved primarily through endocytotic processes.[211–213] Nanoparticles are often found in vesicular structures along various trafficking pathways associated with endocytosis. A schematic illustrating the cellular uptake of nanoparticles and the subsequent intracellular trafficking is shown in Figure 2.2a. A study by Mobius *et al.* examined the morphological characteristics and uptake kinetics of bovine serum albumen (BSA) coated gold nanoparticles in the endocytic pathway of B lymphocytes and further classified the organelles of endocytotic pathway in to several sub-divisions, as depicted schematically in Figure 2.2c, with six different endocytotic organelles identified. Figure 2.2d shows a schematic representation of the endocytic compartments and their internal pH,comprising initial entry → uptake in a trafficking vesicle → transfer in to an early endosome → multivesicular body → late-stage endosome/ lysosome with the associated timescale for each stage.[214,215]

Nanoparticle excretion from cells is also an important aspect in their cellular interaction, particularly in the context of drug-delivery or therapeutic applications where cellular tissue and organ clearance is an important consideration. Nanoparticles may be ejected from cells through three possible pathways namely lysosomal secretion, vesicle and non-vesicle related secretion as depicted schematically in Figure 2.2b.[216]

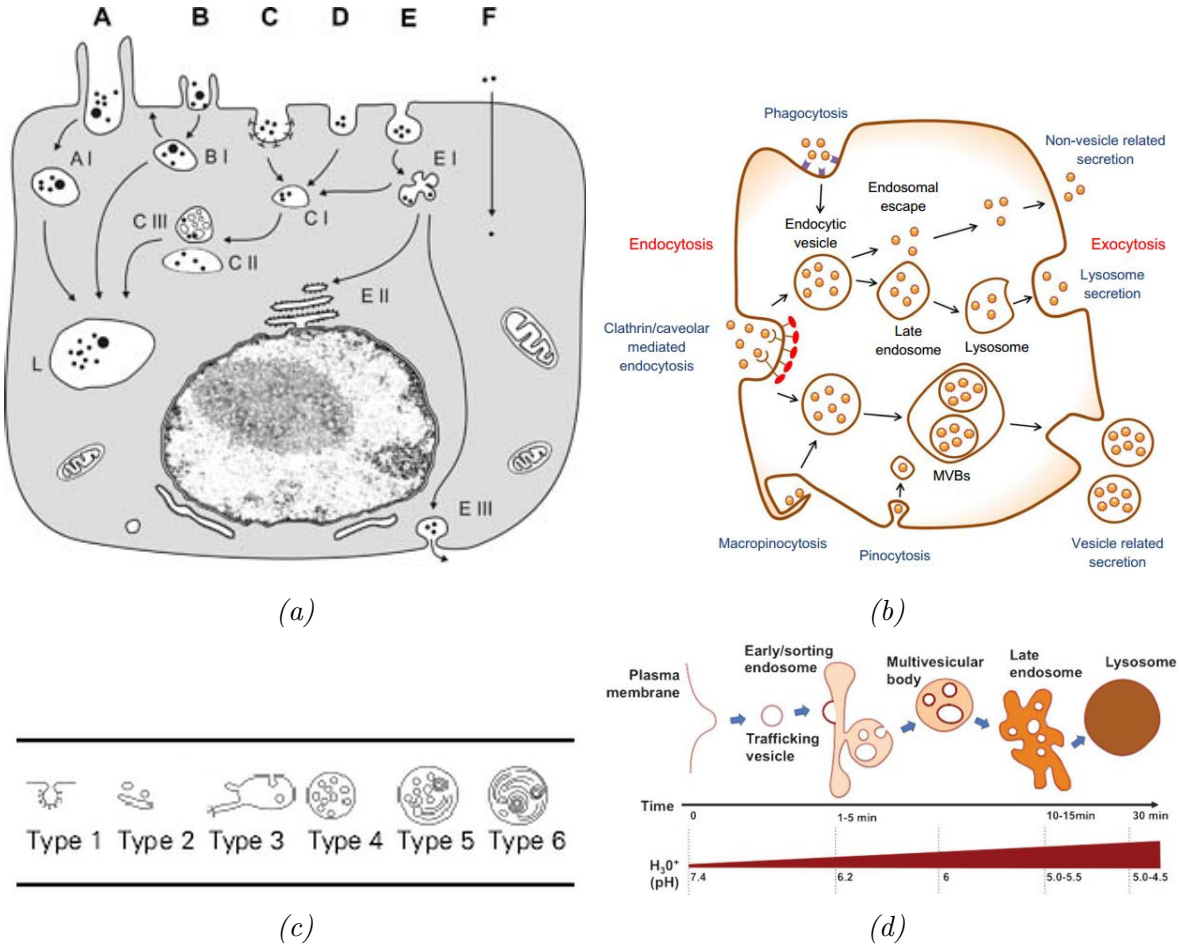

Figure 2.2: (a) Cellular uptake mechanisms of nanoparticles and related intracellular trafficking. A: Phagocytosis - leading to phagosomes (AI) and phago-lysosomes (L). B: Macropinocytosis - leading to macropinosomes (BI) which might be exocytosed or fused with lysosomes (L). C: Clathrin-mediated endocytosis - leading to primary endosomes (CI) and late endosomes (CII)including multivesicular bodies (CIII). D: Clathrin- and caveolae-independent endocytotic pathways. E : Caveolae-mediated endocytosis - leading to caveosomes (EI) which fuse with the endoplasmic reticulum (EII) or translocate through the cell (EIII). F: Particle diffusion/transport through the apical plasma membrane, resulting in particles located freely in the cytosol. Adapted from Brandenberger et al.[217] (b) Schematic of endocytosis and exocytosis mechanisms for nanoparticles. Nanoparticles exit via lysosome secretion, vesicle-related secretion and non-vesicle-related secretion. Adapted from Oh et al.[216] (c) Morphological designations of intracellular compartments in the endocytic pathway. Type 1 - clathrin-coated pits and vesicles, type 2 - vesicular and tubular structures (including primary endocytic vacuoles), type 3 - irregularly shaped MVB with a few internal vesicles, type 4 - globular MVB with abundant internal vesicles, type 5 - an intermediate between the multivesicular (type 4) and the multi-laminar (type 6) vesicles (considered lysosomal in nature), type 6 - multi-laminar vesicle (considered lysosomal in nature). Adapted from Mobius et al.[118] (d) Schematic representation of the endocytic compartments comprising initial entry → uptake in a trafficking vesicle → transfer in to an early endosome → multivesicular body → late-stage endosome/ lysosome with the associated timescale for each stage.,[214] as well as the internal pH of each compartment. Adapted from Canton et al.[131]

It is important to note that many studies can reveal contrasting findings when studying nanoparticle uptake in cells perhaps indicative of the intricate relationship between the physico-chemical properties of the nanoparticle and the internalisation mechanisms. Raynal *et al.* for example showed that iron oxide nanoparticle uptake in macrophages occurred via receptor-mediated endocytosis.[218] Anionic nanoscale micelles were also found to be internalised by the same mechanism in macrophages by Chnari et al.[219,220] Gold nanoparticle uptake in macrophages however was shown to occur through pinocytosis,[221] whilst polystyrene nanoparticles uptake were shown to internalise via an actin-independant mechanism by Geiser *et al.*[222] The actin cytoskeleton is crucial to endocytosis as it is responsible for the membrane protrusions which encompass extracellular entities,[223] hence endocytotic uptake of the polystyrene nanoparticles could be excluded. In the study by Geiser *et al* the polystyrene nanoparticles were found in the macrophage cytoplasm and were thus proposed to have acheived uptake through direct particle diffusion through the cell membrane. Carbon nanotubes were also observed to achieve uptake in HeLa cells in a study by Pantarotto *et al.* in what was referred to as the "needle-effect" where uptake was attributed to the shape and hydrophobic nature of the nanotubes allowing direct physical penetration of the cell membrane.[224]

Surface topology has also been demonstrated to be important factor in uptake. Verma *et al.* studied the uptake of gold nanoparticles coated with self-assembled organic ligand monolayers. It was found that nanoparticles on which there were alternating anionic and hydrophobic groups entered cells via membrane pores, whilst nanoparticles coated with a random distribution of the same surface ligands entered by endocytosis.[105] The consequences of such uptake were nanoparticles free of vesicle restriction with potential access to intracellular proteins, organelles and DNA.[212]

2.1.4 Nanoparticle Uptake and the Cell Cycle

Although nanoparticle related investigations comprise a large field of research many of biological properties of the nanoparticles remain relatively less well understood, one of

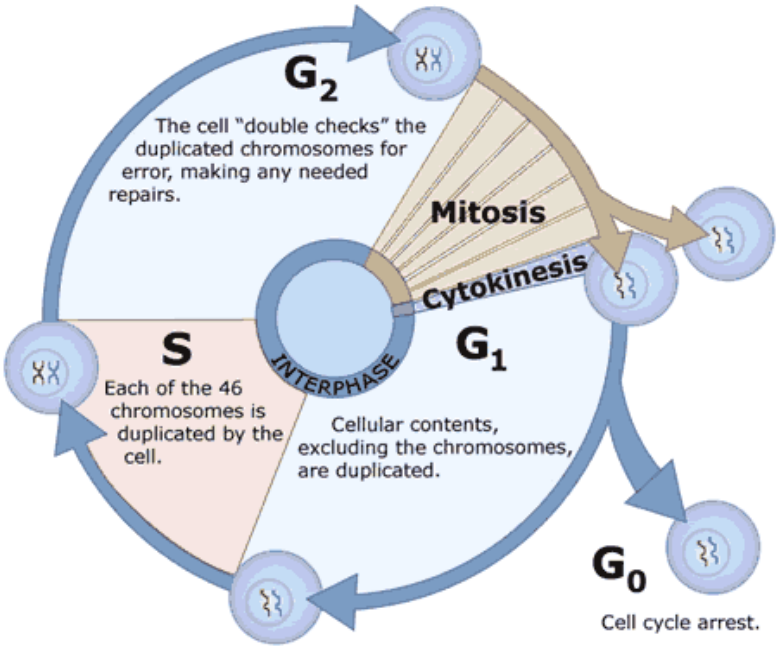

Figure 2.3: Cell cycle in eukaryotes: G1 phase - Cell prepares for division, once it reaches the "restriction point" the cell is committed to division. S phase - genetic material is duplicated. G2 phase - cytoplasmic materials are prepared for division and cytokinesis (the physical process of division). M phase - Nuclear division (mitosis) followed by a cell division (cytokinesis) starting with constriction of the cytoplasm. Interphase - The time period between mitotic divisions (G1, S and G2). (Figure adapted from Clinical Tools Inc.[226])

the most important of which is the effect of nanoparticles on the cell cycle. Nanoparticles can induce a wide range of cellular responses including cell death which is closely linked to the cell cycle.[225] Multiple check points in the cell cycle control the division process and if any of these criteria aren't achieved the cell can undergo necrosis and/or apoptosis with arrest in more or more of the division stages.[200] The method by which nanoparticles induce toxicity is also important in this context in regards to both targeted toxicity in therapy and inadvertent toxicity in diagnostics.

The cell cycle of a cell refers to a chain of events resulting in its duplication and division.[227–229] The cell cycle in eukaryotic cells can be divided in to two periods namely interphase - comprising cell growth and preparation for DNA replication, and mitosis (M phase) - when the cell divides in to two daughter cells (Figure 2.3). Interphase is further split in to three stages; G1 phase when the cell grows and produces the enzymes require for cell division, S phase when DNA undergoes replication and G2 phase when the cell

continues growth and prepares for mitosis. The division process can vary in length from 12 hours to several days depending on the cell type.

Nanoparticles can exhibit many effects on cells following cellular uptake including interaction with chemical signalling pathways and induction of stress, cell cycle dysregulation and apoptosis or necrosis.[230] Examining the cell cycle for changes is of particular importance where nanoparticles are used for delivering anti-proliferative drugs.[231,232] One of the most popular methods for analysing the cell cycle is fluorescent activated cell sorting (FACS). Also known as flow cytometry this technique examines cells in flow thereby allowing fast examination of the properties of large cell populations.[233] For the purposes of cell cycle analysis this technique uses the fact that the DNA content of a cell is closely related to the various stages of the cell cycle. In G0/G1 phase cells will have half the DNA content of cells in G2/M phase, referred to as 2N and 4N amounts of chromasomal DNA. In S-phase, the stage between these two phases, the DNA content is between 2N and 4N (Figure 2.4a). Cells with lower than 2N amounts of chromasomal DNA are cell debris or apoptotic cells which have suffered loss or damage to their chromosomal DNA.

The cells can be stained with a fluorescent dye, the most popular of which is propidium iodide (PI) which binds to the double-stranded nuclear DNA, thus fluorescent signal intensity is directly correlated to the amount of DNA and therefore the stage of the cell cycle (Figure 2.4a).[234] The resulting fluorescence intensity data can be analysed using computer software which applies mathematical models to determine the number of cells in each stage of the cell cycle (Figure 2.4a). The problem of nonspecific binding to double-stranded RNA is avoided by the addition of RNaseA to the propidium iodide staining solution.[234,235] Cell doublets and debris artefacts are also excluded using scatter and fluorescence intensity plots (Figure 2.4b).[236,237]

The effect of nanoparticles on the cell cycle can be ascertained on non-synchronised cells using the FACS protocol. However dysregulation of the cell cycle may potentially be masked by cells' natural distribution in different phases. An alternative approach is therefore to synchronise the cells before nanoparticles are introduced, usually achieved

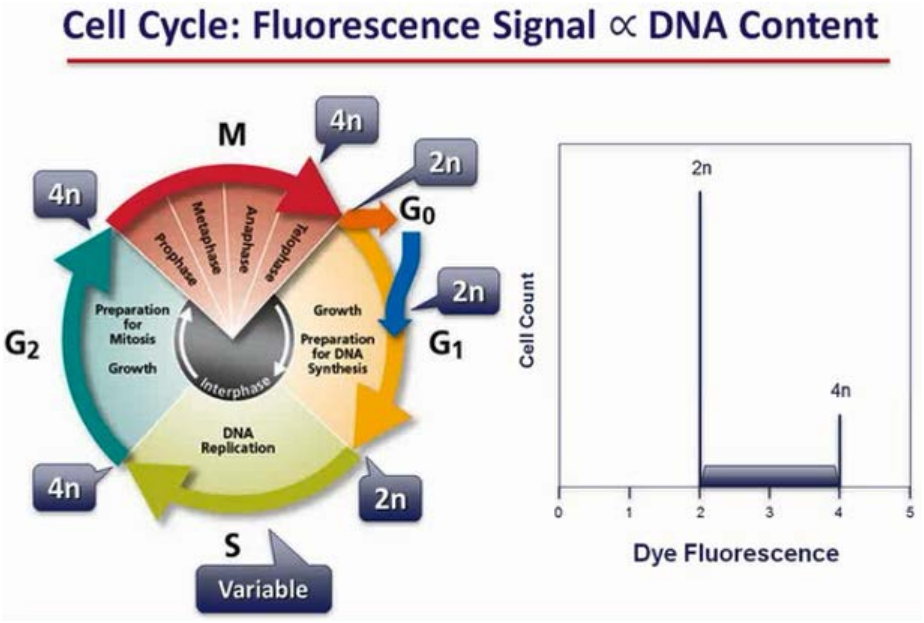

(a)

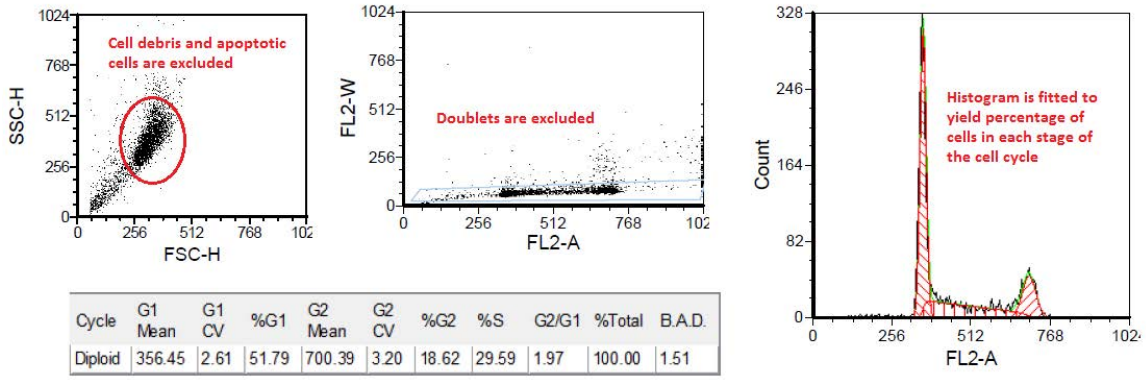

Cycle	G1 Mean	G1 CV	%G1	G2 Mean	G2 CV	%G2	%S	G2/G1	%Total	B.A.D.
Diploid	356.45	2.61	51.79	700.39	3.20	18.62	29.59	1.97	100.00	1.51

(b)

Figure 2.4: (a) Cell cycle schematic showing amount of DNA in a cell at each stage (left) and the theoretical intensity profile that would be obtained (right). Figure adapted from FCS Express Flow Webinar.[238] *(b) Analysis of a typical HeLa cell culture. Cell debris and apoptotic cells (left) and doublets (right) are excluded. The fluorescence intensity histogram is then fitted - the first prominent peak corresponds to G0/G1 phase, followed by the S phase continuum leading up to the second prominent peak corresponding to G2/M phase.*

by removing growth factors from the cell medium to arrest the cells at the desired cell cycle stage. This is followed by reintroduction of the depriving factor to allow the cells to continue through the cycle in a synchronised manner.[239]

Several investigations have indicated that gold nanoparticles can affect the cell cycle. An investigation by Kang *et al.* demonstrated nuclear targeted gold nanoparticles caused cytokinetic arrest in cancer cells inducing apoptosis through failure of complete cell divi-

sion.[150] Although an exact mechanism was not established the study demonstrated that nuclear localised nanoparticles can have specific and significant effects on cellular functioning. It was furthermore proposed that these results demonstrated a novel method by which gold nanoparticles could be used as an anticancer therapy if conjugated to a nuclear-targeting ligand. Furthermore the cytokinetic arrest observed was proposed as being a general consequence of nuclear uptake of the nanoparticles.[150] This is of particular relevance to this chapter which discusses conjugation of the Hoechst DNA binding dye to gold nanoparticles and evaluates uptake of the nanoparticle construct in cells.

In a further study by Kang *et al* it was demonstrated that pre-treating cells with nuclear targeted gold nanoparticles caused an increase in the efficacy of the 5-Fluorouracil chemotherapy drug, with cell arrest observed as an accumulation of cells in the S-phase and depletion of the cells in the G2/M phase.[240] This illustrates how nuclear localised nanoparticles may effect drug efficacy. A further point of interest is the effect of the cell cycle stage on the uptake of nanoparticles.

2.2 Chapter Outline

Luminescent gold nanoparticle constructs for the purposes of imaging are desirable for uptake in cultured cells. The synthesis of a surface-active lumiphore based on the Hoechst 33258 organic dye thiol functionalised to achieve binding to citrate-stabilised gold nanoparticles is initially discussed. Coating of gold nanoparticles with the dye is subsequently explored through surfactant and peptide mediated methods. The colloidal preparations are characterised and their uptake and intracellular interactions explored in two human cancer cell lines. Cells are also evaluated for cell cycle dysregulation in the context of the striking nuclear uptake observed.

2.3 Results and Discussion

2.3.1 Synthesis and Characterisation of HoechstSS

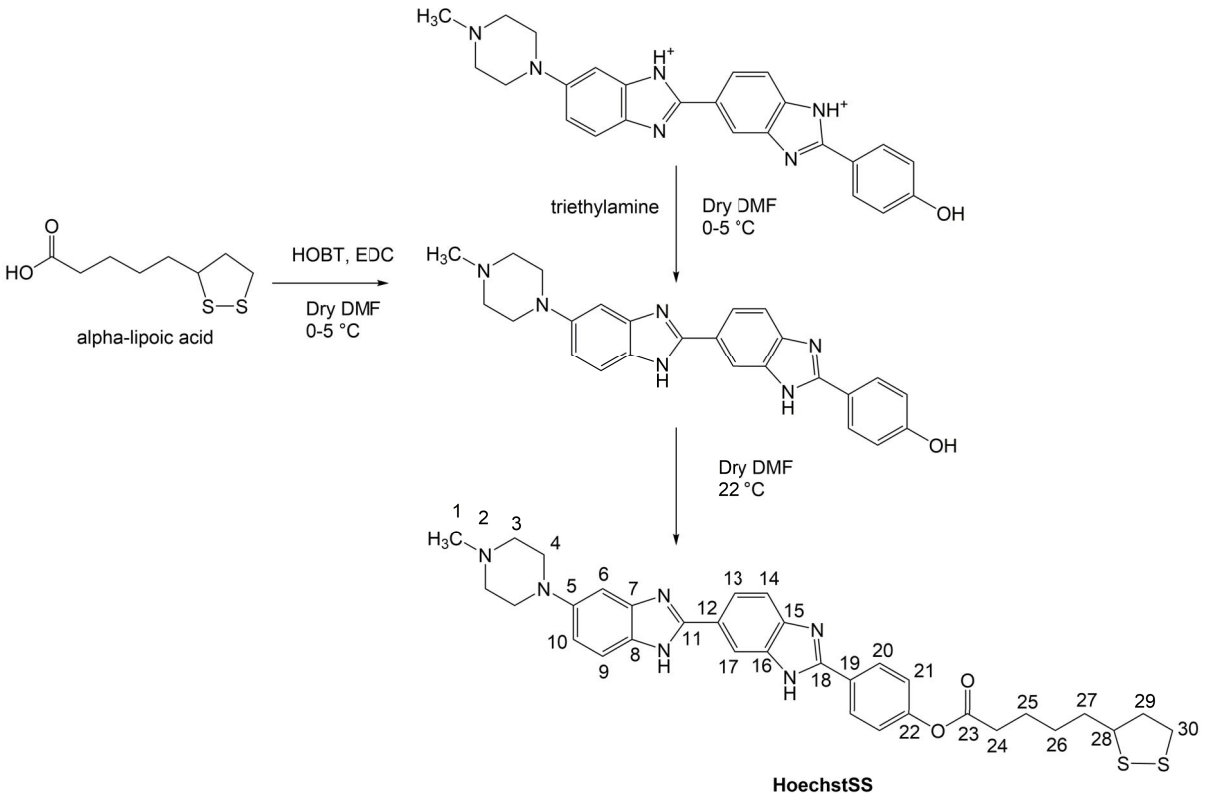

Figure 2.5: Synthesis of the surface-binding HoechstSS (HSS) complex.

The first derivatisation of **Hoechst 33258** incorporates a disulphide group attached to the OH terminal of the **Hoechst 33258** for binding to the gold surface (Figure 2.1). Referred to as **HoechstSS** (**HSS**) this derivative was synthesised by the ester coupling reaction of **Hoechst 33258** with **alpha-lipoic acid** (Figure 2.5). Production of the **HoechstSS** was confirmed by ^{1}H and ^{13}C(^{1}H) NMR spectroscopy and mass spectrometry (Appendix B). Synthesis of **HoechstSS** was performed by the author, with assistance on NMR characterisation provided by Dr. Samuel Adams, School of Chemistry, University of Birmingham.

The **HoechstSS** was however subject to decomposition after purification on a silica column with the product fraction indicating the presence of the **Hoechst 33258** starting material after a few hours as confirmed by NMR and mass spectrometry (Appendix B).

This is possibly due to pH sensitivity and hydrolysis of the ester bond and although column purification was attempted on a neutral alumina column the issue was not rectified. An alternative derivative (**HoechstSH**) was therefore synthesised.

2.3.2 Synthesis and Characterisation of HoechstSH

HoechstSH incorporates a surface-binding thioacetyl group to the OH terminal of the **Hoechst 33258** for binding to the gold surface. The ancillary ligand was synthesised by the Williamson reaction of 6-bromohexene with thioacetic acid (**bromoSAc**) complexed to **Hoechst 33258** by refluxing in DMF (Figure 2.6). Successful production of **HoechstSAc** and **HoechstSH** was confirmed by ^{1}H and ^{13}C pendant NMR spectroscopy and mass spectrometry (Appendix C). Synthesis of **HoechstSH** was performed by the author, with assistance on NMR characterisation provided by Dr. Samuel Adams, School of Chemistry, University of Birmingham.

Solution-based photophysical properties of **Hoechst 33258** have been thoroughly characterised in the literature.[203–205,241] UV-Vis absorption, steady-state luminescence emission and excitation spectra and characterisation of Hoechst 33258 are provided in Appendix A (Figures A1-6) for convenience. When attached to citrate-stabilised gold nanoparticles the **HoechstSS** and **HoechstSAc** complexes are exposed to an aqueous environment, hence the photophysical properties of both are measured in water. Table 2.1 summarises the UV-Vis absorbance, excitation and emission maxima of the **Hoechst 33258** and the two surface-binding derivatives **HoechstSS** and **HoechstSH**. Further photophysical data is provided in Appendix D (Figure D1).

2.3.3 Surfactant Modification of Gold Nanoparticles

Synthesis of 13 nm Gold Nanoparticles

There are a number of ways of synthesizing both spherical and non-spherical metal nanoparticles consisting of top-down[66] and bottom-up approaches.[242] An example of

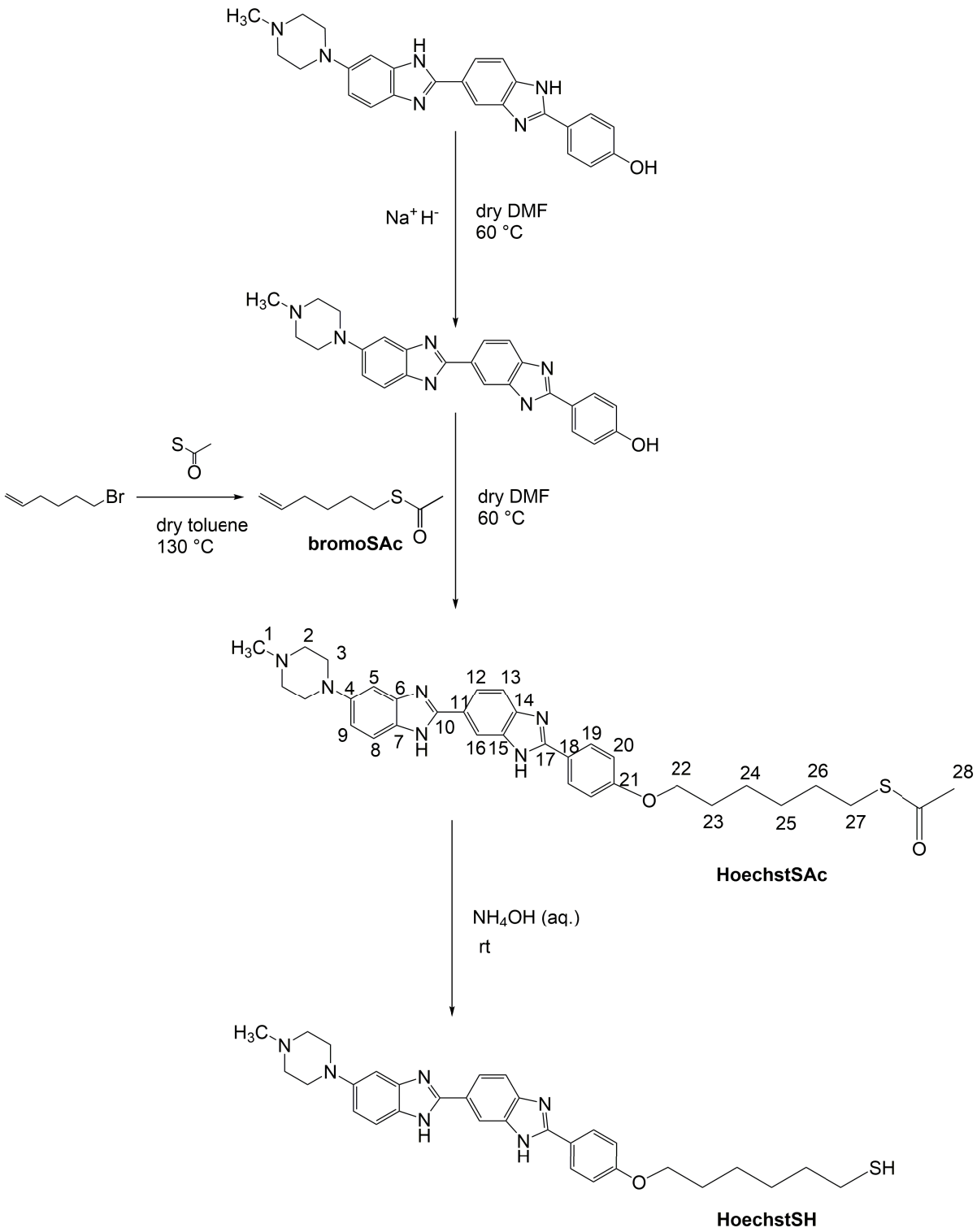

*Figure 2.6: Synthesis of the surface-binding **HoechstSH** complex.*

	λ_{abs}/ nm	λ_{exc}/ nm	λ_{emm}/ nm
Hoechst 33258	263, 342	263, 345	505
HoechstSS	258, 338	264, 345	509
HoechstSAc	258, 340	264, 345	486

Table 2.1: Summary of the photophysical properties of ***Hoechst 33258****,* ***HoechstSS*** *and* ***HoechstSH*** *in water (1 μM). (λ_{exc} = 350 nm, λ_{em} = 500 nm) (Errors are approximated as ±1 nm*

a bottom-up approach is to produce metal nanoparticles by the reduction of the metal ion from its salt in the presence of a suitable stabilising agent. The commonly used approach for the production of aqueous gold nanoparticles involves the citrate reduction of $HAu^{3+}Cl_4$, in which the Au^{3+} is reduced to Au^0.[209] In this method the gold nanoparticles are surrounded by a layer of citrate ions, chloride ions and cations. The Coulombic repulsion between these capping layers stabilises the nanoparticles from coalescing due to van der Waals attractions between metal centres.[243] Gold nanoparticles (AuNP) were produced according to Grabar *et al.*[244] using a method originally developed by Turkevitch in 1951.[52] This preparation is highly reproducible and gives a narrow size distribution, 13±1.7 nm as measured by Transmission Electron Microscopy (TEM) analysis of 100 nanoparticles.[244] Due to it's facile nature and reproducibility, this method of nanoparticle synthesis has been employed by the Pikramenou research group several times for a range of applications.[76,77,82,196,245]

13 nm citrate-stabilised gold nanoparticles were thus synthesised by the reduction of the Au^{3+} salt ($HAuCl_4$).[244] After dissolving the gold salt in water, the trisodium citrate is added whilst the solution is rapidly stirred, reducing the Au^{3+} ions to form neutral gold atoms. As their concentration rises and the solution exceeds saturation, sub-nanometer particles begin to precipitate and the nanoparticles form via a nucleation process with the remaining gold atoms. Providing the solution is stirred vigorously the particles formed will be uniform in size and electrostatically stabilised by citrate ions, thus the trisodium citrate acts as a capping and reducing agent (Figure 2.7).

Using the concentration of the Au^{3+} used and assuming all ions form nanoparticles,

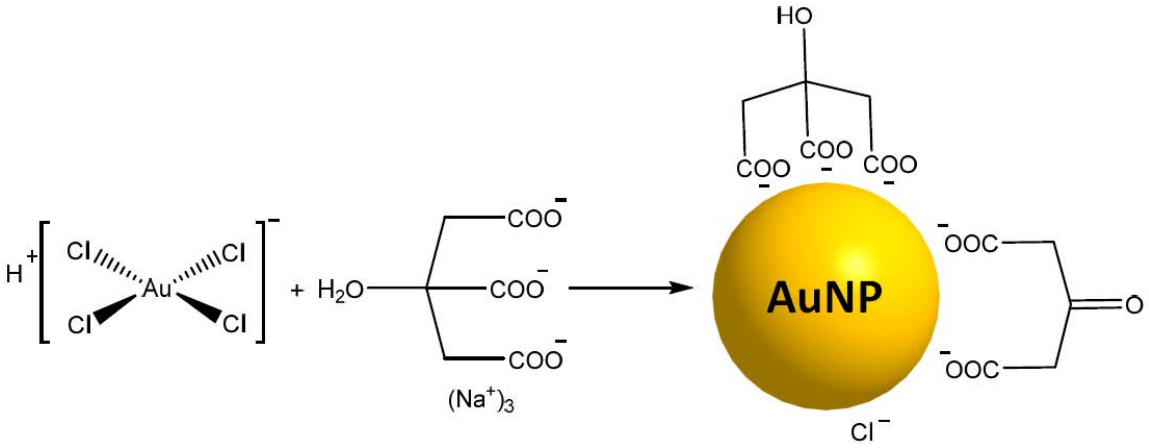

Figure 2.7: Synthesis of 13 nm citrate-stabilised gold nanoparticles.

the concentration of the aqueous colloid produced is estimated at 9 nM (Appendix E.1). The nanoparticles were characterised by UV-Vis absorption spectroscopy, TEM, dynamic light scattering (DLS), and electrophoretic light scatting (zeta potential) measurements. Data are presented in Appendix E.

The UV-Vis absorption of the 9 nM citrate-coated gold nanoparticles exhibit the characteristic SPR peak at 520 nm. DLS sizing of the nanoparticles gives an average intensity distribution of 28±14 nm and an average number distribution of 12 ±4 nm. An interesting observation is the scattering intensity contribution from aggregates several hundred nanometers in size. They contribute 10 % of the intensity distribution but are not evident in the number distribution. This can be explained using Rayleigh's approximation which states that the scattering intensity from a particle is proportional to the sixth power of its diameter, thus larger particles scatter much more than smaller particles.[246,247] When the intensity distribution is converted in to a number distribution this factor is accounted for and it is apparent that these aggregates, although contributing an appreciable scattering intensity, are negligible in quantity.

The nanoparticles possess a zeta potential of -34±2 measured in water at a 1 nM concentration. The zeta potential is measured by performing electrophoresis on the sample and measuring the velocity of the particles using Laser Doppler Velocimetry. Thus the electrophoretic mobility of the sample can be determined by applying the Henry equa-

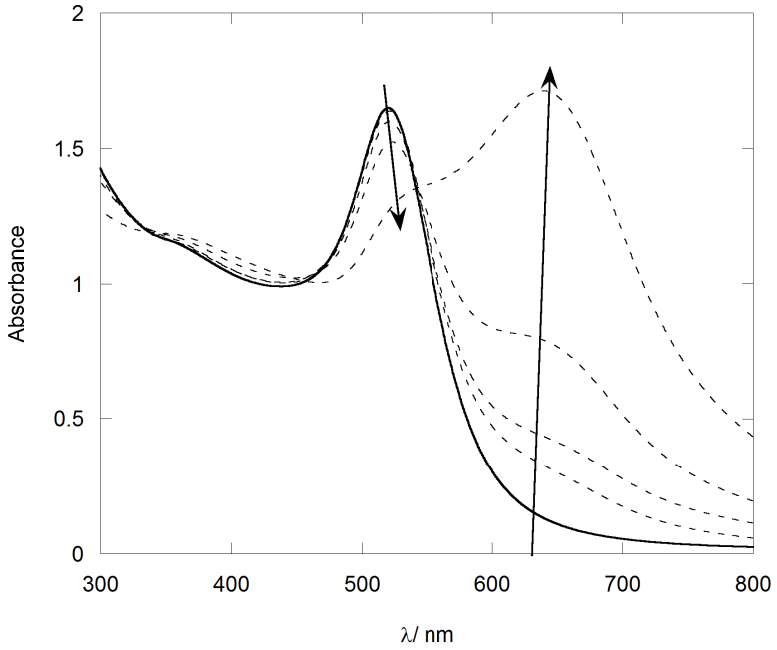

(a)

Figure 2.8: UV-Vis absorption spectra of citrate gold nanoparticles (3 ml, 4.5 nM) (bold) with the addition of 1-25 µl ***HoechstSH*** *[0.6 mM, MeOH] (dashed lines). (****HoechstSH*** *achieves a final concentration of 5 µM.)*

tion.[248] The greater the magnitude of this potential, either positive or negative, in a colloid gives an indication of its stability, where we define a colloid as a system in which one of the three states of matter is finely dispersed in another. In this case the solid nanoparticles are finely dispersed in liquid water. A large negative or positive zeta potential means that colloidal particles will repel each other. The gold colloid possesses a zeta potential of -34±2 mV which is significant enough to stabilise the nanoparticles against aggregation.

Direct Addition of HoechstSH to Gold Nanoparticles

Direct addition of the **HoechstSH** to 13 nm citrate-stabilised gold nanoparticles was initially attempted and monitored by UV-Vis absorption spectroscopy (Figure 2.8). An addition of the **HoechstSH** up to a final concentration of 5 μM was however unsuccessful with the prompt formation of a new SPR band in the UV-Vis spectrum between 600 - 800 nm.

The emergence of the new SPR band occurs upon the first 1 μl addition of the **HoechstSH**, suggesting plasmon coupling between agglomerating nanoparticles and particle flocculation.[57] This corresponds to a gold nanoparticle concentration of 4.5 nM and a dye concentration of 0.2 μM. The new SPR band eventually convolves with the SPR of the 13 nm gold nanoparticles, resulting in a red-shift and a broadening of the convoluted SPR.[57,249]

Previous work in the group includes the successful addition of neutral lanthanide complexes to citrate-stabilised gold nanoparticles without the problem of particle flocculation.[75,82] This is possible because the citrate-stabilised nanoparticles are stable due to the negative electrostatic repulsion between the citrate coating, and the addition of a neutral complex to the nanoparticles causes no electrostatic peturbation. Upon addition and binding of the **HoechstSH** to the surface of a nanoparticle however, its positive charge attracts neighbouring negatively charged partially-coated nanoparticles, leading to their flocculation. Coupled with the displacement of the electrostatically stabilising citrate anions from the gold surface this eventually causes the aggregation of the particles. This is confirmed by visual inspection of the colloid with a colour change from red to blue accompanied by sedimentation of gold aggregates.

Surfactant-mediated Labelling of Gold Nanoparticles with HoechstSH

An alternative strategy to attach the **HoechstSH** complex to citrate-stabilised gold nanoparticles was thus required to circumvent the issue of aggregation. One method of achieving this is through surface modification where the surfactant is added to displace the negative citrate layer on the nanoparticle surface, thus sterically/electrostatically stabilising the particles prior to addition of a cationic complex. Such a method was previously employed by Aslan *et al.* to coat citrate-stabilised gold nanoparticles with peptide nucleic acid.[249]

A study evaluating two commercially available surfactants, Tween 20 and Zonyl 7950, as pre-coating moieties to enable subsequent attachment of a cationic complex to citrate-

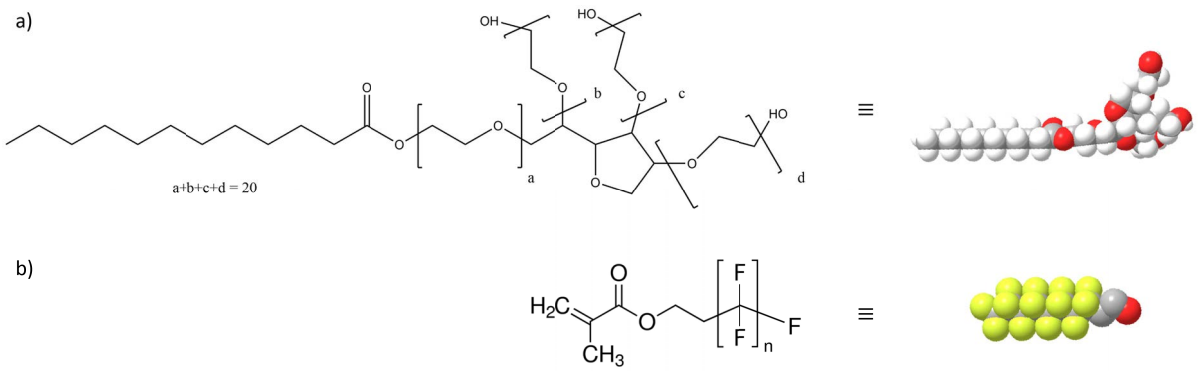

Figure 2.9: Structures of (a) ***Tween 20*** *and (b)* ***Zonyl 7950***

stabilised gold nanoparticles was performed by Dr. N. J. Rogers.[190] The nonionic surfactant polyoxyethylene (20) sorbitan monolaurate (**Tween 20**) has four hydrophilic polyethylene oxide chains and a single aliphatic chain (Figure 2.9).

The **Zonyl 7950** is a fluorosurfactant with a hydrophilic methyl-methacrylate headgroup an a hydrophobic perfluorinate alkyl chain (Figure 2.9). Both surfactants were titrated into the gold colloid which was monitored by UV-Vis absorption spectroscopy with each addition of the surfactant to the gold nanoparticles accompanied by an SPR shift.

For the purposes of attaching the **HoechstSH** to gold nanoparticles a similar method was employed and monitored by UV-Vis absorption spectroscopy to ensure the surfactant-mediated approach was possible across multiple nanoparticle preparations. A schematic of the surfactant-coated nanoparticle constructs is shown in Figure 2.10. UV-Vis spectra monitoring the addition of 1.5 ml Tween 20 [1.2 mM] to 1.5 ml (9 nM) 13 nm citrate-stabilised gold nanoparticles (**Au13-T20**), and the addition of 1.5 μl (1 mg ml^{-1}) **Zonyl 7950** to 3 ml (4.5 nM) 13 nm citrate gold nanoparticles (**Au13-Z**) are shown in Figure 2.11. Addition of the **Tween 20** and the **Zonyl 7950** produced a 5 nm and 1 nm bathochromic shift to the SPR of the gold nanoparticles respectively. This is due to the absorption of the surfactant to the gold nanoparticles which modifies their surface dielectric constant.[68,75]

Further characterisation on the surfactant-coated nanoparticles was performed with

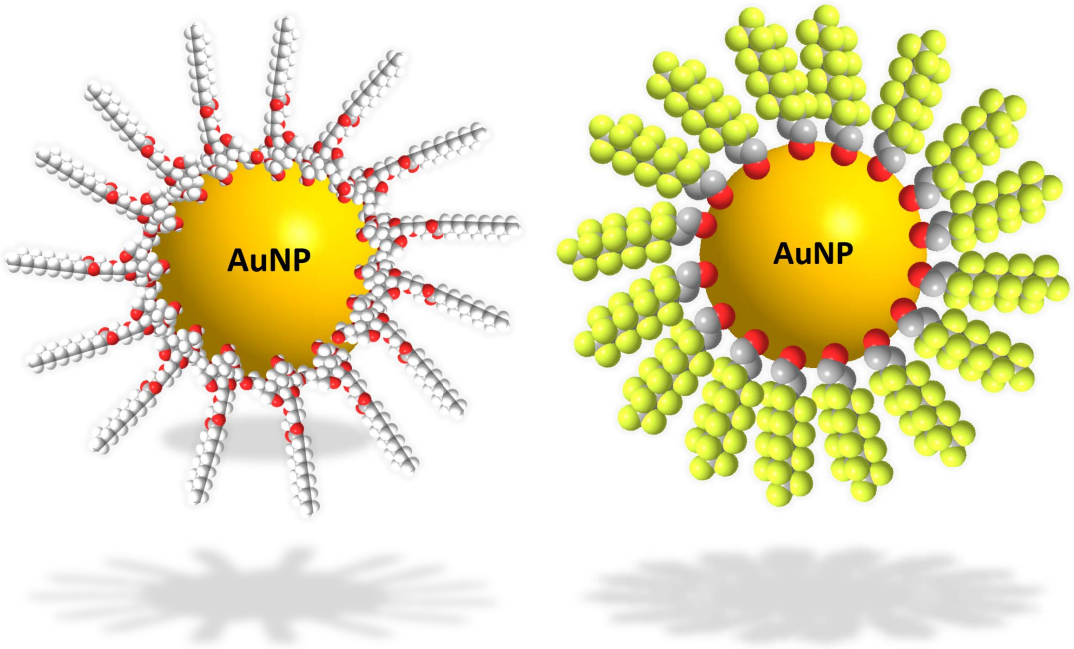

(a) *(b)*

Figure 2.10: Schematics of 13 nm gold nanoparticles coated with (a) Tween 20 and (b) Zonyl 7950.

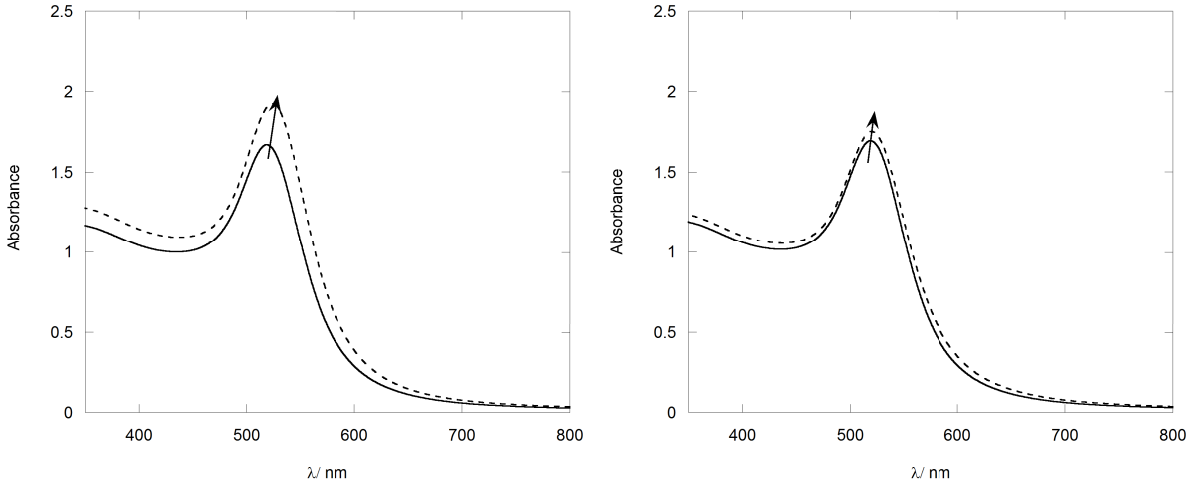

(a) Addition of Tween 20 *(b) Addition of Zonyl 7950*

Figure 2.11: UV-Vis absorption spectra of the addition of (a) 1.5 ml (1.2 mM) Tween 20 and (b) 1.5 µl (1 mg ml^{-1}) Zonyl 7950 (dashed line) to 9.0 nM and 4.5 nM 13 nm citrate-stabilised gold nanoparticles respectively (solid line).

Particle Coating	Citrate	Tween 20	Zonyl 7950
DLS Intensity Distribution/ nm	28±14	43±22	34±13
DLS Number Distribution/ nm	12±4	17±5	18±5
Zeta Potential/ mV	-34±2	-16±5	-69±3
PDI	0.153	0.243	0.157

*Table 2.2: Summary of the DLS intensity, DLS number and zeta potential measurements of 13 nm gold nanoparticles coated with Tween 20 (**Au13-T20**) and Zonyl 7950 (**Au13-Z**). All errors are quoted as ±1 SD.*

DLS and zeta potential measurements to afford the hydrodynamic radii and the magnitude of the electrostatic charge between particle (Figure 2.12). Prior to uniform dilution to 1 nM for DLS and zeta potential measurements, **Au13-T20** and **Au13-Z** were isolated to remove excess/unbound surfactant by size-exclusion chromatography.

The addition of the **Tween 20** and **Zonyl** increased the hydroynamic radii with respect to the citrate-stabilised gold nanoparticles, indicative of the surfactant coating adding steric bulk to the nanoparticles and slowing down their diffusion in solution (Figure 2.12). Data are summarised in Table 2.2.

The citrate-stabilised gold nanoparticles exhibited a zeta potential of -34±2 mV which changed to -16±5 mV upon addition of the neutral Tween 20 surfactant, indicating the negatively charged citrate ions on the nanoparticle surface are being displaced by the Tween 20 surfactant. Interestingly immediate aggregation is not induced by the reduction in surface charge, as illustrated by the DLS data which exhibits intensity and number distribution peaks of 43±22 and 17±5 nm respectively. The addition of the Zonyl 7950 caused a decrease in the zeta potential to -69±3 mV. Although the Zonyl 7950 is itself neutral, the decrease in the zeta potential was attributed to the perfluorinated alkyl chain of the molecule (Figure 2.9). These chains consist of multiple polarised C-F bonds are assumed to present negative charges on the outer surface of the hydrodynamic radii of the particles.[169] Following the production of stable surfactant-coated nanoparticles, **Au13-T20** and **Au13-Z** were investigated as scaffolds for the addition of the thiolated **HoechstSH**. It must be noted here that an attempt was made to functionalise the sur-

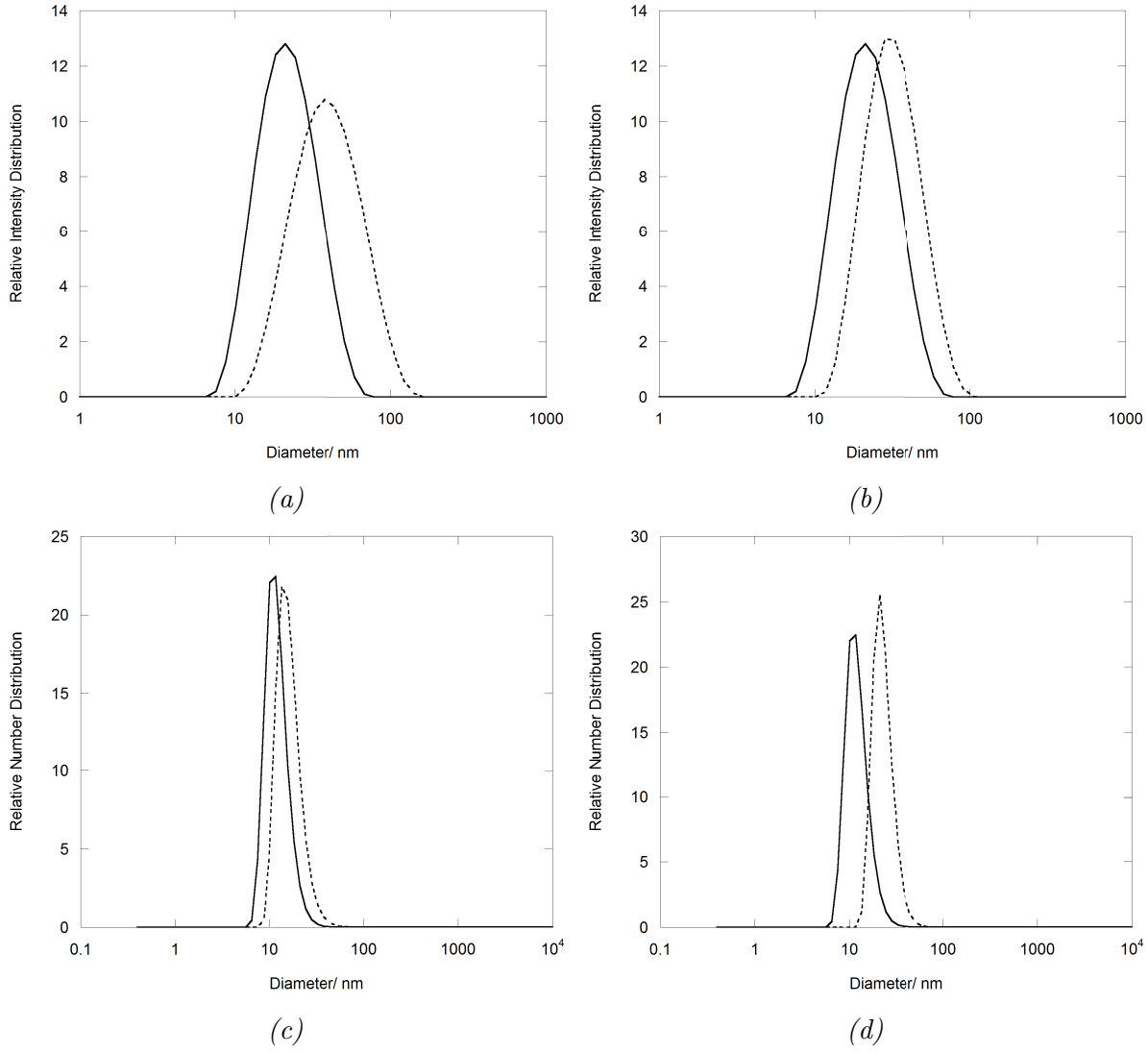

Figure 2.12: DLS intensity (a, b) and number distributions (c, d) of citrate-stabilised gold nanoparticles (solid line) coated with (a, c) Tween 20 and (b, d) with Zonyl 7950 (dashed lines). Gold nanoparticles were diluted to 1 nM for DLS measurements following purification by size-exclusion chromatography and centrifugation respectively.

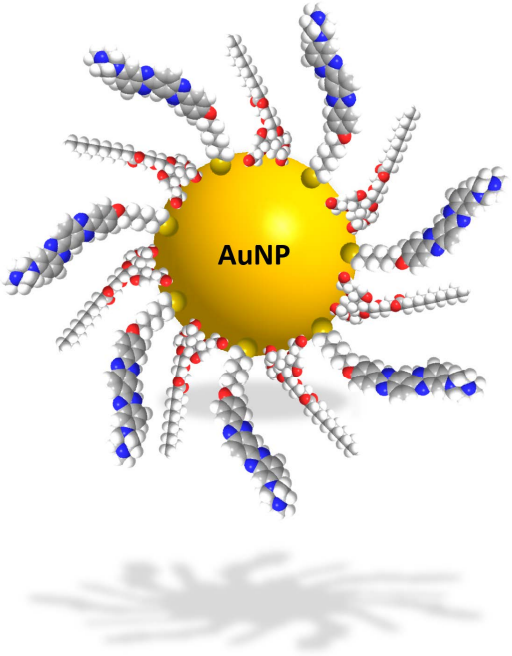

*Figure 2.13: Schematic of **Au13-T20-HSH** nanoparticle construct.*

factant coated gold nanoparticles with **HoechstSS**. The resulting colloid was relatively unstable with aggregates of gold nanoparticles visible within a few hours of the addition of the **HoechstSS**. This is most likely a result of the impurities remaining from the synthesis. As such the **HoechstSH** was utilised as the sole thiolated Hoechst derivative for addition to gold nanoparticles.

Synthesis and Characterisation of Au13-T20-HSH

The **Tween 20** coated gold nanoparticles were investigated as a scaffold for the addition of the **HoechstSH** complex. Titration of the **HoechstSH** into the Tween 20 coated gold nanoparticles was monitored by UV-Vis absorption spectroscopy and caused a 1 nm redshift in the SPR λ_{max} of the gold nanoparticles, as determined computationally by the UV-Vis SPR Analyser (Appendix J.1). The redshift was also accompanied by the emergence of the Hoechst absorption band at 350 nm (Figure 2.14). The redshift is observed in Figure 2.14b which exhibits a plot of the SPR λ_{max} as a function of the molar concentration of the **HoechstSH** added.

It is interesting to note that the increase in the SPR is not linear. The SPR stays

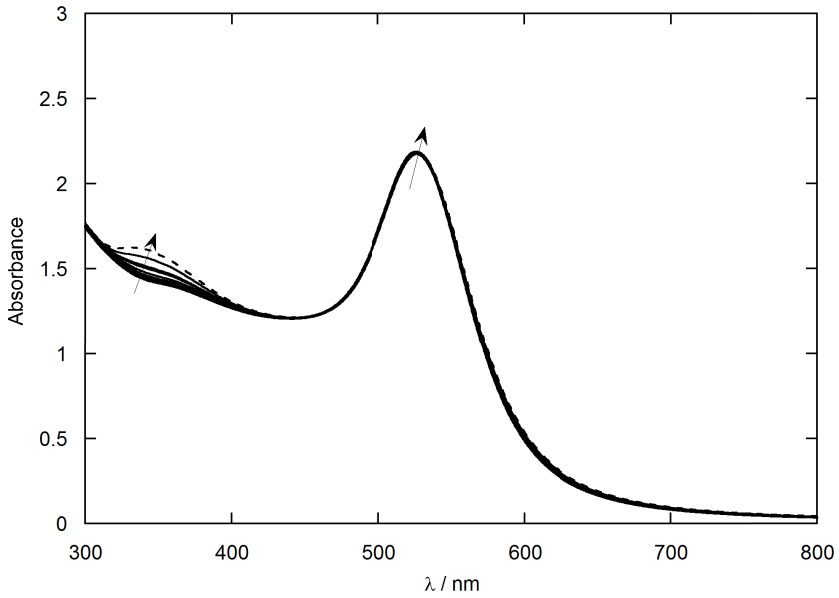

(a)

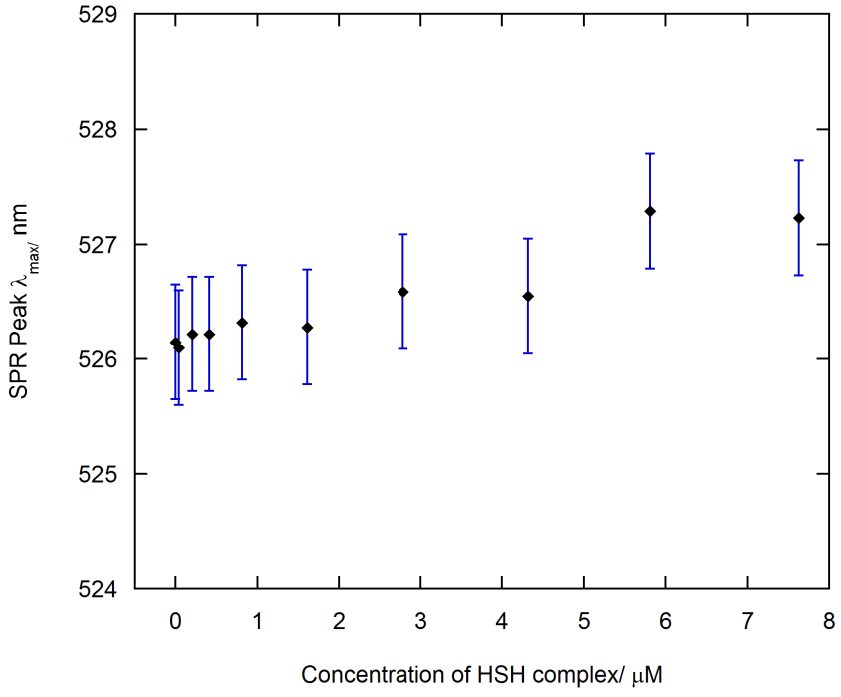

(b)

Figure 2.14: (a) UV-Vis absorption spectra of 13 nm Tween 20 coated gold nanoparticles (3 ml, 4.5 nM) (black) and the addition of 0.04-8 μM (1-200 μl) ***HoechstSH*** *(dashed line). (b) Corresponding plot monitoring the change in SPR λ_{max} during the titration as a function of the concentration of* ***HoechstSH*** *added. (Error bars are applied according to variations in the computational fitting method used to determine SPR maxima (Appendix J.1).)*

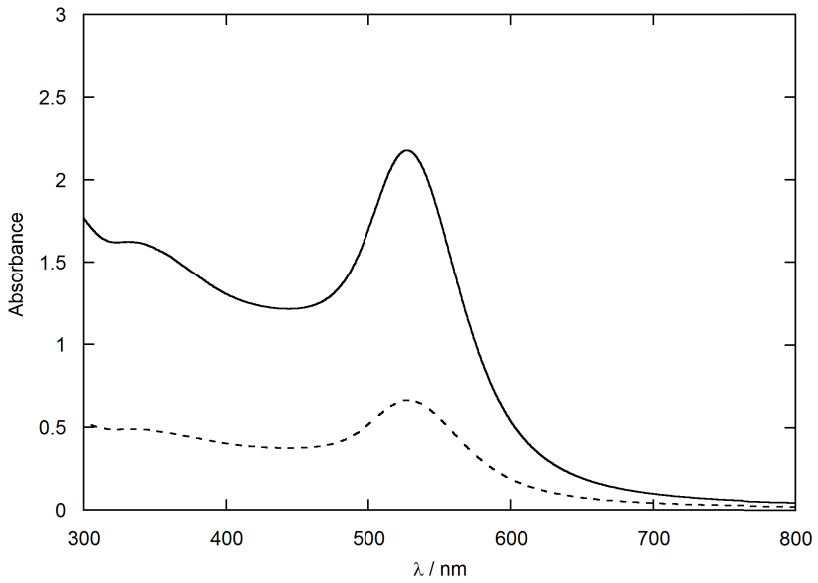

*Figure 2.15: UV-Vis absorption spectra of 13 nm HoechstSH coated Tween 20 coated gold nanoparticles (**Au13-T20-HSH**) before (solid line) and after (dashed line) purification by size-exclusion chromatography.*

below 527 nm following the addition of 4.3 μM **HoechstSH** with a shift from 526.1 nm to 526.5 nm. A rather more abrupt shift is then observed following the next titration point, corresponding to a further 150 μl addition of the **HoechstSH** (to achieve a dye concentration of 7.63 μM) with the SPR shifting to 527.3 nm. This is suggestive of a secondary binding event and that a 4.3 μM addition of **HoechstSH** is enough to achieve maximal surface coverage on the nanoparticles by displacing some of the adsorbed neutral **Tween 20**. Further addition of the **HoechstSH** complex beyond this point may then be in excess. A further important observation is the lack of SPR broadening or emergence of a new SPR band other than the gold nanoparticle band (520 - 527 nm), indicating the nanoparticles are not flocculating and/or aggregating and the colloid is stable.

Purification of the **HoechstSH** coated **Au13-T20** to remove unbound **HoechstSH** was attempted by centrifugation. Following resuspension of the nanoparticle pellet the particles immediately aggregated and sedimented out of solution. Size-exclusion chromatography on superfine Sephadex G-25 was therefore again utilised, affording**Au13-**

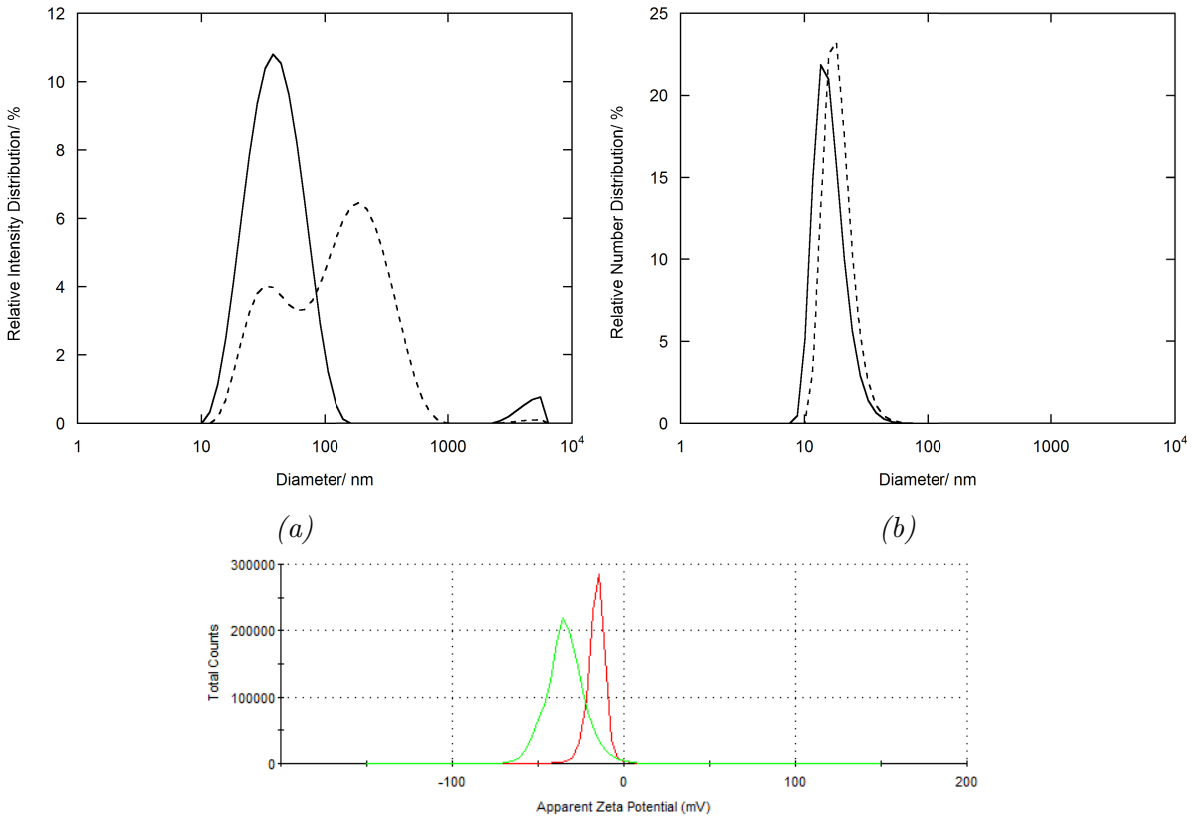

Figure 2.16: (a) DLS intensity distributions and (b) DLS number distributions of ***Au13-T20*** *(solid line) and* ***Au13-T20-HSH*** *(dashed line). (c) Zeta potential distribution of* ***Au13-T20*** *(green) and* ***Au13-T20-HSH*** *(red). (Nanoparticles are diluted to 1 nM for DLS and zeta measurements).*

T20-HSH (Figure 2.15). A schematic of isolated **Au13-T20-HSH** is shown in Figure 2.13.

To estimate the amount of **HoechstSH** remaining on the nanoparticles following column purification, the UV-Vis spectrum of the **Au13-T20** was subtracted from UV-Vis spectrum of the **Au13-T20-HSH** before and after column purification. By integrating the area under the resulting curves and taking the ratio of the quantity of the resultant area, the amount of **HoechstSH** remaining can be estimated. This is possible as a known quantity is added prior to purification. Performing these calculations on the UV-Vis spectra between 300 - 450 nm, corresponding to the **HoechstSH** absorption, indicates a 6.7 μM concentration of **HoechstSH** remaining in the nanoparticle colloid, a reduction from a 7.63 μM concentration prior to purification. With a gold nanoparticle concentration of 4.5 nM this corresponds to approximately 1400 **HoechstSH** complexes per nanoparticle.

The zeta potential of the **Au13-T20** changes to -34±1 mV following addition of the **HoechstSH** and isolation following size-exclusion chromatography (Figure 2.16c). This is a decrease from the zeta potential of **Au13-T20** (-16±5). The DLS intensity distribution increases from 43±22 (97%), 4506±877, (3%) for the **Au13-T20** to 207 ±127 (70%), 36±13 (30%) for the **Au13-T20-HSH**, indicating the presence of flocculates (Figure 2.16a). The number distribution of the **Au13-T20-HSH** gives a single peak of 19±6 nm, an increase from the 17±5 nm of the **Au13-T20** (Figure 2.16b)indicating that the large flocculates observed in the intensity distribution are negligible in quantity.

Synthesis and Characterisation of Au13-Z-HSH

The Zonyl 7950 coated gold nanoparticles were also investigated as a scaffold for the addition of the **HoechstSH** complex. Citrate-coated 13 nm gold nanoparticles were synthesised and coated with **Zonyl 7950** as previously described, with the addition of 1.5 μl (1 mg ml^{-1}) **Zonyl 7950** to 3 ml (4.5 nM) of the nanoparticles. The nanoparticles exhibited a 1 nm redshift in the λ_{max} from 518 nm to 519 nm following centrifugation (Figure 2.18a). The **HoechstSH** complex was then titrated in to the Zonyl 7950 coated

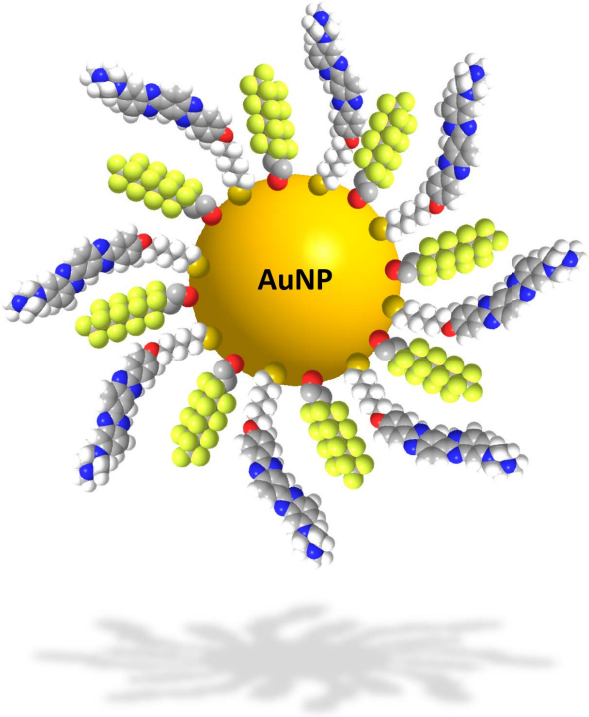

*Figure 2.17: Schematic of **Au13-Z-HSH** nanoparticle construct.*

nanoparticles up to a final **HoechstSH** concentration of 38 μM in the gold colloid (Figure 2.18c).

Addition of **HoechstSH** induces a redshift in the SPR accompanied by an increase in the absorption peak of the **HoechstSH** at 350 nm. The SPR can also be observed to broaden during the titration however there is no emergence of a secondary peak in the absorption profile in the 600 nm region to suggest nanoparticle flocculation/aggregation. To further analyse the addition of the **HoechstSH** with respect to the SPR shift and SPR broadening, the SPR λ_{max} was again determined using the computational SPR analyser. SPR broadening was quantified by fitting the SPR with a Gaussian curve and determining its full-width at half-maximum (FWHM) (Appendix J.1). Results of the analysis are exhibited in Figure 2.18c.

Figure 2.18c shows that the FWHM does not go under any significant change up to an addition of 10 μM **HoechstSH** whilst the SPR increases by approximately 1.5 nm. After this point in the titration the FWHM increases at a constant rate from 90 to 97 nm accompanied by an increase in the SPR from 520.5 nm to 526 nm. Although no

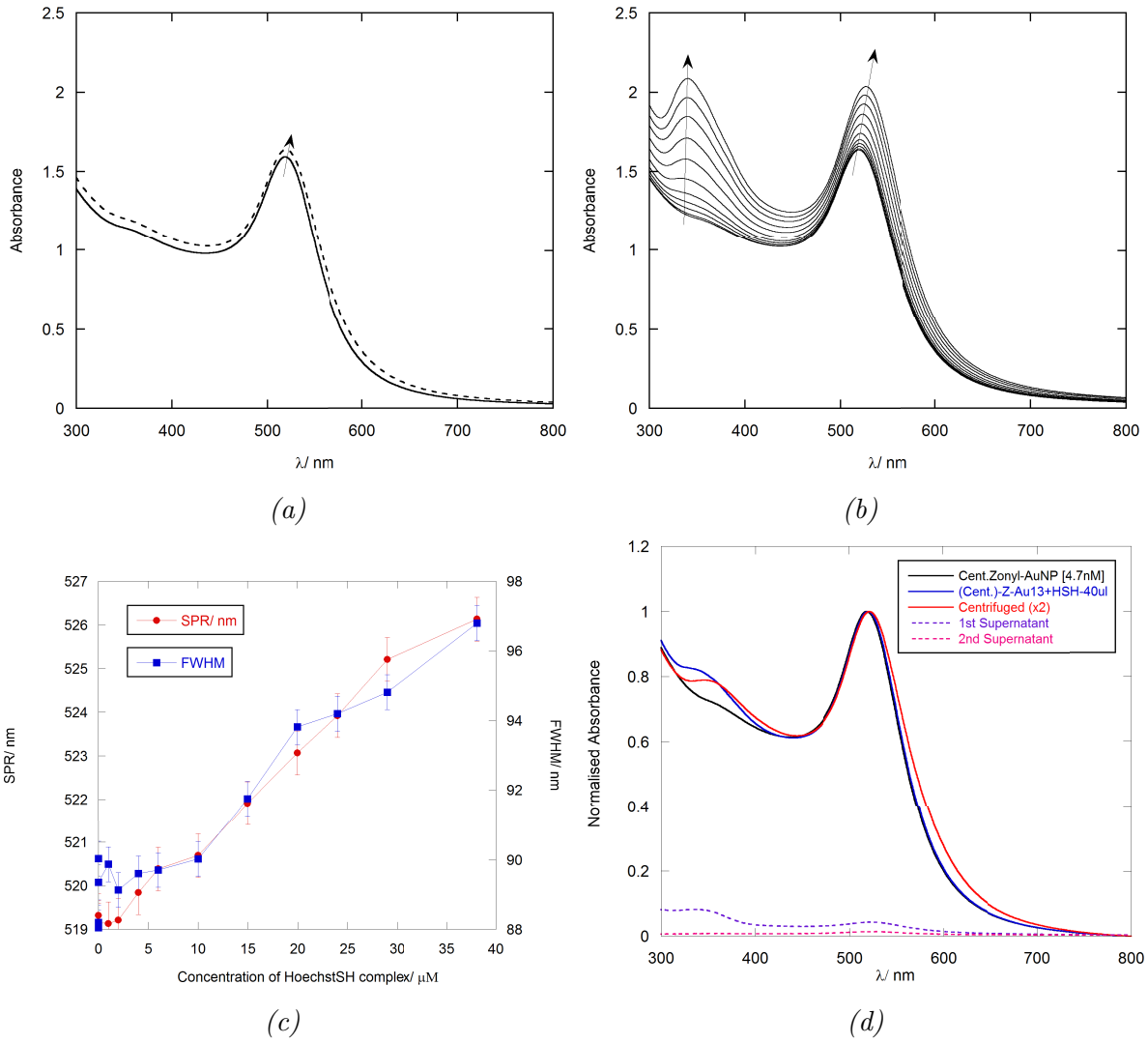

Figure 2.18: UV-Vis absorption spectra (a) of the addition of ***Zonyl 7950*** *to (dashed) coated 13 nm citrate-stabilised gold nanoparticles (solid line) (****Au13-Z****). (b) UV-Vis spectra monitoring the addition of* ***HoechstSH*** *up to 38 μM* ***HoechstSH*** *to AuNP13-Z. (c) Plot of the SPR λ_{max} and full-width at half-maximum (FWHM) as a function of the molar amount of* ***HoechstSH*** *added. (d) Normalised UV-Vis spectra monitoring the addition of 8 μM* ***HoechstSH*** *to* ***Au13-Z*** *and isolated* ***Au13-Z-HSH****. Also exhibited are the supernatants following centrifugation.*

emergence of a secondary band in the absorption profile on the gold nanoparticles was observed, there is the possibility that this relatively abrupt increase in the FWHM could be indicative of the start of nanoparticle flocculation. To ensure optimal nanoparticle stability in terms of avoiding possible flocculation, an 8 μM addition of **HoechstSH** was thus adopted.

Isolation of the nanoparticles to remove excess/unbound **HoechstSH** was achieved by centrifugation as described in the Section 2.6.2. The supernatant was discarded and the nanoparticle pellet resuspended in deionised water affording **Au13-Z-HSH**. Figure 2.18d shows UV-Vis absorption spectra following the addition of the **HoechstSH** and isolation, including spectra of the supernatant following each centrifugation step. The supernatant from the second centrifugation step does not exhibit a **HoechstSH** absorption peak so it can be concluded that two centrifugation steps are sufficient to render isolated **Au13-Z-HSH**. From the normalised spectra it is also apparent that the centrifuged **Au13-Z-HSH** possess the **HoechstSH** absorption peak at 350 nm, indicating the nanoparticles are successfully coated with the **HoechstSH** complex (Figure 2.18d).

To estimate the amount of **HoechstSH** remaining on the nanoparticles following centrifugation the UV-Vis spectrum of the **Au13-Z** was subtracted from spectrum of the **Au13-Z-HSH** before and after centrifugation. By integrating the area under the resulting curves and taking the ratio of the quantity of the result, as a known quantity is added prior to centrifugation the amount of **HoechstSH** remaining can be estimated. Performing these calculations on the UV-Vis spectra between 300 - 450 nm corresponding to the **HoechstSH** absorption indicates a 7.1 μM concentration of **HoechstSH** remaining in the nanoparticle colloid. With a colloidal concentration of 4.5 nM this corresponds to approximately 1500 **HoechstSH** complexes per nanoparticle.

DLS and zeta potential measurements were performed on the 13 nm citrate-stabilised gold nanoparticles, isolated **Au13-Z** and isolated **Au13-Z-HSH** (Figure 2.19c). The citrate-stabilised nanoparticles exhibit a peak in the intensity distribution diameter of 28$\pm$14 nm, **Au13-Z** a diameter of 34$\pm$13 nm and the isolated **Au13-Z-HSH** a diameter

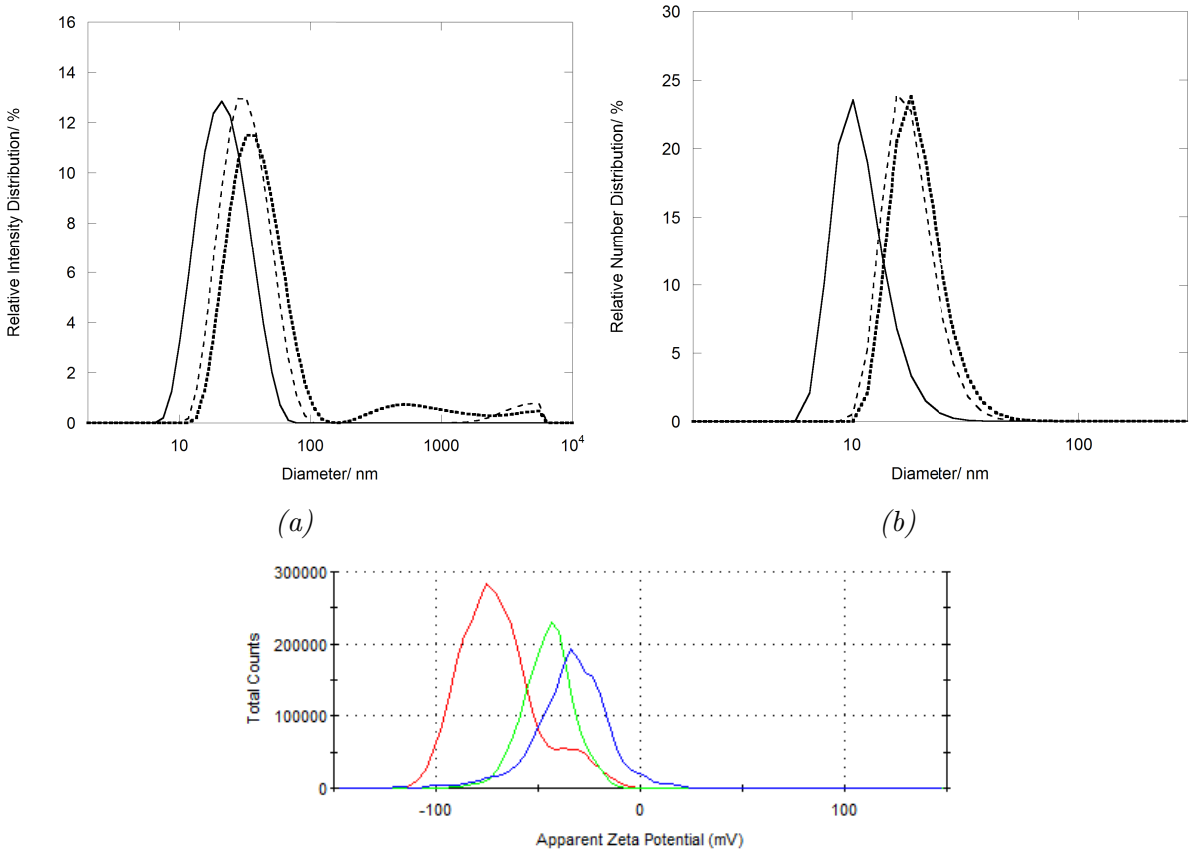

Figure 2.19: (a) DLS intensity distributions, (b) DLS number distribution of 1 nM citrate gold nanoparticles (solid line), isolated 1 nM ***Au13-Z*** *(dashed line) and isolated 1 nm* ***Au13-Z-HSH*** *coated Zonyl 7950 coated nanoparticles (bold dashed line) (****Au13-Z-HSH****). (c) of 1 nM citrate gold nanoparticles (blue), isolated 1 nM* ***Au13-Z*** *(green) and isolated 1 nm* ***Au13-Z-HSH*** *coated Zonyl 7950 coated nanoparticles (red) (****Au13-Z-HSH****).*

of 41 ±18 nm. The corresponding number distributions yield values of 12±4 nm, 18±5 nm and 20±6 nm respectively.

The 20% increase in the intensity distribution and change in the number distribution from 18±5 to 20±6 nm following addition of **HoechstSH** to the **Au13-Z**, indicates an increase in the hydrodynamic radius of the particle, attributed to the binding of the **HoechstSH** to the nanoparticle surface. Although a small number of flocculates are present in the intensity distribution of the isolated **Au13-Z-HSH**, as indicated by the broad peak at approximately 900 nm in Figure 2.19a, these are negligible in quantity as indicated by the single peak in the number distribution for the **Au13-Z-HSH**.

These results suggest a stable colloid with no evidence of nanoparticle aggregation. This is confirmed by the zeta potential measurements (Figure 2.19c). The citrate-stabilised gold nanoparticles possess a zeta potential of -34±2 mV which increases in magnitude to -69±3 mV for the isolated **Au13-Z**. Following addition of the **HoechstSH** complex the zeta potential reduces in magnitude to -45±12 mV which indicates that the **HoechstSH** complex displaces some of the electronegative surfactant. With the zeta potential of the **Au13-Z-HSH** greater in magnitude than the citrate-stabilised gold nanoparticles it suggests that the **Au13-Z-HSH** colloid remains electrostatically stable with significant amounts of surfactant remaining with the **HoechstSH** on the nanoparticle surface. A summary of the DLS and zeta potential measurements of **Au13-T20-HSH**, **Au13-Z-HSH** and all precursors are presented in Appendix E, Figure E.1.

Photophysical Characterisation of Au13-T20-HSH and Au13-Z-HSH

Photophysical properties of **Au13-T20-HSH** and **Au13-Z-HSH** were characterised as isolated dispersions and following the addition of calf-thymus DNA (CT-DNA) to examine the DNA binding capability of the **HoechstSH** complex when bound to nanoparticles. The free **HoechstSH** complex was thus similarly characterised following the addition of CT-DNA in the presence of the Tween20 and Zonyl 7950 surfactants.

Figure 2.20 exhibits the steady-state excitation and emission spectra of the isolated

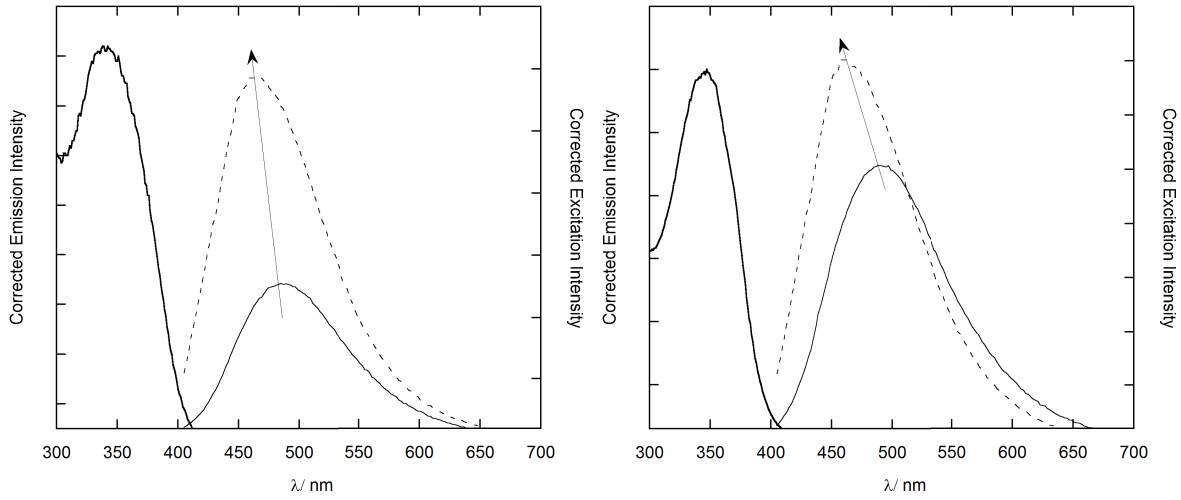

(a) HoechstSH *(b) HoechstSH-T20*

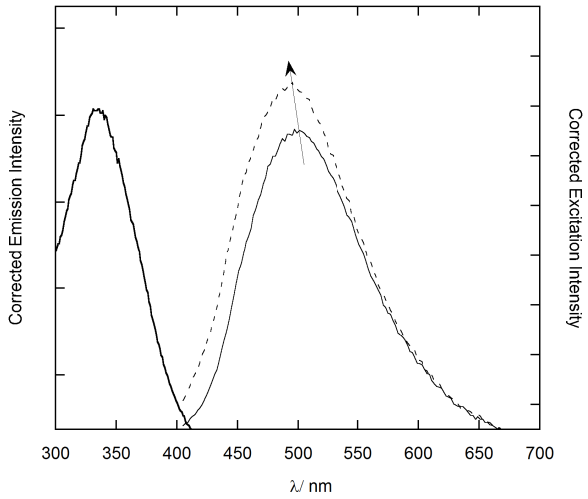

(c) HoechstSH-Zonyl

Figure 2.20: Steady-state luminescence excitation (bold line) and emission spectra of ***HoechstSH*** *[0.1 mM] (solid line) and* ***HoechstSH*** *following the addition of CT-DNA to achieve a final concentration of 180 mM (dashed lined) with prior addition of: (a) Tween20 [0.5 mM] and (b) 0.5µl (1 mg ml^{-1}) Zonyl 7950. (λ_{exc} = 350 nm, λ_{em} = 500 nm. Measurements were performed in Tris-HCl [10 mM], NaCl [100 mM] buffer (pH 7.4). Spectra corrected for instrument response, as described in General Experimental).*

HoechstSH complex following addition of CT-DNA and the same addition in the presence of the Tween 20 and Zonyl 7950 surfactants. The free **HoechstSH** possesses an excitation maximum of $\lambda_{ex_{max}} = 340$ nm which is red-shifted by 5 nm following the addition of the Tween20 and blue-shifted by 5 nm following the addition of the Zonyl 7950. These shifts are attributed to the change in the polarity of the environment of the **HoechstSH** complex due to the surfactants.[241]

The emission spectra of the **HoechstSH** and **HoechstSH** in the presence of the surfactants exhibit the characteristic blueshifts and increase in emission intensity after the addition of the CT-DNA.[241] The **HoechstSH** exhibits an emission maximum of 484 nm and the addition of 10 molar equivalents of the CT-DNA produces a 20 nm blueshift to 464 nm. Presence of the **Tween 20** redshifts the emission maximum to 490 nm and addition of the CT-DNA causes a 30 nm blueshift to 460 nm.

The presence the Zonyl 7950 causes the **HoechstSH** to exhibit an emission maximum of 499 nm which blueshifts to 493 nm following the addition of CT-DNA. Notably both surfactants cause a redshift in the emission maximum of the **HoechstSH**. A previous investigation of the effect of the Tween 20 and indeed a number of other nonionic surfactants on the fluorescent sulfonephthalein dye attributed the redshift in the emission maxima of the organic dye to the interaction with Tween 20 micelles.[250]

Excitation and emission spectra were also recorded of the gold nanoparticles stabilised with the surfactants and coated with the **HoechstSH** complex. The **Au13-T20-HSH** and **Au13-Z-HSH** exhibit excitation maxima of 350 nm and emission maxima of 445 nm and 480 nm respectively (Figure 2.21). The UV-Vis absorption spectra of the **Au13-T20-HSH** and **Au13-Z-HSH** exhibit the SPR of the gold colloid and an absorption peak at 350 nm matching the excitation profile of the **HoechstSH**. The emission maximum of the **Au13-T20-HSH** ($\lambda_{max} = 445$ nm) is blue-shifted considerably with respect to the free **HoechstSH** ($\lambda_{max} = 487$ nm), and also with respect to the **HoechstSH** in the presence of the **Tween 20** ($\lambda_{max} = 490$ nm). This could be due to the hydrophobic polyoxyethylene side chains of the **Tween 20** which are in close proximity to the **HoechstSH** complex on

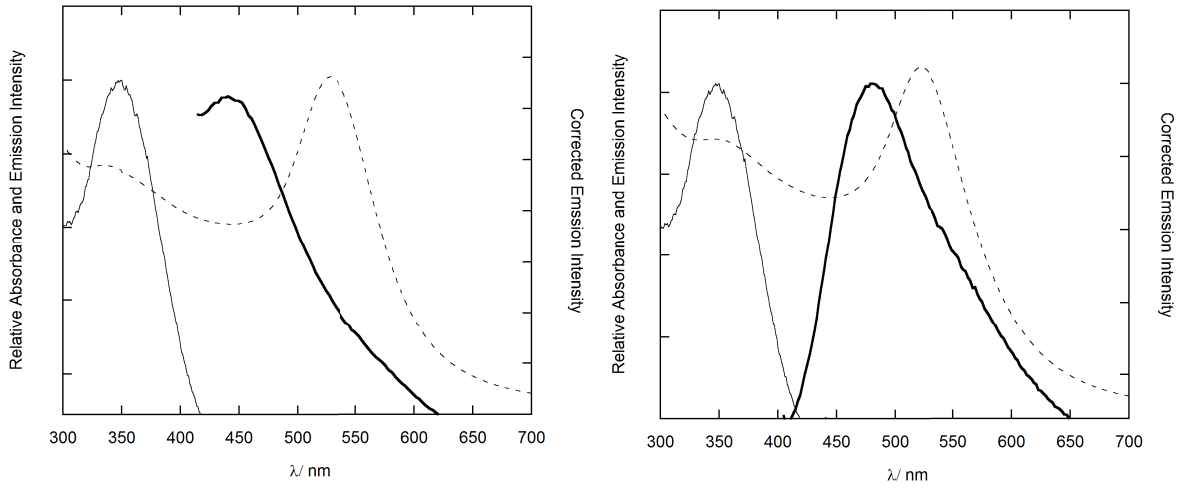

(a) Au13-T20-HSH *(b) Au13-Z-HSH*

*Figure 2.21: UV-Vis absorption spectrum (dashed line), excitation spectrum (λ_{em} = 500 nm, dashed line) and steady-state emission spectrum (λ_{exc} = 350 nm, bold solid line) of (a) **Au13-T20-HSH** (1 nM) and (b) **Au13-Z-HSH** (1 nM). Measurements were performed in Tris-HCl [10mM], NaCl [100mM] buffer (pH 7.4). (All spectra corrected for instrument response).*

the surface of the gold nanoparticle where it is packed between molecules of the adsorbed surfactant.[251] Free in solution however **HoechstSH** complex is not in such close proximity and may furthermore not be exposed to the side chains due to the micelle formation of Tween 20.[252,253] A similar effect is perhaps occurring with the **Zonyl 7950** with its hydrophobic perfluorinated alkyl chain. The **Au13-Z-HSH** exhibits a λ_{max} = 480 nm which is blueshifted by 7 nm and 16 nm respectively from the isolated **HoechstSH** complex (λ_{max} = 487 nm) and the **HoechstSH** with **Zonyl 7950** (λ_{max} = 496 nm).

Addition of calf-thymus DNA (CT-DNA) to **HoechstSH**, **HoechstSH-Tween20** and **HoechstSH- Zonyl7950** solutions causes a blueshift in the emission maxima of the **HoechstSH** as discussed previously (Figure 2.20). This characteristic shift is again observed following the addition of CT-DNA to **Au13-T20-HSH** and **Au13-Z-HSH** which exhibited 3 and 12 nm blueshifts to the **HoechstSH** emission maxima relative to the respective colloids in isolation (Figure 2.22). These shifts as well as the increase in emission intensity upon addition of CT-DNA to the gold colloids suggest that the **HoechstSH** complex is still able to interact with DNA when bound to the nanoparticle surface. Data are summarised in Table 2.3.

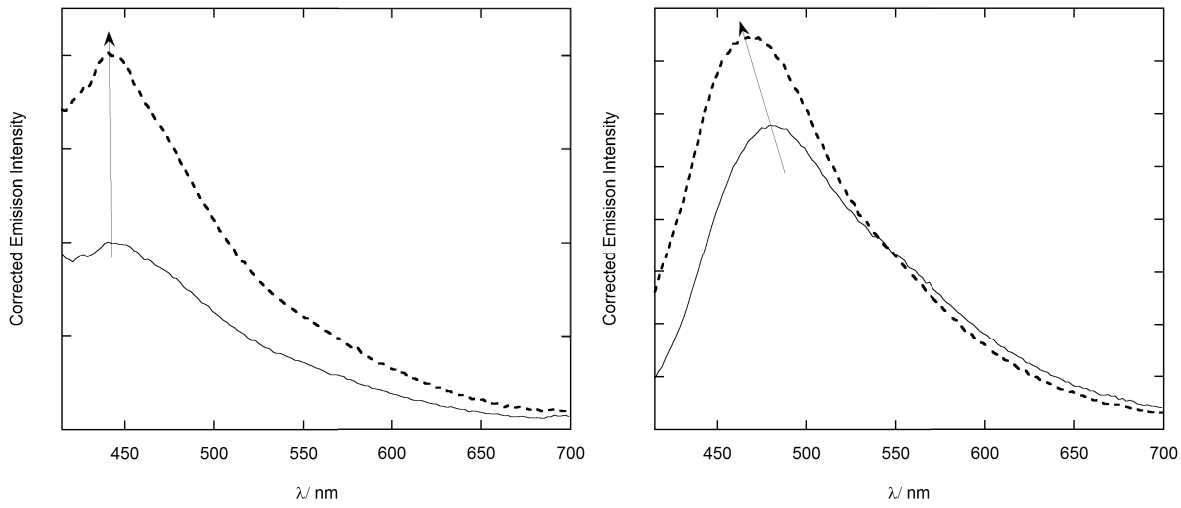

(a) *(b)*

Figure 2.22: Steady-state luminescence emission spectra of (a) ***Au13-T20-HSH*** *(1ml, 1 nM, solid line) and (b)* ***Au13-Z-HSH*** *(1ml, 1 nM, solid) with the addition of CT-DNA (50 µl, 3 mM, dashed line). (λ_{exc} = 350 nm. Measurements were performed in Tris-HCl [10mM], NaCl [100mM] buffer (pH 7.4). All spectra corrected for instrument response).*

	λ_{ex}/ nm	λ_{max}/nm
HoechstSH	340	484
HoechstSH + CT-DNA	-	464
HoechstSH + T20	345	490
HoechstSH + T20 + CT-DNA	-	460
Au13-T20-HSH	350	445
Au13-T20-HSH + CT-DNA	-	440
HoechstSH + Zonyl	335	500
HoechstSH + Zonyl + CT-DNA	-	493
Au13-Z-HSH	350	480
Au13-Z-HSH + CT-DNA		468

Table 2.3: Summary of the photophysical properties of aqueous free ***HoechstSH****,* ***Au13-T20-HSH*** *and* ***Au13-Z-HSH****, with the addition of Tween 20, Zonyl 7950 and CT-DNA.* ***HoechstSH*** *[1 mM, MeOH] added to Milli-Q H_2O to achieve a concentration of 1µM. Addition of Tween 20 [1.2 mM, Milli-Q H_2O] to* ***HoechstSH*** *to achieve a final concentration of 0.5 mM. Addition of Zonyl 7950 [1 mg ml^{-1}] to* ***HoechstSH*** *to achieve a final concentration of 0.5 mM.* ***Au13-T20-HSH*** *and* ***Au13-Z-HSH*** *at 1 nM with the addition of CT-DNA [3 mM, Milli-Q H_2O] to achieve a final concentration of 150 µM. (Estimated error = ±1 nm).*

Synthesis and Characterisation of Au100-Z-HSH

There are several methods for producing gold nanoparticles above 20 nm in diameter, including one-pot reactions[254] and seed-mediated processes.[255–258] One-pot reactions generally produce particles with a low concentration, high polydispersity and limited shape control. Post-synthetic clean up steps are possible in such synthesis, for example cetyl trimethylammonium bromide (CTAB)-stabilised nanoparticles can be grown via a seed-mediated process and subsequently purified to leave only spherical particles.[255] An alternative synthesis by Perrault *et al.* uses hydroquinone as a reducing agent however the oxidation product is toxic and particle polydispersity relatively high.[256] The method therefore adopted in this study is an adapted synthesis by Ziegler and Eychmüller which does not require a post-synthetic clean up and uses a biocompatible reducing agent, producing nanoparticles of a nominal 100 nm diameter.[259]

The nanoparticles are produced in a three step process which starts with 13 nm citrate-stabilised gold nanoparticles (Section 2.3.3). The 13 nm nanoparticles act as seeds to which $HAuCl_4$ is added with a mixture of sodium citrate and ascorbic acid to reduce the gold^{3+} ions to gold^0. Nucleation of the gold^0 on the nanoparticle seeds then produces larger nanoparticles as illustrated in Figure 2.23.

An approximate doubling in size is achieved in the each of the three growth steps due to the ratio of seed (gold nanoparticles) to gold salt added, the 13 nm seeds thus grow to 25 nm, then to 50 nm and finally to a nominal 100 nm. An increase in nanoparticle diameter causes a decrease in the resonant frequency of the electron oscillations in the conduction band of the gold, thus a 566 nm SPR λ_{max} is observed for the 100 nm gold nanoparticles.[50] The resulting 40 pM aqueous gold colloid were subsequently studied as scaffolds for attachment of the thiolated **HoechstSH** complex using the Zonyl 7950 surfactant. (Concentration calculation provided in Appendix E.1).

As described in Section 2.3.3 direct addition of **HoechstSH** to 13 nm citrate-stabilised gold nanoparticles gives rise to their immediate aggregation. This was again observed upon addition of the **HoechstSH** to the 100 nm gold nanoparticles as evident by a colour

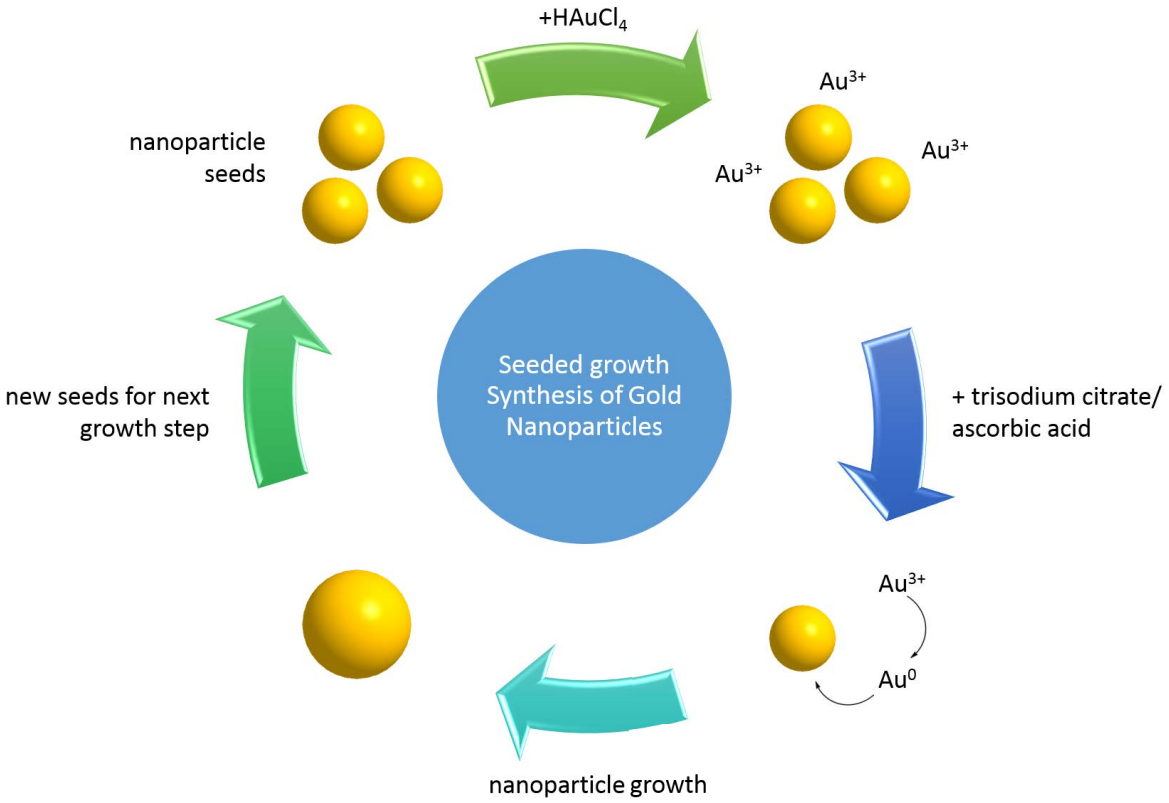

Figure 2.23: Schematic of the seeded-growth synthesis method to produce 100 nm gold nanoparticles.

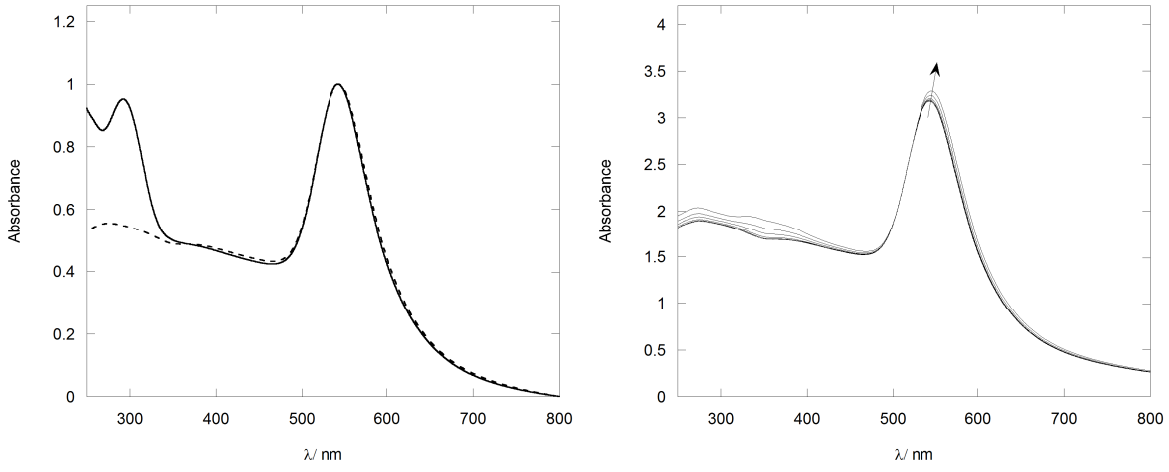

(a) *(b)*

*Figure 2.24: (a) UV-Vis absorption spectra of 100 nm citrate-stabilised gold nanoparticles (solid line) and isolated **Au100-Z** (dashed line). (b) UV-Vis spectra monitoring the addition of 50µl (10µM) **HoechstSH** to **Au100-Z**.*

change from purple to grey accompanied by sedimentation of the gold. To circumvent this the **Zonyl 7950** was again employed in a method analogous to that used for the 13 nm gold nanoparticles.

Coating of the nanoparticles was monitored by UV-Vis absorption spectrscopy. The addition of 1.5 μl (1 mg ml^{-1}) **Zonyl 7950** to 1 ml (40 pM) 100 nm gold nanoparticles caused a 1 nm red-shift in the SPR from 542.5 nm to 543.5 nm (Figure 2.24a). This is similarly observed with the 13 nm gold nanoparticles where addition of the **Zonyl 7950** causes a 1 nm redshift (Figure 2.18a). The UV-Vis spectrum also shows the absorption band at 295 nm due to the ascorbic acid remaining from the nanoparticle synthesis. Ascorbic acid and excess/unbound **Zonyl 7950** is removed following isolation by centrifugation affording **Au100-Z**.

Following isolation of **Au100-Z**, 50 μl **HoechstSH** (0.6 mM MeOH) was titrated in to 1 ml (40 pM) **Au100-Z**. This induced a 1.5 nm red-shift in the SPR from 543.5 nm to 545 nm in the UV-Vis absorption spectrum, indicated by the arrow in Figure 2.24b. Also evident is the absorption band at 350 nm of the **HoechstSH** convoluted with the absorption profile of the particles. This is similar to the addition of **HoechstSH** to **Au13-Z** particles where a red-shift is also observed (Figure 2.18).

The gold colloid was twice centrifuged with removal of the supernatant and resuspension of the nanoparticle pellet in deionised water on each occasion to remove excess/unbound **HoechstSH** complex. Figure 2.25 shows the UV-Vis absorption spectra before and after centrifugation. The spectra show no change in the SPR band (λ_{max} = 545 nm) of the particles and indeed no widening of the band. This indicates that the colloid is stable and the particles are not subject to flocculation and/or aggregation, the indications of which would be widening of the SPR and the emergence of an absorption band beyond 600 nm (Figure 2.8).[57,249] A further noticeable feature is the absorption band of the **HoechstSH** at 350nm following centrifugation steps. With unbound/excess **HoechstSH** removed by the centrifugation this feature originates from **HoechstSH** bound to the gold nanoparticles.

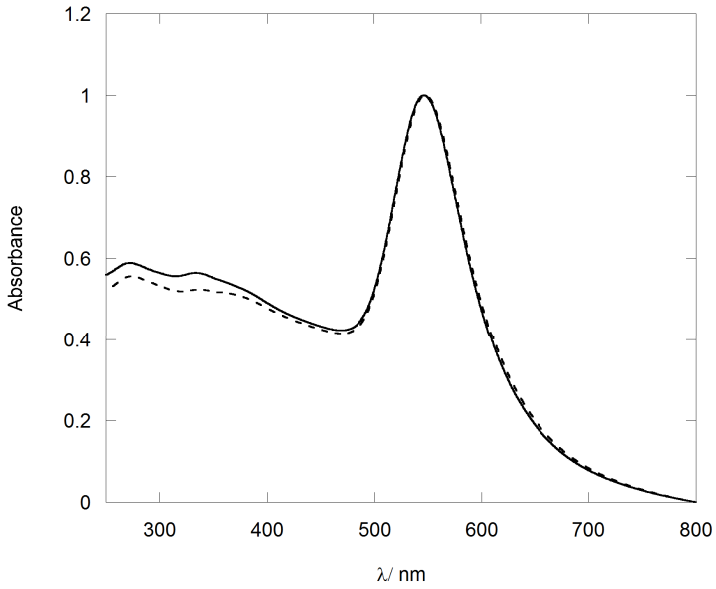

*Figure 2.25: UV-Vis absorption spectra of **Au100-Z-HSH** before (solid line) and after (dashed line) isolation by centrifugation.*

To estimate the amount of **HoechstSH** remaining on the nanoparticles following centrifugation, the UV-Vis spectrum of the **Au100-Z** was subtracted from the spectrum of the **Au100-Z-HSH** before and after centrifugation. By integrating the area under the resulting curves and taking the ratio of the quantity of the resultant, as a known amount is added prior to centrifugation the amount of **HoechstSH** remaining on the particles can be estimated. Performing these calculations on the UV-Vis spectra between 300 - 450 nm, corresponding to the **HoechstSH** absorption, indicates a 2.4 μM concentration of **HoechstSH** remaining in the nanoparticle colloid. With a gold nanoparticle concentration of 29 pM this corresponds to approximately 8x10^4 **HoechstSH** complexes per nanoparticle. The 100 nm gold nanoparticles have a greater surface area by a factor of sixty compared to the 13 nm particles, thus it would be expected that there are a greater number of **HoechstSH** complexes on the surface by this same factor. An analogous calculation as performed above for **Au13-Z-HSH** (Section 2.3.3) indicates approximately 1500 **HoechstSH** complexes per nanoparticle; a factor of fifty less than what is calculated for the **Au100-Z-HSH**. Both calculations are thus consistent with each other taking in to account the difference in surface area. Furthermore it would indicate that this method

of using the UV-Vis spectra to determine the number of **HoechstSH** complexes per nanoparticle provides a valid estimate.

Isolated 100 nm gold particles were further characterised by DLS following addition of the **Zonyl 7950** and subsequently the **HoechstSH** complex (Figure 2.26). DLS measurements of the 100 nm gold nanoparticles and isolated **Zonyl 7950** coated nanoaparticles show a single peak in the intensity and number distributions. The 100 nm gold nanoparticles possess a single peak at 93±37 nm in the intensity distribution which increases to 98±37 nm following addition of the **Zonyl 7950** (Figure 2.26a). A single peak is also observed in the number distribution at 72±17 nm which also increases to 80±19 nm (Figure 2.26b) following addition of the **Zonyl 7950**. Both distributions demonstrate an absence of aggregates in all cases. Following coating with the **HoechstSH** complex and purification by centrifugation, a single peak in the intensity and number distributions is again observed. A peak in the intensity distribution of 100±37 nm is observed for the isolated **Au100-Z-HSH** (Figure 2.26c), and the number distribution exhibits a peak at 83±19 nm (Figure 2.26d). The incremental increases in the nanoparticle diameter following addition of the **Zonyl 7950** and the **HoechstSH** in addition to the increase in the SPR observed (Figure 2.24), indicate successful surface binding of the **HoechstSH** on the 100 nm gold nanoparticles.

DLS measurements of the 100 nm nanoparticles and particles coated with the **Zonyl 7950** and the **HoechstSH** were conducted at 10 pM concentrations (Figure 2.26e). Addition of the **Zonyl 7950** fluorosurfactant increases the magnitude of the zeta potential from -30±15 mV to -50±11 mV, followed by a decrease in magnitude to -40±12 mV upon addition of the **HoechstSH** complex. This is similar to the preparation of **Au13-Z-HSH** where the citrate-stabilised gold nanoparticles possess a zeta potential of -34±2 mV which increases in magnitude to -69±3 mV for the isolated **Au13-Z**. Following addition of the **HoechstSH** complex to **Au13-Z** the zeta potential then reduces in magnitude to -45±12 mV. The increase in magnitude of the zeta potential after the addition of the **Zonyl 7950** is due to the C-F bonds on the peralkyl chains of the Zonyl fluoropolymer which are ex-

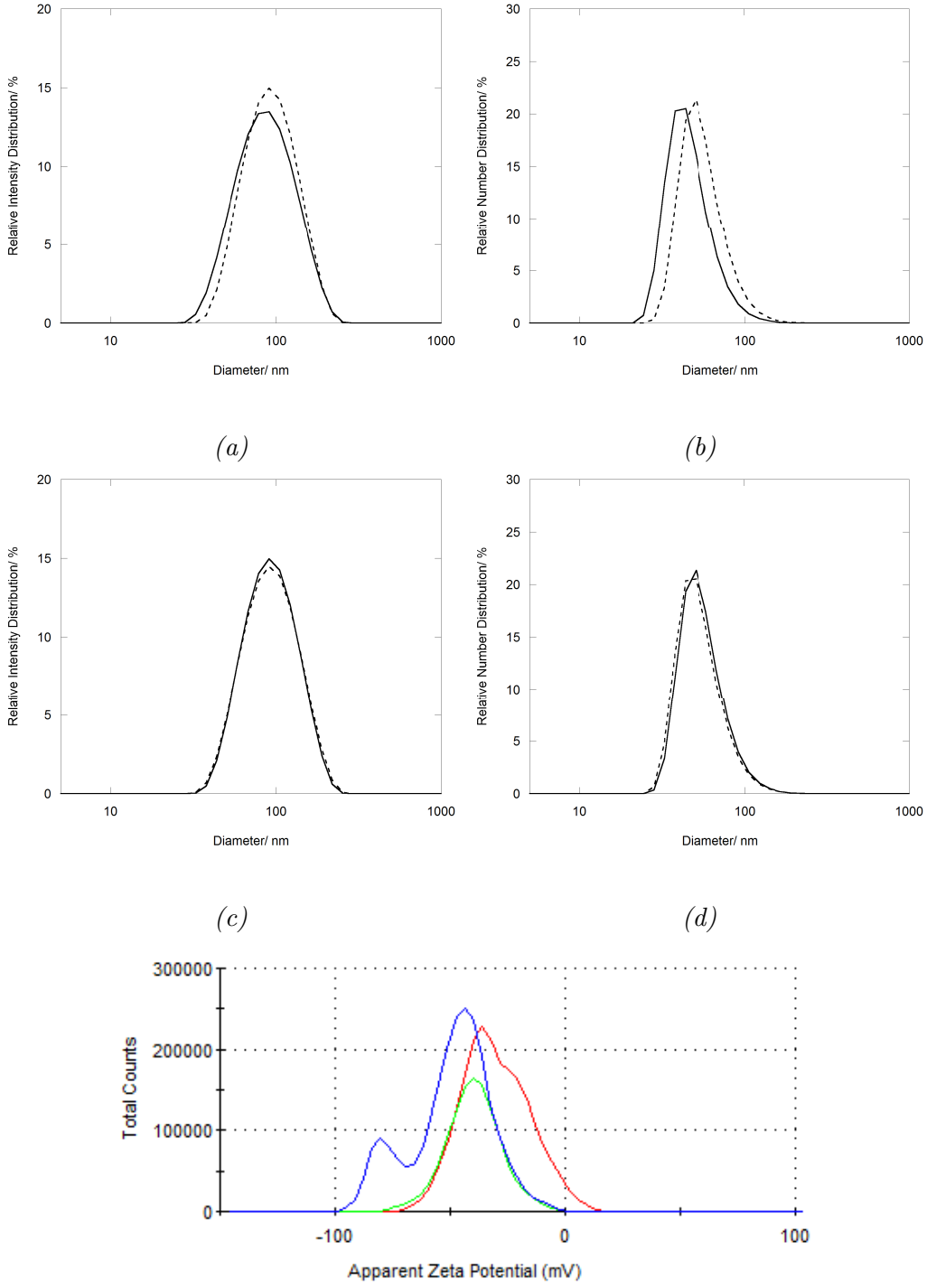

Figure 2.26: (a) DLS intensity and (b) DLS number distributions of ***Au100-Z****. (c) DLS intensity and (d) DLS number distributions of* ***Au100-Z-HSH****. (e) zeta potential distributions of* ***Au100*** *(green),* ***Au100-Z*** *(blue) and* ***Au100-Z-HSH*** *(red). (All measurements performed at 10 pM concentration).*

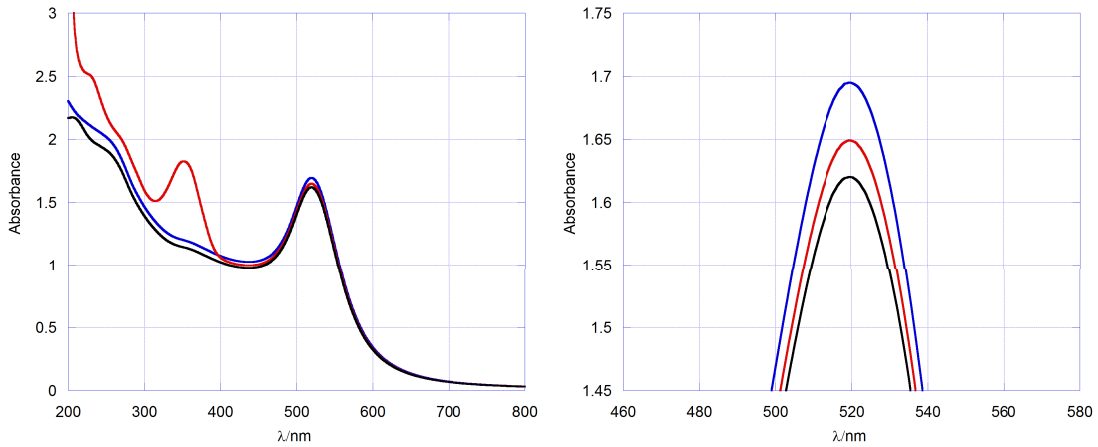

(a) *(b)*

*Figure 2.27: (a) UV-Vis absorption spectra of isolated (**Au13-Z** (blue)), the addition of 22 μM (17 μl) **Hoechst 33258** to **Au13-Z** (red) and subsequent centrifugation (black). (b) Magnifications of the SPR peak.*

posed to the outer region of the hydrodynamic radii of the particles. The **HoechstSH** complex then decreases the magnitude of the zeta potential when it displaces of some of the electronegative fluorosurfactant on the nanoparticle surface.

Addition of Hoechst 33258 to Gold Nanoparticles

A control study was performed to determine whether the SPR shift observed in the UV-Vis absorption spectrum of the Zonyl 7950 coated gold nanoparticles following addition of the **HoechstSH** (Figure 2.18b) was indeed due to the sulphur-gold bonding between the **HoechstSH** complex and the nanoparticle surface. A solution of **Hoechst 33258**, the starting material for the synthesis of the **HoechstSH** which possesses a hydroxyl group in place of the thiolated ligand on the **HoechstSH**, was thus titrated in to isolated Zonyl 7950 coated 13 nm gold nanoparticles.

UV-Vis spectra monitoring the addition of the **Hoechst 33258 Au13-Z** are shown in Figure 2.27. As expected a large absorption band centred at 350 nm is observed following addition of the **Hoechst 33258** and importantly the SPR band of the nanoparticles does not shift, remaining at 520 nm (Figure 2.27b). The SPR of the gold nanoparticles is

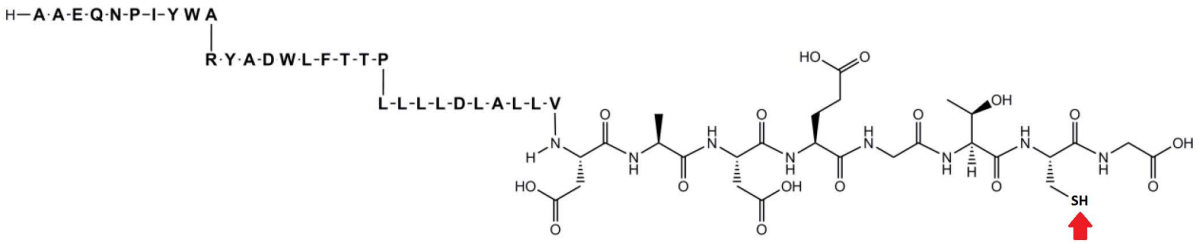

Figure 2.28: Structure of the pHLIP peptide (cysteine group indicated by the red arrow)

dependant on the dielectric constant of the local surrounding medium and any changes due to binding at the nanoparticle surface,[249] hence the absence of an observed SPR shift indicated a lack of binding of **Hoechst 33258** to the nanoparticle. Following centrifugation to isolate the nanoparticles from the unbound **Hoechst 33258** the UV-Vis spectrum exhibits a complete absence of the Hoechst absorption band at 350 nm. This supports the conclusion that the SPR observed upon the addition of the **HoechstSH** to the **Zonyl 7950** gold nanoparticles is due to the sulphur-gold bond.

2.3.4 Peptide Modification of Gold Nanoparticles

Synthesis and Characterisation of Au13-P-HSH

Citrate-stabilised 13 nm gold nanoparticles were synthesised as reported in Section 2.3.3. The pHLIP peptide (purchased from Alta Biosciences) is insoluble in water and therefore dissolved in a 10% DMSO phosphate buffer saline solution, analogous to the preparation by Davies et al.[82] The pHLIP peptide sequence contains a single cysteine amino acid with a free thiol group for binding to gold (Figure 2.28) and was investigated to mediate the attachment of the **HoechstSH** to gold nanoparticles (Figure 2.29).

Coating of the 13 nm citrate-stabilised gold nanoparticles with the pHLIP peptide sequence was monitored by UV-Vis absorption spectroscopy (Figure 2.30a). Addition of the pHLIP peptide resulted in a redshift of 1 nm from (519 - 520 nm) in the SPR λ_{max} of the gold nanoparticles, affording (**Au13-P**). Such a shift indicates a change in the surface dielectric constant and therefore binding of the pHLIP peptide to the nanoparticles.[68,75,82]

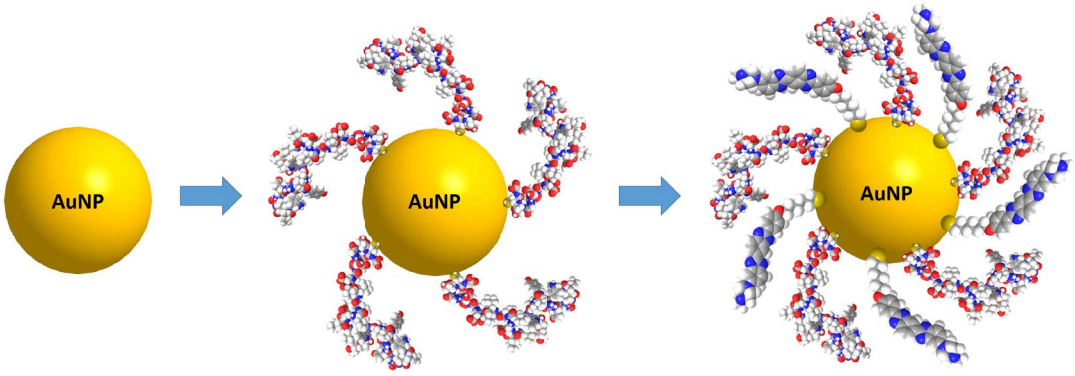

Figure 2.29: Schematic of Au13-P-HSH nanoparticle construction starting with the gold nanoparticle, followed by addition of the pHLIP peptide and ***HoechstSH****.*

The magnitude of the shift is less than that reported in the study by Davies et al. in which a 5 nm red shift in the SPR λ_{max} is observed.[82] This is not however unexpected as the 5 nm shift was attributed to the 80 μM addition of the pHLIP peptide whereas here 8 μM of the peptide is added.

The **HoechstSH** complex was subsequently added to gold nanoparticles pre-coated with the pHLIP peptide **Au13-P**. The SPR λ_{max} was again monitored by UV-Vis absorption spectroscopy (Figure 2.30b). The **HoechstSH** was titrated in to the gold nanoparticles up to a final concentration of 45 μM. The **HoechstSH** was induced a further redshift in the SPR λ_{max} of the nanoparticles with a shift from 520 nm to 522 nm. Significantly no indication of particle flocculation or aggregation was observed with the FWHM of the SPR showing no increase in magnitude and no new formation of an SPR band at 600 nm or beyond (Figure 2.8).[57,249]

Nanoparticles were isolated from excess free **HoechstSH** complex and pHLIP peptide by size-exclusion chromatography on superfine Sephadex G-25 (GE Healthcare HiTrap Column) affording **Au13-P-HSH**. UV-Vis absorption spectra of the particles before and after size-exclusion chromatography are presented in Figure 2.31a. Following isolation the spectra also exhibit a further redshift in the SPR λ_{max} of the particles to 524 nm, indicating a change in the surface environment of the particles. This may be due to excess peptide and/or **HoechstSH** which was adsorbed to the particles in the outer region of the hydrodynamic radius, but was removed upon size-exclusion chromatography. A further

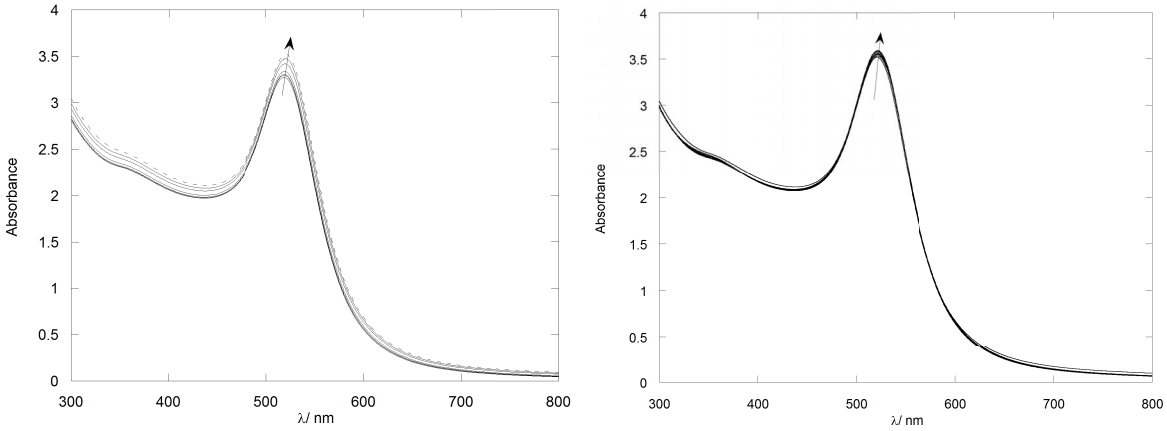

(a) *(b)*

*Figure 2.30: UV-Vis absorption spectra (a) of the addition of 8 μM (20 μl) pHLIP peptide (dashed) to 13 nm citrate-stabilised gold nanoparticles - **Au13-P** (solid line). (b) UV-Vis spectra monitoring the addition of λ_max to **Au13-P** up to a final concentration of 45 μM (200 μl).*

point of note is the dilution factor of 1.5 and again an absence of any signs of particle flocculation and/or aggregation.

In analagous fashion to the surfactant coated nanoparticles, to estimate the amount of **HoechstSH** remaining on the nanoparticles following centrifugation, the UV-Vis spectrum of the **Au13-P** was subtracted from UV-Vis spectrum of the **Au13-P-HSH** before and after centrifugation. By integrating the area under the resulting curves and taking the ratio of the quantity of the resultant, the amount of **HoechstSH** remaining can be estimated. This is possible as a known quantity is added prior to centrifugation. Performing these calculations on the UV-Vis spectra between 300 - 450 nm, corresponding to the **HoechstSH** absorption, indicates a 4 μM concentration of **HoechstSH** remaining in the nanoparticle colloid. With a gold nanoparticle concentration of 9 nM this corresponds to approximately 400 **HoechstSH** complexes per nanoparticle. This compares to 1400 - 1500 complexes for the surfactant coated 13 nm nanoparticles. This would perhaps not be unexpected as the pHLIP peptide is larger than the surfactants and may occlude more of the nanoparticle surface, thus fewer **HoechstSH** are able to bind.

DLS and zeta potential measurements were performed (Figure 2.31). The citrate-

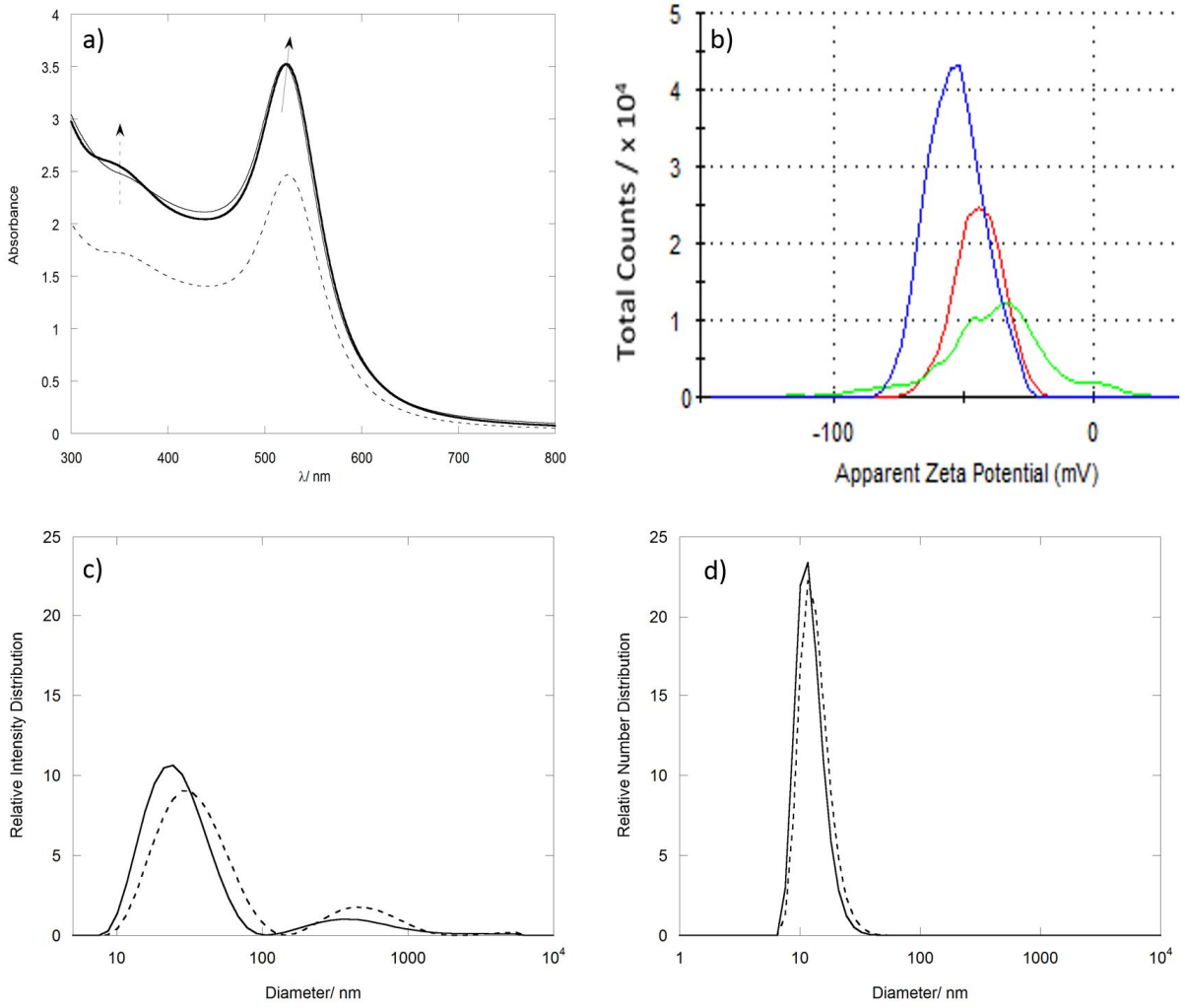

Figure 2.31: (a) UV-Vis spectra of ***Au13-P*** *(solid line) and* ***Au13-P-HSH*** *before (bold line) and after (dashed line) centrifugation. (b) zeta potential distributions of 13 nm citrate-stabilised gold nanoparticles (red),* ***Au13-P*** *(green) and isolated* ***Au13-P-HSH*** *(blue). DLS intensity (c) and number (d) distributions of 13 nm citrate-stabilised gold nanoparticles (solid line) and* ***Au13-P-HSH*** *(dashed line).*

stabilised nanoparticles exhibit an intensity distribution diameter of 28±13 nm and the **Au13-P-HSH** a diameter of 36±19 nm. The number distributions yield diameters of 13±4 for the citrate-stabilised gold nanoparticles and 14±4 for **Au13-P-HSH** respectively. The increase in hydrodynamic radius observed upon addition of the pHLIP peptide and the **HoechstSH** complex indicates binding to the nanoparticles. Furthermore no evidence of flocculates/aggregates are apparent with single distributions observed in the DLS number distributions.

Zeta potential measurements of the 13 nm citrate-stabilised gold nanoparticles yield

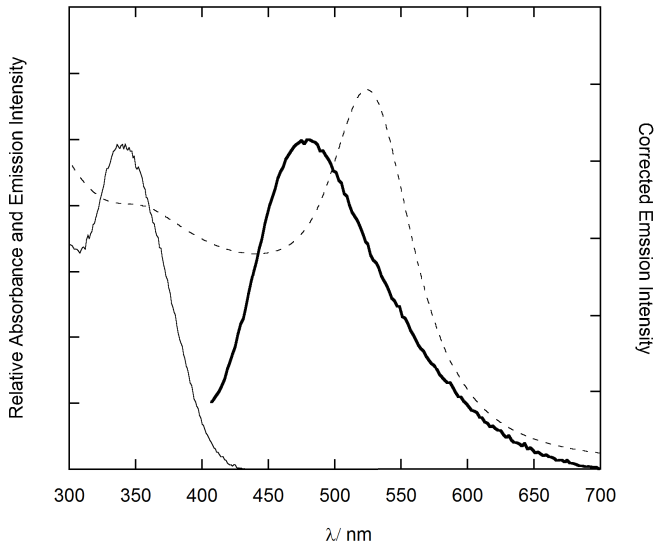

Figure 2.32: UV-Vis absorption spectrum (dashed line), excitation spectrum (λ_{em} = 500 nm, solid line) and steady-state emission spectrum (λ_{exc} = 350 nm, bold solid line) of ***Au13-P-HSH****.*

a zeta potential of -38±3 mV which increases in magnitude to -44±3 mV upon addition of the pHLIP peptide (Figure 2.31b). With the peptide possessing an overall negative charge this would be expected.[260] Following addition of the **HoechstSH** complex the zeta potential again increases in magnitude to -53±12 mV. This is surprising considering the **HoechstSH** is cationic, thus a decrease in magnitude would be expected as it binds on the pHLIP coated gold nanoparticle. The increase in magnitude may be due to the **HoechstSH** complex binding to the nanoparticle in such a way the negatively charged pHLIP peptide rearranges on the nanoparticle surface to become more exposed, thus yielding a more negative zeta potential.

Photophysical Characterisation of Au13-P-HSH

The photophysical properties of **Au13-P-HSH** were characterised as isolated dispersions and following the addition of calf-thymus DNA (CT-DNA) due to the DNA binding property of the **HoechstSH** complex. For comparison the **HoechstSH** complex was similarly characterised in isolation and following addition of the pHLIP peptide.

Upon excitation at 350 nm the **Au13-P-HSH** exhibits blue (cyan) emission with λ_{max}

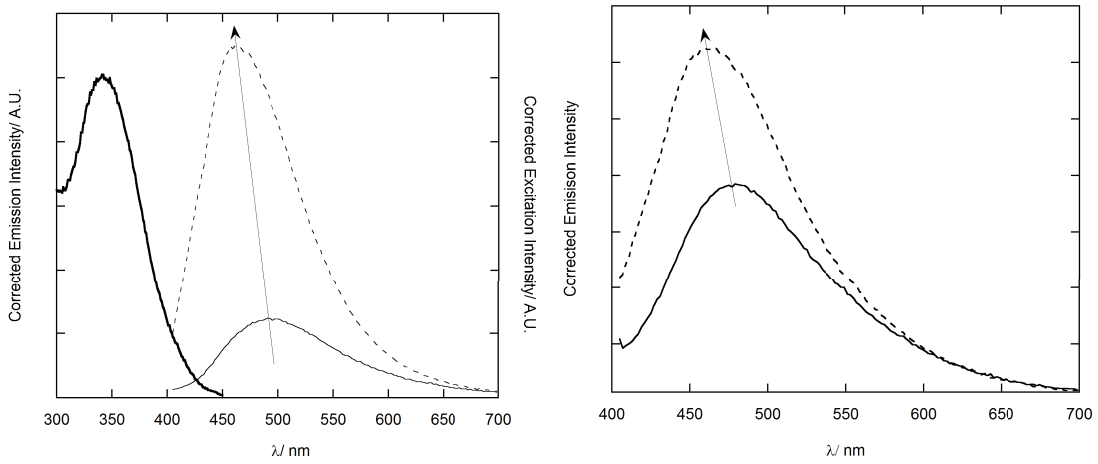

(a) *(b)*

Figure 2.33: (a) Steady-state excitation (bold line) and emission spectra of ***HoechstSH*** *[0.1 mM, Milli-Q H_2O] and pHLIP peptide before (solid line) and after the addition of 10 molar equivalents of CT-DNA (dashed line). (b) emission spectra of* ***Au13-P-HSH*** *(1 nM) before (solid line) and after (dashed line) the addition of CT-DNA to achieve a final concentration of 17 μM. (All spectra corrected for instrument response).*

= 478 nm (Figure 2.32. The UV-Vis absorption spectra of the **Au13-P-HSH** although dominated by the SPR of the gold colloid exhibits a peak at 350 nm corresponding to the excitation peak of the **HoechstSH**. The emission maximum of the **Au13-P-HSH** (λ_{max} = 478 nm) is blue-shifted with respect to the isolated **HoechstSH** (λ_{max} = 487 nm) and the **HoechstSH** with pHLIP (λ_{max} = 493 nm) (Figure 2.332.33a). This could be due to the close proximity of the **HoechstSH** complex with the negatively charged pHLIP peptide on the surface of the gold nanoparticle.

Figure 2.33a shows the excitation and emission spectra of the isolated **HoechstSH** and **HoechstSH-pHLIP** solution before and after the addition of CT-DNA. The **HoechstSH** possesses an excitation maximum of λ_{ex} = 340 nm which is unchanged following the addition of the pHLIP. The emission spectrum of the **HoechstSH** with the pHLIP following the addition 10 molar equivalents CT-DNA exhibits the characteristic blueshift and increase in emission intensity, with a shift from 493 nm to 463 nm. The addition of CT-DNA to **Au13-P-HSH** also causes an increase in the emission intensity and a blueshift of approximately 30 nm from 478 nm to 461 nm (Figure 2.33b).

Synthesis and Characterisation of Au100-P-HSH

Coating of 100 nm gold nanoparticles with the pHLIP peptide was performed analogously to the preparation for the 13 nm gold nanoparticles. Coating of the 100 nm citrate-stabilised gold nanoparticles (40 pM, 2.5 ml) with the pHLIP peptide sequence was monitored by UV-Vis absorption spectroscopy (Figure 2.34a). An addition of 2 μM (5 μl) pHLIP peptide resulted in a redshift of 1 nm in the SPR λ_{max} of the gold nanoparticles with a shift from 595 nm to 596 nm. Addition of 50 μl (10 μM) **HoechstSH** followed by isolation by centrifugation induces a blueshift of 8 nm to 588 nm, affording **Au100-P-HSH**.

Isolated **Au100-P-HSH** were further characterised by DLS (Figure 2.34). DLS measurements of the 100 nm gold nanoparticles and isolated **Au100-P-HSH** show a single peak in the intensity and number distributions. The 100 nm gold nanoparticles possess a single peak at 93±37 nm in the intensity distribution which increases to 154±50 nm for the **Au100-P-HSH** (Figure 2.34c). A single peak in the number distribution is also observed at 72±17 nm which increases to 113±41 nm for the **Au100-P-HSH**, demonstrating an absence of aggregates in all cases.

To estimate the amount of **HoechstSH** remaining on the nanoparticles following centrifugation, the UV-Vis spectrum of the **Au100-P** was subtracted from UV-Vis spectrum of the **Au100-P-HSH** before and after centrifugation. By integrating the area under the resulting curves and taking the ratio of the quantity of the resultant, the amount of **HoechstSH** remaining can be estimated. This is possible as a known quantity is added prior to centrifugation. Performing these calculations on the UV-Vis spectra between 300 - 450 nm, corresponding to the **HoechstSH** absorption, indicates a 2 μM concentration of **HoechstSH** remaining in the nanoparticle colloid. With a gold nanoparticle concentration of 40 pM this corresponds to approximately 5x10^5 **HoechstSH** complexes per nanoparticle. Taking in to account the increase in surface area of the 100 nm particles compared to the 13 nm particles, and the result of the same calculation above for the smaller particles, one would expect to find approximately 2.4x10^4 **HoechstSH** com-

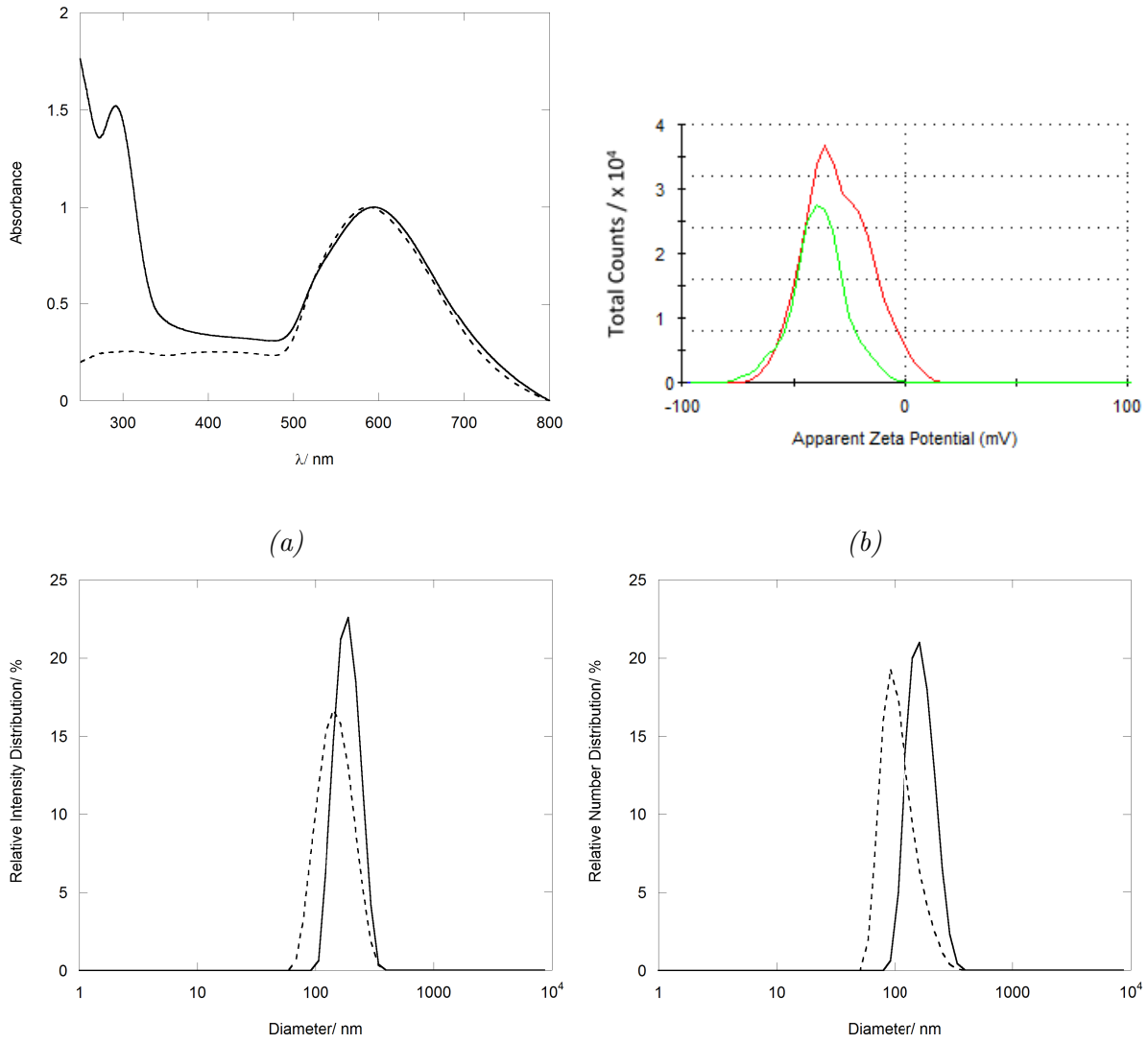

Figure 2.34: (a) UV-Vis spectra of 100 nm gold nanoparticles (solid line), ***Au100-P*** *(dashed line) and* ***Au100-P-HSH*** *(bold line). (b) zeta potential distributions of 100 nm gold nanoparticles (red) and* ***Au100-P-HSH*** *(green). DLS intensity (c) and number (d) distributions of 100 nm gold nanoparticles (dashed line) and* ***Au100-P-HSH*** *(solid line). (PDI = 0.088 for both distributions)*

plexes per nanoparticle. This variation could be attributed to variations in size (particle sizes quoted are nominal values), or perhaps due to a different surface orientation of the pHLIP peptide on the larger particles that allows a great number of **HoechstSH** to bind compared to the 13 nm particles.

Following coating with the **HoechstSH** complex and purification by centrifugation, the single peak in the intensity and number distributions is again observed. A peak in the intensity distribution of 99±37 nm is observed for **Au100-P-HSH** (Figure 2.34c). The number distribution shows a peak at 83±19 nm for **Au100-P-HSH**. The incremental increases in the diameters following addition of the Zonyl 7950 and subsequently the **HoechstSH** in addition to the increase in the SPR, indicate surface functionalisation of the gold nanoparticles with the **HoechstSH** complex.

Electrophoretic light scattering measurements of the 100 nm nanoparticles and **Au100-P-HSH** were conducted at 10 pM concentrations (Figure 2.34). Addition of the pHLIP and **HoechstSH** followed by isolation by centrifugation yields an increases in the zeta potential. The magnitude of the zeta potential increases from -30±15 mV for the 100 nm gold nanoparticles to -39±12 mV for the **Au100-P**, followed by a decrease in magnitude to -40±12 mV upon addition of the **HoechstSH** complex **Au100-P-HSH**.

2.3.5 Preliminary Study: Circular Dichroism of Au13-Z-HSH and Au13-P-HSH

Preliminary circular dichroism (CD) spectroscopy studies monitoring the conformational changes of calf-thymus (CT-DNA) upon addition of the **Au13-Z-HSH** and **Au13-P-HSH** were performed. Circular dichroism refers to the differential absorption of left and right-handed circularly polarised light by a molecule that contains one of more chiral molecules. CD is used to assess the conformation of a range of macromolecules such as proteins and DNA as their structures are sensitive to their environment (pH, temperature) and interaction with other molecules. The Hoechst dye possesses the ability to bind to DNA, thus the **Au13-Z-HSH** and **Au13-P-HSH** were similarly examined to assess their

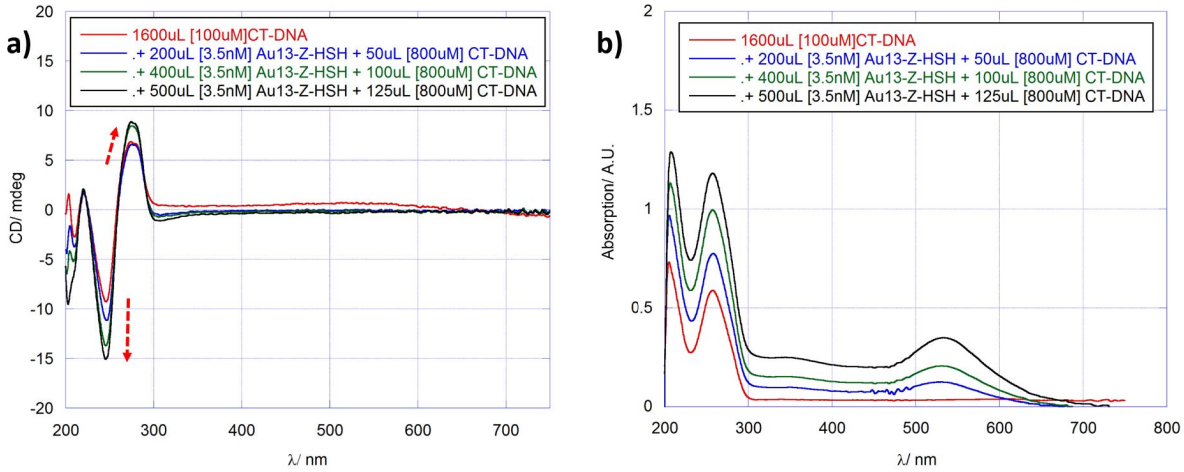

*Figure 2.35: Circular dichroism (a) and UV-Vis absorption (b) spectra of 100 μM CT-DNA plus the addition of **Au13-Z-HSH** as per the figure legend. Addition of the **Au13-Z-HSH** induces changes in the circular dichroism spectra as indicated by the dashed red-arrows. Changes in the DNA structure may be due to conformational changes and/or stiffening upon binding with the HoechstSH complex on the gold nanoparticles. (CT-DNA was added upon each titration to keep DNA concentration consistent. Measurements were performed in Tris-HCl [10mM], NaCl [100mM] buffer (pH 7.4). CT-DNA was dissolved in milli-Q water, and all solutions were sonicated and vortexed before measurement).*

interaction with DNA. Spectra of CT-DNA addition of the **Au13-Z-HSH** and **Au13-P-HSH**are presented in Figure 2.35 and 2.36. In both spectra the increases in magnitude and shifts in wavelength of the CD spectra between 200 and 300 nm indicate stiffening of the three-dimensional structure of the DNA.[261] This is perhaps due to interaction/binding with the nanoparticle bound **Hoechst-SH**, indicating that the both the nanoparticle **HoechstSH** conjugates still possess the ability to bind to DNA. This is of great relevance considering that cellular and nuclear uptake in cells will be examined, as the nanoparticles may possess the potential to interact with nuclear DNA in cells.

2.3.6 Cellular Uptake of Au13-T20-HSH, Au13-Z-HSH and Au100-Z-HSH

One of the major areas of interest in nanotechnology is the interaction of nanoparticles with cells, specifically their ability to achieve uptake and the fate of the nanoparticles once intracellular localisation is achieved. Visualisation of populations of cells exposed to nanoparticles is thus required. A widely used technique in the life sciences for cellular

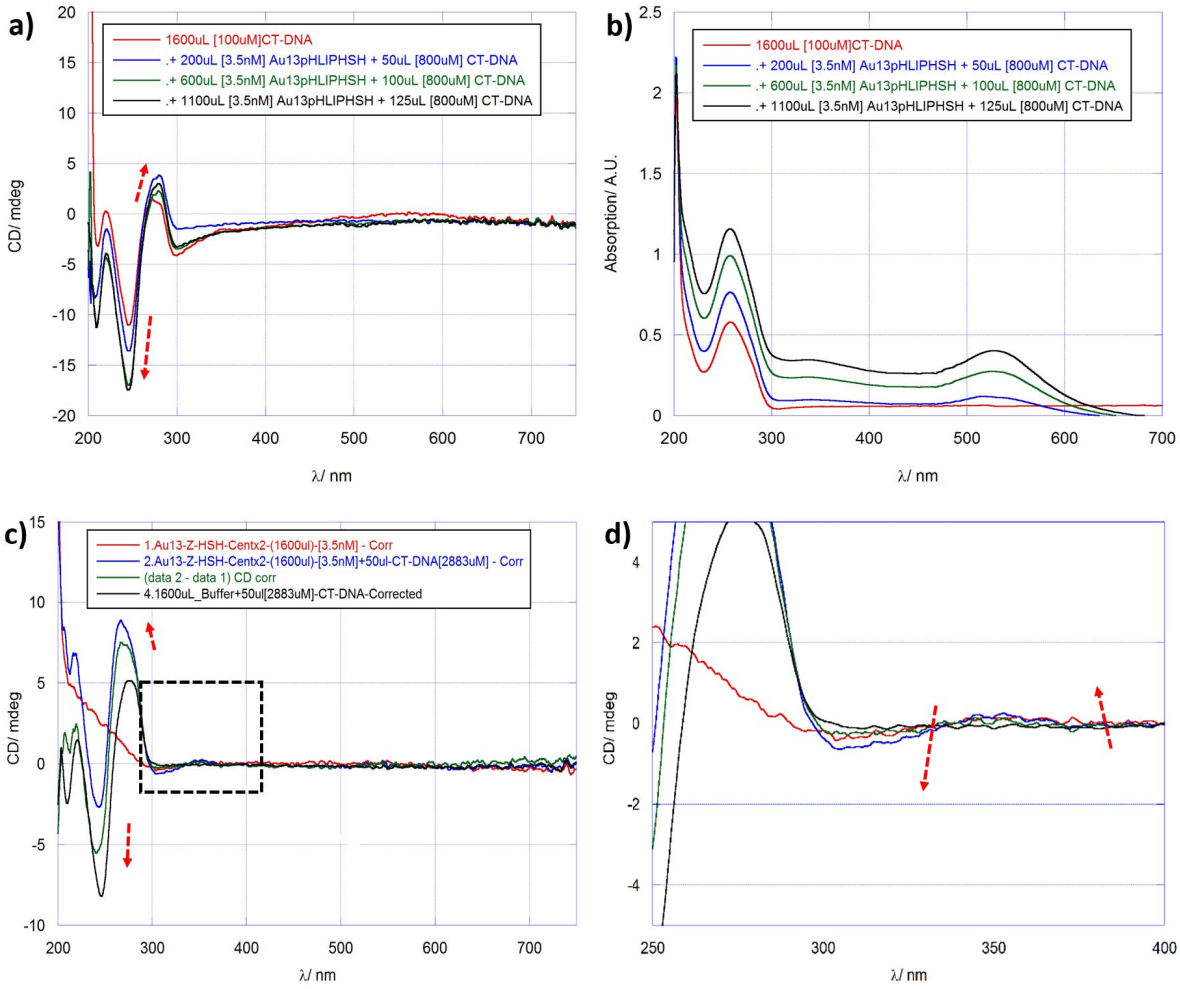

Figure 2.36: Circular dichroism (a) and UV-Vis absorption (b) spectra of 100 μM CT-DNA plus the addition of ***Au13-P-HSH*** *as per the figure legend. Addition of the* ***Au13-P-HSH*** *induces changes in the circular dichroism spectra as indicated by the dashed red-arrows. Changes in the DNA structure may be due to conformational changes and/or stiffening upon binding with the HoechstSH complex on the gold nanoparticles. A reverse titration comprising the addition of CT-DNA to* ***Au13-P-HSH*** *(as denoted by the Figure legend) is shown in (c) with magnification of the inset in (d). Changes in the circular dichroism spectra indicated by the dashed red-arrows again indicated changes in DNA structure/stiffening. (CT-DNA was added upon each titration to keep DNA concentration consistent. Measurements were performed in Tris-HCl [10mM], NaCl [100mM] buffer (pH 7.4). CT-DNA was dissolved in milli-Q water, and all solutions were sonicated and vortexed before measurement).*

imaging is light microscopy which allows the interrogation of living or fixed cells with relatively minimal sample preparation time. Light microscopes can use a range of contrast methods including label free techniques such as brightfield microscopy. The most widely used form of light microscopy is however fluorescence based. The diffraction-limit places a fundamental limit on the resolution achievable in light microscopy (approximately half of the incident wavelength used), thus individual nanoparticles may not be completely resolved depending on their size.[262] Although this limit can be reduced or overcome using specialised "super-resolution" techniques, light microscopy can still be used to image nanoparticles which would instead appear as blurred point sources.

Gold nanoparticles are particularly suited to bright-field and reflection microscopy, exploiting the absorption and scattering properties of gold nanoparticles.[263] Nanoparticles functionalised with luminescent moieties are widely employed due to their potentially higher luminescence when multiple lumiphores can be conjugated to a nanoparticle relative to single lumiphores alone. Also possible are an array of excitation and emission wavelength/bands, thus multiple "channels" of luminescence/fluorescence can be monitored. The most common form of fluorescence microscopy is epifluorescence in which an arc lamp is used to illuminate the field-of-view (FOV) with filters selecting the required excitation and emission wavelengths. The contrast and resolution achieved via this technique is however not ideal as the wide field of illumination allows for out-of-focus planes to be superimposed on the objects of interest in the desired focal plane. In confocal laser scanning microscopy excitation is achieved via a laser that is rastered across the FOV with both the incident laser and emitted light passing through a pinhole in the focal plane of the objective. Out-of-focus fluorescence is thus removed providing improved contrast and resolution relative to epifluorescence microscopy. A great advantage of confocal microscopy is the ability to create three-dimensional reconstructions and to record emission spectra by examining pixel/image intensity in a discrete series of wavelength bands.

To investigate their potential as cellular imaging agents and to evaluate the biological consequences of functionalising the nanoparticles with the Hoechst DNA binding dye,

A549 human adenocarcinomic alveolar basal epithelial cells and HeLa human adenocarcinomic cervical epithelial cells were incubated with **Au-T20-HSH**, **Au-Z-HSH** and **Au-P-HSH**. Cells were incubated for a range of time periods and imaged using confocal microscopy to image **HoechstSH**. Confocal reflectance and transmission brightfield microscopy was used to image the nanoparticles and cellular features.

Images of untreated cells and the appropriate controls for the counterstains used are shown in Appendix H. Confocal microscopy instrument settings and parameters are provided in Section 6.0.8. UV-Vis absorption spectra of **Au13-T20-HSH**, **Au13-Z-HSH** and **Au13-P-HSH** in complete cell media at the same concentration used for the imaging studies were measured. Spectra were void of any indications of particle aggregation/flocculation, demonstrating the stability of the nanoparticles in cell culture medium (Appendix F).

Confocal Microscopy of Au13-T20-HSH in Cells

Initial cell work was performed with the A549 human lung adenocarcinoma epithelial cell line (Appendix G.2). Confocal luminescence and reflection microscopy images of **Au13-T20-HSH** in A549 cells following a 20 minute incubation are exhibited in (Figure 2.37). In brief, widefield and magnifications of representative cells show **Au13-T20-HSH** in the outer regions of the cells as would be expected following a relatively short exposure time. Co-localisation analysis (described in Figure 2.37) on the nanoparticles confirms **HoechstSH** luminescence from bright pixels in the reflectance channel corresponding to scatter gold nanoparticles. This demonstrates the stability of the **HoechstSH** complex on gold nanoparticles upon exposure to a cellular environment/medium (Figure 2.37). Furthermore nanoparticles are relatively disperse in their distribution in the cell and are not localised to one area in particular. This is again what would be expected with such a relatively short exposure time as the cells would most likely not have had enough time to "process" the nanoparticles and either expel them or compartmentalise them in to lysosomal/endosomal vesicles, assuming this would be their eventual fate. The dark spots

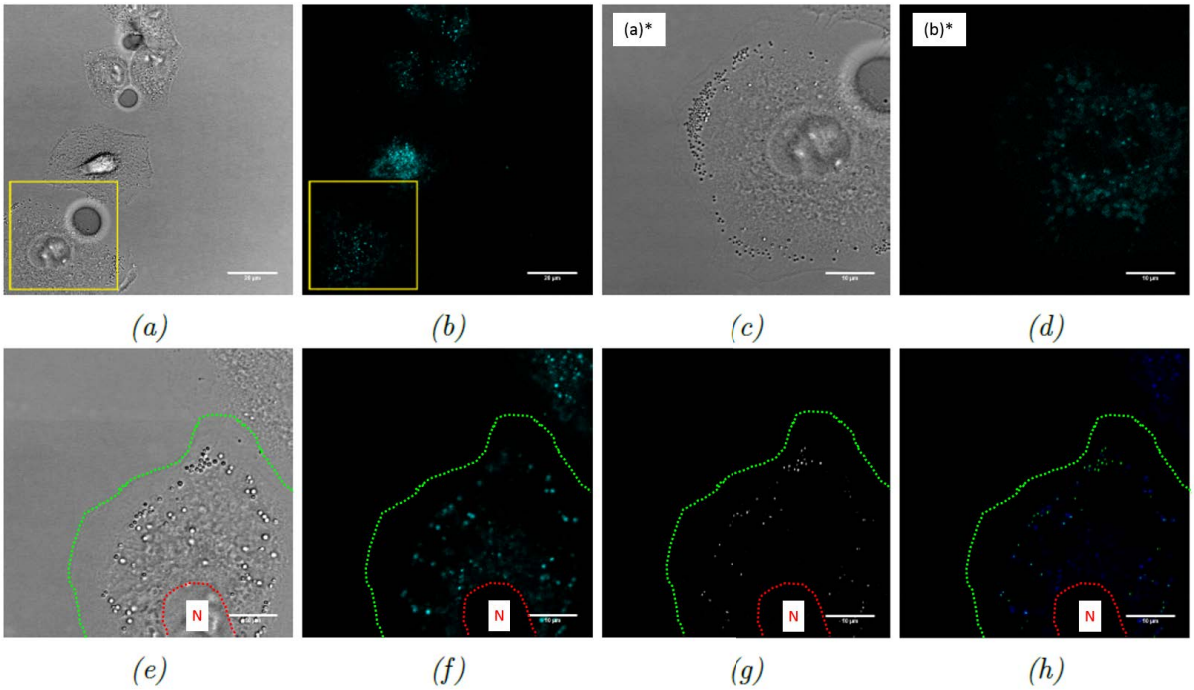

Figure 2.37: Images of Au13-T20-HSH nanoparticles in A549 cells monitored by confocal luminescence and reflection microscopy. Cells were incubated with ***Au13-T20-HSH*** *at a concentration of 0.25 nm in complete cell media for 20 minutes before fixing. (a) and (b) white light transmission and blue HoechstSH luminescence channel image. Magnifications of yellow inset boxes are shown in (c) and (d) respectively, designated (a*) and (b*). (e), (f) and (g) - magnifications of another cell with white light transmission, blue HoechstSH luminescence and reflection images respectively. Nanoparticles are observed as dark spots, cyan (from the HoechstSH surface coating) spots and white spots respectively in these images. Co-localised pixels in the blue HoechstSH luminescence and reflection images indicate HoechstSH emission from spatial locations corresponding to white spots i.e. nanoparticles in the reflection image. Co-localisation was performed using the ImageJ Colocalisation Analyser plugin. NB. Not all pixels "cross-correlate" because of differences in intensity, namely scattering of some of the reflection signal by the cellular material in the reflectance channel image. Cell-membrane and nuclear (N) envelope are manually drawn as indicated by the green and red dashed lines respectively. Reflection image* λ_{exc} *= 633 nm,* λ_{em} *= 623-643 nm, HoechstSH luminescence, blue channel,* λ_{exc} *= 405 nm,* λ_{em} *= 405-550 nm. (Scale bar (a, b) = 20* μ*m, (c - h) = 10* μ*m).*

evident in the transmission image are also notably very similar to observations made in a study on lipid-coated gold nanoparticle uptake in A549 cells by Wang *et al.*[264] Such features were attributed as lamellar bodies which were concluded to help internalise the gold nanoparticles in the cells (Figure 3.2).

Subsequent imaging studies were performed with the HeLa human cervical adenocarcinoma epithelial cell line. Confocal and brightfield images of HeLa cells incubated with **Au13-T20-HSH** for 24 hours are shown in Figure 2.38. Figure 2.38a shows an

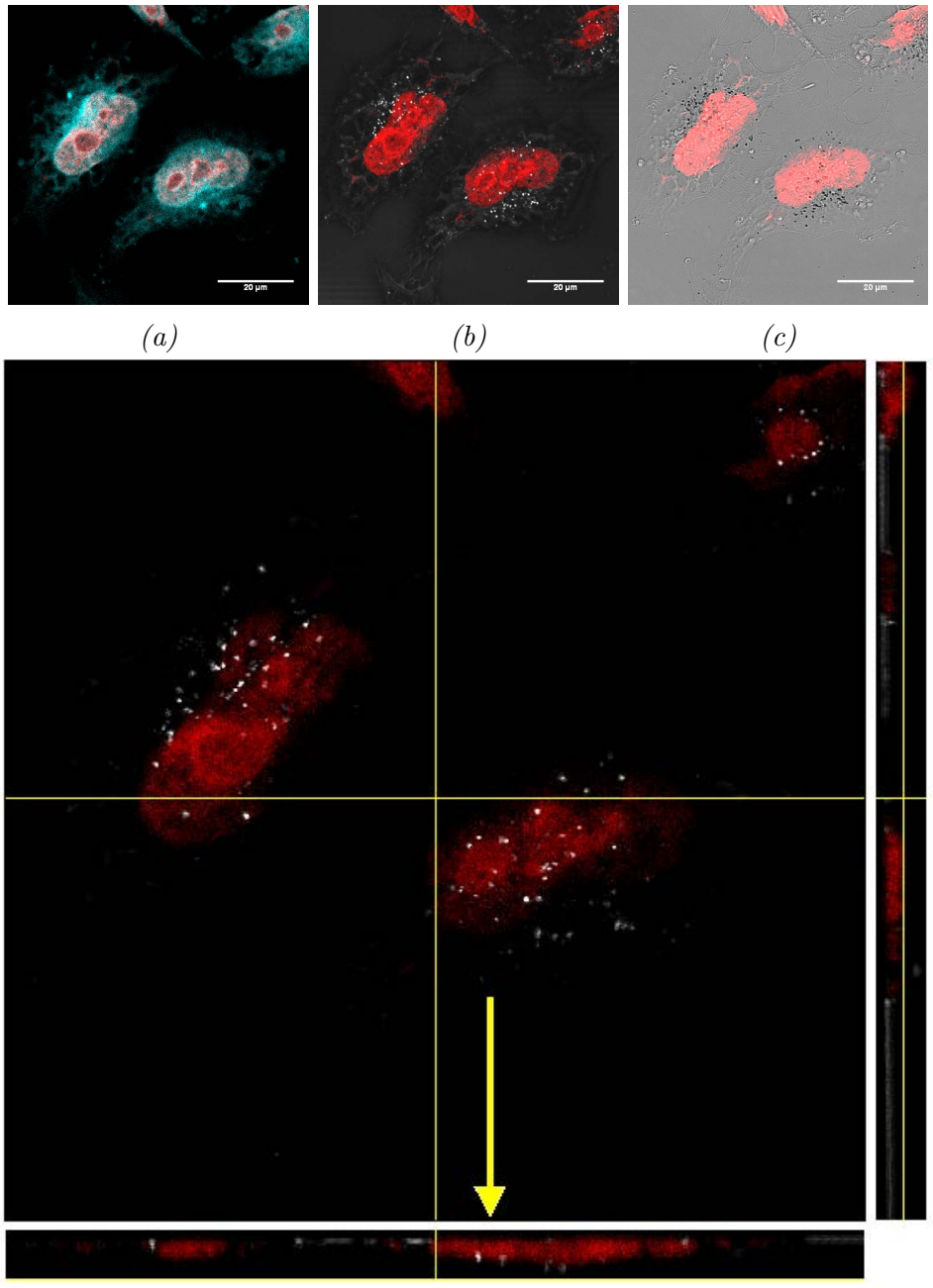

(a) *(b)* *(c)*

(d)

Figure 2.38: Images of ***Au13-T20-HSH*** *in HeLa cells monitored by confocal luminescence and reflection microscopy. Cells were incubated with* ***Au13-T20-HSH*** *at a concentration of 0.25 nM in complete cell media for 24 hours before fixing. (a)* ***HoechstSH*** *and DRAQ5 overlay. (b) Reflection and DRAQ5 overlay. (c) Transmission and DRAQ5 overlay. (d) "Orthogonal View" of Reflection and DRAQ5 overlay. Reflection image* λ_{exc} *= 633 nm,* λ_{em} *= 623-643 nm.* ***HoechstSH*** *luminescence, (blue channel),* λ_{exc} *= 405 nm,* λ_{em} *= 410-550 nm, DRAQ5, (red channel),* λ_{exc} *= 633 nm,* λ_{em} *= 640-800. (Scale bar 20 µm).*

overlay of the red and blue luminescence image channels, corresponding to the DRAQ5 nuclear counterstain and the **HoechstSH** luminescence respectively. It is evident from that these image slices that the most intense cyan emission is in the perinuclear region. Figure 2.38b shows an overlay of the red channel and the reflectance channel, in which gold nanoparticles appear as bright white spots due to their high elastic scattering cross-section of the gold nanoparticles at 633 nm relative to biological tissue.[263] This image overlay indicates cellular uptake with localisations of the nanoparticles within the cell periphery again localised mostly to the perinuclear region, corresponding to the areas of cyan emission observed in Figure 2.38a.

Evidence of some nuclear uptake is also evident with nanoparticles localised within the red area corresponding to the nucleus. Due to the nature of confocal microscopy, when recording an image the focal plane is chosen such that the nucleus is at its largest, thus the image slice is of a central plane in the cell and not above or below the cell. Nanoparticles observed in the nucleus are thus in the same focal plane.

Using line-intensity profiles, where pixel intensity along a selected line of interest is examined, it is possible to determine the size of a typical cluster and compare spatial positions of the peak emissions from different image channels (Figure 2.40). Figure 2.40a shows a magnification of a cell in the **HoechstSH** image in Figure 2.38, and Figure 2.40b the corresponding cell in the reflectance channel. In both images an identical line of interest (yellow) is drawn for the intensity profile measurement shown in Figure 2.40c. The intensity profiles obtained by measuring pixel intensity along the line of interest for the **HoechstSH** image channel (blue-dashed line) and the reflectance (black-solid line) exhibit peaks at approximately the same spatial localisation on the line of interest with peaks at approximately 2860 nm and 2760 nm along the line. This suggests that the **HoechstSH** is stable on the nanoparticle after a 24 hr period of exposure to a cellular environment. The lack of an exact correlation between the peaks and indeed the intensity of the peaks is likely due to the relatively diffuse nature of the **HoechstSH** emission, emanating from multiple **HoechstSH** complexes on multiple nanoparticles.

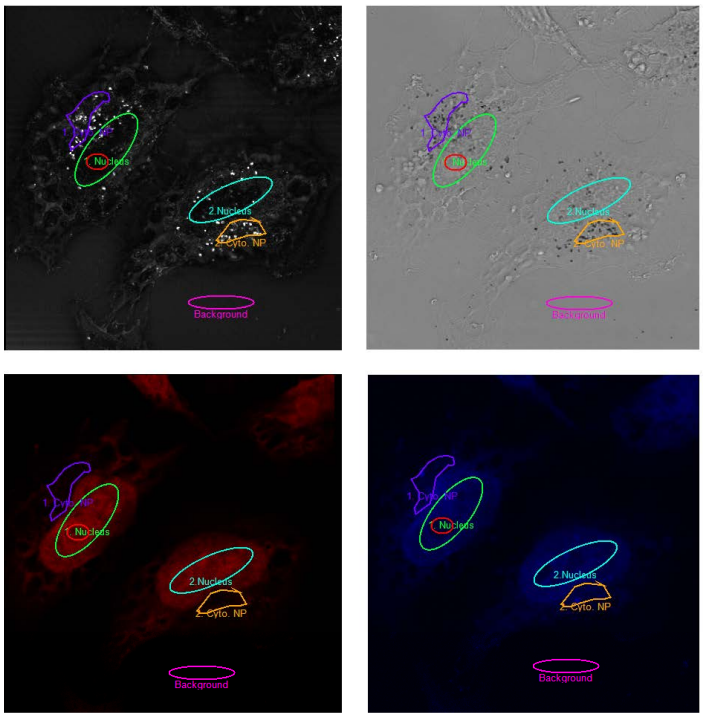

(a)

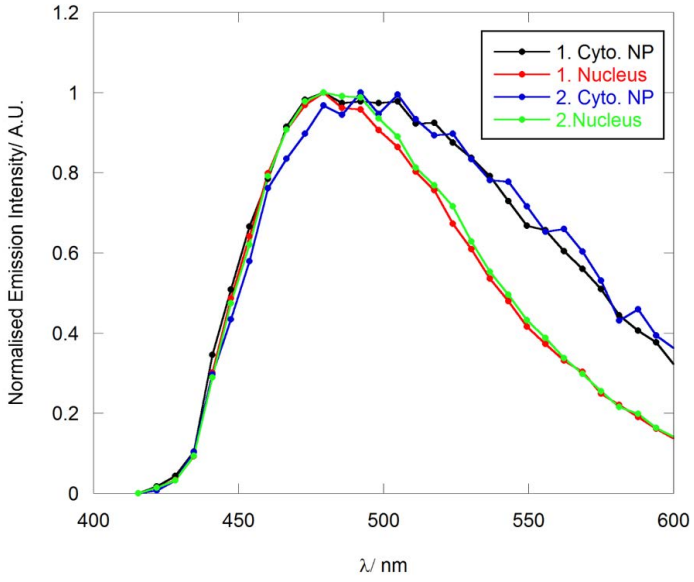

(b)

Figure 2.39: Images of ***Au13-T20-HSH*** *in HeLa cells monitored by confocal luminescence and reflection microscopy. Cells were incubated with* ***Au13-T20-HSH*** *at a concentration of 0.25 nM in complete cell media for 24 hours before fixing. (a) Regions of interest (ROIs) for spectral scans. (b) Spectral scans from (ROIs). Reflection image* λ_{exc} *= 633 nm,* λ_{em} *= 623-643 nm.* ***HoechstSH*** *luminescence, (blue channel),* λ_{exc} *= 405 nm,* λ_{em} *= 410-550 nm, DRAQ5, (red channel),* λ_{exc} *= 633 nm,* λ_{em} *= 640-800. (Scale bar 20 µm).*

The size of the cluster of nanoparticles can also be estimated using the full-width at half-maximum of the intensity profile from the reflectance channel, indicting a group of nanoparticles comprising a cluster approximately 600 nm in diameter. This would indicate the nanoparticles are subject to compartmentalisation once inside the cell where they are translocated into late stage endosomes/lysosomes, as depicted in Figure 2.2d.

A further analysis performed on the cells in Figure 2.38 is imaging of multiple focal planes such that a three-dimensional image stack can be reconstructed. The nuclear localisation is confirmed in Figure 2.38d which provides an orthogonal view of the three-dimensional image stack. The central image square is a single image slice from the stack as indicated by the yellow lines/cross-hairs in the coronal (YZ) and transverse (XZ) cross-sections displayed to the right and below. The nanoparticle-nucleolus association is evident in the transverse view as indicated by the yellow arrow with nanoparticles localised at discrete foci on the periphery of the nucleolus. This is quite significant as the nucleolus is a nuclear substructure responsible for assembling the cells ribosomal subunits for protein synthesis in eukaryotic cells. It consist of chromosomes which contain the genes for pre-ribosomal ribonucleic acid (rRNA) as well as proteins and RNAs that are not related to ribosome assembly.[265] Of particular relevance to the clusters of nanoparticles in Figure 2.38d is the location of the centromeres which are located on the periphery of the nucleolus.[266,267] Centromeres consist of protein structures responsible for directing the chromosomal DNA they are attached to during mitotic cell division. It is interesting to note the apparent affinity of the nanoparticles to these areas of the nucleolus and specifically the centromere/chromosomes. The presence of the surface bound **HoechstSH** complex on the nanoparticles may indeed have a role to play in this occurrence due to its DNA binding affinity.

Spectral emission scans of regions of interest (Figure 2.39a) can also be constructed by plotting the intensity of the emission in those regions of interest as a function of discrete wavelength gates. The ROIs chosen characterised the emission from the **HoechstSH** in the cells, both in the cytoplasm/perinuclear region where the dense clusters of

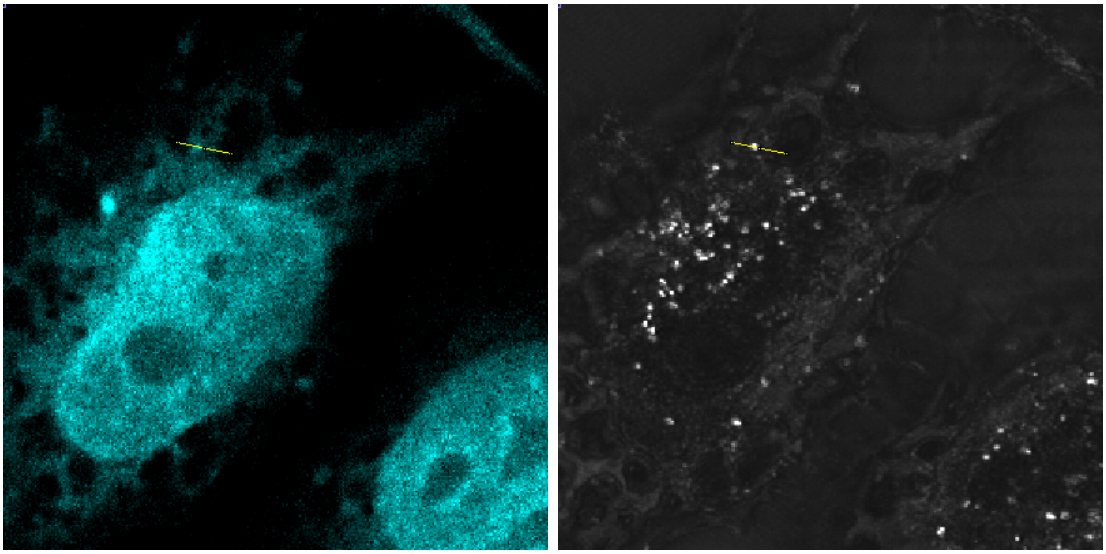

(a) *(b)*

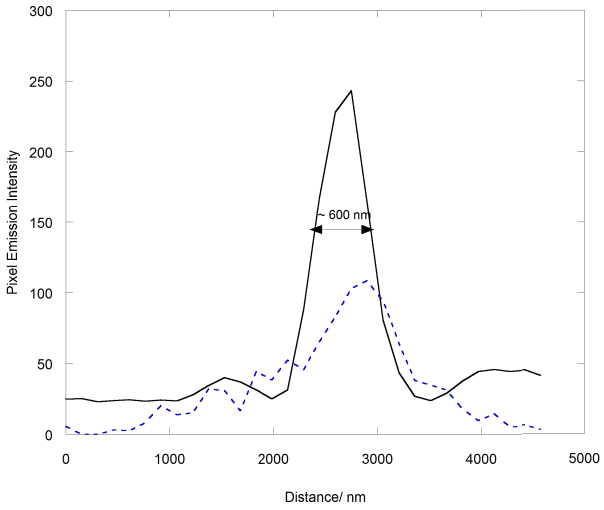

(c)

Figure 2.40: Images and line profiles of ***Au13-T20-HSH*** *in HeLa cells monitored by confocal luminescence and reflection microscopy. Cells were incubated with* ***Au13-T20-HSH*** *at a concentration of 0.25 nM in complete cell media for 24 hours before fixing. (a)* ***HoechstSH*** *and (b) reflectance channel and line of interest (yellow) drawn for intensity profile measurement. (c) Intensity profiles obtained by measuring pixel intensity along the line of interest for the* ***HoechstSH*** *image channel (blue-dashed line) and the reflectance (black-solid line). Distance on x-axis refers to distance along the yellow line of interest in (a) and (b). Reflection image* λ_{exc} *= 633 nm,* λ_{em} *= 623-643 nm.* ***HoechstSH*** *luminescence, (blue channel),* λ_{exc} *= 405 nm,* λ_{em} *= 410-550 nm.*

nanoparticles are observed and in the nucleus/nucleolus. The emission from these areas is characteristic of the Hoechst with peak emission observed at approximately 490 nm. (Figure 2.39b) Upon binding to DNA the Hoechst dye exhibits a characteristic blueshift,[241] and interestingly this is observed in the nucleolus which exhibits an emission maximum of approximately 480 nm. This observation again suggests the surface-bound **HoechstSH** dye is bound to DNA.

In conclusion the A549 and HeLa human adenocarcinomic cell lines were investigated as subjects for uptake of **Au13-T20-HSH**. Both cell lines were observed to internalise the nanoparticles and co-localisation of the peaks along line intensity profiles of **HoechstSH** emission with the positions of nanoparticles demonstrate the stability of the dye on the nanoparticle following exposure to a cellular environment. The majority of the nanoparticles were found in the perinuclear region after 24 hours, indicative of an endocytotic uptake mechanism which can lead to nanoparticle compartmentalisation in late-stage endosomal/lysosomal structures in the perinuclear region.[268,269] Line intensity profiles furthermore indicate nanoparticle clusters several hundred nanometres in diameter, again indicative of the endocytotic and subsequent endosomal/lysosomal processing mechanism. Spectral emission scans compiled from confocal images obtained over a range of wavelengths also confirm the cyan emission observed emanates from the **HoechstSH**.

Interestingly nuclear uptake of nanoparticles was observed and was confirmed using three-dimensional image stacks and orthogonal views of the cells. The most striking features were nanoparticles located on the periphery of the nucleolus. This is of great interest considering the DNA binding ability of the **HoechstSH** complex on the nanoparticles. There is thus great scope to further investigate the uptake and nuclear interactions of these nanoparticles as imaging and indeed as potential therapeutic agents.

Confocal Microscopy of Au13-Z-HSH in Cells

Initial cell work was performed with the A549 human lung adenocarcinoma epithelial cell line (Appendix G.3). Confocal luminescence and reflection microscopy images of **Au13-**

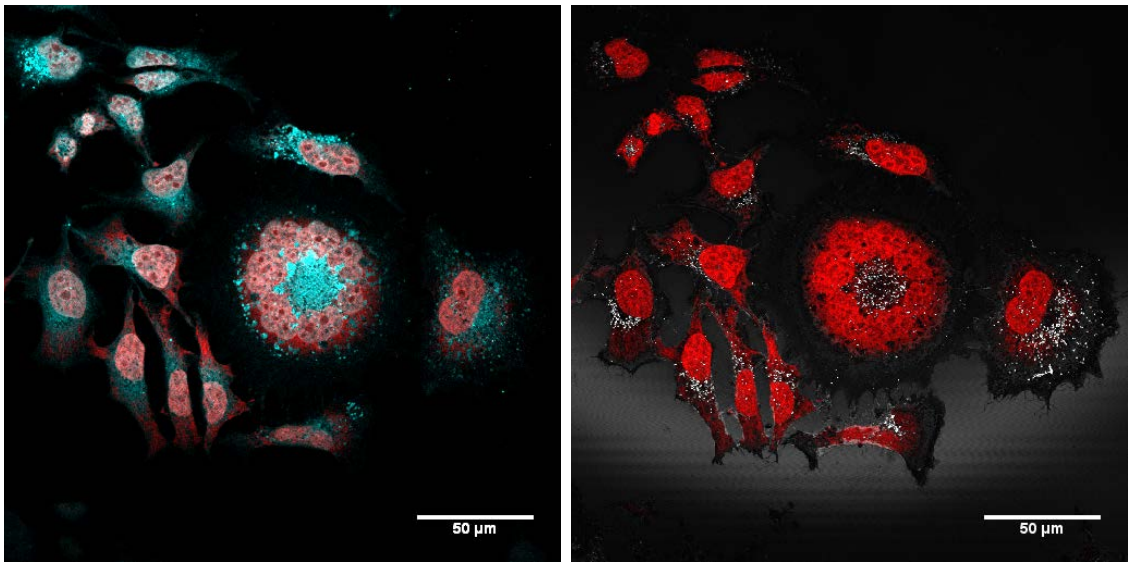

(a) *(b)*

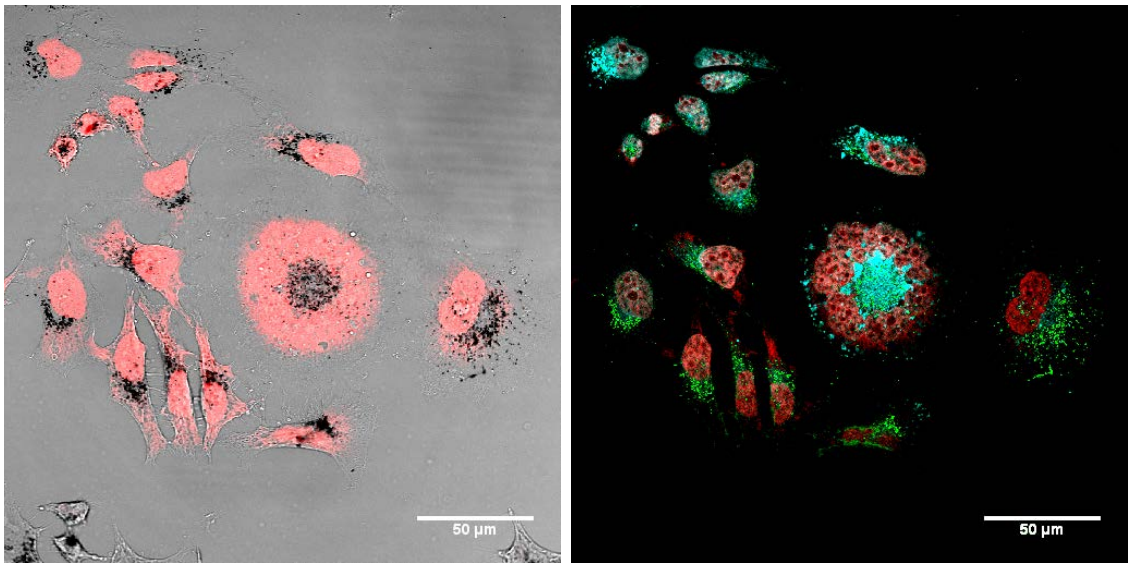

(c) *(d)*

Figure 2.41: Images of ***Au13-Z-HSH*** *in HeLa cells monitored by confocal luminescence and reflection microscopy. Cells were incubated with* ***Au13-Z-HSH*** *at a concentration of 0.25 nM in complete cell media for 24 hours before fixing. (a)* ***HoechstSH*** *and DRAQ5 overlay. (b) Reflection and DRAQ5 overlay. (c) Transmission and* ***HoechstSH*** *overlay. (d)* ***HoechstSH****, DRAQ5 overlay and reflection overlays (green false colour has been applied to reflection image). Reflection image* λ_{exc} *= 633 nm,* λ_{em} *= 623-643 nm.* ***HoechstSH*** *luminescence, (blue channel),* λ_{exc} *= 405 nm,* λ_{em} *= 410-550 nm, DRAQ5, (red channel),* λ_{exc} *= 633 nm,* λ_{em} *= 640-800. (Scale bar 50 µm)*

Z-HSH in A549 cells following a 20 minute incubation are exhibited in (Figure G.3). The dark spots evident in the transmission image are similar to observations of the **Au13-T20-HSH** in A549 cells after a 20 minute exposure (Figure 2.37), with nanoparticles located toward the periphery of the cells. The features are again very similar to observations of lamellar bodies in a study on lipid-coated gold nanoparticle uptake in A549 cells by Wang *et al.*[264] The presence of these features in A549 cells exposed to the different preparations of **HoechstSH** coated gold nanoparticles, namely **Au13-T20-HSH** and **Au13-Z-HSH**, and indeed lipid coated gold nanoparticles in the study by Wang *et al.*, suggest it is a common mechanism of the A549 cell line for gold nanoparticles.

Subsequent imaging studies were performed with the HeLa human cervical adenocarcinoma epithelial cell line. (Further images are provided in Appendix G.3). Confocal and brightfield images of HeLa cells incubated with **Au13-Z-HSH** for 24 hours are shown in Figure 2.41. Figure 2.41a shows an overlay of the red and blue luminescence image channels, corresponding to the DRAQ5 nuclear counterstain and the **HoechstSH** luminescence respectively. It is evident from that these image slices that the most intense cyan emission is in the perinuclear region, exemplified by the cell in the extreme top-left and the cell above the spherical cluster of cells in the centre of the image. Figure 2.41b shows an overlay of the red and reflectance channels in which gold nanoparticles appear as bright white spots. This image overlay again indicates cellular uptake with clusters of nanoparticles within the cell periphery, localised mostly to the perinuclear region. Notably the cells in Figure 2.41a which exhibited intense **HoechstSH**/cyan emission do not show many white spots in the corresponding locations in Figure 2.41b. This can be explained due to uneven illumination in the images, particularly in the reflection image in which a lighter background is seen in the bottom half of the image. The visual correlation in these images between the white spots of nanoparticles and the intense cyan emission observed in the middle of the central spherical cluster of cells, and indeed in the cell above indicates that the **HoechstSH** is stable on the nanoparticle after a 24 hr period of exposure to a cellular environment.

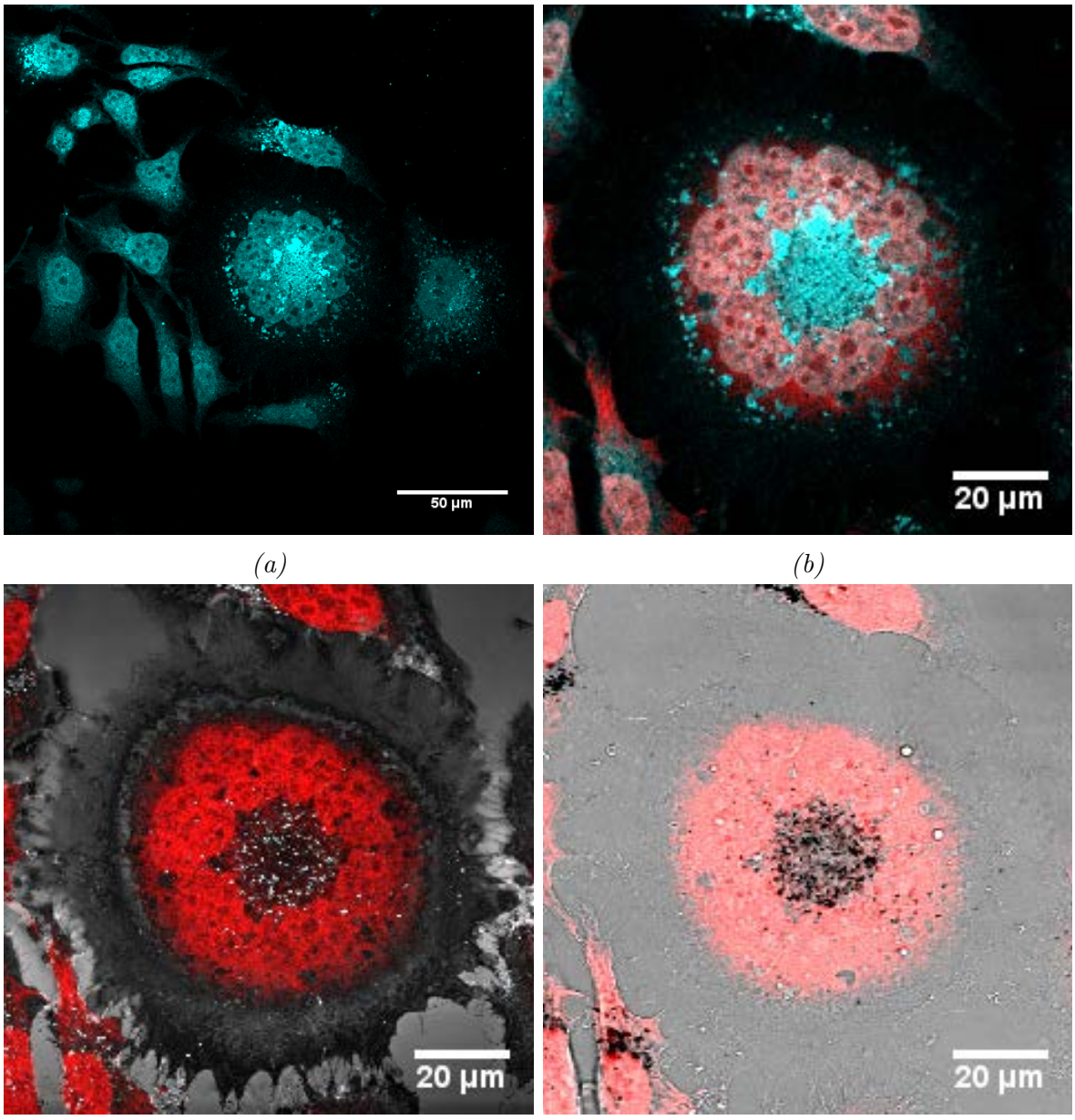

(a) *(b)*

(c) *(d)*

Figure 2.42: Images of ***Au13-Z-HSH*** *in a multicellular spheroid of HeLa cells, monitored by confocal luminescence and reflection microscopy. Cells were incubated with* ***Au13-Z-HSH*** *at a concentration of 0.25 nM in complete cell media for 24 hours before fixing. (a)* ***HoechstSH*** *and DRAQ5 overlay. (b) Reflection and DRAQ5 overlay. (c) Transmission and DRAQ5 overlay. Reflection image* λ_{exc} *= 488 nm,* λ_{em} *= 478-498 nm.* ***HoechstSH*** *luminescence, (blue channel),* λ_{exc} *= 405 nm,* λ_{em} *= 410-550 nm, DRAQ5, (red channel),* λ_{exc} *= 633 nm,* λ_{em} *= 640-800. (Scale bar 50 µm)*

The problem of uneven illumination can be an issue when recording a confocal image but is not an issue on the brightfield transmission image in Figure 2.41d, which shows an overlay of the brightfield image in which the nanoparticles appear as dark spots and the red channel. In this image the perinuclear localisation of the majority of the nanoparticles is clear in all cells. As in Figure 2.38 which presents **Au13-T20-HSH** in HeLa cells after 24 hours, the nanoparticles in the images are of aggregates or clusters, observed as such due to the cells' processing mechanism for spherical gold nanoparticles. Figure 2.41d shows an overlay of the DRAQ5 red image, the cyan **HoechstSH** image and the reflection image which has been given a green false colour for easier visualisation of the nanoparticles in the presence of the cyan emission. It is again apparent from this image that perinuclear localisation is dominant, however the cell on the extreme right shows some nuclear uptake of the nanoparticles. Figure 2.38d showing uptake of the **Au13-T20-HSH** in HeLa cells after 24 hours exhibits similar nuclear localisation, with nanoparticles located around the periphery of the nucleolus.

Figure 2.42 shows magnified images of the most prominent feature in Figure 2.41, the spherical cluster of cells known as a multicellular spheroid. Figure 2.42b exhibits the overlay of the blue and red channel shows the intense cyan emission from the **HoechstSH**. Figure 2.42c shows the overlay of the red channel with the reflection image which was recorded with 488 nm (as opposed to 633 nm for the previous images). At this wavelength it is possible to examine the cell membranes of the cluster of cells more clearly due to the greater contrast they exhibit relative to the background, although The nanoparticles scatter less at this wavelength than at 633 nm. The image overlay shows multiple clusters of nanoparticles enclosed within a ring of cell nuclei.

The cluster of cells in the centre of the image spans 90 μm in diameter and as mentioned is known as a multicellular spheroid. Multicellular spheroids are commonly used three-dimensional cell culture systems for cancer research, possessing an advantage over two-dimensional cultures due to their close resemblance of physiological tumour conditions in humans.[270–273] Specific culture methods are traditionally used to grow multicellular

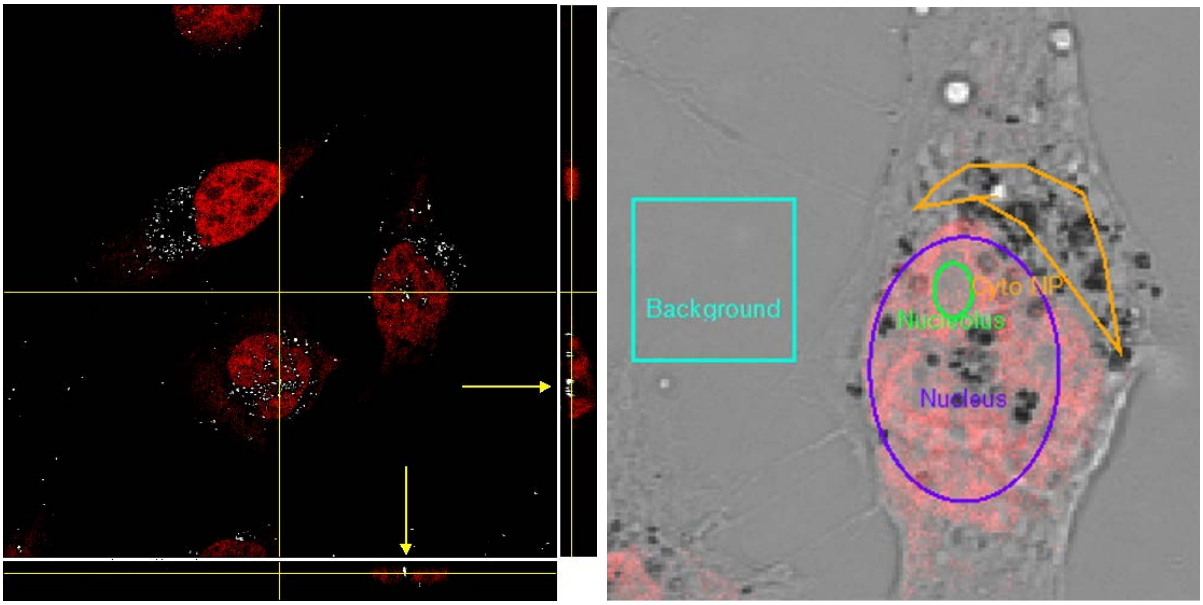

(a) *(b)*

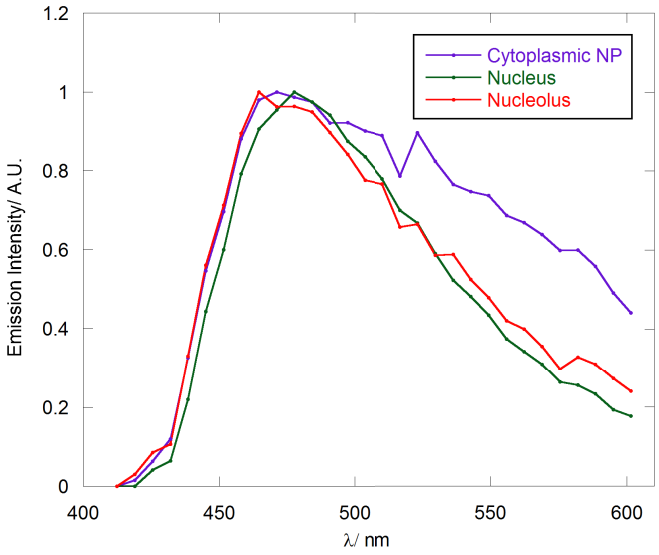

(c)

Figure 2.43: Images of ***Au13-Z-HSH*** *in HeLa cells monitored by confocal luminescence and reflection microscopy. Cells were incubated with* ***Au13-Z-HSH*** *at a concentration of 0.25 nM in complete cell media for 24 hours before fixing. (a) "Orthogonal View" of Reflection and DRAQ5 overlay. (c) Regions of interest (ROI) for Spectral scans. (d) Spectral scans from (ROI). Reflection image* λ_{exc} *= 633 nm,* λ_{em} *= 623-643 nm.* ***HoechstSH*** *luminescence, (blue channel),* λ_{exc} *= 405 nm,* λ_{em} *= 410-550 nm, DRAQ5, (red channel),* λ_{exc} *= 633 nm,* λ_{em} *= 640-800. (Scale bar 20 µm)*

spheroids, such as cell scaffolds or non-physiological matrix compounds.[274] It is therefore surprising that in this study no specific measures were taken to induce the growth of the multicellular spheroid yet such a structure was still observed. The dense clusters of nanoparticles in the centre spanning 20 μm in diameter is particularly striking and it would be interesting to determine with the aid of further investigations whether longer incubation times with the nanoparticles yield growth of more multicellular spheroids, if indeed they are responsible for their production. It is difficult without continuous imaging of the cell population to conclude whether the nanoparticles have caused growth of the spheroid, or whether they were simply internalised by an existing spheroid. Although the multicellular spheroid feature was observed only once in this microscopy sample which contains a population of many hundreds of cells, the dense clustering of the nanoparticles within the spheroid that closely mimics tumours in a physiological environment nevertheless holds great theranostic potential for these nanoparticles.

Nuclear uptake was also observed in another sample of cells shown in Figure 2.43. Examining an image slice from the three-dimensional stack in greater detail using an orthogonal view, nuclear uptake is again obvious in both cells to the right and to the bottom (Figure 2.43a). The yellow arrows in the image directed at transverse views of the left cell show the location of the nanoparticles in the direct centre of the nucleus. Performing a line intensity profile on several of these clusters indicate they range in size from 400 - 800 nm and thus composed of several tens of nanoparticles suggesting the nanoparticles have undergone extensive accumulation within the cell possibly in to late stage endosomes/lysosomes. Surprisingly some particles have however still achieved nuclear localisation.

Spectral emission scans of the same cell exhibiting nuclear uptake are shown in Figures 2.43b and 2.43c. The ROIs chosen for obtaining spectral scans characterise the emission from the **HoechstSH** in the cells in the cytoplasm/perinuclear region, in the nucleus and in the nucleolus. The emission from these areas is characteristic of the Hoechst dye with peak emission observed at approximately 470 nm. It is notable that the emission

spectrum from nanoparticles in the cytoplasm is notably broader that those in the nucleus. This may due to a contribution to the emission spectrum from autofluorescence such as mitochondria and lysosomes which are located in this cytoplasm and perinuclear region.[275]

Uptake of **Au13-Z-HSH** in a sample of the HeLa cells also afforded the opportunity to study the dynamics of internalised nanoparticles during cell division (Figure 2.44). Cell division was discussed in Section 2.1.4 and is an important factor in the uptake of nanoparticles. A study by Kim *et al.* on the role of the cell cycle in nanoparticle uptake and dilution concluded uptake of nanoparticles is affected by the cell cycle phase. Furthermore nanoparticles internalized by cells are not exported from cells were found to be split between daughter cells when the parent cell divides.[276]

Figures 2.44a-c show a widefield view of a selection of newly divided cells or cells just prior to division. Magnifications of a pair of cells from this FOV that have just divided are shown in Figures 2.44d-f. It is noticeable that the clusters of nanoparticles in these cells are located at the terminus where the cells would have separated, suggesting that the nanoparticles have been split between the two daughter cells. Figures 2.44g-i shows a binuclear cell prior to separation and illustrates how the nanoparticles will be divided into the daughter cells as they pull away from each other, thus confirming the conclusions of Kim *et al.*[276]

Uptake of **Au13-Z-HSH** was also examined in live HeLa cells after a 24 hour incubation allowing for the examination of cells in a natural physiological state. Widefield confocal images are shown in Figure 2.45 and show nanoparticle uptake in all of the cells (approximately twenty cells in the field-of-view). Magnifications of representative cells from these images are shown in Figure 2.46. Figure 2.46a-c exhibits a pair of cells which show significant uptake of **Au13-Z-HSH**. This is indicated in the **HoechstSH** and DRAQ5 overlay by the bright cyan spots of luminescence within the red DRAQ stained area which denotes the cell nucleus (Figure 2.46a). The DRAQ5 nuclear stain defines the nuclear membrane very distinctly in live cells so it is clear that nearly all of the nanoparticles are in the nucleus. This is further evident in the top-left cell in the reflectance and

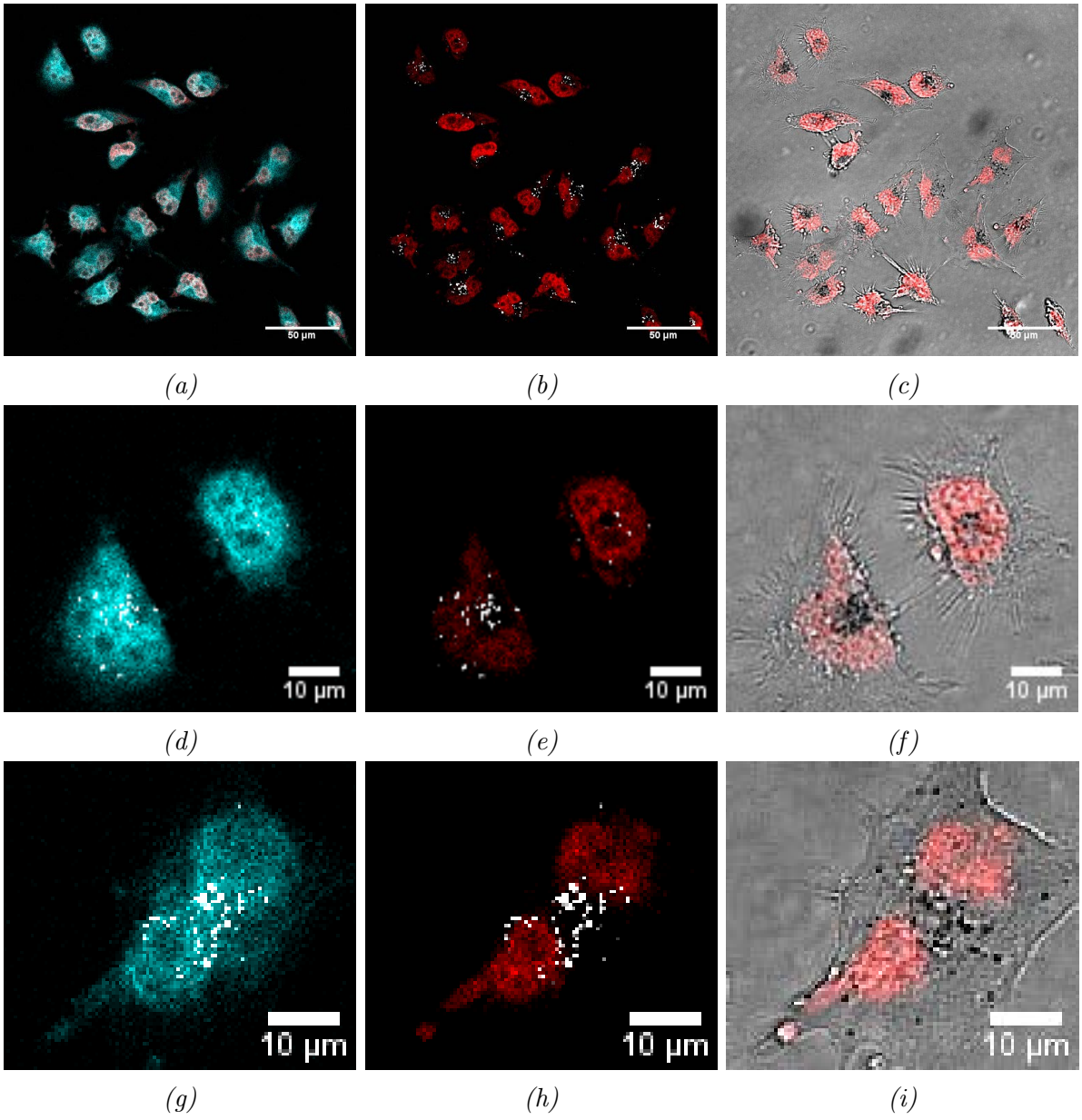

(a) *(b)* *(c)*

(d) *(e)* *(f)*

(g) *(h)* *(i)*

Figure 2.44: Images of ***Au13-Z-HSH*** *in HeLa cells monitored by confocal luminescence and reflection microscopy. Cells were incubated with* ***Au13-Z-HSH*** *at a concentration of 0.25 nM in complete cell media for 24 hours before fixing. (a-c) widefield view of cells: (a)* ***HoechstSH*** *and DRAQ5 overlay. (b) Reflection and DRAQ5 overlay. (c) Transmission and DRAQ5 overlay. (d-f) magnifications of a newly divided cell: (d)* ***HoechstSH*** *and reflection overlay. (e) Reflection and DRAQ5 overlay. (f) Transmission and DRAQ5 overlay. (g-i) magnifications of a dividing cell: (g)* ***HoechstSH*** *and reflection overlay. (h) Reflection and DRAQ5 overlay. (i) Transmission and DRAQ5 overlay. Reflection image λ_{exc} = 633 nm, λ_{em} = 623-643 nm.* ***HoechstSH*** *luminescence, (blue channel), λ_{exc} = 405 nm, λ_{em} = 410-550 nm, DRAQ5, (red channel), λ_{exc} = 633 nm, λ_{em} = 640-800. (Scale bar 50 µm)*

DRAQ5 overlay (Figure 2.46b). In this cell only a few clusters of nanoparticles are outside the nucleus on the top-left edge of the cell. Another point of note is the constriction in the nucleus observed on the left side. This "pinching" of the nucleus indicates the cell is in the cytokinesis stage of cell division.[229]

Figure 2.46c-f shows another cell exhibiting nuclear uptake with clusters on nanoparticles located on the periphery of the nucleolus, as indicated by the green arrows in Figure 2.46d and Figure 2.48. Performing line intensity profiles on these features indicate they range in size from 400-600 nm in diameter, and are thus composed of several tens of nanoparticles. A further interesting feature is the presence of nanoparticles in the direct centre of the both the nucleoli in the nucleus, as indicated by the dashed-yellow arrows. Performing line intensity profiles indicate they range in size from 400 to 500 nm for the clusters designated "NP^1" and "NP^2" respectively (Figure 2.48), again indicating they are composed of several tens of nanoparticles in close proximity. Figures 2.46e and 2.47 exhibit orthogonal views of the cells and also confirm this with white spots of nanoparticles located in the central plane of the nucleus, as indicated by the yellow arrows and the corresponding transverse views.

In conclusion the A549 and HeLa human adenocarcinomic cell lines were investigated as for uptake of **Au13-Z-HSH** with uptake of observed in both cell lines. Nanoparticle uptake in the A549 cell line induced the formation of lamellar bodies analogous to previous observations of gold nanoparticle uptake in the A549 cell line.[264] In the HeLa cell line after 24 hour exposure **Au13-Z-HSH** were observed primarily in the perinuclear region. Perinuclear localisation of **Au13-T20-HSH** was also observed suggesting the endocytotic uptake and processing mechanism is generally preferred for gold nanoparticles in the HeLa cell line. In confocal observations one of the most striking features was a multicellular spheroid, a spherical mass of cells with a dense cluster of nanoparticles within its centre. It is unclear however whether the nanoparticles induced the formation of this feature or were internalised within an already existing spheroid. The presence of such a large cluster of nanoparticles in the centre provides great impetus for future investigations where the

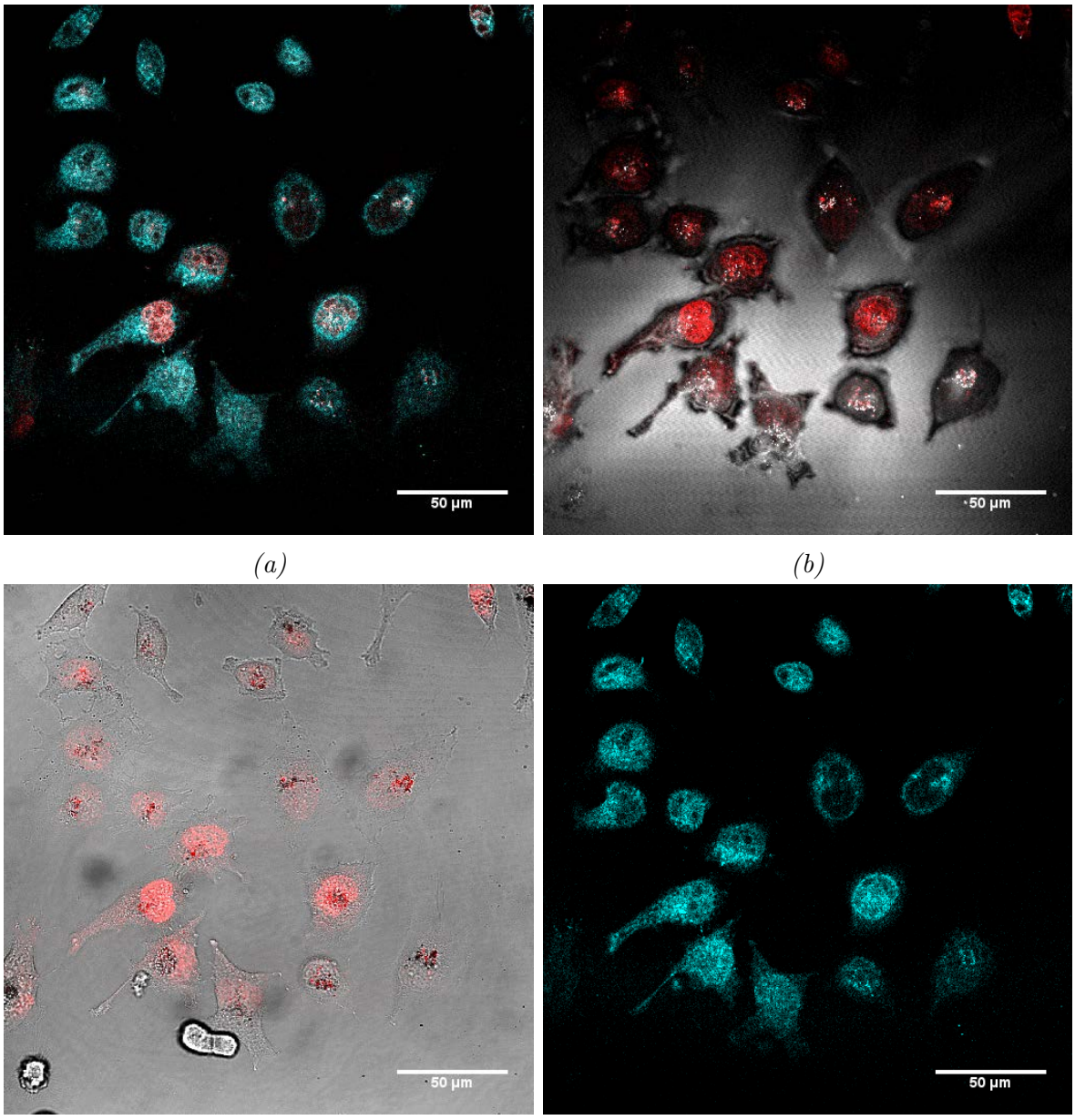

(a) *(b)*

(c) *(d)*

Figure 2.45: Images of ***Au13-Z-HSH*** *in live HeLa cells monitored by confocal luminescence and reflection microscopy. Cells were incubated with* ***Au13-Z-HSH*** *at a concentration of 0.25 nm in complete cell media for 24 hours before (live) imaging. (a)* ***HoechstSH*** *and DRAQ5 overlay. (b) Reflection and DRAQ5 overlay. (c) Transmission and DRAQ5 overlay. (d)* ***HoechstSH*** *image. Reflection image λ_{exc} = 633 nm, λ_{em} = 623-643 nm.* ***HoechstSH*** *luminescence, (blue channel), λ_{exc} = 405 nm, λ_{em} = 410-550 nm, DRAQ5, (red channel), λ_{exc} = 633 nm, λ_{em} = 640-800. (Scale bar 50 µm)*

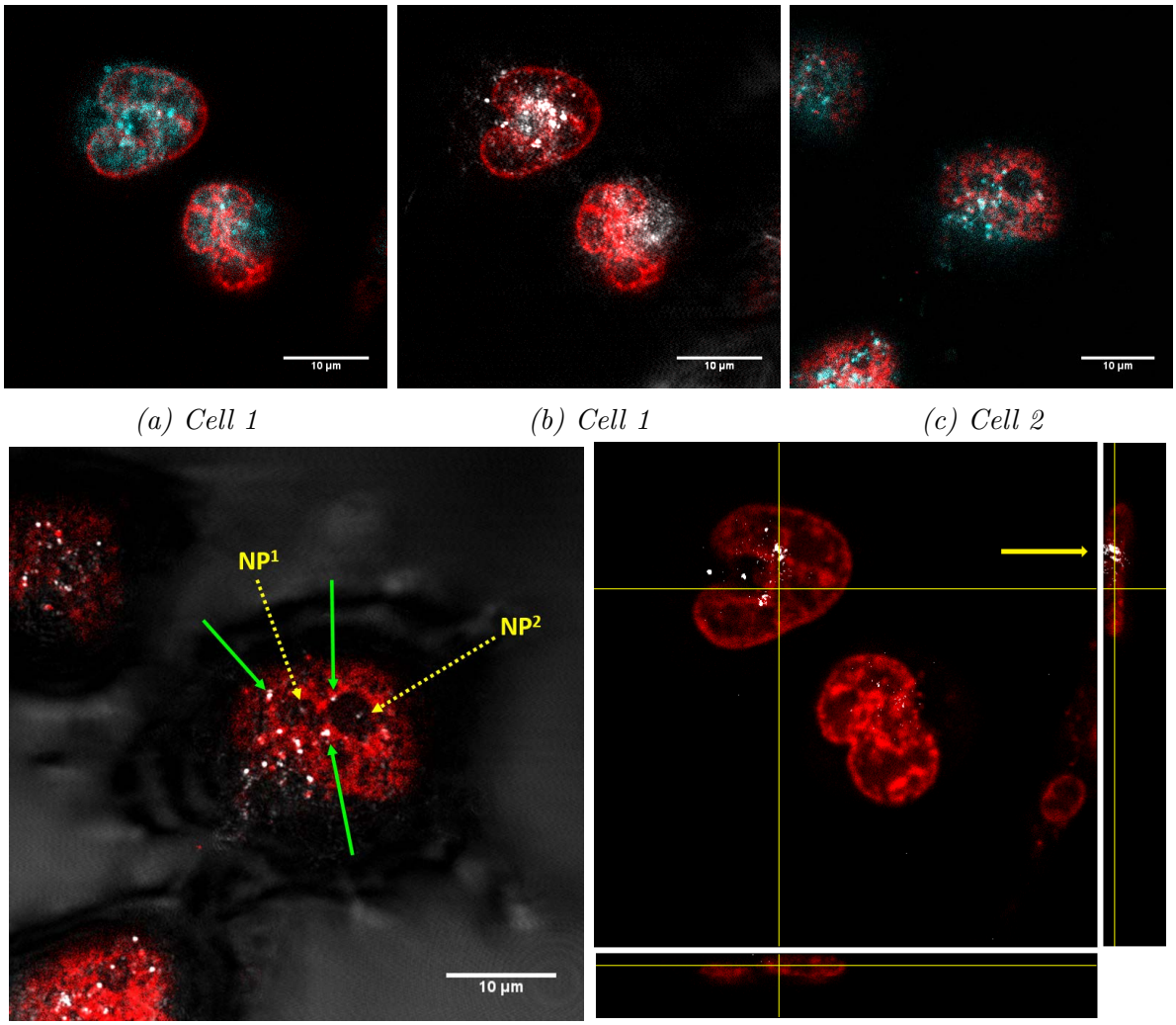

(a) Cell 1 *(b) Cell 1* *(c) Cell 2*

(d) Cell 2 *(e) Orthogonal View of Cell 1*

*Figure 2.46: Images of **Au13-Z-HSH** in live HeLa cells monitored by confocal luminescence and reflection microscopy. Cells were incubated with **Au13-Z-HSH** at a concentration of 0.25 nM in complete cell media for 24 hours before (live) imaging. (a, b) image overlays of cell 1: (a) **HoechstSH** and DRAQ5 overlay. (b) Reflection and DRAQ5 overlay. (c, d) image overlays of cell 2: (c) **HoechstSH** and DRAQ5 overlay. (d) Reflection and DRAQ5 overlay. (e) Orthogonal view of cell 1. Reflection image λ_{exc} = 633 nm, λ_{em} = 623-643 nm. **HoechstSH** luminescence, (blue channel), λ_{exc} = 405 nm, λ_{em} = 410-550 nm, DRAQ5, (red channel), λ_{exc} = 633 nm, λ_{em} = 640-800. (Scale bar 50 µm)*

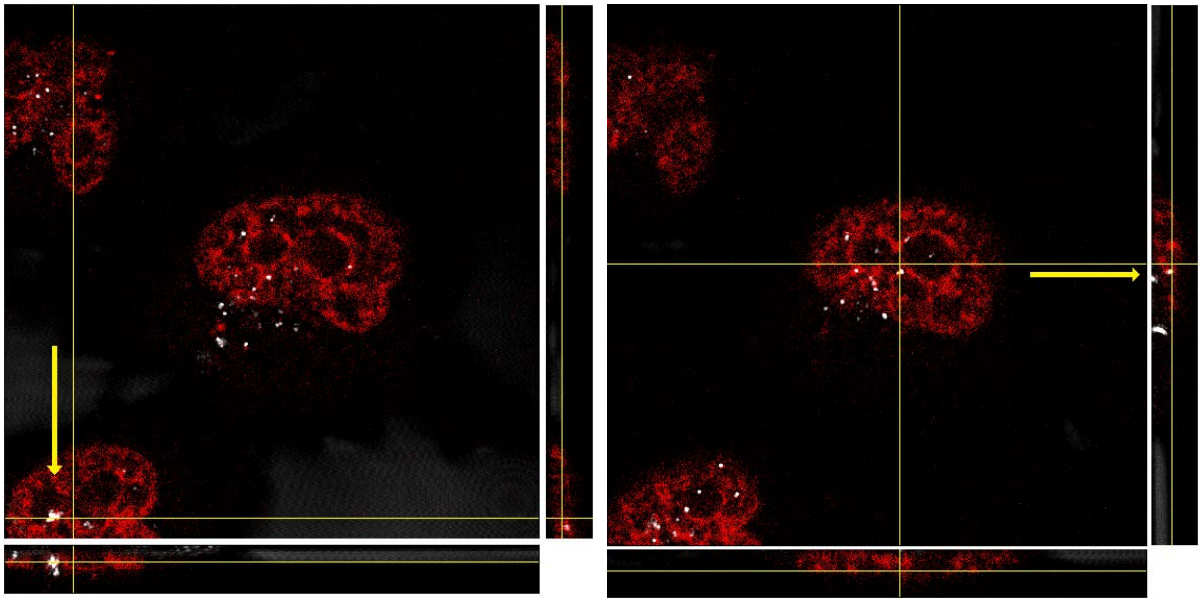

(a) Orthogonal View of Cell 2 *(b) Orthogonal View of Cell 2*

*Figure 2.47: Images of **Au13-Z-HSH** in live HeLa cells monitored by confocal luminescence and reflection microscopy. Cells were incubated with **Au13-Z-HSH** at a concentration of 0.25 nM in complete cell media for 24 hours before (live) imaging. (a) and (d) Orthogonal views of cell 2. Reflection image λ_{exc} = 633 nm, λ_{em} = 623-643 nm. **HoechstSH** luminescence, (blue channel), λ_{exc} = 405 nm, λ_{em} = 410-550 nm, DRAQ5, (red channel), λ_{exc} = 633 nm, λ_{em} = 640-800. (Scale bar 50 µm)*

interactions of multicellular spheroids and nanoparticles are studied in greater detail.

Similarly to HeLa cells exposed to **Au13-T20-HSH** nuclear uptake of **Au13-Z-HSH** was also observed in single confocal image slices and confirmed in three-dimensional image stacks and orthogonal image views. Spectral emission measurements of **HoechstSH** from areas corresponding to nanoparticle localisation yield the characteristic Hoechst emission peak at 480 nm. Line intensity profiles of nuclear localised nanoparticles indicate they are clusters composed of several tens of nanoparticles in close proximity, again indicative of compartmentalisation which is a signature of the endocytotic internalisation mechanism. Images of dividing cells also indicate how internalised nanoparticles are divided in to daughter cells, supporting conclusions made by Kim *et al.*[276]

Uptake of **Au13-Z-HSH** was also observed in live cells. The three-dimensional aspect of cellular imaging with live cells afforded clear evidence of nuclear uptake with well defined nuclear boundaries and centralised nanoparticle localisation within. This is of

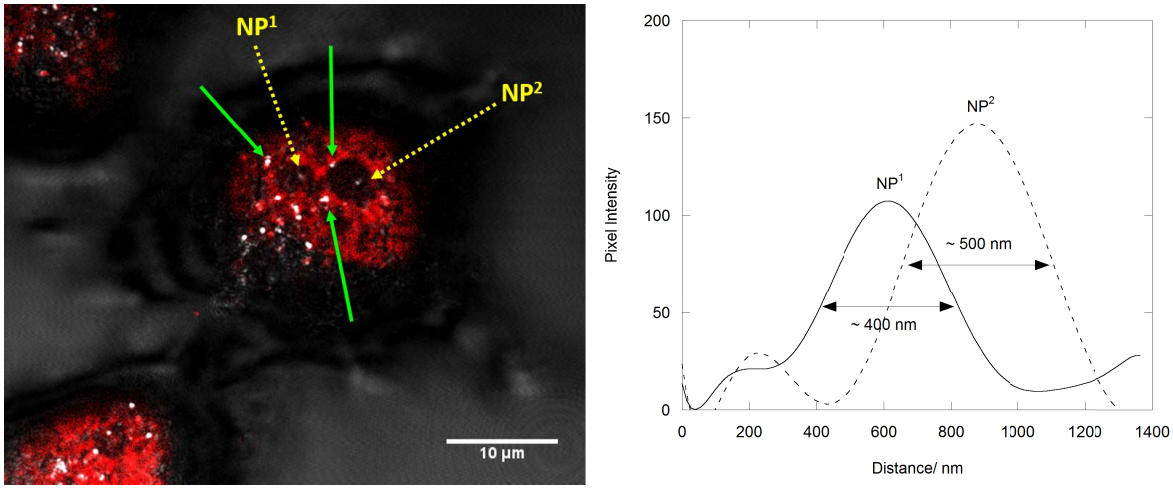

(a) *(b)*

*Figure 2.48: Image of **Au13-Z-HSH** in HeLa cells monitored by confocal luminescence and reflection microscopy. Cells were incubated with **Au13-Z-HSH** at a concentration of 0.25nM in complete cell media for 24 hr before imaging. (a) reflection and DRAQ5 overlay. (b) Line intensity profile measurements performed on the nanoparticle clusters designated NP^1 and NP^2. Size was estimated by measuring the full-width at half-maximum of the intensity profiles. Reflection image λ_{exc} = 633 nm, λ_{em} = 623-643 nm. DRAQ5, (red channel), λ_{exc} = 633 nm, λ_{em} = 640-800. (Scale bar 10 µm)*

.

great interest considering the DNA binding ability of the **HoechstSH** complex and offers further impetus to investigate the uptake and nuclear interactions of these nanoparticles. The nanoparticles exhibit use as imaging and indeed as potential therapeutic agents in light of these observations.

Preliminary Study: Confocal Microscopy of Au13-Z-HSH in Cells with Lysotracker

As depicted schematically in Figure 2.2, nanoparticles can be internalised by cells in to endosomes that ultimately fuse with late-stage acidic lysomosomes as the cell attempts to degrade the cargo with lysosomal enzymes.[277] To explore this possibility for uptake of **Au13-Z-HSH** lysotracker (a red fluorescent dye) was used to stain lysosomes in HeLa cells following 24 hour incubation with the nanoparticles. HeLa cells were subsequently fixed and examined by confocal microscopy.

Figure 2.49a shows a widefield image of fixed HeLa cells incubated with **Au13-Z-**

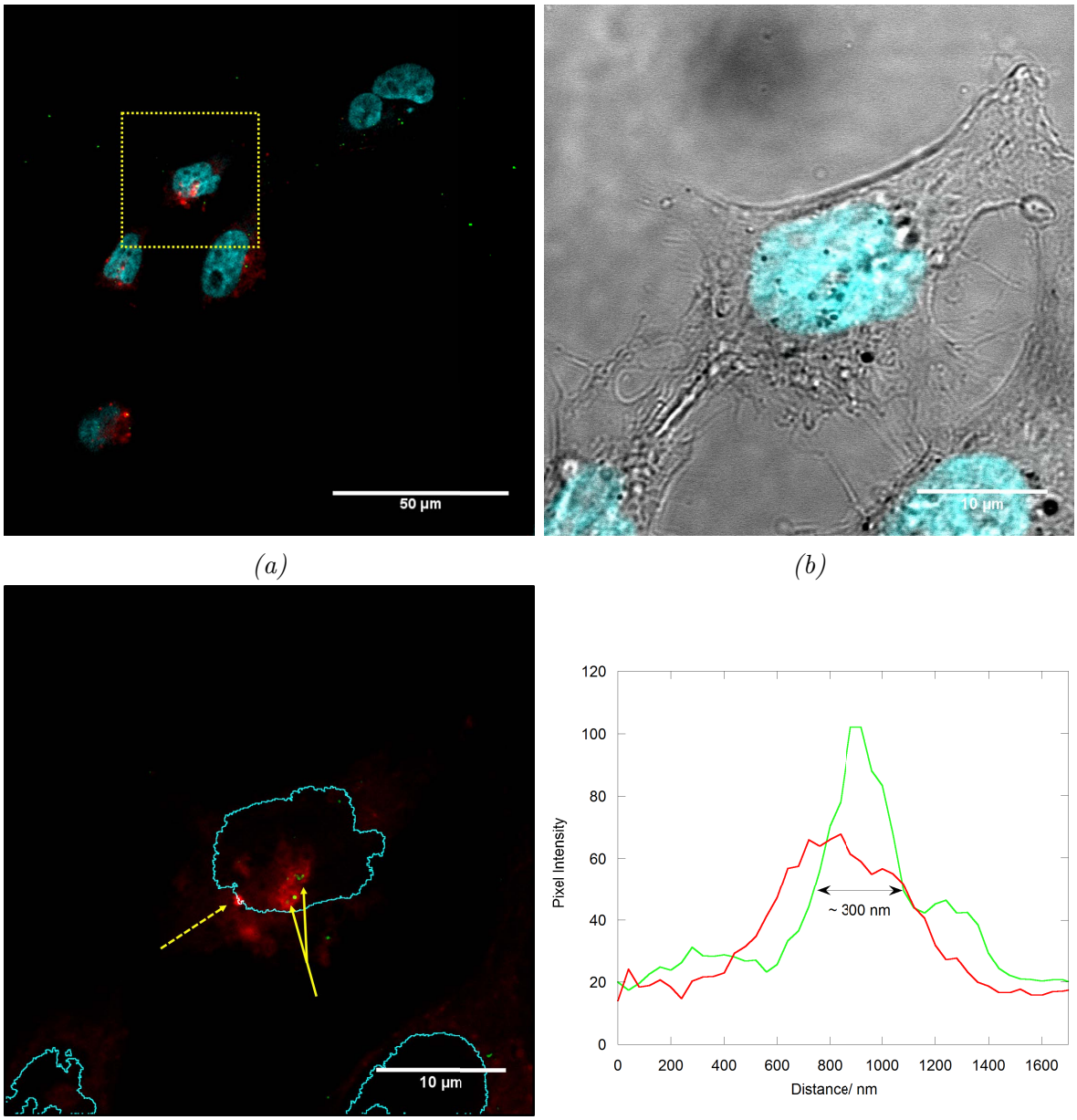

(a) *(b)*

(c) *(d)*

Figure 2.49: Images of ***Au13-Z-HSH*** *in HeLa cells monitored by confocal luminescence and reflection microscopy. Cells were incubated with* ***Au13-Z-HSH*** *at a concentration of 0.25 nM in complete cell media for 24 hours, incubated with Lysotracker for 30 minutes (1 µM concentration) and then fixed. (a)* ***HoechstSH****, lysotracker and reflection (green false colour) image channel overlay. Magnification of yellow inset box: (b) transmission and* ***HoechstSH*** *image channel overlay, (c) reflection (green false colour) and lysotracker overlay. (d) Line intensity profile taken in reflectance (green (false colour) channel) and lysotracker (red channel) taken at the yellow-dashed arrow. Reflection image* λ_{exc} *= 633 nm,* λ_{em} *= 623-643 nm.* ***HoechstSH*** *luminescence, (blue channel),* λ_{exc} *= 405 nm,* λ_{em} *= 410-550 nm, lysotracker, (red channel),* λ_{exc} *= 633 nm,* λ_{em} *= 640-800. (Scale bar (a) 50 µm, (b,c) 10 µm)*

HSH for 24 hours and co-stained with Lysotracker. An overlay of the transmission and **HoechstSH** image channels of the area enclosed by the yellow inset box is shown in Figure 2.49b and exhibits dark spots of nanoparticles in the cytoplasm and in the nucleus. By performing an intensity based image segmentation on the HoechstSH image it possible to derive an outline of the nucleus of the cell. An overlay of the nuclear outline, the lysotracker (red) channel and the reflectance (green false colour) channel is shown in Figure 2.49c. The yellow arrows in this magnification indicate nuclear localised nanoparticles co-localised with diffuse red emission. Due to the diffuse nature of the emission it is however difficult to categorically state the nanoparticles are in lysosomes.

The cluster of nanoparticles indicated by the yellow dashed arrow is on the periphery of the nucleus indeed on the nuclear membrane itself. The cluster of nanoparticles is co-localised with discrete spot of red emission, as indicated by line intensity profiles taken in the lysotracker (red) and reflectance (green) channels which show peaks in the intensity at the same location (Figure 2.49d). The full-width at half-maximum of the peak indicates the nanoparticles are indeed in a cluster of several tens of nanoparticles. It is interesting to observe such a large cluster of nanoparticles virtually on the nuclear membrane in addition to nanoparticles in the nucleus. Both clusters of nanoparticles were localised to areas of red emission suggestive of endosomal/lysosomal compartmentalisation, potentially indicating a trafficking mechanism of these organelles into the nucleus.

Confocal Microscopy of Au100-Z-HSH in HeLa Cells

Uptake of **Au100-Zonyl-HSH** is investigated in HeLa cells where 100 nm gold nanoparticles are large enough to be imaged as single nanoparticles as opposed to the 13 nm gold nanoparticles which are only visible in clusters consisting of several tens of nanoparticles.[77] Images of HeLa cells incubated with **Au100-Z-HSH** nanoparticles for 90 minutes are shown in Figure G.5 (Appendix G.3.3), representative magnified images are shown in Figure 2.50. After 90 minutes significant nanoparticle uptake has occurred in all cells (Figure 2.50a). Nanoparticles are dispersed throughout the whole cell (Figure 2.50b) and

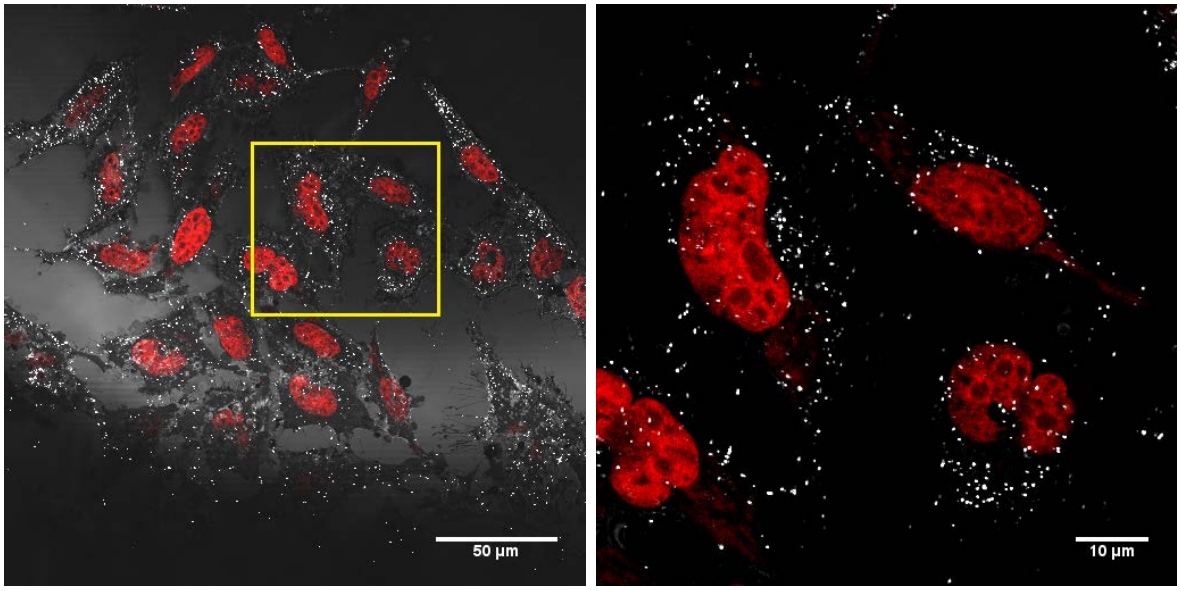

(a) *(b)*

Figure 2.50: Images of Au100-Z-HSH nanoparticles in HeLa cells monitored by confocal luminescence and reflection microscopy. Cells were incubated with Au100-Z-HSH at a concentration of 0.10 pM in complete cell media for 90 min before fixing. (a) widefield reflection and DRAQ5 overlay. (b) magnified inset of reflection and DRAQ5 overlay. Reflection image λ_{exc} = 633 nm, λ_{em} = 623-643 nm. ***HoechstSH*** *luminescence, (blue channel), λ_{exc} = 405 nm, λ_{em} = 410-550 nm, DRAQ5, (red channel), λ_{exc} = 633 nm, λ_{em} = 640-800. (Scale bar (a) 50 µm) (b) 10 µm*

are not specifically localised to the perinuclear region. Figure G.6 (Appendix G.3.3) shows a further set of images of a cell in the metaphase stage of cell division, exhibiting another example of cytoplasmic nanoparticle localisation.[278]

To establish whether the **Au100-Z-HSH** were eventually transferred in to the perinuclear region HeLa cells were incubated with **Au100-Z-HSH** nanoparticles for 24 hours. Images are shown in (Appendix G.3.3), images of representative cells are shown in Figure 2.51. DRAQ5 overlays with the reflectance and brightfield images are shown in Figures 2.51b and 2.51c and constitute magnifications of the yellow-boxed region in Figure 2.51a. The amount of cellular uptake of the nanoparticles is quite striking and indeed all of the cells in the field-of-view show evidence of nuclear uptake indicated by the white and dark spots in the nuclei stained red with the DRAQ5 stain. To confirm these nanoparticles were in the same plane as the nucleus three-dimensional z-stacks were again recorded. Examining orthogonal views of each of the cells it is apparent that the nanoparticles are in the central plane of the nuclei as denoted by the crosshairs (Figures 2.51d-f).

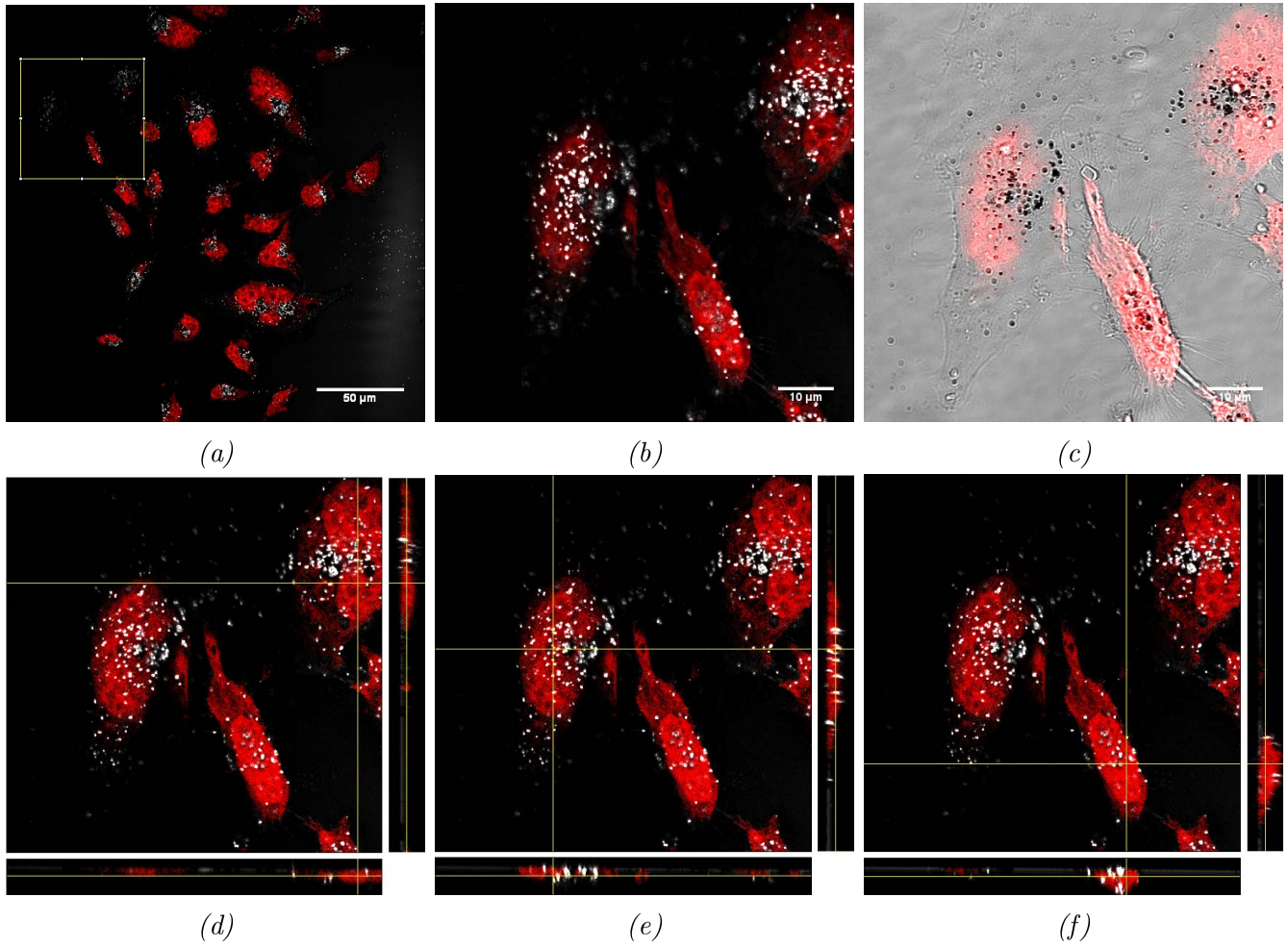

Figure 2.51: Images of ***Au100-Z-HSH*** *in HeLa cells monitored by confocal luminescence and reflection microscopy. Cells were incubated with Au100-Z-HSH at a concentration of 0.10 pM in complete cell media for 24 hours before fixing. (a) widefield reflection and DRAQ5 overlay. (b,c) magnification of inset (yellow dashed box) - (b) reflection and DRAQ5 overlay, (c) transmission brightfield and DRAQ5 overlay. (d-f) orthogonal views of reflection and DRAQ5 overlays examining nuclear uptake. Reflection image* λ_{exc} *= 633 nm,* λ_{em} *= 623-643 nm. DRAQ5, (red channel),* λ_{exc} *= 633 nm,* λ_{em} *= 640-800. (Scale bar (a) 50 µm) (b) 10 µm*

To further evaluate the cytoplasmic and nuclear uptake another cell was imaged and was subject to the segmentation protocol (ImageJ). Image segmentation uses the principle of creating boundaries in an image based on differences in pixel intensity, thus the cell membrane and nuclear boundary were extracted using blue and red channel images as shown in Figure 2.52. The boundary extraction protocol was applied to the cell shown in Figure 2.53. Nanoparticle uptake is obvious in the image overlays but the extent to which nuclear localisation is clear in Figure 2.53d, most strikingly with a dense area in the centre of the nucleus. By taking a ratio of the total pixel intensity of the area enclosed within the magenta boundary and comparing it to the total pixel intensity from the area bounded by the green and magenta boundaries, it is possible to obtain a crude comparison between the relative amount of nanoparticles in the nucleus and the cell cytoplasm respectively. The results of this calculation indicate that 80 % of the nanoparticles in this image slice of the cell are in the within the nuclear boundary.

Line intensity profiles enable nanoparticle size to be estimated. Line intensities were measured on the two of the smallest white spots and two of the larger spots to ascertain a crude measure of the size range of the nanoparticle clusters (Appendix G). Single nanoparticles can be modelled computationally and are determined to appear as spots 300 nm in diameter, as described in Section 3.3.2.[77] The measurements performed indicate that the smaller spots measure are single nanoparticles and the larger spots clusters of two to three nanoparticles in close proximity to each other. It is perhaps surprising to see such significant nanoparticle uptake in to the nucleus considering the size of nanoparticles. Nuclear pore complexes traditionally govern the transfer of a variety of biomolecules between the cytoplasm and the nucleus. Nuclear pores typically allow passage of cargo the order of a few tens of nanometres in diameter,[279] this would therefore suggest an alternative mode of nuclear translocation of **Au100-Z-HSH** in to the cells.

In conclusion uptake of **Au100-Z-HSH** was readily observed with significant uptake after a 90 minute exposure with nanoparticles observed dispersed throughout the cells. After a 24 hour exposure nuclear uptake had also occurred. It is difficult to compare the

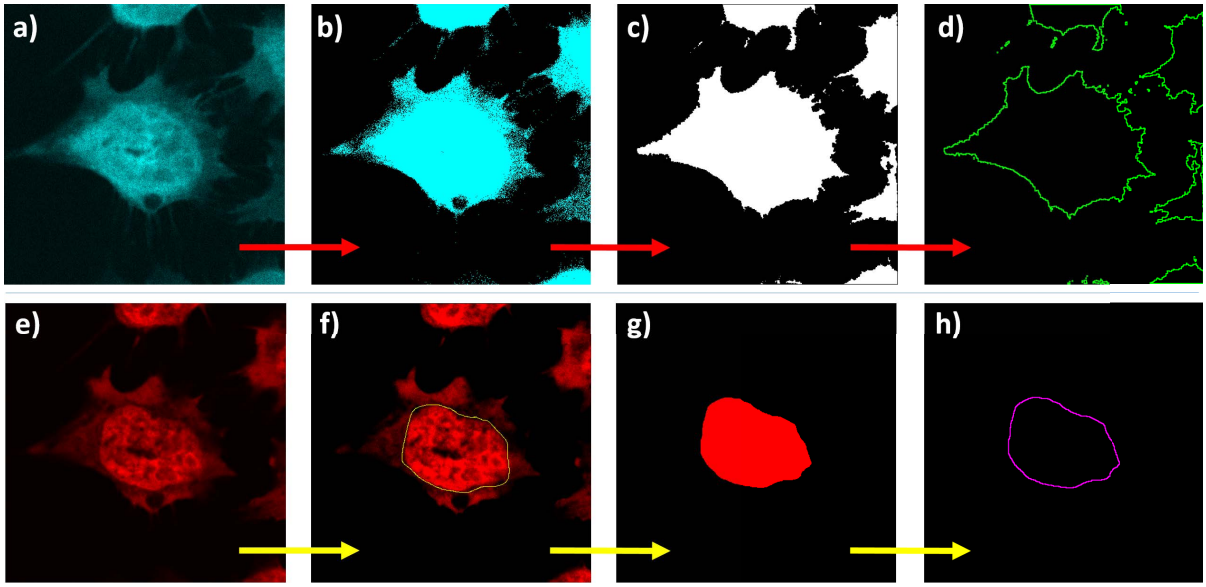

Figure 2.52: Segmentation protocol to extract Cell (a-d) and nuclear boundary (e-h) in HeLa cell. Cell boundary is extracted using the raw blue channel image (a) which is saturated by brightening the pixels (b). The image in then binarised by choosing an appropriate pixel intensity threshold and using the erode and fill functions (c). Boundaries are drawn (green) around the binarised region using the Find Edges function (d). Nuclear boundary is extracted using the red channel (e). The nucleus is manually cropped from the image (f) and saturated in terms of pixel intensity/brightness (g). Boundaries are drawn (magenta) around the binarised region using the Find Edges function (h).

extent of nuclear uptake of the **Au100-Z-HSH** with the **Au13-Z-HSH** as the 13 nm nanoparticles are beyond the resolution limit until they form clusters composed of several tens of nanoparticles. Line intensity profiles of **Au100-Z-HSH** within the nucleus indicate they are composed of small clusters of two to three nanoparticles in close proximity. Taking in to account the size of the nuclear pores, (Pante *et al.* state that the nuclear pore complex is able to transport macromolecules no greater than 39 nm in size[165]), also suggests an alternative mechanism of internalisation rather than transit through the nuclear pores.

Transmission Electron Microscopy of Au13-Z-HSH in Cells

Transmission electron microscopy (TEM) was performed on HeLa cells incubated with the **HoechstSH** functionalised nanoparticles. In TEM a beam of electrons is passed through an ultra-thin sample to afford nanometre resolution.[207] In addition to high spatial

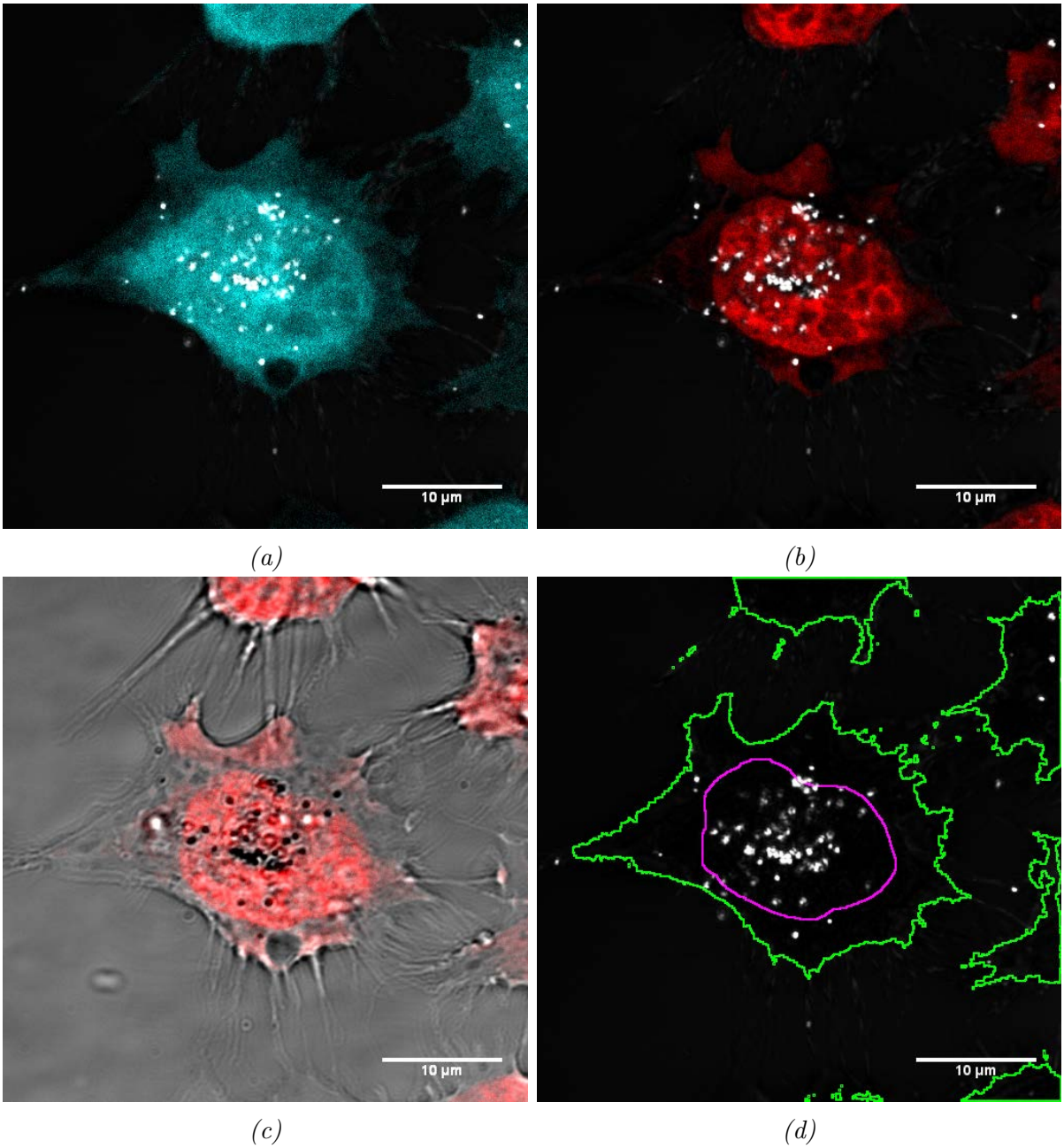

(a) *(b)*

(c) *(d)*

Figure 2.53: Images of Au100-Z-HSH nanoparticles in HeLa cells monitored by confocal luminescence and reflection microscopy. Cells were incubated with Au100-Z-HSH at a concentration of 0.10 pM in complete cell media for 24 hours before fixing. (a) ***HoechstSH*** *and reflection image overlay. (b) reflection image and DRAQ5 overlay. (c) transmission brightfield and DRAQ5 overlay magnification. (d) cell and nuclear boundaries superimposed on reflection image. Reflection image* λ_{exc} *= 633 nm,* λ_{em} *= 623-643 nm. DRAQ5, (red channel),* λ_{exc} *= 633 nm,* λ_{em} *= 640-800. (Scale bar 10* μm

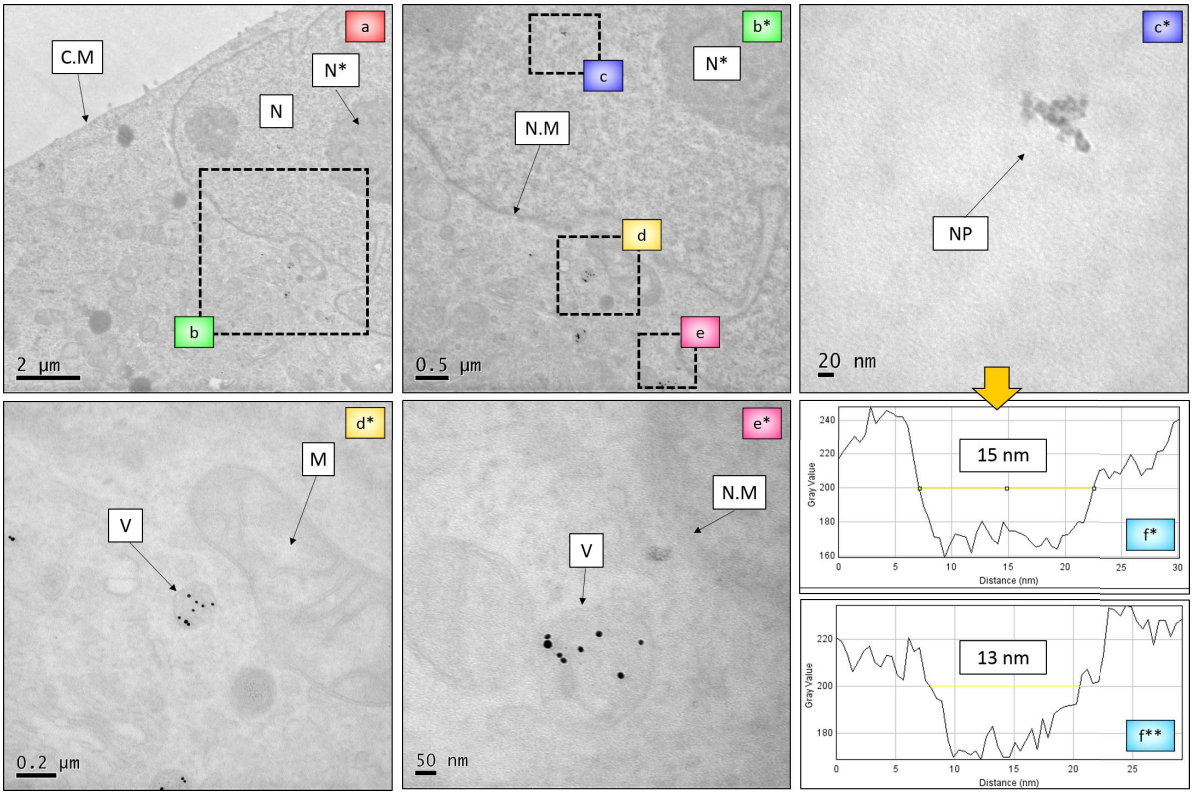

*Figure 2.54: TEM images of **Au13-Z-HSH** in HeLa cells. Cells were incubated with **Au13-Z-HSH** at a concentration of 0.25 nM in complete cell media for 2 hours before fixing. Widefield image is shown in (a). Magnifications of insets (b - e) are in shown in (b* - (e*)) respectively. Line profiles of nanoparticles in (c*) are exhibited in (f*) and (f**) C.M - cell membrane, N.M - nuclear membrane, N - nucleus, N* - nucleolus, V - vesicle, NP - nanoparticles.*

resolution the high contrast provided by electron dense materials such as gold allows for single nanoparticle imaging in the intracellular environment. Cells were incubated with nanoparticles at the same concentration and conditions as for confocal imaging studies and all TEM samples were left unstained. Although this reduces contrast of cellular organelles artefacts from the staining process are avoided.

Figure 2.54 shows HeLa cells incubated with **Au13-Z-HSH** for 2 hours with Figure 2.54a exhibiting a widefield view in which gold nanoparticles are observed as dark spheres due to their high electron density. Figure 2.54b shows a magnification of the intracellular area, depicted by the inset box (b). The magnification shows the nuclear membrane, cytoplasm and nucleus can be observed. It is interesting to note that a cluster of electron dense particles are seen within the nuclear membrane (Figure 2.54c*). Line intensity profiles indicate the cluster is approximately 13 - 15 nm in diameter (Figure 2.55f*),

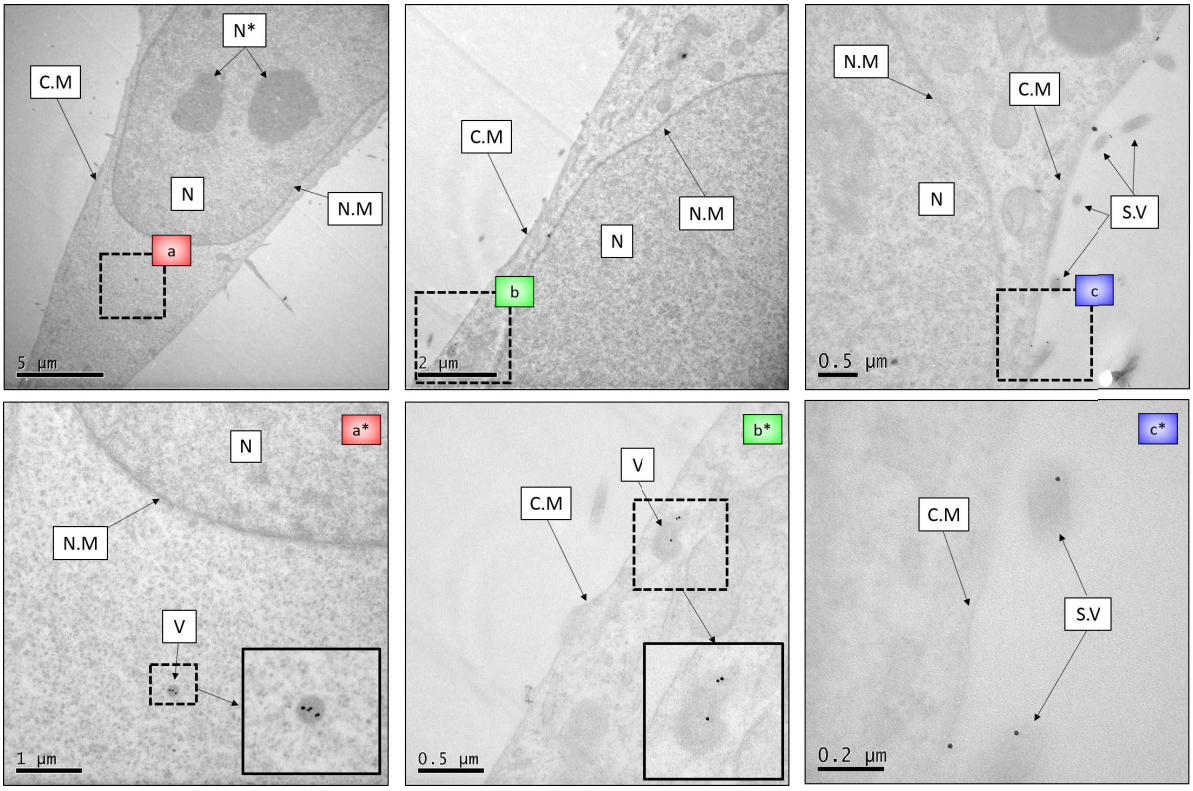

*Figure 2.55: TEM images of **Au13-Z-HSH** in HeLa cells. Cells were incubated with **Au13-Z-HSH** at a concentration of 0.25 nM in complete cell media for 2 hours before fixing. Widefield images are shown in top panel. Magnifications of insets (a), (b) and (c) are shown in (a*), (b*) and (c*) respectively. C.M - cell membrane, N.M - nuclear membrane, N - nucleus, N* - nucleolus, V - vesicle, S.V - secretory vesicles.*

corresponding well to the size of the **Au13-Z-HSH**.

Further magnifications are shown in Figure 2.54d* and 2.54e*. Nanoparticles in these images are observed in membrane bound vesicles approximately 200 nm in diameter with vesicles in the respective images both containing eight nanoparticles. Referring to the uptake mechanisms and vesicle designations described in Figure 2.2, these vesicles are Type 2 in nature and are likely to be trafficking vesicles in the early stages of endocytosis.

Figure 2.55 shows further HeLa cells incubated with **Au13-Z-HSH** for 2 hours. Figures 2.55a-c show widefield views of the cells and Figures 2.55a*-c* magnifications of the respective insets. Nanoparticles in Figures 2.55a* and b* are again observed in membrane bound vesicles approximately 200 - 300 nm in diameter. The vesicle in Figure 2.55a*,b* contains three nanoparticles. The vesicles in Figure 2.55b* are in close proximity and without well defined membranes may be in the process of merging together.

Notably in Figure 2.55c nanoparticles appear to be in extracellular vesicles. Denoted as secretory vesicles (S.V) these may be vesicles that have been ejected by cells as depicted schematically in Figure 2.2. It is interesting to note that nanoparticles are seen on the cell membrane in Figure 2.55c. The single nanoparticle magnified in Figure 2.55c* in particular is not in an obviously apparent vesicle and as such may be entering the cell by passive diffusion through the cell membrane. Alternatively an extracellular vesicle containing the nanoparticle have just been re-internalised by the cell with the membrane of the vesicle breaking down in the process. Re-uptake of exocytosed nanoparticles as demonstrated in a study by Bartczak *et al.* in which re-uptake of extracellular vesicles containing 15 nm peptide coated gold nanoparticles was observed after four hours in HUVEC cells (human umbilical vein endothelial cells).

TEM images of HeLa cells incubated with **Au13-Z-HSH** for 24 hours are exhibited in Figures 2.56-2.58. Examining the first set of images in Figure 2.56 the most prominent feature in the widefield view of a cell (Figure 2.56a) is the presence of several densely packed vesicles containing nanoparticles. The first of these, magnified in Figure 2.56b* contains approximately forty clearly defined nanoparticles with several more appearing as dense indistinguishable flocculations, confirming the endocytotic pathway of uptake as the primary means of nanoparticle internalisation. Quite striking with regards to its extremely dense nanoparticle uptake is the organelle in Figure 2.56c*, a multi-vesicular body containing many lamellar folds. A similar feature was observed by Nativo *et al.* in HeLa cells and was also observed to contain internalised nanoparticles.[119] Referring to the schematic shown in Figure 2.2, this structure can be designated as a Type 6 multi-laminar vesicle (multivesicular body - M.L.V), defined as comprising the latter stage of the endocytotic mechanism of uptake and serving as precursors for lysosomal degradation.[280]

Another possibility is that the structure is part of the endoplasmic reticulum or Golgi network of the cell. Several studies have stated that the payloads contained in endocytotic vesicles can be delivered to the endoplasmic reticulum or Golgi network in cells.[281–283] Indeed the study by Dragoni *et al.* shows gold nanoparticle uptake in a similar structure

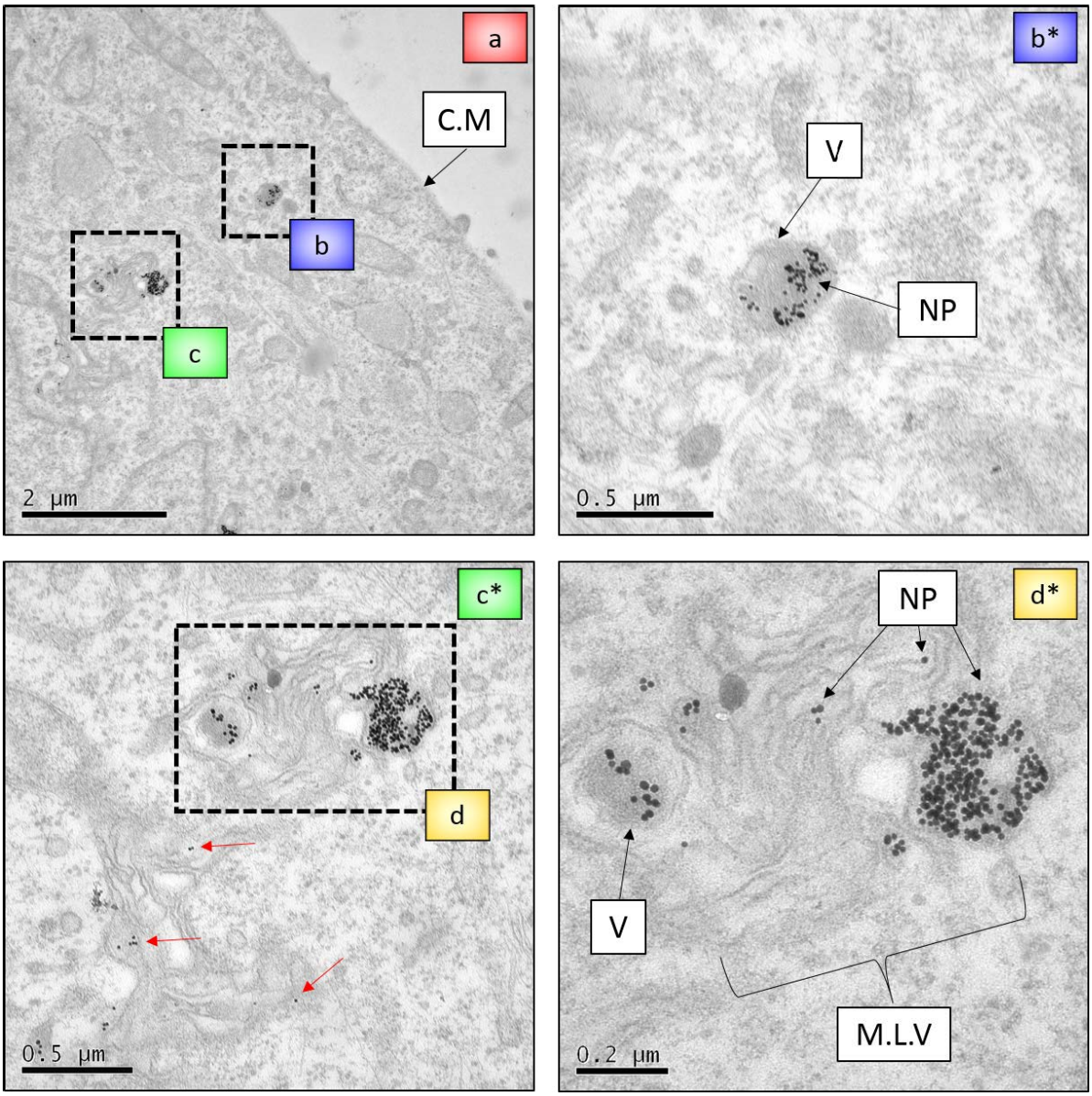

Figure 2.56: TEM images of ***Au13-Z-HSH*** *in HeLa cells. Cells were incubated with* ***Au13-Z-HSH*** *at a concentration of 0.25 nM in complete cell media for 24 hours before fixing. Widefield image is shown in (a). Magnifications of insets (b), (c) and (d) are in shown in (b*), (c*) and (d*) respectively. C.M - cell membrane, V - vesicles, M.L.V - multi-laminar vesicle, NP - nanoparticles.*

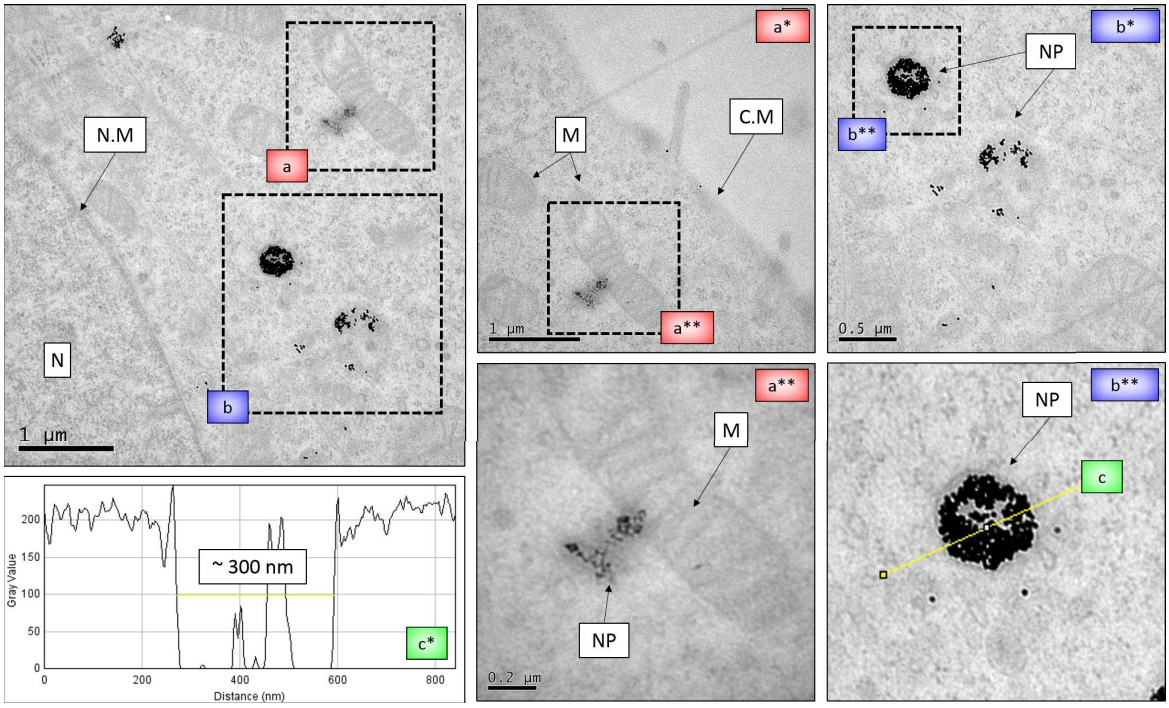

Figure 2.57: TEM images of ***Au13-Z-HSH*** *in HeLa cells. Cells were incubated with* ***Au13-Z-HSH*** *at a concentration of 0.25 nM in complete cell media for 24 hours before fixing. Magnifications of insets (a) and (b) are in shown in (a*) and (b*) respectively. Line profile of nanoparticle cluster denoted by (c) are exhibited in (c*). Size is approximated by the full-width at half-maximum. C.M - cell membrane, V - vesicle, M - mitochondrion, NP - nanoparticles.*

in rat liver cells which is denoted as the Golgi complex.[283] A study on the exocytosis of nanoparticles by cells by Sakhtianchi *et al.*[284] also stated that on the pathway to late-stage vesicles/endosomes, such as that observed in the left of Figure 2.56b*, nanoparticles may escape vesicular restriction and enter the cytoplasm. This is interesting with respect to the nanoparticles denoted by the red arrows in Figure 2.56c* and black arrows in Figure 2.56d* as these nanoparticles although in close proximity to the folds are not in well-defined membrane bound vesicles. In the same study by Sakhtianchi *et al* it was also stated that nanoparticles located in the cytoplasm or confined in vesicles can enter the nucleus, mitochondria, endoplasmic reticulum, and Golgi apparatus by hitherto unknown mechanisms.[284]

Figure 2.57 shows a further set of images of HeLa cells following a 24 hour incubation with **Au13-Z-HSH**. Notable features in the magnified images (Figures 2.57a*,a**) is possible interaction of a cluster of nanoparticles with a mitochondrion. Figures 2.57b*,

b** also illustrate the efficiency of cells to process nanoparticles with an extremely densely populated vesicle measuring approximately 300 nm in diameter observed (Figure 2.57c*).

Further images exhibiting a HeLa cell following 24 hour exposure to **Au13-Z-HSH** are shown in Figure 2.58 and significantly show nuclear uptake of nanoparticles, confirming confocal imaging observations. A section of the widefield image of the cell is shown in Figure 2.58a where nuclear uptake is seen in the bottom of the image. Outlined in red is the nuclear membrane including a dashed section where it is not well defined and invaginated inwards. Examining the magnified inset (b) in Figure 2.58b*, the extent of nuclear uptake is apparent with nanoparticles observed dispersed in an area spanning over 3 μm in length. Interestingly when examined at a higher magnification (Figure 2.58c*) the nanoparticles are localised on the periphery of an area of condensed chromatin, possibly the nucleolus, as outlined in blue.[285] This supports the observations made with confocal microscopy images of the nanoparticles in cells where they were also observed on the periphery of the nucleolus (Figure 2.46).

The section of undefined nuclear membrane is shown in Figure 2.58d* and 2.58d** with and without outlines depicting the nuclear membrane (red) and a vesicle (green) near to where the nuclear membrane breaks (red dashed line). The vesicle also possesses an internal vesicle (I.V) suggesting it is multi-vesicular and has it's origin in the latter stages of endocytosis in the lysosomal degradation pathway as previously discussed. Such vesicles are known to contain nanoparticles so it is possible that the nanoparticles observed in the nucleus may have achieved nuclear translocation via a similar vesicle based mechanism. Eukaryotic cells predominantly undergo open mitotic cell division which is characterised by the breakdown of the nuclear envelope prior to daughter chromosomes migrating apart, with new nuclei assembling around them.[286] Although unreported in the literature it is possible that vesicles containing nanoparticles which are observed in close proximity to the nucleus or indeed free nanoparticles in the cytoplasm, are enclosed by the reforming nuclear membrane in the latter stages of cell division. Without an imaging study over the whole cell division cycle, it is however difficult to resolutely conclude this as the

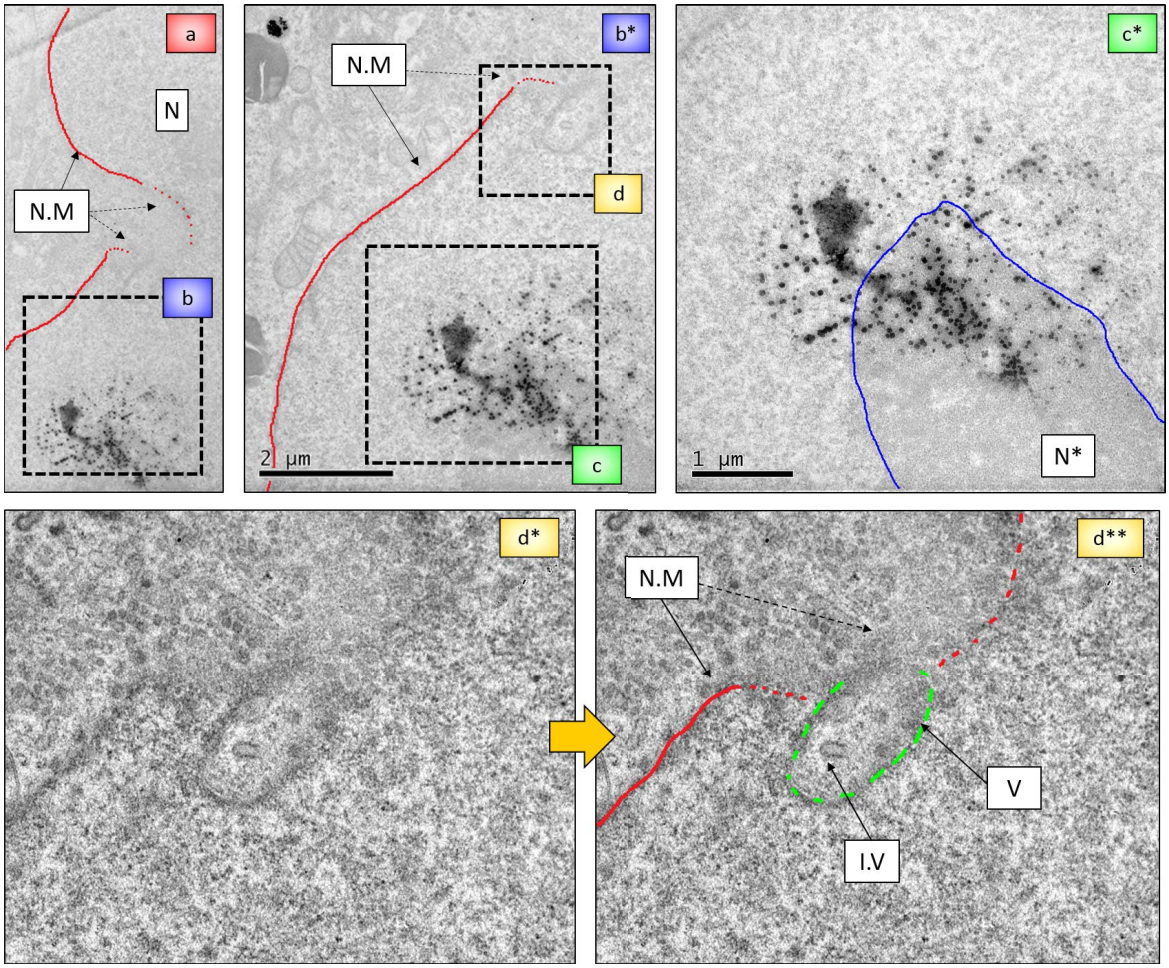

*Figure 2.58: TEM images of **Au13-Z-HSH** in HeLa cells. Cells were incubated with **Au13-Z-HSH** at a concentration of 0.25 nM in complete cell media for 24 hours before fixing. Widefield image is shown in (a). Magnifications of insets (a), (b) and (c) are in shown in (a*), (b*) and (c*) respectively. Magnifications of inset (c) are shown in (c*) and (c*) with and without annotations. N.M - nuclear membrane (red), N* - nucleolus (boundary defined in blue) V - vesicle (boundary defined in green), I.V (internal vesicle).*

mechanism of nuclear uptake.

In conclusion the TEM images yield similar observations to those afforded by confocal imaging of **Au13-Z-HSH**. Some nanoparticles are observed in clusters compartmentalised in late stage endosomes/lysosomes in the perinuclear region with nuclear uptake is also observed. The high resolution afforded by TEM allows individual nanoparticles to be imaged and the extent to which they are observed as large clusters illustrates how effective the cellular machinery is in processing internalised nanoparticles.

2.3.7 Cellular Uptake of Au13-P-HSH and Au100-P-HSH

Confocal Microscopy of Au13-P-HSH in A459 Cells

Confocal and brightfield images of A459 cells incubated with **Au13-P-HSH** are shown in Figure 2.59. Figures 2.59a-b show overlays of the transmission brightfield image and the reflection image with the DRAQ5 red channel image respectively. In these widefield views the nanoparticles are visible as dark spots in the transmission image and white spots in the reflection image with uptake clearly observed in all cells. Notably the cells were incubated in complete media at neutral pH. This suggests that the majority of the nanoparticles have achieved uptake through endocytosis and not via the pHLIP peptide's pH dependence mechanism which would potentially insert the nanoparticles through the membrane at acidic pH as discussed in Section 1.2.

Magnifications of the representative cell indicated by the yellow-dashed inset are shown in Figure 2.59c-e. These images exhibit the **HoechstSH** and reflection (green false colour) image overlay, the transmission brightfield and DRAQ5 overlay and the reflection and DRAQ5 overlay respectively. The green spots in Figure 2.59c correspond to the locations of the nanoparticles with the reflection image given a green false colour to provide clarity with the cyan **HoechstSH** image overlay. The locations of the nanoparticles are co-localised with spots of cyan emission from the **HoechstSH** as indicated by the overlay of the intensity profile peaks measured in the reflection and **HoechstSH** images (Figure 2.60a). This confirms the stability of the **HoechstSH** complex on this pHLIP peptide mediated preparation of nanoparticles after 24 hour exposure to a cellular environment. Performing further intensity profile measurements on several of the white spots in the reflectance image (Figure 2.60) indicates they are composed of nanoparticle clusters approximately 400 nm in size. The largest feature measured is 700 nm in diameter indicating significant compartmentalising of the nanoparticles in the cell. Smaller clusters or indeed single nanoparticles may also be present but not exhibit a high enough (scattering/luminescent) signal over background noise, autofluorescence and scatter from cellular material

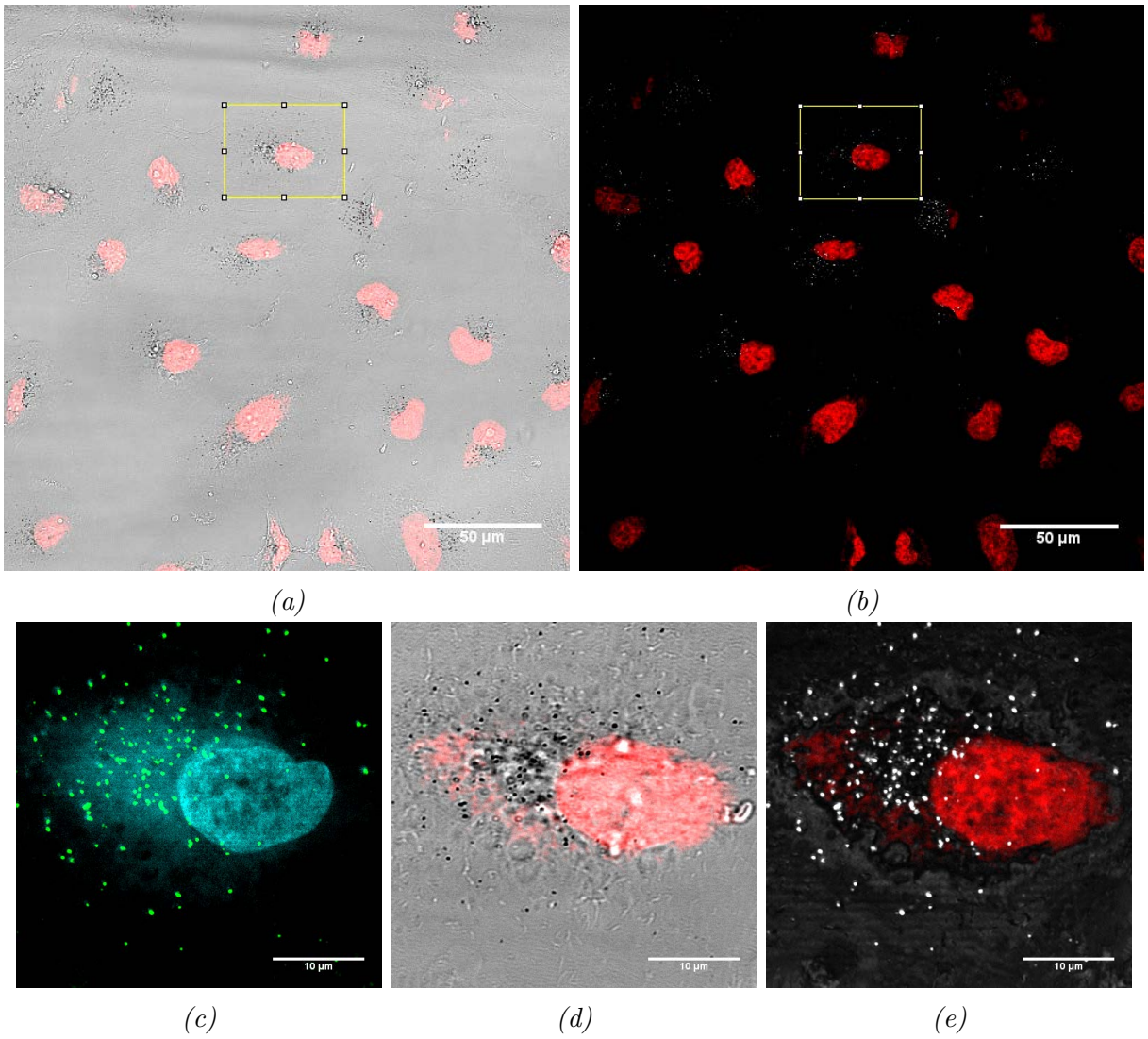

(a) *(b)*

(c) *(d)* *(e)*

Figure 2.59: Images of ***Au13-P-HSH*** *in A549 cells monitored by confocal luminescence and reflection microscopy. Cells were incubated with* ***Au13-P-HSH*** *at a concentration of 0.25 nM in complete cell media for 24 hours before fixing. (a) Widefield transmission brightfield and DRAQ5 overlay. (b) Widefield reflection and DRAQ5 overlay. (c-e) Magnifications of yellow-dashed inset. (c) reflection (green false colour has been applied) and* ***HoeschstSH*** *overlay. (d) Widefield transmission brightfield. (e) Reflection and DRAQ5 overlay. Reflection image* λ_{exc} *= 633 nm,* λ_{em} *= 623-643 nm.* ***HoechstSH*** *luminescence, (blue channel),* λ_{exc} *= 405 nm,* λ_{em} *= 410-550 nm. DRAQ5, (red channel),* λ_{exc} *= 633 nm,* λ_{em} *= 640-800. (Scale bar (a,b) 50 µm, (c-e) 10 µm)*

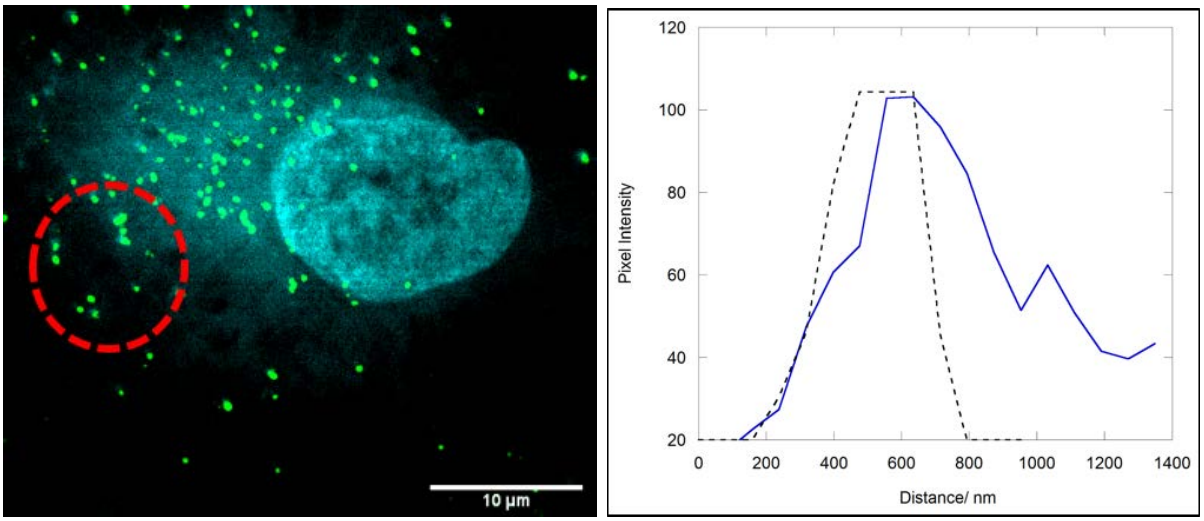

(a) *(b)*

Figure 2.60: Image of ***Au13-P-HSH*** *in an A549 cell monitored by confocal luminescence and reflection microscopy. Cells were incubated with* ***Au13-P-HSH*** *at a concentration of 0.25 nM in complete cell media for 24 hours before fixing. (a) reflection (green false colour has been applied) and HoeschstSH overlay. (b) Line intensity profile of a nanoparticle compared in the* ***HoechstSH*** *(blue solid line) and reflectance (black dashed line) images. (c) Line intensity profiles of nanoparticles in the red-dashed inset in the reflectance (black dashed line) image. Sizes are approximated as the full-width at half-maximum of the intensity profiles. Reflection image* λ_{exc} *= 633 nm,* λ_{em} *= 623-643 nm.* ***HoechstSH*** *luminescence, (blue channel),* λ_{exc} *= 405 nm,* λ_{em} *= 410-550 nm.*

for them to be visible. Further images are provided in Appendix G.4.1.

Four further orthogonal are presented in Figure 2.61 which exhibits **Au13-P-HSH** in fixed A549 cells after 24 hours. The orthogonal views are centred on two groups of cells in the field-of-view with the **HoechstSH** blue channel and DRAQ5 red channel overlaid with the reflectance channel. The cells in these images have been image prior to cell division as several nuclei are grouped very closely in the top cluster of cells, and are presumably in the process of pulling away from each other. The single cell below is slightly earlier in the cell division cycle, with the nuclear chromatin condensing ready for duplication. Although these are fixed cell samples the transverse views in all the orthogonal views are not "squashed" as can be the case with fixed cell samples. As such the localisation of the particles is much clearer in the side-views with nanoparticles (white spots) distinctly evident in the central plane in the nucleus. This is most apparent in the single cell lower down in the field-of-view and the corresponding orthogonal views in Figure 2.61c and 2.61d. It is interesting to note that nuclear uptake of nanoparticles in these cells coincides with cell division, providing impetus to study this potential relationship further.

Confocal Microscopy of Au13-P-HSH in HeLa Cells

Confocal luminescence and reflection microscopy images of **Au13-P-HSH** in HeLa cells following a 30 minute incubation are shown in Appendix G (Figure G.10). It is difficult to confirm localisation of the **Au13-P-HSH** in the reflection image due to extensive scattering from the cellular material. Spots of cyan emission in the HoechstSH image channel do suggest nanoparticle uptake, however with the absence of corresponding spots in the reflectance and indeed white light transmission image channels this cannot be confirmed.

Confocal and brightfield images of HeLa cells incubated with **Au13-P-HSH** for 24 hours are shown in Figure 2.62. Figures 2.62a and 2.62b show overlays of the reflection image and the transmission brightfield image with the DRAQ5 red channel image respectively. As with the A549 cells it is clear to see nanoparticle uptake in all cells.

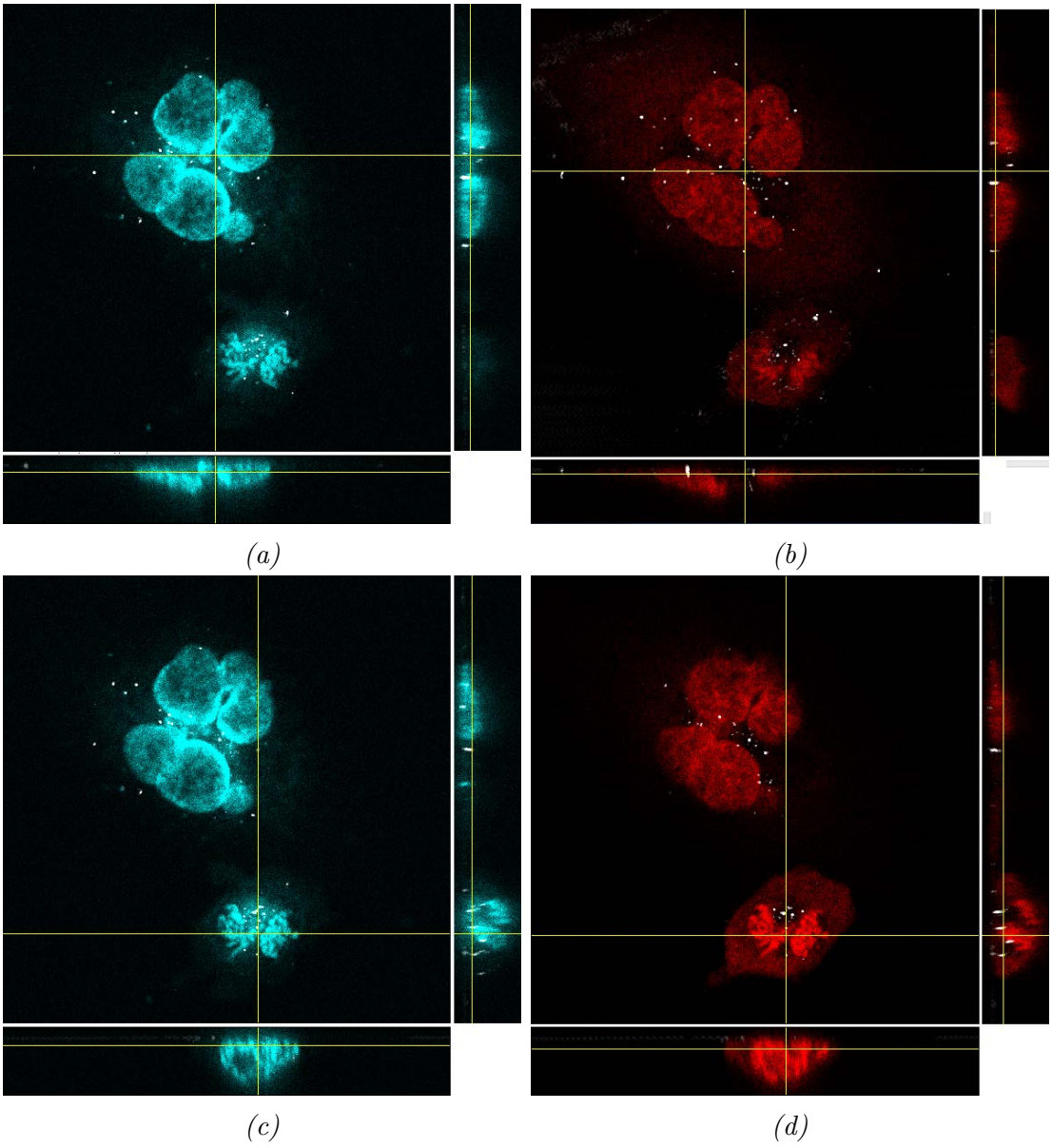

(a) *(b)*

(c) *(d)*

*Figure 2.61: Orthogonal view images of **Au13-P-HSH** nanoparticles in A549 cells monitored by confocal luminescence and reflection microscopy. Cells were incubated with **Au13-P-HSH** at a concentration of 0.25 nm in complete cell media for 24 hours before fixing. (a, c) reflection and HoeschstSH overlay. (b, d) reflection and DRAQ5 overlay. Reflection image λ_{exc} = 633 nm, λ_{em} = 623-643 nm. **HoechstSH** luminescence, (blue channel), λ_{exc} = 405 nm, λ_{em} = 410-550 nm. DRAQ5, (red channel), λ_{exc} = 633 nm, λ_{em} = 640-800. (Scale bar (a,b) 50 µm, (c-e) 10 µm)*

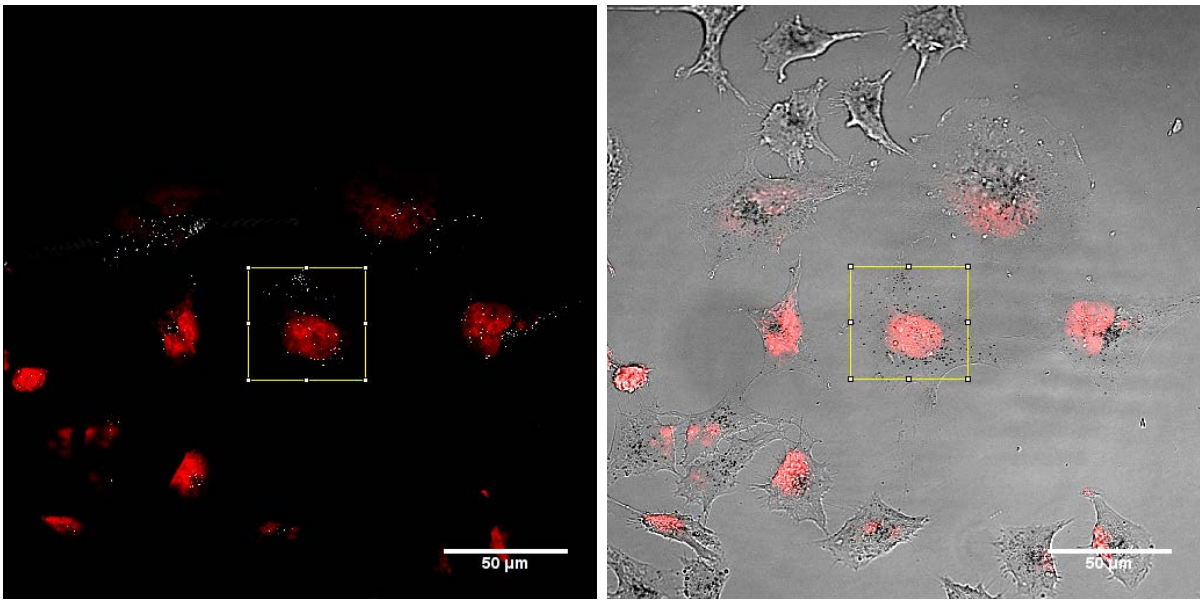

(a) *(b)*

Figure 2.62: Images of ***Au13-P-HSH*** *nanoparticles in HeLa cells monitored by confocal luminescence and reflection microscopy. Cells were incubated with* ***Au13-P-HSH*** *at a concentration of 0.25 nM in complete cell media for 24 hours before fixing. (a) Widefield reflection and DRAQ5 overlay. (b) Widefield transmission brightfield and DRAQ5 overlay. Reflection image* λ_{exc} *= 633 nm,* λ_{em} *= 623-643 nm.* ***HoechstSH*** *luminescence, (blue channel),* λ_{exc} *= 405 nm,* λ_{em} *= 410-550 nm. DRAQ5, (red channel),* λ_{exc} *= 633 nm,* λ_{em} *= 640-800. (Scale bar (a,b) 50 µm, (c,d) 10 µm).*

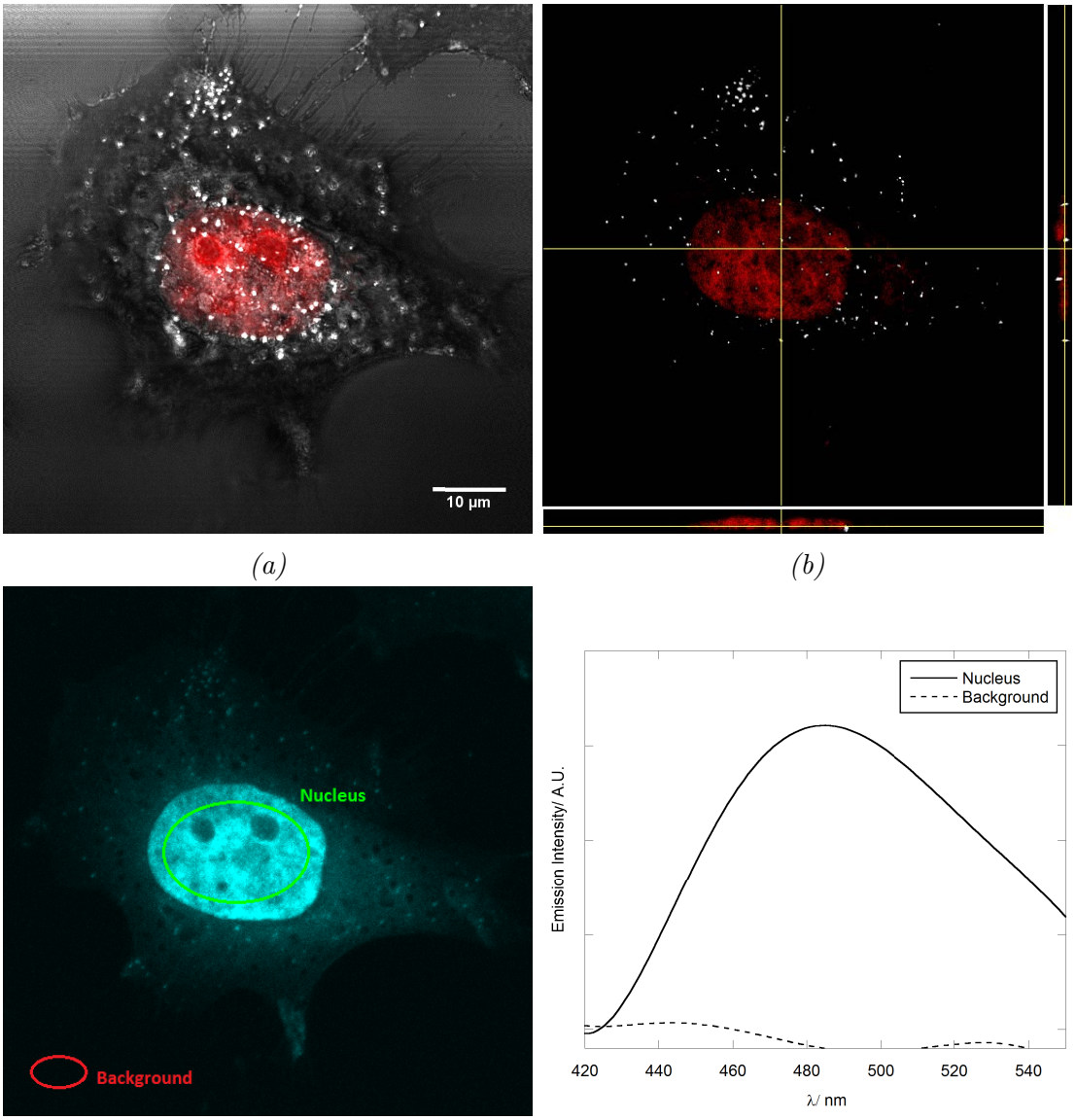

Figure 2.63: Images of ***Au13-P-HSH*** *nanoparticles in HeLa cells monitored by confocal luminescence and reflection microscopy. Cells were incubated with* ***Au13-P-HSH*** *at a concentration of 0.25 nM in complete cell media for 24 hours before fixing. (a-c) Magnifications of yellow-dashed inset (Figure 2.62). (a) Reflection and DRAQ5 overlay. (d) Transmission brightfield and DRAQ5 overlay. (b) Orthogonal view of the reflection and DRAQ5 image stack overlay. (c)* ***HoechstSH*** *image indicating ROIs for spectral scans. (d) Spectral emission scans taken from ROIs. Reflection image* λ_{exc} *= 633 nm,* λ_{em} *= 623-643 nm.* ***HoechstSH*** *luminescence, (blue channel),* λ_{exc} *= 405 nm,* λ_{em} *= 410-550 nm. DRAQ5, (red channel),* λ_{exc} *= 633 nm,* λ_{em} *= 640-800. (Scale bar (a,b) 50 µm, (c,d) 10 µm).*

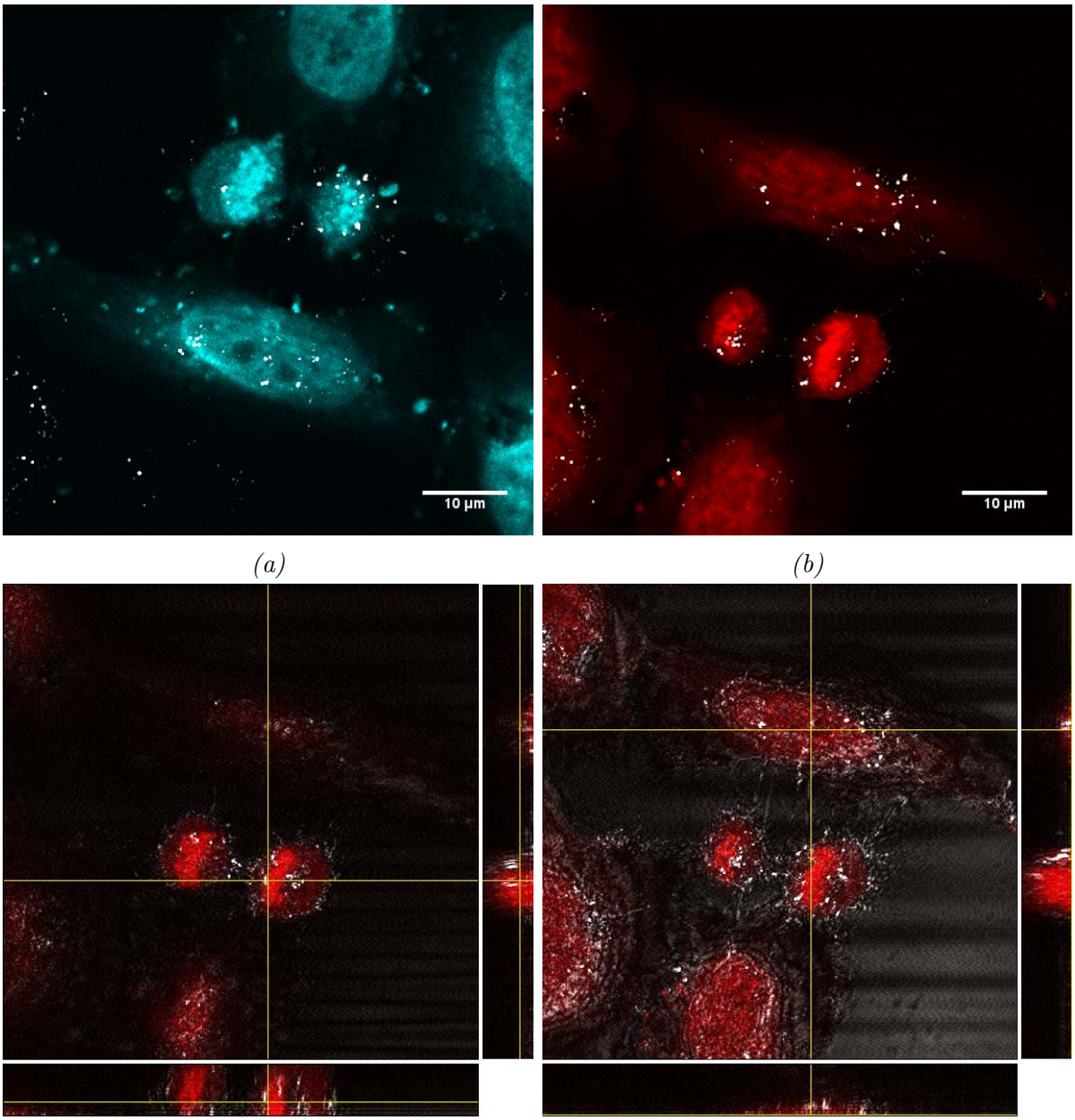

Figure 2.64: Images of ***Au13-P-HSH*** *nanoparticles in HeLa cells monitored by confocal luminescence and reflection microscopy. Cells were incubated with* ***Au13-P-HSH*** *at a concentration of 0.25 nm in complete cell media for 24 hours before fixing. (a)* ***HoechstSH*** *and reflection image overlay. (b) DRAQ5 and reflection image overlay. (c, d) Orthogonal views of the reflection and DRAQ5 image stack overlay. Reflection image* λ_{exc} *= 633 nm,* λ_{em} *= 623-643 nm.* ***HoechstSH*** *luminescence, (blue channel),* λ_{exc} *= 405 nm,* λ_{em} *= 410-550 nm. DRAQ5, (red channel),* λ_{exc} *= 633 nm,* λ_{em} *= 640-800. (Scale bar (a, b) 10 µm)*

Nanoparticles have most likely accumulated or compartmentalised within the cells such that they are now resolvable compared to the shorter 30 minute exposure. With the limited resolution of confocal microscopy it is of course possible that nanoparticles were internalised after 30 minutes exposure but were not in large enough accumulations to exhibit a detectable scattering or luminescent signal. Cells were furthermore incubated in complete media at neutral pH suggesting that the majority of the nanoparticles have most likely been internalised by endocytosis and not via the pHLIP peptide's pH dependence mechanism. Further studies measuring the scatter due to nanoparticle uptake from the cells via flow cytometry could be performed in future to quantitatively assess the pH dependance of uptake of **Au13-P-HSH**.

Magnifications of the representative cell indicated by the yellow-dashed inset are shown in Figure 2.63. The prominent feature of the cell shown in these magnifications is the localisation of the nanoparticles throughout the cell cytoplasm. The uptake in the A549 cells (Figure 2.59) and indeed the majority of the HeLa cells in the widefield view show dense nanoparticle localisation in the perinuclear region. The cell exhibited in Figure 2.63c-g is relatively squamous compared to the other cells in the widefield view indicating it may be ready to divide having duplicated many organelles and increased in size.

The reflection/transmission and DRAQ5 overlays also show evidence of nuclear uptake very similar to that observed in Figure 2.38d and Figure 2.46d which exhibit **Au13-T20-HSH** and **Au13-Z-HSH** uptake in HeLa cells after 24 hours. As in these images **Au13-P-HSH** are also observed in clusters around the periphery of the nucleolus (Figure 2.63b) indicating that the nuclear uptake of the nanoparticles may also be independent of the pHLIP and surfactant coating. Spectral scans of the nuclear region exhibit the characteristic Hoechst emission with a peak at 485 nm (Figure 2.63d). Further confocal images are exhibited in Figure 2.64.

Two further orthogonal are presented in Figure 2.64 which exhibits **Au13-P-HSH** in fixed HeLa cells after 24 hours. The orthogonal views are centred on two groups of cells in the field-of-view with the **HoechstSH** blue channel and DRAQ5 red channel overlaid

with the reflectance channel. The bottom pair of cells in this set of images is clearly in the latter stages of cell division as both cells can be seen pulling away from each other but still joined by a region of constricted cytoplasm. Again although these are fixed cell samples the transverse views in all the orthogonal views are not "squashed" as can be the case with fixed cell samples. As such the localisation of the particles is much distinct in the side-views, this is most clear in Figure 2.64c where nanoparticles (white spots) are located throughout the central plane in the nucleus. As with the A549 cells incubated with **Au13-P-HSH**, it is interesting to note that nuclear uptake of nanoparticles in these cells coincides with cell division, providing impetus to study this potential relationship further.

Confocal Microscopy of Au100-P-HSH in HeLa Cells

Uptake of **Au100-P-HSH** was investigated in HeLa cells. Images and magnifications of yellow-dashed insets showing HeLa cells incubated with **Au100-P-HSH** for 2 hours are exhibited in Figure 2.65. The widefield images show two clusters of cells in which all cells show nanoparticle uptake. The **HoechstSH** and reflectance image overlay indicate that uptake mostly perinuclear (Figure 2.65a). Magnifications of the uppermost cluster of cells confirm this (Figure 2.65c-d) with large clusters of nanoparticles observed on the nuclear periphery in the cells. Line intensity profile measurements performed on a cluster of nanoparticles towards the cell periphery in this cell are shown in Figure 2.66b.

Single 100 nm nanoparticles can be modelled computationally and are determined to appear as spots 300 nm in diameter due to diffraction effects,[77] the peak widths measured therefore indicate the clusters spanning 500 - 600 nm in width are likely comprised of pairs of nanoparticles. It is interesting to note that the **HoechstSH** image measurement yields two clearly defined peaks, indicating a spatial separation of over 1500 nm between the two clusters however in the reflection image the two peaks merge. This is due to diffraction effects, specifically the wavelength dependence, due to excitation at 405 nm for the **HoechstSH** image and 633 nm for the reflection image.[262] The general overlap

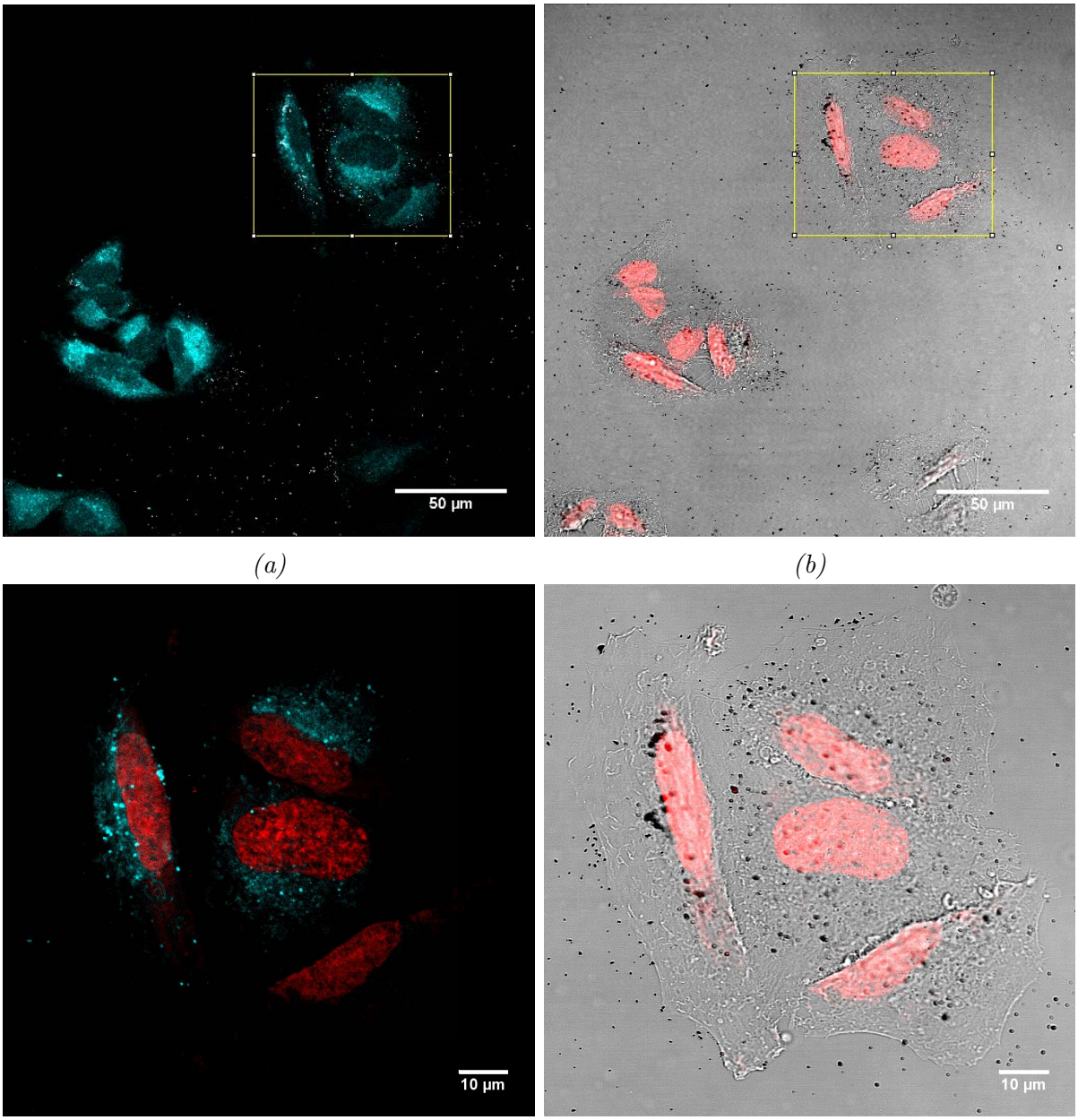

(a) *(b)*

(c) *(d)*

Figure 2.65: Images of ***Au100-P-HSH*** *nanoparticles in HeLa cells monitored by confocal luminescence and reflection microscopy. Cells were incubated with* ***Au100-P-HSH*** *at a concentration of 0.10 pM in complete cell media for 2 hours before fixing. (a,b) widefield views: (a) reflection and* ***HoechstSH*** *overlay. (b) transmission and DRAQ5 overlay. (c,d) magnifications of yellow-dashed inset: (c)* ***HoechstSH*** *and DRAQ5 overlay. (d) transmission and DRAQ5 overlay. (e) orthogonal view of three-dimensional z-stack of DRAQ5 and reflection overlays. (f) line intensity profile measurements performed on the nanoparticles shown in the image insets (****HoechstSH*** *image - blue-dashed line, reflection image - black-solid line). Sizing is estimated using the full-width at half-maximum. Reflection image* λ_{exc} *= 633 nm,* λ_{em} *= 623-643 nm.* ***HoechstSH*** *luminescence, (blue channel),* λ_{exc} *= 405 nm,* λ_{em} *= 410-550 nm, DRAQ5, (red channel),* λ_{exc} *= 633 nm,* λ_{em} *= 640-800. (Scale bar: (a,b) 50 µm, (c, d) 10 µm).*

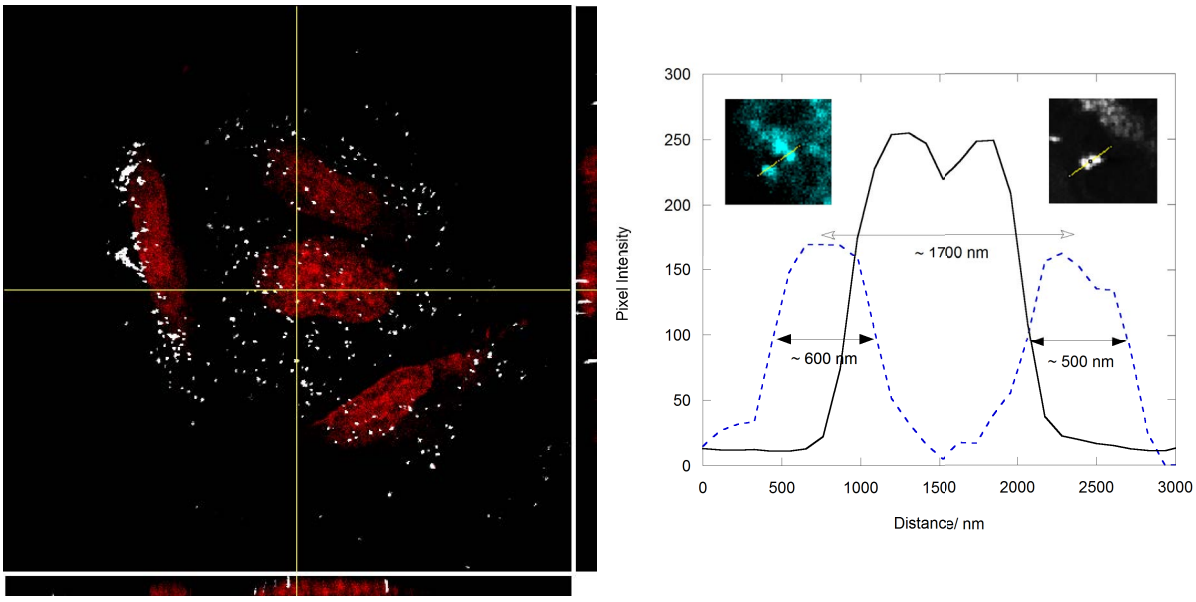

(a) *(b)*

Figure 2.66: Images of ***Au100-P-HSH*** *nanoparticles in HeLa cells monitored by confocal luminescence and reflection microscopy. Cells were incubated with* ***Au100-P-HSH*** *at a concentration of 0.10 pM in complete cell media for 2 hours before fixing. (a) orthogonal view of three-dimensional z-stack of DRAQ5 and reflection overlays. (b) line intensity profile measurements performed on the nanoparticles shown in the image insets (****HoechstSH*** *image - blue-dashed line, reflection image - black-solid line). Sizing is estimated using the full-width at half-maximum. Reflection image* λ_{exc} *= 633 nm,* λ_{em} *= 623-643 nm.* ***HoechstSH*** *luminescence, (blue channel),* λ_{exc} *= 405 nm,* λ_{em} *= 410-550 nm, DRAQ5, (red channel),* λ_{exc} *= 633 nm,* λ_{em} *= 640-800. (Scale bar: (a,b) 50 µm, (c, d) 10 µm).*

in the peaks of the intensity profiles does also indicate the **HoechstSH** emission is co-localised to the nanoparticles and is thus stable on the nanoparticles after exposure to a cellular environment.

Uptake of **Au100-P-HSH** was investigated in HeLa cells following a 24 hour incubation. Widefield images are shown in Appendix G.4.4. Magnifications of representative cells are shown in Figure 2.67 and Figure 2.68. The transmission brightfield and DRAQ5 image overlay is shown in Figure 2.67a. Nanoparticle uptake is evident in all of the cells in the FOV however the most prominent feature is the nanoparticle uptake observed in the cell nucleus denoted by the yellow-dashed circle. The extent of the uptake is evident in the DRAQ5 and reflectance image overlay (Figure 2.67c) where nanoparticles are seen in the nucleus and indeed on the periphery of the nucleolus as previously observed. The green arrows indicate such features in all three of the cells in the image indicating this is not an isolated occurrence.

Sizing measurements performed on the several of the white spots indicated by the arrows suggest diameters ranging from 400 - 600 nm, indicating they are composed of one or two nanoparticles taking in to account diffraction effects.[77] (Line intensity profiles are provided in Figure G.13, Appendix G.4.4). The confocal image slice shown in Figure 2.67d corresponds to an section from a three-dimensional image stack of the cells in which further uptake in the nucleus, particularly around the nucleolus is evident. The nanoparticles are confirmed as being in the same central plane as the nucleus by the transverse views as indicated by the yellow arrow.

Figure 2.68 shows the HeLa cells and spectral scans recorded from the indicated ROIs. All three cells (1-3) in the the image were analysed with ROIs corresponding to cytoplasmic localised and nuclear localised nanoparticles. ROIs are provided in Figure 2.68a on the DRAQ5, **HoechstSH** and reflectance (green false colour) image overlay. The emission intensity profiles are shown in Figures 2.68b, 2.68c and 2.68d. It is evident that in both cells 1 and 2 the emission is blueshifted in the nucleus compared to the cytoplasm. To confirm this the data were fitted with a ninth-order polynomial to obtain crude emission

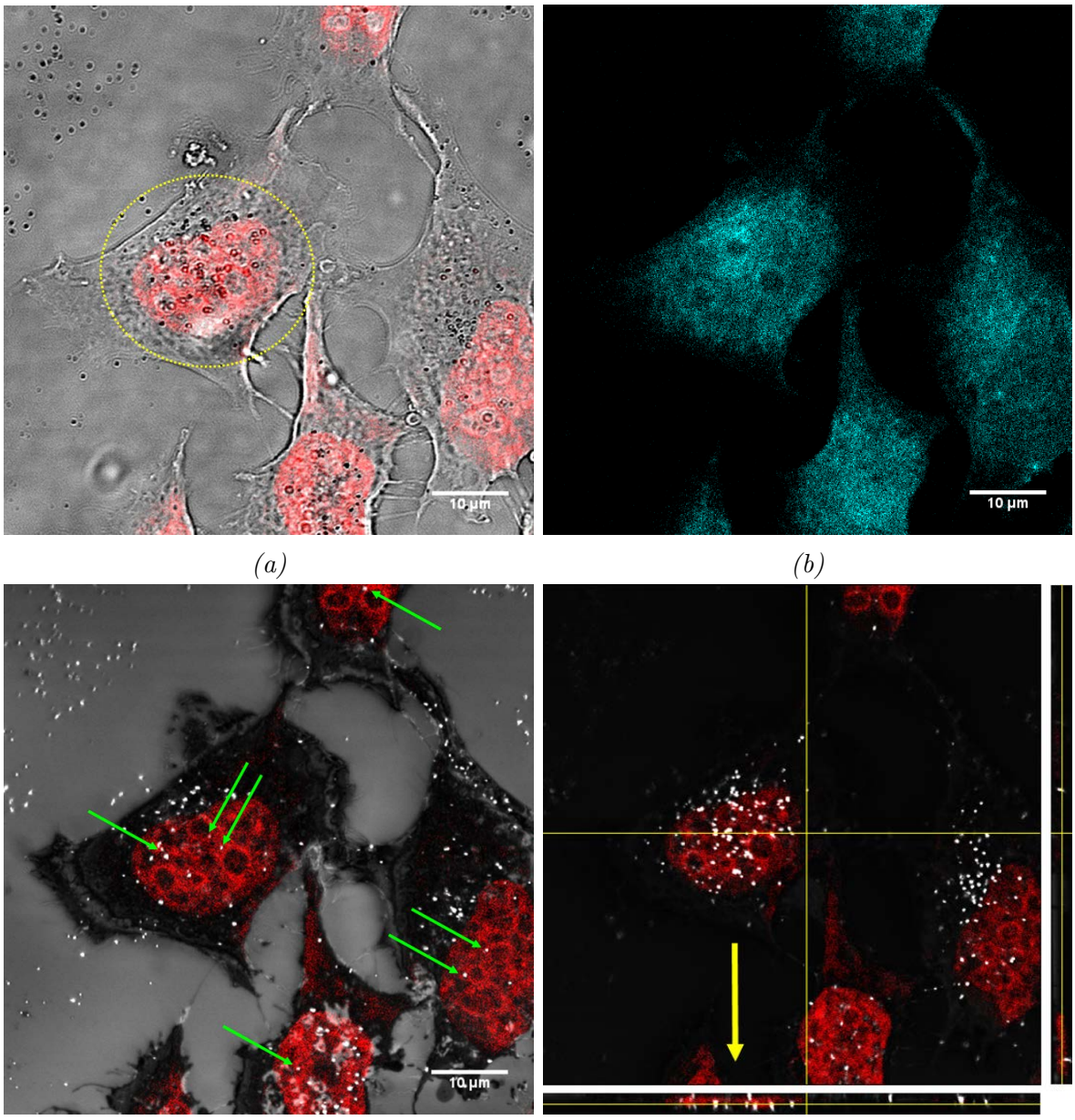

(a) *(b)*

(c) *(d)*

Figure 2.67: Images of ***Au100-P-HSH*** *nanoparticles in HeLa cells monitored by confocal luminescence and reflection microscopy. Cells were incubated with* ***Au100-P-HSH*** *at a concentration of 0.10 pM in complete cell media for 24 hours before fixing. (a) transmission brightfield and DRAQ5 overlay. (b)* ***HoechstSH*** *image. (c) reflection and DRAQ5 overlay. (d) orthogonal view of three-dimensional z-stack of reflectance and DRAQ5 overlay. Reflection image* λ_{exc} *= 633 nm,* λ_{em} *= 623-643 nm.* ***HoechstSH*** *luminescence, (blue channel),* λ_{exc} *= 405 nm,* λ_{em} *= 410-550 nm, DRAQ5, (red channel),* λ_{exc} *= 633 nm,* λ_{em} *= 640-800. (Scale bar) 10 µm*

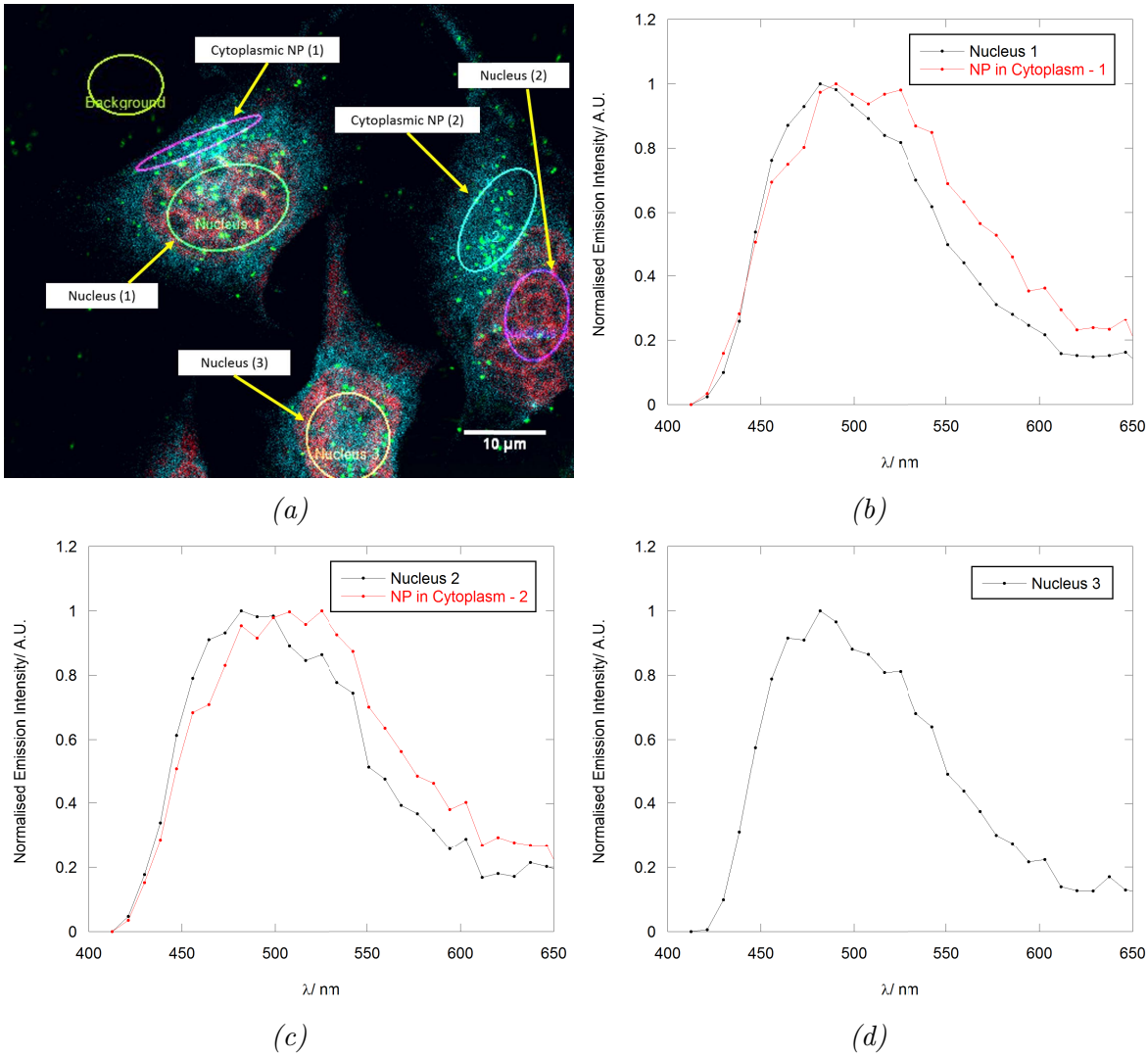

Figure 2.68: Images of ***Au100-P-HSH*** *nanoparticles in HeLa cells monitored by confocal luminescence and reflection microscopy. Cells were incubated with* ***Au100-P-HSH*** *at a concentration of 0.10 pM in complete cell media for 24 hours before fixing. (a) regions used for spectral emission scans shown on DRAQ5,* ***HoechstSH*** *and reflectance overlay (green false colour applied to reflectance channel). transmission and DRAQ5 overlay. (b, c, d) spectral emission scans taken from corresponding cells and regions. Reflection image* λ_{exc} *= 633 nm,* λ_{em} *= 623-643 nm.* ***HoechstSH*** *luminescence, (blue channel),* λ_{exc} *= 405 nm,* λ_{em} *= 410-550 nm, DRAQ5, (red channel),* λ_{exc} *= 633 nm,* λ_{em} *= 640-800. (Scale bar 10 µm).*

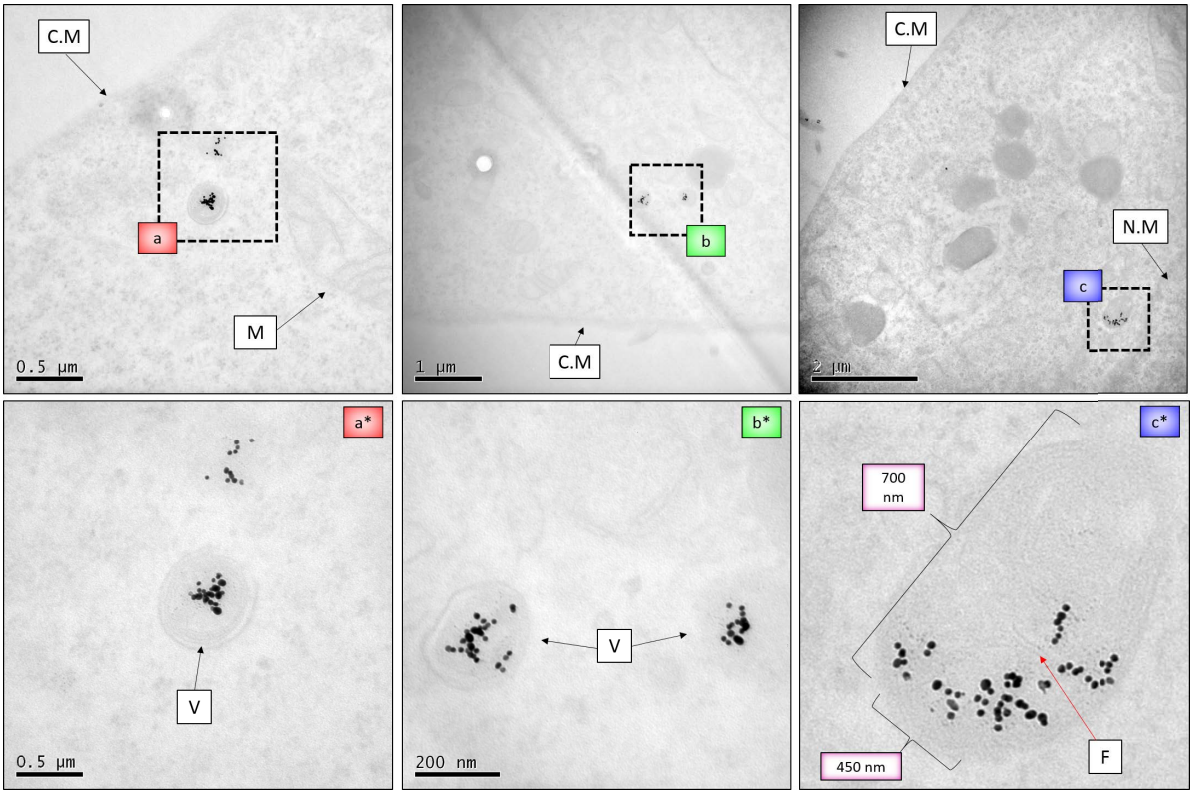

*Figure 2.69: TEM images of **Au13-P-HSH** in HeLa cells. Cells were incubated with **Au13-P-HSH** at a concentration of 0.25 nM in complete cell media for 24 hours before fixing. Widefield images of the cytoplasm of the cell are shown in top panel. Magnifications of insets (a), (b) and (c) are shown in (a*), (b*) and (c*) respectively. C.M - cell membrane, V - vesicle, F - vesicular folds.*

maxima (data not shown). Peaks were thus observed in cell 1 at (nucleus) 485 nm and (cytoplasm) 500 nm, in cell 2 at (nucleus) 485 nm and (cytoplasm) 510 nm and in cell 3 (nucleus) 485 nm. The blueshift observed is characteristic of the **HoechstSH** binding to DNA (Appendix D).

Transmission Electron Microscopy of Au13-P-HSH in Cells

Figure 2.69 exhibits TEM images of HeLa cells incubated with **Au13-P-HSH** for 24 hours. (Images after 2 hour exposure are provided in Appendix G.4.3). The top panel of images show widefield views of the cells and Figures 2.69a*-c* magnifications of the respective insets. **Au13-P-HSH** are observed as dark spheres due to their high electron density. They are observed in vesicles approximately 1-2 μm from the cell membrane inside the cells in Figure 2.69a* and 2.69b*, which enclose 15-20 nanoparticles. Referring

to the uptake mechanisms and vesicle designations described in Figure 2.2 these vesicles are probably of Type 4 or 5. The vesicle observed in Figure 2.69c is much further within the cell at a distance of approximately 6 μm away from the cell membrane placing it close to the nuclear membrane as indicated. Examining the vesicle at a higher magnification reveals it is elliptical in shape, measures 700 x 450 nm along the major and minor axis respectively and contains upwards of 50 nanoparticles. Multiple folds are also evident (red-arrow) indicating the vesicle is part of the latter stages of endocytosis (Figure 2.2). The presence of multiple membrane bound vesicles suggests endocytosis as the predominant uptake mechanism of the **Au13-P-HSH** as also indicated by confocal imaging observations. A single nanoparticle is however observed in the cytoplasm (red-dashed arrow) suggesting that passive uptake directly through the cell membrane or endosomal/vesicular release may also occur on occasion.

Figure 2.70 exhibits another HeLa cell following incubation with **Au13-P-HSH**. Figure 2.70a shows a widefield view of the cell with the nuclear membrane and nucleolar boundary indicated by red and blue dashed lines respectively. The most striking feature in this image is the distribution of nanoparticles observed in the nucleus denoted by the inset box (b) and magnified in the corresponding image comprising Figure 2.70b*. The distribution of nanoparticles is almost identical to that observed in Figure 2.58 which shows nuclear localised **Au13-Z-HSH** in a HeLa cell after 24 hours. Interestingly a magnification of this region in Figure 2.70d* reveals an elliptical vesicular structure containing clusters of nanoparticles approximately 50 nm in diameter (see inset). This is typical of some of the nanoparticles observed in the late stage endosomal/lysosomal compartments in Figure 2.69 which measure many tens of nanometres on diameter and can contain several tens of nanoparticles.

Unlike the vesicles in Figure 2.69 the vesicular compartment observed here in the nucleus contains only three nanoparticles spots inside (green arrows) with two on the periphery (red arrows). A late stage endosome/vesicle would presumably have many more nanoparticles as previously observed. Coupled with the lack of a distinct membrane

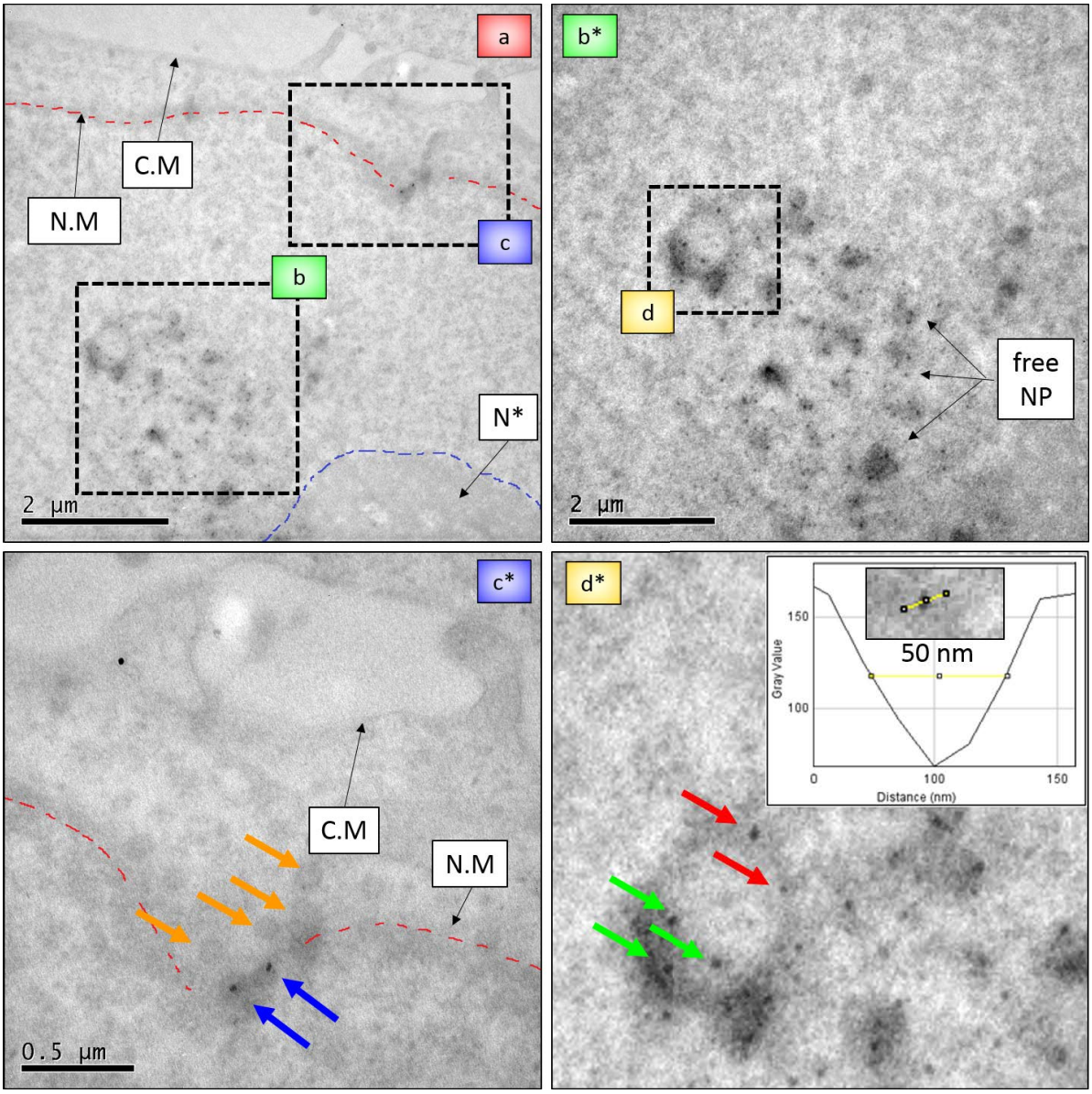

Figure 2.70: TEM images of ***Au13-P-HSH*** *in HeLa cells. Cells were incubated with* ***Au13-P-HSH*** *at a concentration of 0.25 nM in complete cell media for 24 hours before fixing. Widefield image is shown in (a). Magnifications of insets (b), (c) and (d) are shown in (b*), (c*) and (d*) respectively. Line intensity profile of representative NP is shown in inset of (d*). Vesicles indicated by orange arrows, including two containing nanoparticles as indicated by blue arrows, seem to be traversing the broken nuclear membrane. The vesicular compartment observed in the nucleus contains three nanoparticles inside (green arrows), with two on the periphery of the vesicle (red arrows). C.M - cell membrane, N.M - nuclear membrane (red dashed-line), N* - nucleolus (outlined by blue dashed-line), NP - nanoparticles.*

in some areas and clusters of nanoparticles observed just outside the vesicle indicates the nanoparticles have achieved release or expulsion from the compartment. It is possible that with late stage endosomes/vesicles possessing an acidic internal environment (Figure 2.2) the pHLIP peptide on the nanoparticles has enabled them to insert through the membrane as previously discussed (Section 1.2). Similar uptake is observed with the **Au13-Z-HSH** however indicating that this may not be the case.

Without a temporal based TEM study examining uptake over a range of time points it is difficult to be certain of the exact mechanism of nuclear uptake. However another feature of significance is observed in Figure 2.70d* which shows a magnification of an undefined section of nuclear membrane above the nuclear localised nanoparticles. Figure 2.58 shows **Au13-Z-HSH** in the nucleus of a HeLa cell also in close proximity to what appears to be a break in the nuclear membrane. Furthermore a vesicle is observed at the location of the membrane dissolution Figure 2.58d**. A similar such feature is observed in here in Figure 2.70d* where multiple vesicles indicated by orange arrows, including two containing nanoparticles indicated by blue arrows seem to be traversing the broken nuclear membrane. The nuclear localised vesicle in this cell may thus have achieved uptake through this pathway.

Nuclear membrane dissolution occurs when the cell divides via mitosis and it is known that endoplasmic reticulum derived vesicles are used by the cells to reform the nuclear membrane.[287,288] With vesicles containing nanoparticles known to potentially translocate to the endoplasmic reticulum[284] it is possible that these vesicular compartments form part of the same pathway. An alternative hypothesis is that the dense nanoparticle cargo contained in these compartments makes them difficult for cells to translocate away from the nuclear vicinity, and they subsequently become trapped when the nuclear envelope reforms after cell division. Again further investigations would be required to confirm these hypotheses. Notably nanoparticles were also observed to be associated with acidic endosomal/lysosomal compartments in the nucleus of the HeLa cell in the preliminary study using the Lysotracker stain (Section 2.3.6), furthermore indicating nuclear uptake

via such vesicles is not an isolated occurrence in the cells.

Figure 2.71 shows another HeLa cell exhibiting nuclear uptake of a cluster of nanoparticles. Figure 2.71 shows a widefield view of the cell where the nuclear membrane is denoted by the red dashed line. Immediately apparent is a vesicular structure near the centre of the nucleus which is magnified in in Figure 2.71b*. An interesting feature is seen to the left of the image where the nuclear membrane invaginates inwards and is apparently broken, as indicated by the break in the red dashed line. The bold red arrow indicates the possible path traversed by the vesicle in to the nucleus hypothesising a similar mechanism to that proposed for nuclear localised vesicle/nanoparticles in Figure 2.70. Figure 2.71c* shows a magnification of the vesicle that is cylindrical in shape and over 3 μm in length and exhibits three further internal vesicles (Figure 2.71d*). The largest of the internal vesicular compartments is 600 nm in diameter and contains upwards of 30 distinguishable nanoparticles, and furthermore in the vesicle to the extreme right two further nanoparticles as well as another smaller internal vesicle are observed. The collection of vesicles as a whole are thus indicative of a Type 4 endocytotic vesicle which denotes multi-vesicular bodies. (Figure 2.2)

In conclusion confocal microscopy of A549 and HeLa cells exposed to **Au13-P-HSH** indicated cellular uptake of the nanoparticles. Cells were exposed to the nanoparticles in complete media at neutral pH suggesting an uptake mechanism independent of the pHLIP peptides pH dependant mechanism. Colocalisation of the nanoparticles with the **HoechstSH** emission indicate stability of the **HoechstSH** complex on the nanoparticles when prepared via pHLIP peptide mediation and following exposure to a cellular environment. Line profiles of nanoparticles in the A549 cells indicate they are composed of clusters of nanoparticles the majority of which are approximately 400 nm in size suggesting significant compartmentalisation of the nanoparticles, indicative of endocytosis. Nuclear uptake of **Au13-P-HSH** is also readily observed with nanoparticles localised to the periphery of the nucleolus. Interestingly uptake of **Au13-T20-HSH**, **Au13-Z-HSH** and **Au100-Z-HSH** exhibits similar nuclear translocation. TEM images of **Au13-P-HSH** present

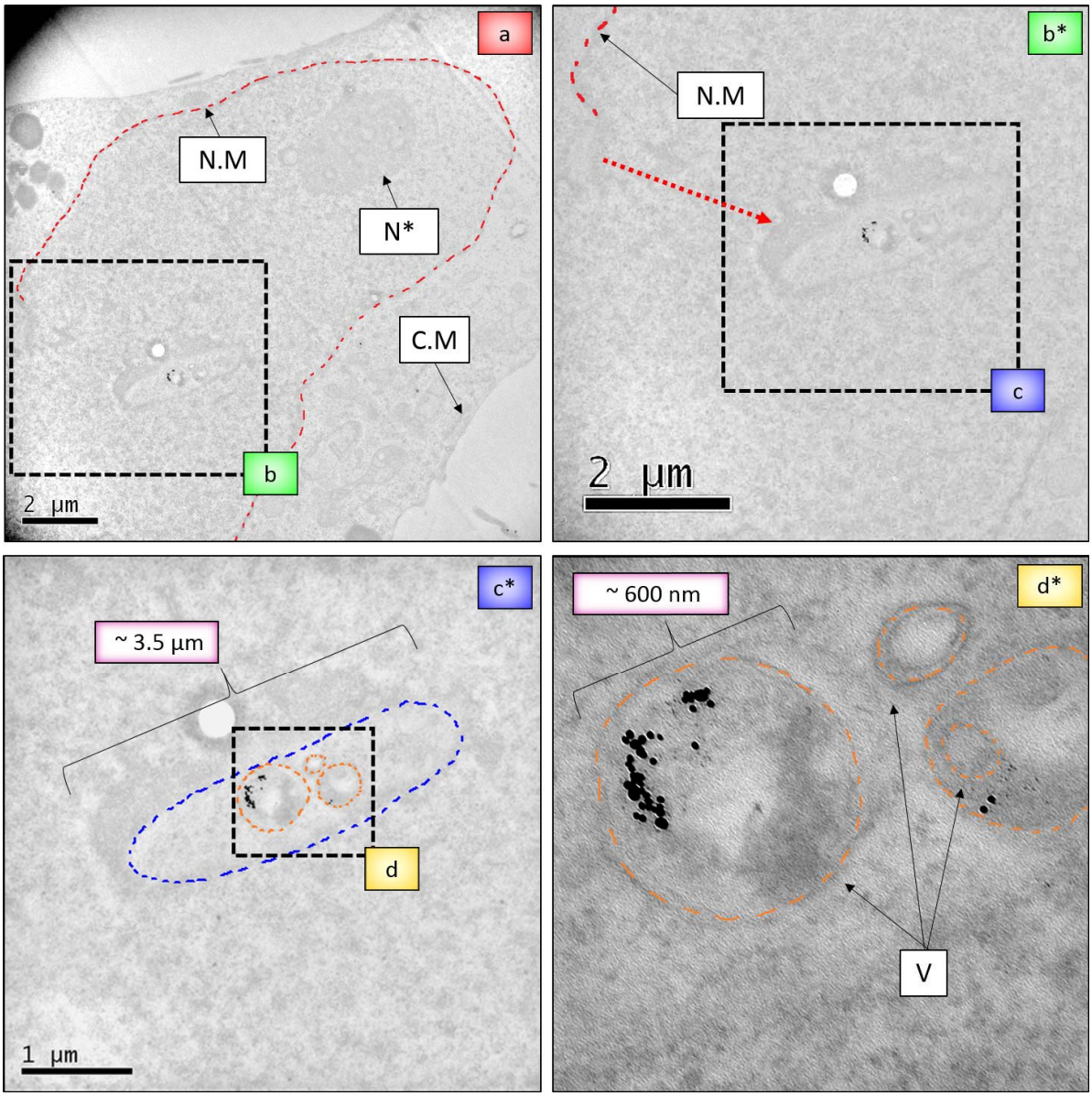

Figure 2.71: TEM images of ***Au13-P-HSH*** *in HeLa cells. Cells were incubated with* ***Au13-P-HSH*** *at a concentration of 0.25 nM in complete cell media for 24 hours before fixing. Widefield image is shown in (a). Magnifications of insets (b), (c) and (d) are shown in (b*), (c*) and (d*) respectively. Yellow arrow in (d*) denotes possible path of nanoparticle containing structure in to the nucleus. C.M - cell membrane, N.M - nuclear membrane (red dashed-line), N* - nucleolus, V - vesicles, NP - nanoparticles.*

further evidence of nuclear localised nanoparticles. Most strikingly a cluster of nanoparticles seemingly achieving vesicular escape within the nucleus was observed located close to a break in the nuclear membrane. Another example of nuclear localised nanoparticles were also identified in a cell nucleus where a structure several micrometers in diameter containing multiple vesicles within was observed. This is extremely interesting as such structures are usually found in the perinuclear region and provides great impetus for further studies monitoring uptake and nuclear translocation. Distinct attention should be afforded to cells undergoing division when the nuclear membrane breaks down and reforms in light of the hypotheses presented to explain the observed nuclear uptake, particularly as it is known that endoplasmic reticulum derived vesicles are used by the cells to reform the nuclear membrane.[287,288]

2.3.8 Nanoparticle Uptake - Effect on the Cell Cycle

Due to the nuclear localisation of **Au13-Z-HSH** and **Au13-P-HSH** and **HoechstSH** coating on these nanoparticles, the cell cycle of populations of HeLa cells was examined for signs of cell cycle dsyregulation. Cells were furthermore synchronised such that they could be incubated with nanoparticles for time periods where the cell population was enriched in the G0/G1, S and G2/M phases. As such to establish appropriate time points HeLa cells were initially cultured to 60 % confluence and deprived of serum (0 % FBS media) for 48 hours to induce cells in to the G0-G1 phase. Following serum deprivation cells were stimulated back in to progression through the cell cycle in phase by the re-introduction of serum containing media (10 % FBS media). Cells were harvested at 2 hour time points to establish the times the cells peaked in the S and G2/M phases (Figure 2.72).

It was hypothesised that nuclear uptake of the nanoparticles observed by confocal microscopy and TEM may be related to cell division, particularly the breakdown of the nuclear membrane which occurs during the latter G2 phase and the early M-phase. Cells were therefore synchronised as described and incubated with nanoparticles for 2 hour time periods corresponding to when the largest fraction of cells were in the required phase of

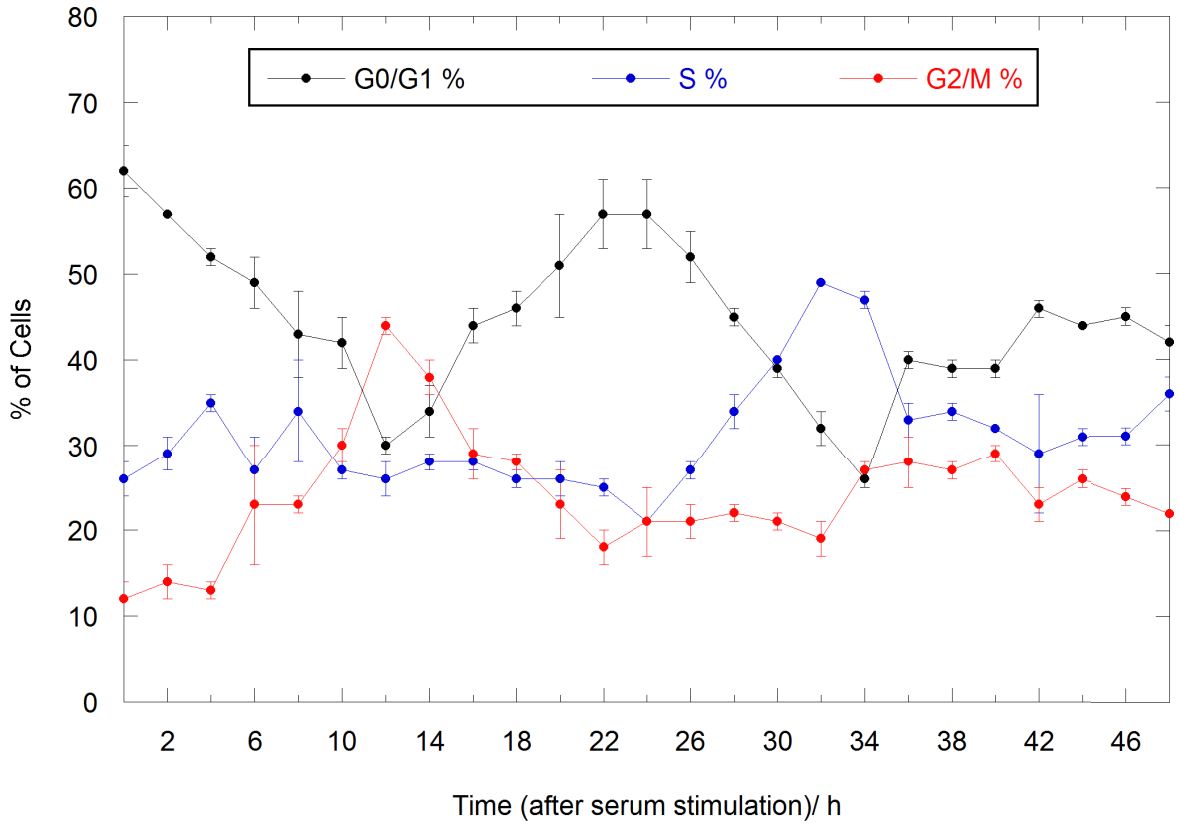

Figure 2.72: Distribution of cells in the G0/G1, S and G2/M phases of the cell cycle after serum re-stimulation following 48 hour serum deprivation. After serum stimulation for the appropriate time period cells were harvested by trypsinisation and fixed in 70 % ethanol. For analysis cells were washed in PBS, treated with RNaseA and stained with the fluorescent nucleic acid propidium iodide dye. Cell fluorescence was analysed using a FACS Calibur 14 flow cytometer (BD Biosciences). G0/G1, S and G2/M proportions were calculated using FCS Express Flow 5 software (De Novo Software) with fitting performed via chi-squared minimisation. Results are reported as the average % of cells in each phase ± 1SD.

the cell cycle. Thus the potential of the nanoparticles to dysregulate the cell cycle could be assessed in relation to the cell cycle phase. Cells were therefore incubated with **Au13-Z-HSH** and **Au13-P-HSH** from 11-13, 22-24 and 30-32 hours after serum-stimulation, corresponding to peak fractions in G2/M phase, G0/G1 phase and S phase respectively (Figure 2.72).

Following exposure to **Au13-Z-HSH** and **Au13-P-HSH** the fraction of cells in the respective phases was determined and compared to an undosed control population of cells at the same phase/time in the cell cycle (Figure 2.73). No significant change in the proportions of cells in the G2/M phase, G0/G1 phase and S phase were observed relative

to the undosed cell population ($P < 0.05$). This suggests that in cells with nuclear uptake the vesicular confinement of the majority of internalised nanoparticles may prevent them from dysregulating the cell cycle. (Data and statistical analysis are presented in Appendix I). Exposure to **Au13-Z-HSH** and **Au13-P-HSH** in unsynchronised cell populations was also shown to exhibit no significant ($P < 0.05$) cell cycle dysregulation (Appendix I).

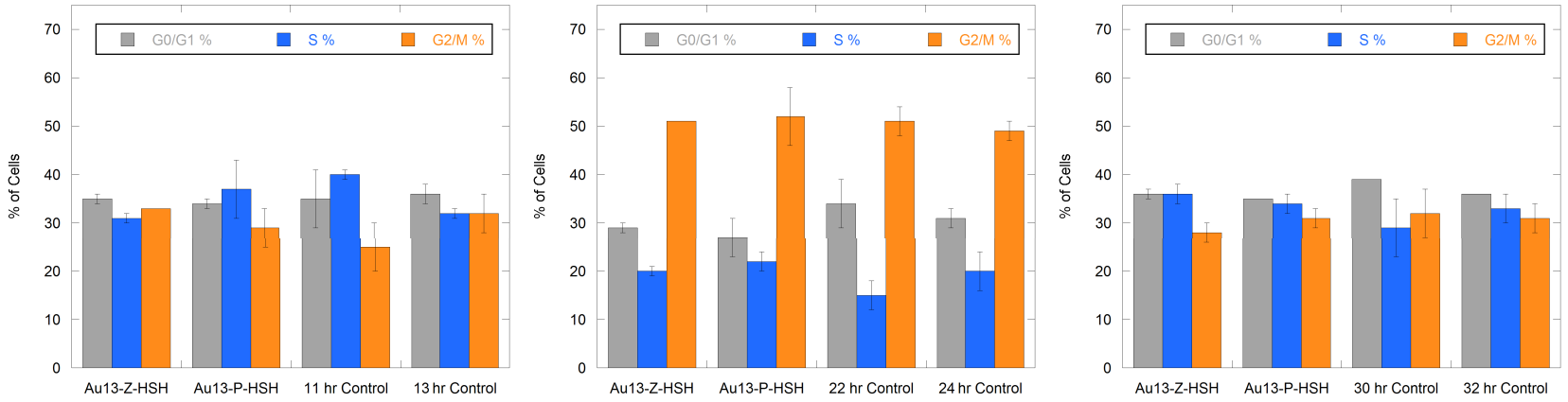

(a) 11-13hr Incubation *(b) 22-24hr Incubation* *(c) 30-32hr Incubation*

Figure 2.73: Distribution of cells in the G0/G1, S and G2/M phases of the cell cycle after serum re-stimulation (following 48 hour serum deprivation) and nanoparticle incubation. Cells were incubated with ***Au13-Z-HSH*** *and* ***Au13-P-HSH*** *for the times indicated (0.25 nM concentration) for the times indicated which refer to time after start of serum re-stimulation. Cells were subsequently harvested by trypsinisation and centrifugation and fixed in 70 % ethanol. For analysis cells were washed in PBS, treated with RNaseA and stained with the fluorescent nucleic acid propidium iodide dye. Cell fluorescence was analysed using a FACS Calibur 14 flow cytometer (BD Biosciences). G0/G1, S and G2/M proportions were calculated using FCS Express Flow 5 software (De Novo Software), with fitting performed to minimise the chi-squared value. Results are reported as the average % of cells in each phase ± 1SD. Statistical significance was tested with an independent t-test. $P < 0.05$, significant differences compared with undosed control cells harvested at identical time points.*

2.4 Conclusion

Gold nanoparticles were successfully synthesised to provide a scaffold for the thiolated **HoechstSH** complex. This was achieved by addition of the **Tween 20** and **Zonyl 7950** surfactants, and **pHLIP** peptide respectively. Luminescent nanoparticles bearing the optical signature of the **HoechstSH** and exhibiting the characteristic photophysical properties of the Hoechst dye upon addition of CT-DNA were produced and characterised.

Cellular uptake of the **HoechstSH** nanoparticle preparations were examined in the A549 and HeLa human cancer cell lines. Uptake of **Au13-T20-HSH**, **Au13-Z-HSH** and **Au100-Z-HSH** were examined in A549 and HeLa cells by confocal microscopy with significant nanoparticle uptake to the perinuclear regions in all cells. Analysis of the nanoparticles in cells indicate the stability of the **HoechstSH** complex on nanoparticles after prolonged exposure to a cellular environment. Uptake of **Au13-P-HSH** and **Au100-P-HSH** as also examined in A549 and HeLa cells. Most striking was nuclear uptake in some cells of all the nanoparticle preparations, with notable localisation of clusters of nanoparticles to the periphery of the nucleoli.

Nuclear localised **Au13-Z-HSH Au13-P-HSH** are again observed in TEM microscopy of HeLa cell sections. This is particularly surprising as nanoparticle uptake is believed to occur primarily via endocytosis and would in theory result in endosomal/lysosomal restriction. Large clusters of nanoparticles are indeed observed in membrane bound organelles in TEM images and preliminary Lysotracker staining studies corroborate this observation. Nuclear localised nanoparticles are also observed in vesicles and freely dispersed within the nucleus, indicating a translocation mechanism for nanoparticles across the nuclear envelope potentially related to it's dissolution upon cell division. Furthermore a vesicular release mechanism or indeed compromised membrane integrity of the nuclear localised vesicles may subsequently lead to free dispersion of the nanoparticles in the intra-nuclear space. In the context of the aforementioned nuclear uptake of nanoparticles and the DNA binding ability of the Hoechst complex, **Au13-Z-HSH** and **Au13-P-HSH** are examined for their ability to induce dysregulation to the HeLa cell cycle in both synchronised and

non-synchronised cell populations. Flow cytometry analysis of the cell cycle indicates no significant dysregulation following exposure to **Au13-Z-HSH** and **Au-P-HSH** compared to undosed controls ($P < 0.05$).

In summary luminescent gold nanoparticles have been synthesised and with the use of surfactants and a peptide as a pre-coating, the particles have been utilised as a scaffold for the addition of the **HoechstSH** complex. Thus nanoprobes exhibiting the optical signature of the **HoechstSH** lumiphore and it's capability of DNA interaction were produced, as indicated by photophysics and circular dichroism studies. Cellular uptake of the nanoparticles is readily observed in two carcinomic human cell lines with extremely interesting nuclear interactions, as observed by confocal and transmission electron microscopy.

2.5 Acknowledgements

Thank you to Dr. Samuel Adams and Dr. Suleman Khan (School of Chemistry, University of Birmingham) for their assistance in the synthesis and characterisation of the Hoechst dyes. Thank you to Dr. Nikolas Hodges and Mr Shrikant Jondhale (School of Biosciences, University of Birmingham) for advice on the cell work and general lab assistance. Thank you to all the analytical staff at the University of Birmingham for their support with NMR, mass-spectrometry. Thank you to Mrs Theresa Morris and Mr Paul Stanley (School of Metallurgy and Materials, University of Birmingham) for the TEM preparation of cell sections. Thanks also to the EPSRC for funding. Some instruments used in this study were supplied through Birmingham Science City: Innovative Uses for Advanced Materials in the Modern World (West Midlands Centre for Advanced Materials Project 2) with support from Advantage West Midlands (AWM) and partial funding from the European Regional Development Fund (ERDF).

2.6 Experimental

2.6.1 Synthesis of Au13-T20-HSH

Tween 20 (1.5 ml at 1.2 mM in dH_2O) purchased from Sigma-Aldrich,was added to 13 nm citrate-stabilised gold nanoparticles (9 nM, 1.5 ml) to give a final particle concentration of 4.5 nM, and a final surfactant concentration of 0.6 mM. The solution was stirred for 2 minutes. **HoechstSH** complex (200 -l, 0.6 mM stock) (made in situ; NH_4OH (aq. 30 % w/w sol.): HoechstSAc (1.2 mM, MeOH)) was added into the nanoparticle/surfactant solution. The solution was stirred for 2 minutes. Final concentration of HoechstSH in nanoparticles 8 μM. Nanoparticles were isolated by size-exclusion chromatography on Sephadex G-25 Hi-trap column, eluting with water, to give a final nanoparticle concentration of approximately 4 nM (estimated by UV-Vis absorption spectroscopy) **Au13-T20-HSH**. UV-Vis (H_2O) λ_{max} = 527 nm (SPR). Diameter = 19±6 nm (DLS number distribution). Diameter = 43±21 nm (DLS intensity distribution), zeta potential = -34±3 mV (isolated, 1 nM in deionised water diluent). Emission (H_2O, λ_{exc} = 350 nm) λ_{max} = 445 nm.

2.6.2 Synthesis of Au13-Z-HSH

Zonyl 7950 (1 μl, 1.15 g ml^{-1}, purchased from Sigma-Aldrich and used without further purification) was added to 13 nm citrate-stabilised gold nanoparticles (3 ml, 4.5 nM fluorosurfactant coated nanoparticles. The solution was stirred for 2 minutes. Fluorosurfactant coated nanoparticles were isolated by centrifugation twice at 13,000 rpm for 30 minutes (decanting the supernatant and re-suspension of the pellet in dH_2O. **HoechstSH** complex (40 μl, 0.6 mM stock) (made in situ; NH_4OH (aq. 30 % w/w sol.)): HoechstSAc (1.2 mM, MeOH) was added into the nanoparticle/surfactant solution. HoechstSH achieves 8 μM final concentration. The particles were centrifuged twice at 13,000 rpm for 30 minutes (decanting the supernatant and re-suspension of the pellet in dH_2O) to give **Au13-Z-HSH**. UV-Vis (dH_2O) λ_{max} [nm] = 521 (SPR). Diameter = 20±6 nm (DLS number distribu-

tion). Diameter = 41±18 nm (DLS intensity distribution), zeta potential = -45±12 mV (isolated, 1 nM in deionised water diluent). Emission (H_2O, λ_{exc} = 350 nm) λ_{max} = 480 nm.

2.6.3 Synthesis of Au100-Z-HSH

Zonyl 7950 (1 μl, 1.15 g ml^{-1}) was added to 100 nm citrate-stabilised gold nanoparticles (1 ml, 40 pM fluorosurfactant coated nanoparticles. The solution was stirred for 2 minutes. Fluorosurfactant coated nanoparticles were isolated by centrifugation twice at 13,000 rpm for 90 seconds (decanting the supernatant and re-suspension of the pellet in dH_2O. HoechstSH**HoechstSH** complex (50 μl, 0.6 mM stock) (made in situ; NH_4OH (aq. 30 % w/w sol.): HoechstSAc (1.2 mM, MeOH) was added into the nanoparticle/surfactant solution. HoechstSH achieves 10 μM final concentration. The particles were centrifuged twice at 13,000 rpm for 90 seconds (decanting the supernatant and re-suspension of the pellet in dH_2O) to give isolated **Au100-Z-HSH**. UV-Vis (dH_2O) λ_{max} [nm] = 545 (SPR). Diameter = 72±17 nm (DLS number distribution). Diameter = 98±37 nm (DLS intensity distribution), zeta potential = -40±12 mV (isolated, 10 pM in dH_2O).

2.6.4 Synthesis of Au13-P-HSH

Procedure was adapted from gold nanoparticle preparation by Davies et al.[82] A 20 μl solution of pHLIP (1 mM in 10 % DMSO, phosphate buffer saline (PBS) solution) was added to 13 nm citrate-stabilised gold nanoparticles (2.5 ml, 4.5 nM), to a final peptide concentration of 8 μM. The solution was stirred for 2 minutes. **HoechstSH** complex (200 μl, 0.6 mM stock) (made in situ; NH_4OH (aq. 30 % w/w sol.): HoechstSAc (1.2 mM, MeOH)) was added into the nanoparticle/surfactant solution (final concentration of HoechstSH in nanoparticles 45 μM). Nanoparticles were isolated by size-exclusion chromatography on Sephadex G-25 Hi-trap column **Au13-P-HSH**. UV-Vis (H_2O) λ_{max} = 524 nm (SPR). Diameter = 14±4 nm (DLS number distribution). Diameter = 36±19 nm

(DLS intensity distribution), zeta potential = -53±12 mV (isolated, 1 nM in deionised water diluent). Emission (H_2O, λ_{exc} = 350 nm) λ_{max} = 445 nm.

2.6.5 Synthesis of Au100-P-HSH

Procedure was adapted from gold nanoparticle preparation by Davies et al.[82] A 5 μl solution of pHLIP (1 mM in 10 % DMSO, phosphate buffer saline (PSB) solution) was added to 100 nm citrate-stabilised gold nanoparticles (2.5 ml, 40 pM), giving a final peptide concentration of 2 μM. The solution was stirred for 2 minutes. **HoechstSH** complex (50 μl, 0.6 mM stock) (made in situ; NH_4OH (aq. 30 % w/w sol.): HoechstSAc (1.2 mM, MeOH)) was added into the nanoparticle/surfactant solution (final concentration of HoechstSH in nanoparticles 10 μM). The particles were centrifuged twice at 13,000 rpm for 90 seconds (decanting the supernatant and re-suspension of the pellet in dH_2O) affording **Au100-P-HSH**. UV-Vis (dH_2O) λ_{max} [nm] = 588 (SPR). Diameter = 113±41 nm (DLS number distribution). Diameter = 154±50 nm (DLS intensity distribution), zeta potential = -40±12 mV (isolated, 10 pM in dH_2O).

2.6.6 Cell Cycle Analysis

HeLa cells were seeded in flasks or six-well plates and cultured in complete cell medium containing 10% FBS. Upon 50% confluence cell medium was removed and cells washed thrice with PBS. For synchronisation cells were incubated in serum-free medium (0% FBS) for 48 hr. Control cells were incubated in 10% FBS for 48 hr. After 48 hrs elapsed cells were gently washed in PBS thrice and incubated in complete cell medium (containing 10% FBS) with a 0.25 nM (final concentration) addition of gold nanoparticles as require. Cells were harvested at the required time points for fixing.

For fixing cells were transferred to Falcon tubes to achieve approximately 10^6 cells per tube. Cells were centrifuged 300 g for 5 min, the supernatant was discarded and the pellet re-suspended in 2 ml PBS. The cells were again centrifuged, supernatant discarded

followed by resuspension of the pellet in 500 μl PBS. Cells were vortexed accompanied by the drop-wise addition of 70 % ice-cold ethanol. Tubes were transferred to the freezer (-20C) before staining (minimum 24 hr).

For propidium iodide (PI) staining and analysis cells were centrifuged for 8 min at 300 g. The supernatant was aspirated off and the pellet washed with 3 ml PBS. Cells were centrifuged for 5 min at 300 g, the supernatant discarded and the pellet resuspended in 500 μl PBS. To each cell sample 5 0μl RNAse A solution and 5 μl of PI (1 mg/ml) was added. Followed by incubation at room temperature for a minimum 30 min in the dark. For each sample, a minimum of 10,000 cells were analyzed by fluorescence activated cell sorting (FACS) with a flow cytometer (BD FACS Calibur 14, BD Biosciences, Erembodegem-Dorp 86, 9320 Erembodegem, Belgium). The percentage of cells in the G0/G1, S and G2/M phases was calculated using FCS Express Flow 5 software, with fitting performed to minimise the chi-squared value (De Novo Software, 400 N. Brand Blvd., Suite 850, Glendale, CA 91203).

2.6.7 Circular Dichroism

Circular dichroism spectra were recorded on a JASCO J180 spectropolarimeter using quartz emission cells with 1 cm path length. Spectra were recorded at an internal temperature of 22 C. Solutions of CT-DNA were stocked at 100 μM and 800 μM in milli-Q water. Stocks of **Au13-Z-HSH** and **Au13-P-HSH** were at 3.5 nM concentration, diluted in Tris-HCl [10 mM], NaCl [10 mM] buffer as required from initial synthesis. Instrument parameters were as follows: sensitivity - standard, band width 2 - μM, data pitch 0.5 nm, scanning speed - 200 nm/min, accumulations - 12. DNA concentrations were measured and adjusted by measuring UVV absorbance at 260 nm (ε = 6600 $mol^{-1}dm^3cm^{-1}$), and sonicated/vortexed for approximately 30 seconds before each measurement.

3

Cellular Uptake of Gold Nanoparticles Labelled with a Luminescent Ruthenium(II) Complex

3.1 Introduction

Research in to the use of metal complexes as cellular probes has attracted much interest due to their distinct physico-chemical properties.[289–291] Detection platforms utilising nanoparticles that incorporate luminescent probes can offer improved sensitivity and stability in addition to the potential for multiplexing with the integration of multiple probes on to a single nanoprobe.[9–13]

Luminescent nanoprobes offer scope for imaging with multiple modalities and can be functionalised to target specific cells and/or tissues. They can therefore be designed to interrogate a range of biomolecular processes opening new avenues in disease diagnosis and therapy.[14–17,77] Gold nanoparticles and quantum dots have attracted particular interest for a wide range of applications.[13,17,47,119] Functionalising gold nanoparticles with luminescent probes enables construction of a nanoprobe that bears the distinct optical characteristics of the lumiphore.[75] Luminescent probes such as these can also exploit the high electron density of gold and its light scattering properties to offer multimodal imaging and furthermore do not suffer from blinking as observed in quantum dots.

One such example is the attachment of neutral lanthanide lumophores to gold nanoparticles co-coated with a pH sensitive peptide. These nanoparticles have demonstrated

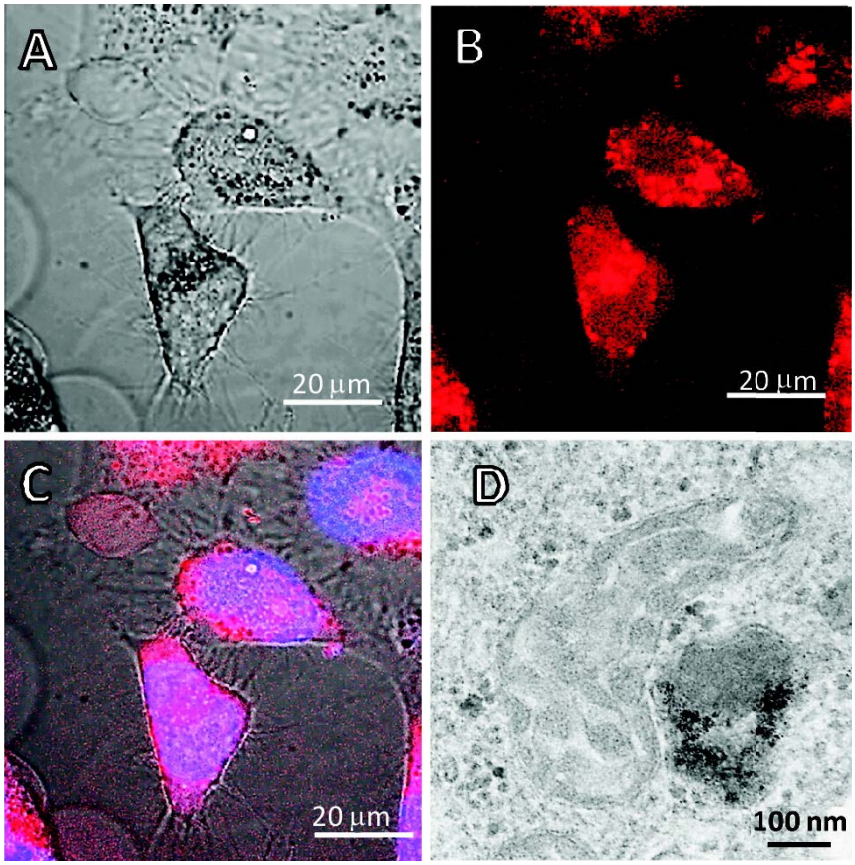

Figure 3.1: Confocal microscopy and TEM of images of live HeLa cells incubated with ruthenium polypyridyl functionalized gold nanoparticles for 4 hours. (A) brightfield image, (B) ruthenium emission from the red channel from 600 to 700 nm, (C) overlay of the red luminescence, the blue channel (exhibiting the DAPI nuclear costain), and the brightfield image, (D) TEM image of internalised following incubation with HeLa cells. Figure adapted from Elmes et al.[300]

selective cellular uptake and have been imaged using their luminescence in the intracellular environment.[82] Ruthenium polypyridyl complexes are amongst the most studied lumiphores and are particularly advantageous due to their photophysical properties[292] which have seen their application for the purposes of luminescence recognition, sensing[293] and as both sensitive and structurally specific DNA probes.[294] In addition to excitation and emission in visible wavelengths they also exhibit large Stoke's shifts and relatively long lifetimes (of the order of several hundred nanoseconds) compared to cellular autofluorescence and organic dyes ($\leq$ 50 nanoseconds) and good photostability.[77,278,295,296] The long lifetime makes the ruthenium complex particularly suited to fluorescence-lifetime imaging microscopy (FLIM), where the lifetime of a fluorescent signal as opposed to its intensity is used to form an image.[297–299]

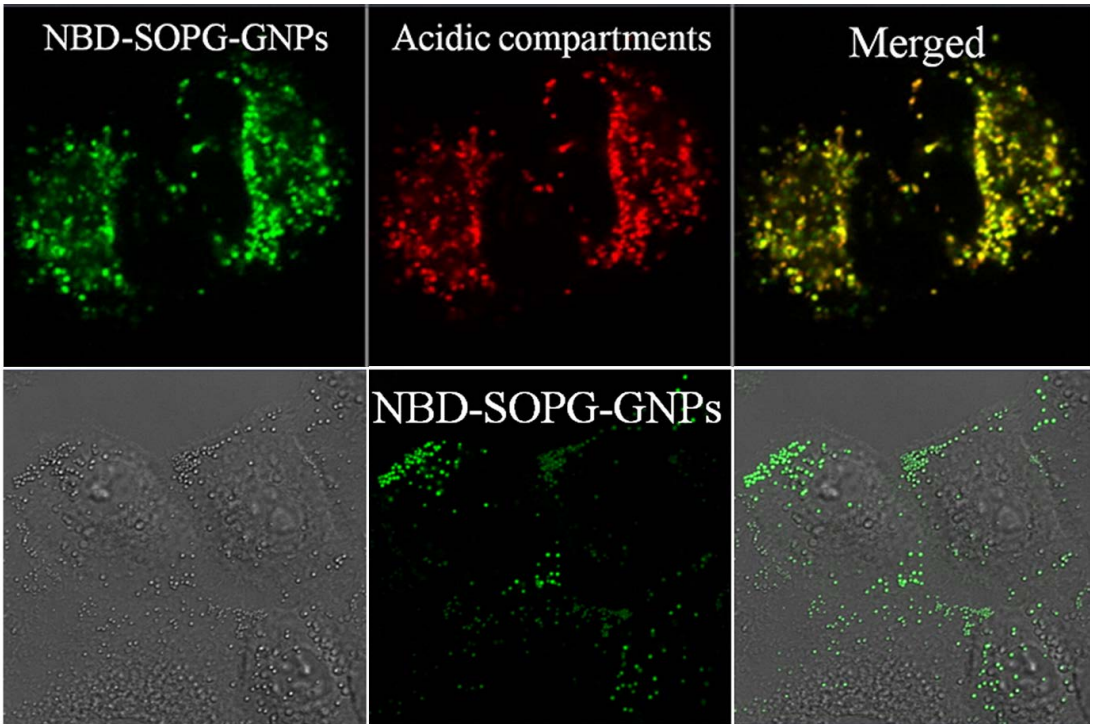

Figure 3.2: Top panel - confocal microscopy images of A549 cells incubated with lipid coated gold nanoparticles (green) for 72 hours (a), with acidic compartments in the cells labelled with Lyso Tracker Red (b) and an image overlay exhibited in (c). Images show co-localisation of nanoparticles with acidic compartments (lysosomes and/or endosomes). Bottom panel - brightfield DIC (d) and confocal microscopy image (e) of A549 cells incubated with lipid coated gold nanoparticles (green) for 48 hours with an image overlay exhibited in (f). Images show formation of lamellar bodies which have internalised the nanoparticles. (Figure adapted from Wang et al.[264])

The association of luminescent ruthenium complexes to gold nanoparticles has traditionally exploited methods exploiting electrostatic interactions,[191] thiol exchange,[192] or by direct reduction of Au^{3+}.[193–195] Such methods have their intrinsic limitations however, for example nanoparticles are restricted to sizes smaller than 10 nm, are relatively polydisperse and control over the coating of the ruthenium probe is non-trivial. An alternative is the use of surfactant based mediation. The interaction of the Zonyl family of fluorosurfactants with gold surfaces has previously been investigated by Lu et al., in which gold nanoparticles were capped with Zonyl FSN which were stable in solution even at high salt concentrations.[301] Tang et al. also used Zonyl FSN self-assembly on gold surfaces.[302]

Cellular uptake of gold nanoparticles functionalised with ruthenium(II) polypyridyl complexes has previously been investigated by Elmes et al. using confocal microscopy and TEM.[300] Synthesis of the ruthenium(II) polypyridyl in the study by Elmes et al.

used the Brust thiol exchange method which lasts 12 hours in duration followed by isolation steps after synthesis.[192] The ruthenium(II) polypyridyl gold nanoparticles were internalised by HeLa cells through what was hypothesised as receptor-mediated endocytosis or plasma membrane driven transport. Figure 3.1 shows a brighfield image (A) where the gold nanoparticle clusters as dark spots which are co-localised with areas of red ruthenium luminescence in the red channel image (B). The TEM image (D) indicates that the nanoparticles are clustered and confined to vesicles in the intracellular environment.

Gold nanoparticle uptake is also readily observed in other cell lines. Wang et al. explored nanoparticle uptake in the A549 human lung cancer epithelial cell line, a type II alveoloar epithelial cell line whose most important role is the secretion of lung surfactants which aid diffusion in the alveolar spaces.[303] Gold nanoparticles (20 - 30 nm) were coated with a phospholipid bilayer and uptake studied with flow cytometry, confocal microscopy and TEM.[264] Nanoparticle exposure in humans can occur via inhalation in which case the lung epithelial cells will be amongst the first to be exposed. The A549 cell line, although adenocarcinomic, does afford the opportunity to therefore explore important biological interactions as an *in vitro* model for the epithelial cells of the lung.[304]

Although the nanoparticles in this study by Wang *et al.* were not coated with ruthenium, interesting and notable interactions between particles and A549 cells were observed. Microscopy revealed the lipid coated gold nanoparticles localised to acidic compartments and lysosomes in the cells and were subsequently cleared from the cells via an exocytosis mechanism (Figure 2.2). Exposure to the nanoparticles was also seen to induce formation of lamellar bodies, exhibited as bright vesicular structures in the cytoplasm of exposed cells which were absent from undosed control cells (Figure 3.2). The lamellar bodies were also shown to contain nanoparticles by confocal microscopy and confirmed by TEM imaging. It was concluded that as the nanoparticles were similarly (negatively) charged to the lipid surfactant that the lung epithelial cells naturally internalise and secrete they were readily internalised via the same mechanism. Furthermore the increase in the number of lamellar bodies, which serve the purpose of exporting lipid surfactant, was explained

as a cellular response to increase the number of compartments that were in turn able to remove the nanoparticles. The results of the study illustrate how the physico-chemical properties of nanoparticles can influence uptake and ejection of nanoparticles in cells.

3.2 Chapter Outline

Direct addition of the thiol derivatised ruthenium complex to gold nanoparticles leads to irreversible aggregation of the particles due to the positive charge of the complex, thus a novel coating strategy was adopted for gold nanoparticles. In work performed by Dr. Nicola Rogers addition of the ruthenium complex was achieved by pre-coating the nanoparticle with a fluorinated surfactant prior to addition of the thiolated ruthenium complex.[77,190] The large gold cores of the nanoparticles provide scaffolds for extensive labelling with the surface active ruthenium(II) polypyridyl complex producing a luminescent water soluble gold colloid. The work discussed herein presents an investigation in to the uptake of the highly luminescent ruthenium coated nanoparticles in A549 human lung cancer cells by the author. Confocal and transmission electron microscopies reveal significant internalisation of the particles and interestingly single nanoparticles were observed in the intracellular environment. Furthermore significant nuclear uptake of the nanoparticles occurred but was not observed to induce toxicity as assessed by mitochondrial and cell membrane integrity assays. The work performed in this chapter contributes to the appended publication.

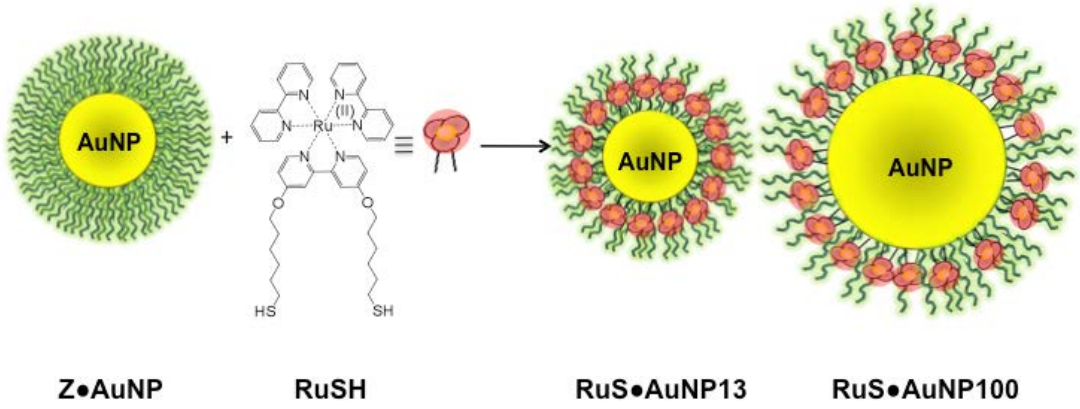

*Figure 3.3: Preparation method for **Au13-Z-RuSH** and **Au100-Z-RuSH**. Nanoparticle were pre-coated with the Zonyl 7950 surfactant prior to labelling with the luminescent ruthenium complex, thus irreversible nanoparticle flocculation and aggregation was avoided.*

3.3 Results and Discussion

3.3.1 Synthesis and Characterisation of Au13-Z-RuSH and Au100-Z-RuSH

Preparation and characterisation of the nanoparticles was performed by Dr. Nicola Rogers.[77,190] Gold nanoparticles were synthesised as described in Chapter 2. In brief Zonyl 7950 was employed to pre-coat the nanoparticle surface. Following isolation of the surfactant coated particles was addition of the ruthenium complex (**RuSH**) as illustrated in Figure 3.3. (Further details on synthesis and characterisation are provided in Appendix K for convenience). Nanoparticles were isolated by centrifugation affording 13 **Au13-Z-RuSH** and 100 nm **Au100-Z-RuSH** gold nanoparticles coated with the ruthenium complex.

3.3.2 Cellular Uptake of Au13-Z-RuSH and Au100-Z-RuSH

The application of **Au13-Z-RuSH** and **Au100-Z-RuSH** as cellular imaging probes was explored by exposure to the A549 human lung cancer epithelial cell line. Uptake of **Au13-Z-RuSH** was readily observed after a 24 hour incubation with uptake evident primarily to the perinuclear region of the cells (Appendix K, Figure K.1). Qualitative

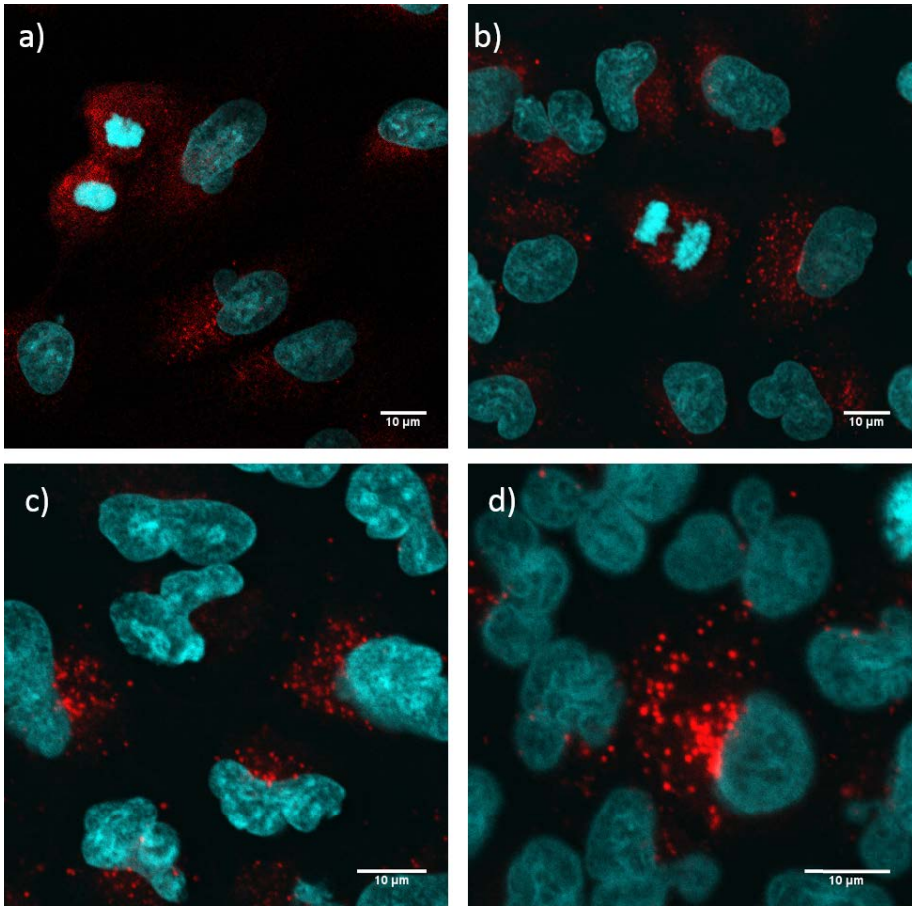

Figure 3.4: Ruthenium luminescence and Hoechst nuclear stain overlay images of ***Au13-Z-RuSH*** *in fixed A549 cells monitored by confocal luminescence microscopy. Cells were incubated with nanoparticles at a concentration of 0.9 nM in complete cell media for 24 hours. Cells were imaged: (a) immediately after the 24 hr incubation, (b) 1 day, (c) 2 days and (d) 3 days post-incubation. Hoechst (blue channel),* λ_{exc} *= 405 nm,* λ_{em} *= 410-455 nm. Ruthenium luminescence (red channel),* λ_{exc} *= 633 nm,* λ_{em} *= 640-800. (Scale bar 10 µm).*

comparisons of the nanoparticle localisation from the reflection and transmission images with the ruthenium luminescence from the red image channel also illustrates the stability of the ruthenium coating following exposure to a cellular environment.

To evaluate nanoparticle uptake and their intracellular fate over an extended period of time a pulse-chase experiment was performed (Figure 3.4). Following an initial exposure for 24 hours cell media containing **Au13-Z-RuSH** was replaced with fresh media to essentially examine a "batch" of internalised nanoparticles over time. Using the Hoechst 33258 nuclear counterstain the perinuclear localisation of the nanoparticles (red spots) is evident in cells imaged immediately after the initial 24 hour exposure (Figure 3.4a).

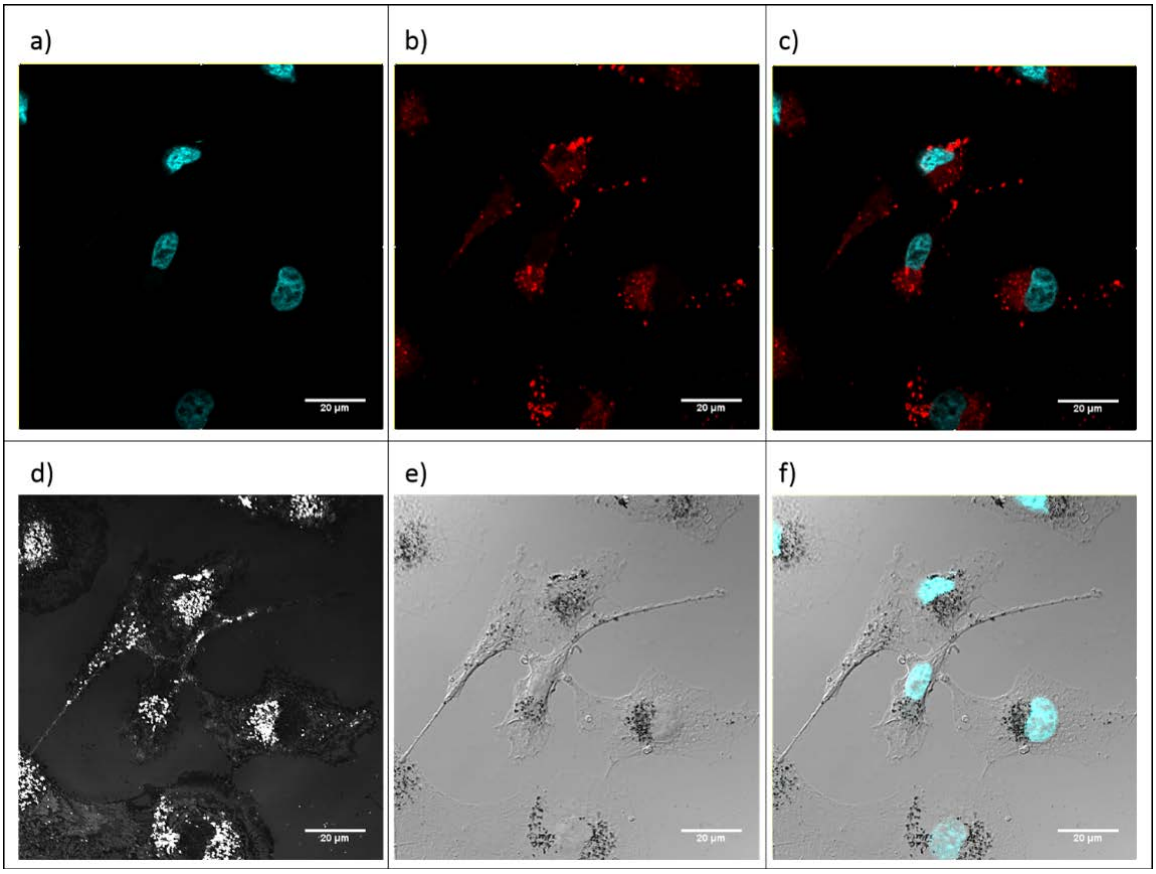

Figure 3.5: Images of ***Au100-Z-RuSH*** *in A549 cells monitored by confocal luminescence and reflection microscopy. Cells were incubated with nanoparticles at a concentration of 0.4 pM in complete cell media for 24 hours before fixing. (a) Hoechst nuclear stain, (b) ruthenium luminescence, (c) ruthenium luminescence and Hoechst overlay, (d) reflectance image, (e) transmission image (f) transmission image and Hoechst nuclear stain overlay, (f) Hoechst nuclear stain and reflection image overlay. Reflection image* λ_{exc} *= 633 nm,* λ_{em} *= 623-643 nm. Hoechst (blue channel),* λ_{exc} *= 405 nm,* λ_{em} *= 410-455 nm. Ruthenium luminescence (red channel),* λ_{exc} *= 633 nm,* λ_{em} *= 640-800. (Scale bar 20* μm*).*

Imaging the cells after a further 24 and indeed 48 hours reveals rather more discrete perinuclear accumulations of nanoparticles several hundred nanometres in diameter, compared to a more qualitatively diffuse and homogenous distribution of nanoparticles immediately after the initial exposure (Figure 3.4b-c). It is interesting to note that even after 72 hours after removal of the media containing the nanoparticles the cells still exhibited internalised **Au13-Z-RuSH** (Figure 3.4d). Based on the number of cell nuclei in the images a 72 hour time period corresponds to approximately three cell-division cycles. The pulse-chase study thus demonstrates not only the long-term stability of the luminescent ruthenium coating but also the poor nanoparticle clearance ability of the cells.

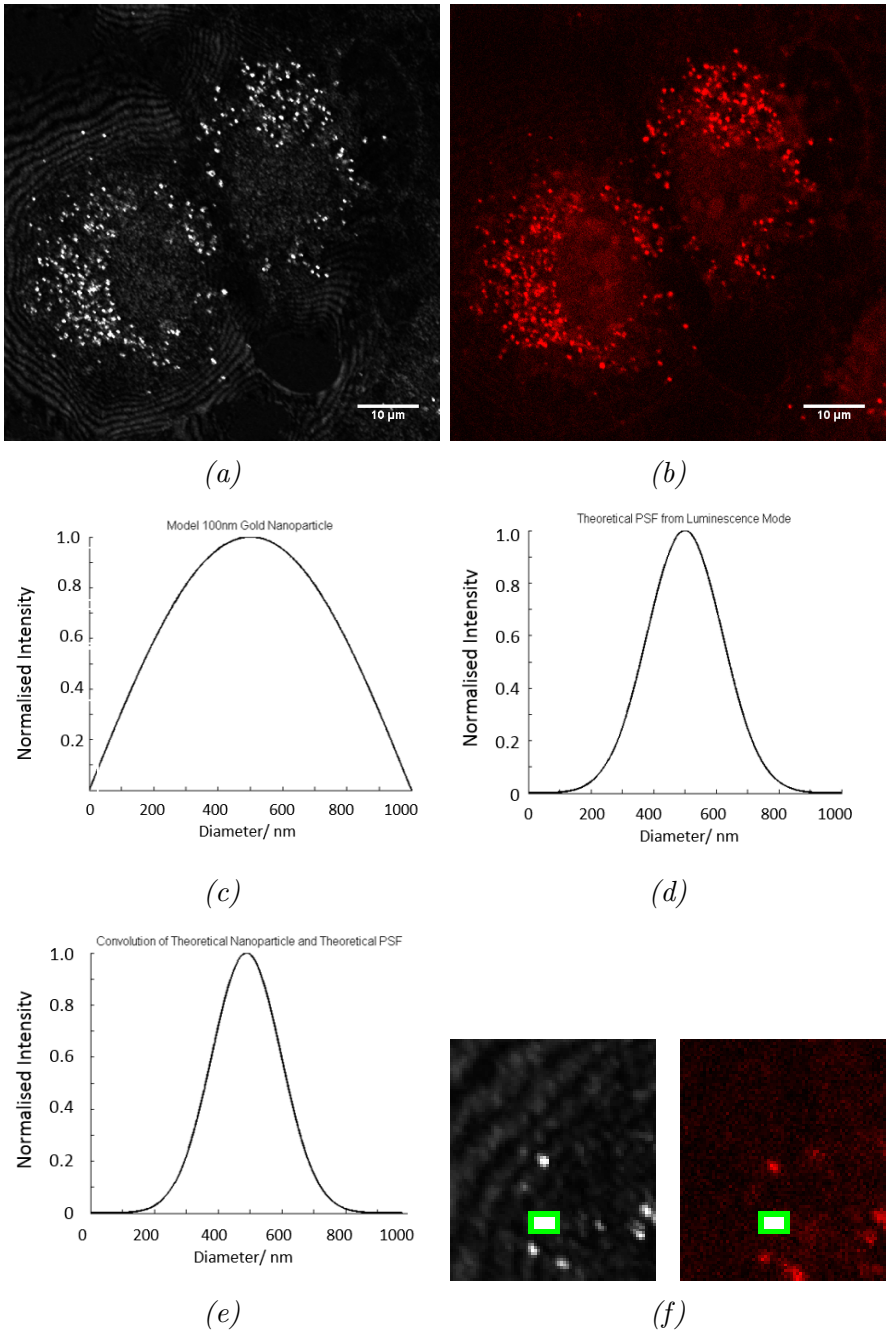

Figure 3.6: Images of ***Au100-Z-RuSH*** *in A549 cells monitored by confocal luminescence and reflection microscopy, and point-spread function analysis to compare observed size and theoretically observed size of single nanoparticles. Cells were incubated with nanoparticles at a concentration of 0.4 pM in complete cell media for 24 hours before fixing. (a) reflectance image, (b) ruthenium luminescence, (c) theoretical 100 nm gold nanoparticle modelled as a section of a sinusoidal wave representing a simple model of the nanoparticle sphere, (d) Gaussian model of the measured point-spread function from confocal luminescence measurements, (e) result of the convolution of the measured point-spread function from confocal luminescence measurements with a simple model of the nanoparticle sphere, f) reflection microscopy image (left) and confocal luminescence image (right) indicating chosen nanoparticle (inset scale-bar 1 µm). (Computational code provided in Appendix J.3).*

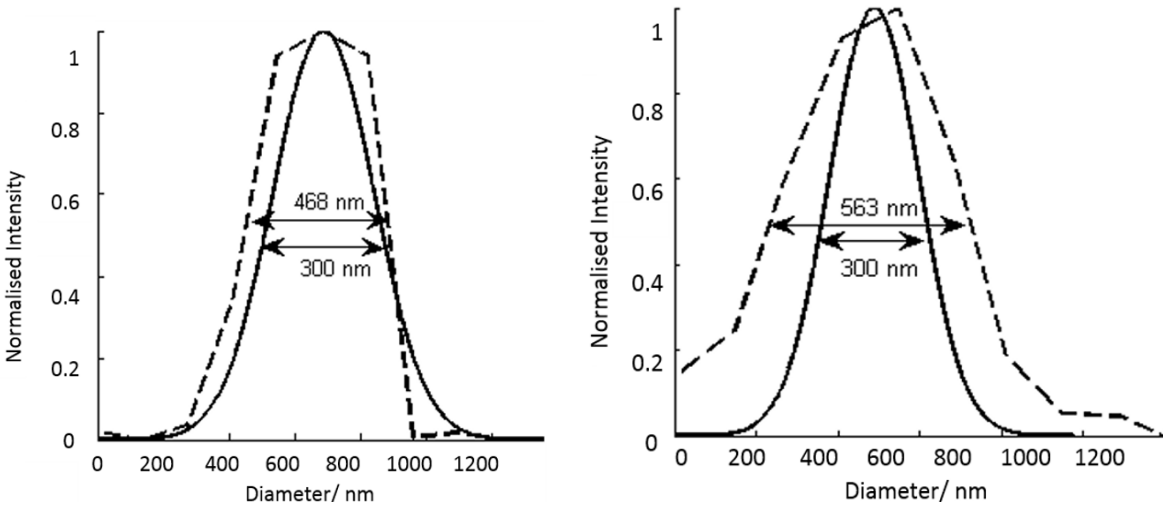

Figure 3.7: (a) and (b) comparison of the result of the convolution of the measured point-spread function with the simple model of the nanoparticle sphere (solid line) and the actual measured intensity profile of a nanoparticle in the reflection and confocal luminescence images ***Au100-Z-RuSH*** *in A549 cells. (Cells were incubated with nanoparticles at a concentration of 0.4 pM in complete cell media for 24 hours before fixing). (Computational code provided in Appendix J.3).*

No immediate nuclear localisation of the **Au13-Z-RuSH** was evident. The luminescence and scattering signal does however have to be above a certain threshold to be detected which single or small clusters of **Au13-Z-RuSH** may be not exhibit. The larger size of **Au100-Z-RuSH** are particularly advantageous in this respect. The 100 nm gold nanoparticles exhibit a larger scattering as discussed in Section 1.2 and a greater luminescence to due to a higher number of ruthenium complexes populating a larger surface area on the 100 nm gold nanoparticle compared to the 13 nm nanoparticles. A549 cells incubated with **Au100-Z-RuSH** for 24 hours show significant uptake of the nanoparticles demonstrating the ability of the cells to internalise a range of particles ranging an order of magnitude in size from 13 to 100 nm.

Confocal microscopy images are presented in Figure 3.5. Cells exhibit nuclear Hoechst staining (cyan) and nanoparticles are exhibited as red spots in the ruthenium luminescence red channels and as black and white spots in the transmission and reflection images, exploiting the absorption and scattering of gold respectively.[263] Qualitative colocalisation of the red ruthenium luminescence and the nanoparticles again indicates the stability of

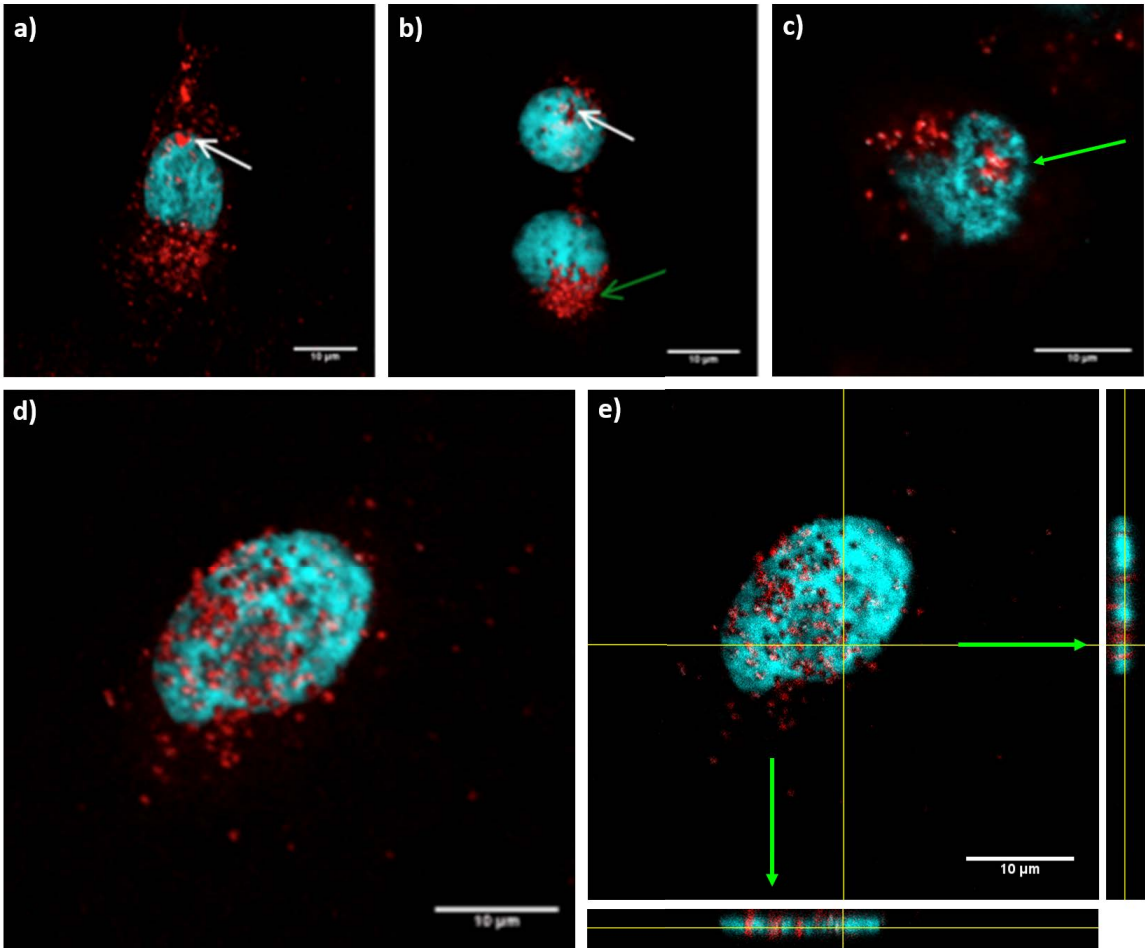

Figure 3.8: Images of ***Au100-Z-RuSH*** *in A549 cells monitored by confocal luminescence and reflection microscopy. Cells were incubated with nanoparticles at a concentration of 0.4 pM in complete cell media for 24 hours before fixing. (a-d) ruthenium luminescence and Hoechst overlays, (e) Orthogonal view of image (d) Reflection image* λ_{exc} *= 633 nm,* λ_{em} *= 623-643 nm. Hoechst (blue channel),* λ_{exc} *= 405 nm,* λ_{em} *= 410-455 nm. Ruthenium luminescence (red channel),* λ_{exc} *= 633 nm,* λ_{em} *= 640-800. (Scale bar 10 µm).*

the ruthenium probe on the 100 nm gold nanoparticles after prolonged exposure to a cellular environment.

The majority of the nanoparticles are perinuclear localised and to further characterise the size of the nanoparticles a computational analysis was performed on particles observed in Figure 3.6). Initially a theoretical 100 nm gold nanoparticle was created by using a section of a sinusoidal wave, thus representing a simple model of the nanoparticle sphere (Figure 3.6c). A theoretical point-spread function of the microscope was then created represented as a Gaussian model, essentially describing the response of the microscope to a point source or object (Figure 3.6d). A convolution of these two models thus represents

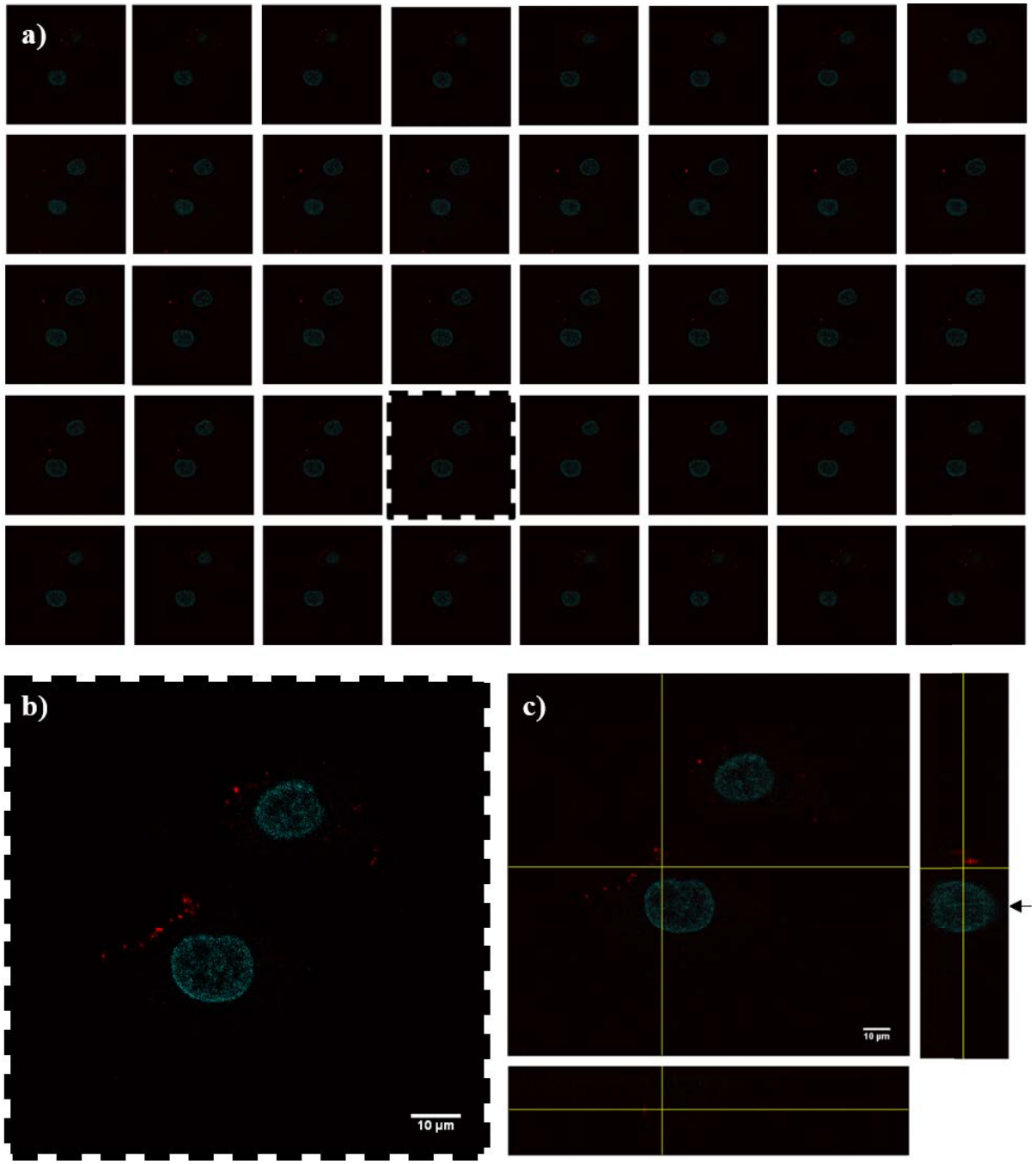

Figure 3.9: Images of ***Au13-Z-RuSH*** *in A549 cells monitored by confocal luminescence and reflection microscopy. Cells were incubated with nanoparticles at a concentration of 0.9 nM in complete cell media for 24 hours before imaging. (a) Confocal image sequence from 3D z-stack of live cells with ruthenium luminescence and nuclear Hoechst overlay, with enlargement of highlighted slice shown in (b). (c) orthogonal view of the central z-stack slice (xz plane below, yz plane-right) illustrating ruthenium luminescence from within the same z-plane as the nuclear Hoechst luminescence (arrow). Reflection image* λ_{exc} *= 633 nm,* λ_{em} *= 623-643 nm. Hoechst (blue channel),* λ_{exc} *= 405 nm,* λ_{em} *= 410-455 nm. Ruthenium luminescence (red channel),* λ_{exc} *= 633 nm,* λ_{em} *= 640-800. (Scale bar 50* μm*).*

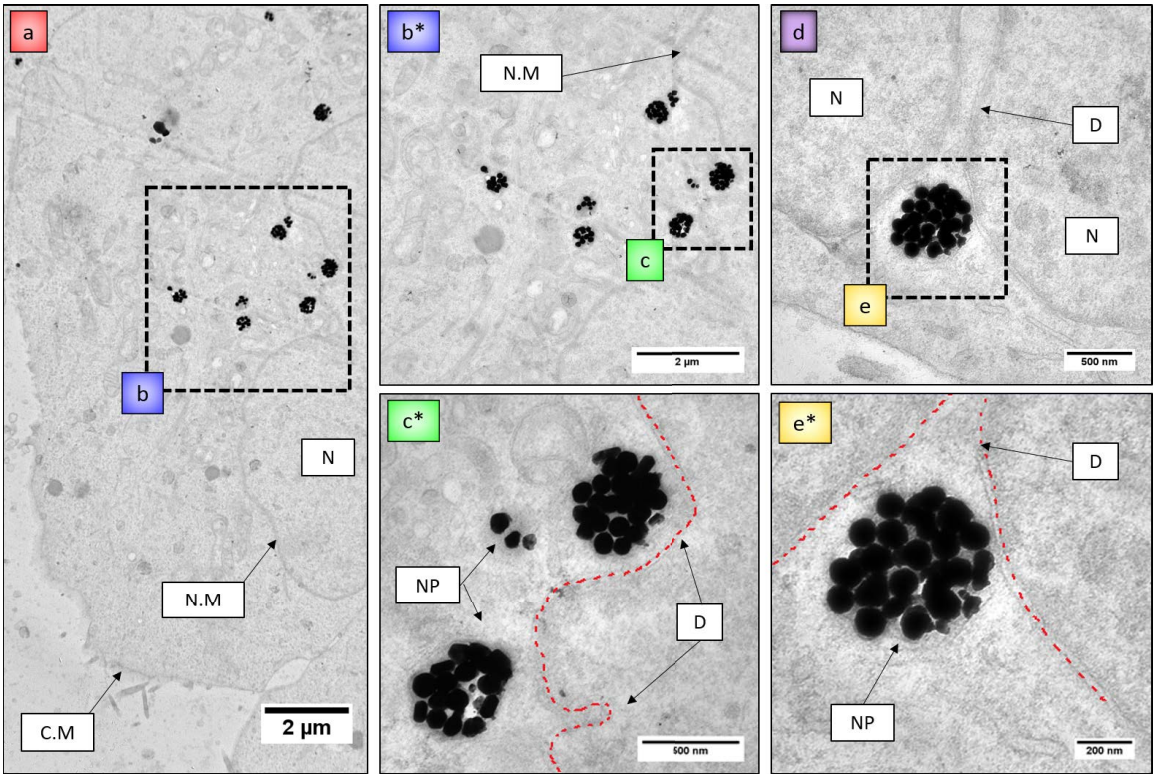

*Figure 3.10: Transmission Electron Microscopy of **Au100-Z-RuSH** in A549 cells. Cells were incubated with **Au100-Z-RuSH** at a concentration of 0.4 pM in complete cell media for 24 hours before fixing. Widefield image is shown in (a). Magnifications of insets (b), (c), (d) and (e) are shown in (b*-e *). C.M - cell membrane, N.M - nuclear membrane, N - nucleus, D - deformation(s), NP - nanoparticle. (Scale bars (a,b *) 2 µm, (c*, d) 500 nm, (e*) 200 nm).*

the theoretically observed image of a single 100 nm gold nanoparticle (Figure 3.6e). The theoretical observation can then be compared with the actual observed intensity profiles of a nanoparticle in the reflectance and ruthenium luminescence imaging channels (Figure 3.6f). Direct comparisons of the theoretical and actual observations are exhibited in (Figures 3.7a and 3.7h) for the reflection and luminescence imaging modes respectively. According to the computational model the observable particle width in the luminescence channel should be approximately 250 - 300 nm. Close correlation with the actual observed profiles indicate the **Au100-Z-RuSH** analysed are single nanoparticles Figure 3.6).

One of the most striking observations of the A549 cells incubated with **Au100-Z-RuSH** were several cells exhibiting nuclear uptake as indicated by the arrows in Figure 3.8. The cell nucleus exhibited in Figure 3.8d was amongst those which showed the greatest nuclear uptake of the nanoparticles with a homogenous distribution of **Au100-**

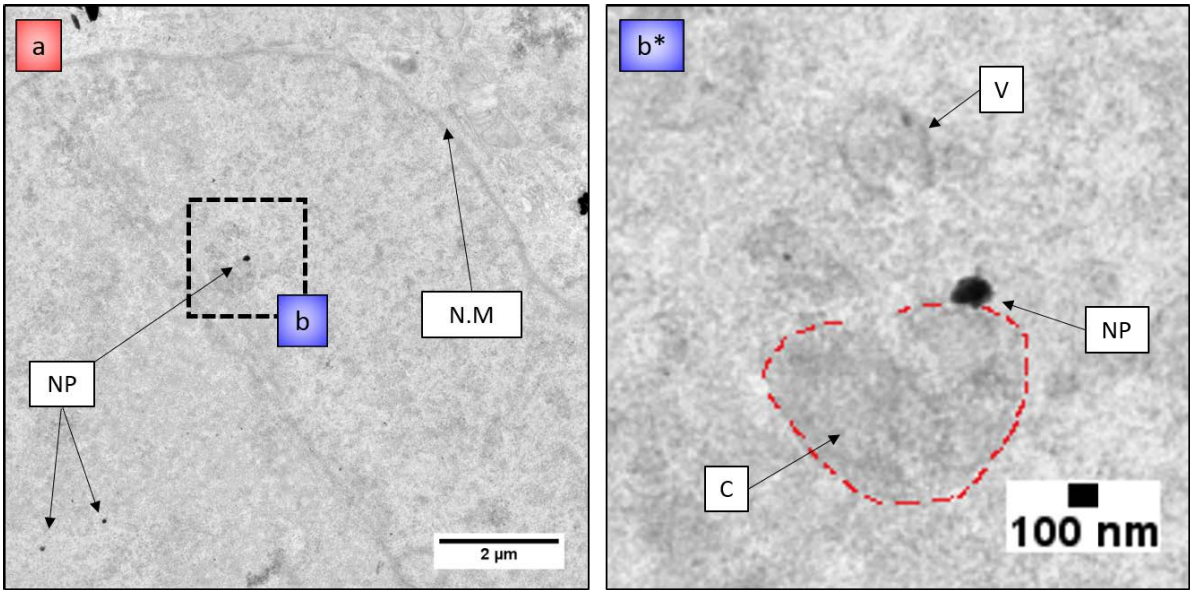

*Figure 3.11: Transmission Electron Microscopy of **Au100-Z-RuSH** in A549 cells. Cells were incubated with **Au100-Z-RuSH** at a concentration of 0.4 pM in complete cell media for 24 hours before fixing. Widefield image is shown in (a). Magnifications of inset (b) is shown in (b*). N.M - nuclear membrane, V - vesicle, NP - nanoparticle, chromatin denoted with red dashed-line. (Scale bars 2 µm and 100 nm).*

Z-RuSH across the entire nucleus. More revealing is the orthogonal view of a three-dimensional image stack of the cell which exhibits transverse views showing discrete red ruthenium emission throughout the central plane of the nucleus, confirming the nanoparticles imaged are in the nucleus and not above or below as indicated by the green arrows in Figure 3.8e.

Figure 3.9 exhibits images of **Au13-Z-RuSH** in A549 cells. The uptake in these images is similar to those that seen in the majority of the fixed cell specimens discussed, with perinuclear localisation of **Au13-Z-RuSH** observed in both cells in the field-of-view. No cells exhibiting nuclear uptake were observed in the live cell imaging specimen, however as a very small sample of live cells just a single specimen were examined (compared to several fixed cell specimens), this can not be excluded. An ideal solution would involve several live cell imaging experiments to evaluate the proportion of cells exhibiting nuclear localised particles, thus uptake in to the nucleus can be quantified and excluded to be as a result of fixing artefacts.

TEM imaging of A549 cells incubated with **Au100-Z-RuSH** for 24 hours allows the

intracellular localisation of the nanoparticles to be examined at high resolution (Figure 3.10). TEM images show several clusters of approximately twenty nanoparticles in close proximity to each other. The widefield images in Figure 3.10 show the majority are located in the perinuclear region of the cells analogous to observations by confocal imaging microscopy. Examining the inset boxes at higher magnification a striking feature in the cells are the nuclear deformations close to the locations of the nanoparticles (Figures 3.10c* and e*). Without examining cells incubated with nanoparticles over an extended period of time it is difficult to conclude whether the nanoparticles have induced these deformations. Perturbations of the intracellular environment would however be unsurprising considering the large size of the nanoparticle clusters, indeed nuclear deformations caused by gold nanoparticles have previously been observed. Gold nanostars functionalised with nucleolin-specific aptamers (to achieve nuclear uptake) and a Cy5 red fluorescent marker were shown to induce major changes to the shape of the nuclear envelope in areas where the nanoconstructs localised (Figure 1.12). In this study by Dam *et al.* uptake was examined in HeLa cells and furthermore cells displaying these folds in the nuclear envelope showed increased apoptosis and decreased cell viability, thus revealing a new correlation between changes in nuclear phenotype.[148]

Nuclear uptake of **Au100-Z-RuSH** was also observed with single nanoparticles imaged within the nuclear membrane. One such example was located on the periphery of an area of condensed chromatin indicated by the red-dashed line in Figure 3.11, again confirming the nuclear uptake observed in the confocal imaging observations. Interestingly these observations are analogous to those of **Au13-Z-HSH** and **Au13-P-HSH** in HeLa cells where nanoparticles were associated to areas of condensed chromasomal material (Section 2.3.6 and 2.3.7).

In light of the cellular and indeed nuclear uptake of **Au13-Z-RuSH** and **Au100-Z-RuSH** cytotoxicity assays assessing both mitochondrial function (MTT assay) and cell membrane integrity via adenylate kinase release (AK assay) were performed. The MTT assay measures the cytotoxicity of gold nanoparticles based on the activity of mitochondrial

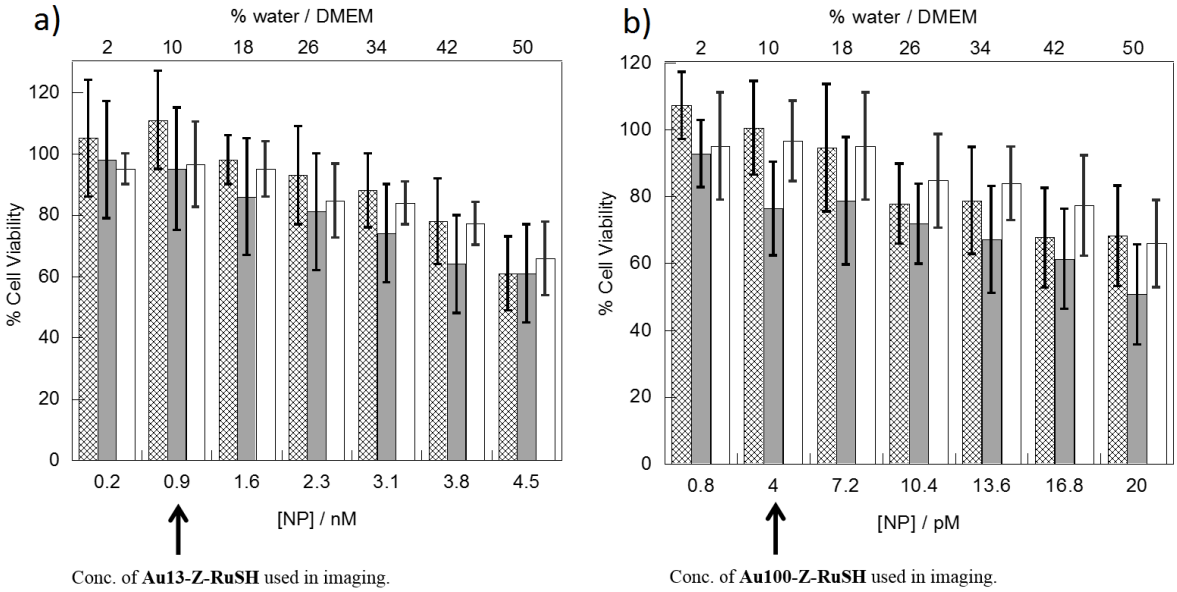

Figure 3.12: MTT assay (a colorimetric assay performed for assessing cell metabolic activity exhibiting percentage cell viability of A549 cells after 24 hour incubation with ***AuNP*** *(hashed) and* ***AuNP-Z-RuSH*** *(grey) for the 13 nm particles (a) and the 100 nm particles (b). Dosing was performed with 0.2-4.5 nM 13 nm particles and 0.8-20 pM 100 nm nanoparticles (equating to 2 - 50% dilutions of the media with water). The equivalent dosing with deionised water blanks (white) are presented on each graph.*

NAD(P)H-dependent cellular oxidoreductase enzymes which is directly proportional to cell viability. The enzymes are able to reduce the trazolium MTT 3-(4,5-dimethylthiazol-2-yl)-2,5-diphenyltetrazolium bromide dye in to insoluble purple formazan.[305] A solution of dimethyl sulfoxide is adde to solubilize the crystals and the absorbance of the resulting solution is measured (between 500 and 600 nm). The higher the absorbance, the greater the amount of formazan, the greater the enzyme activity. Comparing the absorbance to undosed control cells thus allows percentage cell viability to be determined. The adenylate kinase assay to assesses membrane damage to examine whether nanoparticle uptake causes any reduction in the cell membrane integrity. Any ruptures in the cell membrane would cause a release of the "AK" enzyme found naturally in the cell cytoplasm. If the enzyme is detected in the cell media it is indicative of compromised cell membrane integrity. Quantification of the amount present in the media is achieved by adding a reagent that increases in luminescence intensity upon binding with the enzyme, thus the luminescence can be compared to undosed control cells and percentage cell viability determined.

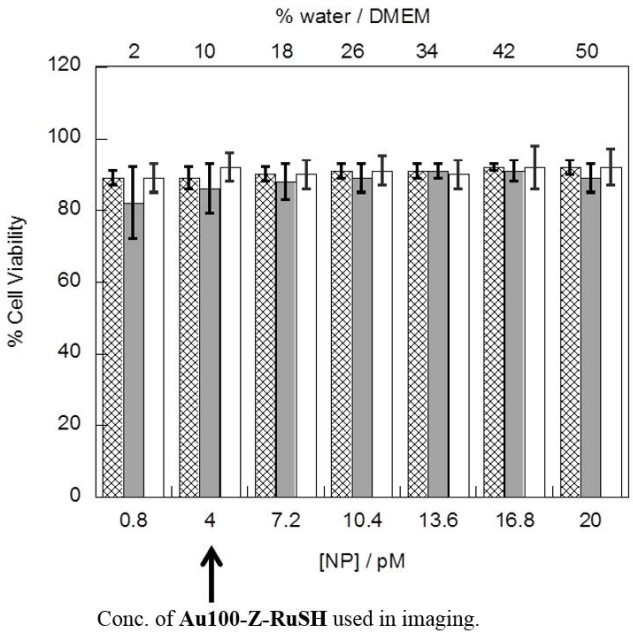

Figure 3.13: AK Assay showing percentage cell viability of A549 cells after 24 hour incubation with ***Au100*** *(hashed) and* ***Au100-Z-RuSH*** *(grey), dosing with 0.8-20 pM nanoparticles (equating to 2 - 50% dilutions of the media with water) and the equivalent dosing with deionised water blanks (white). Viability was measured in four independent experiments; each experiment consisted of duplicate plates with duplicate measurements at each concentration. The error bars for each data point represents the mean 1 standard deviation (SD) of these measurements. Data outside of 1 SD of the mean of these sixteen readings were classified as outliers and disregarded.*

No statistically significant toxicity of the nanoparticles was observed by the MTT assay. Confocal microscopy of the cells dosed with **Au13-Z-RuSH** correspond to a concentration of 0.9 nM and **Au100-Z-RuSH** a concentration of 4 pM, as indicated by the arrows in Figure 3.12. All nanoparticle incubations resulted ina concentration-dependent decrease in the ability of cells to reduce MTT, a measure of mitochondrial activity ($P < 0.001$), as assessed by a 1-way one-way analysis of variance (ANOVA). The ANOVA test is an analysis technique used to compare means of three or more samples and was performed on the data by Dr. N. Hodges, School of Biosciences. As the MTT assay was conducted on five independent samples, each producing a mean percentage cell viability, the ANOVA test was suitable to test statistical significance in the data.

When treatment with particles was compared to the matched water blank there was no statistically significant difference between either the citrate-stabilised gold nanoparticles, **Au13-Z-RuSH** and **Au100-Z-RuSH** with the appropriate water blank, with the

exception of **Au100-Z-RuSH** at 4 pM and 13.6 pM, as assessed by a Bonferoni corrected t-test ($P < 0.05$). The Bonferoni correction was applied to take in to account the multiple repeats (five independent experiments) and comparisons performed on the percentage cell viability measurements from each experiment. Furthermore no statistically significant concentration dependent release of adenylate kinase (a measure of cytoplasmicmembrane integrity) was observed at any of the treatments investigated, as assessed by a 1-way ANOVA. The 1-wat ANOVAh was again aplpied to the data as multiple experiments each yielding mean percentage cell viability were conducted. (Figure 3.13).

3.4 Conclusion

In conclusion the Zonyl 7950 surfactant has enabled coating of gold nanoparticles with the ruthenium transition metal complex. Gold nanoparticles both 13 and 100 nm in diameter are thus functionalised as luminescent nanoprobes exhibiting the distinct optical signature of the ruthenium complex. The nanoparticles are subsequently imaged in the A549 human lung adenocarcinoma cell line via confocal and transmission electron microscopies. The size of the 100 nm coated gold nanoparticles has enabled their imaging at single nanoparticle resolution as demonstrated by comparisons of computational models with actual observations.

Evidence of nuclear uptake is also observed in cell nuclei as well as deformations to the nuclear envelope, potentially caused by clusters of nanoparticles in close proximity to the nucleus. Further investigations are required to ascertain the extent to which nuclear uptake occurs and time-resolved studies to ascertain the cause of peturbations to the envelope. Toxicity assays evaluating mitochondrial function (MTT) and cell membrane integrity (AK) indicate the nanoparticles do not present significant toxicity in cells. The luminescent nanoprobes thus offer great potential in examination of cellular interactions at a single nanoparticle level.

3.5 Acknowledgements

Thank you to Dr. Nicola Rogers for providing the nanoparticles used in this study. Thank you to Dr. Nikolas Hodges and Dr. Bob Harris (School of Biosciences, University of Birmingham) for help with the cell work. Thank you to Mrs Theresa Morris and Mr Paul Stanley (School of Metallurgy and Materials, University of Birmingham) for TEM preparation of cell sections. Thanks also to the EPSRC for funding. Some instruments used in this study were supplied through Birmingham Science City: Innovative Uses for Advanced Materials in the Modern World (West Midlands Centre for Advanced Materials Project 2) with support from Advantage West Midlands (AWM) and partial funding from the European Regional Development Fund (ERDF).

3.6 Experimental

3.6.1 Synthesis and Characterisation of RuSAc

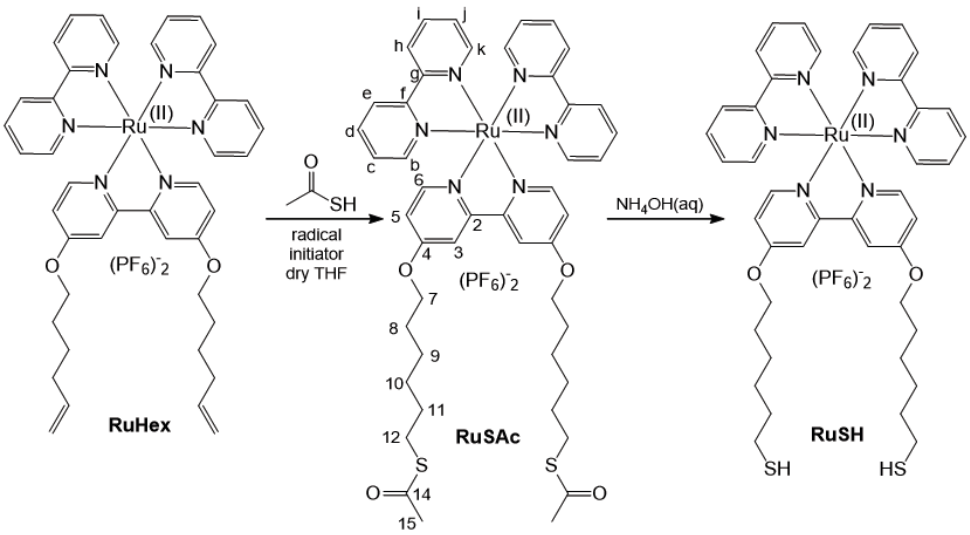

Figure 3.14: Schematic reaction scheme for the preparation of RuSH

Synthesis and characterisation of RuSAc performed by Dr. Nicola Rogers.:[190] Synthesis described in SI of attached publication.[77]

3.6.2 Synthesis and Characterisation of Au-Z-RuSH

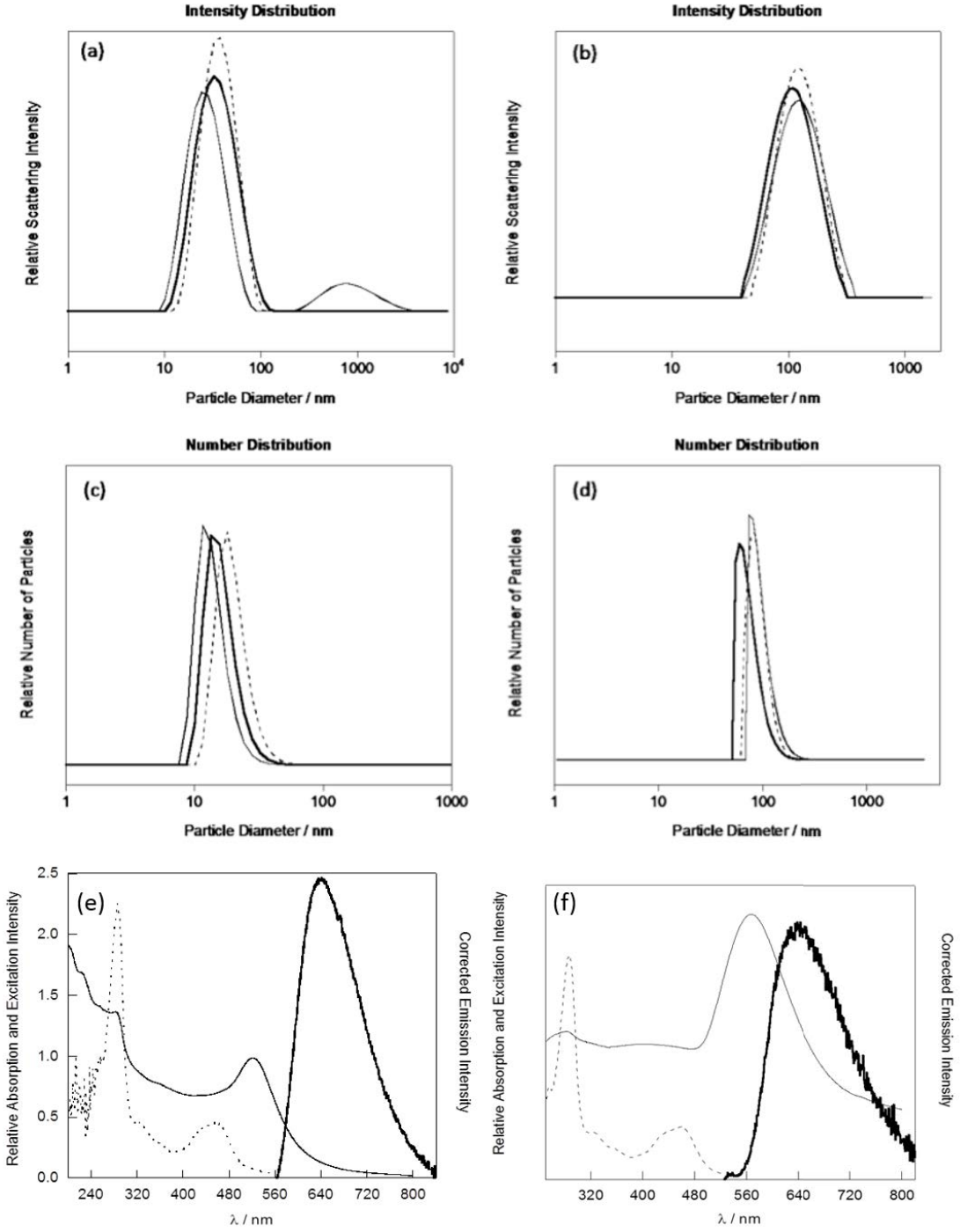

Figure 3.15: DLS intensity distributions (a) and (b), and number distributions (c) and (d). In (a) and (c): ***Au13-Z-RuSH*** *(bold full line),* ***Au13-Z*** *(dashed line) and Au13 (full line). In (b) and (d)* ***Au100-Z-RuSH*** *(bold full line),* ***Au100-Z*** *(dashed line) and Au100 (full line). UV-Vis absorption spectra (solid line), excitation spectra, λ_{em} = 630 nm (dashed line), and luminescence spectra, λ_{exc} = 450 nm (bold solid line) of 2 nM* ***Au13-Z-RuSH*** *(e) and 10 pM* ***Au100-Z-RuSH*** *(f).*

Synthesis and Characterisation of **Au13-Z-RuSH** and **Au100-Z-RuSH** performed by Dr. Nicola Rogers.[190] Au13 synthesised according to Grabar et al.[244] UV-Vis (H_2O) λ_{max} [nm]: 520 (SPR), 260. Diameter = 13 ± 1 nm (DLS number distribution). Zeta potential = -40 ± 5 mV (2 nM in deionised water). Method of Ziegler and Eychmller was followed for Au100 preparation.[77] UV-Vis (H_2O) λ_{max} [nm] = 566 (SPR). Diameter = 98 ± 27 nm (DLS number distribution). Zeta potential = -33 ± 3 mV (4 pM in deionised water).

Au13-Z and **Au100-Z**: Zonyl 7950 1 μl, (1.15 g ml^{-1}) was added to Au13 (1 ml, 9 nM), or Au100 (1 ml, 40 pM), to give fluorosurfactant coated nanoparticles. 13 nm coated particles were centrifuged twice at 13,000 rpm for 30 min, and the 100 nm particles at 13,000 rpm for 90 s (twice), and the supernatant was decanted from each pellet to remove unbound material. Au13-Z, with a zeta potential of - 61 ± 4 mV (2 nM in deionised water), a diameter of 20 ± 2 nm (DLS number distribution). Au100-Z, with a zeta potential of - 47 ± 3 mV (4 pM in deionised water) and diameter of 92 ± 21 nm (DLS number distribution).

Au13-Z-RuSH and **Au100-Z-RuSH** A solution of RuSH (20 μl, 3.5 mM) added to Au13-Z (1 ml, 9 nM) or Au100-Z (1 ml, 40 pM), was stirred for 20 min. The Au13-Z and Au100-Z were prepared as above and used without centrifugation. The 13 nm coated particles were centrifuged at 13,000 rpm for 15 min, and the 100 nm particles at 13,000 rpm for 90 s, and the supernatant was decanted from each pellet to remove unbound material. The nanoparticles were re-suspended in deionised water (1 ml), and the procedure was repeated twice. **Au13-Z-RuSH** : UV-Vis (H_2O) λ_{max}[nm] = 522 (SPR). Diameter = 18 ± 5 nm (DLS number distribution), zeta potential = -48 ± 2 mV (2 nM in deionised water). Emission (λ_{exc} = 450 nm) λ_{max}[nm] = 640. **Au100-Z-RuSH**: UV-Vis ($_2$) λ_{max}[nm] = 567 (SPR). Diameter = 76 ± 22 nm (DLS number distribution), 100 nm (mean diameter by NanoSight Particle Tracking), zeta potential= -35 ± 3 mV (4 pM in deionised water). Emission (λ_{exc} = 450 nm) λ_{max}[nm] = 640.

3.6.3 Photophysical Measurements

All photophysical measurements of **RuSAc** and **Au-Z-RuSH** were performed by Dr. Nicola Rogers. In brief, UV-Vis absorption spectroscopy measurements were performed on a Varian Cary 5000 spectrometer and steady-state luminescence measurements were performed on an Edinburgh Instruments FLS920 spectrophotometer. Emission lifetimes were measured using a 445 nm diode LASER and the time-correlated single-photon counting module integrated within the FLS920 spectrometer, and were tail-fitted with the Edinburgh Instruments F900 software.

3.6.4 MTT Assay

Cells were seeded in a 96-well plate at a density of 8000 cells per well. Following incubation for 24 hours at 37 C in 5 % CO_2, removal of media and a PBS wash, particles or water in complete media at the required concentrations were added for a further 24 hour incubation. The media was removed (and retained for the adenylate kinase assay) and the cells washed twice with PBS followed by incubation in 10 μl MTT (5 mg mL-1 stock in PBS) in 100 μl per well complete media. After 3 hours incubation the supernatant was discarded and DMSO (200 μl per well) added to dissolve the resultant formazan crystals. Absorbance against a DMSO blank was immediately read in a microplate reader at 590 nm. Percentage cell viability was expressed relative to the untreated cells in complete media.

3.6.5 Adenylate Kinase Release Assay

The Adenylate Kinase (AK) assay was performed using the commercially available bioluminescent ToxiLight kit (Lonza Ltd., Wokingham, UK). AK detection reagent (100 μl) was added to each well of a 96-well white luminescence plate (Greiner Bio-One Ltd, UK). Upon reaching room temperature 20 μl aliquots of the test supernatant was transferred to each well and samples incubated for 5 min. Bioluminescence was then immediately

measured with a microplate reader (Bio-tek Instruments Inc., Kineticalc software for Windows). The assay was performed on duplicate plates with duplicate measurements for each concentration tested. Percentage viability was expressed relative to 100 % lysed cells (positive controls), using Biosoft N25-9 detergent.

3.6.6 Flow Cytometry

Cells were cultured in 6-well plates to approximately 60 % confluence before treatment with **Au100-Z-RuSH** (4 pM) for 24 hours. Cells were washed in PBS, detached with trypsin-EDTA solution (3 min, 37C), and pelleted by centrifugation. The supernatant was removed and cell pellets re-suspended in PBS and transferred to flow cytometry tubes for analysis (FACScalibur, BD Biosciences, USA). Forward scatter, side scatter and red fluorescence ($\lambda_{exc} = 488$ nm with light collected through a 670 nm band pass filter) of 50,000 cells were collected and Weasel freeware software was used for data analysis: `http://www.wehi.edu.au/faculty/advanced_research_technologies/flow_cytometry/weasel_for_flow_cytometry_data_analysis/`

ChemComm

COMMUNICATION

View Article Online
View Journal | View Issue

Cite this: *Chem. Commun.*, 2014, **50**, 617

Received 4th October 2013,
Accepted 5th November 2013

DOI: 10.1039/c3cc47606e

www.rsc.org/chemcomm

High coating of Ru(II) complexes on gold nanoparticles for single particle luminescence imaging in cells†

Nicola J. Rogers,‡[a] Sunil Claire,‡[b] Robert M. Harris,[c] Shiva Farabi,[a] Gerald Zikeli,[a] Iain B. Styles,[d] Nikolas J. Hodges*[c] and Zoe Pikramenou*[a]

Gold nanoparticles are efficiently labelled with a luminescent ruthenium complex, producing 13 and 100 nm diameter, monodisperse red-emissive imaging probes with luminescence lifetimes prolonged over the molecular unit. Single, 100 nm particles are observed in whole cell luminescence imaging which reveals their biomolecular association with chromatin in the nucleus of cancer cells.

The design of coordination metal complexes as cellular probes has attracted much research interest based on their distinctive/unique photophysical and electrochemical properties.[1–3] However, nanoscale probes are more ideal for detecting spatially localised cellular probes in luminescence imaging. Indeed, gold nanoparticles and quantum dots have been used for a plethora of biochemical and therapeutic applications.[4–7] We have combined these approaches, and demonstrated labelling gold nanoparticles (AuNPs) with luminescent metal complexes, so that the nanoprobes bear the distinct optical signature of the luminescent agent, independent of the particle properties.[8,9] Such designed probes offer multimodal detection taking advantage of gold's high electron density, and also lack the blinking effect observed in quantum dots. We demonstrated 13 nm AuNP coated with neutral (uncharged) lanthanide lumophores and different modalities to image them in cells.[10] When co-coated with a pH sensitive peptide, selective cell uptake could be achieved.[11]

To explore metal lumophores with still more efficient light excitation in the visible region, we have now chosen highly photostable ruthenium(II) polypyridyl complexes. However, a new strategy is required for the coating of AuNPs since the positive charge of the ruthenium complex leads to flocculation of the AuNPs in aqueous solutions; this challenge is addressed herein. Association of ruthenium complexes with AuNPs has previously been studied using electrostatic interactions,[12] thiol exchange methods using Brust-type[13] nanoparticles,[14–17] or by direct reduction of Au^{3+} by $NaBH_4$.[18–20] All of these methods lead to nanoparticles with sizes smaller than 10 nm that are relatively polydisperse, with limited control over the coating of the ruthenium probe. To increase sensitivity and spatial resolution in imaging,[21] nanoparticles with large Au cores and high number of labels are desirable.

In this communication, we now report an efficient coating method for water soluble gold nanoparticles, 13 (AuNP13) and 100 (AuNP100) nm in diameter, with a ruthenium complex that allows luminescence imaging of non-aggregated, single nanoparticles in cells, revealing interesting biomolecular interactions. The preparation of **RuS·AuNP13** and **RuS·AuNP100** was achieved by controlling the coating of the nanoparticle surface with a non-ionic fluorinated surfactant, Zonyl 7950 (Scheme 1) prior to the addition of the surface-active ruthenium complex, **RuSH** (ESI†). **RuSH** has two thiol groups for attachment to gold nanoparticles and a hexyl spacer group to distance the ruthenium centre from the surface.[22]

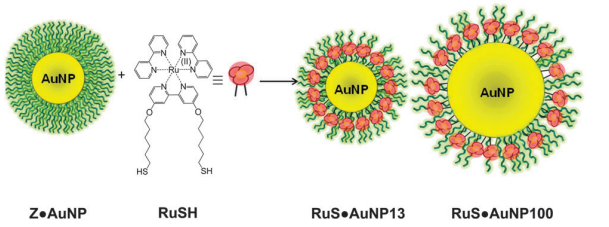

Scheme 1 Controlling nanoparticle labelling with metal complexes to avoid flocculation. Method for preparation of **RuS·AuNP13** and **RuS·AuNP100**.

[a] *School of Chemistry, The University of Birmingham, Edgbaston, B15 2TT, UK. E-mail: z.pikramenou@bham.ac.uk*
[b] *PSIBS Doctoral Training Centre, The University of Birmingham, Edgbaston, B15 2TT, UK*
[c] *School of Biosciences, The University of Birmingham, Edgbaston, B15 2TT, UK. E-mail: hodgesn@adf.bham.ac.uk*
[d] *School of Computer Sciences, The University of Birmingham, Edgbaston, B15 2TT, UK*

† Electronic supplementary information (ESI) available: Details of methods used in compound and nanoparticle synthesis and characterisation are provided together with cell imaging information and cytotoxicity results. See DOI: 10.1039/c3cc47606e

‡ Share equal contribution.

Zonyl® 7950 was chosen to stabilize nanoparticles and inhibit flocculation induced from the positively charged ruthenium complex. It bears a hydrophilic polar head group and a hydrophobic chain and its interaction with gold surfaces has been demonstrated.[23–25] We isolated and characterised the **Z·AuNP13** and **Z·AuNP100** and then added the **RuSH** complex to yield **RuS·AuNP13** and **RuS·AuNP100** (ESI†). The surface environment of the nanoparticle changes with the addition of the cationic complex and partial displacement of the surfactant as confirmed using zeta potential studies and X-ray photoelectron spectroscopy analysis of the Au 4f region. Analysis of the inductively-coupled plasma optical emission spectroscopy (ICP-OES) results, based on the Au : Ru ratio, gives 10^3 ruthenium complexes per **AuNP13** (ESI†). For the case of **RuS·AuNP100**, the number of RuS complexes per AuNP, was estimated to be 10^5 based on calculations from the ^{1}MLCT UV-Vis absorption of the supernatant from centrifugation due to their insufficient digestion for ICP-OES. The Zonyl enables a very high loading on the nanoparticles and the extent of loading per surface area is similar in both sizes, allowing for an estimated surface area of $\sim 0.5 \times 0.5$ nm per ruthenium complex. The TEM images and dynamic light scattering studies confirm the uniformity of the nanoparticles. The **RuS·AuNP100** can also be tracked as single particles by NanoSight analysis (ESI†).

It is striking that isolated **RuS·AuNP13** and **RuS·AuNP100** display luminescence lifetimes of 340 ns and 360 ns (±10%), indicating not only no quenching from the gold surface but indeed an enhancement compared to the free molecular **RuSH** complex 260 ± 6% ns in water with 1% CH_3CN. The larger particles can also be imaged as a *single* **RuS·AuNP100** in flow in a microchannel using luminescence microscopy (Fig. 1a). A luminescence spectrum, collected from the image, confirms the characteristic ^{3}MLCT profile centred at 640 nm with a blue shift from the free **RuSH** complex emission (650 nm), attributed to the influence of the Zonyl hydrophobic environment. To further examine the effect of the addition of **Z·AuNP** to **RuSH**, the luminescence lifetime of **RuSH** was monitored during addition of a solution of **Z·AuNP** to **RuSH** (Fig. 1b). A 50% increase of the luminescence lifetime is observed upon binding of **RuSH** to **Z·AuNP100** or **Z·AuNP13** (Fig. 1b and ESI†). These titration results are consistent with the isolated **RuS·AuNP13** and **RuS·AuNP100** lifetimes. The saturation point in Fig. 1b is consistent with the 10^5 loading estimated above from UV-Vis absorption. The luminescence lifetime of **RuSH** mixed with Zonyl 7950 is 400 ns (±3%), indicating that the effect of the Zonyl is the dominant cause of the extended lifetime of the nanoparticles.

To study the potential of **RuS·AuNP13** and **RuS·AuNP100** in cellular imaging, they were incubated with A549 human lung cancer cells. Cytotoxicity assays using both MTT (mitochondrial function) and adenylate kinase release (cell membrane integrity) showed that there was no statistically significant toxicity of the nanoparticles when compared to a water matched control, at concentrations of up to 5 times the concentration used for imaging studies (ESI†). To monitor the uptake and accumulation of particles in cells over time we performed a pulse-chase experiment (ESI†) using confocal fluorescence microscopy for detection. Interestingly, even after 3 days of the chase experiment, which we estimate as representing approximately three cell divisions based on the number of nuclei per field of view, many cells still contained labelled **RuS·AuNP13** particles, demonstrating the stability, long half-life and poor clearance of **RuS·AuNP13** particles. Although nuclear localisation could not be excluded, there was little or no evidence of **RuS·AuNP13** within the nucleus at any of the time points investigated. However, when the larger nanoparticles were used, more detailed information could be extracted. Cells incubated with **RuS·AuNP100** displayed clear visualisation of individual **RuS·AuNP100** nanoparticles as evidenced by both confocal luminescence and confocal reflection microscopy (Fig. 2).

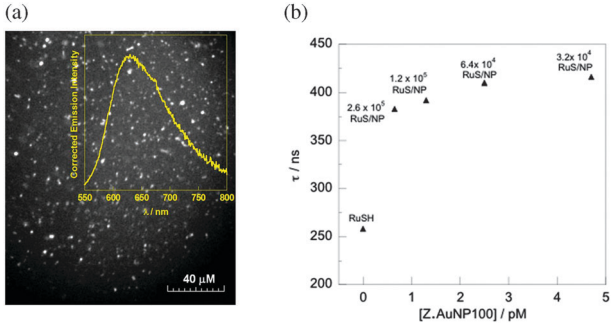

Fig. 1 (a) Luminescence image and spectrum (inset) of a solution of **RuS·AuNP100** in flow within a 100 μm deep, 1 mm wide ibidi microchannel, using epiluminescence microscopy. λ_{exc} = 450 nm, λ_{em} > 510 nm. The emission spectrum (inset) is taken from the field of view in the image. (b) Effect of nanoparticle addition to the lifetime of **RuSH** (0.17 μM, 1% CH_3CN in H_2O) by monitoring the luminescence at 630 nm upon titration of **Z·AuNP100** 0–400 μl (40 pM), λ_{exc} = 450 nm.

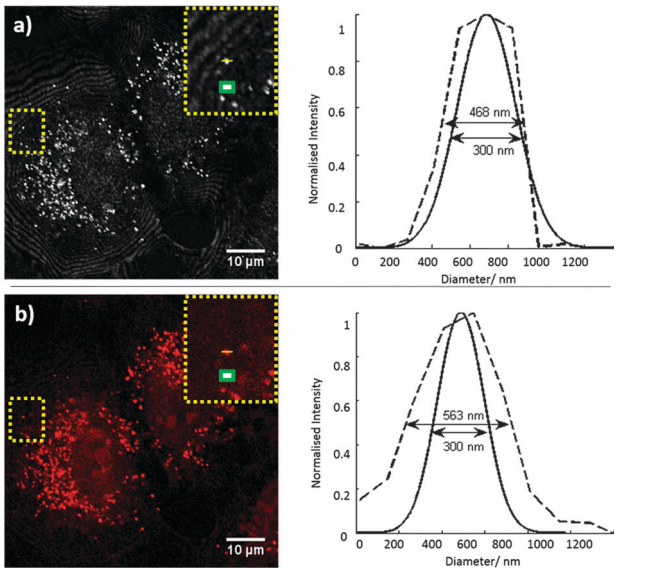

Fig. 2 Confocal images of single **RuS·AuNP100** nanoparticles in A549 cells. (a) Reflection microscopy image λ_{exc} = 488 nm, λ_{em} = 478–498 nm and (b) ruthenium luminescence image λ_{exc} = 453 nm, λ_{em} = 555–800 nm. Respective comparisons of the measured point-spread function of the microscope convolved with a model of the nanoparticle sphere (solid-line), and the experimental intensity profile of a nanoparticle from the inset (dashed-line) are shown on the right. Scale bar 10 μm, inset scale-bar 1 μm, acquisition time 70 s.

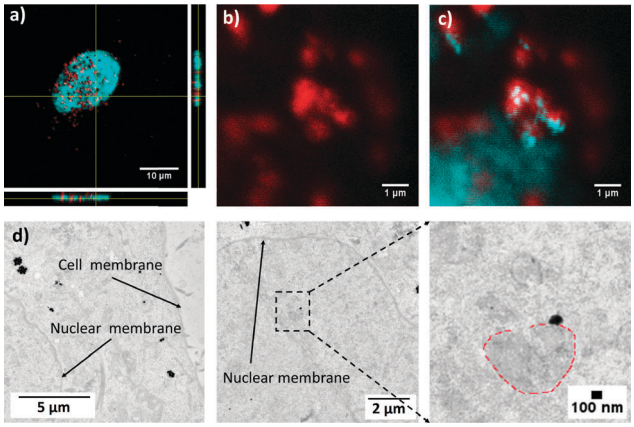

Fig. 3 Imaging nuclear localisation of **RuS·AuNP100** in A549 cells. (a) Orthogonal view of the central *z*-stack slice (*xz* plane below, *yz* plane-right) from a single cell, illustrating ruthenium luminescence from within the central *z*-planes containing the Hoechst luminescence. (Scale bar 10 μm; acquisition time 75 s). (b) Ruthenium luminescence image and (c) corresponding overlay with Hoechst nuclear stain; acquisition time = 60 s, showing association of chromatin with **RuS·AuNP100** particles inside the nucleus (Scale bar 1 μm; acquisition time = 60 s). (d) Transmission electron micrographs (70–90 nm slice width) of A549 cell dosed with **RuS·AuNP100**; magnified inset shows interaction of nanoparticles with condensed chromatin (red dashed-line). Scale bars 5 μm, 2 μm and 100 nm.

Gold nanoparticles appear as bright spots in the confocal reflection images based on the strong scattering signal of the gold. The confocal luminescence signal confirms the ruthenium red luminescence of the particles (Fig. 2). Co-localisation of signals in the red and the reflection images confirm the stability of the nanoprobe after 24 h incubation. To further analyse the results, we used a convolution of the measured point-spread function from the confocal luminescence measurements using a simple model of the nanoparticle sphere (Fig. 2). The model predicts the estimated observable particle width in the luminescence images to be 250–300 nm (due to light diffraction effects) and is consistent with actual measurements performed. In complementary cell studies, the **RuS·AuNP13** are observed only as accumulations of nanoparticles, due to their smaller diameter and limited resolution (ESI†).

Analysis of the confocal luminescence images of the cells treated with **RuS·AuNP100** reveal co-localisation of red particles and Hoechst 33258 emission in some cells, confirming that few of these nanoparticles can localise in the nucleus (Fig. 3). This is in contrast to **RuS·AuNP13** which were absent from the nucleus, although this could be attributed to low spatial resolution as accumulations of the 13 nm AuNPs are required for their visualisation. Still more revealing is that some of the single nanoparticles appear to be localized to a condensed area of Hoechst staining, indicative of nuclear chromatin material containing genomic DNA (Fig. 3). The confocal luminescence images are further supported by TEM studies (Fig. 3). In the TEM images of the A549 cells treated with **RuS·AuNP100**, particles can be seen in close proximity to optically dense regions of the nucleus, which are attributed to condensed chromatin. These results indicate an interaction of the nanoparticles with chromatin that is visualised using the aforementioned microscopy techniques.

In conclusion, by employing the Zonyl 7950 surfactant we have achieved a very high loading of a luminescent transition metal complex on AuNPs of different sizes. This has enabled the design of nanoprobes that can be imaged at single nanoparticle resolution in cells by conventional and widely available optical microscopy methods. These nanoparticles do not present any significant cytotoxicity in cells and are stable in cells without losing their coating. Their strong luminescence allows imaging of particle association with DNA condensed material in the nucleus. These nanoprobes therefore present great potential in the detection and monitoring of biomolecular interactions at the level of a single nanoprobe. Applications may also be envisaged in the development of new nanomaterials with properties encoded by the grafted transition metal complex.

We wish to thank EPSRC, the Leverhulme Trust and the University of Birmingham for funding and support. Some instruments used in this study were supplied through Birmingham Science City: Innovative Uses for Advanced Materials in the Modern World (West Midlands Centre for Advanced Materials Project 2) with support from Advantage West Midlands (AWM) and partial funding from the European Regional Development Fund (ERDF).

Notes and references

1 N. P. E. Barry and P. J. Sadler, *ACS Nano*, 2013, **7**, 5654–5659.
2 D.-L. Ma, H.-Z. He, K.-H. Leung, D. S.-H. Chan and C.-H. Leung, *Angew. Chem., Int. Ed.*, 2013, **52**, 7666–7682.
3 E. J. New, A. Congreve and D. Parker, *Chem. Sci.*, 2010, **1**, 111–118.
4 E. C. Dreaden, A. M. Alkilany, X. Huang, C. J. Murphy and M. A. El-Sayed, *Chem. Soc. Rev.*, 2012, **41**, 2740–2779.
5 D. A. Gilijohann, D. S. Seferos, W. L. Daniel, M. D. Massich, P. C. Patel and C. A. Mirkin, *Angew. Chem., Int. Ed.*, 2010, **49**, 3280–3294.
6 K. Saha, A. Bajaj, B. Duncan and V. M. Rotello, *Small*, 2011, **7**, 1903–1918.
7 P. Nativo, I. A. Prior and M. Brust, *ACS Nano*, 2008, **2**, 1639–1644.
8 D. J. Lewis, T. M. Day, J. V. MacPherson and Z. Pikramenou, *Chem. Commun.*, 2006, 1433–1435.
9 A. C. Savage and Z. Pikramenou, *Chem. Commun.*, 2011, **47**, 6431–6433.
10 D. J. Lewis, C. Bruce, S. Bohic, P. Cloetens, S. P. Hammond, D. Arbon, S. Blair-Reid, Z. Pikramenou and B. Kysela, *Nanomedicine*, 2010, **5**, 1547–1557.
11 A. Davies, D. J. Lewis, S. P. Watson, S. G. Thomas and Z. Pikramenou, *Proc. Natl. Acad. Sci. U. S. A.*, 2012, **109**, 1852–1867.
12 T. Huang and R. W. Murray, *Langmuir*, 2002, **18**, 7077–7081.
13 M. Brust, M. Walker, D. Bethell, D. J. Schiffrin and R. Whyman, *Chem. Commun.*, 1994, 801–802.
14 M. Jebb, P. K. Sudeep, P. Pramod, K. G. Thomas and P. V. Kamat, *J. Phys. Chem. B*, 2007, **111**, 6839–6844.
15 P. Pramod, P. K. Sudeep, K. G. Thomas and P. V. Kamat, *J. Phys. Chem. B*, 2006, **110**, 20737–20741.
16 R. B. P. Elmes, K. N. Orange, S. M. Cloonan, D. C. Williams and T. Gunnlaugsson, *J. Am. Chem. Soc.*, 2011, **133**, 15862–15865.
17 L. Zedler, F. Theil, A. Csaki, W. Fritzsche, S. Rau, M. Schmitt, J. Popp and B. Dietzek, *RSC Adv.*, 2012, **2**, 4463–4471.
18 M. S. Vickers, J. Cookson, P. D. Beer, P. T. Bishop and B. Thiebaut, *J. Mater. Chem.*, 2006, **16**, 209–215.
19 Y. Yu, M. Zhou and H. Cui, *J. Mater. Chem.*, 2011, **21**, 12622–12625.
20 C. R. Mayer, E. Dumas, A. Michel and F. Sécheresse, *Chem. Commun.*, 2006, 4183–4185.
21 W. S. Chang, B. Willingham, L. S. Slaughter, S. Dominguez-Medina, P. Swanglap and S. Link, *Acc. Chem. Res.*, 2012, **45**, 1936–1945.
22 P. Bertoncello, E. T. Kefalas, Z. Pikramenou, P. R. Unwin and R. J. Forster, *J. Phys. Chem. B*, 2006, **110**, 10063–10069.
23 C. Lu, Y. Zu and V. W.-W. Yam, *Anal. Chem.*, 2007, **79**, 666–672.
24 Y. Tang, J. Yan, X. Zhou, Y. Fu and B. Mao, *Langmuir*, 2008, **24**, 13245–13249.
25 F. Li and Y. B. Zu, *Anal. Chem.*, 2004, **76**, 1768–1772.

4 Deposition and Imaging of Silica particles in Dentine

4.1 Introduction

The use of artificially engineered nanoparticles in dentistry is attracting much research interest due to the many clinical applications nanotechnology can be used for.[306] One such example is the use of nanofillers to aid in the restorative aspect of dentistry to repair the physiological and mechanical functions of the tooth. Such treatments are of great relevance for nanoparticle applications involving dentinal tubules where they can be used to help strengthen the dentine, reduce hypersensitivity by tubule occlusion or exhibit an antibacterial efficacy.

The dentine itself is composed of hydrated mineralised tissue that underlies the enamel surface layer and constitutes much of the bulk of the tooth (Figure 4.1). The dentine composition by weight is 70% inorganic, 20% organic and 10% water with hydroxyapatite and collagen constituting much of the inorganic and organic phases. The characteristic channels which permeate the dentine are called dentinal tubules and range in diameter from 2.5 μm in the vicinity of the pulp, 1.2 μm in the middle of the dentine and 0.9 μm at the dentino-enamel junction.[307] Interestingly tubule density also varies. Tubules cover 45,000 mm^2 near the pulp, 29,000 mm^2 in the middle of the dentine and 20,000 mm^2 at the dentino-enamel junction.[181,182,307–309]

The porous nature of the dentine due to it's organic components and high water

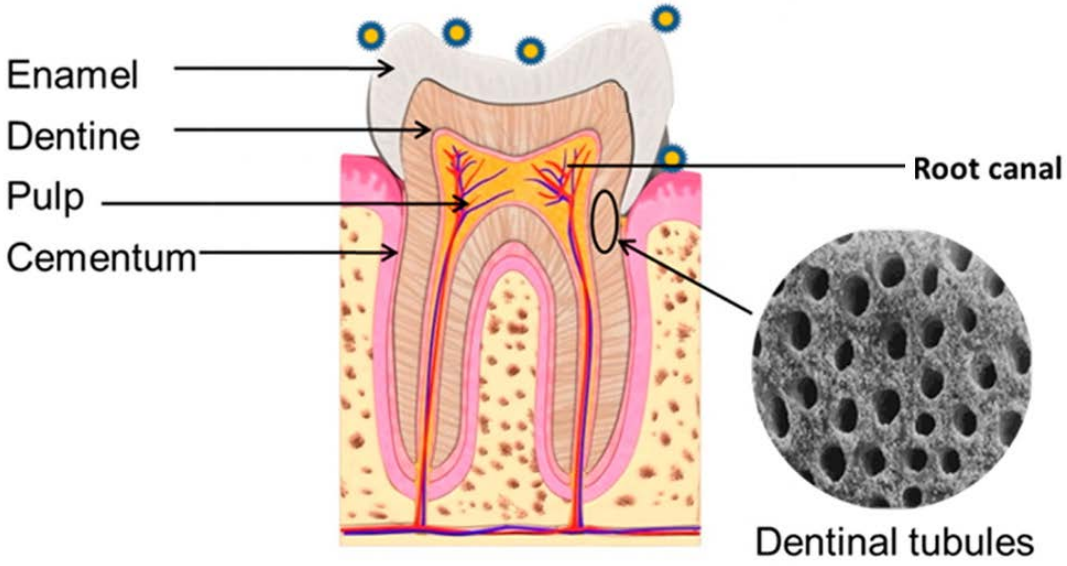

Figure 4.1: Schematic of human tooth anatomy showing the four main components of the tooth, namely enamel, dentine, cementum, and pulp. Characteristic microscopic channels that permeate the dentine are known as dentinal tubules. Dental research studies have investigated the use of nanomaterials in different clinical applications including enamel remineralization, antibacterial applications, caries management, dentine hypersensitivity and root canal therapy. Figure adapted from Besinis et al.[306]

concentration, in addition to the presence of the dentinal tubules, can make them prone to causing dentine hypersensitivity. The main causes of hypersensitivity are gingival recession (receding gums) leading to exposure of root surfaces, loss of the surface layers and tooth wear.[310]

Nanomaterials can aid in the treatment of dentine hypersensitivity by the occlusion of the dentinal tubules.[311,312] Earl *et al.* investigates tubule occlusion with nanoscale hydroxyapatite particles and found that shape and size of the particles used was of great importance.[313] Hydroxyapatite particles 100 nm in size were found to be optimal in achieving tubule occlusion whilst larger 600 nm needle like particles showed very limited infiltration. Demineralisation of the dentine surface also enhanced tubule infiltration and occlusion thus demonstrating the complexities of achieving tubule occlusion with regards to particle shape, size and indeed chemistry with the surface environment of the dentine itself.

Besinis *et al.* further illustrated the dependence of particle size on occlusion ability

with extensive infiltration achieved with spherical hydroxyapatite and silica nanoparticles below 15 nm in size.[188] Interestingly in a follow-up study the hydroxyapatite and silica nanoparticles were also found to enhance remineralisation of the dentine.[314] Silica nanoparticles have also found application in tubule occlusion with 40 nm silica particles shown to prevent the movement of fluid with the tubules, thus addressing one of the primary causes of hypersensitivity.[313]

A further notable point of relevance regards a number of investigations addressing the use of toothpastes specifically designed for sensitive teeth that have indicated they do in fact have an adverse effect, causing dentine erosion and exacerbating dentinal tubule exposure.[315] These studies using nanoparticles thus offer great potential as more viable solutions in dental healthcare. Optimisation of the nanotechnology and monitoring its applications with imaging is thus of great importance.

In the context of the aforementioned studies using silica nanoparticles to aid tubule occlusion, silica nanomaterials engineered to encapsulate luminescent agents are of particular interest. Imaging applications of these materials range from use as optical sensors *in vitro* to the use of silica nanoparticles in cells and tissues for biological applications.[167,168] Silica nanoparticles are particularly advantageous due to their robustness, mechanical stability and ability to protect the encapsulated or embedded lumiphores in imaging applications. The synthesis of monodisperse nanoparticles with encapsulated lumiphores is also relatively trivial with further potential for functionalisation via surface conjugation.[23]

These properties have allowed for use of silica nanoparticles used in variety of applications. Wang *et al.* incorporated quantum dots in a silica based nanosphere which was able to measure local pH in a ratiometric fashion.[167] Sung *et al.* also incorporated quantum dots within porous silica nanoparticles which were able to sense for Cu^{2+} ions.[168] Zhang *et al.* demonstrated surface functionalisation of silica nanoparticles with pairs of DNA strands that "uncap" in the presence of Hg^{2+} ions, releasing a fluorescent dye resulting in a measurable increase in fluorescence signal Encapsulation of multiple lumiphores within a single nanoparticles also affords a much higher signal intensity compared to single lu-

miphores. Encapsulation of luminescent ruthenium(II) tris-bipyridyl complexes within 500 nm diameter colloidal silica nanoparticles demonstrated this in a study by Lewis *et al* where the luminescence from the encapsulated lumiphore was used to analyse fluid flow in microchannels.[170] A subsequent study established a method of immobilizing a cyclometalated iridium(III) complex on to the surface of silica nanoparticle using a fluorinated polymer.[169] These particles exhibited better stability than those prepared without the polymer along with a seven-fold increase in the luminescence intensity and luminescence lifetime. The surfactant prepared particles were also successfully used in fluid flows for microparticle imaging velocimetry, exploiting the enhanced particle brightness and demonstrating the potential for using the nanoparticles as nanotracers in microchannels.

Nano- and sub-micron particles offer the potential for use as multi-functional dental agents by exhibiting the ability to deliver anti-pathogenic or analgesic drugs into the tubules, in addition to being able to occlude the internal space and aid in the prevention of infection and pulp infiltration.[313,316,317] Tubule occlusion can be achieved with a variety of different types of particles including calcium fluoride,[318] combinations of carbonate-hydroxyapatite nanocrystals[319–321] and bioactive glass.[188,314] The aforementioned strategies aim to increase the mineral content of enamel and dentine where the particles are employed as protagonists for further growth of the crystalline structure of the dentine via seed mediation, eventually leading to dentinal tubule closure. The stability and ability of the silica nanoparticle to adhere to the dentinal surface has seen their application for occlusion of dentinal tubules.[185] Their water solubility allows them to be easily deposited into the irregular spaces composing the dentine surface[186] and their large surface area also allows for further functionalisation.[169]

4.2 Chapter Outline

Successful tubule occlusion has been demonstrated using silica nanoparticles. A common problem with the use of such particles however is their liability to aggregate which can

prevent them from entering a dentinal tubule prior to inducing seed based remineralisation.[322] A possible method to help prevent this occurrence is the addition of surfactant coatings to the particles, however the interaction of surfactant coated particles with dentine is an unexplored avenue of research. In this context the aim of the following research is to investigate the interaction of silica particles with human molar teeth sections with particular emphasis on examining how the particles interact with the tubule openings via scanning electron and confocal microscopy imaging modalities. The use of different surfactants as coatings for the particles is also explored in the context of their ability to influence surface interactions with the dentine. The work performed in this chapter forms the appended publication.

4.3 Results and Discussion

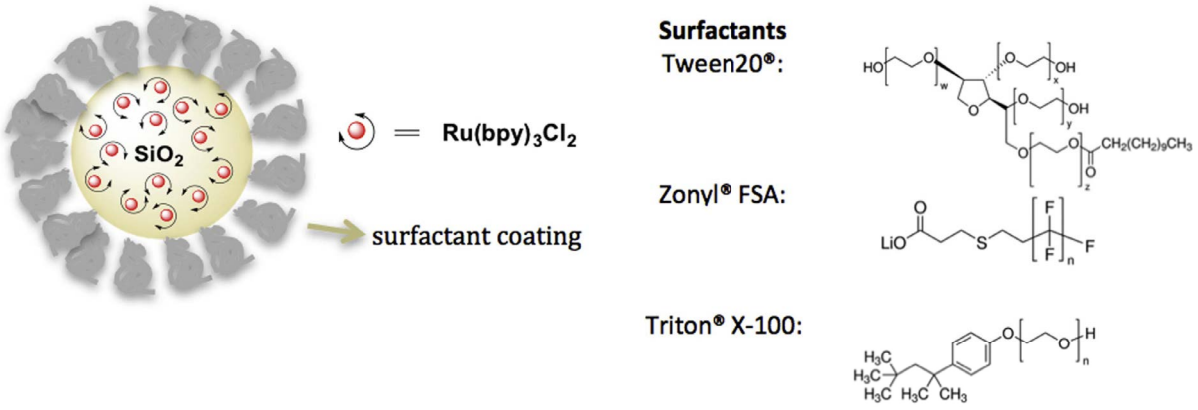

Figure 4.2: Schematic diagram of silica particles with encapsulated luminescent ruthenium probe (SiO_2-Ru) and surfactants used for coating.

The particles investigated in this study for their interaction with dentine consisted of spherical silica particles 640 nm in diameter encapsulating a luminescent ruthenium complex (tris-(2,2'-bipyridyl) ruthenium(II) dichloride). These were denoted as (SiO_2-Ru-640) with surfactant coated particles were also prepared as follows (Figure 4.2):

1. SiO_2-Ru-640: control sample (no surfactant).

2. Zonyl-SiO_2-Ru-640: (a) 10 ml SiO_2-Ru + 10 μl Zonyl FSA (1.3 g/ml), (b) 10 ml SiO_2-Ru + 100 μl Zonyl FSA (1.3 g/ml).

3. Tween20-SiO_2-Ru-640: 10 ml SiO_2-Ru + 10 μl Tween 20 (1.095 g/ml).

4. Triton-SiO_2-Ru-640: 10 ml SiO_2-Ru + 10 μl Triton X-100 (1.7 M).

In brief for surfactant coated nanoparticle preparations Zonyl FSA, Triton X-100 or Tween20 were added to solutions of the SiO_2-Ru-640 followed by ultrasonication and centrifugation/resuspension to remove excess surfactant. The surfactant coatings did not change the size within the error limit of the particle size analysed. For confocal fluorescence imaging studies three different sized particles were prepared: SiO_2-Ru-130 (130 $\pm$ 50 nm), SiO_2-Ru-430 (430 $\pm$ 50 nm), SiO_2-Ru-810 (810 $\pm$ 160 nm). Dentine

surfaces used to examine interaction with the aforementioned particles were acid etched with 10 % citric acid for 60 seconds to simulate hypersensitive dentine. Particles were pipetted on to the tooth surface with no mechanical agitation. For the SiO_2-Ru-640, Zonyl-SiO_2-Ru-640, Tween20-SiO_2-Ru-640 and the Triton-SiO_2-Ru-640 applications 10 μl of the solutions detailed above were uniformly pipetted on to the dentine surface. The surface was left to air-dry completely and washed three-times with 10 μl of de-ionised water. Particle application was performed by Hayley Floyd (PSIBS Doctoral Training Centre, School of Chemistry, University of Birmingham).

Scanning electron microscopy (SEM) examination revealed unique interactions of the particles with the dentine surface. After application to the surface **SiO_2-Ru-640** particles formed large aggregates several micrometers in diameter the majority of which were clustered together (Figure 4.3A). Although these clusters are large enough to potentially occlude tubule openings it seemed that the majority of **SiO_2-Ru-640** attached to the area surrounding the tubule periphery (Figure 4.3A*). Partial occlusion is thus only achieved in a small minority of the tubules where small clusters or single particles have been able to enter.

The Triton X-100 coated particles (**Triton-SiO_2-Ru-640**) show similar interactions with the dentine surface section as the **SiO_2-Ru-640**. Particle aggregation has however qualitatively occurred to a lesser degree (Figure 4.3B). Nevertheless, the particle clusters that formed were still too large to occlude the tubule openings and as such again seemed restricted to the periphery of the tubule opening. The few tubules that were partially occluded were blocked with small clusters or single particles (Figures 4.3B* and 4.3B**)

The **Tween20-SiO_2-Ru-640** preparation of particles were markedly less aggregated on the acid etched dentine surface. Clusters were qualitatively smaller in size than the **SiO_2-Ru-640** or the **Triton 100-SiO_2-Ru-640** preparations (Figure 4.3C). With the smaller cluster size it is perhaps easier for the particles/clusters to at least partially occlude the tubules (Figure 4.3C*). The difference with **Tween20-SiO_2-Ru-640** preparation is particularly apparent when compared to the **SiO_2-Ru-640** particles (Figure 4.3A), where

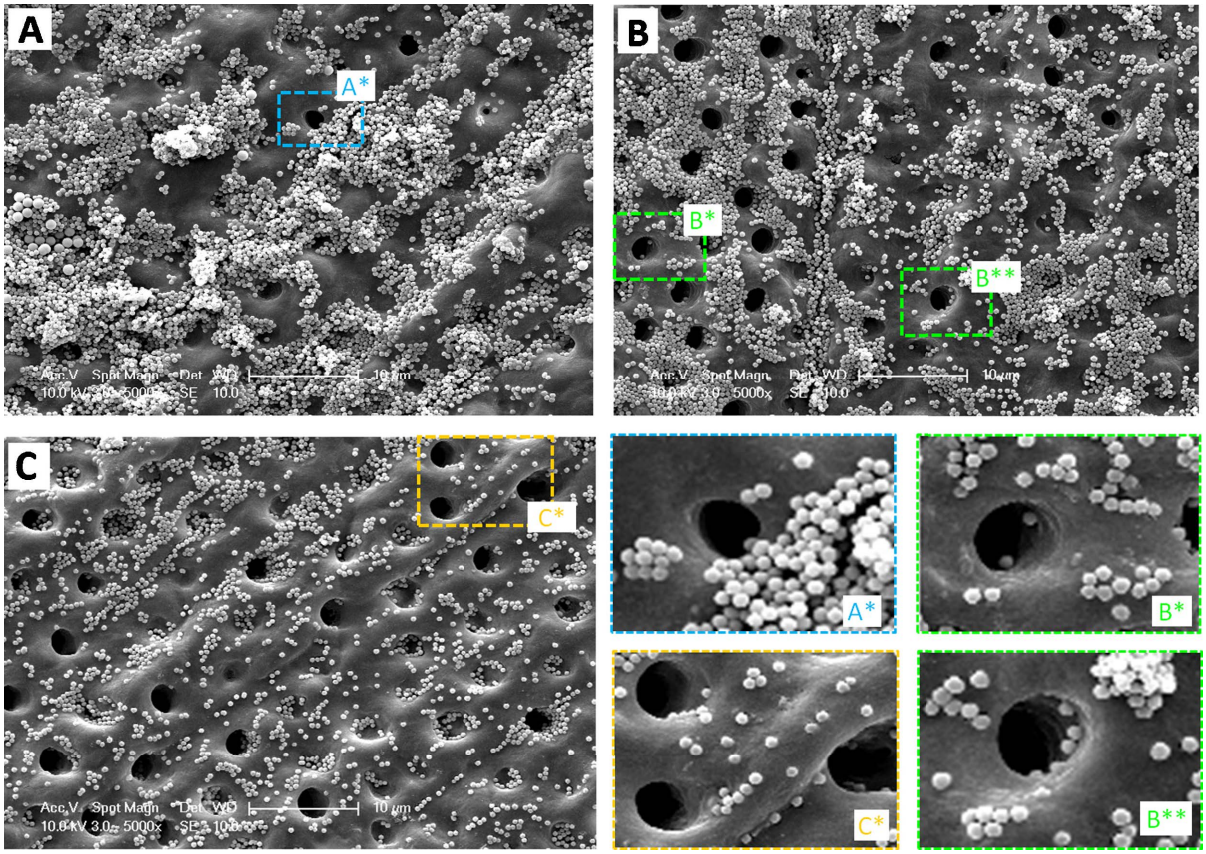

Figure 4.3: SEM images of acid etched molar root surface sections treated with (A) ***SiO$_2$-Ru-640****, **Triton-SiO$_2$-Ru-640**(B) and **Tween20-SiO$_2$-Ru-640** (C). Magnifications of insets provided in "*" images. (Scale bar 10 µm).*

large clusters are seemingly preventing tubule occlusion due to particles/small clusters attaching to and blocking the area surrounding the tubule periphery.

The **Zonyl-SiO$_2$-Ru-640** particles were observed as fairly large aggregated clusters that seem to have an affinity for the tubule openings (Figure 4.4). This may be due to the hydrophobic nature of the Zonyl surfactant which bears polar fluorine groups. The physico-chemical properties of the particles in this instance may be such that the clusters of particles prefer attachment within the tubule as opposed to the tubule periphery, as in the case of the **SiO$_2$-Ru-640** and the **Triton-SiO$_2$-Ru-640**. Furthermore clusters seem to be of a suitable size to occlude the majority of the tubule openings (Figure 4.4A-C).

For the purposes of luminescence imaging of the particles further particle characterisation was performed. The silica particles exhibit red luminescence due to the encapsulated ruthenium bipyridyl complex. Spectroscopic studies to quantify the effects of the sur-

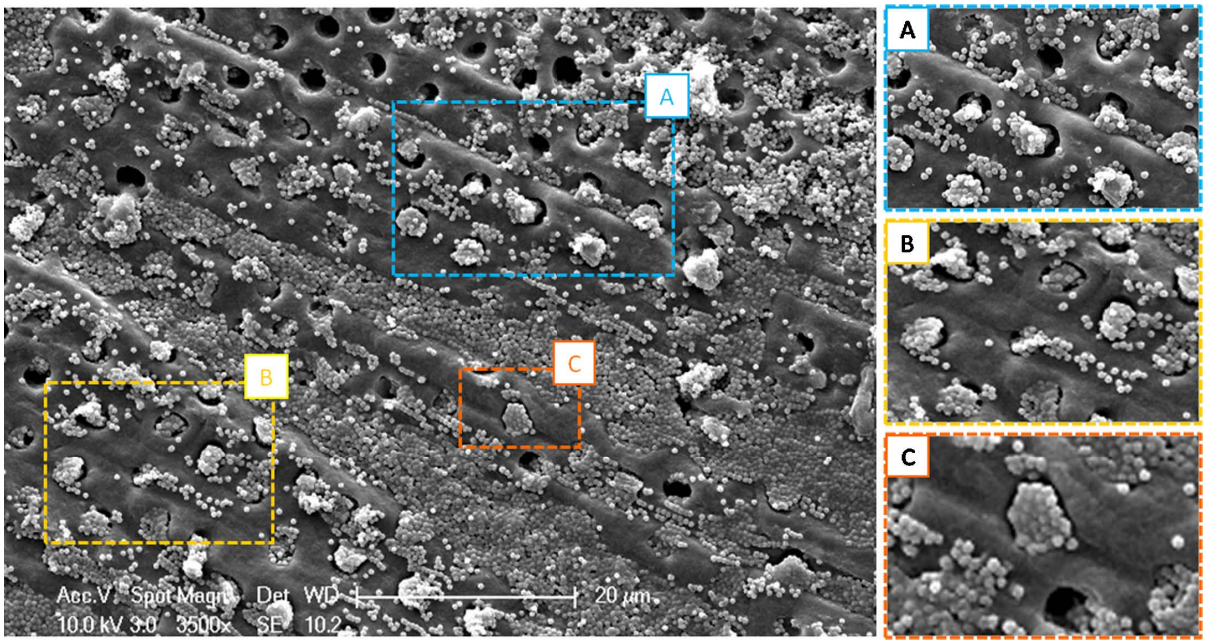

Figure 4.4: SEM images of acid etched molar root surface sections treated with ***Zonyl-SiO$_2$-Ru-640****. Magnifications of insets provided in (A-C). (Scale bar 20 µm).*

factants on the luminescence were performed by taking emission scans before and after the addition of the surfactants (Appendix L). Upon excitation with visible light at 450 nm, where the characteristic absorption of the ruthenium complex occurs, the particles luminesce in the red region of the spectrum with a peak around 615 nm.

Confocal luminescence microscopy of dentine sections exposed to SiO_2-Ru-130, SiO_2-Ru-430 and SiO_2-Ru-810 was performed, exploiting the luminescence of the encapsulated ruthenium. Overlays of the red luminescence channel and the reflectance channel which affords the dentine surface demonstrate nanoparticle association for all size preparations (Figure 4.5). Due to the diffraction limit of confocal microscopy only the larger SiO_2-Ru-430 and SiO_2-Ru-810 were individually resolved and were readily observed as clusters occluding multiple tubules (Figure 4.5B-C).

4.4 Conclusion

There is increasing interest in the use of sub-micron particles in dentistry for applications in the remineralisation of dentine and for the treatment of hypersensitivity by tubule

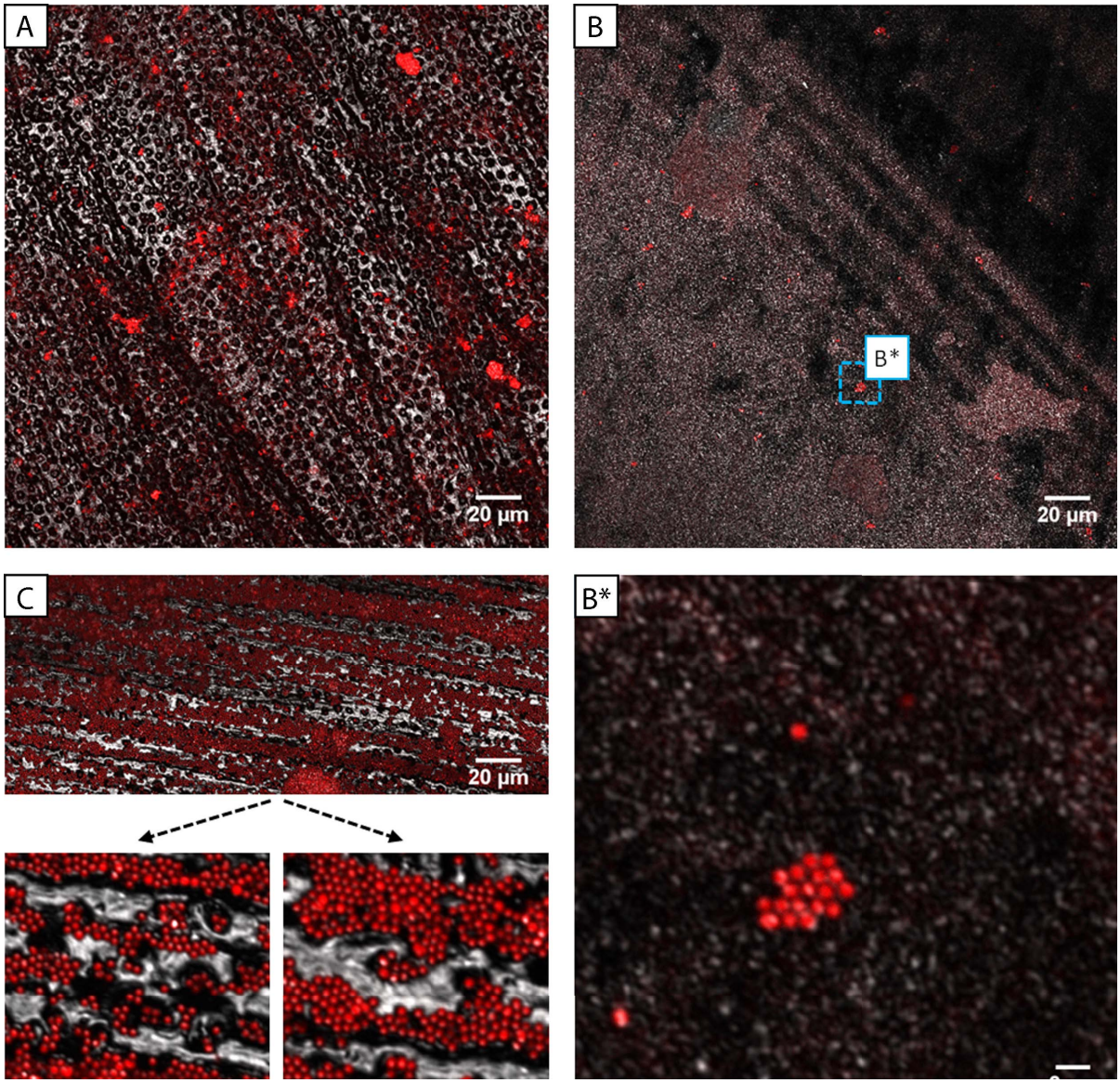

Figure 4.5: Confocal luminescence and reflection microscopy image overlays (and corresponding magnifications) of molar root surfaces treated with ***SiO$_2$-Ru-130*** *(A),* ***SiO$_2$-Ru-640*** *(B) and* ***SiO$_2$-Ru-810*** *(C). (Magnified image, scale bar 2 µm).*

occlusion. Various nanosized particles of different materials have been introduced into the dentinal tubules to this effect including calcium fluoride, hydroxyapatite and bioactive glass.[318,319,323] These approaches use particles to occlude the tubules or furthermore to initiate a scaffold for the remineralisation of the dentine. The silica particles used in this project have a porous structure and therefore have the potential to be a carrier for a range of molecules including calcium based compounds. It is thus of great encouragement that tubule occlusion is evident in both the SEM (Figure 4.3, 4.4) and confocal imaging

observations (Figure 4.5).

These particles may also serve as a carrier for antimicrobial compounds and therefore offer an approach to treating contaminated hard tissues,[324,325] indeed preliminary studies of **SiO_2-Ru-640** with a surfactant and silver coating have been shown to reduce bacterial growth in solution (Appendix L).

Previous studies have shown the ability of particles to infiltrate dentinal tubules although the difficulty of such applications in practice is preventing the particles from aggregating due to physico-chemical interactions.[188] In this study when the particles with surfactant coatings were applied to the dentine surfaces qualitative differences in the aggregation characteristics were observed with SEM observations. The absence of a surfactant and Triton X-100 treated preparations resulted in the greatest aggregation of the particles with little surface spread or tubule occlusion. Dentinal tubule occlusion was greater with the Tween20 coated particles but was most readily observed with the Zonyl preparation, most likely due to the physico-chemical properties of the sub-micron particles when coated with the hydrophobic Zonyl surfactant. The properties of this Zonyl coating are such that the particles seem to achieve an interaction with the surface and cluster such that optimal tubule occlusion is achieved. Indications that the surfactant coating influence surface interactions in such a manner, coupled with the encapsulation of luminescent complex in the particles to enable luminescence imaging, provides great impetus for further investigations studying particle/dentine interactions. There is also great scope for further analysis on the images to assess tubule occlusion and particle kinematics on the dentine surface in greater detail.

4.5 Acknowledgements

Thank you to Hayley Floyd, Sophie Glinton, Dr. Phillip Tomson, Dr. Rachel Sammons and Prof. Damien Walmsley. Thanks also to the EPSRC for funding through the PSIBS Doctoral Training Centre. Some instruments used in this study were supplied through

Birmingham Science City: Innovative Uses for Advanced Materials in the Modern World (West Midlands Centre for Advanced Materials Project 2) with support from Advantage West Midlands (AWM) and partial funding from the European Regional Development Fund (ERDF).

4.6 Experimental

4.6.1 Dentine Preparation

Human decay-free lower first permanent molar teeth, which were covered by the United Kingdom Human Tissue Act (HTA), were chosen for the purpose of assessing the entry of sub-micron particles into the tubules. The crown removed and the root sliced in half along the vertical axis using the bone saw. The sectioned roots were ground down using a grinder/polisher with 400/800 papers, to approximately 0.1 mm thick sections measured by a micrometer. This method was used to produce sections with perpendicular tubule openings. Before imaging/nanoparticle application, the sections were etched by a 60 second immersion in a 10% citric acid solution. The sections were then ultrasonicated for 180 seconds. The sections were dehydrated using successive ethanol baths for ten-minute periods of 50 %, 75 % then 100 % before drying for 1 hour in a 60 C oven. Tooth preparation was performed by Dr. Phillip Tomson, School of Dentistry, University of Birmingham.

4.6.2 Particle Preparation

The particles used in this investigation consisted of spherical silica encapsulated with a luminescent complex, tris-(2,2'-bipyridyl)ruthenium(II) dichloride, represented as SiO_2-Ru,[170] with a size of 640 nm were designated as **SiO_2-Ru-640** (640 ± 90 nm). The effect of polymer coating did not change the size within the error limit of the particle size analysed. The sizes were determined by Dynamic Light Scattering measurement us-

ing a Zetasizer Nano ZS, (Malvern Instruments Ltd., Malvern, UK). Visualization of the particles was performed using Nanosight tracking Analysis instrument (Malvern Instruments Ltd., Malvern, UK). For confocal fluorescence imaging studies, three different sizes were used (particle concentration 0.004% w/v). SiO_2-Ru-130 (130 ± 50 nm), SiO_2-Ru-430 (430 ± 50 nm), SiO_2-Ru-810 (810 ± 160 nm) estimated by the confocal reflectance images. They were prepared as 0.004% w/v solutions by addition of 50 ml deionised water to 2 mg particles (dry weight), followed by ultrasonication for 5 min. For surfactant coated nanoparticle preparations Zonyl FSA, Triton X-100 or Tween20 (purchased by Sigma-Aldrich) were added to 0.04% w/v solutions of the **SiO_2-Ru-640**. The 0.04% w/v solution required addition of 10 ml deionized water to 4 mg particles (dry weight), followed by ultrasonication for 5 min. Additions of the various surfactants were done on 10 ml aliquots of the 0.04% w/v **SiO_2-Ru-640**. Preparations are therefore as follows:

1. **SiO_2-Ru-640**: control sample (no surfactant).

2. **Zonyl-SiO_2-Ru-640**: (a) 10 ml SiO_2-Ru + 10 μl Zonyl FSA (1.3 g/ml) (b) 10 ml SiO_2-Ru + 100 μl Zonyl FSA (1.3 g/ml). The excess of Zonyl FSA in (b) was used to examine if this affected the particle interaction with dentine.

3. **Tween20-SiO_2-Ru-640**: 10 ml SiO_2-Ru + 10 μl Tween 20 (1.095 g/ml).

4. **Triton-SiO_2-Ru-640**: 10 ml SiO_2-Ru + 10 μl Triton X-100 (1.7 M).

After addition of the surfactants, 1 ml aliquots were transferred to eppendorf tubes and centrifuged at 6000 rpm for 6 min, the supernatant discarded and the particles re-suspended in deionized water. This wash step was done to remove excess surfactant. The photophysical properties of the luminescent particles were analyzed using Edinburgh Instruments FLS920 Series fluorescence spectrometer.

4.6.3 Particle Application

The particles were dropped on to the tooth surface with no mechanical agitation. For the **SiO_2-Ru-640**, **Zonyl-SiO_2-Ru-640**, **Tween20-SiO_2-Ru-640** and the **Triton-SiO_2-Ru-640** 10 μL of the supplied solution, was pipetted on to the dentine surface and uniformly spread using the pipette tip. The surface was left to dry completely and subsequently washed three-times with 10 μL of de-ionised water by pipetting it on to the surface and aspirating it off. Dentine samples were then prepared for imaging. Particle Application was performed by Hayley Floyd, PSIBS Doctoral Training Centre, School of Chemistry, University of Birmingham.

4.6.4 Particle Imaging

All of the samples were prepared by mounting onto a carbon coated aluminium stub before splutter coating with gold using a Quorum Emitech K550X splutter coater. A scanning electron microscope, SEM (Zeiss EVO MA 10) was used under high vacuum and at a range of electron acceleration voltages between 5 and 15 eV. The confocal microscopy studies were performed using a Leica confocal microscope in reflectance and fluorescence modes. Excitation was at 488 nm at approximately 20% power and at 458, 476 and 488 nm at 100% power, with emission collection at 478 - 498 nm and 580 - 800 nm, respectively. The samples were mounted on 12 mm diameter carbon stubs (used in SEM) and were attached to a glass slide.

4.7 Publication

Journal of Dentistry xxx (2015) xxx–xxx

Contents lists available at ScienceDirect

Journal of Dentistry

journal homepage: www.intl.elsevierhealth.com/journals/jden

The deposition and imaging of silica sub-micron particles in dentine

Sunil Claire[a], Anthony Damien Walmsley[b,*], Sophie Glinton[a], Hayley Floyd[a], Rachel Sammons[b], Zoe Pikramenou[c]

[a] Physical Sciences of Imaging in the Biological Sciences, University of Birmingham, Birmingham B15 2TT, United Kingdom
[b] School of Dentistry, University of Birmingham, Birmingham, B15 2TT, United Kingdom
[c] School of Chemistry, University of Birmingham, Birmingham, B15 2TT, United Kingdom

ARTICLE INFO

Article history:
Received 2 June 2015
Received in revised form 1 August 2015
Accepted 5 August 2015
Available online xxx

Keywords:
Dentine
Sub-micron particles
Surfactants
Dentinal tubules
Microscopy
Surface coating

ABSTRACT

Objectives: Sub-micron particles may assist in the delivery of compounds into dentine tubules. The surface interactions of the particles with dentine may prevent them from entering the tubules. The aim of this study is to investigate whether silica particles, treated with surfactants improves dentine tubules occlusion using both artificial and human tooth models

Methods: Spherical silica particles (size 130–810 nm) bearing an encapsulated ruthenium luminescent complex were coated with the following surfactants: Zonyl® FSA, Triton® X-100 and Tween20®. The particles were prepared as 0.004% w/v and 0.04% w/v solutions with deionized water and were applied to the surface of; (1) in vitro model of PET ThinCert™ cell culture inserts; (2) 0.1 mm thick sections of human molar teeth.

Results: Scanning electron and confocal fluorescence microscopy images show that particles without any coating and with TritonX-100 coating had the highest aggregation. Particles with Tween-20 are less aggregated on the surface and show inclusion in the tubules. Particles coated with fluorosurfactant Zonyl show a preference for aggregation at the tubule. With the ThinCert™ membranes high aggregation within the artificial tubules was increased by particle concentration.

Conclusions: The use of silica sub-micron particles on hard dental tissues is dependent on the modification of the surface chemistry of both the particle and the dentine and the employment of the fluorosurfactant may improve tubule occlusion. The use of ThinCerts™ membrane is useful in vitro model to mimic dentinal tubules and observe the ability of particles to occlude small channels.

Clinical significance: The use of silica sub-micron particles on hard dentine tissues is dependent on the modification of the surface coating of the particles. This may influence how particles are incorporated in potential delivery vehicles applied to the dentine surface with the employment of a fluorosurfactant showing promise.

1. Introduction

Dentinal tubules are microscopic channels within the dentinestructure, which traverse from the junction of the protective outer enamel to the internal pulp containing the soft tissues [1]. They are around 1–4 microns in width and formed via the odontoblast cells [2]. There is variation in both arrangement and width of the tubules depending on their position within the tooth [3]. Once the outer enamel structure is breached, exposure of dentine occurs and allows communication through the tubular space to the pulp underneath. This can lead to irreversible damage to the soft tissues of the tooth. Nano- and sub-micron sized particles offer the possibility of a multi-functional dental agent, by both delivering anti-pathogenic or analgesic drugs into the tubules combined with the ability to occlude of the internal space,thus helping to prevent infection or infiltration into the pulp [4–6]. Their size makes them an attractive vehicle for entering into the dentinal tubule and investigators have looked to different types of particles to undertake such a task. These include calcium fluoride [7], combinations of carbonate-hydroxyapatite nanocrystals [8–10] as well as bioactive glass [11,12]. The general aim of these studies is to increase mineral content of enamel and dentine, where the particle acts as a seed for further growth of crystalline structure leading to the closure of the tubules. One approach is that the sub-micron particles may be introduced into a scaffold of collagen and provide a structure for this growth and subsequent mineralisation [13]. Furthermore, antibacterial actives or compounds may be attached to the particles to inhibit or break up bacterial growth.

* *Corresponding author.
E-mail address: a.d.walmsley@bham.ac.uk (A.D. Walmsley).

http://dx.doi.org/10.1016/j.jdent.2015.08.002
0300-5712/

A problem with the use of such particles is that they are liable to aggregate [14], thus preventing them from entering a dentinal tubule. Methods of preventing this from occurring include adding surfactants to the particles. However, it is not known how the addition of surfactants influences the movement of particles on the dentine surface and into the tubules. Researchers have used mechanical forces such as cavitation form imploding bubbles to push particles into the dentinal tubules [15]. Observing such activity of the sub-micron particles may be problematical due to the complex surface of dentine and a simple *in vitro* model system may assist in observing how particles behave on a dentine like surface.

We have chosen silica particles for their distinct advantages: availability in sizes ranging for nanometer to submicron without altering the particle surface and their porous structure, which can act as a container for molecules. Most studies involving silica particles in dental applications have concentrated in their property as a composite in biomaterials. We have previously introduced the influence of surfactants of metal complexes attached on the outside of the silica surface [16].

The aim of this research is to investigate the interaction of silica particles with human molar teeth sections, with a particular focus on entering the opening of dentine tubules. We have also used different surfactants as coatings for the particles to address their influence upon the surface interactions of the particle with the dentine surfaces. An alternative *in vitro* models has also been evaluated against dentine slices of human teeth to determine its suitability as a research tool.

2. Materials and methods

2.1. Tooth preparation

Human decay-free lower first permanent molar teeth, which were covered by the United Kingdom Human Tissue Act (HTA), were chosen for the purpose of assessing the entry of sub-micron particles into the tubules. The crown removed and the root sliced in half along the vertical axis using the bone saw. The sectioned roots were ground down using a grinder/polisher with 400/800 papers, to approximately 0.1 mm thick sections measured by a micrometer. This method was used to produce sections with perpendicular tubule openings. Before imaging/nanoparticle application, the sections were etched by a 60 s immersion in a 10% citric acid solution. The sections were then ultrasonicated for 180 s. The sections were dehydrated using successive ethanol baths for ten-minute periods of 50%, 75% then 100% before drying for 1 h in a 60° oven.

2.2. Particle preparation

The particles used in this investigation consisted of spherical silica encapsulated with a luminescent complex, tris-(2,2′-bipyridyl)ruthenium(II) dichloride, represented as SiO_2–Ru [17], with a size of 640 nm were designated as SiO_2–Ru-640 (640 ± 90 nm). The effect of polymer coating did not change the size within the error limit of the particle size analysed. The sizes were determined by Dynamic Light Scattering measurement using a Zetasizer Nano ZS, (Malvern Instruments Ltd., Malvern, UK). Visualization of the particles was performed using Nanosight tracking Analysis instrument (Malvern Instruments Ltd., Malvern, UK). For confocal fluorescence imaging studies, three different sizes were used (particle concentration 0.004% w/v). SiO_2–Ru-130 (130 ± 50 nm), SiO_2–Ru-430 (430 ± 50 nm), SiO_2–Ru-810 (810 ± 160 nm) estimated by the confocal reflectance images. They were prepared as 0.004% w/v solutions by addition of 50 ml deionised water to 2 mg particles (dry weight), followed by ultrasonication for 5 min. For surfactant coated nanoparticle preparations Zonyl® FSA, Triton® X-100 or Tween20® (purchased by Sigma–Aldrich) were added to 0.04% w/v solutions of the SiO_2–Ru-640. The 0.04% w/v solution required addition of 10 ml deionized water to 4 mg particles (dry weight), followed by ultrasonication for 5 min. Additions of the various surfactants were done on 10 ml aliquots of the 0.04% w/v SiO_2–Ru-640. Preparations are therefore as follows:

1. SiO_2–Ru-640: control sample—(no surfactant).
2. Zonyl-SiO_2–Ru-640: (a) 10 ml—SiO_2–Ru + 10 μl Zonyl FSA (1.3 g/mL) (b) 10 ml—SiO_2–Ru + 100 μl Zonyl FSA (1.3 g/mL). The excess of Zonyl FSA in (b) was used to examine if this affected the particle interaction with dentine.
3. Tween20–SiO_2–Ru-640:10 ml—SiO_2–Ru + 10 μl Tween20 (1.095 g/mL).
4. Triton–SiO_2–Ru-640:10 ml—SiO_2–Ru + 10 μl TritonX—100 (1.7 M).

After addition of the surfactants, 1 ml aliquots were transferred to Eppendorfs centrifuge tubes and centrifuged at 6000 rpm for 6 min, the supernatant discarded and the particles re-suspended in deionized water. This wash step was done to remove excess surfactant.

The photophysical properties of the luminescent particles were analyzed using Edinburgh Instruments FLS920 Series fluorescence spectrometer.

2.3. Application of particles to dentine

The particles were dropped on to the tooth surface with no mechanical agitation taking place. For the SiO_2–Ru-640, Zonyl–SiO_2–Ru-640, Tween20–SiO_2–Ru-640 and the Triton–SiO_2–Ru-640 10 μL of the supplied NP solution, was pipetted on to the dentine surface and uniformly spread using the pipette tip. The surface was left to dry completely and then subsequently washed three-times with 10 μL of de-ionised water by pipetting it on to the surface and aspirating it off. Dentine samples were then prepared for imaging.

2.4. Imaging of particles

All of the samples were prepared by mounting onto a carbon coated aluminium stub before splutter coating with gold using a Quorum Emitech K550X splutter coater. A scanning electron microscope, SEM (Zeiss EVO MA 10) was used under high vacuum and at a range of electron acceleration voltages between 5 and 15 eV.

The confocal microscopy studies were performed using a Leica confocal microscope in reflectance and fluorescence modes. Excitation was at 488 nm at approximately 20% power and at 458, 476 and 488 nm at 100% power, with emission collection at 478–498 nm and 580–800 nm, respectively. The samples were mounted on 12 mm diameter carbon stubs (used in SEM) and were attached to a glass slide.

2.5. Thinsert™ preparation and imaging

Polyethylene terephthalate (PET) ThinCert™ cell culture inserts, normally used for cell tissue work, were selected with a pore size of approximately 3 μm in diameter. They consisted of a polystyrene housing containing a PET membrane. Prior to application of the particles, one batch of control membranes was not splutter coated; the second batch had one coat of gold applied and the third batch had two coats of gold applied. The gold splutter coating deposition was for 2 min delivering a thickness of 15 nm. Sub-micron particles were applied to the surface of each batch of membranes with no mechanical agitation taking place. The membranes and particles were splutter coated before SEM imaging in a similar manner to the dentine surfaces.

Please cite this article in press as: S. Claire, et al., The deposition and imaging of silica sub-micron particles in dentine, Journal of Dentistry (2015), http://dx.doi.org/10.1016/j.jdent.2015.08.002

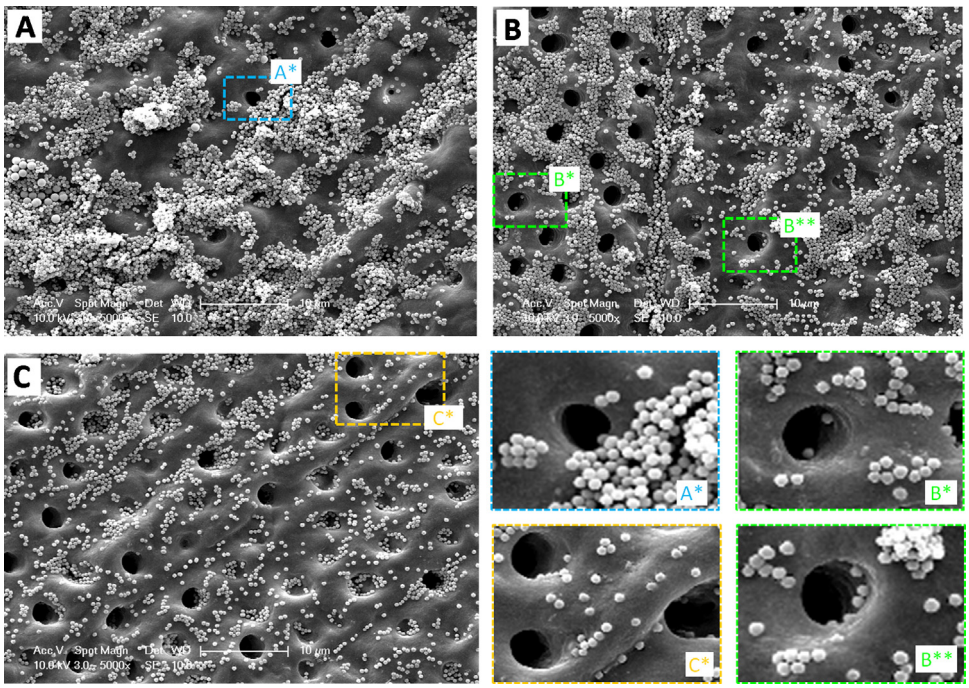

Fig. 1. SEM images of SiO_2–Ru-640 (A) particles suspended in: Triton–SiO_2–Ru-640 (B), Tween20–SiO_2–Ru-640 (C) applied to acid etched root surface sections. (Scale bar 10 μM). Concentrations: Triton–SiO_2–Ru-640:10 ml – SiO_2–Ru + 10 ml TritonX – 100 (1.7 M), Tween20–SiO_2–Ru-640:10 ml – SiO_2–Ru + 10 μl Tween20 (1.095 g/mL)

3. Results

When applied directly to the molar root dentine surfaces that had been acid etched with 10% citric acid for 60 s to simulate hypersensitive dentine, SEM examination revealed unique interactions of the particles with the dentine surface. The 0.04% w/v SiO_2–Ru-640particles formed large aggregates of several micrometers in diameter clustered on top of each other (Fig. 1A). Although these clusters are large enough to potentially occlude a tubule opening it seemed that most of the particles attached to the area surrounding the tubule periphery (Fig. 1A*). Partial occlusion is thus only achieved in a small minority of the tubules where small clusters or single particles have been able to enter.

The Triton® X-100 coated particles, Triton–SiO_2–Ru-640, show similar interactions with the dentine surface section as the SiO_2–Ru-640 (no surfactant); however, particle aggregation occurred to a lesser degree (Fig. 1B). Nevertheless, the particle clusters that formed were still too large to occlude the tubule openings and instead were restricted to the periphery of the tubule opening. The few tubules that were partially occluded to a small degree, were blocked with small clusters or single particles (Fig. 1B* and B**).

Tween20–SiO_2–Ru-640particles were markedly less aggregated on the acid etched dentine surface with clusters qualitatively smaller than the SiO_2–Ru-640 or the Triton100–SiO_2–Ru-640 preparations (Fig. 1C). With these smaller clusters it is perhaps easier for the particles/clusters to at least partially occlude the tubules (Fig. 1C*). This is particular relevant when compared to the SiO_2–Ru-640 particles (Fig. 1A), where large clusters are potentially preventing tubule occlusion by particles/small clusters by attaching to and blocking the area surrounding the tubule periphery.

With regards to the Zonyl–SiO_2–Ru-640 preparation, Zonyl is a relatively hydrophobic surfactant, bearing polar fluorine groups. This may explain why Zonyl–SiO_2–Ru-640 particles were observed as fairly large aggregated clusters that seem to have an affinity for the tubule openings (Fig. 2). The particles were placed on dry dentine and further research on how moisture affects the

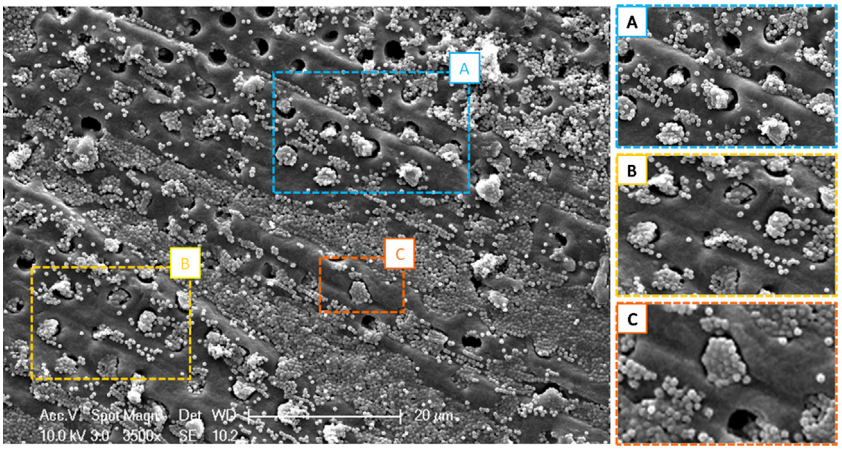

Fig. 2. SEM image of Zonyl–SiO_2–Ru-640 (and corresponding magnifications) applied to molar root surface sections. (Scale bar 20 μM). Concentration: Zonyl–SiO_2–Ru-640: 10 ml – SiO_2–Ru + 100 μl Zonyl FSA (1.3 g/mL).

Please cite this article in press as: S. Claire, et al., The deposition and imaging of silica sub-micron particles in dentine, Journal of Dentistry (2015), http://dx.doi.org/10.1016/j.jdent.2015.08.002

clustering is required. The physico-chemical properties of the particles, in this instance, may be such that these clusters of particles prefer attachment within the tubule as opposed to the tubule periphery, as in the case of the SiO_2–Ru–640 and the Triton–SiO_2–Ru-600. Furthermore, the clusters seem to be of a suitable size to occlude the majority of the tubule openings.

The silica particles exhibited red luminescence based on the properties of the encapsulated ruthenium bipyridyl complex (Fig. 3). We carried out spectroscopic studies to quantify the effects of the surfactants on the luminescence signal. The experiment was carried out by aliquoting silica particles into 1 ml samples, followed by taking emission scans before and after the addition of the surfactants. This approach accounts for any small but significant variations in the concentration of the particles in the stock solution. The luminescence spectra are accompanied by excitation spectra (Fig. 3).

The samples were excited with visible light at 450 nm, where the characteristic absorption of the ruthenium complex occurs based on a metal to ligand charge transfer transition. They luminesce in the red region of the spectrum with a peak around 615 nm. The luminescence is sensitive to the environment, and it clearly showed a blue shift upon coating of the particles with the Zonyl surfactant. The emission studies showed that for all samples of SiO_2–Ru particles, the effect of the surfactant was most pronounced for the Zonyl coating leading to particles with the highest luminescence and a 5 nm blue shift on the emission maximum. The effect of Zonyl is highest when excess of Zonyl was added (sample 2b). The excitation spectra confirmed that the emission originates from the ruthenium core.

The red luminescent particles SiO_2–Ru-130, SiO_2–Ru-430 and SiO_2–Ru-810 (0.004% w/v) can also be observed interacting with molar root sections with confocal luminescence microscopy, utilizing the luminescence of the encapsulated ruthenium. Overlays

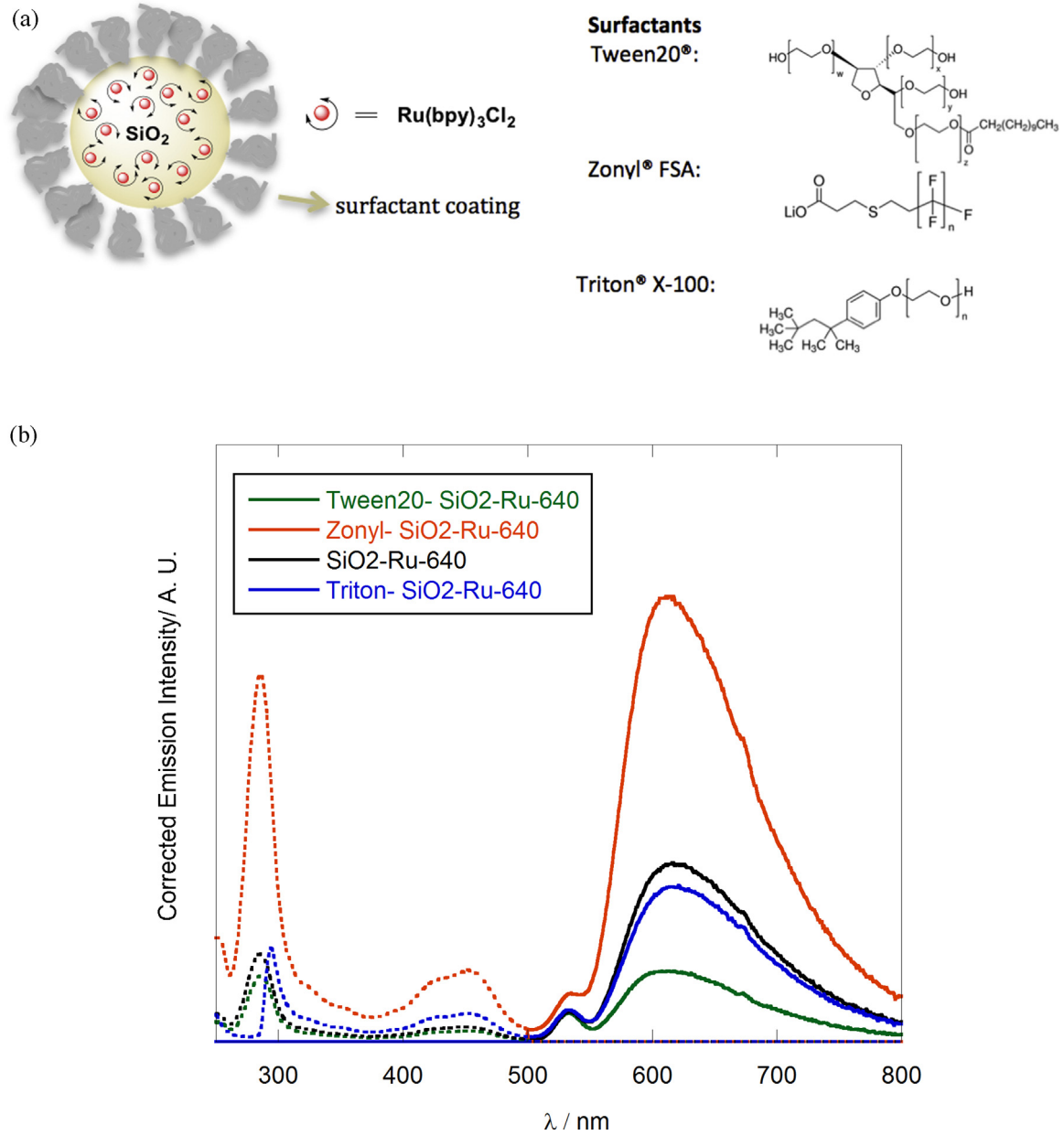

Fig. 3. (a) Schematic diagram of silica particles with encapsulated luminescent ruthenium probe SiO_2–Ru and surfactant coating. (b) Excitation (left) and emission (right) spectra of the silica particles coated with different surfactants, $\lambda_{exc} = 450$ nm, $\lambda_{em} = 620$ nm.

Please cite this article in press as: S. Claire, et al., The deposition and imaging of silica sub-micron particles in dentine, Journal of Dentistry (2015), http://dx.doi.org/10.1016/j.jdent.2015.08.002

of the red luminescence channel and the reflectance channel ($\lambda_{exc/em}$ = 488 nm) of the dentine surface, demonstrated nanoparticle association with the surface (Fig. 4). However, due to the resolution limit of confocal microscopy, only the larger SiO_2–Ru-810 were clearly resolved, and were readily observed as clusters occluding multiple tubules (Fig. 4).

To further characterize the particle–surface interactions, Zonyl coated particles were applied to plain and gold splutter-coated polyethylene terephthalate (PET) micropore sheets (Fig. 5).

A sample of Zonyl–SiO_2–Ru (sample 2b) was applied to the ThinCerts™ in a similar manner. Three ThinCerts™ samples were used. The control sample was an unaltered PET ThinCerts™, the second sample had one splutter coating of gold, and the third sample had two consecutive splutter-coatings of gold before the particles were applied. The most interesting and noticeable result of this experiment is that nanoparticle aggregation is clearly surface-dependent. Aggregation between particles is a well-documented phenomenon that is thought to be mainly driven by Van der Waals forces, and exaggerated by a large surface-to-volume ratio. The repulsive forces between polar surfactant-coated particles and charged ions are overcome in favour of the attractive Van der Waals forces on the PET surface, resulting in obvious aggregation. It is also possible, given the chemical structure of PET, that delta negative charges on the surface repel the delta negative oxygen atoms of the silica shell. On the gold coated polymer surface, surfactant-coated particles adsorb more evenly onto the surface, presumably driven by electrostatic forces. The same particles used in all three gold coated PET samples, were also used on dentine. It is notable that the gold-coated PET membranes bound the particles similar to how the particles bound to dentine. This could be useful for future experiments, but could also be an indicator that similar strength forces are involved. Overall, the particles showed distinct aggregation on the plain PET micropores, and strong surface interaction on the gold-coated version.

4. Discussion

There is much interest in the use of sub-micron particles in dentistry and generally these particles may be used as a method to remineralise dentine. There have been nanosized particles of different materials introduced into the dentinal tubules and these include calcium fluoride, hydroxyapatite and bioactive glass [8,20,21]. All these approaches use the particles to initiate a scaffold for the remineralisaiton of the dentine. The silica particles used in this project have a porous structure and therefore have the potential to be a carrier for a range of molecules including calcium based compounds. These particles may also serve as a carrier for antimicrobial compounds and therefore offer a novel approach to treating contaminated hard tissues [16,17].

Previous work has shown the ability of particles to infiltrate dentinal tubules although the difficulty of preventing the particles from aggregating due to interaction with each other is a challenge [11]. Previous work has suggested that surfactants may prevent this from occurring [16] although this was not conducted in a biological situation.

In this study, when the particles with surfactant coatings were applied to the flat dentine surfaces, differences in the aggregation were observed with SEM. The no surfactant and Triton X-100 treated preparations resulted in the greatest aggregation of the particles with little surface spread or occlusion of the tubules. The dentinal tubule occlusion was greater in the Tween20 preparation, but was most readily observed with the Zonyl preparation, possibly due to the physico-chemical properties of the sub-micron particles when coated with the relatively hydrophobic surfactant containing polar fluorine groups. The properties of this preparation are such that the particles achieve suitable interaction with the surface and clustered to achieve optimum tubule occlusion, compared to the other preparations investigated. The use of luminescent particles also provides an avenue for the use of luminescence imaging to investigate their use on dental surfaces [17].

There may be other factors involved in nanoparticle aggregation, mainly local concentration and surface morphology. However, these observations merit further research to establish the extent of influence the surfactant has with respect to the chemistry, bonding and other interactions. More research should be directed at optimizing the entry of these particles for occluding dentine tubules. If these particles are able to occlude the tubule opening, their novel structure will allow active compounds to be bound onto the particle. Such an approach may be useful in the topical treatment of dentine sensitivity or the treatment of carious dentine.

The particles also showed distinct aggregation on the plain PET micropores and strong surface interaction on the gold-coated PET membranes, again revealing the importance of the surface chemistry of both the nanoparticle, and the surface to which they are binding. Therefore, the occlusion of the dentinal tubules may be assisted by the use of surface chemistry modification prior to delivery of the sub-micron particles.

For the use of particles to occlude, for example, hypersensitive dentine, the interactions of the particles with the dentine surface present a paradox. Electrostatic interactions of the particles with dentine surfaces are a requirement to keep the particles on the tooth surface, but they may prove an obstacle when attempting to deliver the particles deeper into the tubules. It may be that other techniques are required to overcome the surface attractive forces and move the particles to a deeper position in the tubules.

These studies also demonstrated the use of PET ThinCerts™ as potential *in vitro* dentine models for observing the activity of sub-micron particles. Human teeth are difficult to procure and require a Human Tissue Act (HTA) license for handling, as well as inherent variations between individuals. Part of this project involved preliminary examinations of PET ThinCerts™ as a possible model for dentine. The ThinCerts™ are semi-transparent capillary pore membranes produced from polyethylene terephthalate (PET) from which they derive their name. The average tubule diameter for the openings of the dentinal tubules was measured as 2.3 μm (standard deviation: ±0.50 μm). For the ThinCerts™ the average diameter of the pore was calculated at 2.17 μm (standard deviation: ±0.23 μm), and the percentage of the total area covered by the pores was 3.0% which is similar to that of superficial dentine [18]. In Pashley (1996), the area of dentine occupied by the tubules is 2.85–3.96% in mid-coronal dentine [18]. It is only 0.96% in superficial dentine. So the tubules, which are in dentine *vs*. PET membrane,are similar. These values are unsurprising, given the gross appearance of the dentinein comparison to the ThinCerts™. Summing up the similarities and differences, the channel openings are very similar in diameter although the ThinCerts™ are less variable as shown by the standard deviations. The area in the ThinCerts™ occupied by pores is similar to the area of superficial dentine occupied by the dentinal tubules [8]. The other difference is the pattern of arrangement of the pores which is more random than the dentine. However, these images do suggest that the ThinCerts™ may be useful as a dentine model.

This study showed distinct aggregation of the sub-micron particles on plain PET micropore membranes and strong surface interaction on the gold-coated version, revealing the importance of the surface chemistry of both the nanoparticle and the surface to which they are binding. Silica particles offer the possibility of different sizes, coating and inclusion of therapeutic agents and their use on hard dental tissues will be dependent on the modification of the surface chemistry of the dentine prior to drug delivery.

The current study focused on silica particles binding to dentine whilst future work will be directed at how they bind to mineralized

Please cite this article in press as: S. Claire, et al., The deposition and imaging of silica sub-micron particles in dentine, Journal of Dentistry (2015), http://dx.doi.org/10.1016/j.jdent.2015.08.002

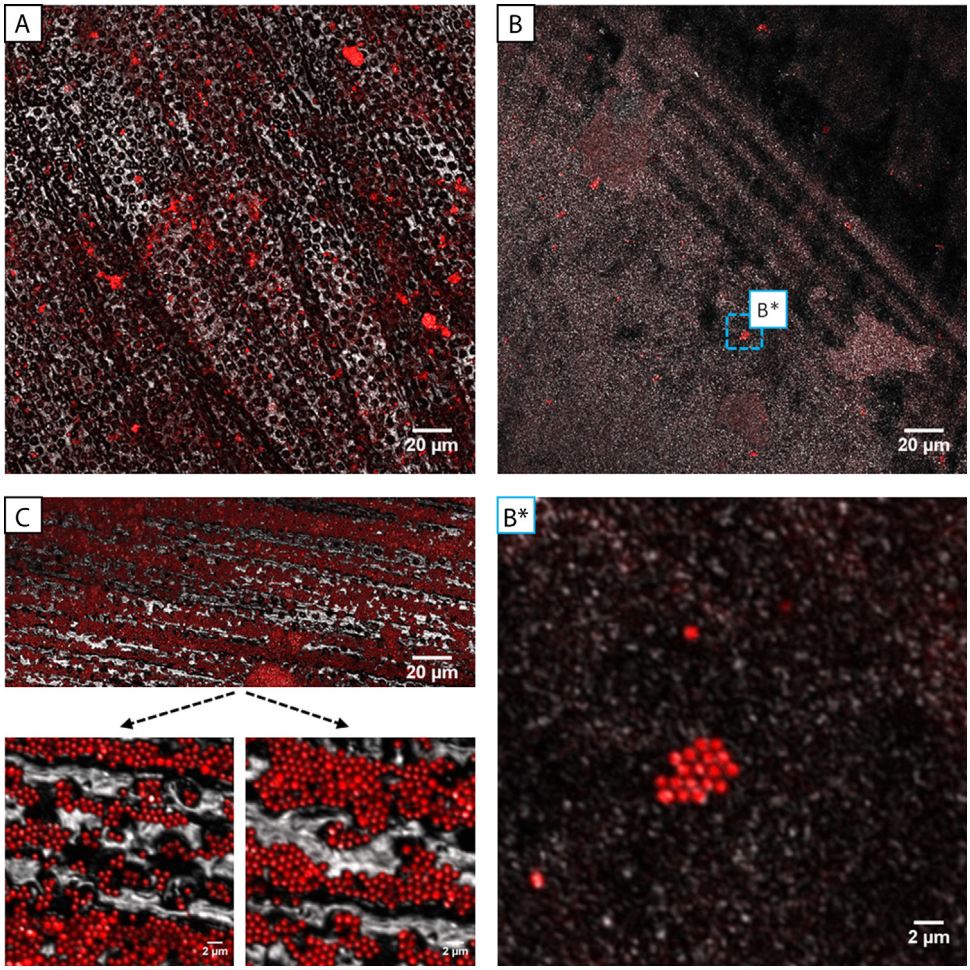

Fig. 4. Confocal luminescence and reflection microscopy image overlays (and corresponding magnifications) of SiO_2–Ru-130 (A), SiO_2–Ru-640 (B) and SiO_2–Ru-810 (C) on the molar root surface. (Magnified image, scale bar 2 µM).

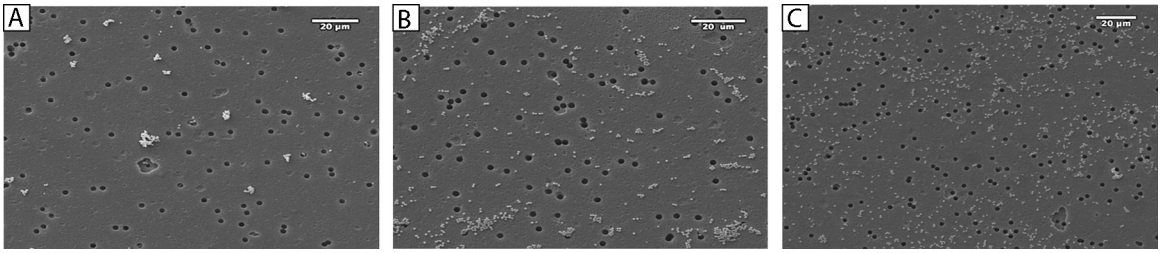

Fig. 5. SEM images of Zonyl–SiO_2–Ru-640 applied to PET ThinCerts™ (A) uncoated, (B) with a single gold splutter coat, (C) with two gold splutter coats. (Scale bar 20 µM).

dentine surfaces that better simulate clinical dentine hypersensitivity [19].

There are several limitations with this work. The deposition of the submicron particles may affect subsequent bonding systems ability to attach to the dentine. The potential effect on bond strength to dentine is an area of future investigation. Furthermore silica absorbs water from the dentine and this in itself could potential cause post-operative discomfort if the particles are to be used as an anti-hypersensitivity agent. Again this will be investigated in further studies.

5. Conclusion

The use of silica sub-micron particles on hard dentine tissues is dependent on the modification of the surface coating of the particles. The hydrophobic Zonyl surfactant coating appeared to allow the most penetration of particles into the tubules. The use of a ThinCerts™ membrane provides a useful *in vitro* model to mimic dentinal tubules and observe the ability of particles to occlude small channels.

Acknowledgements

This work was funded by an Engineering and Physical Sciences Research Council (EPSRC),Physical Sciences Imaging Biological Sciences (PSIBS), Doctoral Training CenterEP/F50053X/1.

The authors declare no potential conflicts of interest with respect to the authorship and/or publication of this article.

Please cite this article in press as: S. Claire, et al., The deposition and imaging of silica sub-micron particles in dentine, Journal of Dentistry (2015), http://dx.doi.org/10.1016/j.jdent.2015.08.002

References

[1] A. Linde, M. Goldberg, Dentinogenesis, Criti. Rev. Oral Biol. Med. 4 (1993) 679–728.
[2] R. Schilke, J.A. Lisson, O. Bauss, W. Geurtsen, Comparison of the number and diameter of dentinal tubules in human and bovine dentine by scanning electron microscopic investigation, Arch. Oral Biol. 45 (2000) 355–361.
[3] H.E. Schroeder, Oral structural biology, Thieme Medical Publishers, New York, 1991 pp. 103–118.
[4] J.S. Earl, D.J. Wood, S.J. Milne, Nanoparticles for dentine tubule infiltration: an in vitro study, J. Nanosci. Nanotechnol. 9 (2009) 6668–6674.
[5] R.P. Allaker, The use of nanoparticles to control oral biofilm formation, J. Dent. Res. 89 (2010) 1175–1186.
[6] M. Hannig, C. Hannig, Nanotechnology and its role in caries therapy, Adv. Dent. Res. 24 (2012) 53–57.
[7] L.M. Sun, L.C. Chow, Preparation and properties of nano-sized calcium fluoride for dental applications, Dent. Mater. 24 (2008) 111–116.
[8] K.L. Lv, J.X. Zhang, X.C. Meng, X.Y. Li, Remineralization effect of the nano-HA toothpaste on artificial caries, Key Eng. Mater. 330-332 (2007) 267–270.
[9] S.H. Jeong, S.J. Hong, C.H. Choi, B.I. Kim, Effect of new dentifrice containing nano-sized carbonated apatite on enamel remineralization, Key Eng. Mater. 330-332 (2007) 291–294.
[10] N. Roveri, E. Battistella, I. Foltran, E. Foresti, M. Iafisco, M. Lelli, B. Palazzo, L. Rimondini, Synthetic biomimetic carbonate-hydroxyapatite nanocrystals for enamel remineralization, Adv. Mater. Res. 47–50 (2008) 821–824.
[11] A. Besinis, N. van, R. oort, N. Martin, Infiltration of demineralized dentin with silica and hydroxyapatite nanoparticles, Dent. Mater. 28 (2012) 1012–1023.
[12] A. Besinis, N. van, R. oort, N. Martin, Remineralization potential of fully demineralized dentin infiltrated with silica and hydroxyapatite nanoparticles, Dent. Mater. 30 (2014) 249–262.
[13] S. Srinivasan, P.T. Kumar, S.V. Nair, S.V. Nair, K.P. Chennazhi, R. Jayakumar, Antibacterial and bioactive alpha- and beta-chitin hydrogel/nanobioactive glass ceramic/nano silver composite scaffolds for periodontal regeneration, J. Biomed. Nanotechnol. 9 (2013) 1803–1816.
[14] W. Zhang, J. Crittenden, K. Li, Y. Chen, Attachment efficiency of nanoparticle aggregation in aqueous dispersions: modeling and experimental validation, Environ. Sci. Technol. 46 (2012) 7054–7062.
[15] A. Shrestha, S.W. Fong, B.C. Khoo, A. Kishen, Delivery of antibacterial nanoparticles into dentinal tubules using high-intensity focused ultrasound, J. Endod. 35 (2009) 1028–1033.
[16] D. Lewis, V. Dore, N.J. Rogers, T. Mole, G. Nash, P. Angeli, Z. Pikramenou, Silica nanoparticles for micro-particle imaging velocimetry: fluorosurfactant improves nanoparticle stability and brightness of immobilized iridium(III) complexes, Langmuir 29 (2013) 14701–14708.
[17] D.J. Lewis, V. Dore, M.J. Goodwin, A.C. Savage, G.B. Nash, P. Angeli, Z. Pikramenou, Luminescent ruthenium(II) tris-bipyridyl complex caged in nanoscale silica for particle velocimetry studies in microchannels, Measurement Sci. Technol. 23 (2012) 084004.
[18] D.H. Pashley, Dynamics of the pulo–dentine complex, Crit. Rev. Oral Biol. Med. 7 (1996) 104–133.
[19] M. Yoshiyama, K. Ozaki, S. Ebisu, Morphological characterization of hypersensitive human radicular dentin and the effect of a light-curing resin liner on tubular occlusion, Proc. Finn. Dent. Soc. 88 (Suppl 1) (1992) 337–344.
[20] L.M. Sun, L.C. Chow, Preparation and properties of nano-sized calcium fluoride for dental applications, Dent. Mater. 24 (2008) 111–116.
[21] M. Vollenweider, T.J. Brunner, S. Knecht, R.N. Grass, M. Zehnder, T. Imfeld, et al., Remineralization of human dentin using ultrafine bioactive glass particles, Acta Biomater. 3 (2007) 936–943.

Please cite this article in press as: S. Claire, et al., The deposition and imaging of silica sub-micron particles in dentine, Journal of Dentistry (2015), http://dx.doi.org/10.1016/j.jdent.2015.08.002

5

General Conclusions and Future Work

Nanoparticles have attracted considerable recent research interest for a variety of applications. The incorporation of luminescent moieties on to or within a nanoparticle can produce an extremely useful imaging agent, that can offer several advantages over the luminescent moiety alone. This thesis presented the development of functionalised gold and silica nanoparticles for use as imaging probes.

Following an introduction on the relevant literature and the instrumentation used for nanoparticle characterisation in the first chapter, the second chapter in this thesis presents the use of two surfactants and a peptide to modify gold nanoparticles. Surface modification using this methodology allows nanoparticle conjugation with the **HoechstSH** complex synthesised by the author. The **Tween 20** and **Zonyl 7950** surfactants, and the pHLIP peptide were utilised to overcome the issue of the aggregation upon direct addition of **HoechstSH** complex to gold nanoparticles. The surfactants and peptides were successfully used to modify 13 and 100 nm gold nanoparticles to produce fully characterised and stable gold colloids.

The **HoechstSH** complex was synthesised from the Hoechst 33258 organic dye with the incorporation of a thiol link, thereby allowing conjugation to gold nanoparticles. The **HoechstSH** was characterised and photophysical studies revealed the complex exhibited similar properties to the Hoechst family of dyes, with an increase in intensity and blueshift in emission upon binding with DNA.

Gold nanoparticles both 13 nm and 100 nm in diameter were then functionalised

with the **Hoechst SH** complex using prior modification with surfactant or peptide precoatings. The resulting gold colloids were fully characterised and stable against aggregation. Upon photophysical characterisation the colloids exhibited the emission characteristics of the **HoechstSH** complex alone and upon addition of DNA, indicating the luminescent nanoparticles are able to interact and bind with DNA through the surface bound **HoechstSH** complex. This was corroborated by preliminary circular dichroism studies that indicated stiffening of the DNA due to binding with the **HoechstSH**. These results illustrate how an organic dye can by successfully functionalised for conjugation with gold nanoparticles whilst retaining its characteristic physical properties. The successful demonstration of surfactants and peptides to produce these organic dye functionalised nanoparticles provide impetus for future development of other organic dyes for their use with nanoprobes. With further functionality with a drug, targeting agent or indeed further imaging moieties, there is great scope for the production a multi-modal theranostic agent.

The cellular interactions of 13 nm and 100 nm **HoechstSH** functionalised gold nanoparticles were studied in the A549 lung cancer and HeLa cervical cancer human cell lines. Confocal microscopy studies of both cell lines show showed particle uptake in all cells incubated with the all the nanoparticle preparations. The characteristic emission of the **HoechstSH** is also observed on the particles inside the cells, illustrating the stability of the nanoparticle-dye conjugate in an intracellular/biological environment. Nuclear uptake of all the nanoparticle preparations was also observed in some cells. Localisation of particles to the nucleus was seemingly related to cell division, with all cells exhibiting nuclear uptake in the cell division stage of the cell cycle as according to their morphology. A future study that could address this is an experiment where cell division is stopped using mitotic inhibitor. These cells could be treated with nanoparticles with the amount of nuclear uptake then compared to an untreated control, thus the proposed relationship with cell division and nuclear uptake could be further scrutinized.

These interesting observations require future studies aimed at quantifying the amount

of nuclear uptake observed in a particular cell. This can be done by developing an image segmentation protocol such as that described in the second chapter, where the pixel intensity due to the DRAQ5 nuclear stain was used to derive the location of the cell nucleus. The co-localisation with nanoparticles can, be examined by extracting their location by means of an intensity threshold algorithm on the reflectance image, exploiting the light scattering properties of the gold nanoparticles. Performed only on a single cell by the author in this thesis, this methodology requires development for high throughput, such that many images/cells can be processed to provide statistical quantification of the percentage of nuclear uptake in a particular cell population. An image analysis algorithm can also thus provide a percentage of the total number of cells in a sample that exhibit nuclear uptake. Confocal imaging fields-of-view were chosen on the basis of the number of cells visible and although the percentage of cells with nuclear uptake in each field-of-view was not recorded, if a crude approximation were provided approximately 10 % of cells imaged exhibited nuclear uptake.

The aforementioned confocal microscopy studies were complemented with transmission electron microscopy to provide intracellular resolution on the uptake of **Au13-Z-HSH** and **Au13-P-HSH** in HeLa cells. A single electron microscopy sample grid contained approximately twenty cells of which half exhibited particle uptake compared to virtually all cells in a confocal sample exhibiting uptake. This would however be expected as the cells on the grid have been prepared as ultra-thin samples of the order of several tens of nanometres in height. Confocal imaging samples are of whole cells of the order of several microns in height. It is therefore difficult to directly compare confocal and electron microscopy and corroborate the number of cells with nuclear uptake, particularly when the sensitivity of the confocal microscope and its ability to image single 13 nm particles is considered. It is however promising that several cells with nuclear uptake, approximately two to three cells out of twenty on the grid, were observed by electron microscopy.

The electron microscopy images themselves were extremely interesting. All cells that exhibited uptake had nanoparticles located in densely packed vesicles in the perinuclear

regions. This is analagous to the majority of confocal imaging observations. The presence of nanoparticles in vesicles of various morphologies was related to observations made in the literature of nanoparticles internalised by cells. Although requiring an extensive review of the literature this examination of nanoparticle uptake provided an important perspective on their cellular interactions, and is furthermore regarding as one of the most important accomplishments of this research.

The most remarkable observations in cells showing nuclear uptake of **Au13-Z-HSH** and **Au13-P-HSH** were apparent breaks in the nuclear membrane in the vicinity of the particles and vesicles containing nanoparticles present in some cell nuclei. Such observations are remarkable particularly as no mechanism for vesicle mediated nuclear uptake of nanoparticles such as this has been presented in the literature to the authors knowledge. Examining this in greater detail in the future would therefore be of great interest. Such studies could examine uptake in a time course experiment to evaluate particle localisation over a period of minutes to hours after initial cellular internalisation.

Cells with nuclear uptake of particles all exhibited morphological indications they were in the cell division stage of the cell cycle. The breaks in the nuclear membrane accompanying localisation of particles to the nucleus also occur during cell/nuclear division. These observations prompted a study in to cell cycle dysregulation due to nanoparticles. HeLa cells were synchronised and treated with **Au13-Z-HSH** and **Au13-P-HSH** in the G0/1, S and G2/M phases of the cell division and examined for signs of dysregulation against undosed controls. Although no significant effects were observed this does provide scope for the use of these nanoparticles as non-toxic nuclear imaging probes, particularly as particles were often localised to the periphery of the nucleoli in the cells. The cell cycle experiments were extremely time consuming and extensive due to the requirement for experimental repeats, and although no significant effects were observed, the author considers these challenging experiments important accomplishments in the research presented.

A further point of consideration when evaluating images of cells with nanoparticle uptake is the comparison between the fixed and live cell specimens. As discussed in

the introduction the fixation protocol for confocal microscopy can produce artefacts in the specimen. Of great relevance for studying nanoparticle uptake is permeabilization of the cell membrane and damage to the DNA structure that can occur with the use of formaldehyde/paraformaldehyde for fixing. It is therefore reassuring that the fixed and live cell specimens exhibit identical uptake with nanoparticles localised to the perinuclear region of cells in both fixed and live cell specimens.

Further aspects of the research presented that would benefit from future studies include the pHLIP peptide coated particles. An investigation on to the pH dependence of uptake in cells would be of great interest. Nanoparticle uptake can be quantified by flow cytometry and confocal imaging after incubation in acidic and neutral buffer, potentially exploiting the ability of the pHLIP peptide-nanoparticle conjugate to "insert" across the cell membrane at acidic pH. Uptake methods could be further studied by incubating cells with particles at 4 C and 37 C or in the presence of chemical endocytosis inhibitors to establish whether passive cellular uptake of particles is significant.

Further accomplishments in the second chapter are the production of stable and luminescent **HoechstSH** coated gold nanoparticles. The work required to produce these particles was very arduous, to study these successfully produced nanoparticles in cells and observe interesting cellular interactions was therefore very rewarding.

The work presented in chapter 3 was also similar in this respect. The **Zonyl 7950** surfactant enabled coating of gold nanoparticles with a luminescent ruthenium polypyridyl transition metal complex. Gold nanoparticles both 13 and 100 nm in diameter were functionalised to produce luminescent nanoprobes exhibiting the distinct optical signature of the ruthenium complex. The nanoparticles were imaged in the A549 human lung adenocarcinoma cell line via confocal and transmission electron microscopies, and toxicity assessed by the MTT and AK assay. The results showed the particles possessed high luminescence in a cellular environment coupled with low cytotoxicity. Although initial particle preparations proved troublesome with regards to achieving optimal coatings on nanoparticles, both in terms of their stability and luminescence, successful production

proved very fruitful in terms of the interesting cellular interactions observed with high quality microscopic observations. Performing confocal and electron microscopy was furthermore novel to the author at the outset of these studies, thus the development of these techniques to obtain the images presented was extremely rewarding.

With regards to further work the ruthenium coated particles could be investigated in the HeLa cell line and cellular uptake in general scrutinized with image analysis based techniques aimed at quantification, both of particle uptake over time and the percentage of nuclear uptake. There is great scope for the use of organelle stains that could be used co-localisation studies with the nanoparticles to ascertain cellular fate. An example is the Lysotracker stain used with the **HoechstSH** gold nanoparticles in chapter 2. Although these were preliminary studies the results were very encouraging as the confocal imaging observations indicated particles in acidic vesicles in the process of achieving nuclear uptake. These results corroborate the observations made with electron microscopy that indicated vesicle mediated nuclear delivery of particles was occurring.

Another aspect of the research presented that would benefit from further study is the nuclear uptake of the ruthenium coated particles. Ideally the amount of nuclear uptake of these particles could be examined and compared with the **HoechstSH** coated nanoparticles and the relevant uncoated controls. Nuclear uptake could also be examined in a more simplified scenario. The majority of nanoparticles in the cellular uptake studies presented in this thesis are observed in the perinuclear region and are found restricted in vesicles, indicative of the endocytotic mechanism of particle uptake. It would therefore be beneficial if nuclear uptake could be examined with "non-restricted" nanoparticles. This could be achieved by isolating cell nuclei from a population of cells and subsequently "reseeding" them. A commonly used protocol in biosciences this technique would provide the opportunity for the investigation of direct interaction between nanoparticles and a cell nuclei in essentially a simplified biological scenario.

Chapter 4 describes an investigation on to the deposition and imaging of silica nanoparticles encapsulating a luminescence probe on citric acid treated dentine surfaces. These

studied were performed with the aim of evaluating the ability of particles to occlude dentinal tubules in the context of providing a clinical treatment for dental hypersensitivity. Using scanning electron and fluorescence microscopy the interaction of the particles with the dentine was examined. The images indicated that both the absence of a surfactant and incubating the particles with the **Triton X-100** resulted in the greatest particle aggregation once they were applied to the dentine, with little tubule occlusion achieved. Dentinal tubule occlusion was greater with **Tween 20** coated particles but was most readily observed with the **Zonyl** preparation. This was attributed to the physico-chemical properties of the sub-micron particles when coated with the hydrophobic **Zonyl** surfactant. The properties of the **Zonyl** are such that the particles exhibit physico-chemical interactions that allow them to cluster such that optimal tubule occlusion is achieved.

Indications that surfactant coating influences surface interactions in such a manner, coupled with the encapsulation of luminescent complex in the particles allowing for luminescence imaging, provides great impetus for further investigations studying particle/dentine interactions. Although particle preparation was relatively trivial it was rewarding to work with silica nanoparticles in addition to gold nanoparticles and furthermore evaluate them in a completely different biological context. With regards to future work there is a requirement to quantify tubule occlusion which the author envisages can be achieved through the development of computation image analysis. The effect of multiple particle treatments is also of interest, as is assessing tubule occlusion on the short, medium and long time scale after treatment. This would be of particular relevance for clinical applications of nanoparticle treatments aimed at relieving dentinal hypersensitivity.

The greatest accomplishment the author hopes to achieve is the eventual clinical application of any of the research performed and presented in this thesis.

Finis.

6 General Experimental

6.0.1 Materials for Synthesis

Solvents were purchased from Fisher or Sigma Aldrich and anhydrous solvents were dried over 3 molecular sieves under N_2(g) for 1 hr. Deuterated solvents for NMR were also purchased from Sigma Aldrich. HPLC grade solvents were used in photophysical studies and water was deionised using an Elga Option 3 water purifier. All compounds were synthesised under N_2(g) unless otherwise indicated, using standard Schlenk techniques.

6.0.2 Experimental Details for Synthesis

^{1}H and ^{13}C spectra were recorded using a Bruker AC 300, AV 300, AMX 400 or AV 400 spectrometer. Electrospray mass spectra were recorded on a Waters Micromass LCT time of flight mass spectrometer, using a nitrogen laser. Elemental analysis was performed on either a Carlo Erba EA1110 Simultaneous CHN elemental analyser (University of Birmingham), or at the London School of Pharmacy, UCL, on an Elemental Analyser, Model 1108 (Carlo-Erba, Milan, Italy) with PC based data system, Eager 200 for WindowsTM and a Sartorious Ultra Micro Balance, 4504MP8.

6.0.3 Synthesis of 13 nm Gold Nanoparticles

13 nm citrate-stabilised gold nanoparticles were synthesised according to Grabar *et al.*[244] All glassware was washed with aqua regia (HCl:HNO_3, 3:1), rinsed with deionised water and dried in an oven for 24 hours. $HAuCl_4.3H_2O$ (49.85 % Au) (0.0988 g, 0.2501 mmol) was dissolved in deionised water (250 ml) with vigorous stirring and the solution was heated to reflux. A solution of trisodium citrate (0.2858 g, 0.9718 mmol) in deionised water (25 ml, 38.87 mM) was rapidly added to the centre of the vortex. The yellow solution slowly darkened to a deep burgundy colour, and was kept at reflux for a further 10 min. The solution was cooled to room temperature with continuous stirring for a further 15 minutes to yield 13 nm gold nanoparticles. Colloids were stored at room temperature, in the dark in airtight flasks. UV-Vis (H_2O) λ_{max} = 520 nm (SPR). Diameter = 12±4 nm (DLS number distribution). Diameter = 28±14 nm, (DLS intensity distribution). Zeta potential = -34±2 mV (1 nM in deionised water).

6.0.4 Synthesis of 100 nm Gold Nanoparticles

The procedure for synthesis of 100 nm gold nanoparticles was an adapted synthesis by Ziegler and Eychmüller.[259] Stock solutions of ascorbic acid (aq) (502 mg, 2.85 mmol, 1% w/v), trisodium citrate dehydrate (aq) (500 mg, 1.70 mmol, 1% w/v) and $AuCl_4.3H_2O$ (aq) (49.85 % Au) (0.0988 g, 0.2501 mmol). Prepared as previously described $HAuCl_4.3H_2O$ (49.85 % Au) (0.0988 g, 0.2501 mmol) were 13 nm citrate-stabilised gold nanoparticle seeds (9 nM). 13 nm citrate gold nanoparticles (6 ml, 9 nM) were diluted in dH_2O to 40 ml under stirring. The Au^{3+} stock solution(4 ml, 0.2% w/v) was diluted to 20 ml in deionised water and added dropwise to the 13 nm citrate-stabilised gold nanoparticle seeds. Ascorbic acid stock solution (1 ml, 1% w/v) was combined with trisodium citrate stock solution (0.5 ml, 1% w/v), diluted to 20 ml in dH_2O and added dropwise over 15 minutes to give a dark red solution. The mixture was refluxed for 30 minutes at 100 C. A 9 ml aliquot of the reaction mixture was diluted to 40 ml. Au^{3+} stock solution (4

ml, 0.2% w/v) diluted to 20 ml was added dropwise to the diluted aliquot over 15 min. Ascorbic acid stock solution (1 ml, 1% w/v) and trisodium citrate stock solution (0.5 ml, 1% w/v) were diluted to 20 ml, and added dropwise. The mixture was refluxed for 30 minutes at 100 C for 30 min to afford a red/purple solution. Au^{3+} stock solution (16 ml, 0.2% w/v) was diluted to 20 ml and added dropwise to a 40 ml aliquot of the reaction mixture. Ascorbic acid stock (4 ml, 1% w/v) and trisodium citrate stock (2 ml, 1% w/v) was diluted to 20 ml and added dropwise to the mixture affording a dark brown colloid. The mixture was refluxed at 100 C for 30 minutes and allowed to cool, yielding 100 nm gold nanoparticles as an orange/light brown colloid in water (40 pM). UV-Vis (H_2O) λ_{max} (SPR) = 567 nm. Zeta potential (10 pM in dH_2O) = -30±15 mV.

6.0.5 Photophysical Characterisation

UV-Vis absorption spectroscopy measurements used a Varian Cary 5000 spectrometer at a 300 nm min^{-1} acquisition rate. Samples were prepared in either 1 cm or 0.4 cm path length low volume quartz cuvettes. Steady-state and time-resolved luminescence measurements were executed on an Edinburgh Instruments FLS920 spectrometer, with a 450 W xenon arc lamp illumination source. The detection system uses a Hamamatsu R928 photomultiplier tube (PMT), and an emission monochromator blazed at 500 nm. Samples were prepared in quartz cuvettes with four transparent faces, and appropriate long-pass filters were employed to eliminate second-order photon scattering. 77 K studies were measured in an in-house built sample holder within a nitrogen cryostat (Oxford Instruments), using the Edinburgh Instruments FLS920 spectrophotometer. All spectra were corrected using a correction file provided by Edinburgh Instruments FLS920 for the Xenon lamp light source, accounting for non-uniform intensity across the output wavelength range.

6.0.6 Dynamic Light Scattering and Zeta Potential

Dynamic light scattering (DLS) measurements were performed using a calibrated Zetasizer Nano ZS (Malvern Instruments). DLS sizing used a standard operating procedure with settings as follows; refractive index 0.47, water dispersant, temperature 25C, equilibration time 120 seconds, disposable DTS0012 cuvettes, automated measurement duration with five runs and no pause between runs. Zeta potentials were also measured using a calibrated Zetasizer Nano ZS (Malvern Instruments) with analagous settings using a standard operating procedure adopting the Smoluchowski model and the DTS1060 cuvettes.

6.0.7 Materials for Cell Culture

Phosphate buffered saline (Dulbecco A) tablets were purchased from Fisher Scientific UK Ltd, Loughborough, UK. Foetal bovine serum (FBS) was purchased from Invitrogen Ltd, Paisley, UK. All other materials were purchased from Sigma-Aldrich Company Ltd, Dorset, UK. Complete cell media was made using 50ml Dulbecco's modified Eagle's medium (DMEM) to which was added 50ml 10% v/v FBS, 5ml 100 μg ml^{-1} penicillin, 5ml 2mM L-glutamine and 5ml 100 μg ml^{-1} streptomycin. Phosphate buffered saline solution (PBS) was made by dissolving 4 Phosphate buffered saline (Dulbecco A) tablets in 400ml distilled water. When not in use all solutions were refrigerated at 4°C.

HeLa Cell Culture

HeLa cells were cultured in 20 ml complete media in T_{75} flasks with vented caps at 37 °C containing 5% CO_2. Complete media, PBS and all other solutions used for cell culture maintenance were warmed to 37°C prior to use. All cell maintenance was conducted in a class II laminar flow cell culture cabinet. Cell media was changed every day according to standard protocol. Cell viability was checked using a Nikon TMS light microscope before and after media change to check confluence and general cell viability.

A549 Cell Culture

The human alveolar adenocarcinoma A549 cell line (line 86012804, HPA) was maintained in Dulbecco's Modified Eagle's Medium (DMEM) supplemented with 10% fetal bovine serum (FBS), penicillin (100 μg ml^{-1}), streptomycin (100 μg ml^{-1}) L-glutamine (100 μg ml^{-1}), hereafter called complete media. Cells were cultured in 20 ml of complete media in vented T75 flasks at 37C in 5 % CO_2.

For both HeLa and A549 cells, cell passage was performed when confluence reached 60-70%. Media was removed and 10 ml PBS was used to wash away cell debris. 3 ml 0.1% v/v trypsin-EDTA solution was added and then incubated in the flask for approximately 3 minutes at 37°C. Cell detachment was monitored under a Nikon TMS light microscope. Upon detachment 8 ml fresh complete media was added. The solution was transferred to a 15 ml Falcon tube and centrifuged at 1500 rpm for 5 minutes. The supernatant was then removed and the cell pellet resuspended in 1 ml fresh cell media. Cells were then diluted in to a sterile T_{75} flask.

Confocal Microscopy Preparation and Treatment of Cells with Nanoparticles

Glass coverslips were sterilised in 100% ethanol and rinsed in phosphate buffered saline solution pH 7.4 (PBS) before being transferred to a six-well plate. Cell passage was performed as described above with 3 ml of the final cell suspension added to each well. Cells were grown in the six-well plate as described above for at least 24 hours until approximately 60-70% cell confluence was attained.

Prior to addition of the nanoparticles, cell media was removed from the six-well plate and each well was washed thoroughly with PBS. 2.7 ml of media was then added to each well with 0.3 ml nanoparticle solution to give a 1 in 10 dilution to prevent osmotic damage. After the required incubation time points coverslips were extensively rinsed with phosphate-buffered saline (PBS) twice. Cells were then were fixed with 4% paraformaldehyde in PBS for 10 min at room temperature and then rinsed and rehydrated in PBS. Glass slides sterilised with a rinse in 100% ethanol and then allowed to dry were used to

mount the coverslips which were placed on a droplet of non-fluorescent aqueous Hydromount media. Fixed coverslips were then sealed with clear nail varnish applied copiously around the rim to help prevent contamination and decay. The coverslips were then allowed to dry for a minimum of 24 hours in the dark at 4°C before microscopy analysis.

6.0.8 Confocal Microscopy

All samples were analysed using a Leica SP2 confocal system with inverted microscope Leica DMIRE2 making use of the 63x/1.4 oil lens. For DAPI and Hoechst fluorescence imaging of cells, samples were excited at 405nm with a beam intensity of 25%, and emission detected between 410-550nm with default standard PMT gain. Transmission images were acquired with the transmission microscopy setting on the microscope with beam intensity 1-3%. For Hoechst-AuNPs, emission was collected with samples excited at 405nm with a beam intensity of 25%, 476nm (75% intensity), 488nm (75% intensity) and 496nm (75% intensity) with fluorescence emission was detected at 410-550nm with default standard PMT gain.

Image processing was conducted using Macbiophotonics ImageJ Version 1.43M. For the batch addition of scale bars a macro was written for conversion of the image parameters from the Leica TCS SP2 microscope image data file, as illustrated in Appendix J.2.

6.0.9 Transmission Electron Microscopy

Cells were treated as described in the protocol above for fluorescence microscopy preparation. Analogously wells were dosed with Ru coated and non-coated gold nanoparticles for 24 hours. Coverslips were then washed with PBS and fixed in 2.5% gluteraldehyde for a further 24 hours at 4°C. Ultrathin sections were cut parallel to the coverslips by P. Stanley and colleagues at the Centre for Electron Microscopy and mounted onto Formvar-coated 200 mesh copper grids. Transmission electron micrographs slice widths are 70-90 nm . Sections were examined using a Jeol 1200 EX Transition Electron Micrograph (Jeol UK

Ltd., Welwyn Garden City, UK) operated at 80kV in the imaging mode. Images were acquired using Digital Micrograph Version 1.83.842 (Gatan Inc., Pleasanton California, USA) with 5 second exposures.

Appendices

A

Characterisation of Hoechst 33258

A.1 NMR Spectra of Hoechst 33258

^{1}H NMR δ_H (300 MHz, MeOD) 3.04(3H, s, H-1), 3.15-3.50(4H, m, H-3',4'), 3.72(2H, d, J 12.1, H-3,4), 4.04(3H, d, J 13.8, H-4), 7.13-7.18(2H, m, H-21), 7.41(1H, d, J 2.1, H-6), 7.50(1H, dd, J 2.2 9.1, H-10), 7.81(1H, d, J 9.09, H-9), 8.08-8.17(3H, m, H-14,20), 8.30(1H, dd, J 1.7 8.7, H-13), 8.6(1H, J 1.2, H-17).

^{1}3C NMR δ_C (100 MHz, MeOD) 228.0, 222.7, 165.2, 151.1, 136.5 (C-16) 134.5, 131.7 (C-20), 127.8, 126.4 (C-13), 121.7, 120.0 (C-10), 118.1 (C-21), 116.3 (C-14), 115.7 (C-9), 114.7 (C-17), 114.1 (C-12), 112.1 (C-22) 100.9, 54.6 (C-2/3), 48.4 (C-3/2), 43.6 (C-1).

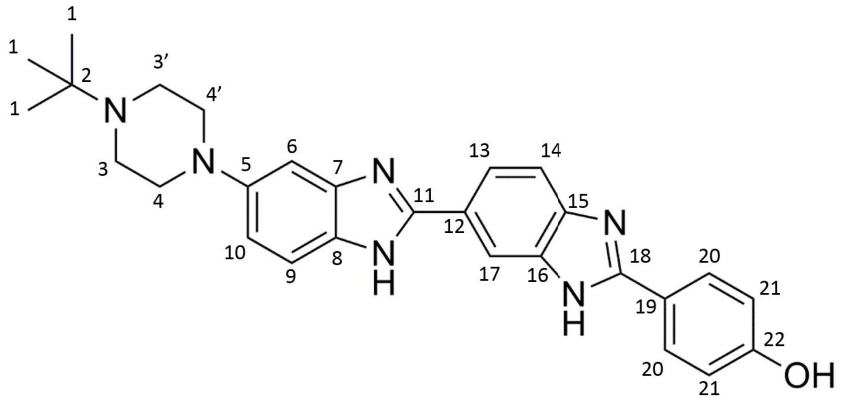

Figure A.1: ^{1}H NMR designations of Hoechst 33258 in MeOD

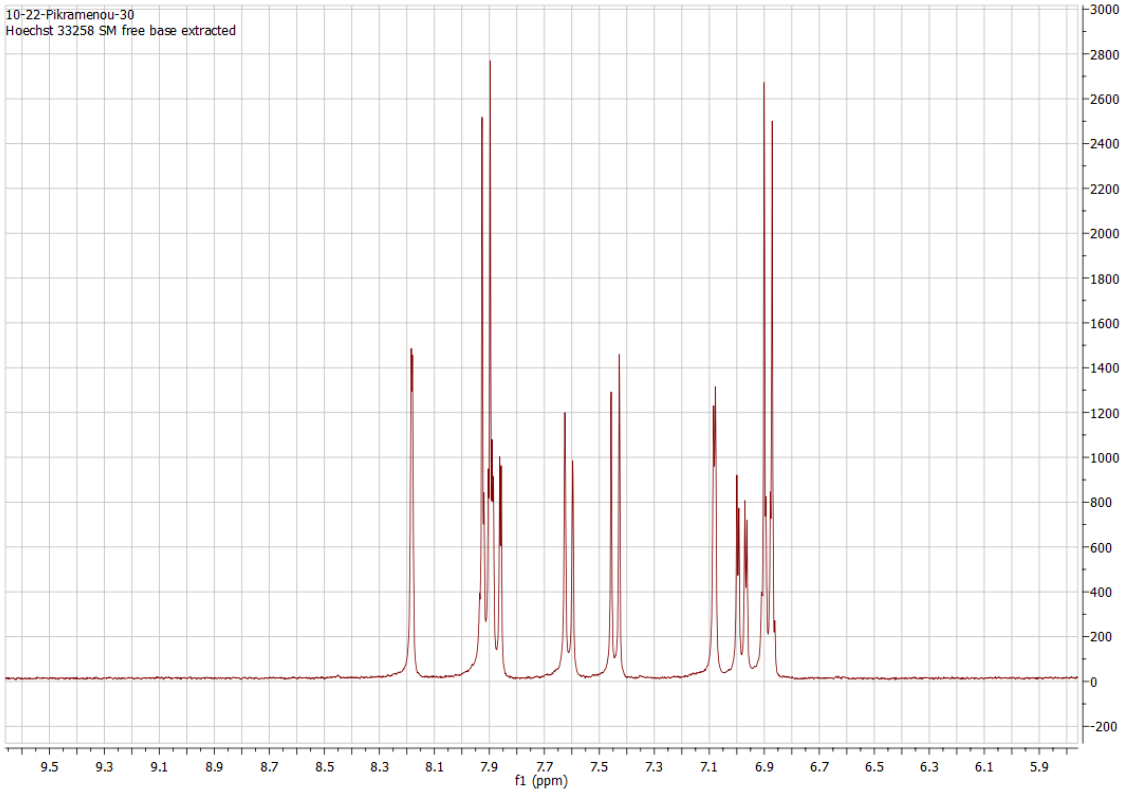

Figure A.2: ^{1}H NMR designations of Hoechst 33258 in MeOD (aromatic)

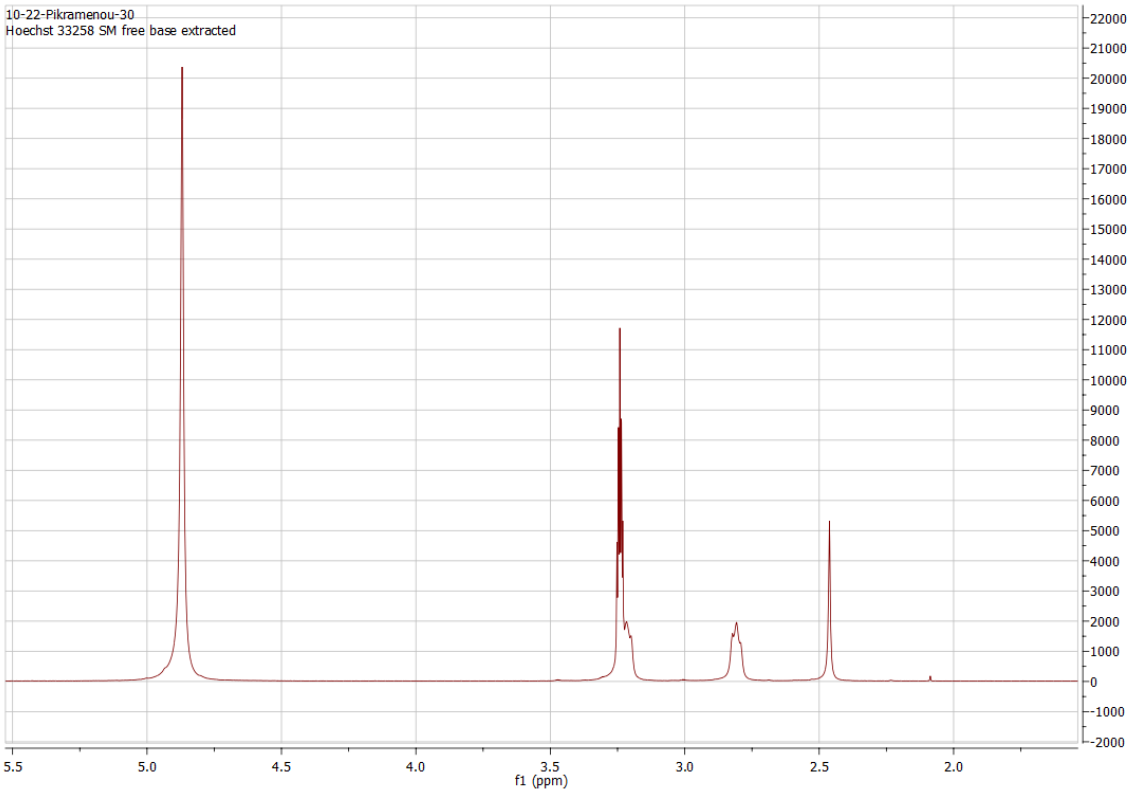

Figure A.3: ^{1}H NMR designations of Hoechst 33258 in spectrum (aliphatic)

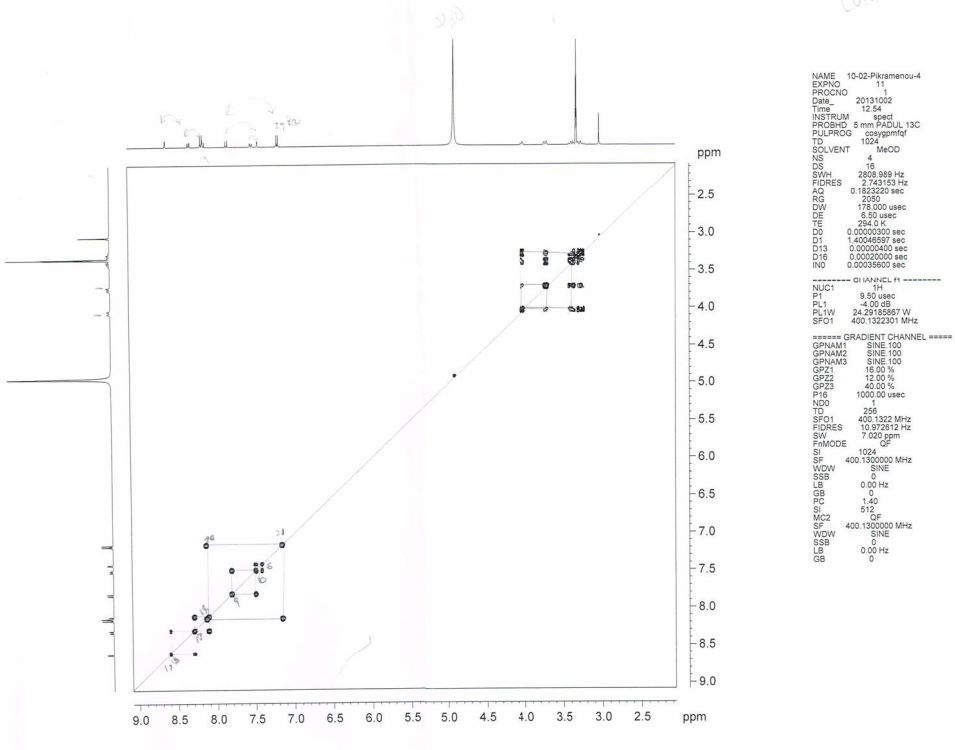

Figure A.4: ^{1}H, ^{13}C COSY NMR spectrum of Hoechst 33258, MeOD

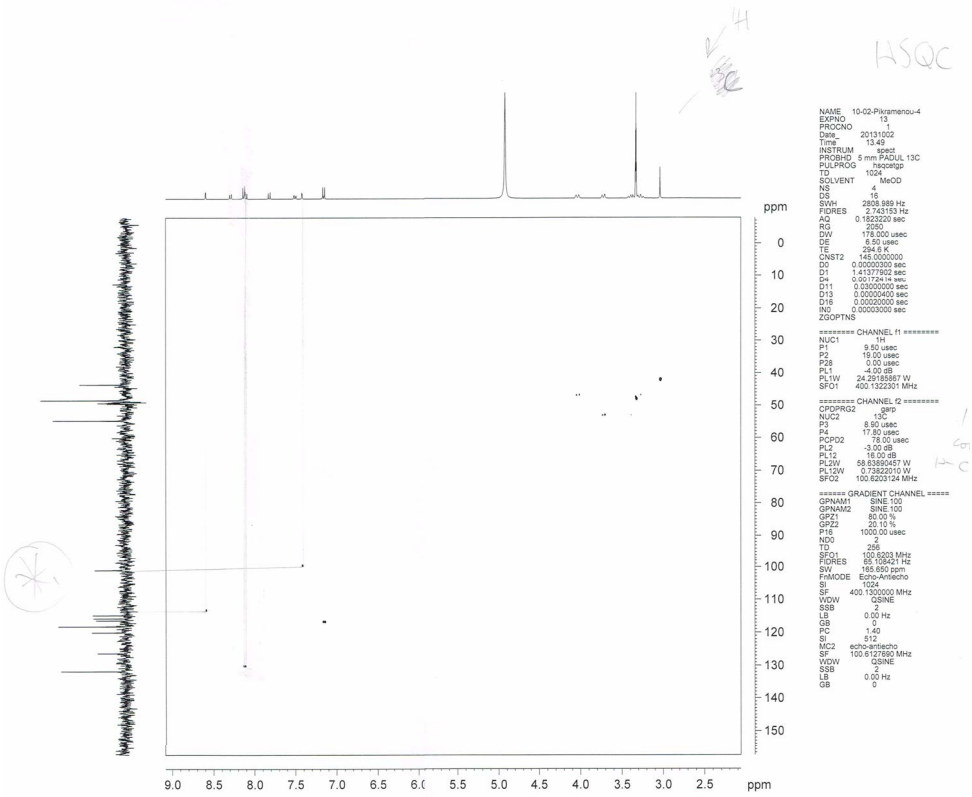

Figure A.5: ^{1}H, ^{13}C HSQC NMR spectrum of Hoechst 33258, MeOD

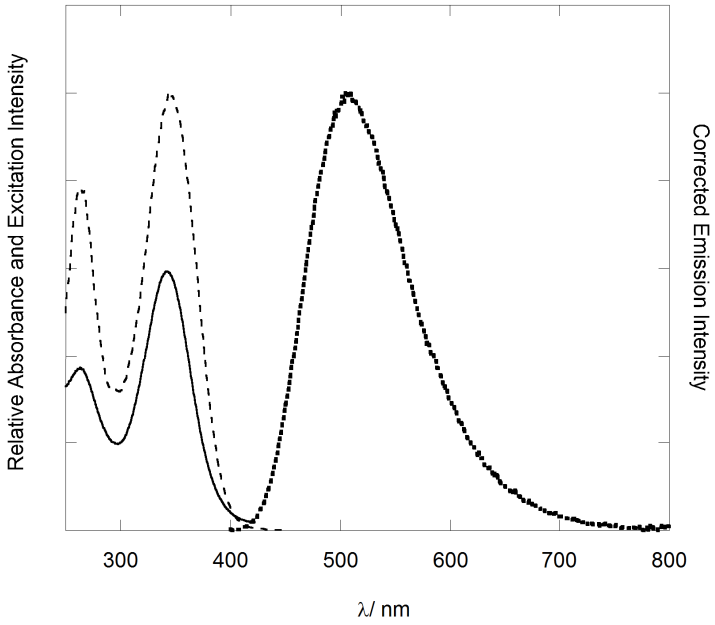

Figure A.6: (a) UV-Vis absorption spectrum of ***Hoechst 33258*** *in water (solid line) and steady-state luminescence emission spectrum (dashed line). (λ_{exc} = 350 nm). (b) Excitation spectrum of* ***Hoechst 33258*** *in water (λ_{em} = 500 nm). Spectra corrected for instrument response. All solutions measured at 1.3 μM concentration.*

B

Synthesis and Characterisation of HoechstSS

The first derivatisation of the Hoechst 33258 incorporates a disulphide group attached to the OH terminal of the Hoechst 33258 molecule for binding to the gold surface (Figure B.1). Referred to as HoechstSS (HSS), this derivative was synthesised by the ester coupling reaction of Hoechst 33258 with α-lipoic acid (Figure B.1). In brief a solution of α-lipoic acid (0.155 mg, 0.75 mmol) and 1-Hydroxybenzotriazole hydrate (0.57 mg, 0.37 mmol) in dry DMF (40 ml) was cooled to 0-5 °C, upon which 1-ethyl-3-(3-(dimethylaminopropyl)carbodiimide (EDC) (116 mg, 0.75 mmol) was added and stirred, (ca. 20 min). A solution of triethylamine (0.420 μL, 3 mmol) was added to Hoechst 33258 Pentahydrate bis-benzimide (400 mg, 0.75 mmol) in dry DMF (20ml) cooled to 0-5 °C and stirred (ca. 20 min) was added to the reaction mixture. The solution was allowed to warm to room temperature and stirred overnight. The solvent was removed *in vacuo* to afford HoechstSS was filtered and dried, and used in the next step without further purification (62 mg, 21 % yield). Production of the HoechstSS was confirmed by ^{1}H and ^{13}C(^{1}H) NMR spectroscopy (Figure B.1) and mass spectrometry.

The HoechstSS complex was subject to decomposition after it was purified on a silica column, with the product fraction indicating the presence of the **Hoechst 33258** starting material after a few hours (NMR and mass spectrometry). This is possibly due to pH sensitivity and hydrolysis of the ester bond and although column purification was attempted on an alumina column, the issue was not rectified. The **HoechstSS** was therefore not purified further and as such NMR characterisation indicates the presence impurities in-

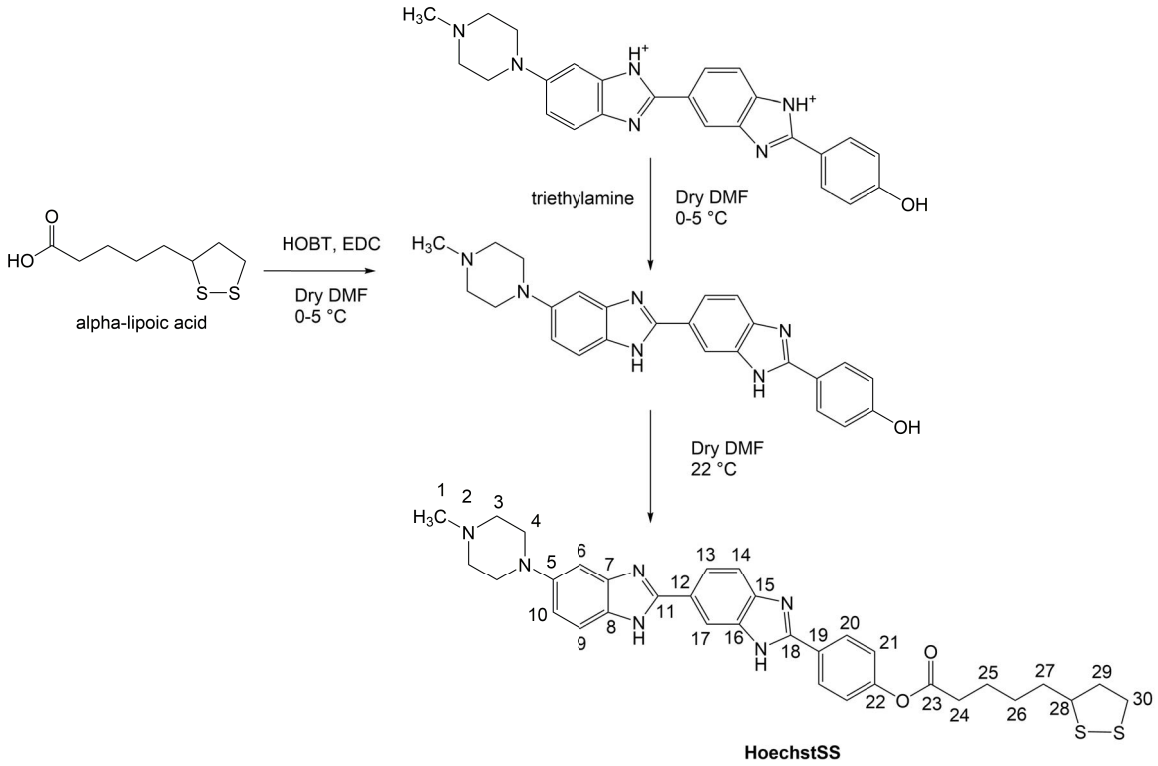

Figure B.1: Synthesis of the surface-binding HoechstSS (HSS) complex.

cluding HOBT remaining from its synthesis and the Hoechst 33258 starting material. An alternative derivative (**HoechstSAc**) was therefore synthesised.

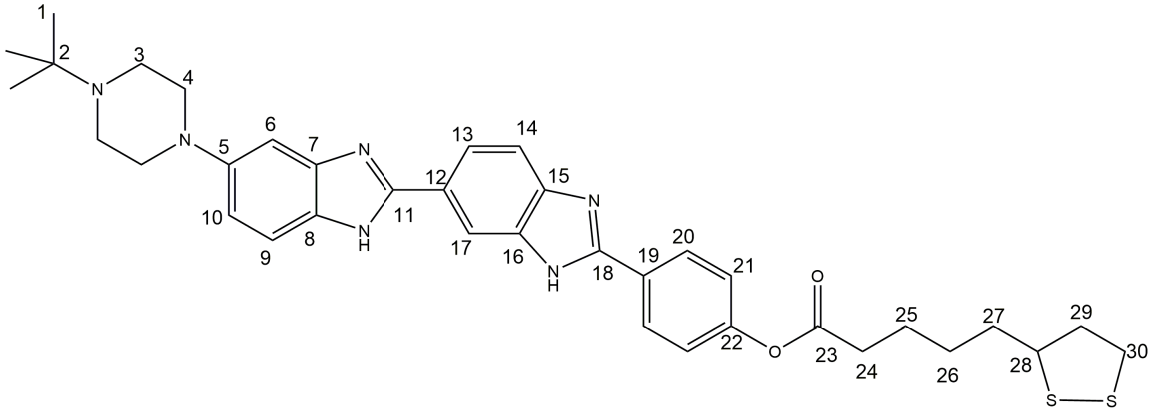

Figure B.2: ^{1}H NMR designations of HoechstSS in spectrum

B.1 NMR Spectra of HoechstSS

Production of the HoechstSS was confirmed by ^{1}H and ^{13}C(^{1}H) NMR spectroscopy (Figure B.1). ^{1}H NMR δ_H (300 MHz, MeOD) 1.40-1.66 (m, H-25,27), 1.68-1.81 (m, H-26,29), 2.17 (2H, t, J= 7.3, H-24), 2.27-2.36 (m, H-29), 2.87(3H, s, H-1), 2.93-3.08 (m, H-3/4,19), 3.14-3.30 (m, H-3/4), 3.38-3.49 (m, H-28), 6.84 (2H, J= 8.8, H-21), 7.15-7.26 (m, H-6,10), 7.53 (1H, J= 8.6, H-14), 7.55-7.65 (m, H-9), 7.80 (1H, dd, J= 1.4, 8.6), 7.83-7.90 (m, H-20), 8.10 (1H, s, H-17). ^{13}C NMR δ_C(100 MHz, MeOD) 25.6, 28.6, 30.3, 33.4, 34.5, 35.6, 35.9, 37.9, 39.9, 41.9, 42.6, 53.7, 55.0, 56.2, 101.5, 110.9, 112.5, 112.9, 114.8, 115.1, 115.3, 115.6, 117.4, 120.1, 121.1, 121.4, 122.2, 123.3, 124.2, 124.2, 127.6, 127.8, 128.4, 138.4, 140.6, 142.9, 147.0, 152.4, 154.4, 160.1, 163.5, 176.9.

H-14, H-17 integrate for 1 proton and H-24 for 2 protons, thus the relative number of hydrogens suggest HoechstOH and α-lipoic acid have bonded together. H-24 is also shifted with respect to the α-lipoic acid starting material, indicating a different chemical environment i.e. due to the Hoechst 33258 (Figure A.1)

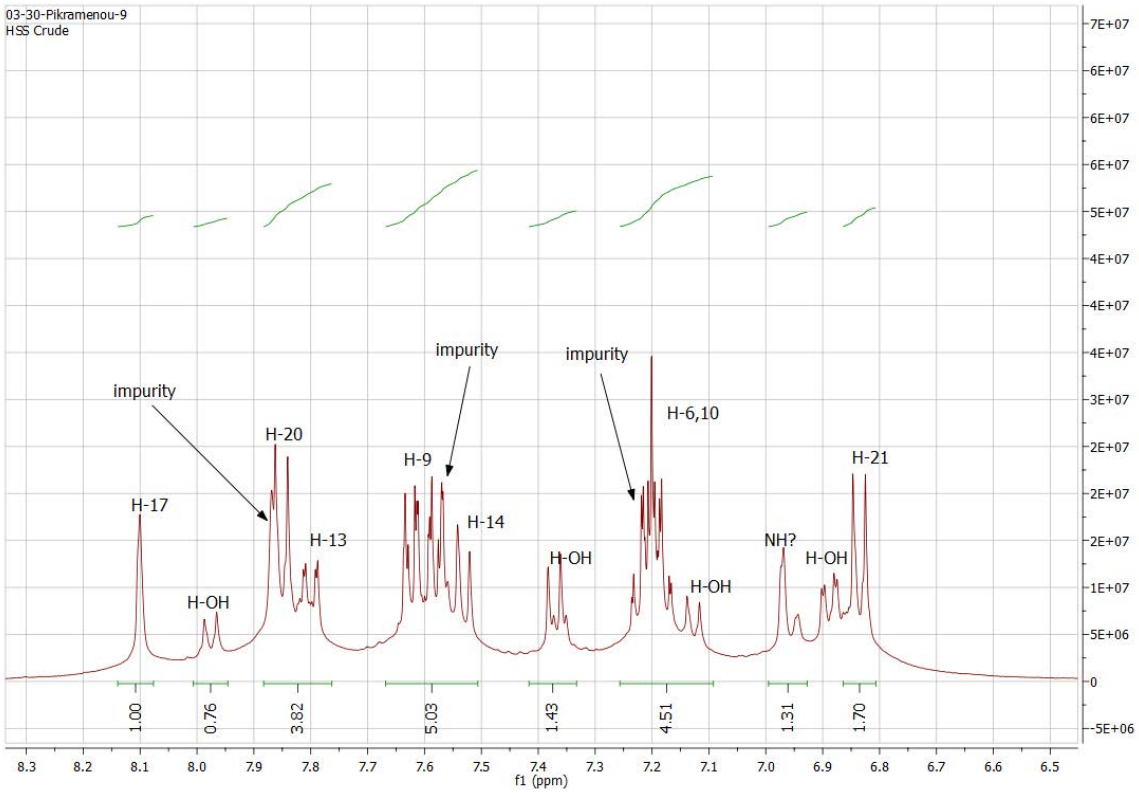

Figure B.3: ^1H NMR spectrum of HoechstSS in MeOD (aromatic)

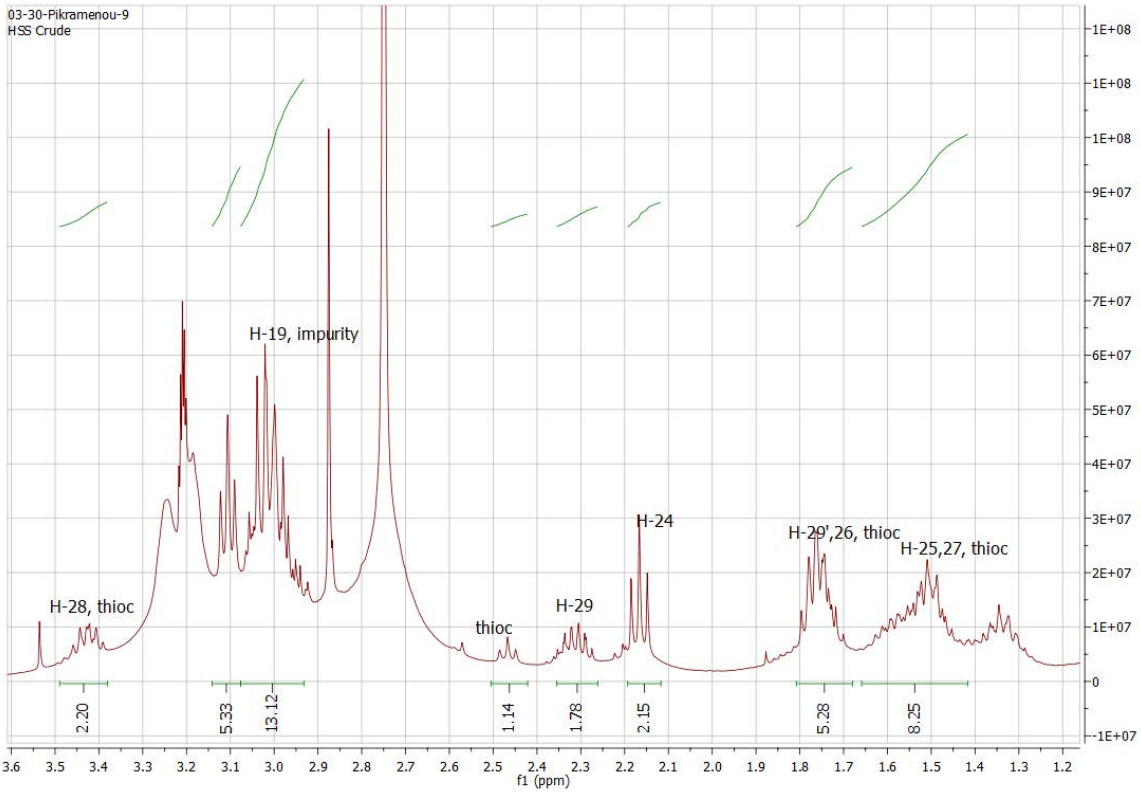

Figure B.4: ^1H NMR spectrum of HoechstSS in MeOD (aliphatic)

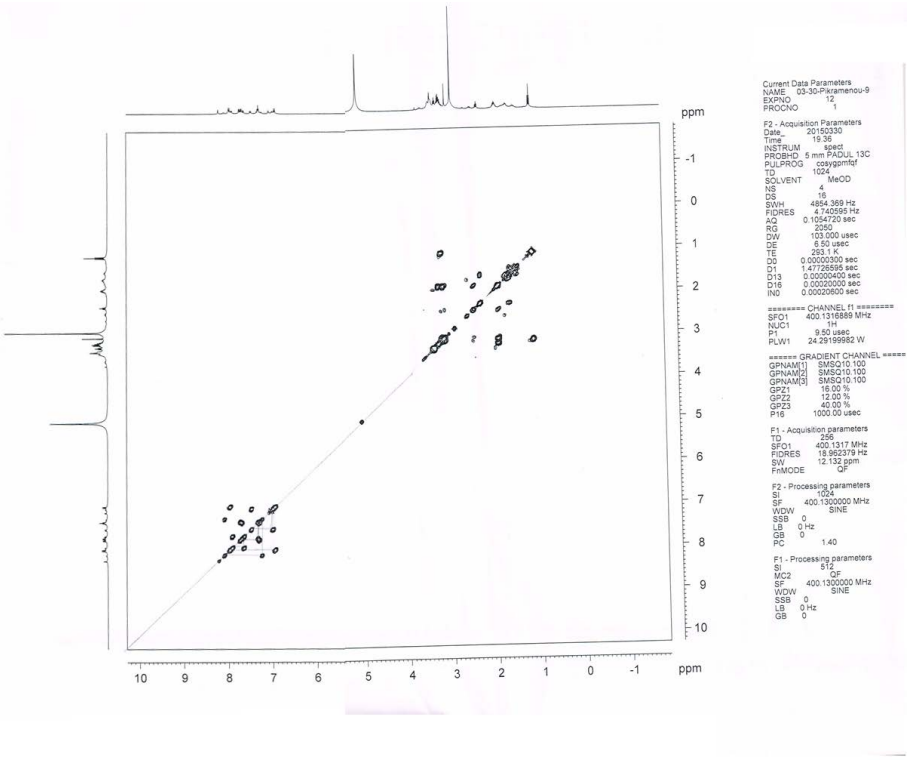

Figure B.5: ^{1}H, ^{13}C COSY NMR spectrum of HoechstSS, MeOD

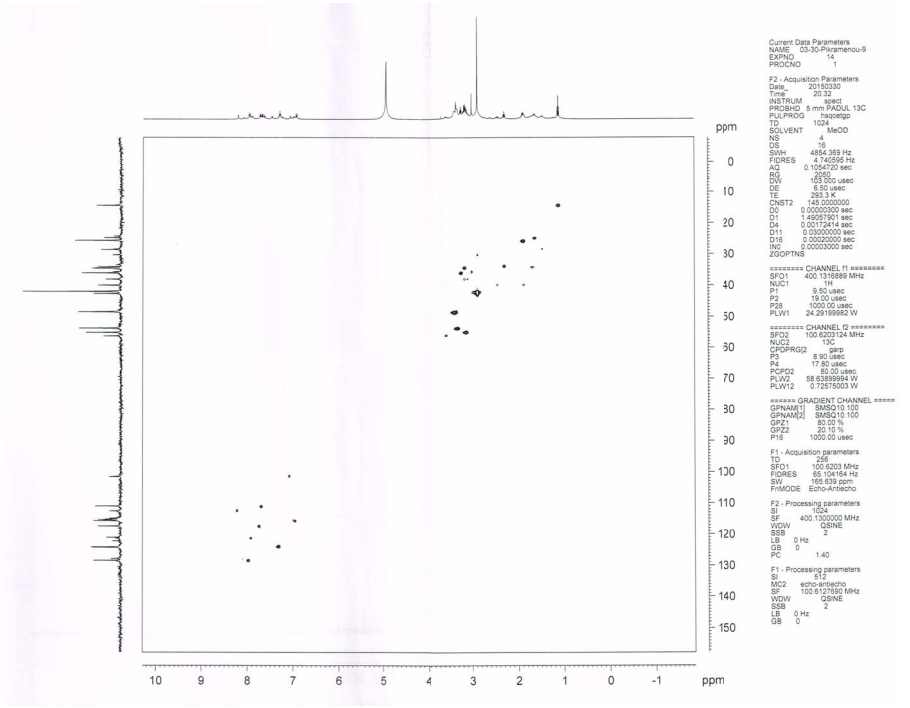

Figure B.6: ^{1}H, ^{13}C HSQC NMR spectrum of HoechstSS, MeOD

C

Synthesis and Characterisation of HoechstSH

HoechstSAc incorporates a surface-binding thiol group to the OH terminal of the **Hoechst 33258** for binding to the gold surface. The ancillary ligand was synthesised by the Williamson reaction of 6-bromohexene with thioacetic acid (**bromoSAc**) complexed to **Hoechst 33258** by refluxing in DMF. (Figure C.1).

In brief, thioacetic acid (1.86 g, 24.6 mmol, 2 eq.) was added to a solution of 6-bromo-1-hexene (2.00 g, 12.3 mmol, 1 eq.) in dry toluene (15 ml) with a catalytic amount of 1,1-azobis(cyclohexanecarbonitrile) (0.025 g). The solution was heated to reflux (130 °C) under N_2 for 30 minutes. The reaction was cooled to room temperature and quenched with $NaHCO_3$(aq) (60 ml, 1 M). The organic layer was extracted in ethyl acetate (120 ml), washed with aqueous sodium bicarbonate (60 ml, 1 M), dried over Na_2SO_4 and filtered. Solvent was removed in vacu to afford S-(5-bromopentyl)-ethanethioate, a yellow oil (2.64 g, 90 % yield).

A solution of Hoechst 33258, pentahydrate(bis-benzamide) (0.150 g, 0.282 mmol, 1 eq. in dry DMF (20 ml) was heated to 60 °C under N_2 for 30 minutes. The reaction was cooled to room temperature and sodium hydride was added (0.135 g, 5.64 mmol, 20 eq.). The mixture was heated to 130 °C under N_2 for 30 minutes. A solution of S-(5-bromopentyl)-ethanethioate (0.190 g, 0.846 mmol, 3 eq.) in dry DMF (5 ml) was added dropwise and the mixture was stirred at 60 °C under N_2 overnight. The solvent was removed in vacuo. The crude product was purified by column chromatography (Silica, methanol: dichloromethane, 1:10) to afford the HoechstSAc as a dark yellow oil (0.035 g,

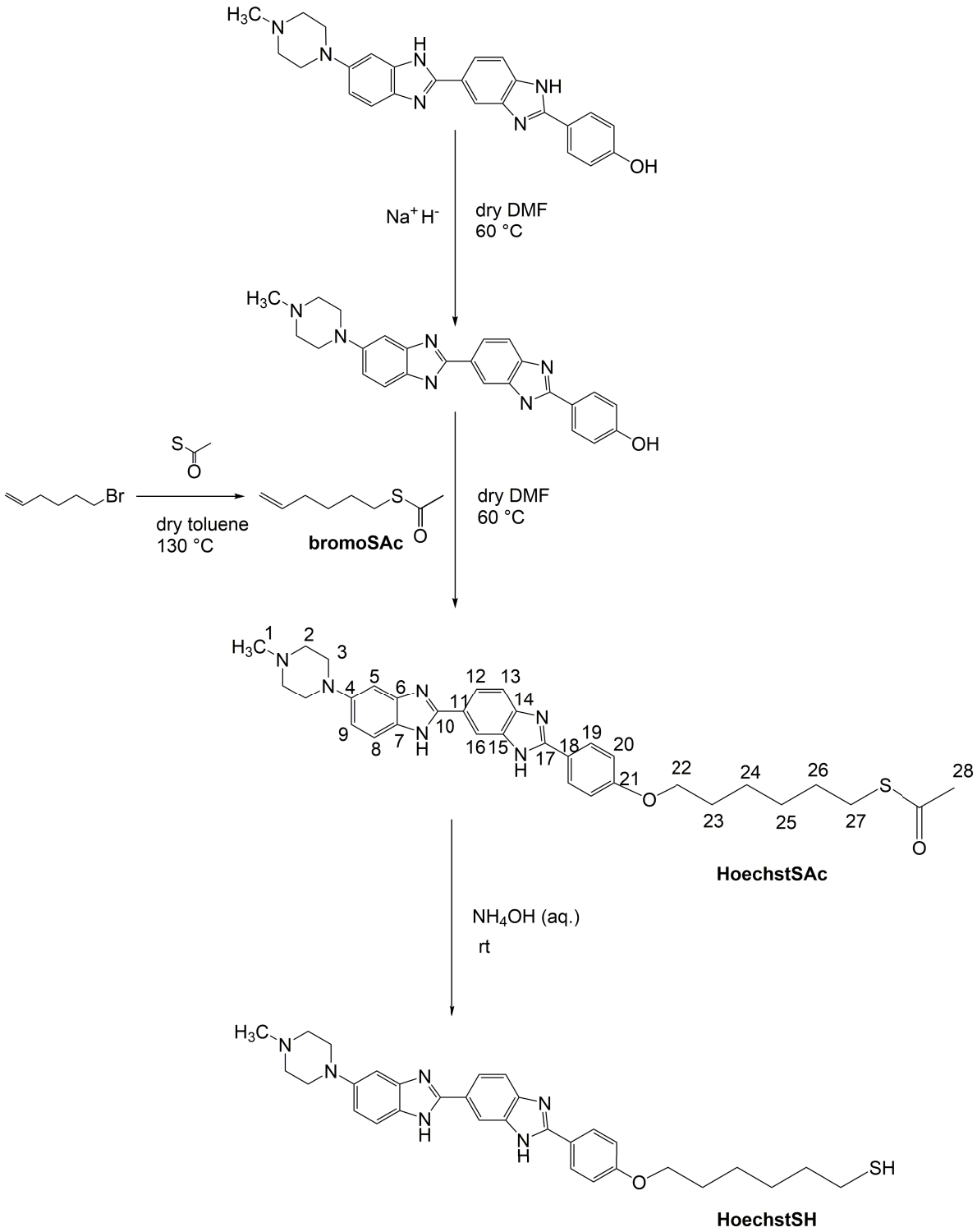

Figure C.1: Synthesis of the surface-binding HoechstSH (HSH) complex.

23 % yield, Rf = 0.28). The thiol group was finally unmasked in situ by thioester hydrolysis with aqueous ammonia (1:1) to afford **HoechstSH** for addition to gold nanoparticles. ε = 46,000 M^{-1} cm^{-1}. Successful production of **HoechstSH** was confirmed by confirmed by ^{1}H and ^{1}3 C^{1}H pendant NMR spectroscopy and mass spectrometry. HRMS for **HoechstSAc** [M+H] (583.2855), found 583.2858 (0.5 ppm). HRMS for **HoechstSH** [M+H] (540.2740), found 541.2750 (0.5 ppm)

C.1 NMR Spectra of HoechstSAc

Production of the HoechstSAc was confirmed by ^{1}H and ^{13}C(^{1}H) NMR spectroscopy (Figure C.1). ^{1}H NMR δ_H (300 MHz, MeOD)1.11-1.80 (8H, m, H-23, H-24, H-25, H-26), 2.19 (1H, s, SAc methyl), 2.62 (3H, s, H-1), 2.77 (2H, t, J= 6.3, H-22/27), 2.95 - 3.05 (4H, m, H-2/3), 3.19 - 3.28 (4H, m, H-2/3), 3.88 (2H, t, J=6.4, H-22/27), 6.93 (2H, d, J=8.7, H-20), 6.96 (1H, dd, J=2.3, H-9), 7.06 (1H, d, J=2.3, H-5), 7.42 (1H, d, J= 8.7, H-8), 7.57 (1H, d, J=8.7, H-13), 7.83 (1H, d, J=8.7, H-12), 7.91 (2H, d, J= 8.7, H-19), 8.13 (1H, s, H-16). ^{13}C NMR δ_C(100 MHz, MeOD) 25.3 (C-23/24/25/26), 27.6-29.8 (C-23/24/25/26), 28.3 (C-22/27) 28.9 (C-SAc methyl), 43.3 (C-H-1), 50.1 (C-2/3), 54.4 (C-2/3), 67.4 (C-22/27), 101.4 (C-5), 112.6 (C-16), 114.8 (C-20), 115.5 (C-8,9,13), 121.5 (C-12), 128.3 (C-19).

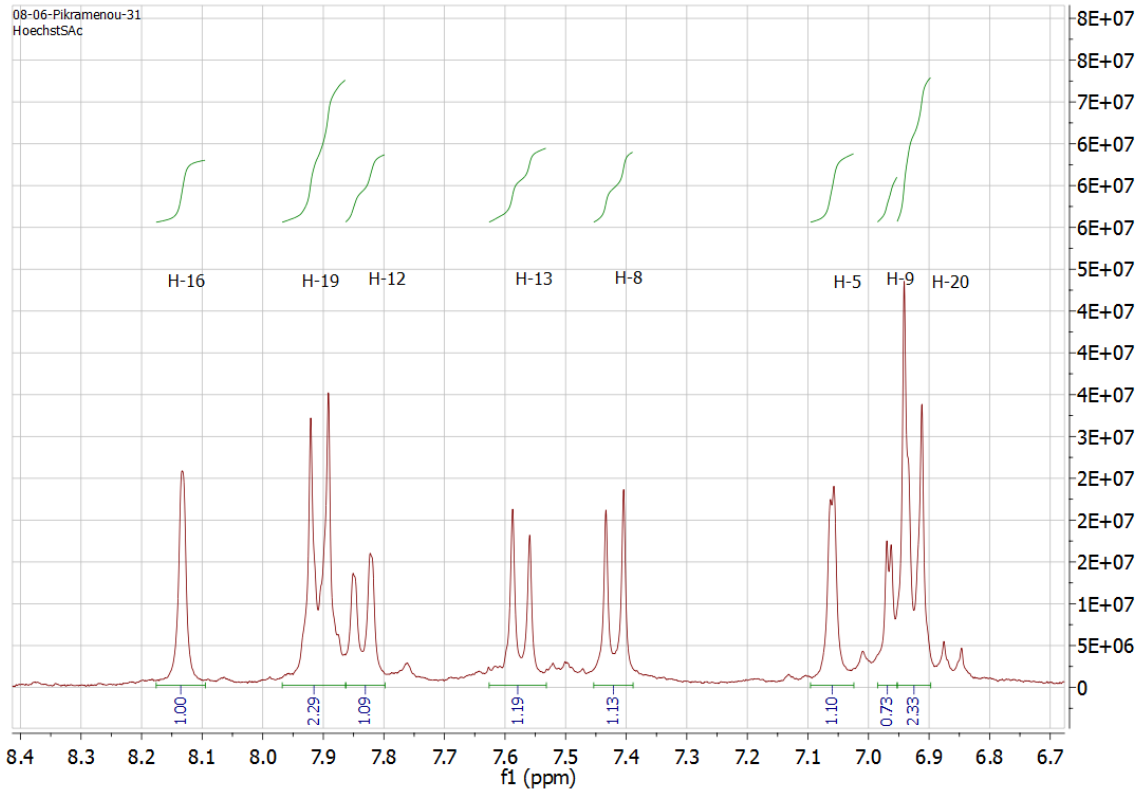

Figure C.2: ^{1}H NMR spectrum of HoechstSS in MeOD (aromatic)

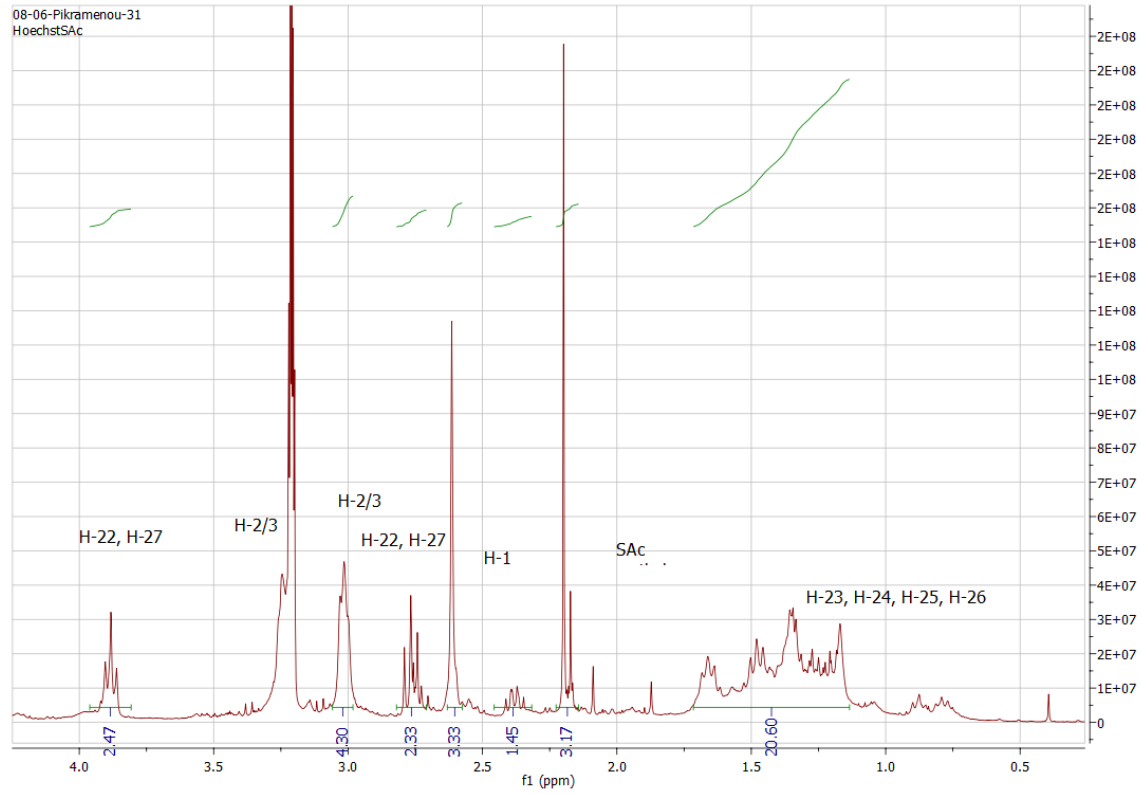

Figure C.3: ^{1}H NMR spectrum of HoechstSAc in MeOD (aliphatic)

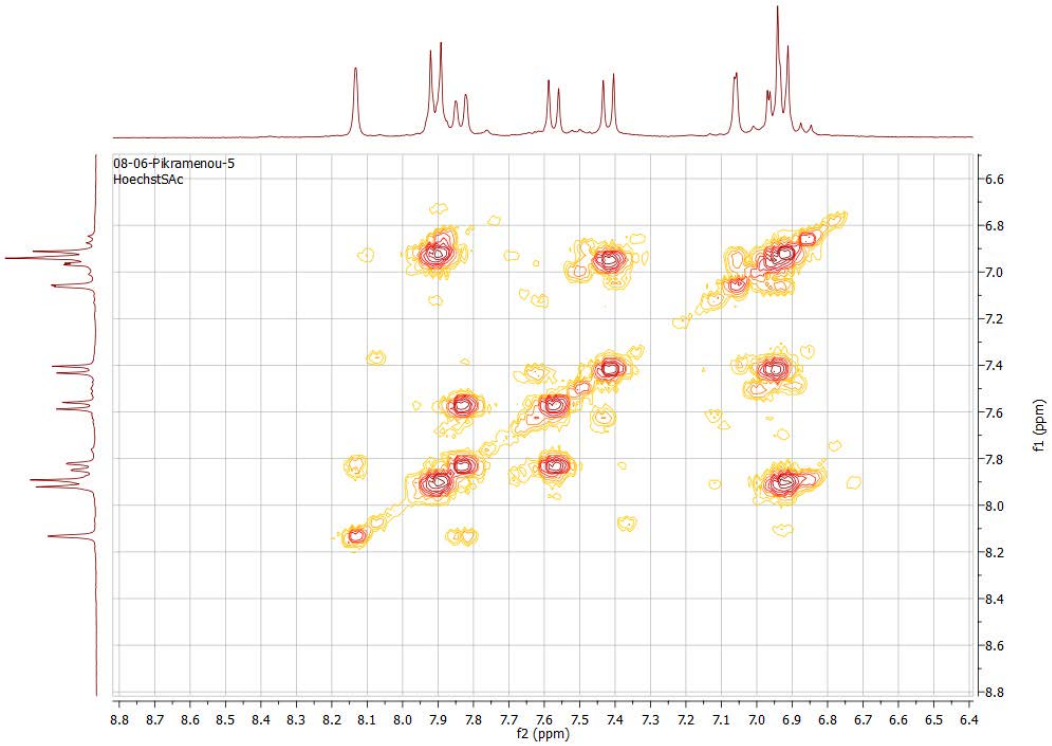

Figure C.4: ^{1}H, ^{13}C COSY NMR (aromatic) spectrum of HoechstSAc, MeOD

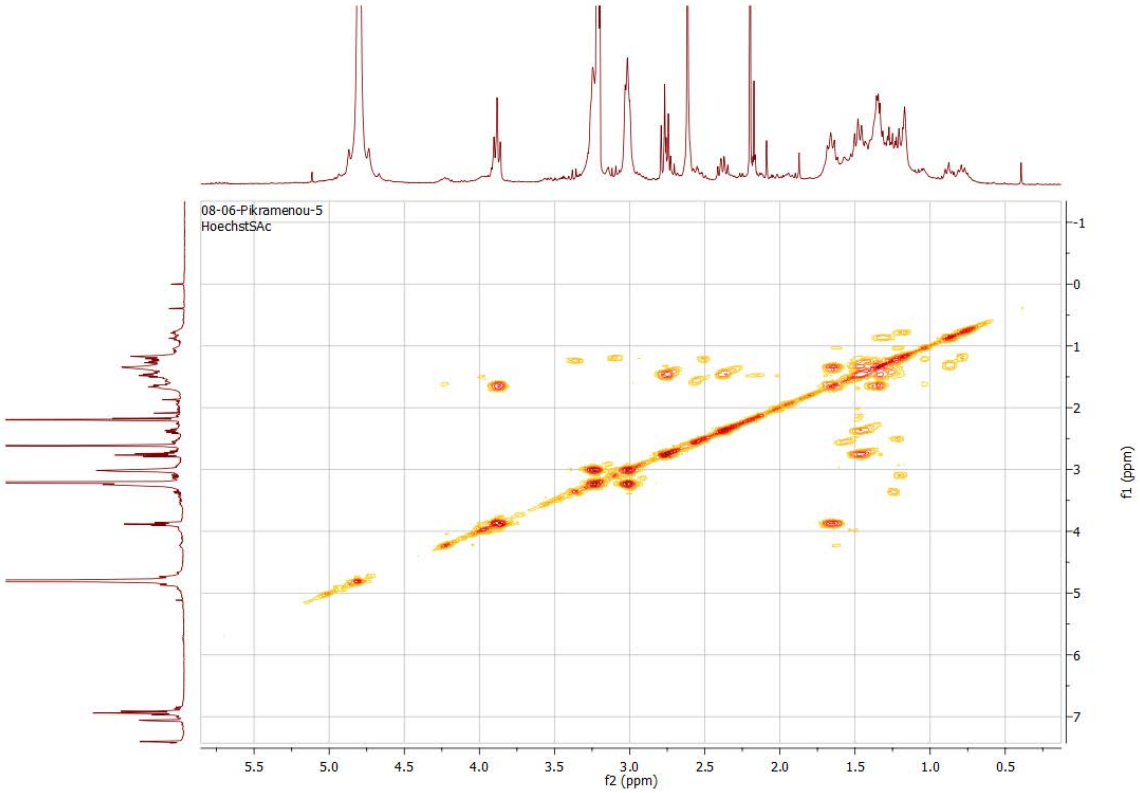

Figure C.5: ^{1}H, ^{13}C COSY NMR (aliphatic) spectrum of HoechstSAc, MeOD

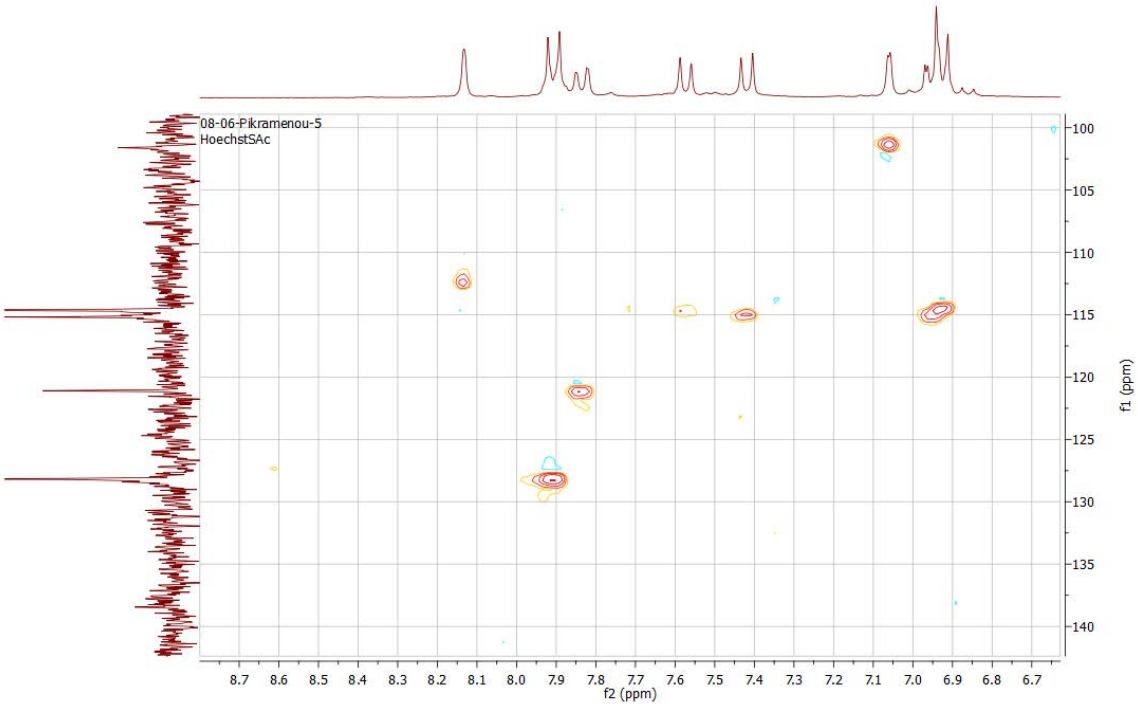

Figure C.6: ^{1}H, ^{13}C HSQC NMR (aromatic) spectrum of HoechstSAc, MeOD

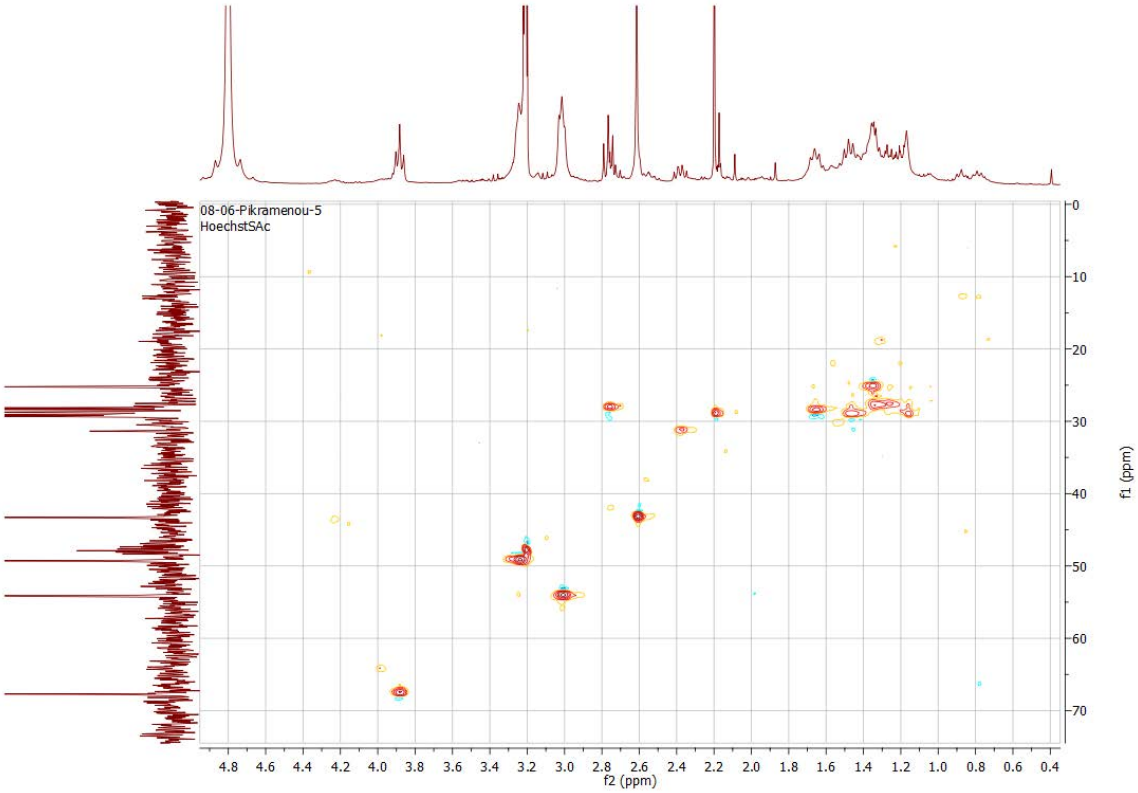

Figure C.7: ^{1}H, ^{13}C HSQC NMR (aliphatic) spectrum of BpyHex ligand, in CDCl3.

D

Photophysical Characterisation of HoechstSS and HoechstSH

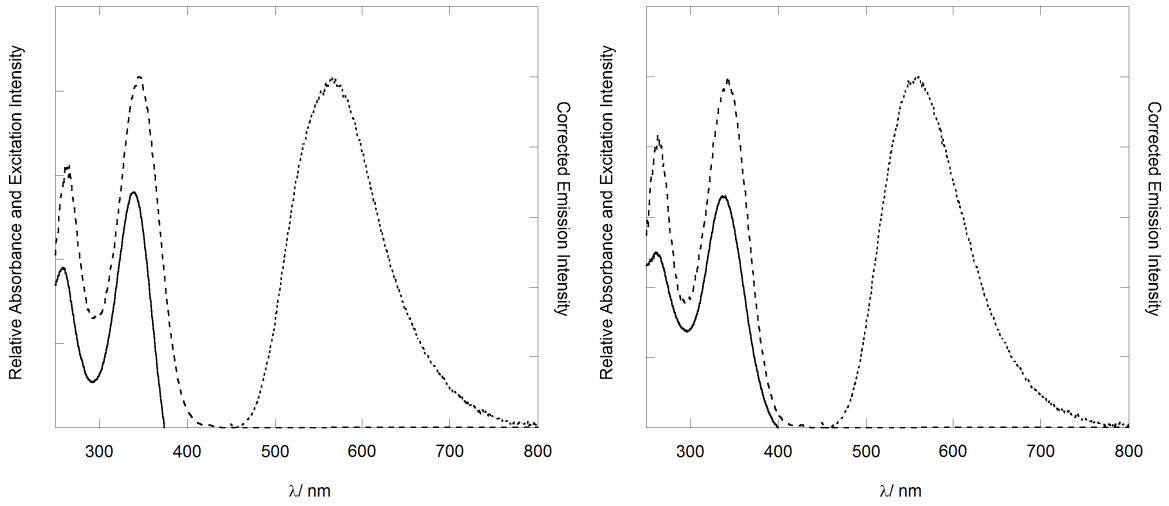

(a) HoechstSS *(b) HoechstSAc*

Figure D.1: UV-Vis absorption spectra (solid line) and steady-state luminescence excitation (dashed line) and emission spectra (bold dashed line) of HoechstSS (a) and HoechstSAc (b) in water (1μM). (λ_{exc} = 350 nm). (λ_{em} = 500 nm). Spectra corrected for instrument response.

E

Gold Nanoparticle Characterisation

E.1 Calculating Concentration of 13 nm Gold Nanoparticles

Mass of $HAuCl_4$ (49 % by assay) = 0.09889 g

Mass of Au = 0.49 x 0.09889 = 0.04846 g

No. moles of Au 0.04846 / 197 = 2.4597 x 10^{-4} moles

Concentration of Au = 2.4597 x 10^{-4} moles / 0.275 dm^3 8.944 x $^{-4}$ M

Estimated atomic radius of gold =140 pm

No. of gold atoms per 13 nm (diameter) nanoparticle (Assuming spherical nanoparticles): $\frac{4}{3}\pi r^3_{nanoparticle}$ / $\frac{4}{3}\pi r^3_{atom}$

$\rightarrow \frac{4}{3}\pi$ (6.5 x 10^{-9})^3 / $\frac{4}{3}\pi$ (140 x 10^{-12})^3

Concentration of 13 nm gold nanoparticles = 8.944 / 100,000 = **9 nM**

E.2 Characterisation of 13 nm Gold Nanoparticles

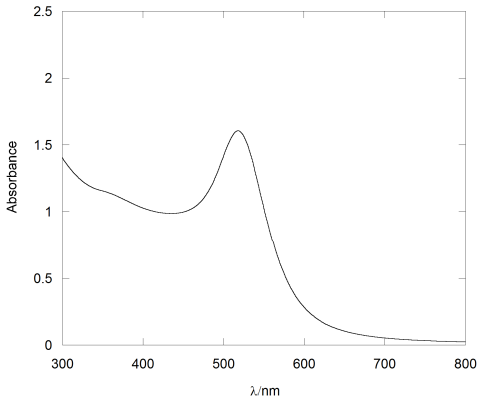

(a) UV-Vis absorption spectrum

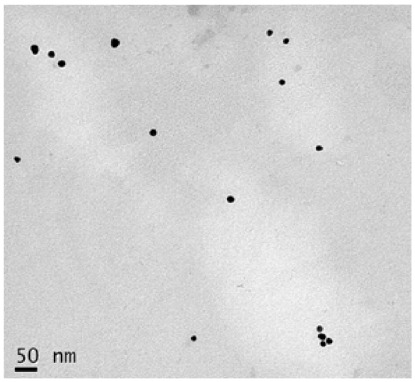

(b) Transmission Electron Micrograph

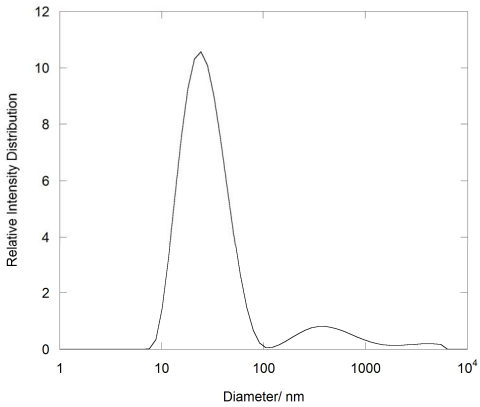

(c) DLS intensity distribution

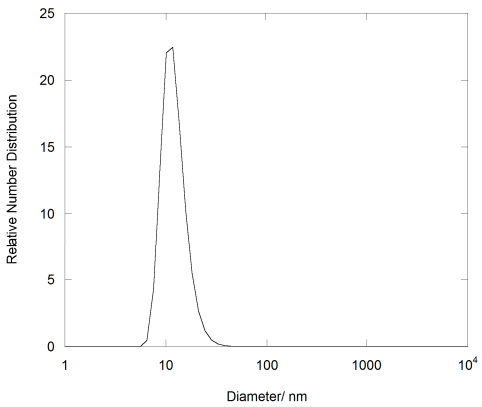

(d) DLS number distribution

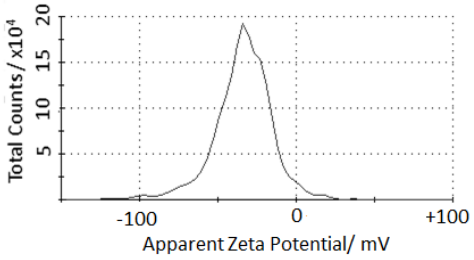

(e) Zeta potential distribution

Figure E.1: Characterisation of 13 nm citrate-stabilised gold nanoparticles: (a) UV-Vis absorption spectrum measured at 4.5 nM particle concentration, (b) TEM sample of nanoparticles at 1 nM particle concentration dried on to formvar-coated copper grids, (c) DLS intensity and (d) number distributions and (e) zeta potential measurements performed at 1 nM particle concentration.

Particle	Au13	Au13-T20	Au13-T20-HSH	Au13-Z	Au13-Z-HSH
DLS Intensity Distribution/ nm	28±14	43±22	36±13	34±13	41 ±18
DLS Number Distribution/ nm	12±4	17±5	19±6	18±5	20±6
Zeta Potential/ mV	-34±2	-16±5	-34±1	-69±3	-45±12
PDI	0.153	0.243	0.516	0.157	0.239

Table E.1: Summary of DLS intensity, DLS number and zeta potential measurements of 13 nm citrate-stabilised gold nanoparticles, ***Au13-T20****,* ***Au13-T20-HSH****,* ***Au13-Z*** *and* ***Au13-Z-HSH****. (All measurements performed at 1 nM particle concentration. All errors are quoted as ±1 SD).*

E.3 Calculating Concentration of 100 nm Gold Nanoparticles

During growth step one, 6 mL of the 13 nm gold nanoparticle seeds (9 nM) are diluted in 80 mL. Assuming no new seeds are formed, the concentration of the 25 nm particles formed = 0.7 nM.

In the second growth step 9 mL of the 25 nm gold nanoparticle seeds (0.7 nM) are diluted to 80 mL. Again, assuming no new seeds are formed, the concentration of the 50 nm particles formed = 80 pM.

In the final growth step, 40 mL of the 50 nm gold nanoparticles (80 pM) are diluted to 80 mL, rendering 100 nm gold nanoparticles at 40 pM.

F

UV-Vis Absorption Spectra of Gold Nanoparticles in Cell Media

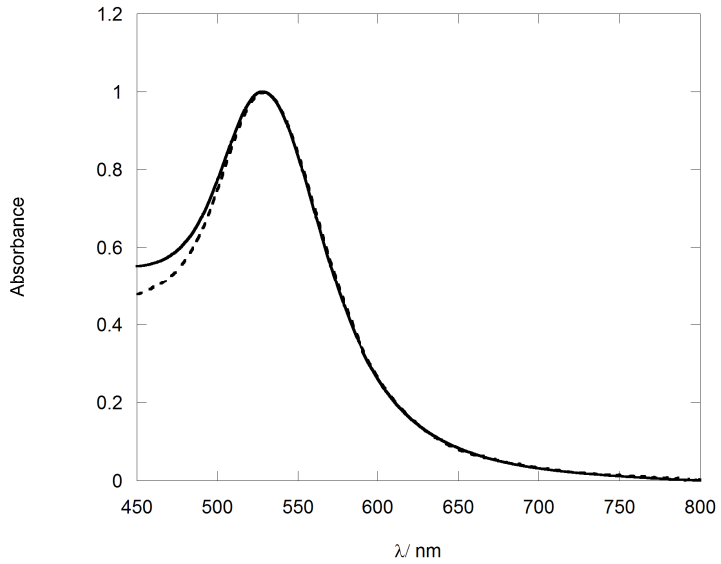

Figure F.1: Normalised UV-Vis Absorption Spectra of (3 ml, 2.5 nM) Au13-T20-HSH (dashed line), and following the addition of phenol red free cell media (solid line). Addition was done to achieve a 1 in 10 dilution (300 µl Au13-T20-HSH: 2700 µl cell media), analogous to concentrations/quantities used for cellular uptake studies.

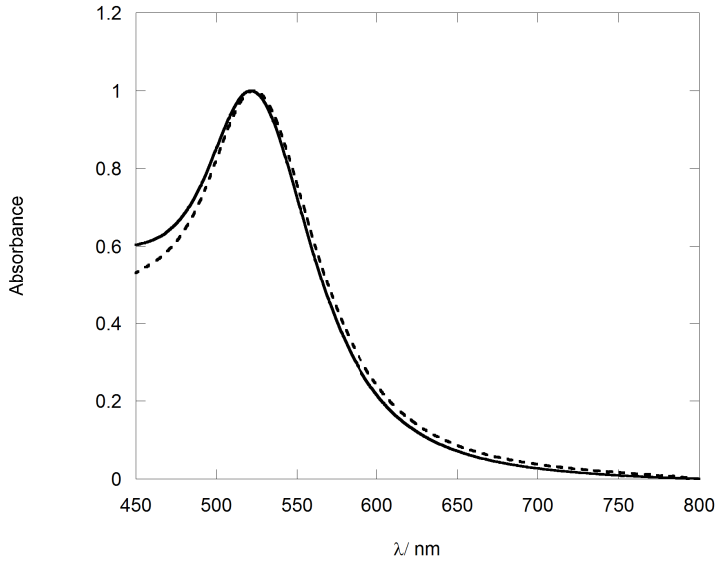

Figure F.2: Normalised UV-Vis Absorption Spectra of (3 ml, 2.5 nM) Au13-Z-HSH (dashed line), and following the addition of phenol red free cell media (solid line). Addition was done to achieve a 1 in 10 dilution (300 µl Au13-Z-HSH: 2700 µl cell media), analogous to concentrations/quantities used for cellular uptake studies.

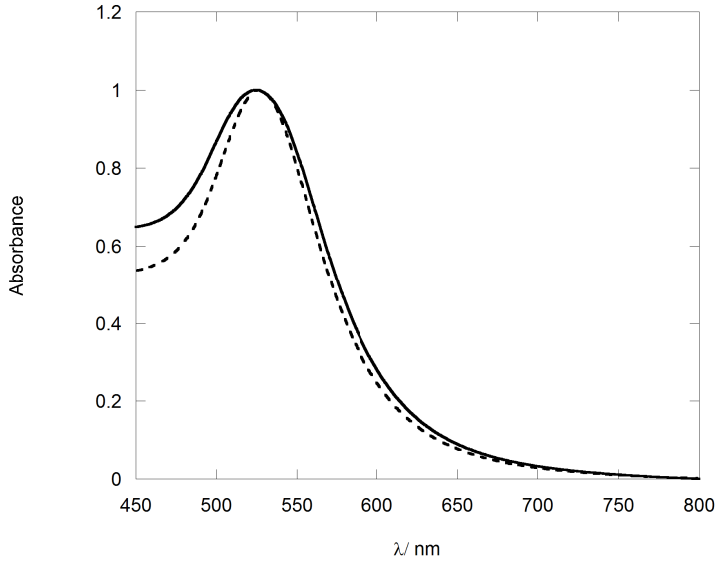

Figure F.3: Normalised UV-Vis Absorption Spectra of (3 ml, 2.5 nM) Au13-P-HSH (dashed line), and following the addition of phenol red free cell media (solid line). Addition was done to achieve a 1 in 10 dilution (300 µl Au13-P-HSH: 2700 µl cell media), analogous to concentrations/quantities used for cellular uptake studies.

G

Cellular Uptake of Au-T20-HSH, Au-Z-HSH and Au-P-HSH

G.1 Confocal Microscopy of Au13 in Cells

G.1.1 Confocal Microscopy of Au13 in A549 Cells - 24 Hour Incubation

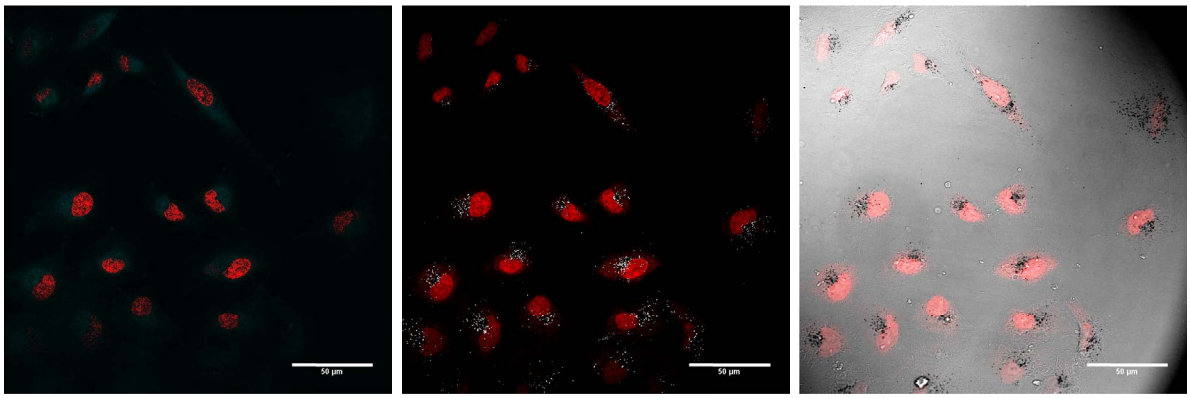

(a) *(b)* *(c)*

Figure G.1: Images of 13 nm citrate-stabilised gold nanoparticles in A549 cells monitored by confocal luminescence and reflection microscopy. Cells were incubated with nanoparticles at a concentration of 0.25 nm in complete cell media for 24 hours before fixing. (a) ***HoechstSH*** *and DRAQ5 overlay. (b) Reflection and DRAQ5 overlay. (c) Transmission and DRAQ5 overlay. Reflection image* λ_{exc} *= 633 nm,* λ_{em} *= 623-643 nm.* ***HoechstSH*** *luminescence, (blue channel),* λ_{exc} *= 405 nm,* λ_{em} *= 410-550 nm, DRAQ5, (red channel),* λ_{exc} *= 633 nm,* λ_{em} *= 640-800. (Scale bar 50* μm*).*

G.1.2 Confocal Microscopy of Au13 in HeLa Cells - 24 Hour Incubation

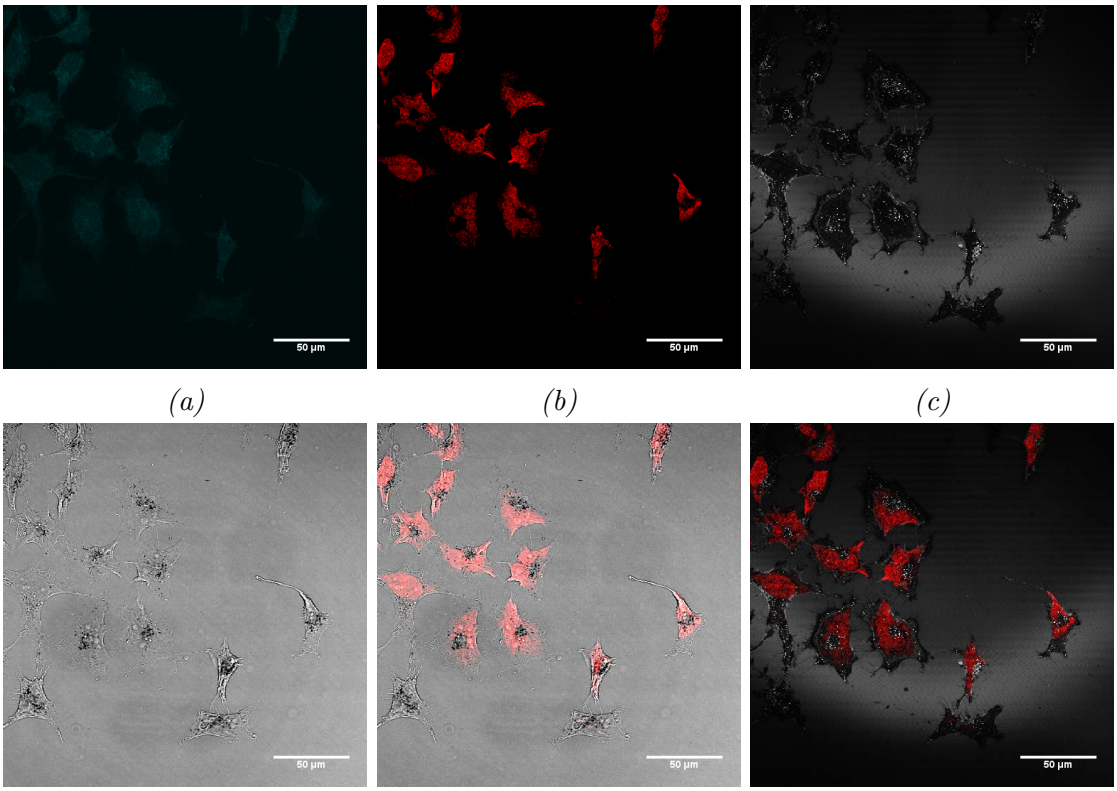

(a) *(b)* *(c)*

(d) *(e)* *(f)*

Figure G.2: Images of 13 nm citrate-stabilised gold nanoparticles in HeLa cells monitored by confocal luminescence and reflection microscopy. Cells were incubated with nanoparticles at a concentration of 0.25 nm in complete cell media for 24 hours before fixing. (a) ***HoechstSH*** *image. (b) DRAQ5 image. (c) Reflection image. (d) Transmission image. (e) Transmission and DRAQ5 overlay. (f) Reflection and DRAQ5 overlay. Reflection image* λ_{exc} *= 633 nm,* λ_{em} *= 623-643 nm.* ***HoechstSH*** *luminescence, (blue channel),* λ_{exc} *= 405 nm,* λ_{em} *= 410-550 nm, DRAQ5, (red channel),* λ_{exc} *= 633 nm,* λ_{em} *= 640-800. (Scale bar 50 µm).*

G.2 Confocal Microscopy of Au13-T20-HSH in Cells

G.2.1 Confocal Microscopy of Au13-T20-HSH in A549 Cells - 20 Minute Incubation

G.3 Confocal Microscopy of Au13-Z-HSH in Cells

G.3.1 Confocal Microscopy of Au13-Z-HSH in A549 Cells - 20 Minute Incubation

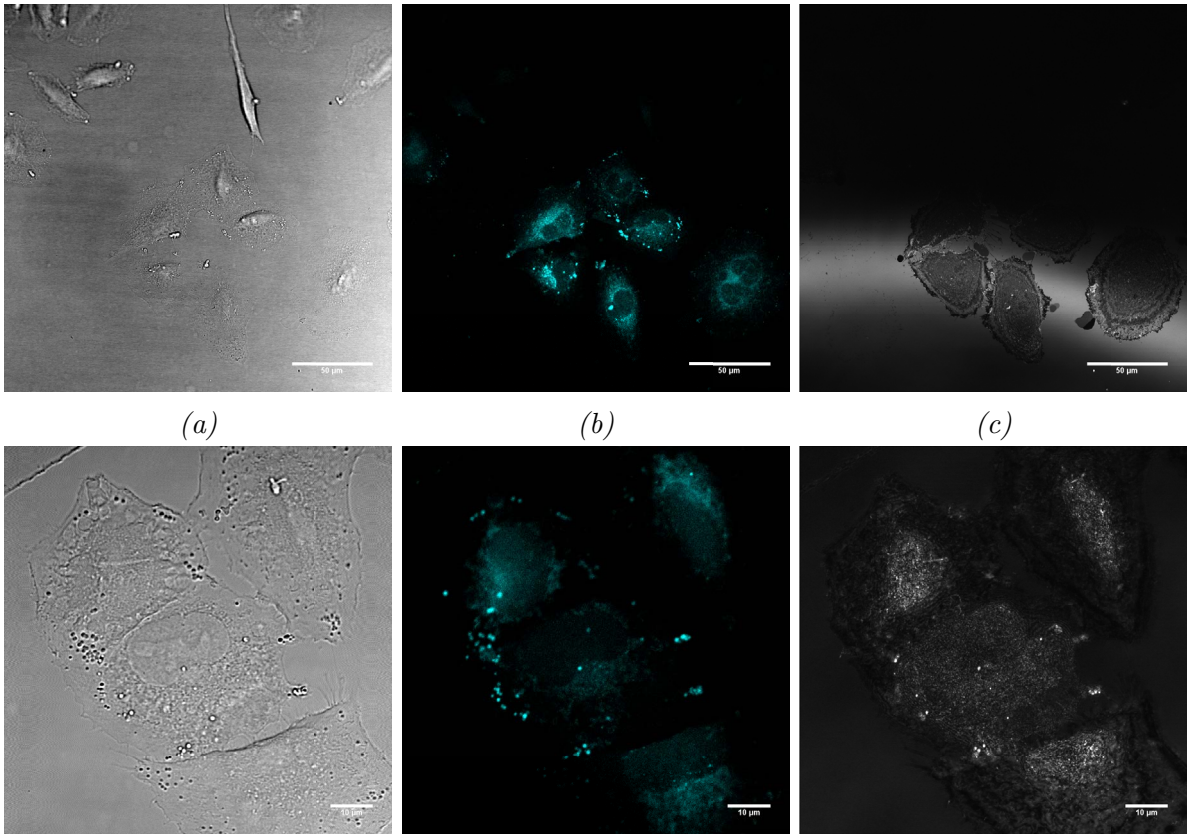

(a) *(b)* *(c)*

(d) *(e)* *(f)*

Figure G.3: Images of Au13-Zonyl-HSH nanoparticles in A549 cells monitored by confocal luminescence and reflection microscopy. Cells were incubated with ***Au13-Z-HSH*** *at a concentration of 0.25 nm in complete cell media for 20 minutes before fixing. (a), (b) and (c) - widefield views of cells with white light transmission, blue HoechstSH luminescence and reflection images respectively. (d), (e) and (f) - magnifications of more cells with white light transmission, blue HoechstSH luminescence and reflection images respectively. Nanoparticles are observed as dark spots, cyan (from the HoechstSH surface coating) spots and white spots respectively in these images. Reflection image λ_{exc} = 633 nm, λ_{em} = 623-643 nm, (c, f) HoechstSH luminescence, blue channel, λ_{exc} = 405 nm, λ_{em} = 405-550 nm. (Scale bar (a, b, c) = 50 µm, (d, e, f) = 10 µm)*

G.3.2 Confocal Microscopy of Au13-Z-HSH in A549 Cells - 24 Hour Incubation

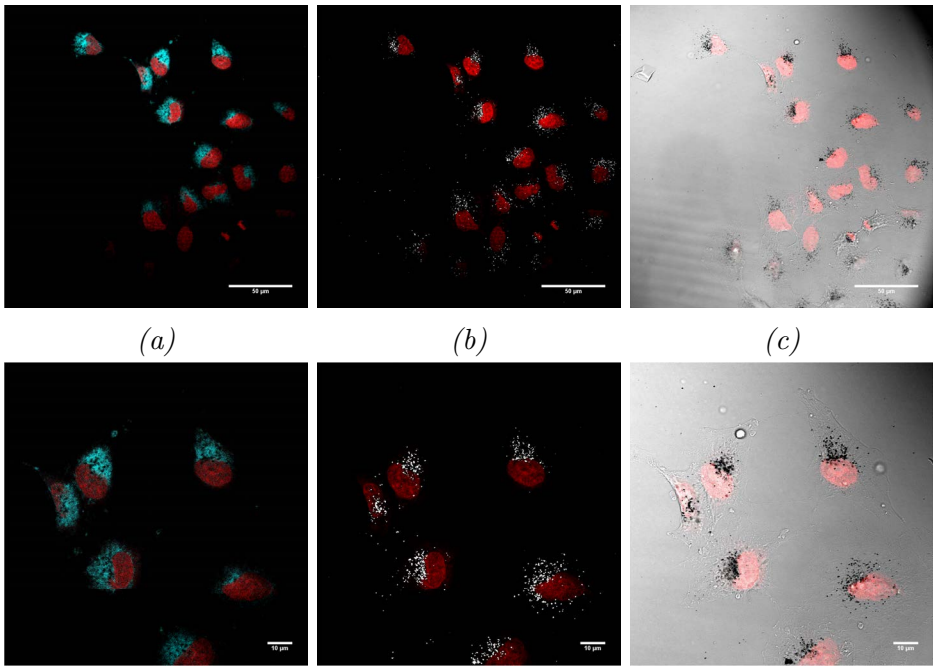

(a) *(b)* *(c)*

(d) *(e)* *(f)*

*Figure G.4: Images of **Au13-Z-HSH** nanoparticles in A549 cells monitored by confocal luminescence and reflection microscopy. Cells were incubated with **Au13-Z-HSH** at a concentration of 0.25 nm in complete cell media for 24 hours before fixing. (a - c) widefield, (d - f) magnifications. (a, d) **HoechstSH** and DRAQ5 overlay. (b, e) Reflection and DRAQ5 overlay. (c, f) Transmission and DRAQ5 overlay. Reflection image λ_{exc} = 633 nm, λ_{em} = 623-643 nm. **HoechstSH** luminescence, (blue channel), λ_{exc} = 405 nm, λ_{em} = 410-550 nm, DRAQ5, (red channel), λ_{exc} = 633 nm, λ_{em} = 640-800. (Scale bar 50 µm)*

G.3.3 Confocal Microscopy of Au100-Z-HSH in HeLa Cells - 90 Minute Incubation

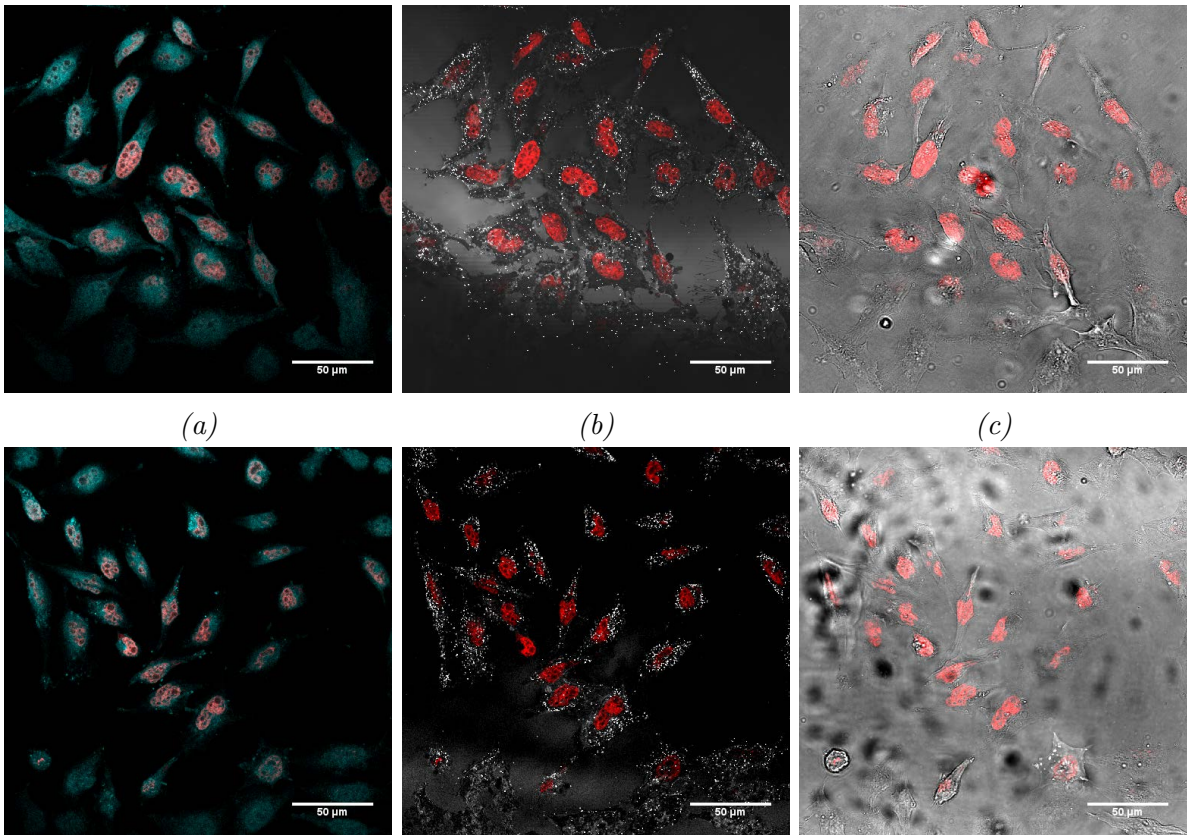

(a) *(b)* *(c)*

(d) *(e)* *(f)*

*Figure G.5: Images of **Au100-Z-HSH** nanoparticles in HeLa cells monitored by confocal luminescence and reflection microscopy. Cells were incubated with Au100-Z-HSH at a concentration of 0.10 pM in complete cell media for 90 min before fixing. (a-c) field-of-view 1. (d-f) field-of-view 2: (a, d) **HoechstSH** and DRAQ5 overlay. (b, e) Reflection and DRAQ5 overlay. (c, f) Transmission and DRAQ5 overlay. Reflection image λ_{exc} = 633 nm, λ_{em} = 623-643 nm. **HoechstSH** luminescence, (blue channel), λ_{exc} = 405 nm, λ_{em} = 410-550 nm, DRAQ5, (red channel), λ_{exc} = 633 nm, λ_{em} = 640-800. (Scale bar 50 µm)*

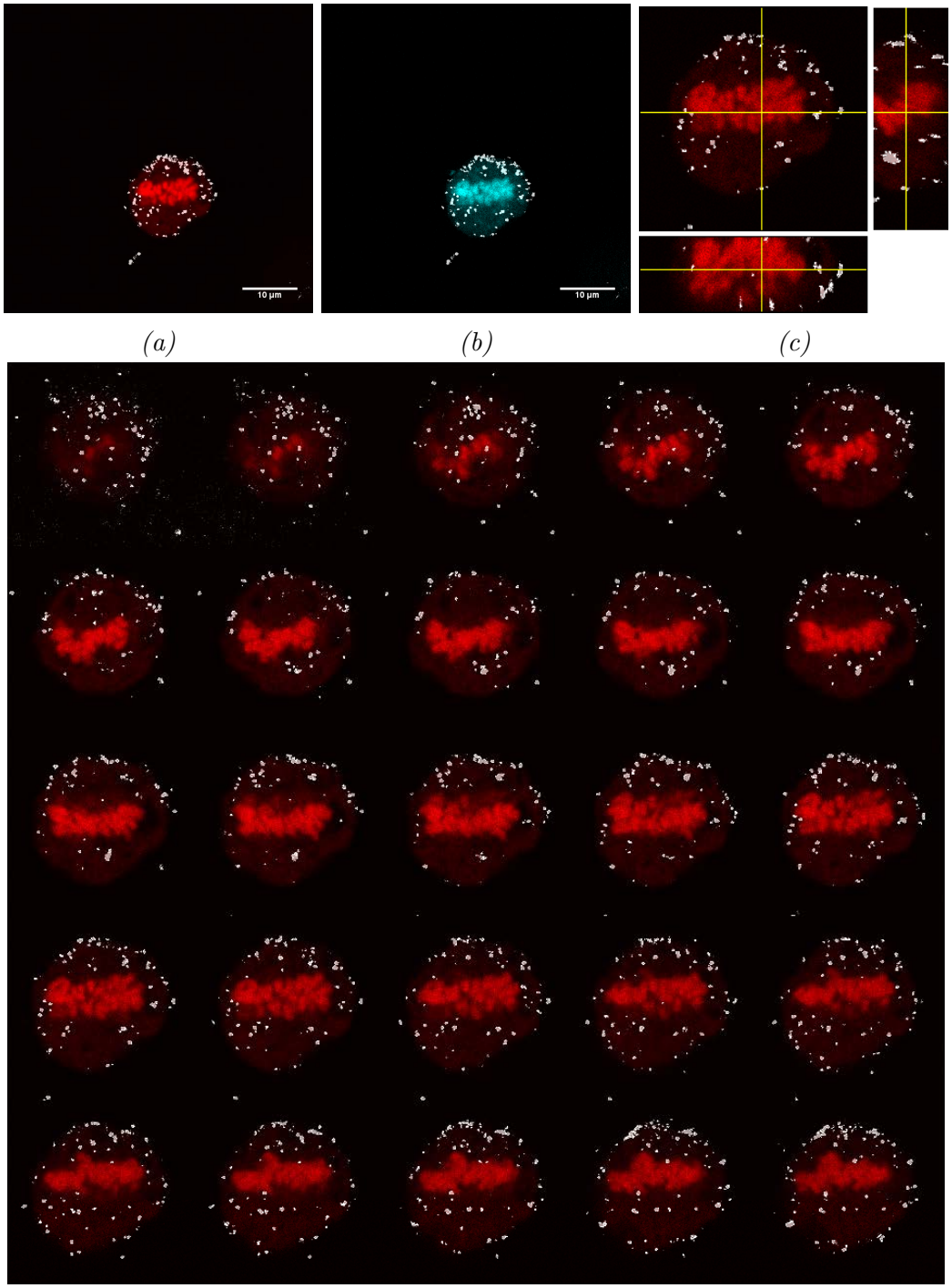

(a) *(b)* *(c)*

(d)

Figure G.6: Images of ***Au100-Z-HSH*** *nanoparticles in metaphasic HeLa cells monitored by confocal luminescence and reflection microscopy. Cells were incubated with* ***Au100-Z-HSH*** *at a concentration of 0.10 pM in complete cell media for 90 min before fixing. (a) reflection and DRAQ5 overlay. (b) reflection and* ***HoechstSH*** *overlay. (c) orthogonal view of reflection and DRAQ5 overlay. (d) Image montage of three-dimensional z-stack image slices. Reflection image,* λ_{exc} *= 633 nm,* λ_{em} *= 623-643 nm.* ***HoechstSH*** *luminescence, (blue channel),* λ_{exc} *= 405 nm,* λ_{em} *= 410-550 nm, DRAQ5, (red channel),* λ_{exc} *= 633 nm,* λ_{em} *= 640-800. (Scale bar 10 µm*

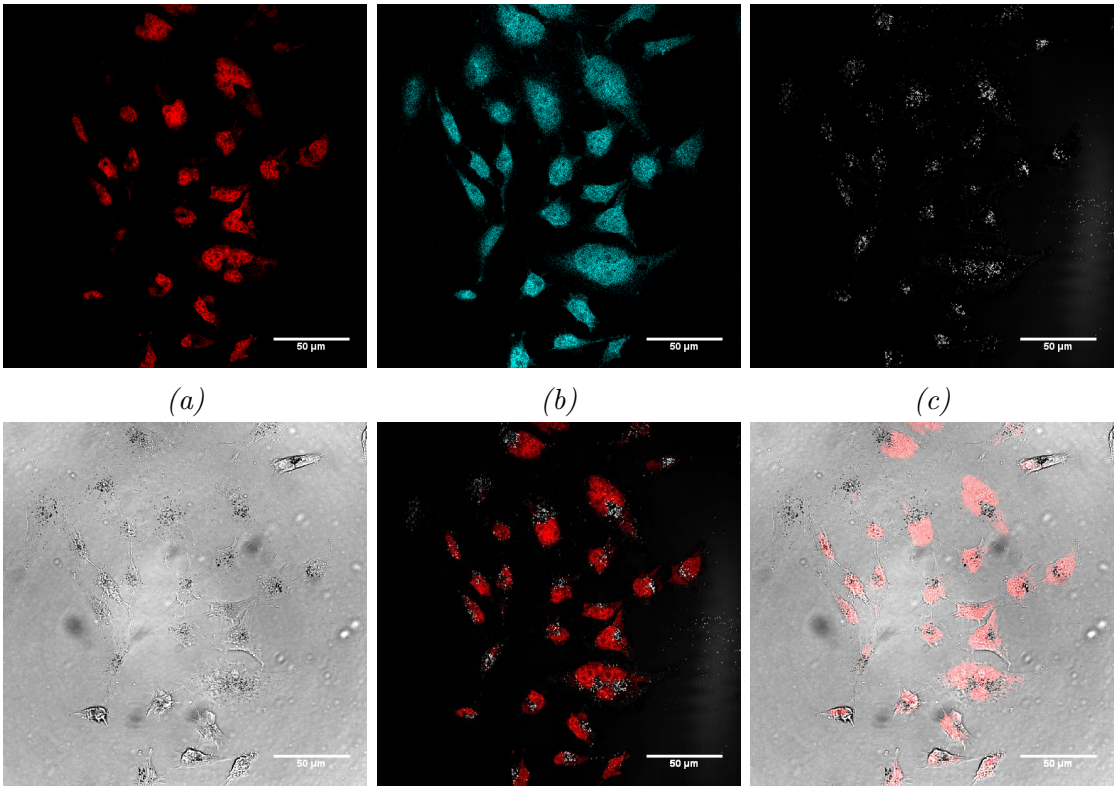

Figure G.7: Images of ***Au100-Z-HSH*** *nanoparticles in HeLa cells monitored by confocal luminescence and reflection microscopy. Cells were incubated with* ***Au100-Z-HSH*** *at a concentration of 0.10 pM in complete cell media for 24 hr before fixing. (a) DRAQ5 image. (b)* ***HoechstSH*** *image. (c) reflection image. (d) transmission brightfield image. (e) reflection and DRAQ5 overlay. (f) transmission and DRAQ5 overlay. Reflection image* λ_{exc} *= 633 nm,* λ_{em} *= 623-643 nm.* ***HoechstSH*** *luminescence, (blue channel),* λ_{exc} *= 405 nm,* λ_{em} *= 410-550 nm, DRAQ5, (red channel),* λ_{exc} *= 633 nm,* λ_{em} *= 640-800. (Scale bar (a) 50 µm) (b) 10 µm*

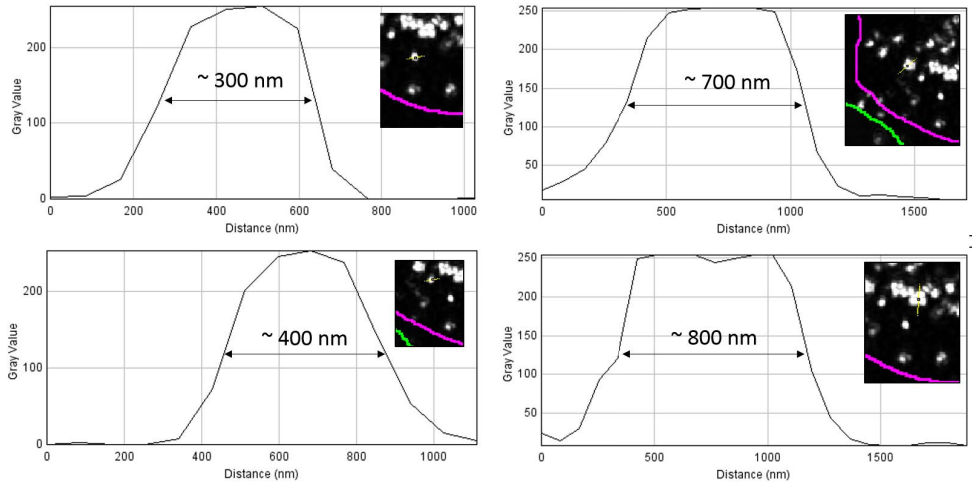

Figure G.8: Line intensity profiles of ***Au100-Z-HSH*** *in HeLa cells particles. (Confocal images shown in insets)*

.

G.4 Microscopy of Au-P-HSH in Cells

G.4.1 Confocal Microscopy of Au13-P-HSH in A549 Cells - 24 Hour Incubation

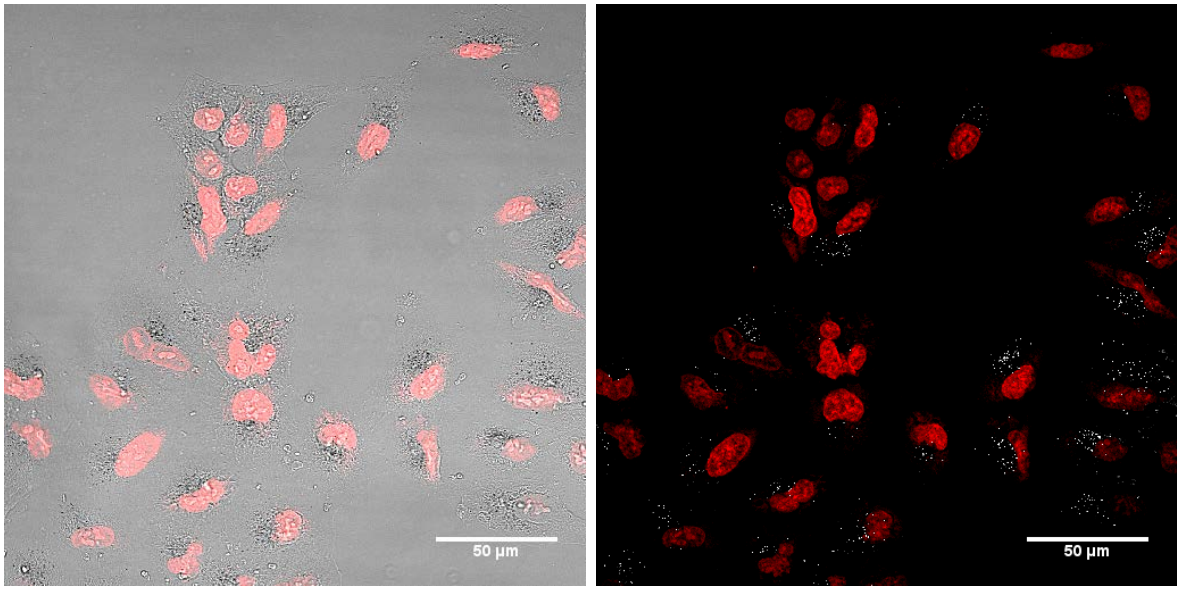

(a) *(b)*

*Figure G.9: Images of **Au13-P-HSH** nanoparticles in A549 cells monitored by confocal luminescence and reflection microscopy. Cells were incubated with **Au13-P-HSH** at a concentration of 0.25 nm in complete cell media for 24 hours before fixing. (a) Transmission brightfield and DRAQ5 overlay. (b) Reflection and DRAQ5 overlay. Reflection image λ_{exc} = 633 nm, λ_{em} = 623-643 nm. DRAQ5, (red channel), λ_{exc} = 633 nm, λ_{em} = 640-800. (Scale bar 50 µm)*

G.4.2 Confocal Microscopy of Au13-P-HSH in A549 Cells - 30 Minute incubation

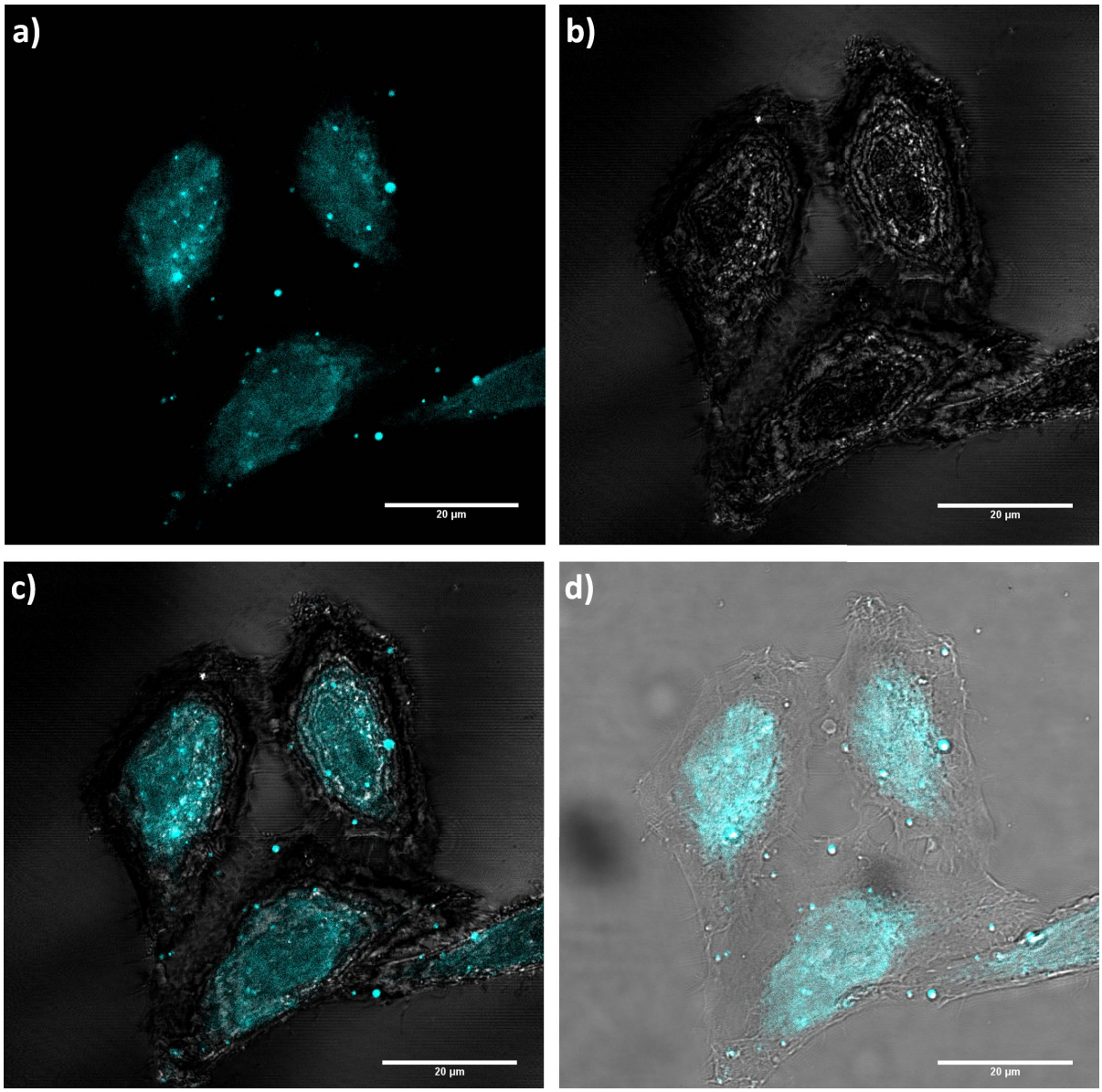

*Figure G.10: Images of **Au13-P-HSH** nanoparticles in HeLa cells monitored by confocal luminescence and reflection microscopy. Cells were incubated with **Au13-P-HSH** at a concentration of 0.25 nm in complete cell media for 30 hours before fixing. (a) **HoechstSH** channel image, (b) reflection channel image overlay, (c) HoechstSH and reflectance channel image overlay, (d) HoechstSH and transmission channel image overlay. Reflection image λ_{exc} = 633 nm, λ_{em} = 623-643 nm. **HoechstSH** luminescence, (blue channel), λ_{exc} = 405 nm, λ_{em} = 410-550 nm. (Scale bar 20 µm)*

G.4.3 Transmission Electron Microscopy of Au13-P-HSH in A549 Cells - 2 Hour Incubation

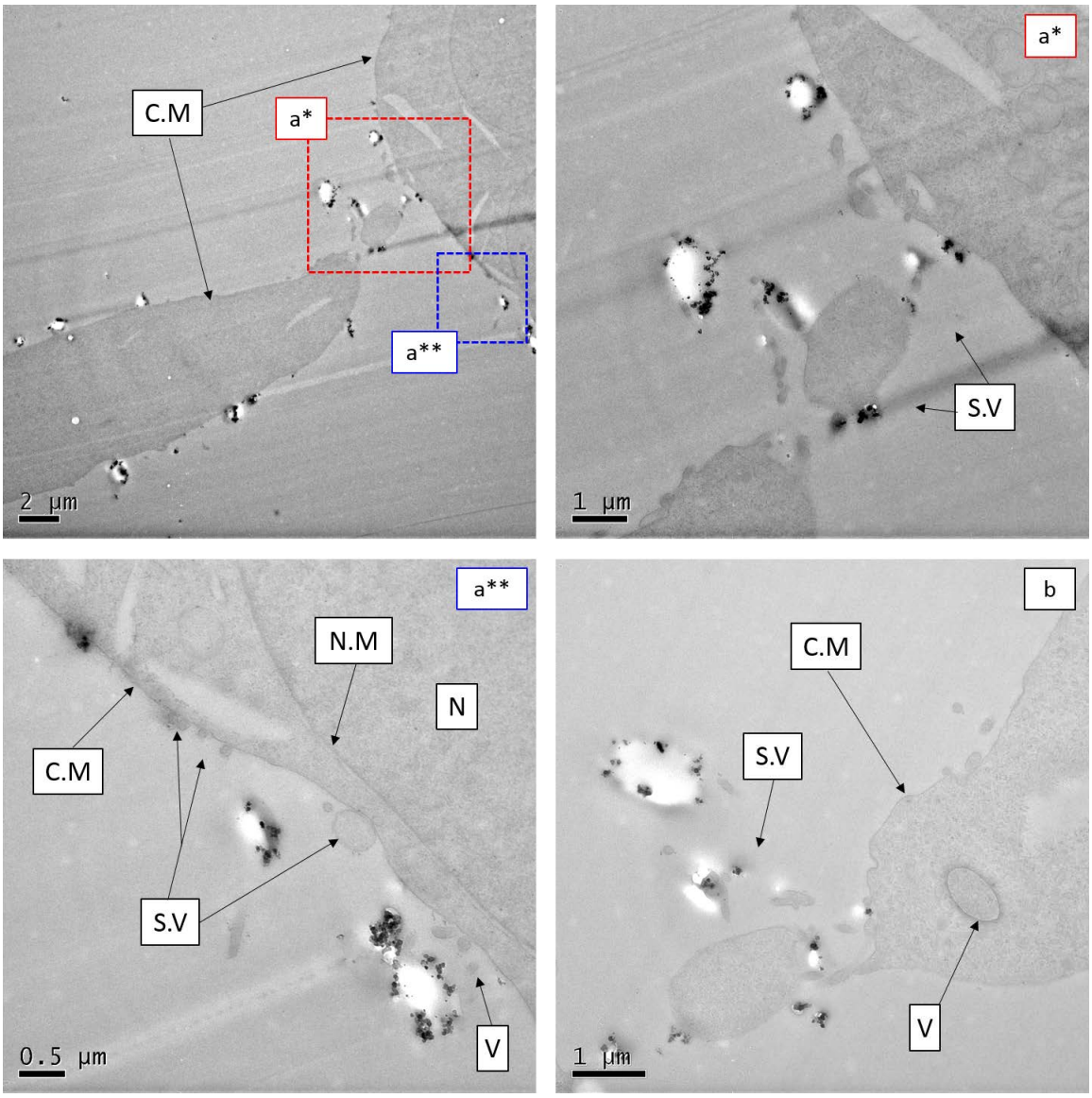

*Figure G.11: TEM images of **Au13-P-HSH** nanoparticles in HeLa cells. Cells were incubated with **Au13-P-HSH** at a concentration of 0.25 nm in complete cell media for 2 hours before fixing. Widefield images are shown in top-left image with magnification of insets (a*) and (a**) shown as labelled. A further cell is shown in (b). and (c) are shown in (a^*), (b^*) and (c^*) respectively. C.M - cell membrane, N - nuclear membrane, N - nucleus, V - vesicle, S.V - secreted vesicle.*

G.4.4 Confocal Microscopy of Au100-P-HSH in HeLa Cells - 24 Hour Incubation

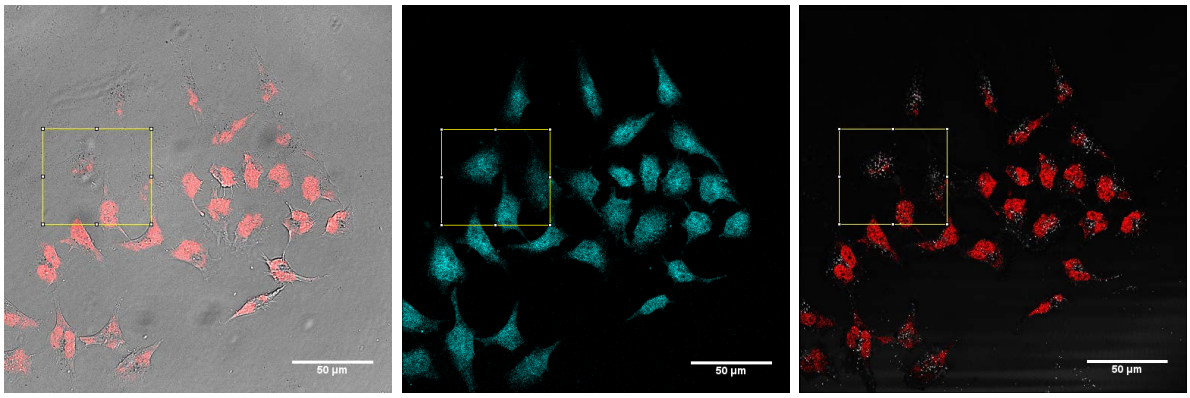

(a) *(b)* *(c)*

Figure G.12: Images of ***Au100-P-HSH*** *nanoparticles in HeLa cells monitored by confocal luminescence and reflection microscopy. Cells were incubated with* ***Au100-P-HSH*** *at a concentration of 0.10 pM in complete cell media for 24 hours before fixing. (a) widefield transmission brightfield and DRAQ5 overlay. (b) widefield* ***HoechstSH*** *image. (c) widefield reflection and DRAQ5 overlay. Reflection image* λ_{exc} *= 633 nm,* λ_{em} *= 623-643 nm.* ***HoechstSH*** *luminescence, (blue channel),* λ_{exc} *= 405 nm,* λ_{em} *= 410-550 nm, DRAQ5, (red channel),* λ_{exc} *= 633 nm,* λ_{em} *= 640-800. (Scale bar (a) 50 µm) (b) 10 µm*

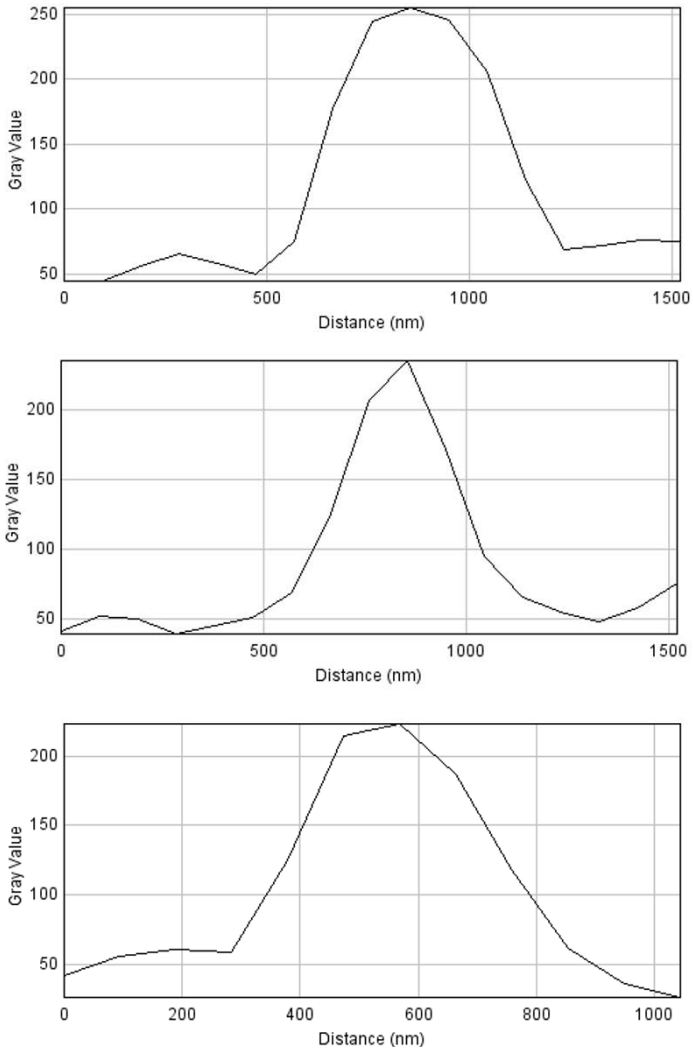

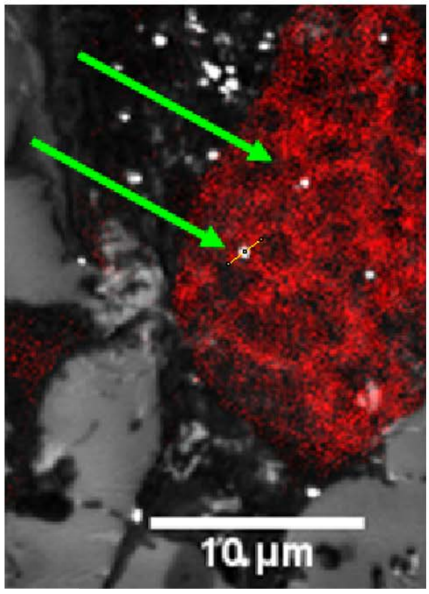

Figure G.13: DRAQ5 and reflection image overlay of ***Au100-P-HSH*** *nanoparticles in HeLa cells monitored by confocal luminescence and reflection microscopy. Cells were incubated with Au100-P-HSH at a concentration of 0.10 pM in complete cell media for 24 hours before fixing. Line intensity profiles were performed on nucleolus associate nanoparticles. Profiles were measured on the reflection and DRAQ5 overlay with nanoparticle diameter estimated as the full-width at half-maximum of the intensity profiles. Reflection image* λ_{exc} *= 633 nm,* λ_{em} *= 623-643 nm. DRAQ5, (red channel),* λ_{exc} *= 633 nm,* λ_{em} *= 640-800. (Scale bar 10 µm*

H

Imaging Controls of Counterstains

H.1 Hoechst 33258 Nuclear Stain

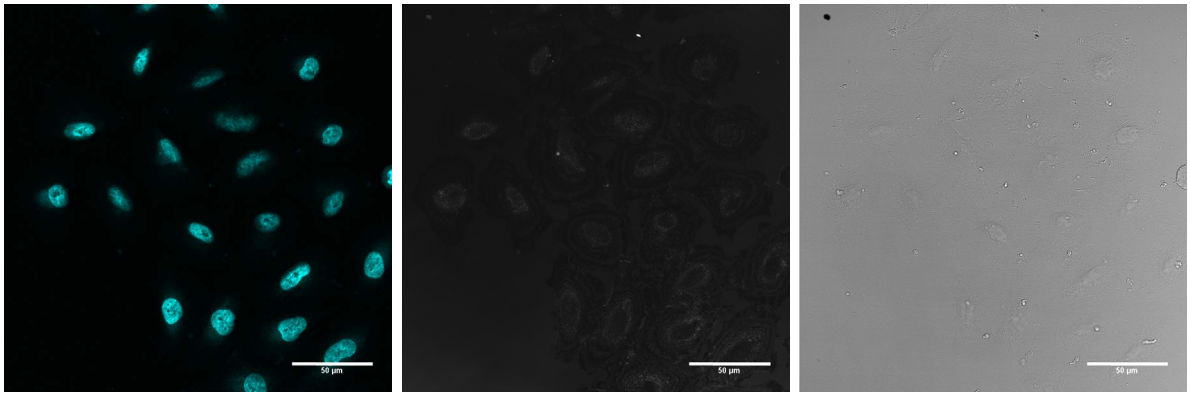

(a) *(b)* *(c)*

Figure H.1: Images of A549 cells monitored by confocal luminescence and reflection microscopy. Cells were incubated with Hoechst 33258 at a concentration of 1 μM in complete cell media for 30 minutes before fixing. (a) ***HoechstSH*** *image. (b) Reflection image. (c) Transmission image. Reflection image λ_{exc} = 633 nm, λ_{em} = 623-643 nm.* ***HoechstSH*** *luminescence, (blue channel), λ_{exc} = 405 nm, λ_{em} = 410-550 nm. (Scale bar 50 μm).*

H.2 DRAQ 5 Nuclear Stain

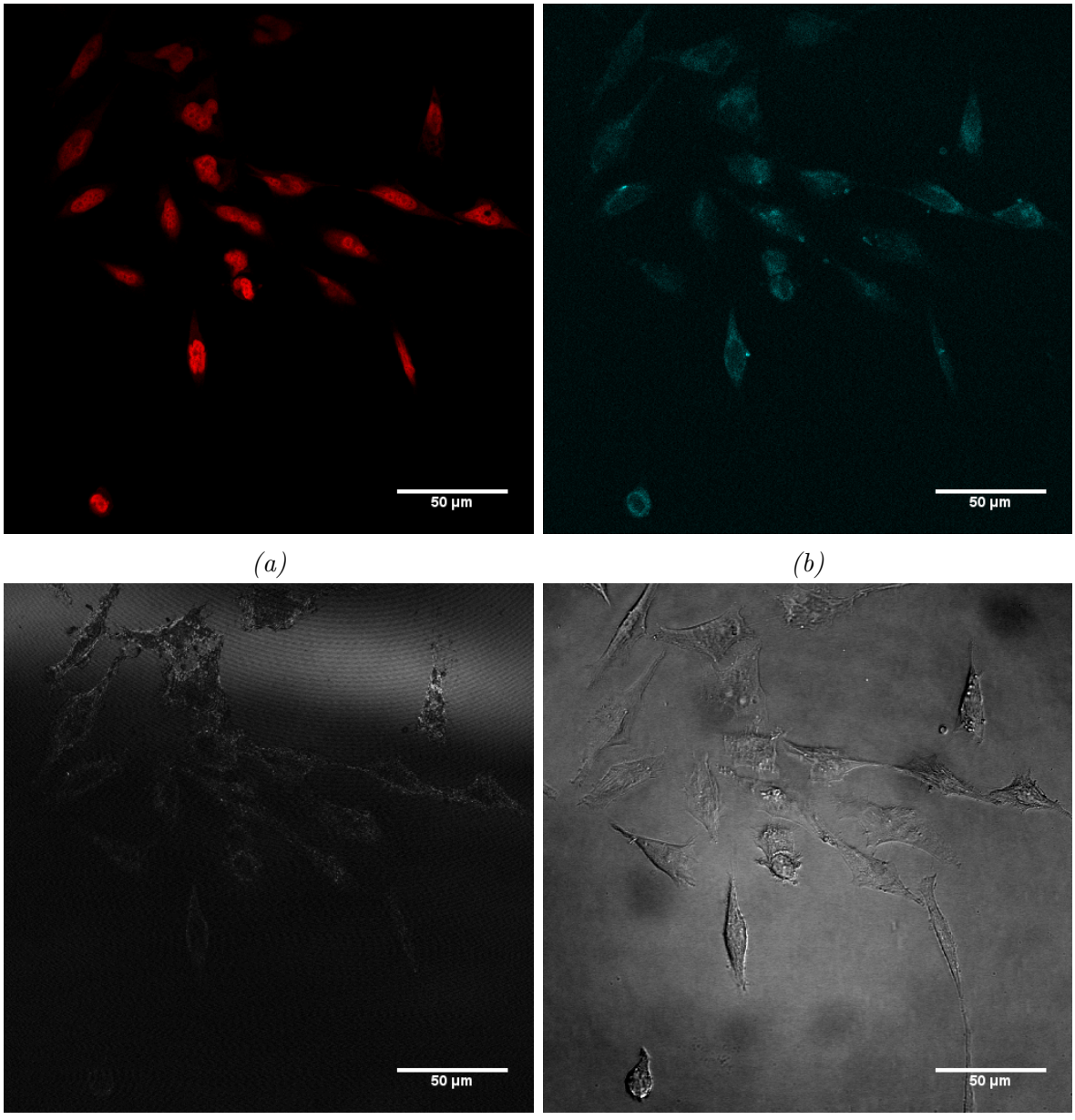

(a) *(b)*

(c) *(d)*

Figure H.2: Images of HeLa cells monitored by confocal luminescence and reflection microscopy. Cells were incubated with DRAQ5 at a concentration of 1 µM in complete cell media for 30 minutes before fixing. (a) DRAQ5 image. (b) ***HoechstSH*** *image. (c) Reflection image. (d) Transmission image. Reflection image* λ_{exc} *= 633 nm,* λ_{em} *= 623-643 nm.* ***HoechstSH*** *luminescence, (blue channel),* λ_{exc} *= 405 nm,* λ_{em} *= 410-550 nm. (Scale bar 50 µm).*

H.3 Lysotracker Lysosome Stain

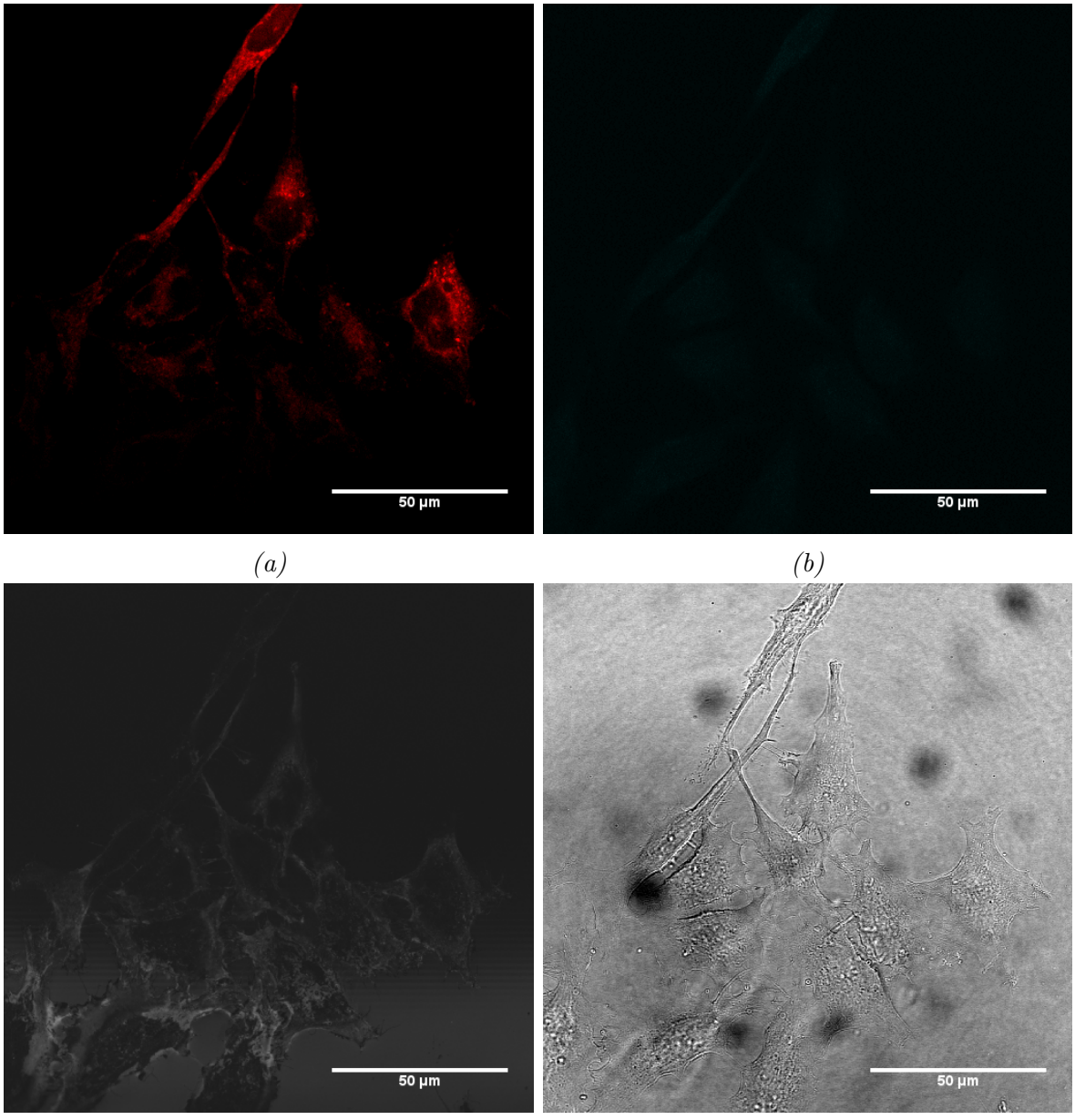

(a) *(b)*

(c) *(d)*

Figure H.3: Images of HeLa cells monitored by confocal luminescence and reflection microscopy. Cells were incubated with Lysotracker Deep Red at a concentration of 1 µM in complete cell media for 30 minutes before fixing. (a) DRAQ5 image. (b) ***HoechstSH*** *image. (c) Reflection image. (d) Transmission image. Reflection image λ_{exc} = 633 nm, λ_{em} = 623-643 nm.* ***HoechstSH*** *luminescence, (blue channel), λ_{exc} = 405 nm, λ_{em} = 410-550 nm. (Scale bar 50 µm).*

I

Cell Cycle Data

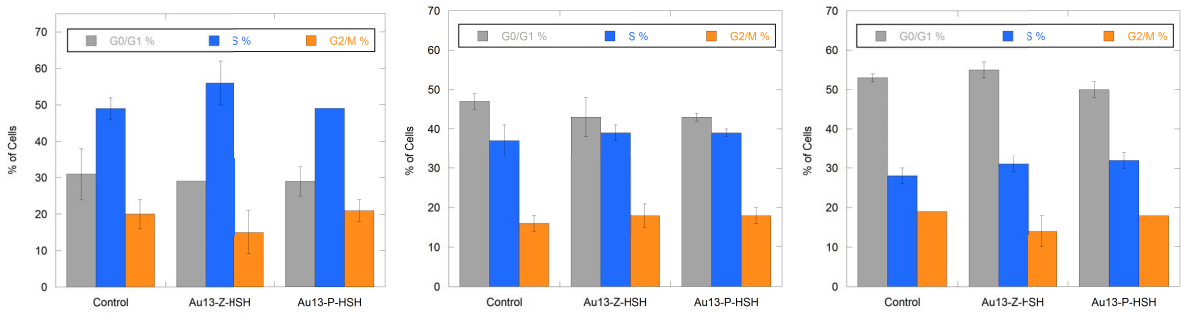

(a) 2hr Incubation *(b) 24hr Incubation* *(c) 48hr Incubation*

Figure I.1: Distribution of cells in the G0/G1, S and G2/M phases of the cell cycle after incubation with ***Au13-Z-HSH*** *and* ***Au13-P-HSH*** *for the times indicated (0.25 nM concentration). Cells were subsequently harvested by trypsinisation and centrifugation and fixed in 70 % ethanol. For analysis cells were washed in PBS, treated with RNaseA and stained with the fluorescent nucleic acid propidium iodide dye. Cell fluorescence was analysed using a FACS Calibur 14 flow cytometer (BD Biosciences). G0/G1, S and G2/M proportions were calculated using FCS Express Flow 5 software (De Novo Software), with fitting performed to minimise the chi-squared value. Results are reported as the average % of cells in each phase ± 1SD. Statistical significance was tested with an independent t-test. $P < 0.05$, significant differences compared with undosed control cells harvested at identical time points.*

	Incubation Time	Nanoaprticle (0.25 nM)	t-value G0/G1	t-value S	t-value G2/M
After serum re-stimulation	11-13 hr	Au13-Zonyl-HSH	0.290	0.567	0.454
After serum re-stimulation	11-13 hr	Au13-pHLIP-HSH	0.963	1.189	0.775
After serum re-stimulation	22-24 hr	Au13-Zonyl-HSH	1.204	0.142	0.872
After serum re-stimulation	22-24 hr	Au13-pHLIP-HSH	1.402	0.706	0.485
After serum re-stimulation	30 - 32 hr	Au13-Zonyl-HSH	0.565	0.924	1.075
After serum re-stimulation	30 - 32 hr	Au13-pHLIP-HSH	1.403	0.222	0.027
Complete media	2 hr	Au13-Zonyl-HSH	0.347	1.430	1.087
Complete media	2 hr	Au13-pHLIP-HSH	0.311	0.064	0.458
Complete media	24 hr	Au13-Zonyl-HSH	1.069	0.885	0.537
Complete media	24 hr	Au13-pHLIP-HSH	2.778	0.997	0.885
Complete media	48 hr	Au13-Zonyl-HSH	1.265	1.371	1.632
Complete media	48 hr	Au13-pHLIP-HSH	1.490	1.816	1.449

Figure I.2: Statistical data - independent t-test for cell cycle analysis following incubation with ***Au13-Z-HSH*** *and* ***Au13-P-HSH****. T-value > 2.920/ P < 0.05 was considered significant.*

I.1 Flow Cytometry Data Analysis

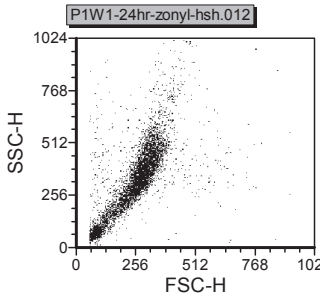

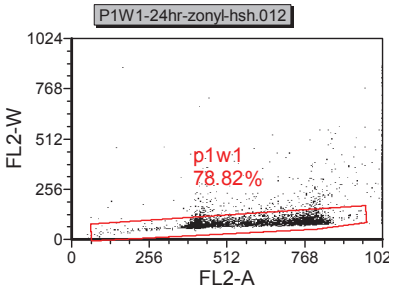

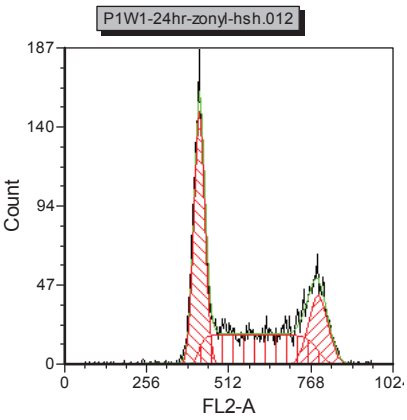

Cycle	G1 Mean	G1 CV	%G1	G2 Mean	G2 CV	%G2	%S	G2/G1	%Total	B.A.D.
Diploid	419.65	4.18	39.91	791.59	3.91	19.50	40.59	1.89	100.00	2.17

Model	Dip %G2	Dip %S	Chis
SL S0	19.90	40.42	0.81
SL CL S0	19.50	40.59	0.80
+G2/G1 Fixed	6.18	52.92	2.07
+Aggregates	6.34	52.82	2.22
+S Order = 1	20.33	40.19	0.81
+CVs Fixed	20.52	40.08	0.81

Interpretation
MultiCycle suggestions (a guideline only):
No abnormal DNA content is observed.
The diploid %S=40.6, %G2=19.5
The S Phase confidence is good

Experiment Statistics
Chi sq: 0.80
BAD: 2.17
Number of cells: 4469.00
Number of cycles: 1.00
Cycle fit model: 1 Cycle

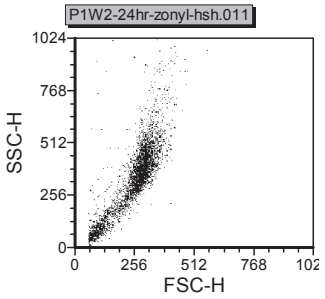

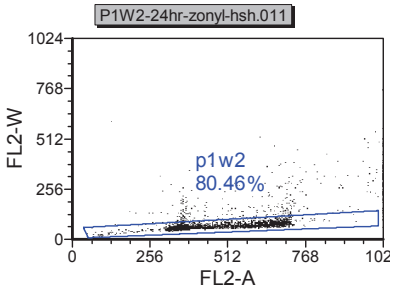

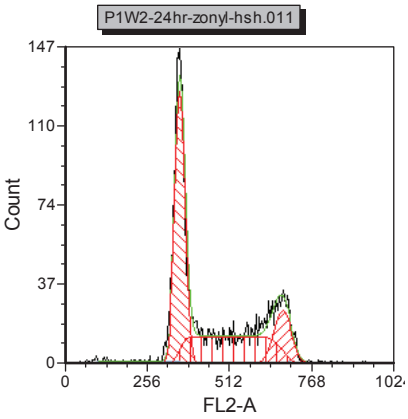

Cycle	G1 Mean	G1 CV	%G1	G2 Mean	G2 CV	%G2	%S	G2/G1	%Total	B.A.D.
Diploid	357.67	4.44	46.59	678.14	3.99	15.56	37.85	1.90	100.00	1.92

Model	Dip %G2	Dip %S	Chis
SL S0	15.95	37.71	0.81
SL CL S0	15.56	37.85	0.80
+G2/G1 Fixed	5.98	46.98	1.19
+Aggregates	5.38	47.22	1.17
+S Order = 1	15.10	38.22	0.81
+CVs Fixed	16.66	37.08	0.82

Interpretation
MultiCycle suggestions (a guideline only):
No abnormal DNA content is observed.
The diploid %S=37.8, %G2=15.6
The S Phase confidence is good

Experiment Statistics
Chi sq: 0.80
BAD: 1.92
Number of cells: 2957.00
Number of cycles: 1.00
Cycle fit model: 1 Cycle

J

Computational Analysis

J.1 UV-Vis Analysis

Absorption of the surfactant molecules to the gold surface also modifies the surface dielectric constant of the particles.[68,75] The change in SPR can furthermore be potentially quite small in magnitude (¡0.5 nm), therefore a computational Matlab algorithm was created to automate precise calculation of the SPR (J.1). A summary of the algorithm is shown in Figure J.1. In brief, the gradient between UV-Vis absorption data points is determined (Figure J.1b) and the data points fitted with a high-degree polynomial. The *roots* of the fitted curve i.e. where the gradient equals zero are determined (Figure J.1c). These *roots* correspond to the SPR and can be plotted in conjunction with the full-width at half-maximum (FWHM) of the SPR band (Figure J.1d) to precisely monitor gold nanoparticles by analysis of their UV-Vis absorption spectra. The FWHM of the SPR band was determined using a computational Matlab algorithm developed by Mr Chris Stepanek (EPSRC Doctoral Training Centre in Physical Science for Imaging in the Biomedical Sciences, The University of Birmingham). Figure J.1e) shows the result of this algorithm which essentially fits a Gaussian curve (red) to the SPR band of the gold nanoparticles (blue). Extracting the FWHM of the Gaussian thus enables the extent of any SPR band broadening to be ascertained.

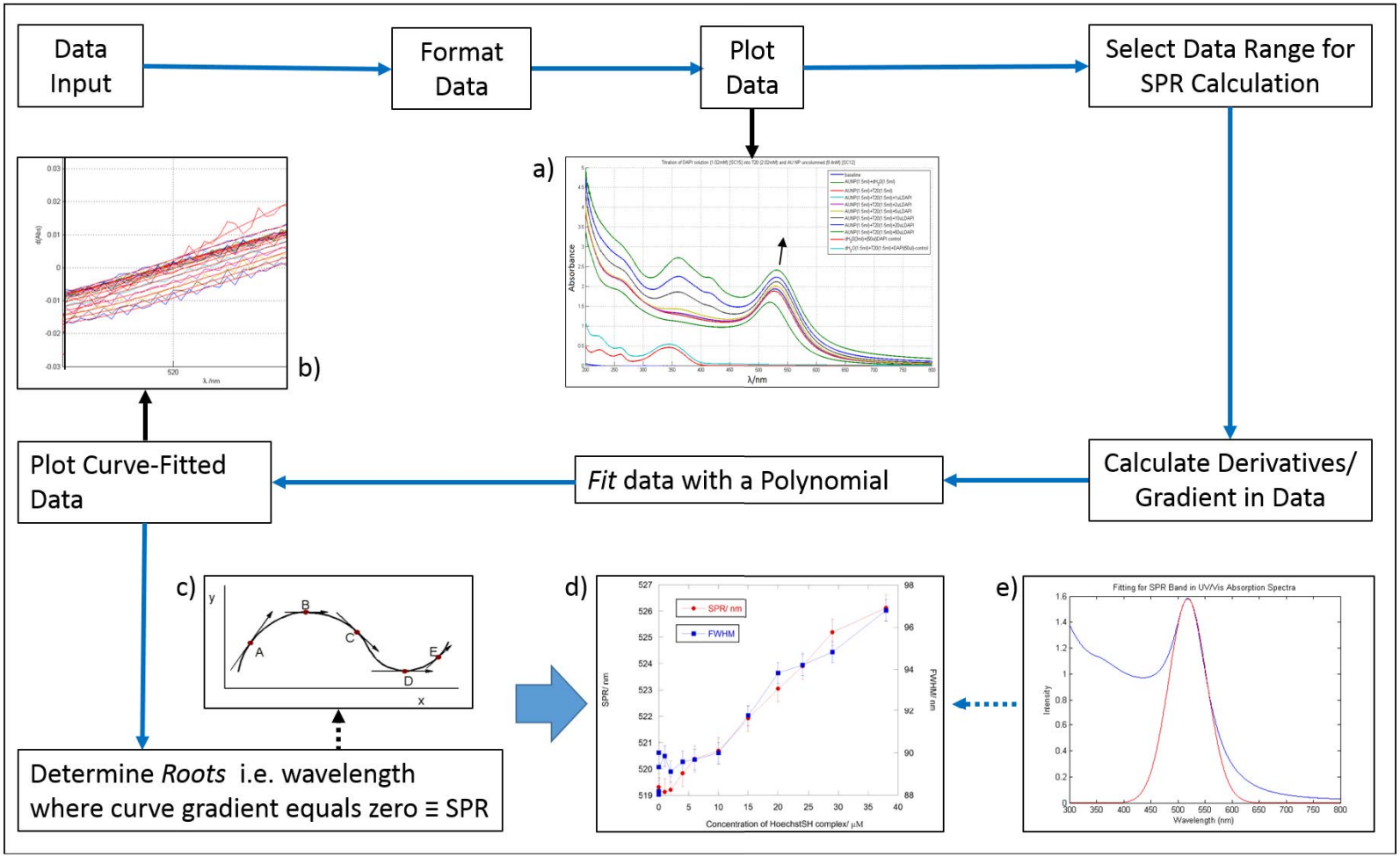

Figure J.1: Algorithmic Summary of UV-Vis Absorption Computational SPR Calculator

```
%% UV-VIS Analysis: Version 1.0 (18-7-12) -
%  Sunil Claire [sxc656@bham.ac.uk]
%% Importing Data...
%% Step 1: delete 'wavelength, abs' row (2nd row) in csv data file.
%% Recommended 'Baseline' columns (columns 1 and 2) are also deleted
%% Step 2: Save csv file with a different file name] and LOAD DATA
%% into Matlab via 'import' option under 'File'
%% Also included with this 'm' file is some UV-Vis data for which
%% the current code works.
%% SPR maxima are output in: TURNING_PT_RESULTS

%% getting some data info.
dim=size(data);
imax=(dim(1,2));

%% get headings
for i=1:2:imax
    headings0(i)=[textdata(1,i)]
end
headings=headings0';
headings(cellfun(@isempty,headings))=[]; % delete empty entries

%%
close all;  clc;

%% NB. If you have a lot of data columns and line colours start...
%%... repeating, 'uncomment' the following line ...
%ColorSet = varycolor(15); %set number of  lines

% ... and in the next 'for loop'
% ... 'COMMENT'   "set(gca, 'XTick', 0:50:800,'FontSize',12);
% ... 'UNCOMMENT' "set(gca, 'XTick', 0:50:800,'ColorOrder',
                        ColorSet,'FontSize',12);
% [NB. Comment and uncomment lines by inserting
```

```
35  % and removing a '%' symbol respectively at the start of the line]
36
37
38  %% Plot Data
39  for i=2:2:imax
40      hold all;
41      axis([250 800 0 5]) % Axis Lengths
42      plot(double(data(1:1201,1)),double(data(1:1201,i)),'linewidth',2);
43      grid on
44      set(gca, 'XTick', 0:50:800, 'FontSize',12);
45      %set(gca, 'XTick', 0:50:800,'ColorOrder', ColorSet, 'FontSize',12);
46      legend(headings,'FontSize',14);
47      title('TITLE', 'FontSize',18);
48      xlabel('\lambda /nm', 'FontSize',14);
49      ylabel('Absorption', 'FontSize',14);
50  end
51
52  %% USER INPUT: Wavelength range within which to calculate
53  %  turning point (SPR)
54  wavelength_range=[550 565];
55
56  %%
57  index=[0 0];
58  index=[double(1601+wavelength_range(1,1)*(-2))
59        double(1601+wavelength_range(1,2)*(-2))];
60
61  %% Precautionary Variable Clearance
62  clearvars turning_point;
63  clearvars turning_point_nm;
64
65  %% Calculate derivative and turning points via curve fitting
66  %% USER INPUT: degree of polynomial
67  dop=8;
68
```

```
69  %% USER INPUT: SELECT data columns to find turning points in
70  %% and enter column numbers in 'for loop' arguement
71  %% NB. See CSV file to get column numbers
72  % Guidelines for entering 'for loop' arguement:
73  % To choose columns 3 to 29 enter "for i=3:29" ....
74  % .... or to choose individual columns eg. 3, 5 and 9,
75  % enter "for i=[3,5,9]"
76
77  clearvars headings_legend;
78  for i=3:29
79  headings_legend(i)=[textdata(1,i)];
80  headings_legend(cellfun(@isempty,headings_legend))=[];
81  % delete empty entries
82  end
83
84  %% USER INPUT: SELECT data columns to plot and
85  %% enter column numbers in 'for loop' arguement
86  % Guidelines for entering 'for loop' arguement:
87  % To choose columns 3 to 29 enter "for i=3:2:29"
88  %....NB. ENSURE the '2' is included
89  % .... or to choose individual columns eg. 3, 5 and 9,
90  % enter "for i=[3,5,9]" ...
91  % ... NB. in this case  ensure the Absorption values
92  % columns are chosen and not the wavelength columns
93
94  figure;
95  for i=3:2:29
96
97  % differential calculus
98  deriv1y=double(diff(data(index(1,2):index(1,1),(i+1)),1));
99  derivy_x=double((double(deriv1y./0.5)));
100
101 % create wavelength vector
102 lam=flipud([wavelength_range(1,1):0.5:
```

```
103     (wavelength_range(1,2)-0.5)]');
104 dydx=cat(2,lam,derivy_x);
105 % concatenate wavelength and data values
106
107 % plotting
108 hold all;
109 plot(dydx(:,1),dydx(:,2),'linewidth',1);
110 grid on
111 set(gca, 'XTick', 0:10:800);
112 %set(gca, 'XTick', 0:10:800,'ColorOrder', ColorSet);
113     legend(headings_legend);
114     title('TITLE');
115     xlabel('\lambda /nm');
116     ylabel('d(Abs)');
117
118 % Curve fitting
119 p=polyfit(dydx(:,1),dydx(:,2),dop);
120 deriv_poly=polyval(p,dydx(:,1));
121 plot(lam,deriv_poly,'r')
122
123 % Root finding
124 roots1=roots(p);
125 roots1=roots1(find(roots1>=wavelength_range(1,1)
126       & roots1<=wavelength_range(1,2)));
127 turning_point(i)=roots1(roots1 == real(roots1));
128 %turning_point(cellfun(@isempty,turning_point))=[];
129 end
130
131 %% display results
132 [r,c,v]=find(turning_point');
133 % get SPR wavelengths together into vector 'v'
134 v
135
136 % add appropriate labels and OUTPUT data
```

```
137 TURNING_PT_RESULTS=[headings_legend' num2cell(v)]
138
139 %% Plotting concentrations vs. SPR
140 %% USER INPUT: ENTER Concentrations
141 concs=[...
142 1;...
143 2;...
144 3;...
145 4;...
146 ];
147
148 %% add SPR wavelengths to appropriate concentration labels
149 results=[TURNING_PT_RESULTS num2cell(concs)]
150 %% Plot SPR vs. concentration
151 figure;
152 plot(concs(:,1),v(:,1),'.r','MarkerSize',20)
153 title('TITLE');
154 xlabel('[conc]/ {\mu}M perhaps');
155 ylabel('\lambda _{SPR} /nm');
156 grid on
```

J.2 ImageJ Batch Image Processing Macro

Image processing was conducted using Macbiophotonics ImageJ Version 1.43M. For the addition of scale bars to batches of confocal images acquired with the Leica TCS SP2 Confocal Microscope, a macro requiring minimal user-input was created:

```
1  Dialog.create("Scale Bars");
2  Dialog.addMessage("Please ensure you have duplicates of all images saved
3  and you have produced all required overlays.");
4  Dialog.addMessage("Please choose the Source and Save
5  directories for your images.");
6
7  Dialog.show();
8
9  dir = getDirectory("Choose a Source Directory ");
10 list = getFileList(dir);
11 dirs = getDirectory("Choose a Save Directory ");
12
13 Dialog.create("Scale Bar Settings");
14 Dialog.addMessage("Please enter the scale bar parameters you require.");
15 Dialog.addMessage("(The 'Physical Length' parameter can be found in
16         the 'txt' file saved with the images by the Leica software).");
17
18    Dialog.create("Scale bar settings");
19    Dialog.addMessage("Set Scale");
20    Dialog.addNumber("Distance in Pixels",512);
21    Dialog.addNumber("Physical Length (metres)",0);
22    Dialog.addNumber("Scalebar Width Required (microns)",50);
23    Dialog.addNumber("Scalebar Thickness (pixels)",4);
24    Dialog.addString("Scalebar Color", "White");
25    Dialog.addNumber("Scalebar Font size", 14);
26    Dialog.show();
27
```

```
28      DistanceinPixels = Dialog.getNumber();
29      PhysicalLength = Dialog.getNumber();
30      PhysicalLengthum = PhysicalLength*(1E6);
31
32      width = Dialog.getNumber();
33      widthum = width*(1E6);
34
35      height = Dialog.getNumber();
36      color = Dialog.getString();
37      font = Dialog.getNumber();
38
39    for (i=0; i<list.length; i++) {
40        path = dir+list[i];
41        //print(i+"  "+path);
42        showProgress(i, list.length);
43        if (endsWith(list[i], "/") == 0) {
44      open(path);
45          title = getTitle();
46  run("RGB Color");
47  run("Set Scale...", "distance=" + DistanceinPixels+
48  " known=" + PhysicalLengthum + " pixel=1 unit=um global");
49  run("Scale Bar...",  "width=" + width+ " height=" + height
50  + " font=" + font + " color=" + color + "
51               background=None location=[Lower Right] bold");
52              saveAs("tiff", dirs+list[i]);
53              close();
54        }
55      }
```

J.3 Computational PSF Analysis

```
clc; close all;
%theroetical NP

x=0:pi/1000:pi;
y=sin(x);
x=(1e-7)*x/pi;
normalised_y=(y-min(y))./(max(y)-min(y));

figure; plot(x,normalised_y,'k','LineWidth',2);
title('Model 100nm Gold Nanoparticle','FontSize',12);
xlabel('diameter/ m ', 'FontSize',12);
ylabel('Normalised Intensity', 'FontSize',12);
grid off;
box off;

% gaussian approximation of PSF - approx 300nm FWHM
%(created from estimate obtained from microscope software).

x_gaus=0:1e-10:1e-6;
y_gaus_PSF=gaussmf(x_gaus,[1.2e-7 0.5e-6]);
normalised_yg=(y_gaus_PSF-min(y_gaus_PSF))
                ./(max(y_gaus_PSF)-min(y_gaus_PSF));
%normalised_yg=y_gaus_PSF/norm(y_gaus_PSF);
figure; plot(x_gaus,normalised_yg,'k','LineWidth',2);
title('Theoretical PSF from Luminescence Mode','FontSize',12);
xlabel('diameter/ {\mu}m ', 'FontSize',12);
ylabel('Normalised Intensity', 'FontSize',12);
grid off;
box off;

```

```
% plot convolution

a=conv(y,y_gaus_PSF);
xp=(1:length(a))*0.89e-10;
a=(a-min(a))./(max(a)-min(a));
%normalised_a=a/norm(a);
figure; plot(xp,a,'k','LineWidth',2);
grid off;
title('Convolution of Theoretical Nanoparticle & PSF','FontSize',12);
xlabel('diameter/ m ', 'FontSize',12);
ylabel('Normalised Intensity', 'FontSize',12);
grid off;
box off;
%250-300nm, lexa 488
hold all;
%%%%%%%%

%figure;
plot(data(:,6),data(:,8),'--k','LineWidth',2);

xlabel('diameter/ m ', 'FontSize',12);
ylabel('Normalised Intensity', 'FontSize',12);
grid off;
plot(xp,a,'k','LineWidth',2);
```

K

Cellular Uptake of Au13-Z-RuSH and Au100-Z-RuSH

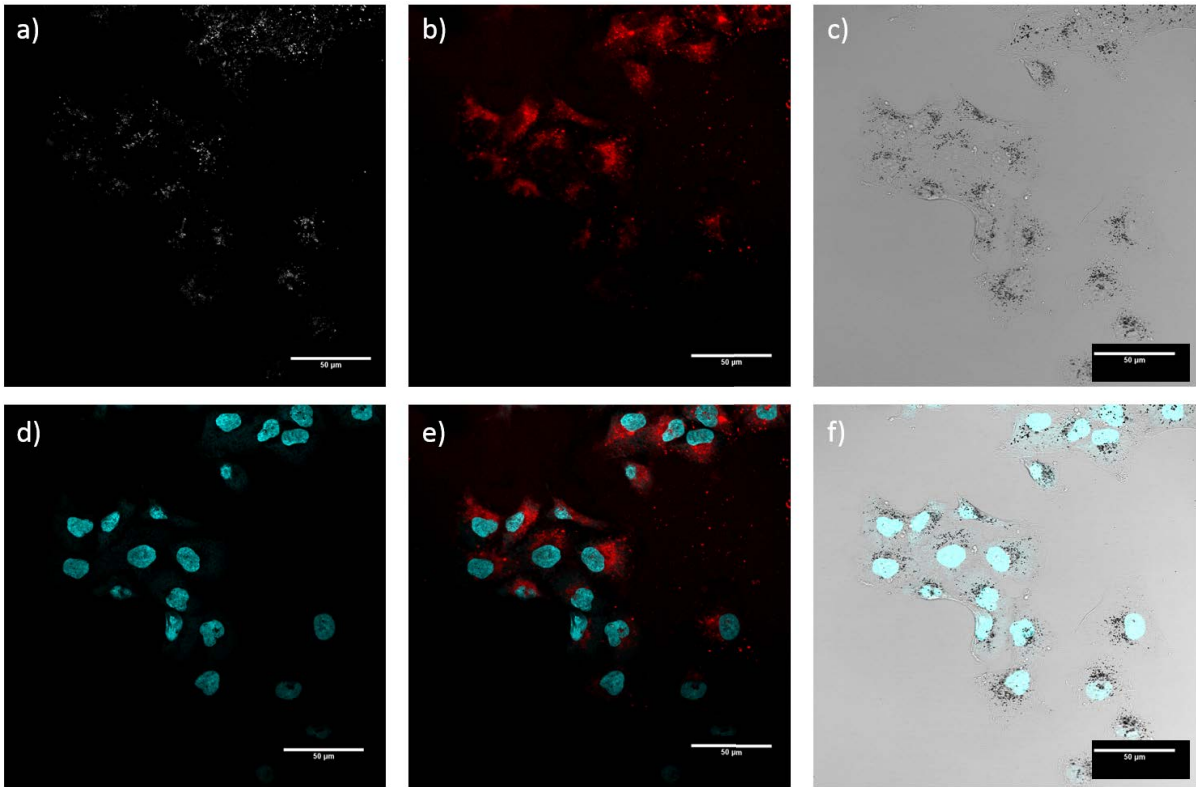

Figure K.1: Images of ***Au13-Z-RuSH*** *in A549 cells monitored by confocal luminescence and reflection microscopy. Cells were incubated with nanoparticles at a concentration of 0.9 nM in complete cell media for 24 hours before fixing. (a) reflectance image, (b) ruthenium luminescence, (c) transmission image, (d) Hoechst nuclear stain,(e) ruthenium luminescence and Hoechst overlay, (f) transmission image and Hoechst nuclear stain overlay. Reflection image* λ_{exc} *= 633 nm,* λ_{em} *= 623-643 nm. Hoechst (blue channel),* λ_{exc} *= 405 nm,* λ_{em} *= 410-455 nm. Ruthenium luminescence (red channel),* λ_{exc} *= 633 nm,* λ_{em} *= 640-800. (Scale bar 50* μm*).*

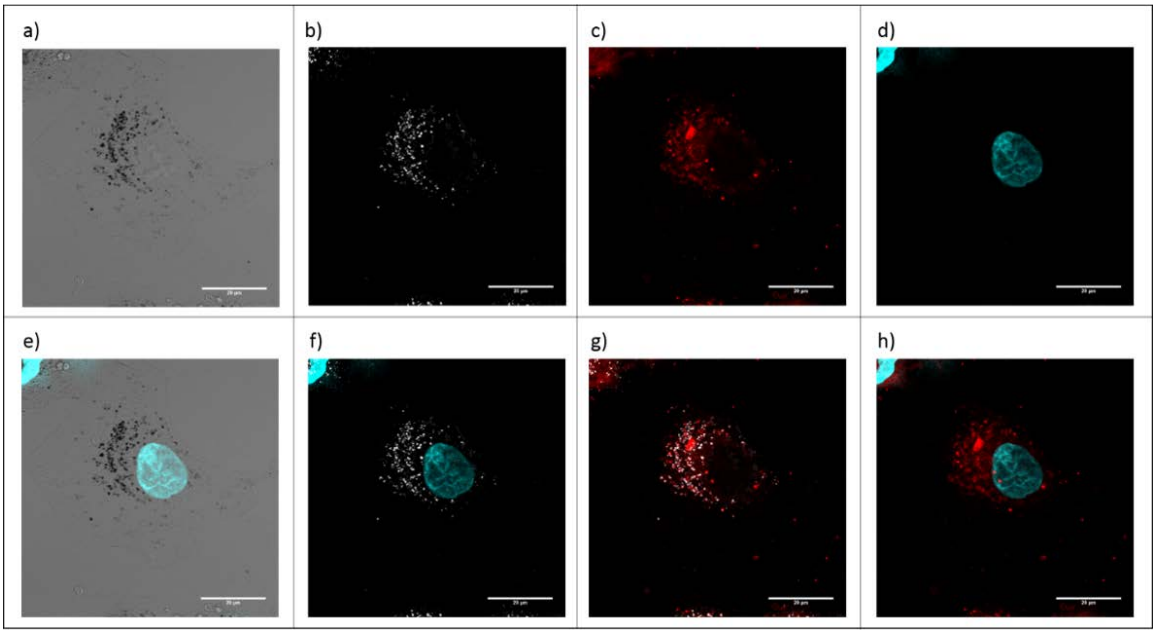

Figure K.2: Images of ***Au13-Z-RuSH*** *in A549 cells monitored by confocal luminescence and reflection microscopy. Cells were incubated with nanoparticles at a concentration of 0.9 nM in complete cell media for 24 hours before fixing. (a) transmission image, (b) reflectance image, (c) ruthenium luminescence, (d) Hoechst nuclear stain, (e) transmission image and Hoechst nuclear stain overlay, (f) Hoechst nuclear stain and reflection image overlay, (g) ruthenium luminescence and reflection image overlay, (h) ruthenium luminescence and Hoechst overlay, Reflection image* λ_{exc} *= 633 nm,* λ_{em} *= 623-643 nm. Hoechst (blue channel),* λ_{exc} *= 405 nm,* λ_{em} *= 410-455 nm. Ruthenium luminescence (red channel),* λ_{exc} *= 633 nm,* λ_{em} *= 640-800. (Scale bar 20* μm*).*

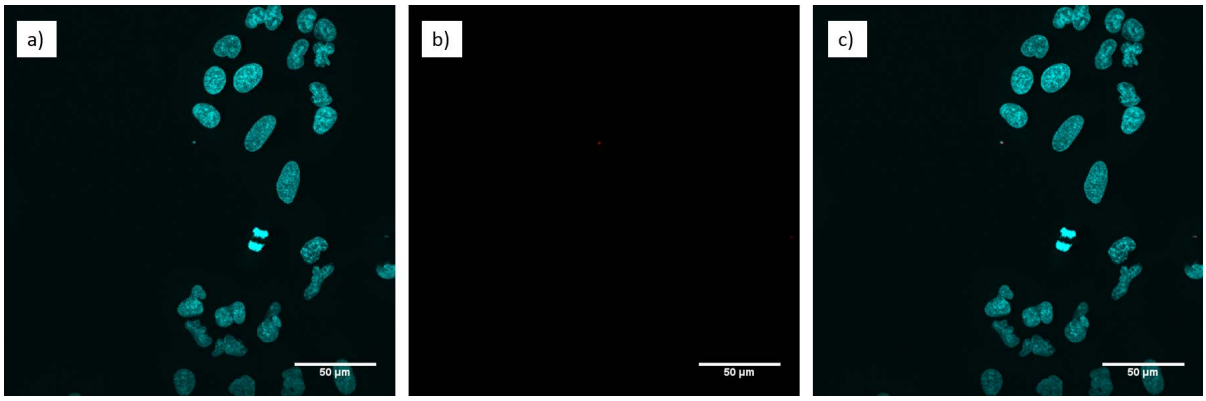

Figure K.3: Images of A549 cells monitored by confocal luminescence and reflection microscopy. Cells were cultured in complete cell media for 24 hours before fixing. (a) Hoechst nuclear stain image, (b) ruthenium luminescence image (c) ruthenium luminescence and Hoechst overlay, (f) transmission image and Hoechst nuclear stain overlay. Hoechst (blue channel), λ_{exc} = 405 nm, λ_{em} = 410-455 nm. Ruthenium luminescence (red channel), λ_{exc} = 633 nm, λ_{em} = 640-800. (Scale bar 50 µm).

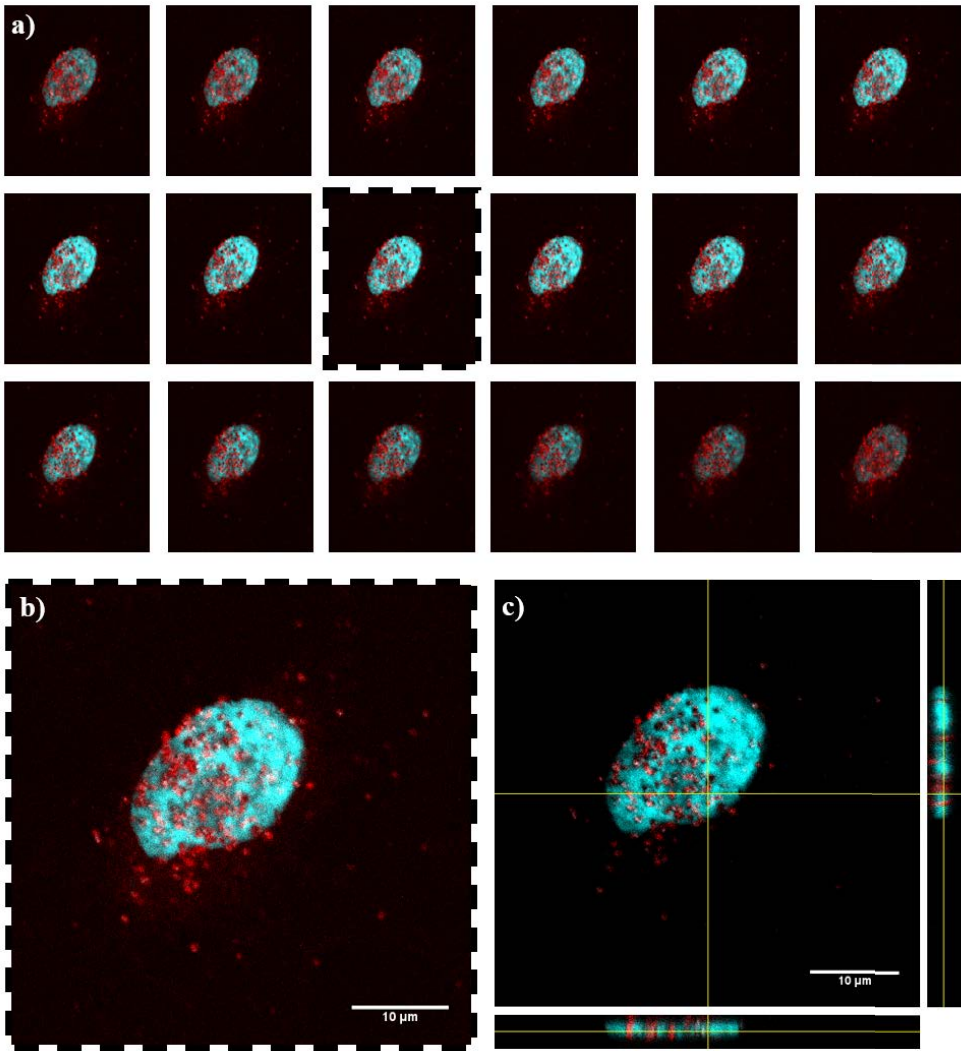

Figure K.4: Images of ***Au100-Z-RuSH*** *in A549 cells monitored by confocal luminescence and reflection microscopy. Cells were incubated with nanoparticles at a concentration of 0.4 pM in complete cell media for 24 hours before imaging. (a) Confocal image slice sequence from 3D z-stack of cells with ruthenium luminescence and nuclear Hoechst overlay, with enlargement of highlighted slice shown in (b) and orthogonal view of the central z-stack slice (xz plane below, yz plane-right) in (c) illustrating ruthenium luminescence from within the same central z-plane as the nuclear Hoechst luminescence (arrow). Reflection image* λ_{exc} *= 633 nm,* λ_{em} *= 623-643 nm. Hoechst (blue channel),* λ_{exc} *= 405 nm,* λ_{em} *= 410-455 nm. Ruthenium luminescence (red channel),* λ_{exc} *= 633 nm,* λ_{em} *= 640-800. (Scale bar 10 µm).*

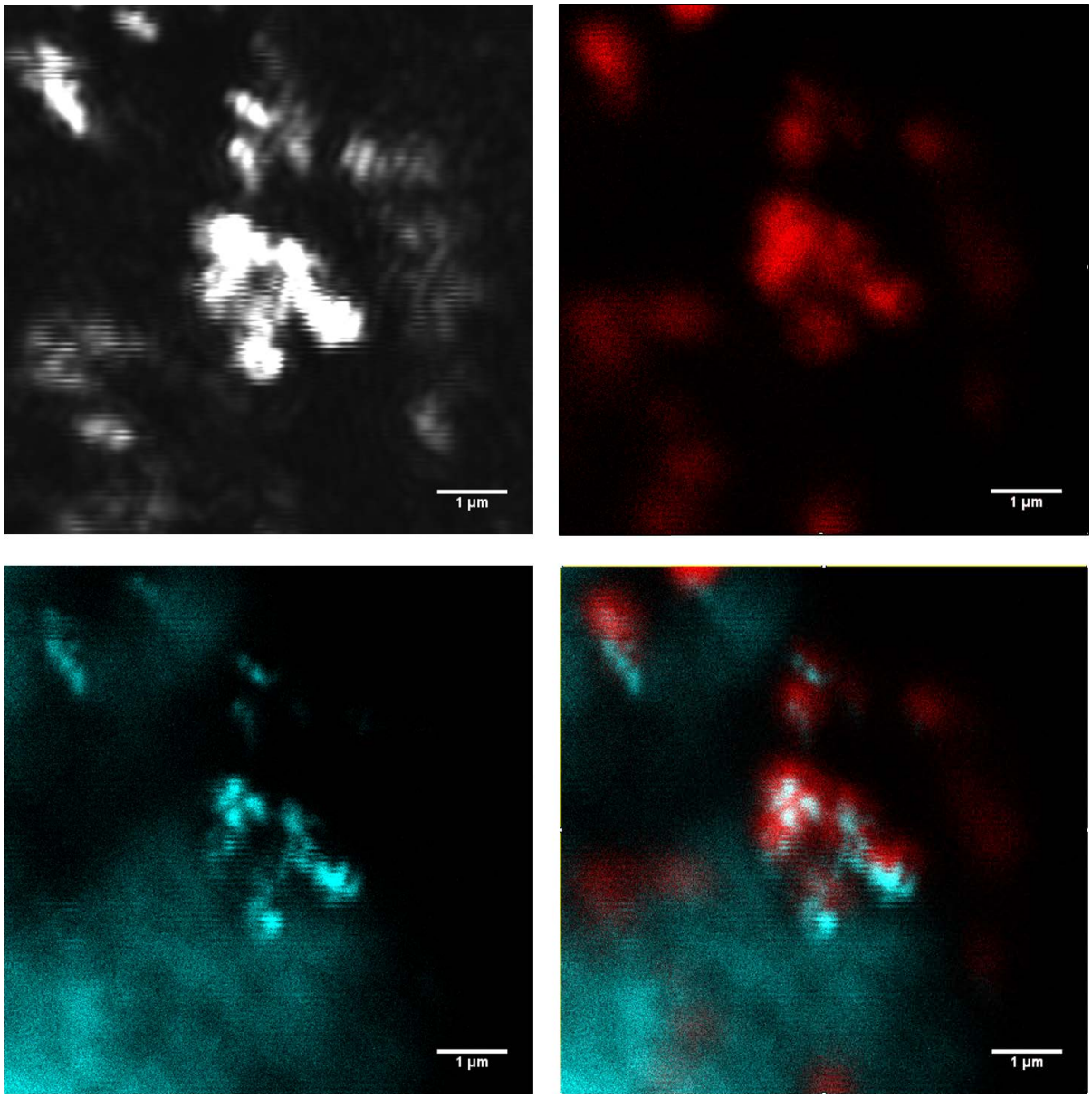

Figure K.5: Images of ***Au100-Z-RuSH*** *in close to proximity to condensed chromatin in the nucleus of an A549 cell. Cells were incubated with nanoparticles at a concentration of 0.4 pM in complete cell media for 24 hours before imaging. (a) Reflection image, (b) ruthenium luminescence image, (c) Hoechst blue channel image and (d) ruthenium luminescence and Hoechst overlay. Reflection image* λ_{exc} *= 633 nm,* λ_{em} *= 623-643 nm. Hoechst (blue channel),* λ_{exc} *= 405 nm,* λ_{em} *= 410-455 nm. Ruthenium luminescence (red channel),* λ_{exc} *= 633 nm,* λ_{em} *= 640-800. (Scale bar 1 µm).*

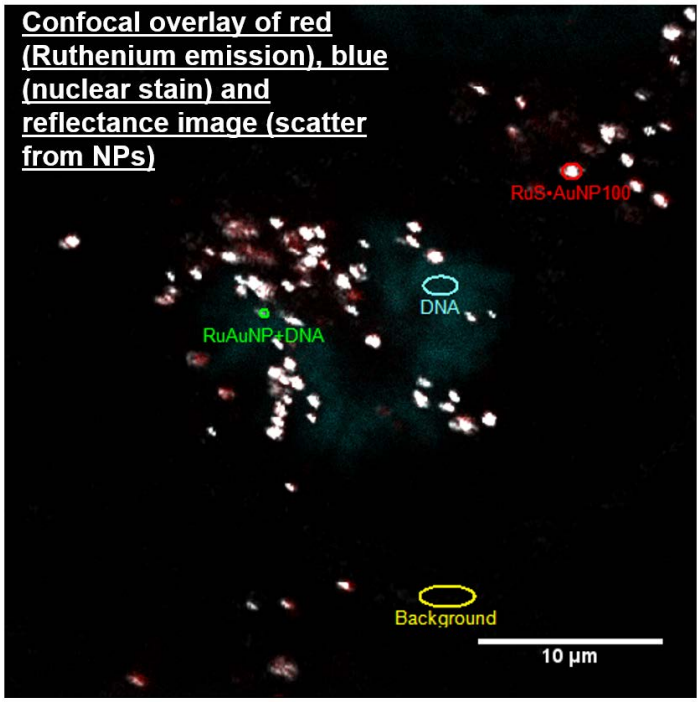

Confocal images showing ROI's corresponding to the locations where spectral scan data was analysed.

Below (clockwise from top-right: reflectance, blue (nucleus) and red channel confocal images.

Red: RuAuNP,
Blue: DNA
Green: RuAuNP in close proximity to DNA,
Yellow: Background

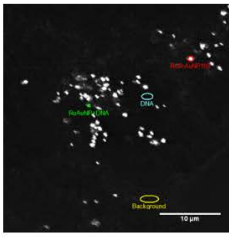

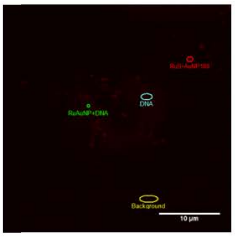

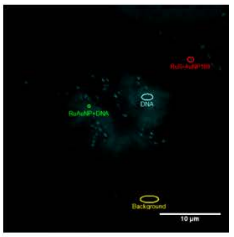

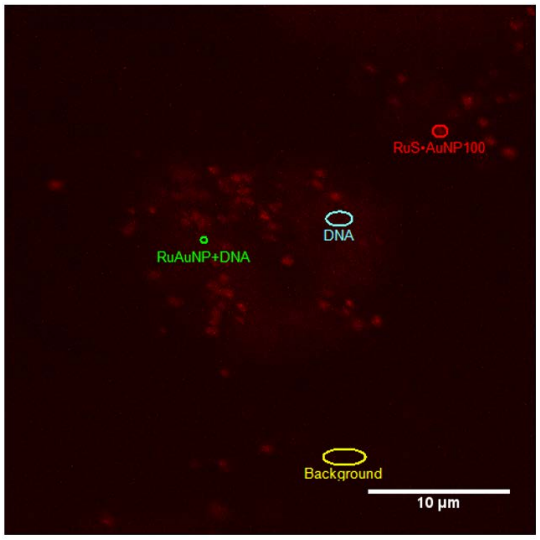

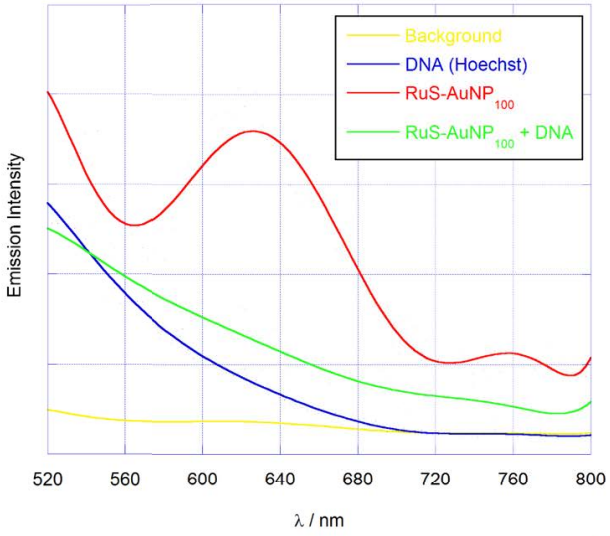

Exported spectral data from Leica Confocal Lite software and fitted 9th order polynomial to data in to smooth out noise (see graph on right).
Curve from the **green** ROI placed on RuAuNPs in close proximity to nuclear stained region
Resulting spectrum – a possible convolution of (**blue** and **red**) spectra from RuAuNP and DNA(Hoechst)

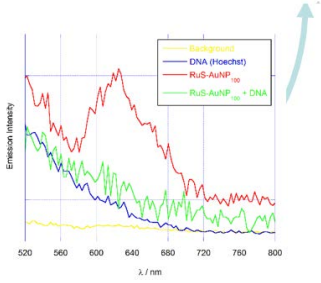

Figure K.6: Images and spectral scans of ***Au100-Z-RuSH*** *in close to proximity to condensed chromatin in the nucleus of an A549 cell. Spectral data is measured and fitted as described in image descriptions.*

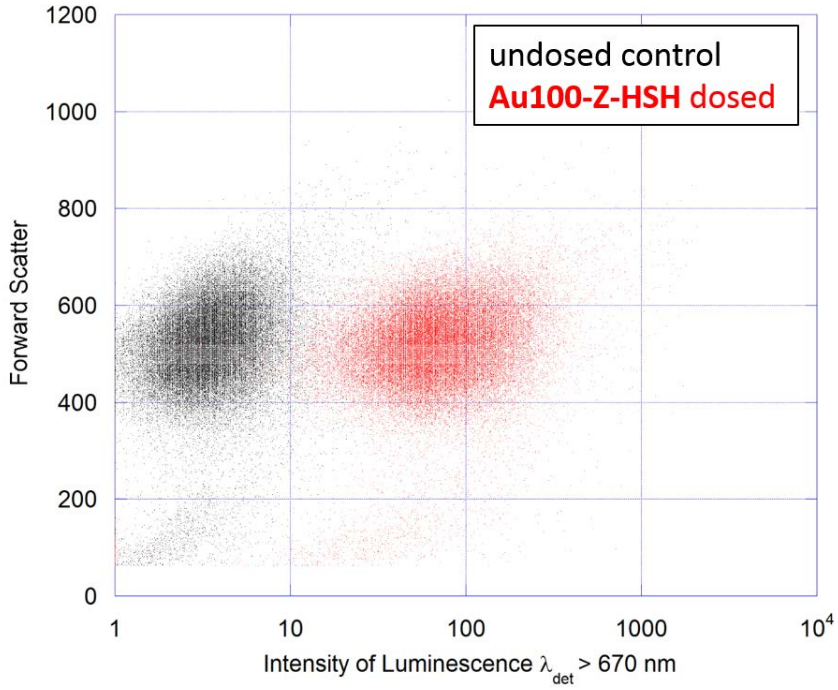

Figure K.7: Flow Cytometry Analysis of A549 Incubated with ***Au100-Z-RuSH*** *for 24 hours. Cells were cultured in 6-well plates to approximately 60 % confluence before treatment with* ***Au100-Z-RuSH*** *(4 pM) for 24 hours. Cells were washed in PBS, detached with trypsin-EDTA solution (3 min, 37C), and pelleted by centrifugation. The supernatant was removed and cell pellets re-suspended in PBS and transferred to flow cytometry tubes for analysis (FACScalibur, BD Biosciences, USA). Forward scatter, side scatter and red fluorescence (λ_{exc} = 488 nm, with emission collected with a 670 nm band pass filter) of 50,000 cells were measured. Weasel freeware software was used for data analysis: Weasel Software*

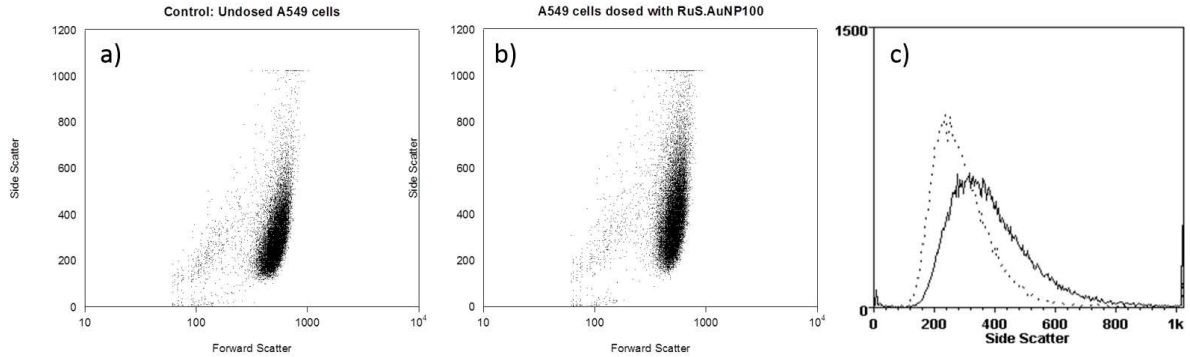

Figure K.8: FACS forward and side scatter data of (a) control (undosed) A549 cells and (b) cells incubated with ***Au100-Z-RuSH*** *(4 pM) for 24 hours (b). (middle and solid line in graph on right). Median side scatter intensity exhibited in (c) - undosed control cells (dashed) and cells incubated with* ***Au100-Z-RuSH*** *(4 pM) for 24 hours (solid line). An increase in the median side scatter, from 273.8 to 361.9 is indicative of increased scattering from the dosed cells, over and above the expected cell granularity, induced by the presence of the gold nanoparticles.*

L

Silica Nanoparticles

L.1 Photophysical Characterisation

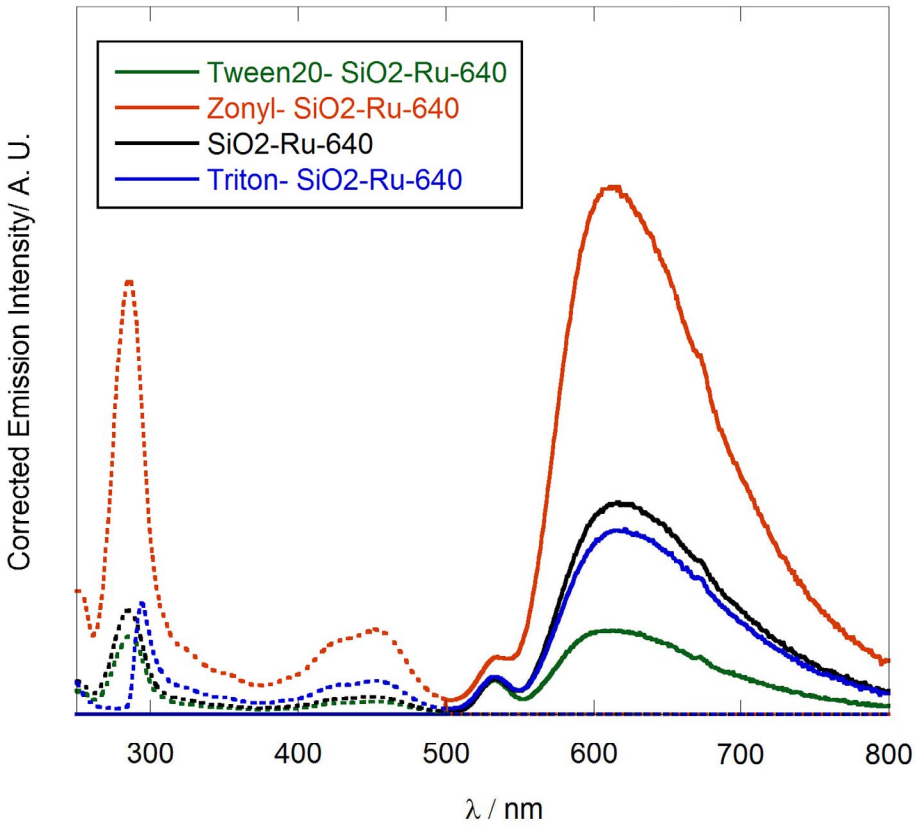

Figure L.1: Excitation (dashed line) and emission (solid line) spectra of the silica particles coated with different surfactants. $\lambda_{exc} = 450$ *nm,* $\lambda_{em} = 620$ *nm.*

L.2 Preliminary Antibacterial Response Studies of SiO_2Ru-640

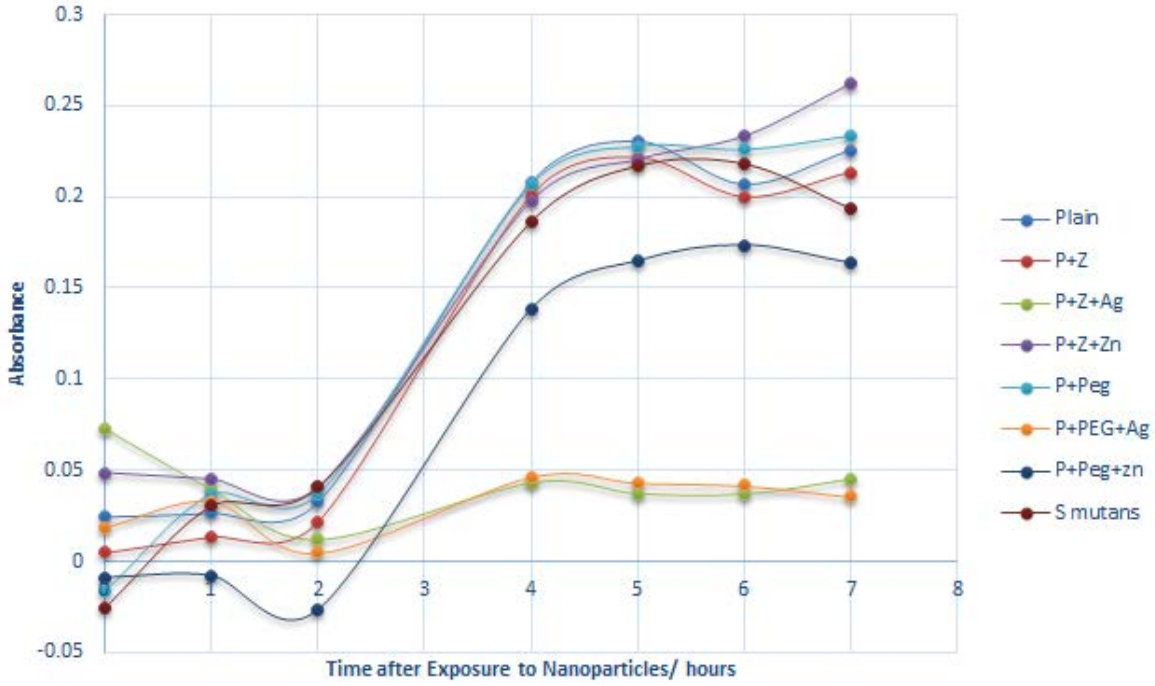

Figure L.2: Growth inhibition effect over time (hours) on Streptococcus Mutans bacteria of functionalised sub-micron silica particles: plain - uncoated particles, P + Z - zonyl coated particles, P + Z + Ag - zonyl and silver coated particles, P + Z + Zn - zonyl and zinc coated particles, P + PEG - PEG coated particles, P + PEG + Ag - PEG and silver coated particles, P + Z + Zn - PEG and zinc coated particles, and S. mutans - undosed control.

List of References

[1] K Imasaka, Y Kanatake, Y Ohshiro, J Suehiro, and M Hara. Production of carbon nanoonions and nanotubes using an intermittent arc discharge in water. *Thin solid films*, 506:250–254, 2006.

[2] Jamie H Warner, Yasuhiro Ito, Mujtaba Zaka, Ling Ge, Takao Akachi, Haruya Okimoto, Kyriakos Porfyrakis, Andrew AR Watt, Hisanori Shinohara, and G Andrew D Briggs. Rotating fullerene chains in carbon nanopeapods. *Nano letters*, 8(8):2328–2335, 2008.

[3] Xu Wang, Yiqing Wang, Zhuo Georgia Chen, and Dong M Shin. Advances of cancer therapy by nanotechnology. *Cancer Research and Treatment*, 41(1):1, 2009.

[4] Elena A Rozhkova. Nanoscale materials for tackling brain cancer: recent progress and outlook. *Advanced Materials*, 23(24):H136–H150, 2011.

[5] Caterina Minelli, Stuart B Lowe, and Molly M Stevens. Engineering nanocomposite materials for cancer therapy. *Small*, 6(21):2336–2357, 2010.

[6] S Moein Moghimi, A Christy Hunter, and J Clifford Murray. Nanomedicine: current status and future prospects. *The FASEB Journal*, 19(3):311–330, 2005.

[7] Feng Zhao, Ying Zhao, Ying Liu, Xueling Chang, Chunying Chen, and Yuliang Zhao. Cellular uptake, intracellular trafficking, and cytotoxicity of nanomaterials. *Small*, 7(10):1322–1337, 2011.

[8] Raman Preet Singh and Poduri Ramarao. Cellular uptake, intracellular trafficking and cytotoxicity of silver nanoparticles. *Toxicology letters*, 213(2):249–259, 2012.

[9] Lin Wang, Meghan B O'Donoghue, and Weihong Tan. Nanoparticles for multiplex diagnostics and imaging. *Nanomedicine*, 2006.

[10] Helmut Goesmann and Claus Feldmann. Nanoparticulate functional materials. *Angewandte Chemie International Edition*, 49(8):1362–1395, 2010.

[11] Elodie Boisselier and Didier Astruc. Gold nanoparticles in nanomedicine: preparations, imaging, diagnostics, therapies and toxicity. *Chemical Society Reviews*, 38(6):1759–1782, 2009.

[12] Nandanan Erathodiyil and Jackie Y Ying. Functionalization of inorganic nanoparticles for bioimaging applications. *Accounts of chemical research*, 44(10):925–935, 2011.

[13] Krishnendu Saha, Avinash Bajaj, Bradley Duncan, and Vincent M Rotello. Beauty is skin deep: A surface monolayer perspective on nanoparticle interactions with cells and bio-macromolecules. *Small*, 7(14):1903–1918, 2011.

[14] Vikash P Chauhan, Zoran Popović, Ou Chen, Jian Cui, Dai Fukumura, Moungi G Bawendi, and Rakesh K Jain. Fluorescent nanorods and nanospheres for real-time in vivo probing of nanoparticle shape-dependent tumor penetration. *Angewandte Chemie*, 123(48):11619–11622, 2011.

[15] B Devika Chithrani, Arezou A Ghazani, and Warren CW Chan. Determining the size and shape dependence of gold nanoparticle uptake into mammalian cells. *Nano letters*, 6(4):662–668, 2006.

[16] Nicholas A Kotov, Jessica O Winter, Isaac P Clements, Edward Jan, Brian P Timko, Stéphane Campidelli, Smita Pathak, Andrea Mazzatenta, Charles M Lieber, Maurizio Prato, et al. Nanomaterials for neural interfaces. *Advanced Materials*, 21(40):3970–4004, 2009.

[17] David A Giljohann, Dwight S Seferos, Weston L Daniel, Matthew D Massich, Pinal C Patel, and Chad A Mirkin. Gold nanoparticles for biology and medicine. *Angewandte Chemie International Edition*, 49(19):3280–3294, 2010.

[18] Larissa Y Rizzo, Benjamin Theek, Gert Storm, Fabian Kiessling, and Twan Lammers. Recent progress in nanomedicine: therapeutic, diagnostic and theranostic applications. *Current opinion in biotechnology*, 24(6):1159–1166, 2013.

[19] Twan Lammers, Silvio Aime, Wim E Hennink, Gert Storm, and Fabian Kiessling. Theranostic nanomedicine. *Accounts of chemical research*, 44(10):1029–1038, 2011.

[20] Margaret A Hamburg and Francis S Collins. The path to personalized medicine. *New England Journal of Medicine*, 363(4):301–304, 2010.

[21] Forrest M Kievit and Miqin Zhang. Cancer nanotheranostics: improving imaging and therapy by targeted delivery across biological barriers. *Advanced materials*, 23(36):H217–H247, 2011.

[22] Elmar Schmälzlin, Joost T Van Dongen, Ingo Klimant, Bettina Marmodée, Martin Steup, Joachim Fisahn, Peter Geigenberger, and Hans-Gerd Löhmannsröben. An optical multifrequency phase-modulation method using microbeads for measuring intracellular oxygen concentrations in plants. *Biophysical journal*, 89(2):1339–1345, 2005.

[23] Maria J Ruedas-Rama, Jamie D Walters, Angel Orte, and Elizabeth AH Hall. Fluorescent nanoparticles for intracellular sensing: a review. *Analytica chimica acta*, 751:1–23, 2012.

[24] Hui Shi, Xiaoxiao He, Kemin Wang, Yin Yuan, Ke Deng, Jiyun Chen, and Weihong Tan. Rhodamine b isothiocyanate doped silica-coated fluorescent nanoparticles (rbitc-dsfnps)–based bioprobes conjugated to annexin v for apoptosis detection and imaging. *Nanomedicine: Nanotechnology, Biology and Medicine*, 3(4):266–272, 2007.

[25] Sungmin Seo, Hye Young Lee, Minsung Park, Jung Mi Lim, Dongmin Kang, Juyoung Yoon, and Jong Hwa Jung. Fluorescein-functionalized silica nanoparticles as a selective fluorogenic chemosensor for cu2+ in living cells. *European Journal of Inorganic Chemistry*, 2010(6):843–847, 2010.

[26] Ronit Freeman, Tali Finder, Ron Gill, and Itamar Willner. Probing protein kinase (ck2) and alkaline phosphatase with cdse/zns quantum dots. *Nano letters*, 10(6):2192–2196, 2010.

[27] Igor L Medintz, Michael H Stewart, Scott A Trammell, Kimihiro Susumu, James B Delehanty, Bing C Mei, Joseph S Melinger, Juan B Blanco-Canosa, Philip E Dawson, and Hedi Mattoussi. Quantum-dot/dopamine bioconjugates function as redox coupled assemblies for in vitro and intracellular ph sensing. *Nature materials*, 9(8):676–684, 2010.

[28] Yu-San Liu, Yinghua Sun, P Thomas Vernier, Chi-Hui Liang, Suet Ying Christin Chong, and Martin A Gundersen. ph-sensitive photoluminescence of cdse/znse/zns

quantum dots in human ovarian cancer cells. *The Journal of Physical Chemistry C*, 111(7):2872–2878, 2007.

[29] Sheila N Baker and Gary A Baker. Luminescent carbon nanodots: emergent nanolights. *Angewandte Chemie International Edition*, 49(38):6726–6744, 2010.

[30] Hyunjong Son, Hye Young Lee, Jung Mi Lim, Dongmin Kang, Won Seok Han, Shim Sung Lee, and Jong Hwa Jung. A highly sensitive and selective turn-on fluorogenic and chromogenic sensor based on bodipy-functionalized magnetic nanoparticles for detecting lead in living cells. *Chemistry-A European Journal*, 16(38):11549–11553, 2010.

[31] Yicheng Wu, Maoquan Chu, Bizhi Shi, and Zonghai Li. A novel magneto-fluorescent nano-bioprobe for cancer cell targeting, imaging and collection. *Applied biochemistry and biotechnology*, 163(7):813–825, 2011.

[32] Guanying Chen, Hailong Qiu, Paras N Prasad, and Xiaoyuan Chen. Upconversion nanoparticles: design, nanochemistry, and applications in theranostics. *Chemical reviews*, 114(10):5161–5214, 2014.

[33] Hye Young Lee, Hyunjong Son, Jung Mi Lim, Jungmin Oh, Dongmin Kang, Won Seok Han, and Jong Hwa Jung. Bodipy-functionalized gold nanoparticles as a selective fluoro-chromogenic chemosensor for imaging cu2+ in living cells. *Analyst*, 135(8):2022–2027, 2010.

[34] Shenfei Zong, Zhuyuan Wang, Jing Yang, and Yiping Cui. Intracellular ph sensing using p-aminothiophenol functionalized gold nanorods with low cytotoxicity. *Analytical chemistry*, 83(11):4178–4183, 2011.

[35] Preeti Nigam, Shobha Waghmode, Amar Yeware, Laxman Nawale, Priyanka Dagde, Amol Dhudhane, and Dhiman Sarkar. Aptamer functionalized multifunctional fluorescent nanotheranostic platform for pancreatic cancer. *Journal of Nanopharmaceutics and Drug Delivery*, 2(4):280–287, 2014.

[36] Chun-Nan Zhu, Peng Jiang, Zhi-Ling Zhang, Dong-Liang Zhu, Zhi-Quan Tian, and Dai-Wen Pang. Ag2se quantum dots with tunable emission in the second near-infrared window. *ACS applied materials & interfaces*, 5(4):1186–1189, 2013.

[37] Xavier Michalet, Fabien F Pinaud, Laurent A Bentolila, James M Tsay, SJJL Doose, Jack J Li, Gobalakrishnan Sundaresan, Anna M Wu, Sanjiv S Gambhir, and Shi-

mon Weiss. Quantum dots for live cells, in vivo imaging, and diagnostics. *science*, 307(5709):538–544, 2005.

[38] Hee-Sun Han, John D Martin, Jungmin Lee, Daniel K Harris, Dai Fukumura, Rakesh K Jain, and Moungi Bawendi. Spatial charge configuration regulates nanoparticle transport and binding behavior in vivo. *Angewandte Chemie International Edition*, 52(5):1414–1419, 2013.

[39] Heebeom Koo, Myung Sook Huh, In-Cheol Sun, Soon Hong Yuk, Kuiwon Choi, Kwangmeyung Kim, and Ick Chan Kwon. In vivo targeted delivery of nanoparticles for theranosis. *Accounts of chemical research*, 44(10):1018–1028, 2011.

[40] Jifang Weng and Jicun Ren. Luminescent quantum dots: a very attractive and promising tool in biomedicine. *Current medicinal chemistry*, 13(8):897–909, 2006.

[41] CV Durgadas, CP Sharma, and K Sreenivasan. Fluorescent gold clusters as nanosensors for copper ions in live cells. *Analyst*, 136(5):933–940, 2011.

[42] Feng Wang, Debapriya Banerjee, Yongsheng Liu, Xueyuan Chen, and Xiaogang Liu. Upconversion nanoparticles in biological labeling, imaging, and therapy. *Analyst*, 135(8):1839–1854, 2010.

[43] Feng Wang and Xiaogang Liu. Multicolor tuning of lanthanide-doped nanoparticles by single wavelength excitation. *Accounts of chemical research*, 47(4):1378–1385, 2014.

[44] Ellen E Connor, Judith Mwamuka, Anand Gole, Catherine J Murphy, and Michael D Wyatt. Gold nanoparticles are taken up by human cells but do not cause acute cytotoxicity. *Small*, 1(3):325–327, 2005.

[45] Matthew D Massich, David A Giljohann, Abrin L Schmucker, Pinal C Patel, and Chad A Mirkin. Cellular response of polyvalent oligonucleotide- gold nanoparticle conjugates. *ACS nano*, 4(10):5641–5646, 2010.

[46] Andrew E Prigodich, Pratik S Randeria, William E Briley, Nathaniel J Kim, Weston L Daniel, David A Giljohann, and Chad A Mirkin. Multiplexed nanoflares: mrna detection in live cells. *Analytical chemistry*, 84(4):2062–2066, 2012.

[47] Erik C Dreaden, Alaaldin M Alkilany, Xiaohua Huang, Catherine J Murphy, and Mostafa A El-Sayed. The golden age: gold nanoparticles for biomedicine. *Chemical Society Reviews*, 41(7):2740–2779, 2012.

[48] Nikolai Khlebtsov and Lev Dykman. Biodistribution and toxicity of engineered gold nanoparticles: a review of in vitro and in vivo studies. *Chemical Society Reviews*, 40(3):1647–1671, 2011.

[49] M Faraday. On the color of colloidal gold. *Phil. Trans. R. Soc. London*, 147:145–181, 1857.

[50] Gustav Mie. Beitrge zur optik trber medien, speziell kolloidaler metallsungen. *Annalen der Physik*, 330(3):377–445, 1908.

[51] Mona Treguer-Delapierre, Jérôme Majimel, Stéphane Mornet, Etienne Duguet, and Serge Ravaine. Synthesis of non-spherical gold nanoparticles. *Gold Bulletin*, 41(2):195–207, 2008.

[52] John Turkevich, Peter Cooper Stevenson, and James Hillier. A study of the nucleation and growth processes in the synthesis of colloidal gold. *Discuss. Faraday Soc.*, 11:55–75, 1951.

[53] Da-Peng Yang and Da-Xiang Cui. Advances and prospects of gold nanorods. *Chemistry–An Asian Journal*, 3(12):2010–2022, 2008.

[54] Hannu Häkkinen. The gold-sulfur interface at the nanoscale. *Nature chemistry*, 4(6):443–455, 2012.

[55] Karen Weintraub. Biomedicine: The new gold standard. *Nature*, 495(7440):S14–S16, 2013.

[56] Marcio A Alencar, Eduardo J Fonseca, Cassio E Santos, Sara F Moraes, Marcos A Gelesky, Mario R Meneghetti, and Jandir M Hickmann. Tuning the surface plasmon resonance of colloidal gold nanoparticles and controlling their linear and nonlinear optical responses. In *Nonlinear Optics: Materials, Fundamentals and Applications*, page NME5. Optical Society of America, 2009.

[57] M Quinten and U Kreibig. Optical properties of aggregates of small metal particles. *Surface Science*, 172(3):557–577, 1986.

[58] K-H Su, Q-H Wei, X Zhang, JJ Mock, David R Smith, and S Schultz. Interparticle coupling effects on plasmon resonances of nanogold particles. *Nano Letters*, 3(8):1087–1090, 2003.

[59] Prashant K Jain, Xiaohua Huang, Ivan H El-Sayed, and Mostafa A El-Sayed. Noble metals on the nanoscale: optical and photothermal properties and some applications in imaging, sensing, biology, and medicine. *Accounts of Chemical Research*, 41(12):1578–1586, 2008.

[60] Konstantin Sokolov, Michele Follen, Jesse Aaron, Ina Pavlova, Anais Malpica, Reuben Lotan, and Rebecca Richards-Kortum. Real-time vital optical imaging of precancer using anti-epidermal growth factor receptor antibodies conjugated to gold nanoparticles. *Cancer research*, 63(9):1999–2004, 2003.

[61] Xiaohua Huang, Prashant K Jain, Ivan H El-Sayed, and Mostafa A El-Sayed. Plasmonic photothermal therapy (pptt) using gold nanoparticles. *Lasers in medical science*, 23(3):217–228, 2008.

[62] Boris Khlebtsov, Vladimir Zharov, Andrei Melnikov, Valery Tuchin, and Nikolai Khlebtsov. Optical amplification of photothermal therapy with gold nanoparticles and nanoclusters. *Nanotechnology*, 17(20):5167, 2006.

[63] Hypothetical dynamic light scattering of two samples. `https://commons.wikimedia.org/wiki/File:DLS.svg`. Accessed: 2016-01-25.

[64] Bruce J Berne and Robert Pecora. *Dynamic light scattering: with applications to chemistry, biology, and physics*. Courier Corporation, 2000.

[65] B Chu. Laser light scattering. *Annual Review of Physical Chemistry*, 21(1):145–174, 1970.

[66] Susie Eustis and Mostafa A El-Sayed. Why gold nanoparticles are more precious than pretty gold: noble metal surface plasmon resonance and its enhancement of the radiative and nonradiative properties of nanocrystals of different shapes. *Chemical Society Reviews*, 35(3):209–217, 2006.

[67] Jie Zheng, Chen Zhou, Mengxiao Yu, and Jinbin Liu. Different sized luminescent gold nanoparticles. *Nanoscale*, 4(14):4073–4083, 2012.

[68] Jiu-Ju Feng, Hong Huang, Dan-Ling Zhou, Lin-Yi Cai, Qi-Qi Tu, and Ai-Jun Wang. Peptide-templated synthesis of wavelength-tunable fluorescent gold nanoparticles. *Journal of Materials Chemistry C*, 1(31):4720–4725, 2013.

[69] Hsiangkuo Yuan, Christopher G Khoury, Hanjun Hwang, Christy M Wilson, Gerald A Grant, and Tuan Vo-Dinh. Gold nanostars: surfactant-free synthesis, 3d modelling, and two-photon photoluminescence imaging. *Nanotechnology*, 23(7):075102, 2012.

[70] Benjamin R Martin, Daniel J Dermody, Brian D Reiss, Mingming Fang, L Andrew Lyon, Michael J Natan, and Thomas E Mallouk. Orthogonal self-assembly on colloidal gold-platinum nanorods. *Advanced Materials*, 11(12):1021–1025, 1999.

[71] Michael Walter, Jaakko Akola, Olga Lopez-Acevedo, Pablo D Jadzinsky, Guillermo Calero, Christopher J Ackerson, Robert L Whetten, Henrik Grönbeck, and Hannu Häkkinen. A unified view of ligand-protected gold clusters as superatom complexes. *Proceedings of the National Academy of Sciences*, 105(27):9157–9162, 2008.

[72] Wenbo Hou, Mita Dasog, and Robert WJ Scott. Probing the relative stability of thiolate-and dithiolate-protected au monolayer-protected clusters. *Langmuir*, 25(22):12954–12961, 2009.

[73] Marie-Christine Daniel and Didier Astruc. Gold nanoparticles: assembly, supramolecular chemistry, quantum-size-related properties, and applications toward biology, catalysis, and nanotechnology. *Chemical reviews*, 104(1):293–346, 2004.

[74] Werner Jahn. Review: chemical aspects of the use of gold clusters in structural biology. *Journal of structural biology*, 127(2):106–112, 1999.

[75] David J Lewis, Thomas M Day, Julie V MacPherson, and Zoe Pikramenou. Luminescent nanobeads: attachment of surface reactive eu (iii) complexes to gold nanoparticles. *Chem. Commun.*, 45(13):1433–1435, 2006.

[76] Alison C Savage and Zoe Pikramenou. Peptide coated gold nanoparticles that bind lanthanide ions. *Chem. Commun.*, 47(22):6431–6433, 2011.

[77] Nicola J Rogers, Sunil Claire, Robert M Harris, Shiva Farabi, Gerald Zikeli, Iain B Styles, Nikolas J Hodges, and Zoe Pikramenou. High coating of ru (ii) complexes on gold nanoparticles for single particle luminescence imaging in cells. *Chemical Communications*, 50(5):617–619, 2014.

[78] Chung Hang J Choi, Jonathan E Zuckerman, Paul Webster, and Mark E Davis. Targeting kidney mesangium by nanoparticles of defined size. *Proceedings of the National Academy of Sciences*, 108(16):6656–6661, 2011.

[79] AS Thakor, J Jokerst, C Zavaleta, TF Massoud, and SS Gambhir. Gold nanoparticles: a revival in precious metal administration to patients. *Nano letters*, 11(10):4029–4036, 2011.

[80] Xiangsheng Liu, Nan Huang, Huan Li, Qiao Jin, and Jian Ji. Surface and size effects on cell interaction of gold nanoparticles with both phagocytic and nonphagocytic cells. *Langmuir*, 29(29):9138–9148, 2013.

[81] Leo YT Chou, Kevin Ming, and Warren CW Chan. Strategies for the intracellular delivery of nanoparticles. *Chemical Society Reviews*, 40(1):233–245, 2011.

[82] Amy Davies, David J Lewis, Stephen P Watson, Steven G Thomas, and Zoe Pikramenou. ph-controlled delivery of luminescent europium coated nanoparticles into platelets. *Proceedings of the National Academy of Sciences*, 109(6):1862–1867, 2012.

[83] Ivan H El-Sayed, Xiaohua Huang, and Mostafa A El-Sayed. Surface plasmon resonance scattering and absorption of anti-egfr antibody conjugated gold nanoparticles in cancer diagnostics: applications in oral cancer. *Nano letters*, 5(5):829–834, 2005.

[84] Huanxin Cai and Ping Yao. In situ preparation of gold nanoparticle-loaded lysozyme–dextran nanogels and applications for cell imaging and drug delivery. *Nanoscale*, 5(7):2892–2900, 2013.

[85] Malini Olivo, Ramaswamy Bhuvaneswari, and Ivan Keogh. Advances in bio-optical imaging for the diagnosis of early oral cancer. *Pharmaceutics*, 3(3):354–378, 2011.

[86] Didier Astruc, Liyuan Liang, Amalia Rapakousiou, and Jaime Ruiz. Click dendrimers and triazole-related aspects: catalysts, mechanism, synthesis, and functions. a bridge between dendritic architectures and nanomaterials. *Accounts of chemical research*, 45(4):630–640, 2011.

[87] Nathaniel L Rosi and Chad A Mirkin. Nanostructures in biodiagnostics. *Chemical reviews*, 105(4):1547–1562, 2005.

[88] Eugenii Katz and Itamar Willner. Integrated nanoparticle–biomolecule hybrid systems: synthesis, properties, and applications. *Angewandte Chemie International Edition*, 43(45):6042–6108, 2004.

[89] George M Whitesides. The'right'size in nanobiotechnology. *Nature biotechnology*, 21(10):1161–1165, 2003.

[90] Robert Bacallao, Kianush Kiai, and Lynn Jesaitis. Guiding principles of specimen preservation for confocal fluorescence microscopy. In *Handbook of biological confocal microscopy*, pages 311–325. Springer, 1995.

[91] Ulrike Schnell, Freark Dijk, Klaas A Sjollema, and Ben NG Giepmans. Immunolabeling artifacts and the need for live-cell imaging. *Nature methods*, 9(2):152–158, 2012.

[92] Wolfgang J Parak, Teresa Pellegrino, and Christian Plank. Labelling of cells with quantum dots. *Nanotechnology*, 16(2):R9, 2005.

[93] Ralph A Sperling, Pilar Rivera Gil, Feng Zhang, Marco Zanella, and Wolfgang J Parak. Biological applications of gold nanoparticles. *Chemical Society Reviews*, 37(9):1896–1908, 2008.

[94] Jessica Rosenholm, Cecilia Sahlgren, and Mika Lindén. Cancer-cell targeting and cell-specific delivery by mesoporous silica nanoparticles. *Journal of Materials Chemistry*, 20(14):2707–2713, 2010.

[95] Maria E Åkerman, Warren CW Chan, Pirjo Laakkonen, Sangeeta N Bhatia, and Erkki Ruoslahti. Nanocrystal targeting in vivo. *Proceedings of the National Academy of Sciences*, 99(20):12617–12621, 2002.

[96] Jasmine Davda and Vinod Labhasetwar. Characterization of nanoparticle uptake by endothelial cells. *International journal of pharmaceutics*, 233(1):51–59, 2002.

[97] Philippe Juvin, Thierry Fournier, Sonja Boland, Paul Soler, Francelyne Marano, Jean-Marie Desmonts, and Michel Aubier. Diesel particles are taken up by alveolar type ii tumor cells and alter cytokines secretion. *Archives of Environmental Health: An International Journal*, 57(1):53–60, 2002.

[98] Tomoko Kato, Takashi Yashiro, Yoshio Murata, Damon C Herbert, Katsuhisa Oshikawa, Masashi Bando, Shoji Ohno, and Yukihiko Sugiyama. Evidence that exogenous substances can be phagocytized by alveolar epithelial cells and transported into blood capillaries. *Cell and tissue research*, 311(1):47–51, 2003.

[99] Alexander T Florence and Nasir Hussain. Transcytosis of nanoparticle and dendrimer delivery systems: evolving vistas. *Advanced drug delivery reviews*, 50:S69–S89, 2001.

[100] Margot Lundborg, Urban Johard, Lena Låstbom, Per Gerde, and Per Camner. Human alveolar macrophage phagocytic function is impaired by aggregates of ultrafine carbon particles. *Environmental research*, 86(3):244–253, 2001.

[101] Günter Oberdörster, Zachary Sharp, Viorel Atudorei, Alison Elder, Robert Gelein, Alex Lunts, Wolfgang Kreyling, and Christopher Cox. Extrapulmonary translocation of ultrafine carbon particles following whole-body inhalation exposure of rats. *Journal of Toxicology and Environmental Health Part A*, 65(20):1531–1543, 2002.

[102] Sushmita Mukherjee, Thwe Thwe Soe, and Frederick R Maxfield. Endocytic sorting of lipid analogues differing solely in the chemistry of their hydrophobic tails. *The Journal of cell biology*, 144(6):1271–1284, 1999.

[103] Olivier Le Bihan, Pierre Bonnafous, Laszlo Marak, Thomas Bickel, Sylvain Trépout, Stéphane Mornet, Felix De Haas, Hugues Talbot, Jean-Christophe Taveau, and Olivier Lambert. Cryo-electron tomography of nanoparticle transmigration into liposome. *Journal of structural biology*, 168(3):419–425, 2009.

[104] Andre E Nel, Lutz Mädler, Darrell Velegol, Tian Xia, Eric MV Hoek, Ponisseril Somasundaran, Fred Klaessig, Vince Castranova, and Mike Thompson. Understanding biophysicochemical interactions at the nano–bio interface. *Nature materials*, 8(7):543–557, 2009.

[105] Ayush Verma and Francesco Stellacci. Effect of surface properties on nanoparticle–cell interactions. *Small*, 6(1):12–21, 2010.

[106] Zhuang Liu, Weibo Cai, Lina He, Nozomi Nakayama, Kai Chen, Xiaoming Sun, Xiaoyuan Chen, and Hongjie Dai. In vivo biodistribution and highly efficient tumour targeting of carbon nanotubes in mice. *Nature nanotechnology*, 2(1):47–52, 2007.

[107] Volker Mailander and Katharina Landfester. Interaction of nanoparticles with cells. *Biomacromolecules*, 10(9):2379–2400, 2009.

[108] Sean D Conner and Sandra L Schmid. Regulated portals of entry into the cell. *Nature*, 422(6927):37–44, 2003.

[109] Oshrat Harush-Frenkel, Eva Rozentur, Simon Benita, and Yoram Altschuler. Surface charge of nanoparticles determines their endocytic and transcytotic pathway in polarized mdck cells. *Biomacromolecules*, 9(2):435–443, 2008.

[110] Oshrat Harush-Frenkel, Yoram Altschuler, and Simon Benita. Nanoparticle-cell interactions: drug delivery implications. *Critical Reviews in Therapeutic Drug Carrier Systems*, 25(6), 2008.

[111] Xiue Jiang, Carlheinz Rocker, Margit Hafner, Stefan Brandholt, Rene M Dorlich, and G Ulrich Nienhaus. Endo-and exocytosis of zwitterionic quantum dot nanoparticles by live hela cells. *ACS nano*, 4(11):6787–6797, 2010.

[112] Christina Greulich, Jörg Diendorf, T Simon, G Eggeler, Matthias Epple, and Manfred Köller. Uptake and intracellular distribution of silver nanoparticles in human mesenchymal stem cells. *Acta biomaterialia*, 7(1):347–354, 2011.

[113] Zhuang Liu, Scott Tabakman, Kevin Welsher, and Hongjie Dai. Carbon nanotubes in biology and medicine: in vitro and in vivo detection, imaging and drug delivery. *Nano research*, 2(2):85–120, 2009.

[114] J Rappoport. Focusing on clathrin-mediated endocytosis. *Biochem. J*, 412:415–423, 2008.

[115] Janette Contreras, Jiansong Xie, Yin Jie Chen, Hua Pei, Guoqing Zhang, Cassandra L Fraser, and Sarah F Hamm-Alvarez. Intracellular uptake and trafficking of difluoroboron dibenzoylmethane- polylactide nanoparticles in hela cells. *ACS nano*, 4(5):2735–2747, 2010.

[116] Kathryn C Partlow, Gregory M Lanza, and Samuel A Wickline. Exploiting lipid raft transport with membrane targeted nanoparticles: a strategy for cytosolic drug delivery. *Biomaterials*, 29(23):3367–3375, 2008.

[117] Deirdre P McIntosh, Xiang-Yang Tan, Phil Oh, and Jan E Schnitzer. Targeting endothelium and its dynamic caveolae for tissue-specific transcytosis in vivo: a pathway to overcome cell barriers to drug and gene delivery. *Proceedings of the National Academy of Sciences*, 99(4):1996–2001, 2002.

[118] W Möbius, E Van Donselaar, Y Ohno-Iwashita, Y Shimada, HFG Heijnen, JW Slot, and HJ Geuze. Recycling compartments and the internal vesicles of multivesicular bodies harbor most of the cholesterol found in the endocytic pathway. *Traffic*, 4(4):222–231, 2003.

[119] Paola Nativo, Ian A Prior, and Mathias Brust. Uptake and intracellular fate of surface-modified gold nanoparticles. *ACS nano*, 2(8):1639–1644, 2008.

[120] Antonios G Kanaras, Fadhil S Kamounah, Kjeld Schaumburg, Christopher J Kiely, and Mathias Brust. Thioalkylated tetraethylene glycol: a new ligand for water soluble monolayer protected gold clusters. *Chem. Commun.*, 9(20):2294–2295, 2002.

[121] Lucas Pelkmans, Thomas Bürli, Marino Zerial, and Ari Helenius. Caveolin-stabilized membrane domains as multifunctional transport and sorting devices in endocytic membrane traffic. *Cell*, 118(6):767–780, 2004.

[122] Lennart Treuel and Gerd Ulrich Nienhaus. Toward a molecular understanding of nanoparticle–protein interactions. *Biophysical Reviews*, 4(2):137–147, 2012.

[123] Tommy Cedervall, Iseult Lynch, Martina Foy, Tord Berggård, Seamas C Donnelly, Gerard Cagney, Sara Linse, and Kenneth A Dawson. Detailed identification of plasma proteins adsorbed on copolymer nanoparticles. *Angewandte Chemie International Edition*, 46(30):5754–5756, 2007.

[124] Julia S Gebauer, Marcelina Malissek, Sonja Simon, Shirley K Knauer, Michael Maskos, Roland H Stauber, Wolfgang Peukert, and Lennart Treuel. Impact of the nanoparticle–protein corona on colloidal stability and protein structure. *Langmuir*, 28(25):9673–9679, 2012.

[125] Marco P Monopoli, Dorota Walczyk, Abigail Campbell, Giuliano Elia, Iseult Lynch, Francesca Baldelli Bombelli, and Kenneth A Dawson. Physical- chemical aspects of protein corona: relevance to in vitro and in vivo biological impacts of nanoparticles. *Journal of the American Chemical Society*, 133(8):2525–2534, 2011.

[126] Martin Lundqvist, Johannes Stigler, Giuliano Elia, Iseult Lynch, Tommy Cedervall, and Kenneth A Dawson. Nanoparticle size and surface properties determine the protein corona with possible implications for biological impacts. *Proceedings of the National Academy of Sciences*, 105(38):14265–14270, 2008.

[127] Tiantian Wang, Jing Bai, Xiue Jiang, and G Ulrich Nienhaus. Cellular uptake of nanoparticles by membrane penetration: a study combining confocal microscopy with ftir spectroelectrochemistry. *ACS nano*, 6(2):1251–1259, 2012.

[128] Barbara M Rothen-Rutishauser, Samuel Schürch, Beat Haenni, Nadine Kapp, and Peter Gehr. Interaction of fine particles and nanoparticles with red blood cells visualized with advanced microscopic techniques. *Environmental science & technology*, 40(14):4353–4359, 2006.

[129] Mathieu Laurencin, Thomas Georgelin, Bernard Malezieux, Jean-Michel Siaugue, and Christine Ménager. Interactions between giant unilamellar vesicles and charged core-shell magnetic nanoparticles. *Langmuir*, 26(20):16025–16030, 2010.

[130] Liangfang Zhang and Steve Granick. How to stabilize phospholipid liposomes (using nanoparticles). *Nano letters*, 6(4):694–698, 2006.

[131] Irene Canton and Giuseppe Battaglia. Endocytosis at the nanoscale. *Chemical Society Reviews*, 41(7):2718–2739, 2012.

[132] Jiaqi Lin, Hongwu Zhang, Zhen Chen, and Yonggang Zheng. Penetration of lipid membranes by gold nanoparticles: insights into cellular uptake, cytotoxicity, and their relationship. *ACS nano*, 4(9):5421–5429, 2010.

[133] Ayush Verma, Oktay Uzun, Yuhua Hu, Ying Hu, Hee-Sun Han, Nicki Watson, Suelin Chen, Darrell J Irvine, and Francesco Stellacci. Surface-structure-regulated cell-membrane penetration by monolayer-protected nanoparticles. *Nature materials*, 7(7):588–595, 2008.

[134] Lennart Treuel, Xiue Jiang, and Gerd Ulrich Nienhaus. New views on cellular uptake and trafficking of manufactured nanoparticles. *Journal of The Royal Society Interface*, 10(82):20120939, 2013.

[135] Raphaël Lévy, Nguyen TK Thanh, R Christopher Doty, Irshad Hussain, Richard J Nichols, David J Schiffrin, Mathias Brust, and David G Fernig. Rational and combinatorial design of peptide capping ligands for gold nanoparticles. *Journal of the American Chemical Society*, 126(32):10076–10084, 2004.

[136] Linlin Sun, Dianjun Liu, and Zhenxin Wang. Functional gold nanoparticle- peptide complexes as cell-targeting agents. *Langmuir*, 24(18):10293–10297, 2008.

[137] Robert A Gatenby, Edward T Gawlinski, Arthur F Gmitro, Brant Kaylor, and Robert J Gillies. Acid-mediated tumor invasion: a multidisciplinary study. *Cancer research*, 66(10):5216–5223, 2006.

[138] Yana K Reshetnyak, Oleg A Andreev, Ursula Lehnert, and Donald M Engelman. Translocation of molecules into cells by ph-dependent insertion of a transmembrane helix. *Proceedings of the National Academy of Sciences*, 103(17):6460–6465, 2006.

[139] Eugene A Sosunov, Evgeny P Anyukhovsky, Alexander A Sosunov, Anna Moshnikova, Dayanjali Wijesinghe, Donald M Engelman, Yana K Reshetnyak, and Oleg A Andreev. ph (low) insertion peptide (phlip) targets ischemic myocardium. *Proceedings of the National Academy of Sciences*, 110(1):82–86, 2013.

[140] John F Hunt, Parshuram Rath, Kenneth J Rothschild, and Donald M Engelman. Spontaneous, ph-dependent membrane insertion of a transbilayer α-helix. *Biochemistry*, 36(49):15177–15192, 1997.

[141] Dhammika Weerakkody, Anna Moshnikova, Mak S Thakur, Valentina Moshnikova, Jennifer Daniels, Donald M Engelman, Oleg A Andreev, and Yana K Reshetnyak. Family of ph (low) insertion peptides for tumor targeting. *Proceedings of the National Academy of Sciences*, 110(15):5834–5839, 2013.

[142] Lan Yao, Jennifer Daniels, Anna Moshnikova, Sergey Kuznetsov, Aftab Ahmed, Donald M Engelman, Yana K Reshetnyak, and Oleg A Andreev. phlip peptide targets nanogold particles to tumors. *Proceedings of the National Academy of Sciences*, 110(2):465–470, 2013.

[143] Monika Musial-Siwek, Alexander Karabadzhak, Oleg A Andreev, Yana K Reshetnyak, and Donald M Engelman. Tuning the insertion properties of phlip. *Biochimica et Biophysica Acta (BBA)-Biomembranes*, 1798(6):1041–1046, 2010.

[144] Oleg A Andreev, Donald M Engelman, and Yana K Reshetnyak. Targeting acidic diseased tissue: New technology based on use of the ph (low) insertion peptide (phlip). *Chimica oggi*, 27(2):34, 2009.

[145] Zilong Zhao, Hongmin Meng, Nannan Wang, Michael J Donovan, Ting Fu, Mingxu You, Zhuo Chen, Xiaobing Zhang, and Weihong Tan. A controlled-release nanocarrier with extracellular ph value driven tumor targeting and translocation for drug delivery. *Angewandte Chemie International Edition*, 52(29):7487–7491, 2013.

[146] Gang Han, Chang-Cheng You, Byoung-jin Kim, Rosemary S Turingan, Neil S Forbes, Craig T Martin, and Vincent M Rotello. Light-regulated release of dna and its delivery to nuclei by means of photolabile gold nanoparticles. *Angewandte Chemie*, 118(19):3237–3241, 2006.

[147] Alexander G Tkachenko, Huan Xie, Donna Coleman, Wilhelm Glomm, Joseph Ryan, Miles F Anderson, Stefan Franzen, and Daniel L Feldheim. Multifunctional gold nanoparticle-peptide complexes for nuclear targeting. *Journal of the American Chemical Society*, 125(16):4700–4701, 2003.

[148] Duncan Hieu M Dam, Jung Heon Lee, Patrick N Sisco, Dick T Co, Ming Zhang, Michael R Wasielewski, and Teri W Odom. Direct observation of nanoparticle–cancer cell nucleus interactions. *ACS nano*, 6(4):3318–3326, 2012.

[149] Adegboyega K Oyelere, Po C Chen, Xiaohua Huang, Ivan H El-Sayed, and Mostafa A El-Sayed. Peptide-conjugated gold nanorods for nuclear targeting. *Bioconjugate chemistry*, 18(5):1490–1497, 2007.

[150] Bin Kang, Megan A Mackey, and Mostafa A El-Sayed. Nuclear targeting of gold nanoparticles in cancer cells induces dna damage, causing cytokinesis arrest and apoptosis. *Journal of the American Chemical Society*, 132(5):1517–1519, 2010.

[151] Sridharan Soundararajan, Li Wang, Vijayalakshmi Sridharan, Weiwei Chen, Nigel Courtenay-Luck, David Jones, Eleanor K Spicer, and Daniel J Fernandes. Plasma membrane nucleolin is a receptor for the anticancer aptamer as1411 in mv4-11 leukemia cells. *Molecular pharmacology*, 76(5):984–991, 2009.

[152] Mohamed Kodiha, Yi Meng Wang, Eliza Hutter, Dusica Maysinger, and Ursula Stochaj. Off to the organelles-killing cancer cells with targeted gold nanoparticles. *Theranostics*, 5(4):357, 2015.

[153] Jennifer P Leung, Sherry Wu, Keng C Chou, and Ruth Signorell. Investigation of sub-100 nm gold nanoparticles for laser-induced thermotherapy of cancer. *Nanomaterials*, 3(1):86–106, 2013.

[154] Steven K Libutti, Giulio F Paciotti, Adriana A Byrnes, H Richard Alexander, William E Gannon, Melissa Walker, Geoffrey D Seidel, Nargiza Yuldasheva, and Lawrence Tamarkin. Phase i and pharmacokinetic studies of cyt-6091, a novel pegylated colloidal gold-rhtnf nanomedicine. *Clinical Cancer Research*, 16(24):6139–6149, 2010.

[155] Colleen M Alexander, Kristen L Hamner, Mathew M Maye, and James C Dabrowiak. Multifunctional dna-gold nanoparticles for targeted doxorubicin delivery. *Bioconjugate chemistry*, 25(7):1261–1271, 2014.

[156] S Jain, DG Hirst, and JM O'sullivan. Gold nanoparticles as novel agents for cancer therapy. *The British journal of radiology*, 2014.

[157] I Jose, Dzmitry G Batrakou, and Eric C Schirmer. Cancer biology and the nuclear envelope: a convoluted relationship. In *Seminars in cancer biology*, volume 23, pages 125–137. Elsevier, 2013.

[158] Kyle B Matchett, Suzanne McFarlane, Sophie E Hamilton, Yousef SA Eltuhamy, Matthew A Davidson, James T Murray, Ahmed M Faheem, and Mohamed El-Tanani.

Ran gtpase in nuclear envelope formation and cancer metastasis. In *Cancer Biology and the Nuclear Envelope*, pages 323–351. Springer, 2014.

[159] Predrag Jevtić, Lisa J Edens, Lidija D Vuković, and Daniel L Levy. Sizing and shaping the nucleus: mechanisms and significance. *Current opinion in cell biology*, 28:16–27, 2014.

[160] C M Feldherr and D Akin. The permeability of the nuclear envelope in dividing and nondividing cell cultures. *The Journal of Cell Biology*, 111(1):1–8, 1990.

[161] Carl M Feldherr and Debra Akin. Signal-mediated nuclear transport in proliferating and growth-arrested balb/c 3t3 cells. *The Journal of cell biology*, 115(4):933–939, 1991.

[162] Carl M Feldherr and Debra Akin. Regulation of nuclear transport in proliferating and quiescent cells. *Experimental cell research*, 205(1):179–186, 1993.

[163] Mohamed Kodiha, Eliza Hutter, Sebastien Boridy, Michal Juhas, Dusica Maysinger, and Ursula Stochaj. Gold nanoparticles induce nuclear damage in breast cancer cells, which is further amplified by hyperthermia. *Cellular and Molecular Life Sciences*, 71(21):4259–4273, 2014.

[164] Yan-Juan Gu, Jinping Cheng, Chun-Chi Lin, Yun Wah Lam, Shuk Han Cheng, and Wing-Tak Wong. Nuclear penetration of surface functionalized gold nanoparticles. *Toxicology and applied Pharmacology*, 237(2):196–204, 2009.

[165] Nelly Panté and Michael Kann. Nuclear pore complex is able to transport macromolecules with diameters of 39 nm. *Molecular biology of the cell*, 13(2):425–434, 2002.

[166] Fenghua Meng, Yinan Zhong, Ru Cheng, Chao Deng, and Zhiyuan Zhong. ph-sensitive polymeric nanoparticles for tumor-targeting doxorubicin delivery: concept and recent advances. *Nanomedicine*, 9(3):487–499, 2014.

[167] Xiaojuan Wang, Chiara Boschetti, Maria Jose Ruedas-Rama, Alan Tunnacliffe, and Elizabeth AH Hall. Ratiometric ph-dot ansors. *Analyst*, 135(7):1585–1591, 2010.

[168] Ti-Wen Sung and Yu-Lung Lo. Highly sensitive and selective sensor based on silica-coated cdse/zns nanoparticles for cu 2+ ion detection. *Sensors and Actuators B: Chemical*, 165(1):119–125, 2012.

[169] David J Lewis, Valentina Dore, Nicola J Rogers, Thomas K Mole, Gerard B Nash, Panagiota Angeli, and Zoe Pikramenou. Silica nanoparticles for micro-particle imaging velocimetry: Fluorosurfactant improves nanoparticle stability and brightness of immobilized iridium (iii) complexes. *Langmuir*, 29(47):14701–14708, 2013.

[170] David J Lewis, Valentina Dore, Mark J Goodwin, Alison C Savage, Gerard B Nash, Panagiota Angeli, and Zoe Pikramenou. Luminescent ruthenium (ii) tris-bipyridyl complex caged in nanoscale silica for particle velocimetry studies in microchannels. *Measurement Science and Technology*, 23(8):084004, 2012.

[171] Brian G Trewyn, Supratim Giri, Igor I Slowing, and Victor S-Y Lin. Mesoporous silica nanoparticle based controlled release, drug delivery, and biosensor systems. *Chemical communications*, (31):3236–3245, 2007.

[172] Igor I Slowing, Juan L Vivero-Escoto, Chia-Wen Wu, and Victor S-Y Lin. Mesoporous silica nanoparticles as controlled release drug delivery and gene transfection carriers. *Advanced drug delivery reviews*, 60(11):1278–1288, 2008.

[173] Se Won Bae, Weihong Tan, and Jong-In Hong. Fluorescent dye-doped silica nanoparticles: new tools for bioapplications. *Chemical communications*, 48(17):2270–2282, 2012.

[174] Zongxi Li, Jonathan C Barnes, Aleksandr Bosoy, J Fraser Stoddart, and Jeffrey I Zink. Mesoporous silica nanoparticles in biomedical applications. *Chemical Society Reviews*, 41(7):2590–2605, 2012.

[175] Xiaoxiao He, Hailong Nie, Kemin Wang, Weihong Tan, Xu Wu, and Pengfei Zhang. In vivo study of biodistribution and urinary excretion of surface-modified silica nanoparticles. *Analytical chemistry*, 80(24):9597–9603, 2008.

[176] Tianlong Liu, Linlin Li, Xu Teng, Xinglu Huang, Huiyu Liu, Dong Chen, Jun Ren, Junqi He, and Fangqiong Tang. Single and repeated dose toxicity of mesoporous hollow silica nanoparticles in intravenously exposed mice. *Biomaterials*, 32(6):1657–1668, 2011.

[177] NB Cramer, JW Stansbury, and CN Bowman. Recent advances and developments in composite dental restorative materials. *Journal of dental research*, 90(4):402–416, 2011.

[178] JW Kim, LU Kim, and CK Kim. Size control of silica nanoparticles and their surface treatment for fabrication of dental nanocomposites. *Biomacromolecules*, 8(1):215–222, 2007.

[179] Sumita B Mitra, Dong Wu, and Brian N Holmes. An application of nanotechnology in advanced dental materials. *The Journal of the American Dental Association*, 134(10):1382–1390, 2003.

[180] RM Gaikwad and I Sokolov. Silica nanoparticles to polish tooth surfaces for caries prevention. *Journal of dental research*, 87(10):980–983, 2008.

[181] DG Gillam, HS Seo, HN Newman, and JS Bulman. Comparison of dentine hypersensitivity in selected occidental and oriental populations. *Journal of oral rehabilitation*, 28(1):20–25, 2001.

[182] EG Absi, M Addy, and D Adams. Dentine hypersensitivity. *Journal of Clinical Periodontology*, 14(5):280–284, 1987.

[183] Martin Brännström. Dentin sensitivity and aspiration of odontoblasts. *The Journal of the American Dental Association*, 66(3):366–370, 1963.

[184] NX West, JA Hughes, and M Addy. Dentine hypersensitivity: the effects of brushing toothpaste on etched and unetched dentine in vitro. *Journal of oral rehabilitation*, 29(2):167–174, 2002.

[185] M Addy and P Mostafa. Dentine hypersensitivity. ii. effects produced by the uptake in vitro of toothpastes onto dentine. *Journal of Oral Rehabilitation*, 16(1):35–48, 1989.

[186] SY Lee, HK Kwon, and BI Kim. Effect of dentinal tubule occlusion by dentifrice containing nano-carbonate apatite. *Journal of oral rehabilitation*, 35(11):847–853, 2008.

[187] Sunil Claire, Anthony Damien Walmsley, Sophie Glinton, Hayley Floyd, Rachel Sammons, and Zoe Pikramenou. The deposition and imaging of silica sub-micron particles in dentine. *Journal of dentistry*, 2015.

[188] Alexandros Besinis, Richard van Noort, and Nicolas Martin. Infiltration of demineralized dentin with silica and hydroxyapatite nanoparticles. *Dental Materials*, 28(9):1012–1023, 2012.

[189] Lili Tian, Ce Peng, Ying Shi, Xuan Guo, Bo Zhong, Juanjuan Qi, Guanhong Wang, Qiang Cai, and Fuzhai Cui. Effect of mesoporous silica nanoparticles on dentinal tubule occlusion: An in vitro study using sem and image analysis. *Dental materials journal*, 33(1):125–132, 2014.

[190] Nicola Rogers. *The Development of Gold Nanoparticles Labelled with Transition Metal Complexes for Imaging Applications*. PhD thesis, School of Chemistry, University of Birmingham, The address of the publisher, 7 2014. An optional note.

[191] Tao Huang and Royce W Murray. Quenching of [ru (bpy) 3] 2+ fluorescence by binding to au nanoparticles. *Langmuir*, 18(18):7077–7081, 2002.

[192] Mathias Brust, Merryl Walker, Donald Bethell, David J Schiffrin, and Robin Whyman. Synthesis of thiol-derivatised gold nanoparticles in a two-phase liquid–liquid system. *J. Chem. Soc., Chem. Commun.*, 1(7):801–802, 1994.

[193] Matthew S Vickers, James Cookson, Paul D Beer, Peter T Bishop, and Benedicte Thiebaut. Dithiocarbamate ligand stabilised gold nanoparticles. *Journal of Materials Chemistry*, 16(2):209–215, 2006.

[194] Yuqi Yu, Ming Zhou, Wen Shen, Hongli Zhang, Qiao Cao, and Hua Cui. Synthesis of electrochemiluminescent graphene oxide functionalized with a ruthenium (ii) complex and its use in the detection of tripropylamine. *Carbon*, 50(7):2539–2545, 2012.

[195] Frédéric Dumur, Cédric R Mayer, Eddy Dumas, Fabien Miomandre, Michel Frigoli, and Francis Sécheresse. New chelating stilbazonium-like dyes from michler's ketone. *Organic letters*, 10(2):321–324, 2008.

[196] Zoe Pikramenou and Nicola Rogers. Coated nanoparticles, June 28 2012. US Patent App. 14/130,254.

[197] Laurent Bouffier, Humphrey HP Yiu, and Matthew J Rosseinsky. Chemical grafting of a dna intercalator probe onto functional iron oxide nanoparticles: a physicochemical study. *Langmuir*, 27(10):6185–6192, 2011.

[198] Hongjie An and Bo Jin. Prospects of nanoparticle–dna binding and its implications in medical biotechnology. *Biotechnology advances*, 30(6):1721–1732, 2012.

[199] Vijay K Varadan, Linfeng Chen, and Jining Xie. *Nanomedicine: design and applications of magnetic nanomaterials, nanosensors and nanosystems*. John Wiley & Sons, 2008.

[200] Morteza Mahmoudi, Kayhan Azadmanesh, Mohammad A Shokrgozar, W Shane Journeay, and Sophie Laurent. Effect of nanoparticles on the cell life cycle. *Chemical reviews*, 111(5):3407–3432, 2011.

[201] Nolan T Flynn, Thanh Nga T Tran, Michael J Cima, and Robert Langer. Long-term stability of self-assembled monolayers in biological media. *Langmuir*, 19(26):10909–10915, 2003.

[202] Brent S Gaylord, Alan J Heeger, and Guillermo C Bazan. Dna hybridization detection with water-soluble conjugated polymers and chromophore-labeled single-stranded dna. *Journal of the American Chemical Society*, 125(4):896–900, 2003.

[203] Katrin Steinmetzer and Karl-Ernst Reinert. Multimode interaction of hoechst 33258 with eukaryotic dna; quantitative analysis of the dna conformational changes. *Journal of Biomolecular Structure and Dynamics*, 15(4):779–791, 1998. PMID: 9514253.

[204] Himanshu Ojha, Bhaskar Mohan Murari, Sneh Anand, Mohd Imtaiyaz Hassan, Faizan Ahmad, and Nabo Kumar Chaudhury. Interaction of dna minor groove binder hoechst 33258 with bovine serum albumin. *Chemical and Pharmaceutical Bulletin*, 57(5):481–486, 2009.

[205] Vekshin Nikolai. Binding of hoechst with nucleic acids using fluorescence spectroscopy. *Journal of Biophysical Chemistry*, 2011, 2011.

[206] Catherine J Murphy, Anand M Gole, John W Stone, Patrick N Sisco, Alaaldin M Alkilany, Edie C Goldsmith, and Sarah C Baxter. Gold nanoparticles in biology: beyond toxicity to cellular imaging. *Accounts of chemical research*, 41(12):1721–1730, 2008.

[207] Ratna Tantra and Alex Knight. Cellular uptake and intracellular fate of engineered nanoparticles: a review on the application of imaging techniques. *Nanotoxicology*, 5(3):381–392, 2011.

[208] Krishnendu Saha, Sarit S Agasti, Chaekyu Kim, Xiaoning Li, and Vincent M Rotello. Gold nanoparticles in chemical and biological sensing. *Chemical reviews*, 112(5):2739–2779, 2012.

[209] Yi-Cheun Yeh, Brian Creran, and Vincent M Rotello. Gold nanoparticles: preparation, properties, and applications in bionanotechnology. *Nanoscale*, 4(6):1871–1880, 2012.

[210] Dorota Bartczak, Otto L Muskens, Simone Nitti, Tilman Sanchez-Elsner, Timothy M Millar, and Antonios G Kanaras. Interactions of human endothelial cells with gold nanoparticles of different morphologies. *Small*, 8(1):122–130, 2012.

[211] Hervé Hillaireau and Patrick Couvreur. Nanocarriers entry into the cell: relevance to drug delivery. *Cellular and Molecular Life Sciences*, 66(17):2873–2896, 2009.

[212] Klaus Unfried, Catrin Albrecht, Lars-Oliver Klotz, Anna Von Mikecz, Susanne Grether-Beck, and Roel PF Schins. Cellular responses to nanoparticles: target structures and mechanisms. *Nanotoxicology*, 1(1):52–71, 2007.

[213] C Muhlfeld, Peter Gehr, and Barbara Rothen-Rutishauser. Translocation and cellular entering mechanisms of nanoparticles in the respiratory tract. *Swiss medical weekly*, 138(27/28):387, 2008.

[214] Paul R Pryor, Lauren Jackson, Sally R Gray, Melissa A Edeling, Amanda Thompson, Christopher M Sanderson, Philip R Evans, David J Owen, and J Paul Luzio. Molecular basis for the sorting of the snare vamp7 into endocytic clathrin-coated vesicles by the arfgap hrb. *Cell*, 134(5):817–827, 2008.

[215] Cameron C Scott and Jean Gruenberg. Ion flux and the function of endosomes and lysosomes: ph is just the start. *Bioessays*, 33(2):103–110, 2011.

[216] Nuri Oh and Ji-Ho Park. Endocytosis and exocytosis of nanoparticles in mammalian cells. *International journal of nanomedicine*, 9(Suppl 1):51, 2014.

[217] Christina Brandenberger, Christian Mühlfeld, Zulqurnain Ali, Anke-Gabriele Lenz, Otmar Schmid, Wolfgang J Parak, Peter Gehr, and Barbara Rothen-Rutishauser. Quantitative evaluation of cellular uptake and trafficking of plain and polyethylene glycol-coated gold nanoparticles. *Small*, 6(15):1669–1678, 2010.

[218] Isabelle Raynal, Philippe Prigent, Sophie Peyramaure, Abderrahim Najid, Cécile Rebuzzi, and Claire Corot. Macrophage endocytosis of superparamagnetic iron oxide nanoparticles: mechanisms and comparison of ferumoxides and ferumoxtran-10. *Investigative radiology*, 39(1):56–63, 2004.

[219] Evangelia Chnari, Jessica S Nikitczuk, Kathryn E Uhrich, and Prabhas V Moghe. Nanoscale anionic macromolecules can inhibit cellular uptake of differentially oxidized ldl. *Biomacromolecules*, 7(2):597–603, 2006.

[220] Evangelia Chnari, Jessica S Nikitczuk, Jinzhong Wang, Kathryn E Uhrich, and Prabhas V Moghe. Engineered polymeric nanoparticles for receptor-targeted blockage of oxidized low density lipoprotein uptake and atherogenesis in macrophages. *Biomacromolecules*, 7(6):1796–1805, 2006.

[221] Ravi Shukla, Vipul Bansal, Minakshi Chaudhary, Atanu Basu, Ramesh R Bhonde, and Murali Sastry. Biocompatibility of gold nanoparticles and their endocytotic fate inside the cellular compartment: a microscopic overview. *Langmuir*, 21(23):10644–10654, 2005.

[222] Marianne Geiser, Barbara Rothen-Rutishauser, Nadine Kapp, Samuel Schürch, Wolfgang Kreyling, Holger Schulz, Manuela Semmler, Vinzenz Im Hof, Joachim Heyder, and Peter Gehr. Ultrafine particles cross cellular membranes by nonphagocytic mechanisms in lungs and in cultured cells. *Environmental health perspectives*, pages 1555–1560, 2005.

[223] Olivia L Mooren, Brian J Galletta, and John A Cooper. Roles for actin assembly in endocytosis. *Annual review of biochemistry*, 81:661–686, 2012.

[224] Davide Pantarotto, Ravi Singh, David McCarthy, Mathieu Erhardt, Jean-Paul Briand, Maurizio Prato, Kostas Kostarelos, and Alberto Bianco. Functionalized carbon nanotubes for plasmid dna gene delivery. *Angewandte Chemie*, 116(39):5354–5358, 2004.

[225] DuncanA. Rouch, BarryT.O. Lee, and AndyP. Morby. Understanding cellular responses to toxic agents: a model for mechanism-choice in bacterial metal resistance. *Journal of Industrial Microbiology*, 14(2):132–141, 1995.

[226] Clinical tools inc. `http://tfscientist.hubpages.com/hub/Stages-of-the-Cell-Cycle-Mitosis-Part-1-of-2`. Accessed: 2015-05-30.

[227] David Owen Morgan. *The cell cycle: principles of control*. New Science Press, 2007.

[228] Benjamin Lewin. *Cells*. Jones & Bartlett Learning, 2007.

[229] Bruce Alberts, Dennis Bray, Karen Hopkin, Alexander Johnson, Julian Lewis, Martin Raff, Keith Roberts, and Peter Walter. *Essential cell biology*. Garland Science, 2013.

[230] Clinton F Jones and David W Grainger. In vitro assessments of nanomaterial toxicity. *Advanced Drug Delivery Reviews*, 61(6):438–456, 2009.

[231] Padmaparna Chaudhuri, Abhimanyu Paraskar, Shivani Soni, Raghunath A Mashelkar, and Shiladitya Sengupta. Fullerenol- cytotoxic conjugates for cancer chemotherapy. *Acs Nano*, 3(9):2505–2514, 2009.

[232] VF Chekhun, IN Todor, N Yu Lukyanova, SI Shpyleva, LA Naleskina, IK Khaetsky, and GI Kulik. The use of nanoferromagnetics to increase the cytotoxic effect of antitumor drugs. *Exp oncol*, 31:163–7, 2009.

[233] Sreemanti Basu, Hope M Campbell, Bonnie N Dittel, and Avijit Ray. Purification of specific cell population by fluorescence activated cell sorting (facs). *Journal of visualized experiments: JoVE*, (41), 2010.

[234] Zbigniew Darzynkiewicz and Hong Zhao. Cell cycle analysis by flow cytometry. *eLS*, 2014.

[235] Zbigniew Darzynkiewicz, Harry Crissman, and James W Jacobberger. Cytometry of the cell cycle: cycling through history. *Cytometry Part A*, 58(1):21–32, 2004.

[236] Rafael Nunez. Dna measurement and cell cycle analysis by flow cytometry. *Current issues in molecular biology*, 3:67–70, 2001.

[237] Robert P Wersto, Francis J Chrest, James F Leary, Christa Morris, MaryAlice Stetler-Stevenson, and Edward Gabrielson. Doublet discrimination in dna cell-cycle analysis. *Cytometry*, 46(5):296–306, 2001.

[238] Fcs express flow seminar. `https://www.denovosoftware.com/`. Accessed: 2015-05-30.

[239] Shing Huang, Pin Ju Chueh, Yun-Wei Lin, Tung-Sheng Shih, and Show-Mei Chuang. Disturbed mitotic progression and genome segregation are involved in cell transformation mediated by nano-tio2 long-term exposure. *Toxicology and applied pharmacology*, 241(2):182–194, 2009.

[240] Megan A Mackey and Mostafa A El-Sayed. Chemosensitization of cancer cells via gold nanoparticle-induced cell cycle regulation. *Photochemistry and photobiology*, 90(2):306–312, 2014.

[241] G. Cosa, K.-S. Focsaneanu, J. R. N. McLean, J. P. McNamee, and J. C. Scaiano. Photophysical properties of fluorescent dna-dyes bound to single- and double-stranded dna in aqueous buffered solution. *Photochemistry and Photobiology*, 73(6):585–599, 2001.

[242] Christy L Haynes and Richard P Van Duyne. Nanosphere lithography: a versatile nanofabrication tool for studies of size-dependent nanoparticle optics. *The Journal of Physical Chemistry B*, 105(24):5599–5611, 2001.

[243] Sujit Kumar Ghosh, Anjali Pal, Subrata Kundu, Sudip Nath, and Tarasankar Pal. Fluorescence quenching of 1-methylaminopyrene near gold nanoparticles: size regime dependence of the small metallic particles. *Chemical physics letters*, 395(4):366–372, 2004.

[244] Katherine C. Grabar, R. Griffith. Freeman, Michael B. Hommer, and Michael J. Natan. Preparation and characterization of au colloid monolayers. *Analytical Chemistry*, 67(4):735–743, 1995.

[245] David J Lewis, Christopher Bruce, Sylvain Bohic, Peter Cloetens, Stephen P Hammond, Darren Arbon, Sarah Blair-Reid, Zoe Pikramenou, and Boris Kysela. Intracellular synchrotron nanoimaging and dna damage/genotoxicity screening of novel lanthanide-coated nanovectors. *Nanomedicine*, 5(10):1547–1557, 2010.

[246] Phuoc Long Truong, Xingyi Ma, and Sang Jun Sim. Resonant rayleigh light scattering of single au nanoparticles with different sizes and shapes. *Nanoscale*, 6(4):2307–2315, 2014.

[247] CE Barnett. Some applications of wave-length turbidimetry in the infrared. *The Journal of Physical Chemistry*, 46(1):69–75, 1942.

[248] Michael Kaszuba, Jason Corbett, Fraser Mcneil Watson, and Andrew Jones. High-concentration zeta potential measurements using light-scattering techniques. *Philosophical Transactions of the Royal Society of London A: Mathematical, Physical and Engineering Sciences*, 368(1927):4439–4451, 2010.

[249] Kadir Aslan and Víctor H Pérez-Luna. Surface modification of colloidal gold by chemisorption of alkanethiols in the presence of a nonionic surfactant. *Langmuir*, 18(16):6059–6065, 2002.

[250] Mercedes Novo, Suren Felekyan, Claus AM Seidel, and Wajih Al-Soufi. Dye-exchange dynamics in micellar solutions studied by fluorescence correlation spectroscopy. *The Journal of Physical Chemistry B*, 111(14):3614–3624, 2007.

[251] Seema Acharya and Babulal Rebery. Fluorescence spectrometric study of eosin yellow dye–surfactant interactions. *Arabian Journal of Chemistry*, 2(1):7–12, 2009.

[252] C Carnero Ruiz, J Molina-Bolívar, J Aguiar, G MacIsaac, S Moroze, and R Palepu. Effect of ethylene glycol on the thermodynamic and micellar properties of tween 20. *Colloid and Polymer Science*, 281(6):531–541, 2003.

[253] Soumen Ghosh and SP Moulik. Interfacial and micellization behaviors of binary and ternary mixtures of amphiphiles (tween-20, brij-35, and sodium dodecyl sulfate) in aqueous medium. *Journal of colloid and interface science*, 208(2):357–366, 1998.

[254] G Frens. Controlled nucleation for the regulation of the particle size in monodisperse gold suspensions. *Nature*, 241(105):20–22, 1973.

[255] Jessica Rodríguez-Fernández, Jorge Pérez-Juste, F Javier García de Abajo, and Luis M Liz-Marzán. Seeded growth of submicron au colloids with quadrupole plasmon resonance modes. *Langmuir*, 22(16):7007–7010, 2006.

[256] Steven D Perrault and Warren CW Chan. Synthesis and surface modification of highly monodispersed, spherical gold nanoparticles of 50- 200 nm. *Journal of the American Chemical Society*, 132(33):11824–11824, 2010.

[257] Nikhil R Jana, Latha Gearheart, and Catherine J Murphy. Seed-mediated growth approach for shape-controlled synthesis of spheroidal and rod-like gold nanoparticles using a surfactant template. *Advanced Materials*, 13(18):1389, 2001.

[258] Kenneth R Brown, Daniel G Walter, and Michael J Natan. Seeding of colloidal au nanoparticle solutions. 2. improved control of particle size and shape. *Chemistry of Materials*, 12(2):306–313, 2000.

[259] Christoph Ziegler and Alexander Eychmuller. Seeded growth synthesis of uniform gold nanoparticles with diameters of 15- 300 nm. *The Journal of Physical Chemistry C*, 115(11):4502–4506, 2011.

[260] Lin Guo and Feng Gai. Heterogeneous diffusion of a membrane-bound phlip peptide. *Biophysical journal*, 98(12):2914–2922, 2010.

[261] Christina EB Caesar, Richard Johnsson, Ulf Ellervik, Keith R Fox, Per Lincoln, and Bengt Nordén. A polarized-light spectroscopy study of interactions of a hairpin polyamide with dna. *Biophysical journal*, 91(3):904–911, 2006.

[262] Max Born and Emil Wolf. *Principles of optics: electromagnetic theory of propagation, interference and diffraction of light*. Cambridge university press, 1999.

[263] Prashant K Jain, Kyeong Seok Lee, Ivan H El-Sayed, and Mostafa A El-Sayed. Calculated absorption and scattering properties of gold nanoparticles of different size, shape, and composition: applications in biological imaging and biomedicine. *The Journal of Physical Chemistry B*, 110(14):7238–7248, 2006.

[264] Meijing Wang and Nils O Petersen. Lipid-coated gold nanoparticles promote lamellar body formation in a549 cells. *Biochimica et Biophysica Acta (BBA)-Molecular and Cell Biology of Lipids*, 1831(6):1089–1097, 2013.

[265] Mark OJ Olson and Miroslav Dundr. Nucleolus: Structure and function. *eLS*, 2010.

[266] Jan Padeken and Patrick Heun. Centromeres in nuclear architecture. *Cell Cycle*, 12(22):3455–3456, 2013.

[267] Eva Bártová, Jana Krejčí, Andrea Harničarová, Gabriela Galiová, and Stanislav Kozubek. Histone modifications and nuclear architecture: a review. *Journal of Histochemistry & Cytochemistry*, 56(8):711–721, 2008.

[268] Ilaria Fratoddi, Iole Venditti, Cesare Cametti, and Maria Vittoria Russo. The puzzle of toxicity of gold nanoparticles. the case-study of hela cells. *Toxicology Research*, 2015.

[269] Chiara Uboldi, Daniele Bonacchi, Giada Lorenzi, M Iris Hermanns, Christine Pohl, Giovanni Baldi, Ronald E Unger, and C James Kirkpatrick. Gold nanoparticles induce cytotoxicity in the alveolar type-ii cell lines a549 and ncih441. *Part Fibre Toxicol*, 6(1):18, 2009.

[270] Andrew I Minchinton and Ian F Tannock. Drug penetration in solid tumours. *Nature Reviews Cancer*, 6(8):583–592, 2006.

[271] Siew-Min Ong, Ziqing Zhao, Talha Arooz, Deqiang Zhao, Shufang Zhang, Tiehua Du, Martin Wasser, Danny van Noort, and Hanry Yu. Engineering a scaffold-free 3d tumor model for in vitro drug penetration studies. *Biomaterials*, 31(6):1180–1190, 2010.

[272] Ruei-Zhen Lin and Hwan-You Chang. Recent advances in three-dimensional multicellular spheroid culture for biomedical research. *Biotechnology journal*, 3(9-10):1172–1184, 2008.

[273] M Pickl and CH Ries. Comparison of 3d and 2d tumor models reveals enhanced her2 activation in 3d associated with an increased response to trastuzumab. *Oncogene*, 28(3):461–468, 2009.

[274] Jens M Kelm, Nicholas E Timmins, Catherine J Brown, Martin Fussenegger, and Lars K Nielsen. Method for generation of homogeneous multicellular tumor spheroids applicable to a wide variety of cell types. *Biotechnology and bioengineering*, 83(2):173–180, 2003.

[275] Monica Monici. Cell and tissue autofluorescence research and diagnostic applications. volume 11 of *Biotechnology Annual Review*, pages 227 – 256. Elsevier, 2005.

[276] Jong Ah Kim, Christoffer Åberg, Anna Salvati, and Kenneth A Dawson. Role of cell cycle on the cellular uptake and dilution of nanoparticles in a cell population. *Nature nanotechnology*, 7(1):62–68, 2012.

[277] Hemant Sarin, Ariel S Kanevsky, Haitao Wu, Kyle R Brimacombe, Steve H Fung, Alioscka A Sousa, Sungyoung Auh, Colin M Wilson, Kamal Sharma, Maria A Aronova, et al. Effective transvascular delivery of nanoparticles across the blood-brain tumor barrier into malignant glioma cells. *Journal of Translational Medicine*, 6(1):80, 2008.

[278] Martin R Gill, Jorge Garcia-Lara, Simon J Foster, Carl Smythe, Giuseppe Battaglia, and Jim A Thomas. A ruthenium (ii) polypyridyl complex for direct imaging of dna structure in living cells. *Nature chemistry*, 1(8):662–667, 2009.

[279] Dagmar Mohr, Steffen Frey, Torsten Fischer, Thomas Güttler, and Dirk Görlich. Characterisation of the passive permeability barrier of nuclear pore complexes. *The EMBO journal*, 28(17):2541–2553, 2009.

[280] Radek Dobrowolski and Edward M De Robertis. Endocytic control of growth factor signalling: multivesicular bodies as signalling organelles. *Nature reviews Molecular cell biology*, 13(1):53–60, 2012.

[281] Robert C Piper and David J Katzmann. Biogenesis and function of multivesicular bodies. *Annual review of cell and developmental biology*, 23:519, 2007.

[282] Longfa Kou, Jin Sun, Yinglei Zhai, and Zhonggui He. The endocytosis and intracellular fate of nanomedicines: implication for rational design. *Asian Journal of Pharmaceutical Sciences*, 8(1):1–10, 2013.

[283] Stefania Dragoni, Giulia Franco, Marì Regoli, Monica Bracciali, Vittorio Morandi, Giampietro Sgaragli, Eugenio Bertelli, and Massimo Valoti. Gold nanoparticles uptake and cytotoxicity assessed on rat liver precision cut slices. *Toxicological Sciences*, page kfs150, 2012.

[284] Ramin Sakhtianchi, Rodney F Minchin, Ki-Bum Lee, Alaaldin M Alkilany, Vahid Serpooshan, and Morteza Mahmoudi. Exocytosis of nanoparticles from cells: role in cellular retention and toxicity. *Advances in colloid and interface science*, 201:18–29, 2013.

[285] Mark OJ Olson, Miroslav Dundr, and Attila Szebeni. The nucleolus: an old factory with unexpected capabilities. *Trends in cell biology*, 10(5):189–196, 2000.

[286] Brian Burke and Larry Gerace. A cell free system to study reassembly of the nuclear envelope at the end of mitosis. *Cell*, 44(4):639–652, 1986.

[287] Ian G Macara. Transport into and out of the nucleus. *Microbiology and molecular biology reviews*, 65(4):570–594, 2001.

[288] Cornelia Wandke and Ulrike Kutay. Enclosing chromatin: reassembly of the nucleus after open mitosis. *Cell*, 152(6):1222–1225, 2013.

[289] Nicolas PE Barry and Peter J Sadler. Challenges for metals in medicine: how nanotechnology may help to shape the future. *ACS nano*, 7(7):5654–5659, 2013.

[290] Dik-Lung Ma, Hong-Zhang He, Ka-Ho Leung, Daniel Shiu-Hin Chan, and Chung-Hang Leung. Bioactive luminescent transition-metal complexes for biomedical applications. *Angewandte Chemie International Edition*, 52(30):7666–7682, 2013.

[291] Elizabeth J New, Aileen Congreve, and David Parker. Definition of the uptake mechanism and sub-cellular localisation profile of emissive lanthanide complexes as cellular optical probes. *Chemical Science*, 1(1):111–118, 2010.

[292] Aline M Nonat, Susan J Quinn, and Thorfinnur Gunnlaugsson. Mixed f- d coordination complexes as dual visible-and near-infrared-emitting probes for targeting dna. *Inorganic chemistry*, 48(11):4646–4648, 2009.

[293] Robert BP Elmes and Thorfinnur Gunnlaugsson. Luminescence anion sensing via modulation of mlct emission from a naphthalimide–ru (ii)–polypyridyl complex. *Tetrahedron Letters*, 51(31):4082–4087, 2010.

[294] Maria Matson, Frida R Svensson, Bengt Nordén, and Per Lincoln. Correlation between cellular localization and binding preference to rna, dna, and phospholipid membrane for luminescent ruthenium (ii) complexes. *The Journal of Physical Chemistry B*, 115(7):1706–1711, 2011.

[295] Shashi Pandya, Junhua Yu, and David Parker. Engineering emissive europium and terbium complexes for molecular imaging and sensing. *Dalton Transactions*, (23):2757–2766, 2006.

[296] Marc AMJ van Zandvoort, Cees J de Grauw, Hans C Gerritsen, Jos LV Broers, Frans Ramaekers, Dick W Slaaf, et al. Discrimination of dna and rna in cells by a vital fluorescent probe: Lifetime imaging of syto13 in healthy and apoptotic cells. *Cytometry*, 47(4):226–235, 2002.

[297] Wei Zhong, Paul Urayama, and Mary-Ann Mycek. Imaging fluorescence lifetime modulation of a ruthenium-based dye in living cells: the potential for oxygen sensing. *Journal of Physics D: Applied Physics*, 36(14):1689, 2003.

[298] Frida R Svensson, Maria Abrahamsson, Niklas Stromberg, Andrew G Ewing, and Per Lincoln. Ruthenium (ii) complex enantiomers as cellular probes for diastereomeric interactions in confocal and fluorescence lifetime imaging microscopy. *The journal of physical chemistry letters*, 2(5):397–401, 2011.

[299] Mikhail Y Berezin and Samuel Achilefu. Fluorescence lifetime measurements and biological imaging. *Chemical reviews*, 110(5):2641–2684, 2010.

[300] Robert BP Elmes, Kim N Orange, Suzanne M Cloonan, D Clive Williams, and Thorfinnur Gunnlaugsson. Luminescent ruthenium (ii) polypyridyl functionalized gold nanoparticles; their dna binding abilities and application as cellular imaging agents. *Journal of the American Chemical Society*, 133(40):15862–15865, 2011.

[301] Chao Lu, Yanbing Zu, and Vivian Wing-Wah Yam. Specific postcolumn detection method for hplc assay of homocysteine based on aggregation of fluorosurfactant-capped gold nanoparticles. *Analytical chemistry*, 79(2):666–672, 2007.

[302] Yongan Tang, Jiawei Yan, Xiaoshun Zhou, Yongchun Fu, and Bingwei Mao. An stm study on nonionic fluorosurfactant zonyl fsn self-assembly on au (111): large domains, few defects, and good stability. *Langmuir*, 24(23):13245–13249, 2008.

[303] Tatsiana Mironava, Michael Hadjiargyrou, Marcia Simon, Vladimir Jurukovski, and Miriam H Rafailovich. Gold nanoparticles cellular toxicity and recovery: effect of size, concentration and exposure time. *Nanotoxicology*, 4(1):120–137, 2010.

[304] Kimberly A Foster, Christine G Oster, Mary M Mayer, Michael L Avery, and Kenneth L Audus. Characterization of the a549 cell line as a type ii pulmonary epithelial cell model for drug metabolism. *Experimental cell research*, 243(2):359–366, 1998.

[305] Michael V Berridge, Patries M Herst, and An S Tan. Tetrazolium dyes as tools in cell biology: new insights into their cellular reduction. *Biotechnology annual review*, 11:127–152, 2005.

[306] Alexandros Besinis, Tracy De Peralta, Christopher J Tredwin, and Richard D Handy. Review of nanomaterials in dentistry: Interactions with the oral microenvironment, clinical applications, hazards, and benefits. *ACS nano*, 9(3):2255–2289, 2015.

[307] R Garberoglio and M Brännström. Scanning electron microscopic investigation of human dentinal tubules. *Archives of Oral Biology*, 21(6):355–362, 1976.

[308] Grayson W Marshall, Sally J Marshall, John H Kinney, and Mehdi Balooch. The dentin substrate: structure and properties related to bonding. *Journal of dentistry*, 25(6):441–458, 1997.

[309] Anders Linde and Michel Goldberg. Dentinogenesis. *Critical Reviews in Oral Biology & Medicine*, 4(5):679–728, 1993.

[310] Lars G Petersson. The role of fluoride in the preventive management of dentin hypersensitivity and root caries. *Clinical oral investigations*, 17(1):63–71, 2013.

[311] Y-C Chiang, H-J Chen, H-C Liu, S-H Kang, B-S Lee, F-H Lin, H-P Lin, and C-P Lin. A novel mesoporous biomaterial for treating dentin hypersensitivity. *Journal of dental research*, 89(3):236–240, 2010.

[312] JS Earl, DJ Wood, and SJ Milne. Dentine infiltration. a cure for sensitive teeth. *American Ceramic Society Bulletin*, 85(7):22–25, 2006.

[313] JS Earl, DJ Wood, and SJ Milne. Nanoparticles for dentine tubule infiltration: an in vitro study. *Journal of nanoscience and nanotechnology*, 9(11):6668–6674, 2009.

[314] Alexandros Besinis, Richard van Noort, and Nicolas Martin. Remineralization potential of fully demineralized dentin infiltrated with silica and hydroxyapatite nanoparticles. *Dental Materials*, 30(3):249–262, 2014.

[315] Tetsuo Kodaka, Masaru Kuroiwa, Mie Kuroiwa, Junko Okumura, Ryoichi Mori, Shoji Hirasawa, and Megumi Kobori. Effects of brushing with a dentifrice for sensitive teeth on tubule occlusion and abrasion of dentin. *Journal of electron microscopy*, 50(1):57–64, 2001.

[316] RP Allaker. The use of nanoparticles to control oral biofilm formation. *Journal of dental research*, 89(11):1175–1186, 2010.

[317] M Hannig and C Hannig. Nanotechnology and its role in caries therapy. *Advances in dental research*, 24(2):53–57, 2012.

[318] Limin Sun and Laurence C Chow. Preparation and properties of nano-sized calcium fluoride for dental applications. *dental materials*, 24(1):111–116, 2008.

[319] Kui Long Lv, Jiu Xing Zhang, Xiang Cai Meng, and Xing Yi Li. Remineralization effect of the nano-ha toothpaste on artificial caries. In *Key Engineering Materials*, volume 330, pages 267–270. Trans Tech Publ, 2007.

[320] SH Jeong, Suck Jin Hong, Choong Ho Choi, and BI Kim. Effect of new dentifrice containing nano-sized carbonated apatite on enamel remineralization. In *Key Engineering Materials*, volume 330, pages 291–294. Trans Tech Publ, 2007.

[321] Norberto Roveri, Elisa Battistella, Ismaela Foltran, Elisabetta Foresti, Michele Iafisco, Marco Lelli, Barbara Palazzo, and Lia Rimondini. Synthetic biomimetic carbonate-hydroxyapatite nanocrystals for enamel remineralization. In *Advanced Materials Research*, volume 47, pages 821–824. Trans Tech Publ, 2008.

[322] Wen Zhang, John Crittenden, Kungang Li, and Yongsheng Chen. Attachment efficiency of nanoparticle aggregation in aqueous dispersions: modeling and experimental validation. *Environmental science & technology*, 46(13):7054–7062, 2012.

[323] Meret Vollenweider, Tobias J Brunner, Sven Knecht, Robert N Grass, Matthias Zehnder, Thomas Imfeld, and Wendelin J Stark. Remineralization of human dentin using ultrafine bioactive glass particles. *Acta Biomaterialia*, 3(6):936–943, 2007.

[324] Berdan Aydin Sevinç and Luke Hanley. Antibacterial activity of dental composites containing zinc oxide nanoparticles. *Journal of Biomedical Materials Research Part B: Applied Biomaterials*, 94(1):22–31, 2010.

[325] Juliana Matos Corrêa, Matsuyoshi Mori, Heloísa Lajas Sanches, Adriana Dibo da Cruz, Edgard Poiate, and Isis Andréa Venturini Pola Poiate. Silver nanoparticles in dental biomaterials. *International journal of biomaterials*, 2015, 2015.